FUSION BONDING OF FIBER REINFORCED SEMI-CRYSTALLINE POLYMERS IN EXTRUSION DEPOSITION ADDITIVE MANUFACTURING

by

Eduardo Barocio Vaca

A Dissertation

Submitted to the Faculty of Purdue University

In Partial Fulfillment of the Requirements for the degree of

Doctor of Philosophy

School of Materials Engineering

West Lafayette, Indiana

December 2018

THE PURDUE UNIVERSITY GRADUATE SCHOOL
STATEMENT OF COMMITTEE APPROVAL

Dr. R. Byron Pipes, Chair
Department of Materials Engineering
Dr. Jan-Anders Månson
Department of Materials Engineering
Dr. Rodney Trice
Department of Materials Engineering
Dr. Alejandro H Strachan
Department of Materials Engineering
Dr. Carlos Martinez
Department of Materials Engineering

Approved by:

Dr. David Bahr
Head of the Graduate Program

Con cariño para mis Papas, Alejandro y Ma. Elena
quienes con su amor, motivación y apoyo incondicional
me hicieron posible llegar hasta este punto.

ACKNOWLEDGMENTS

Firstly, I would like to express my most sincere gratitude to my advisor Prof. R. Byron Pipes for providing unparalleled mentorship and advice during my Ph.D. as well as for his unconditional support in all the dimensions. I will always be grateful for the great opportunity of working with him on this fascinating topic of composites additive manufacturing and for embracing the ideas that led to new creations and patent applications. This was by far the most creative and enriching experience I have had in my life. I'm also honored to have been part of the Composites Manufacturing and Simulation Center of excellence created and directed by Prof. Pipes. He created for a second time a unique world-class center for composites which I am certain will continue to grow its influence in the academia and the composites industry.

I also want to thank the members of my thesis committee, Prof. Carlos Martinez, Prof. Jan-Anders Månson, Prof. Rodney Trice and Prof. Alejandro H Strachan for their insightful comments and encouragement at the different stages of the academic program.

I would like to express my gratitude to my friends Dr. Bastian Brenken and Dr. Anthony Favaloro for the countless fruitful discussions we had and all the things I learned with them during the last four and a half years. I truly enjoyed constructing our research platform CAMRI with Bastian and I am grateful with Tony for his wonderful advice in the numerical implementation of some of the models presented in this dissertation.

I'm also grateful to the newer members of the composites additive manufacturing team, Jorge Ramirez, Sushrut Karmarkar and Miguel Ramirez for all the fruitful discussions we had and their support with the continuous improvement of the CAMRI system as well as with experiments related to the work presented in this dissertation. I want to thank Deba J. Khawas, Pasita Pibulchinda and Logan M. Greenlee for their support with experiments and projects in the additive manufacturing laboratory. I also want to thank the excellent group of professors and researchers in the composites manufacturing and simulation center who also provided valuable inputs for this work.

The last but not the least, I want to express my gratitude to my parents, Alejandro and Ma. Elena and to my siblings Alejandra, Juan Pablo and Alejandro for their continuous encouragement and unconditional support throughout my Ph.D.

TABLE OF CONTENTS

LIST OF TABLES

LIST OF FIGURES

ABSTRACT

Author: Barocio, Eduardo. PhD
Institution: Purdue University
Degree Received: December 2018
Title: Fusion Bonding of Fiber Reinforced Semi-Crystalline Polymers in Extrusion Deposition Additive Manufacturing.
Committee Chair: R. Byron Pipes

Extrusion deposition additive manufacturing (EDAM) has enabled upscaling the dimensions of the objects that can be additively manufactured from the desktop scale to the size of a full vehicle. The EDAM process consists of depositing beads of molten material in a layer-by-layer manner, thereby giving rise to temperature gradients during part manufacturing. To investigate the phenomena involved in EDAM, the Composites Additive Manufacturing Research Instrument (CAMRI) was developed as part of this project. CAMRI provided unparalleled flexibility for conducting controlled experiments with carbon fiber reinforced semi-crystalline polymers and served as a validation platform for the work presented in this dissertation.

Since the EDAM process is highly non-isothermal, modeling heat transfer in EDAM is of paramount importance for predicting interlayer bonding and evolution of internal stresses during part manufacturing. Hence, local heat transfer mechanisms were characterized and implemented in a framework for EDAM process simulations. These include local convection conditions, heat losses in material compaction as well as heat of crystallization or melting. Numerical predictions of the temperature evolution during the printing process of a part were in great agreement with experimental measurements by only calibrating the radiation ambient temperature.

In the absence of fibers reinforcing the interface between adjacent layers, the bond developed through the polymer is the primary mechanisms governing the interlayer fracture properties in printed parts. Hence, a fusion bonding model was extended to predict the evolution of interlayer fracture properties in EDAM with semi-crystalline polymer composites. The fusion bonding model was characterized and implemented in the framework for EDAM process simulation. Experimental verification of numerical predictions obtained with the fusion bonding model for interlayer fracture properties is provided. Finally, this fusion bonding model bridges the gap between processing conditions and interlayer fracture properties which is extremely valuable for predicting regions with frail interlayer bond within a part.

1. MOTIVATION AND PROBLEM STATEMENT

The experimental, analytical and simulation work presented in this dissertation focuses on Extrusion Deposition Additive Manufacturing (EDAM) of fiber reinforced semi-crystalline polymers. This manufacturing process consists of manufacturing three-dimensional objects by depositing beads of molten material in a layer-by-layer basis. Fiber reinforced polymers have enabled printing objects in the scale of a couple of meters by lowering the coefficient of thermal expansion and increasing the stiffness of the printed material. Nevertheless, the flow induced orientation of discontinuous fibers leads to anisotropy in the printed material. The EDAM process is highly non-isothermal and as the manufacturing process of a part progresses, the printed material cools down unevenly and temperature gradients developed within the printed part. The non-isothermal cooling process of the printed part and the anisotropy of the printed material give rise to internal stresses in printed parts. Additionally, the temperature history resulting from the conditions used in the printing process of a part has a strong impact on the bond developed between adjacent layers. A combination of high internal stress and low interlayer strength potentiates delamination of printed parts during manufacturing or during service in the final application. Hence, the complexity in the EDAM process due to all the phenomena occurring simultaneously requires of predictive tools capable for anticipating issues like delamination during manufacturing or during service of the part. Further, this technology is currently utilized for producing tooling where the thermal and thermomechanical performance are of great concern. Thus, approaches for engineering tools printed with anisotropic materials are needed.

The first problem addressed in this dissertation is the development of a research instrument capable of processing high temperature and highly filled polymers. By the time this project started, 2014, extrusion deposition additive manufacturing systems of the kind and scale needed were not commercially available. Thus, the architecture of the mechanical, electronics, and control system used in the Composites Additive Manufacturing Research Instrument (CAMRI) system was developed. The goal of controlling and monitoring all the aspects of the EDAM process was achieved with the CAMRI system.

Heat transfer in the EDAM process is the second problem addressed in this dissertation. Temperature history of the printed material is of great interest in the EDAM process since temperature governs multiple phenomena in the polymer. Phenomena like polymer crystallization,

fusion bonding of adjacent layers, and the evolution of material stiffness during solidification are strongly coupled with temperature. A significant improvement to the predictive capabilities for temperature has been done compared to previous work.

The third problem addressed in this dissertation is with regards to layer-to-layer bonding during the EDAM process. In the absence of fibers reinforcing an interface, fusion bonding of the polymer is the only mechanisms strengthening an interface formed by adjacent layers of printed material. Fusion bonding of semi-crystalline polymers involves first inter-diffusion of polymer chains and second crystallization of the polymer across the interface formed between adjacent layers. A phenomenological model coupling polymer diffusion and polymer crystallization was developed to predict the layer-to-layer properties based on the processing conditions.

2. INTRODUCTION

This chapter begins by introducing the Extrusion Deposition Additive Manufacturing (EDAM) process used for fabricating three-dimensional geometries in a layer-by-layer basis. The state-of-the art in EDAM systems is presented, including the CAMRI system which is the platform used for demonstrating and validating the work presented in this dissertation. However, a whole chapter is dedicated to the CAMRI system since its development was a significant part of this project. The role of fiber reinforced polymers in AM and the material used in this work is discussed after. Then, the focus is turned to the phenomena participating in the manufacturing process. Once the phenomena have been described, a literature review on experimental characterization of printed materials and process simulation of additive manufacturing processes is presented. To finalize this chapter, examples of tooling applications for the EDAM technology are presented.

2.1 Extrusion Deposition Additive Manufacturing

The Extrusion Deposition Additive Manufacturing (EDAM) process is an extrusion-based Additive Manufacturing (AM) method for printing with reinforced and unreinforced polymers. Therefore, EDAM is in the category of "Material extrusion" of the ISO-17296-2 standard for AM process categories and feedstock [1]. In the EDAM process, a digital object is materialized by depositing beads of molten material in a layer-by-layer basis as depicted in **Error! Reference s ource not found.**. Further, the orientation of individual beads within a printed layer can be unique for each layer. The feedstock material used for printing is melted in the printing equipment and delivered through a printing nozzle in the form of beads. The first layer deposited is the foundation for the printed part and this is deposited on a substrate which can be heated to a predefined temperature or maintained at room temperature. After depositing the first layer, a predefined sequence of layers is deposited one after the other, thereby giving rise to a scalloped representation of the three-dimensional geometry.

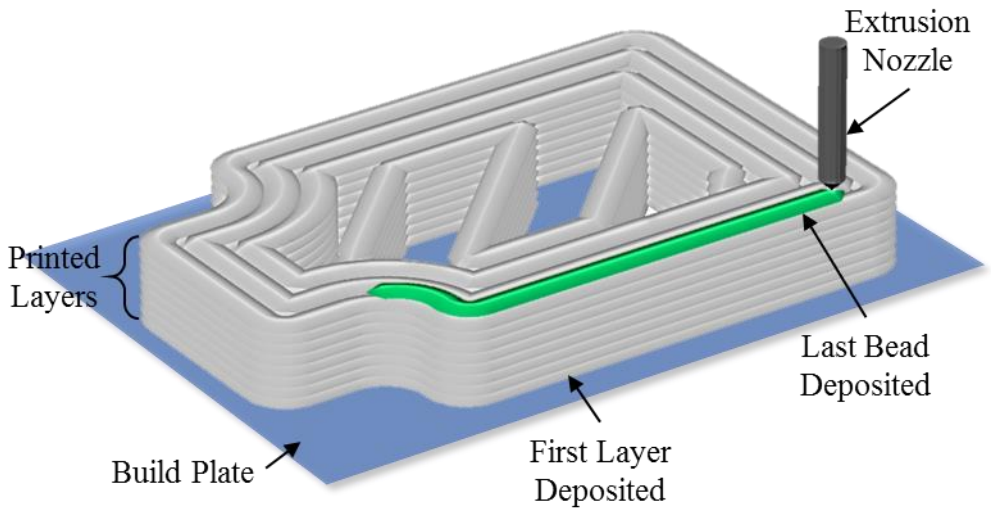

Figure 2.1 Extrusion deposition additive manufacturing process

AM processes analogous to the EDAM process include the Fused Filament Fabrication (FDM) or Fused Deposition Modeling (FDM). Although these methods for manufacturing a part are similar, the following three primary differences exist between EDAM and the others. First difference is the feedstock material. While FDM and FFF technology utilizes a filament material, the EDAM process utilizes pelletized feedstock material, thereby enabling printing with a wider range of commercially available materials. As a consequence, the liquefier commonly used in the FDM and FFF is replaced by a single-screw extruder in the EDAM process. Second difference is in the deposition rates. Since the deposition rated aimed in the EDAM process is higher compared to the FDM or FFF process, parts are printed near the final shape and finished in a second operation. This way, the printing time for parts defined near the volume of traditional FDM systems, which is in the range of less than 1 cubic meter, can be reduced by orders of magnitude. Third difference is in the process conditions and energy cost. The deposition in the EDAM process is carried out at ambient temperature rather than under controlled temperature conditions like in the FDM process. This has a strong impact in the energy embodied per kilogram of material printed which according to Love et al. [2] can represent a reduction in the range of 400% compared to in-oven AM processes. The steps for manufacturing a part utilizing the EDAM process are illustrated in Figure 2.2. Figure 2.2The example illustrated in Figure 2.2 corresponds to one half of a double cavity compression molding tool.

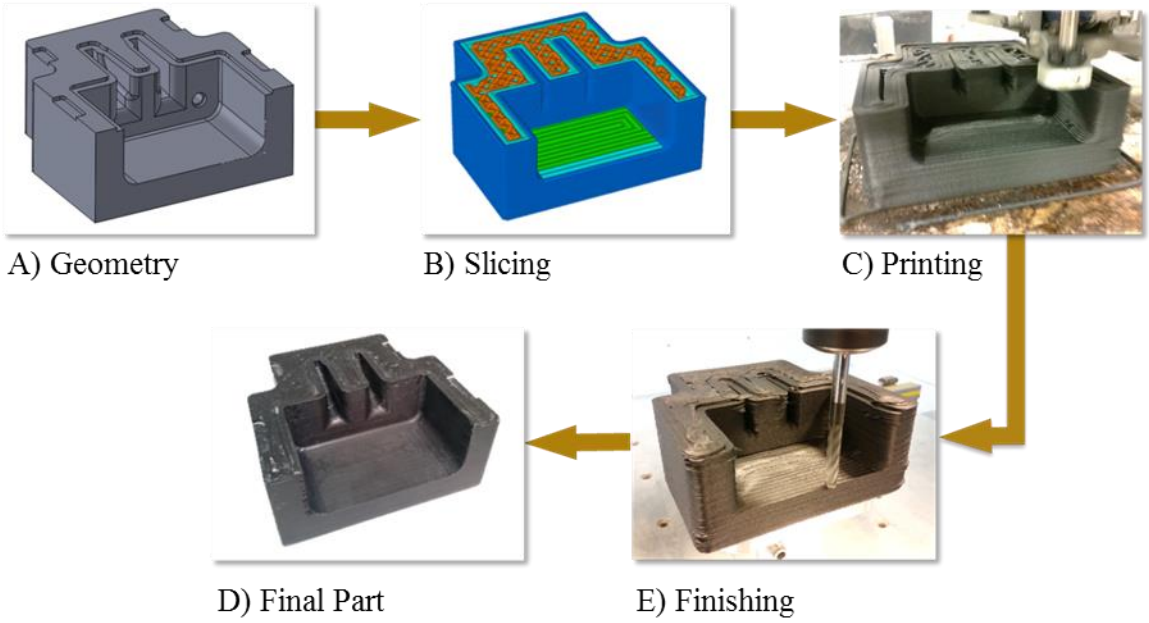

Figure 2.2 Steps for part manufacture with Extrusion Deposition Additive Manufacturing.

The first step in the process is the geometry definition. As part of the geometry definition, the geometry to print should be assessed to determine whether is printable or not. Printability viewed only from the geometry perspective depends not only on manufacturing constraints but also on aspects like material anisotropy and the orientation of the part with respect to the printing direction. Manufacturing constraints are briefly discussed in this chapter. Following the assessment of the geometry for printability, two geometries must be defined. The first geometry is called the nominal geometry and corresponds to the final desired shape. This geometry includes all the geometrical features of the final shape but it is not yet the geometry that is going to be printed. The second geometry, called printed geometry, is generated by offsetting the surfaces in the nominal shape along their normal direction. Features in the nominal shape with dimensions similar to the printed bead might be removed in the process of upscaling process in order to generate a continuous surface that is more suitable for printing. Determining the minimum distance to offset the nominal geometry depends on the dimensions of the printed bead and the smallest overhang in the nominal geometry. The schematic representation of a printed section in Figure 2.3 illustrates the minimum distance, s, required to capture the shape of the nominal geometry in the printed geometry. It should be noted the shape of the beads in this figure was simplified to rectangular cross-sections.

The surface of the nominal shape is represented by the segment AA intersecting the printed section whereas the surface of the printed geometry is represented with the segment $A'A'$ intersecting the printed section.

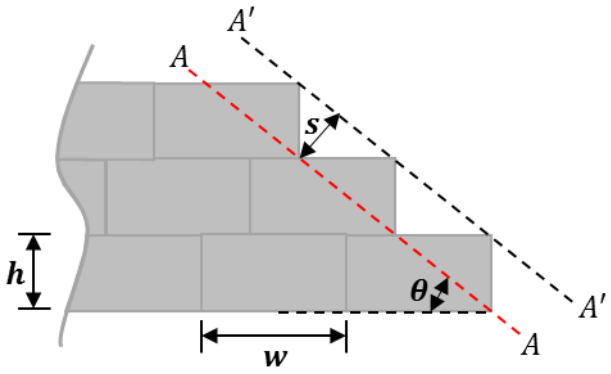

Figure 2.3 Schematic of printed section with overhang angle $\boldsymbol{\theta}$

From the schematic of the printed section shown in Figure 2.3, a relation can be derived for the minimum distance, s, based on the dimensions of the printed bead, h and w, and the minimum overhang angle, θ. Equation 2.1 provides the minimum distance s for overhangs angles, θ, in the range of $0 < \theta < \pi$. The cases of positive and negative overhang correspond to angles θ in the range of $0 < \theta < \frac{\pi}{2}$ and $\frac{\pi}{2} < \theta < \pi$, respectively. In other words, for a positive overhang angle, the layers of printed material are fully supported by the layers underneath, whereas for the negative overhangs, the layers of printed material are partially supported by layers underneath.

$$s = h \cdot \left|\sin\left(\frac{\pi}{2} - \theta\right)\right| \tag{2.1}$$

The offset distance s obtained with Equation 2.1 only accounts for differences in geometry between the printed and the nominal geometries. However, the shrinkage due to cooling of the printed material from the molten state to room temperature has to be considered in the calculation of s. The framework for EDAM process simulation presented in Chapter 4 can be utilized to predict part deformation after printing and considering anisotropy and residual stresses.

The second step in the diagram from Figure 2.2 is discretizing the solid geometry to a collection of layers. This process requires definition of three sets of parameters, namely parameters

for the geometry of the printed bead, parameters for the layer architecture and parameters for the printing conditions. The parameters for the bead geometry can be defined for each layer and include the width, w, and the height, h, of the printed bead (Figure 2.4). Definition of layer architecture can vary from one layer to other and requires parameters such as the infill pattern, the percentage of infill, the angle of the infill, ϕ, and the number of contour beads. Options for infill patterns commonly found in commercial slicers include concentric, grid, honeycomb, wiggle or rectilinear patterns like the one shown in Figure 2.4. The percentage of infill can vary from near zero for a sparsely filled layer to one hundred percent for a solid layer.

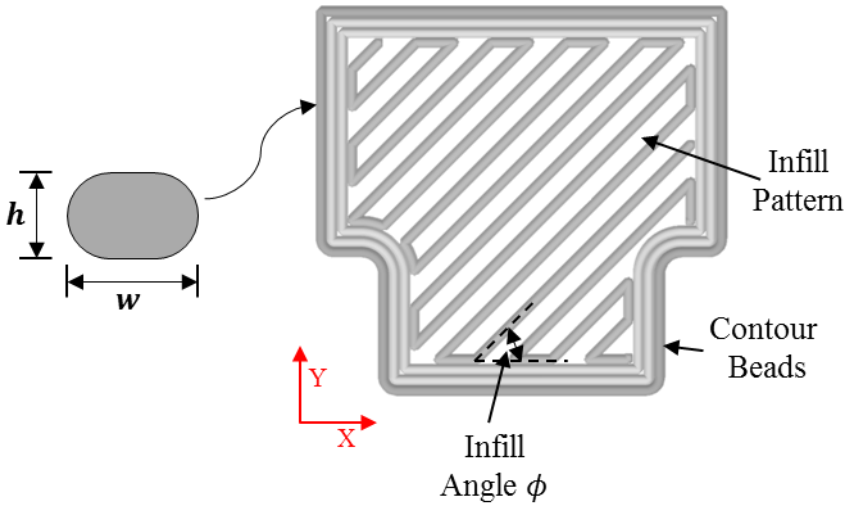

Figure 2.4 Examples of input parameters required for the slicing process

Printing conditions is the last set of parameters required in the slicing and includes the deposition speed, temperatures for the build plate and the extrusion system and definition of support material for areas with overhangs exceeding the maximum permissible angle θ.

The output generated by the slicing process is the machine code which is frequently given in the format of G-code. The machine code provides the EDAM system with the spatial and temporal description of the printing process as well as with the temperatures for the extrusion system and the build plate. Upon slicing of the geometry, the machine code is used to drive the EDAM system and produce a part near the final shape. A finishing step follows the printing process. The finishing process consists of removing the scalloped texture of the printed part to lead to a smooth and continuous surface finish. The finishing step is carried out in a numeric controlled

(NC) milling machines in order to achieve the dimensions and tolerances specified for the nominal shape. Milling tools with different shapes and dimensions provide for material removal and carving of features smaller than then printed bead. This way, geometrical features not possible to generate in the EDAM process can be created in the finishing step. Even though part manufacturing with EDAM requires an extra finishing step, this only implicates light milling operations that are neither time intensive nor require of large-rigid milling machines. Figure 2.5 provides an example of the surface finish before and after finishing a printed part in a NC milling operation. An optional final step in the part manufacture by EDAM involves applying coatings or surface conditioners for improving appearance or reducing roughness of the machined printed surface.

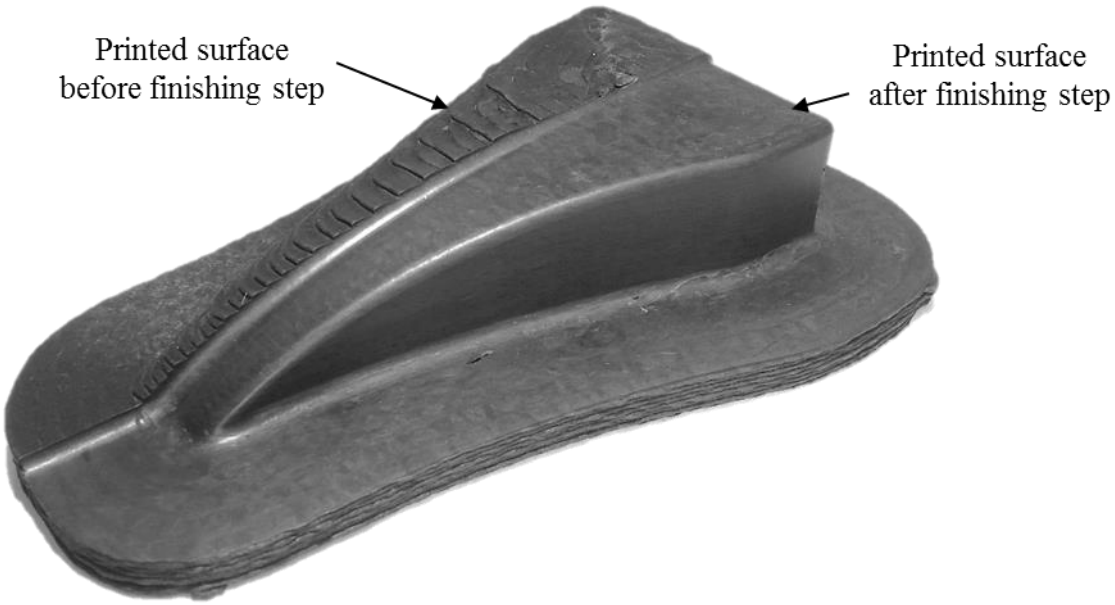

Figure 2.5 Surface of printed part before and after finishing step

AM processes like EDAM have enabled manufacturing of complex shapes that are not possible to manufacture with conventional subtractive methods. For example, printed parts can be manufactured hollow or partially infilled, thereby reducing weight and material cost [ref]. Further, freedom for placement of material in the areas and directions where is needed in a printed component is another virtue of AM processes. Nevertheless, there are also manufacturing constrains inherent to the layer-by-layer manufacturing process. Examples of manufacturing constraints include the maximum overhangs that can be printed, the maximum bridging distance

for unsupported beads, and the maximum deposition rate the EDAM system is capable of. The maximum overhang corresponds to the maximum angle, θ, that can be printed without compromising the shape of the part by sagging of printed material. The maximum bridging is relevant for printing partially filled structures. This parameter determines the maximum unsupported distance an extruded bead can bridge between two points without suffering significant sagging. The upper and lower bounds for the deposition rate are given by the extrusion equipment used in the EDAM system. The maximum deposition rate is defined by the capacity of the extrusion equipment for processing printing material, whereas the minimum deposition rate is limited by the stability of the extrusion system to operate at low deposition rates. Another process parameter consequence of the manufacturing constraints listed previously is the minimum and maximum layer time. The lower bound of the layer time is governed by the cooling process of the printed material. In other words, it corresponds to the minimum time required for the printed material to solidify and develop stiffness so that subsequent layers can be sustained. The upper bound corresponds to the minimum time between depositions of consecutive layers required to develop a strong bond between these. Variation on either process conditions or geometry lead to changes in layer time which ultimately impacts the adhesion between layers. Hence, there is a need for predictive simulation tools capable of anticipating issues prior to the printing process of a part like weak bonding between layers, excessive residual stresses, large residual deformation to name but a few.

2.2 State of the Art: Systems for Extrusion Deposition Additive Manufacturing

The technology for Extrusion Deposition Additive Manufacturing (EDAM) has undergone multiple changes during the last six years due to constant improvement in printing materials and the extrusion equipment. The first public record in the United States of systems of the kind of EDAM was the development made at Oak Ridge National Laboratory (ORNL) in a partnership with Lockheed Martin [3]. This pioneering work at ORNL was partly motivated by the unrivaled freedom for shape generation Additive Manufacturing (AM) offers and the vision of increasing the scale of printed parts from the centimeters size to the meters size. In this first attempt made around 2013 to scale this technology, a multi-axis robotic arm was equipped with a polymer extruder capable of extruding pelletized feedstock material (Figure 2.6-A). This way, the possibilities for materials was extended to printing not only with neat polymers but also with highly

filled polymers that otherwise cannot be processed in the filament based FDM process. This development at ORNL gave rise to the system known as Big Area Additive Manufacturing (BAAM). In a different part of the world, in the Netherlands, a company providing robotic extrusion deposition emerged also around 2013 from a collaborative research project with the institute for advanced architecture of catalonia and the design firm Joris Larrman Lab [4]. The company called Mataerial© developed a process for fabricating three-dimensional objects with printed beads oriented in any direction in the space without the need of support structures. Unlike the thermoplastic resins used in the BAAM system, the technology developed by Mataerial© pumps a thermoset resin to the end effector of a multi-axis robotic arm where material is mixed and dispensed through a nozzle (Figure 2.6-B).

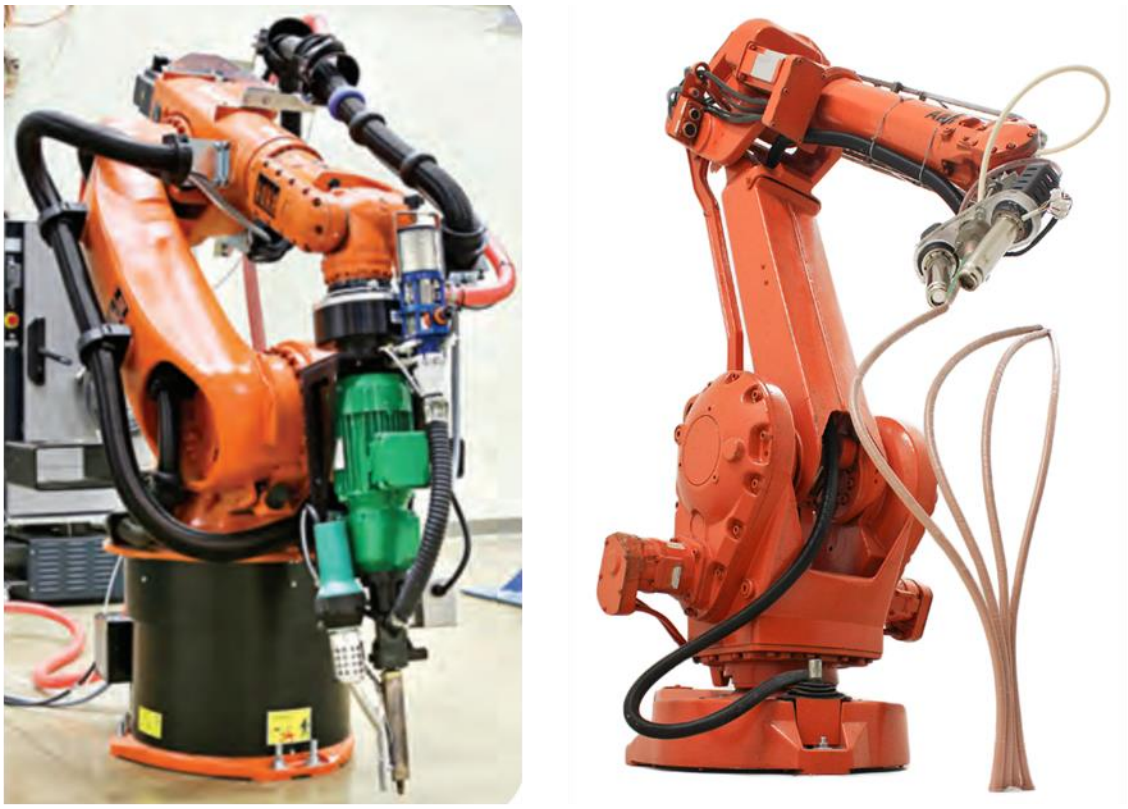

A) B)

Figure 2.6 A) Robotic extrusion deposition systems for thermoplastics developed at ORNL [3]. B) Robotic extrusion deposition system for thermosets developed Mataerial©. Permission for reproducing figure kindly provided by Mataerial©

Following the initial developments at ORNL, in 2014 the company Cincinnati Incorporated© signed a partnership with ORNL to accelerate the development of large-scale additive manufacturing systems [5]. CI© is a US-based machine tool manufacturer located near Cincinnati, Ohio. In this endeavor of producing a commercial large-scale EDAM system, Cincinnati Incorporated© retrofitted one of their commercial solutions for laser cutting with a single-screw extrusion system. At this point in the development of the EDAM process, the platform for the BAAM changed from a multi-axis robot arm to a gantry system. This gave rise to the first version of what would be commercialized later as the Big Area Additive Manufacturing (BAAM) system. The first public demonstration of the BAAM system occurred a few months after signing the partnership with ORNL in 2014 at the IMTS trade show in Chicago, IL. USA [6]. It was during the IMTS show, when the team from CI© featured the BAAM manufacturing of the major components of the first 3D printed vehicle called strati [6].

Figure 2.7 shows the BAAM system currently commercialized by CI©. The current generation of BAAM systems is available in three different size envelopes going from a volume in the range of 3.56 x 1.65 x 1.83 meters to envelopes with volume in the range of 6.1 x 2.3 x 1.83 meters [7]. The BAAM system is equipped with single-screw extruder capable of delivering up to 60 kilograms an hour. Consistency in material deposition is achieved in BAAM through the dynamic flow control implemented for the single-screw extruder [8]. An air pellet conveyor supplies the pelletized feedstock material from material driers to the hopper feeding the extrusion system in BAAM. The motion of the gantry system is driven with electromagnetic linear motors. Further, a tamping system provides for material consolidation during printing. The tamping system developed for BAAM consists of a vibrating ring that surrounds the printing nozzle, thereby consolidating the deposited beads regardless of the direction traveled in the printing process. After producing a part with the BAAM system, the part printed near the final shape is transferred to a NC milling machine to smooth the scalloped printed surface.

Figure 2.7 BAAM – Big Area Additive Manufacturing system developed by Cincinnati Incorporated© [7].

Another vendor of large-scale EDAM systems arose in the last five years in the region of Dale, Indiana, USA. Thermwood, a company emerging from the NC wood routers industry, redesigned one of their existing gantry routers to fit an extrusion system for additive manufacturing. Figure 2.8 shows the LSAM® system developed by Thermwood [9]. The build envelope available in LSAM is in the range of 3.1 meter wide, 1.5 meter height, and with a length that can be up to 31 meter [10]. Unlike the BAAM system, the LSAM is equipped not only with a printing head but also with a trimming head in the same gantry system. This way, both printing and trimming operations can be performed in the same machine without the need of moving the printed part to another machine for finishing. Additionally, the LSAM utilizes a positive displacement pump in series with the single-screw extruder, which provides material flow-rate control over a wide range of printing speeds. Thermwood offers three different melt cores or extrusion systems which corresponds to a 40, 60 and 70 mm single screw extruder. The options available in LSAM for melt cores deliver material at a range of 90 to 230 kilograms per hour. The pelletized feedstock material used in LSAM is dried before being fed into the LSAM through an automatic air conveyor.

LSAM also incorporates a compaction mechanism for improving consolidation of material printed. Instead of using a tamper, LSAM utilizes a compression wheel that orients automatically tangential to the printing trajectory.

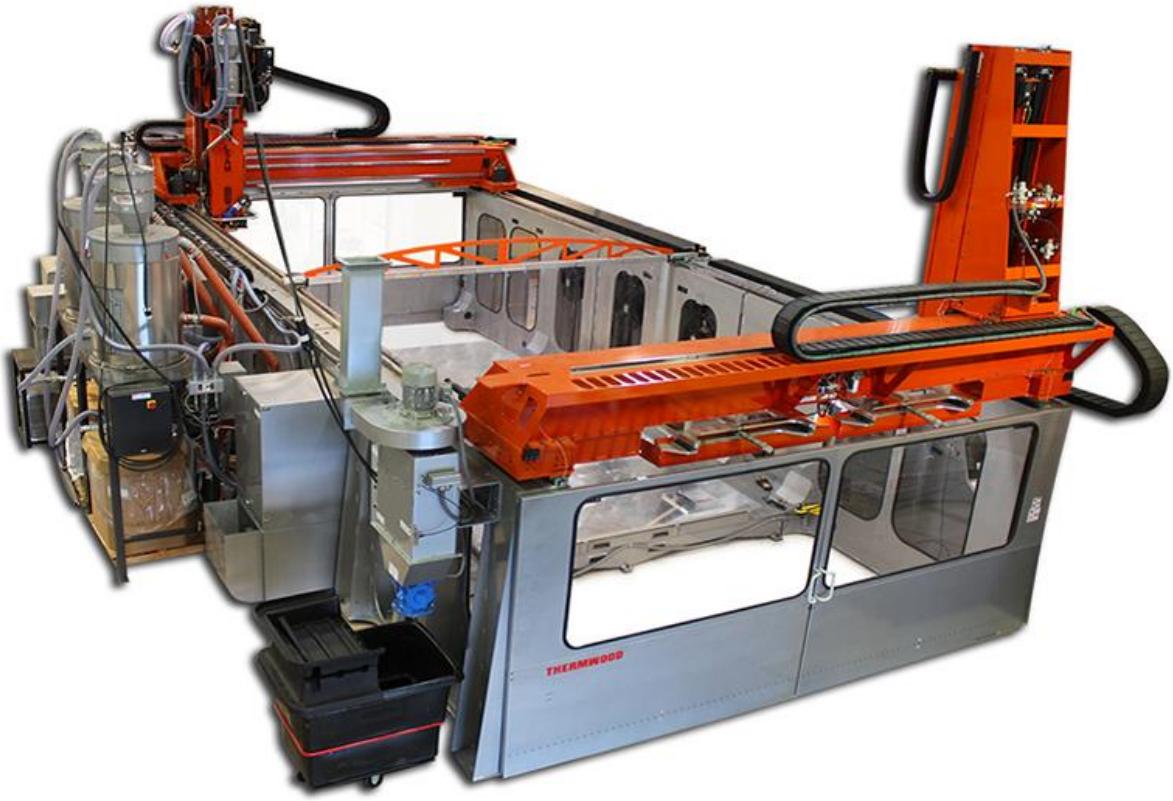

Figure 2.8 LSAM® – Large Scale Additive Manufacturing system developed by Thermwood. Permission to reproducing figure kindly provided by Thermwood.

The LSAM and BAAM system are currently the most matured EDAM systems that are commercially available. Nevertheless, other NC machine manufacturers are beginning to announce products for this technology area. For example, diversified machine systems (DMS) advertises two hybrid additive and subtractive manufacturing systems, one intended for metal and the other for polymer composites [11]. A different company called Ingersoll machine tools announced the development of a wide and high additive manufacturing machine in collaboration with ORNL [12]. Deposition rates in the range of close to 450 kilograms per hour are targeted by Ingersoll according to an early press release [12].

By the time this project started at Purdue University, fall of the 2014, there were not EDAM systems commercially available for investigating this manufacturing process emerging by that time. Further, motivated by the technical and scientific challenges underlying this manufacturing process, our group at Purdue decided to develop a medium size extrusion deposition additive manufacturing apparatus. The goal of this endeavor was to develop a system for investigating the extrusion deposition process of fiber reinforced polymer composites. Therefore, the name of Composites Additive Manufacturing Research Instrument (CAMRI) was coined for the system illustrated in Figure 2.9. CAMRI can deposit up to 6 kilograms per hour of high temperature and highly reinforced polymer composites.

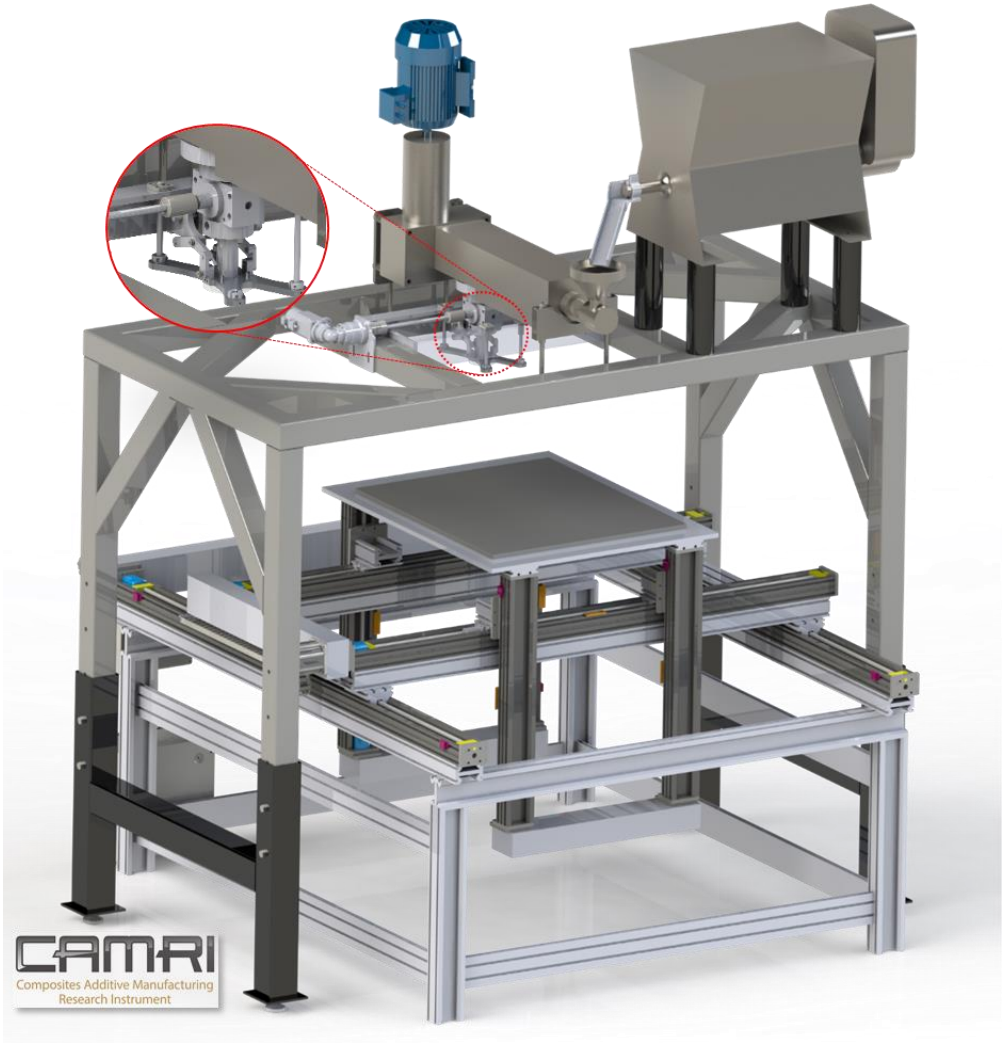

Figure 2.9 Composites Additive Manufacturing Research Instrument (CAMRI) developed at Purdue University.

The build envelope of CAMRI is adjustable in the height direction and provides a maximum of around 0.5 x 0.5 x 0.5 meters. A single screw-extruder with a diameter of $25.4\ mm$ and a length-to-diameter ratio of $24-1$ is the core of the extruder. Processing temperatures of up to 450 °C are possible in CAMRI. In order to achieve a precise material flow rate control over a wide range of deposition rates, a melt pump was incorporated to the system. This enabled printing beads of molten material maintaining consistency in dimensions and texture for a range of speeds from $8\ mm/s$ to $110\ mm/s$. Further, a tamper system provides for consolidation during material deposition. Unlike the majority of commercial systems where the extruder is moved on a gantry system, the inverse approach of moving the build plate was utilized in CAMRI. This is partly because lightweight extruders were not commercially available by the time the system was developed, and due to our interest on monitoring the deposition process from a steady position. Material feeding in CAMRI is by starve feeding rather than by flood feeding as in the BAAM or LSAM systems which enabled processing pellets in CAMRI with different dimensions and aspect ratios. A more detailed description of the CAMRI system is presented in Chapter 3, particularly in the control system developed for CAMRI.

2.3 Additive Manufacturing with Fiber Reinforced Polymer Composites

The second yet, not least important component for upscaling the EDAM process was the materials technology. While most of the work in additive manufacturing preceding the EDAM process was focused on fabricating prototypes with neat polymers, upscaling the size of printed objects from the centimeters scale to the meters scale aggravated the effect of the large Coefficient of Thermal Expansion (CTE) and the low stiffness of neat polymers. Hence, reinforcing the printing polymers with discontinuous fibers was the prominent choice that would not only reduce the CTE in the printed material but also increase the stiffness of the printed material. Love et al. [2] demonstrated this point by printing the two $1.83\ m$ long beams shown in Figure 2.10 with neat and fiber reinforced Acrylonitrile Butadiene Styrene (ABS) in a BAAM system. Reinforcing the ABS with 14% by volume of carbon fiber reduced significantly the residual deformation of the printed beams as illustrated in Figure 2.10. However, the improvement in thermomechanical properties has a directionality dependence that is governed by the orientation of the fibers within the printed bead.

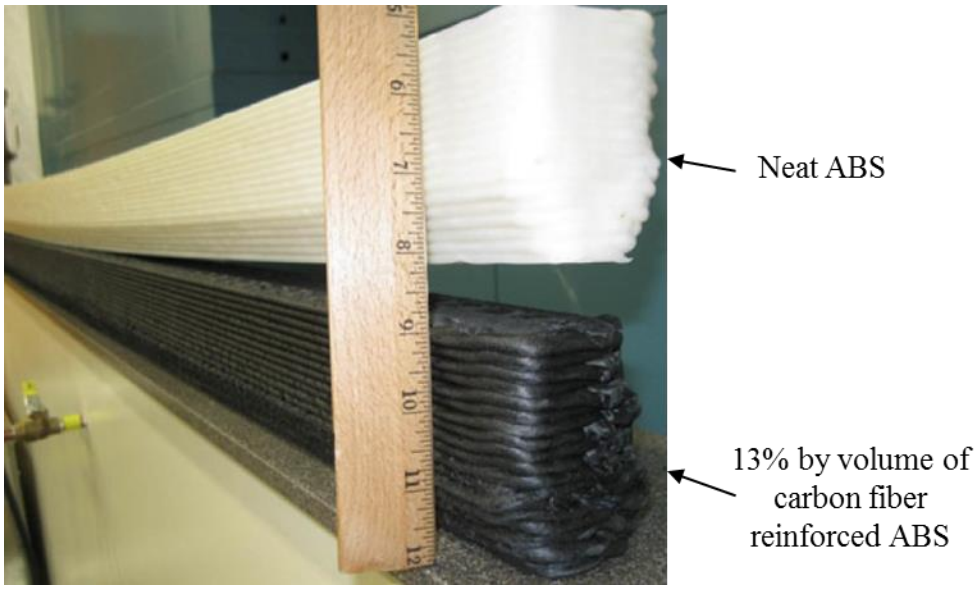

Figure 2.10 Beams printed with neat ABS and 13% by volume of carbon fiber reinforced ABS to demonstrate the role of fiber reinforced composites in the EDAM process [2].

The process-controlled fiber orientation distribution gives rise to anisotropy in the mechanical, transport and flow properties of the printed material. An example of the microstructure resulting from the EDAM process in CAMRI with 50% by weight of carbon fiber reinforced Polyphenylene sulfide (PPS) is shown in Figure 2.11. At this point, a convention for the local coordinate system is defined at the bead level. Referring to the bead located at the bottom left corner of the printed section illustrated in Figure 2.11, the 1-direction corresponds to the deposition direction, the 2-direction corresponds to the transverse in-plane direction and the 3-direction corresponds to the stacking direction. The first level of magnification shown for the printed microstructure in Figure 2.11includes two entire beads and partial sections of neighboring beads. The black regions in this microstructure correspond to voids which can be categorized in two regions. First, the intra-bead voids which correspond to voids inside the bead. Second, the inter-bead voids which correspond to voids located at the boundaries of the printed beads. It should be noted that the voids of the second kind are significantly reduced through the consolidation of the printed material attained with the tamper. Without the compaction from the tamper, these voids would appear as diamond shapes at the intersection of four beads. Void content for this material system is in the range of 7 to 15 %. Further, there are not visual signs of an interface between the adjacent beads in this microstructure. The second level of magnification in Figure 2.11 shows individual carbon fibers

in white surrounded by the polymeric matrix in light gray. The fact that fibers are shown as circles indicate from stereology that fibers are highly oriented in the 1-direction.

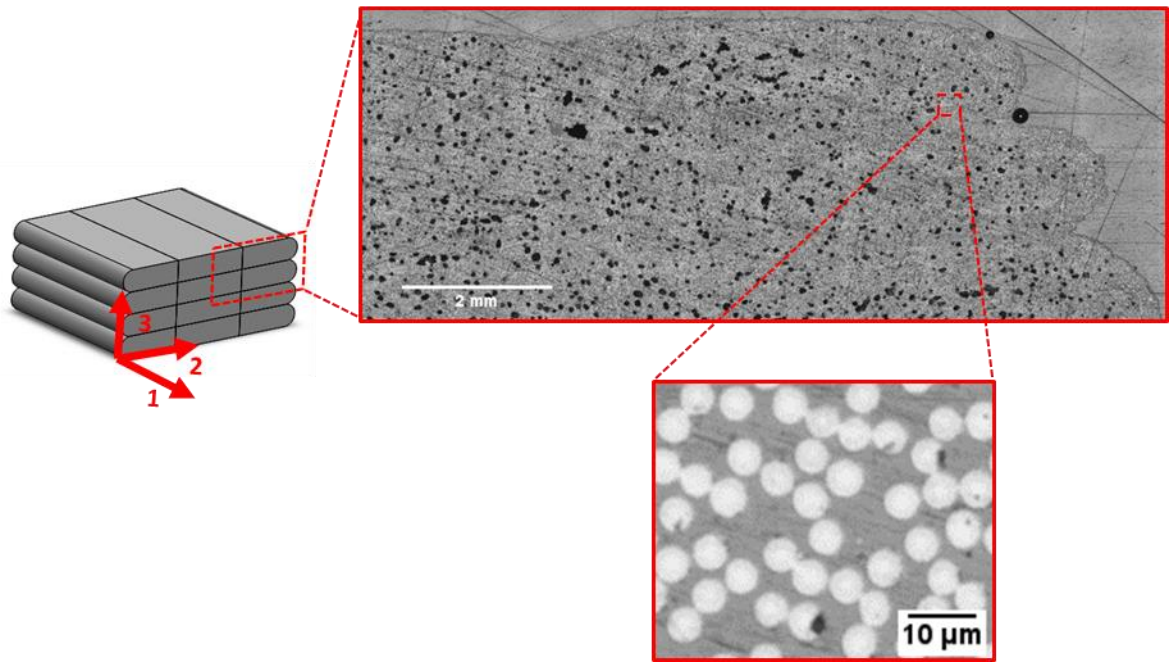

Figure 2.11 Representative microstructure produced with the CAMRI system

Stereology utilizes information from a 2D section of the material to infer information of the 3D orientation state. This way, fibers angled with respect to the direction normal to the plane of observation appear as ellipses. By characterizing the principal dimensions of the ellipses, a set of angles defining the orientation of the fiber in 3D can be defined. However, this method has the limitation that a single ellipse is not sufficient to solve the ambiguity resulting from the fact that fibers oriented at different angles can produce the same ellipses on the plane [13].

2.3.1 Material Selected for Printing with CAMRI

The material selected in the first place for printing in the CAMRI system was Polyphenylene Sulfide (PPS) reinforced with 50% by weight of carbon fiber. This material is supplied in the form of long discontinuous carbon fiber pellets with a length of around 12 mm and a diameter of around 2 mm and it is produced by Celanese© under the name of Celstran® PPS-CF50-01 [14]. Figure 2.12 shows pellets reinforced with long discontinuous fibers produced by Pultrusion by Celanese©. Among the reasons to have chosen this material is because PPS is a semi-crystalline polymer that

offers elevated service temperature, yet it is still economically accessible compared to other high end semi-crystalline polymers like PEEK or PEKK or amorphous polymers like PEI. According to the cost comparison for 3D printing materials made by DeNardo [15] in 2016, the cost per kilogram of an amorphous polymer with similar operation temperature than PPS-CF50-01, namely carbon fiber reinforced PEI, would cost around 60% more than the carbon fiber reinforced PPS. Polymers matrix composite materials with elevated service temperature were the primary focus of this project due the application of this Additive Manufacturing (AM) technology in the production of high-temperature molds or tools. Further details of the applications are provided in the section 2.6 of this chapter. Furthermore, printing with high temperature fiber reinforced semi-crystalline polymers involves more technical challenges that deserve attention from the scientific community.

Figure 2.12 Pellets of Polyphenylene Sulfide reinforced with long discontinuous fibers.

The Celstran® PPS-CF50-01 has been studied extensively in the CAMRI system by the composites additive manufacturing group at Purdue and as a result, a detailed characterization of the material for process simulation has been carried out in the last four years and has been reported in detail in the Ph.D. dissertation of Bastian Brenken [16]. Thermophysical and orthotropic elastic properties are provided in Table A.1 through Table A.6 of the APPENDIX A. Furthermore, the tensor representation proposed by Advani and Tucker [17] has been utilized to describe the fiber

orientation distribution characterized through stereology estimates of fiber orientation within a printed bead. The second order fiber orientation tensor is reported in Table A.7 of the APPENDIX A. In addition to the fiber orientation, the fiber length distribution after the single-screw extrusion process in CAMRI was characterized for the Celstran® PPS-CF50-01 and is reported in Figure A.1 of the APPENDIX A.

Although experimental and simulation work of the EDAM process has been carried out for this material form, the models and methods are applicable to not only other semi-crystalline polymers but also to amorphous polymers. Furthermore, the pelletized feedstock used in the EDAM process can be produced in multiple ways. Pellets with Long Discontinuous Fibers (LDF) are typically manufactured by impregnating continuous fibers in a pultrusion process to produce a continuous filament which is subsequently chopped into pellets of constant length. An example of this material is the Celstran® PPS-CF50-01. A different way to produce the pelletized feedstock material is by compounding fibers with neat polymer resin in a twin-screw extruder. The compounding process provides a continuous filament of homogenized polymer and fibers that can be chopped into small pellets with short aspect ratio (length to diameter ratio). Although both processes for manufacturing pelletized material deliver good impregnation of fibers with the polymer resin, a significant difference in the length of the fibers within the pellets results from the use of either of these techniques.

2.4 Phenomena Involved

The phenomena involved in the EDAM process are detailed in this section. The steps of the EDAM process considered in this section cover the extrusion process of the fiber reinforced polymer composite in the processing equipment, e.g. single-screw extruder, and material deposition. The former includes the phenomena occurring during feeding, melting and extruding of the pelletized material while the latter considers the phenomena after the fiber reinforced molten polymer leaves the extrusion nozzle.

2.4.1 Material Extrusion

The Extrusion Deposition Additive Manufacturing (EDAM) process utilizes either single-screw extruders or a combination of a single-screw extruder and a positive displacement pump for transforming the pelletized feedstock material into a suspension of fibers in molten polymer. A

more detail description of this transformation process along with a brief description of the mechanisms degrading the length of fibers during processing of reinforced polymers is given in this section. The first step consists of feeding the pelletized material through the hopper of the single-screw extruder. Pellets can be supplied to the extrusion equipment either by flooding the hopper in the extruder, which is called flood feeding, or by dispensing pellets in a controlled manner to the hopper in the extruder, which is known as starve feeding [18]. A schematic of a single-screw extruder is shown in Figure 2.13. As the material enters the single-screw extruder through the feed zone, the pellets are conveyed volumetrically by the rotation and the geometry of the screw. After flowing of the pellets through the feed zone in the extruder, these become confined between the screw and the barrel of the extruder.

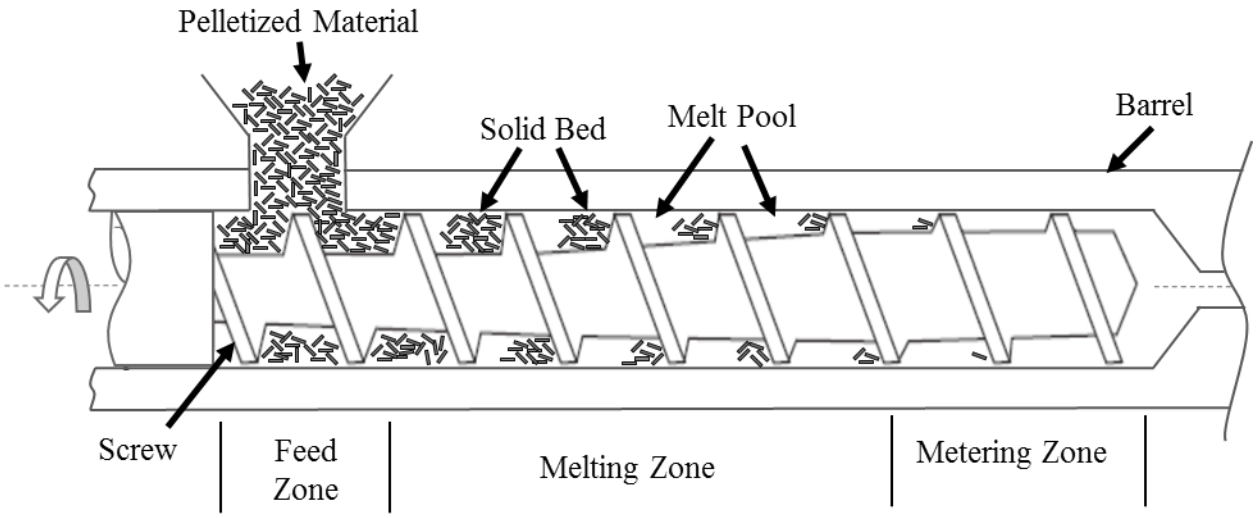

Figure 2.13 Schematic of a single-screw extruder

Electric heaters placed along the barrel of the extruder provide thermal energy to assist the melting process of the pelletized material. Melting of the pellets occurs gradually along the melting zone in the extruder which is located after the feeding zone and before the metering zone shown in Figure 2.13. Furthermore, thermal energy for melting the pellets is not only supplied through conduction from the barrel but also developed through viscous losses in the polymer [18]. The gradual melting of pellets leads to the formation of a melt pool which enlarges as the material is conveyed in the melting zone as illustrated in Figure 2.13. Therefore, variables in the extrusion

process, namely temperature profile along the barrel and screw rotation speed, should be controlled such that the material is fully molten by the time it reaches the metering zone.

Preserving the length of the fibers in single-screw extrusion of composites is desired to leverage the strength of the reinforcing fibers, especially in feedstock materials like the long carbon fiber reinforced PPS utilized throughout the work presented in this dissertation. Nevertheless, degradation of fiber length in single-screw extrusion occurs during the extrusion process due to pellet-to-pellet and pellet-to-extruder interactions. Detailed investigations on single-screw extruders like the ones carried out by Wolf [19] and by Ramani et al. [20] have led to a better understanding of the mechanisms for fiber attrition during the extrusion process. According to their findings, fiber attrition occurs primarily in the development of the melt pool (Figure 2.13) due to movement of the solid bed during the melting process and high shear stresses developed in the region between the barrel and the flights of the screw [19, 20]. From the material and screw design perspective, good impregnation of the fibers with polymer has been found to lessen the fiber attrition whereas features in the screw design like mixers and short compression zones aggravates the attrition of fibers [19, 20]. Furthermore, extrusion systems equipped with melt pumps overall result in higher degradation of fiber length due to additional shear deformation the molten material undergoes as it flows between the gears and the housing of the melt pump.

Upon completion of the melting process in the single-screw extruder or the melt pump, the molten material is pumped through the printing nozzle. The flow behavior of fiber suspensions is highly anisotropic. In other words, the rheological properties of the fiber suspensions are strongly coupled with the local orientation of the fibers [21, 22]. A concentrated suspension with fibers fully oriented in one direction can be used to illustrate the anisotropy in rheological properties. By considering the ratio of the extensional viscosity in the direction of the fibers to the extensional viscosity in the direction transverse to the fibers for the system under consideration, a square dependence on the aspect ratio of the fibers develops for the ratio of viscosities [22, 23].

Printing nozzle, deposition nozzle, or extrusion nozzle is used interchangeably in this dissertation to refer to the nozzle delivering molten material in the EDAM process. Printing nozzles can be designed with reductions in internal diameter from the point where material enters the nozzle to the point where material is delivered in the EDAM process. Features like converging zones are common ways to transition between different internal diameters inside printing nozzles. The combination of converging zones in printing nozzles and shear flow developed inside the

printing nozzle can give rise to a rapid collimation of fibers along the extrusion direction [24, 25]. Hence, initial conditions for fiber orientation distribution at the inlet of the printing nozzle and the geometrical features of the printing nozzle control the fiber orientation distribution delivered at the outlet of the printing nozzle. For example, long nozzles with small extrusion diameter will cause the viscous suspension to experience large shear flow which in turn causes alignment of the fibers in the flow direction. In the opposite case of short nozzles with relatively large extrusion diameter, a flow condition close to plug flow can develop and thus only the regions near the wall of the nozzle experience significant shear flow to align the fibers. As a result, a distribution of fiber orientations will developed across the diameter of the nozzle. The design of the extrusion system in CAMRI is closer to the first kind of nozzle architecture since it includes converging zones and a long extrusion nozzle with a relatively small diameter. Therefore, fibers are considerably oriented in the extrusion direction by the time the fiber suspension reaches the tip of the printing nozzle.

2.4.2 Material Deposition

This section considers the phenomena participating during the deposition process of the fiber suspension described in the previous section. Therefore, the phenomena discussed herein comprise from the point the material leaves the extrusion nozzle to the point the part is removed from the build plate. The schematic shown in Figure 2.14 illustrates the deposition process and highlights the phenomena occurring during the so-called Extrusion Deposition Additive Manufacturing process.

In the early stages of the deposition process, the fiber suspension flows through the printing nozzle which affects the fiber orientation as described before. Upon exciting the printing nozzle, the fiber suspension is considered an extrudate or a printed bead, therefore these two words are used interchangeably in this section. Since the printing nozzle in the EDAM systems is oriented perpendicular to the build plate, a rotation of ninety degree is required to lay down the extrudate horizontally on the build plate. The kinematics of this sharp turn around the tip of the printing nozzle lead to a difference in radii from the back to the front of the deposition as illustrated in Figure 2.14. Such a difference in radii introduces shear deformation in the fiber suspension, thereby promoting further orientation of the fibers along the printing direction. Following this sharp turn around the tip nozzle, compaction of the extrudate with either a roller or a tamping mechanism occurs. Depending on the compaction conditions, changes in fiber orientation inside

the extrudate can be introduced. One of these conditions includes the amount of squeeze defined by the ratio of the height of the printed bead to the diameter of a free extrudate.

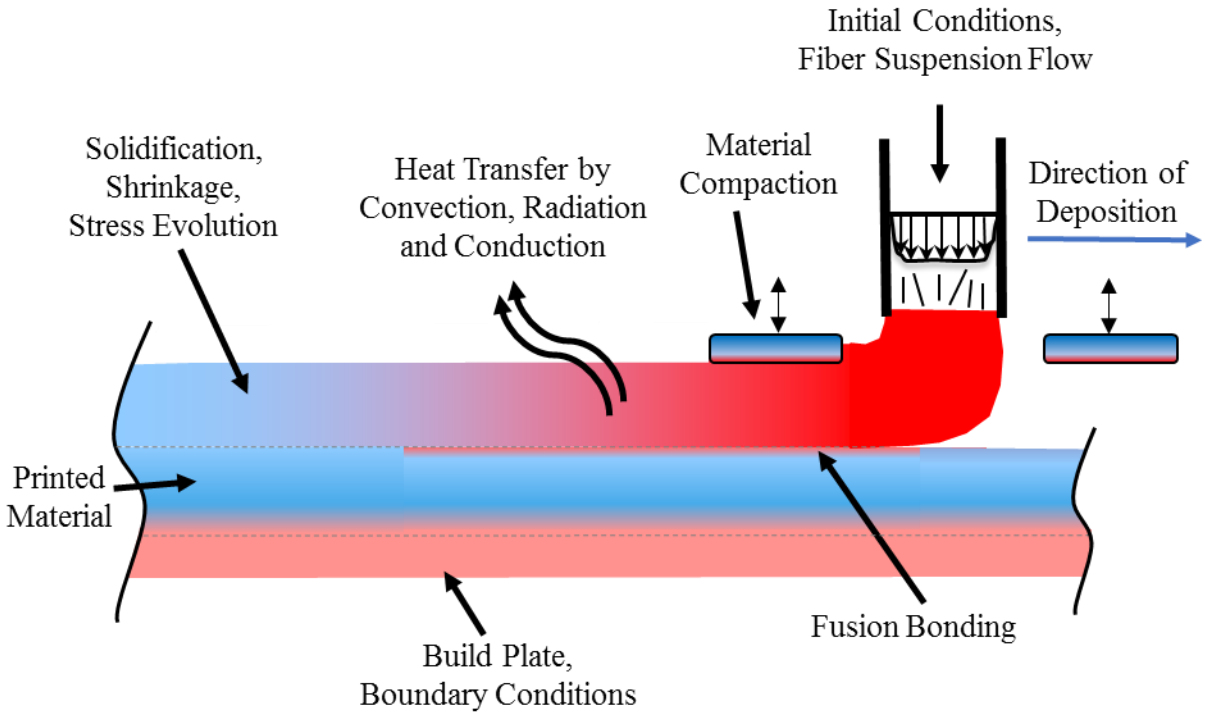

Figure 2.14 Schematic of the deposition process illustrating the phenomena participating in the EDAM process.

Squeezing an extrudate introduces shear and extensional deformation at the top and bottom regions of the extrudate and in the interior of the extrudate, respectively. For the case of an extrudate with fibers highly aligned in the deposition direction, lateral motion of the fiber suspension dominates over motion in the print direction due to the large ratio of extensional viscosities described before [23]. Depending on the amount of squeeze in the extrudate, fibers slightly angled with respect to the deposition direction can experience velocity gradients arising from the lateral flow which lead to further rotation of the originally angled fibers. Flow conditions similar to the squeeze flow introduced with the tamper in the EDAM process can be introduced in the FFF process through manipulation of printing parameters like the gap between the printing nozzle and the build plate. This condition is used commonly to improve the contact of newly deposited beads with either the build plate or previously deposited layers. Experimental evidence of the increase of lateral

realignment of fibers upon deposition is provided by the work of Mulholland et al. [26] where the second order fiber orientation tensor is characterized for multiple printing scenarios. An increase in the tensor components A_{22} and A_{33} accompanied with a reduction of the A_{11} component were observed between a free extrudate and a printed bead in the same work. As a closing statement, the fiber orientation distribution in the printed bead ultimately governs the thermomechanical, mechanical and transport properties of the printed bead. The fact that the fiber orientation distribution within a printed bead is fairly uniform throughout a part suggests that the bead scale is a good starting point for simulating the EDAM process with properties homogenized at this scale.

After defining the mechanisms governing the fiber orientation distribution within a printed bead, the focus can be then turn to the heat transfer in the EDAM process. Temperature history of the printed material during the EDMA process is of major relevance since temperature drives the solidification of the polymer, the transitions during such a solidification process, the bonding process between layers and finally the evolution of stresses. Therefore, special attention is given to the heat transfer analysis so that a whole chapter is dedicated to this topic.

A constant temperature through the extrudate can be assumed as initial conditions for the heat transfer analysis. This initial temperature condition can be stablished based on the temperature of the processing equipment and the processing conditions. However, temperature gradients can develop in large nozzle diameters. Shortly after leaving the printing nozzle, the molten material can be compacted with either a roller or a tamper system as shown in the schematic of Figure 2.14. During compaction, molten material contacts the surface of the compaction system, thereby giving rise to local heat loses through conduction. Temperature at the surface of the compactor is commonly controlled to prevent adhesion of the printed material, as a result the heat flow from tamping a single bead do not change significantly over time. Further, printing sections with multiple beads placed side-by-side causes the tamper to interact with more than the bead being deposited. This is a consequence of the need for a compacting surface that spans beyond the width of a printing bead, otherwise undesired surface irregularities could be introduced. Fiber orientation distribution within the printed bead is practically locked upon compaction of the printed bead therefore, the orthotropic thermal conductivities resulting from the fiber orientation state and the thermal conductivity of the constituent properties govern the heat losses through conduction in the newly deposited bead. Differences in orders of magnitude of thermal conductivity between the

principal directions of the printed bead can arise from the combination of high level of fiber collimation and highly conductive fibers [26]. In addition to the heat losses through conduction with the tamper, newly deposited beads are squeezed on top of either the build plate or previously deposited material. In the former case, the build plate is maintained at a constant temperature which can lead to a difference in temperature between the printed bead and the build plate, thereby driving the diffusion of thermal energy. In the latter case, thermal energy is diffused from the newly deposited bead to previously printed layers as illustrated in Figure 2.14.

Thermal energy is also dissipated through convection and radiation from the exposed surfaces in a printed part. The convective heat losses arise from the interchange of thermal energy with the air surrounding the printed part. Heating of the air surrounding the hot surfaces of the printed part give rise to local changes in the density of the air. Density gradients then lead to buoyancy forces that drive the flow of air around the printed part and thus the buoyancy driven flow also drives the interchange of energy with the air surrounding the part [27]. The interchange of energy with air occurs within the thermal boundary layer that develops around the printed part. This process is known as natural convection. However, air can also be propelled to increase the effectiveness of heat removal which leads to what is known as forced convection. Passive cooling in the EDAM process is of the first kind of convection, however, active cooling which corresponds to the second kind is sometimes used to improve thermal management during printing of small parts.

The second mechanism of heat transfer from the exposed surfaces of printed parts does not need a medium like air to convey thermal energy, instead, the phenomenon of radiation results from the emission of electromagnetic waves. Emission is then related to the oscillations and transitions of the electrons that constitute matter in a thermally excited solid, liquid or gas [28]. However, only the case of emission from surfaces of solid or molten printed material is considered relevant in the EDAM process. There is also heat exchange through radiation with surfaces viewed by the surfaces of a printed part like the build plate, the extrusion equipment, etc.

The next phenomenon to describe is the fusion bonding of adjacent layers. Since the material utilized in the work presented throughout this dissertation is a semi-crystalline polymer, we will focus our attention on the phenomena relevant for fusion bonding of semi-crystalline polymers. However, the methods are also applicable to amorphous polymers. Fusion bonding is one of the primary topics of this thesis and thus a whole chapter is dedicated to this topic. Fusion

bonding of semi-crystalline reinforced polymers involves a sequence of at least three steps which include development of intimate contact, interdiffusion of polymer chains, and solidification [29]. In the context of EDAM, the step of establishment of intimate contact is achieved upon compaction of molten material on top of previously deposited material. As a result, instantaneous wetting can be considered in EDAM. Establishment of intimate contact with the material underneath also reduces the thermal resistance between the adjacent layers, thereby enabling thermal diffusion from the newly deposited bead to the layer underneath. The second step is interdiffusion of polymer chains through the interface formed with two adjacent layers. Interdiffusion requires mobility of polymer chains in the vicinity of the interface; in other words, the material in this region should be in a temperature region where crystallinity has not developed yet, otherwise the polymer chains are trapped in the polymer crystals already formed and the polymer chains mobility is precluded [30]. However, melting of polymer crystals in already crystallized material can occur upon deposition of molten material if certain thermodynamic conditions for melting are satisfied in the material near the interface [31]. This way, the interdiffusion of polymer chains across the interface can proceed until crystallization occurs through the interface again. A characteristic time, which is strongly dependent on temperature, associated with the movement or reptation of polymer chains is required to achieve the maximum interlayer strength [32]. Subsequent to interdiffusion of polymer chains through an interface, the solidification by crystallization of the polymer takes place.

Crystallization in polymers is a two-step process involving nucleation and growth of crystals, which are controlled by the amount of supercooling and by diffusion, respectively [33]. Further, temperature gradients developed in a printed part due to the non-isothermal nature of EDAM drive the evolution of crystallinity. In other words, crystallization evolves in the same direction that cooling occurs in a printed bead or in a printed part. Additionally, the crystallization process, which is a physical and reversible transformation, gives off thermal energy, introduces additional shrinkage in the polymer and sets the start of the transition from molten state to solid state in the polymer [33].

The next phenomenon to be described is the evolution of internal stresses during cooling of the printed material. Stresses are developed at multiple scales that coexist in a part manufactured with EDAM [34]. Further, the evolution of stresses is the result of two competing mechanisms, one building up stresses and a second one relaxing stress which occur simultaneously during the

EDAM process [35]. The scales in the EDAM process are illustrated in Figure 2.15 and comprise from the constituents or microstructure level to the part level. At the microstructure level, stresses are caused by differences in coefficient of thermal expansion between the constituents of the printed composite material. Further, these stresses develop as the composite material is cooled from the processing temperature to room temperature. The next level up in the scales, which is far more relevant for this work, is the internal stresses developed at the mesostructure level (Figure 2.15). Internal stresses at this scale develop due to either anisotropy caused by changes in orientation of printed beads within a printed layer or by temperature differences in adjacent layers. In the former case, the changes of bead orientation within a layer lead to constrained anisotropic shrinkage of the printed beads which results in building up of stresses. In the latter case, the temperature difference between subsequent layers introduces a difference in shrinkage between the two subsequent layers which leads to residual stresses upon cooling of the printed part.

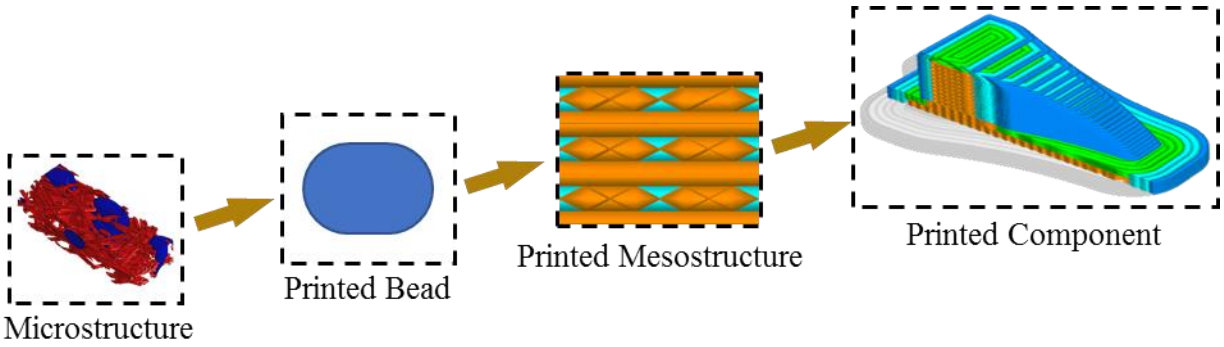

Figure 2.15 Scales in the EDAM process

As described previously, the viscoelastic nature of the polymeric material provides for relaxation of internal stresses. However, in a simplistic scenario if internal stresses exceed the strength of the printed material, failure through different mechanisms can occur in a printed part. One example of failure mechanisms in printed parts is delamination of printed layers. Delamination results from the combination of weak bonding between layers and development internal stresses. This failure mechanism can initiate during manufacturing, during cooling after manufacturing, or during service of a printed component.

Removal of the printed part from the build plate is the last step in the printing process. This step is generally carried out upon cooling the printed part to room temperature while the part is

still on the build plate. At this point, the thermal shrinkage has concluded as well as the development of internal stresses. However, removing the constraint imposed by the build plate on the printed part relieves the stresses induced by this constraint and causes the internal stresses to equilibrate into a new configuration. As a result, additional deformation can occur in the printed part and the internal residual stress state is established for the printed part.

A general description of the phenomena participating in the EDAM process was provided in this section. This section presented the complexity of this manufacturing process due to multiple phenomena occurring simultaneously. This emphasizes the need for predictive simulation tools capable of anticipating fusion bonding, residual stresses, deformation and failure prior to manufacturing of a part. Hence, this dissertation presents not only the investigation of some of the phenomena outlined in this section but also proposes methods to capture those in process simulation of the EDAM process.

2.5 Literature Review on Extrusion Deposition

A throughout review on additive manufacturing is presented in the following two subsections. The first subsection summarizes characterization work carried out for printed fiber reinforced polymers with the aim of setting a reference of what is possible today in terms of mechanical properties of printed material. The second subsection focuses on previous work on process simulation capturing some of the phenomena described in the previous section yet with an emphasis on the topics addressed in this dissertation, namely heat transfer and fusion bonding.

2.5.1 Experimental Characterization

Materials technology for extrusion additive manufacturing processes is one of the primarily elements of AM assisting in the transition of this technology from prototyping technology of 3D models to manufacturing method of end-use components. Significant improvements in mechanical properties, particularly in the print direction, have been achieved by reinforcing printing polymers with carbon fiber [15, 2, 25, 36, 37, 38, 39]. However, the mechanical properties of the printed parts are highly anisotropic and, in some cases, still inferior compared to properties of similar parts produced by traditional manufacturing techniques such as injection molding or compression molding [25]. A clear example of this is the strength in the 3-direction or stacking direction which depends on the bond developed between adjacent layers during the printing process. Hence, this

section on experimental characterization presents a survey on the mechanical properties reported for printed reinforced polymers with the goal of settling a reference for what is currently possible with additive manufacturing of reinforced polymers. The scope of this survey is on the extrusion additive manufacturing methods [1] rather than just EDAM so that a wider spectrum of reinforced materials is covered. The following discussion is limited to mechanical properties in the 1 and 3 directions since these yield the upper and lower bound in mechanical properties, respectively. Previous work by Brenken et al. [40] summarized mechanical properties reported in the literature for a significant number of printed reinforced polymers. This includes both discontinuous fiber reinforced polymers and continuous fiber reinforced polymers. For the discontinuous fiber reinforced polymers reviewed in [40], the maximum tensile modulus reported in the direction parallel to the print direction (1-direction) was of $26.4\ GPa$ and corresponds to the PPS reinforced with 50% by weight of carbon fiber characterized by DeNardo [15]. The specimens tested by DeNardo were produced with EDAM. A maximum tensile strength of $125.3\ MPa$ was reported in the 1-direction for Polyetherimide (PEI) reinforced with 4.7% by weight of carbon nanotubes which was characterized by Gardner et al. [41]. Gardner et al. [41] produced specimens for tensile tests utilizing FFF. With regards to the properties in the 3-direction or stacking direction. A maximum tensile modulus of $8.06\ GPa$ was reported in [40] for epoxy reinforced with 10% of silicon carbide printed by Compton and Lewis [42] whereas a maximum tensile strength of $46\ MPa$ was reported for epoxy reinforced with 15% by weight of carbon fiber printed by Mahajan et al. [43]. The specimens used for characterizing the elastic modulus of silicon carbide reinforced epoxy were made in a three-step process, where specimens are first printed with an epoxy-based ink and then fully cured in two more steps [42]. Printed specimens used in the investigation that yielded the maximum strength were prepared with a method similar to Compton and Lewis [42].

Work published within the last twelve months that is worthwhile to include in this review is summarized next. The materials technology front is advancing rapidly in terms of improving existing materials and enabling new materials for extrusion deposition. Examples of the former case include the reformulation of materials like the Acrylonitrile Butadiene Styrene (ABS) reinforced with 20% by weight of carbon fiber to improve the mechanical properties of parts printed with EDAM in the BAAM system [39]. In the same material development program, a new blend of Polyamide 6 (PA6) with 20% by weight of carbon fiber and 25% by weight of a proprietary filler set the new maximum value of $146.9\ MPa$ for strength in the printing direction.

Examples of the latter case include reinforcing polypropylene (PP) with up to 20% by weight of carbon fiber for extrusion deposition with FFF [44]. Another example is the filament for FFF produced from polyethylene terephthalate glycol (PETG) reinforced with 20% by weight of carbon fiber [45]. However, neither of the last two materials outperformed the maximum mechanical properties reported before. The highest mechanical properties reported in the literature for the printing direction and the stacking direction is summarized in Table 2.1. All the mechanical properties considered in this survey are summarized in Table A.8 and Table A.10 of the APPENDIX A.

Table 2.1 Highest Mechanical Properties Reported in the Literature for Polymers with Discontinuous Reinforcements.

Maximum Tensile Modulus Reported in the Literature				
Source	**Orientation**	**Material**	$\boldsymbol{E}$ $(\boldsymbol{GPa})$	**Manufacturing Process**
DeNardo [15]	1 - Direction	50%wt CF/PPS	26.4	EDAM
Compton and Lewis [42]	3 - Direction	10%wt CF/SiC/ Epoxy	8.1	Ink Extrusion
Maximum Strengths Reported in the Literature				
Source	**Orientation**	**Material**	**Strength** $(\boldsymbol{MPa})$	**Manufacturing Process**
Hill et al. [39]	1 - Direction	20%wt CF/25%wt Prop/ PA6	146.9	EDAM
Mahajan et al. [43]	3 - Direction	15%wt CF/Epoxy	46.0	Ink Extrusion

The following conclusions can be made based on the experimental data published and reviewed thus far. The highest elastic modulus reported by DeNardo [15] can be attributed to both the high degree of fiber alignment in the print direction and the high fiber content of 50% by weight. However, these two conditions not necessary yield the highest strength. The following example can be used to explain this. For a constant fiber length, increasing the fiber volume fraction leads to a larger number of fibers embedded in the matrix and thus to a larger number of stress concentrators. A larger number of stress concentrators also mean more sites with potential for nucleating damage which can accumulate and lead to a rapid reduction of the load carrying capacity of the material. Therefore, is critical to increase the fiber length For the case of the highest strength reported in the print direction [39], this can attributed to improvement in the mechanisms

for load transfer between the polymer and the carbon fibers as well as to other reinforcements added in the proprietary filler used in this new material formulation.

With regards to the highest mechanical properties reported for the stacking direction (3-direction), the maximum tensile modulus and strength reported in [40] were characterized from specimens printed with epoxy-based inks. The section Material Deposition described the fusion bonding occurring between layers in thermoplastic-based composites, however, the fact that printed epoxy-based inks are cured after the shape generation allows for creation of chemical bonds across adjacent layers. This way, the mechanical properties in the 3-direction become independent of the printing conditions used for manufacturing the specimens and stronger bonds are developed between layers.

In addition to the progress made with materials reinforced with discontinuous elements, significant progress has been reported in the literature for additive manufacturing with continuous fibers. Two methods have been developed primarily for printing with continuous fibers yet utilizing the same major hardware components of FDM or FFF. The primary difference between the two methods is in the process of impregnating the continuous fibers with polymer. In the first method, a strand composed of sized continuous fibers is impregnated in-situ in the extrusion nozzle. In this method, impregnation is conducted by simultaneously feeding the strand of continuous fiber and the filament of neat polymer into an extrusion nozzle. However, the quality of the impregnation, measured by the fraction of the strand of continuous fibers covered with polymer, is frequently low due to the short time for the polymer to diffuse into the strand and the low pressure developed in the extrusion nozzle which is necessary to drive the polymer into the strand. This method though, has been demonstrated for different types of fiber including aramid, carbon and glass fiber as well as for both thermoplastics and thermosets [46, 47, 48, 49, 50, 51, 52]. The second method consists in impregnating the strand of continuous fibers in a step prior to the process of additive manufacturing. This way, a filament for FDM or FFF can be produced with a high level of impregnation. The filament can be then fed into a conventional extrusion nozzle used in FFF or FDM. Although this process of filament extrusion assures more consistent results in terms of impregnation and therefore in mechanical properties, the only record found in the literature of this method corresponds to work carried out with the commercial FFF system Markforged [53]. Extensive work has been done with this system exposing shortcomings of this technology like the inadequate impregnation of the continuous fibers [54, 55, 56, 57]. Moreover, limited design

flexibility for continuous fibers, limited control on key process parameters like temperature and print speed, and low fiber volume fraction attained in printed parts recur in the literature [58, 54, 59]. Nevertheless, a substantial leap in the mechanical properties in the direction parallel to the fibers has been attained with the addition of continuous fibers to printed parts. Like previously done with the survey of materials reinforced with discontinuous fibers, the maximum mechanical properties reported in the literature with the two methods described herein are summarized in Table 2.2. In this case, the materials with the highest tensile elastic modulus also corresponded to the materials with the highest tensile strength. All the data considered in the survey of printing with continuous fibers can be found in Table A.11 of the APPENDIX A.

Table 2.2 Highest Mechanical Properties Reported in the Literature for Polymers with Continuous Reinforcements.

Source	**Material**	**Technology**	**Tensile Modulus E_{11} (GPa)**	**Tensile Strength (MPA)**
Hao et al. [51]	CF/Epoxy	In-situ Impregnation	164.4	792.8
Blok et al. [58]	27%vol CF/Nylon	Filament Extrusion	62.5	968.0

The highest tensile strength and modulus reported with in-situ impregnation was achieved with an epoxy resin which generally have lower viscosities than thermoplastic resins, thereby facilitating the impregnation of continuous fibers. However, very limited control on fiber volume fraction was achieved with the method used by Hao et al. [51]. Fiber volume fraction was not characterized in this work, yet the large variability in their experimental results could be the result of variability in fiber volume fraction assuming good impregnation of fibers. It is worthwhile to mention that mechanical properties reported for the same manufacturing method yet for thermoplastic resins are significantly inferior to the ones of thermoset resins due to the implication of the viscosity.

With regards to the highest mechanical properties reported for extrusion of pre-impregnated fiber filament, significant variability in mechanical properties has been noticed in the results reported across the literature reviewed, and the observation of inconsistent fiber impregnation recurs throughout most of the work review. Except for the mechanical properties reported by Blok et al. [58], all the other reports on mechanical properties yielded values below

the ones advertised by Markforged [60]. Nevertheless, the results reported by Blok et al. [58] suggests significant improvements in the consistency of the material form supplied with the Markforged printers, yet further experimental tests should be carried out to provide confidence in the values reported.

This survey on mechanical properties for polymers reinforced with both discontinuous and continuous elements is meant to serve as a reference for what is possible in terms of mechanical properties with extrusion additive manufacturing. Critical issues with both continuous and discontinuous reinforcements were discusses like fiber impregnation in continuous fiber systems or fiber length in discontinuous fiber systems. Finally, printing with polymers reinforced with continuous fibers shows a lot of promise but, additional work must be done on the processing side to make this process not only more reliable but also scalable for larger and more complex geometries. A novel approach on this regard was developed for overcoming the rate limitations of current filament based printing with continuous fibers. This invention is protected under a provisional patent and it is presented in the section Methods and Apparatus to Additively Manufacture by Coextruding Continuous Multifunctional Composite Materials of chapter seven.

2.5.2 Process Simulation

The previous discussion on the phenomena involved during Material Deposition highlighted the primary phenomena in EDAM such as heat transfer, fusion bonding, stress evolution and deformation. Furthermore, the mechanisms causing delamination in printed parts during manufacturing was also mentioned as part of the phenomena. This section now provides a thorough review on analysis and simulations developed in general for extrusion additive manufacturing in the categories of heat transfer, fusion bonding, and solidification, stress evolution and damage modeling. One of the main motivations for developing analytical models and predictive simulation tools has been anticipating the residual deformations and residual stresses not only during manufacturing but also after manufacturing of a part. Unlike traditional subtractive manufacturing methods, the mechanical performance of printed parts depends on conditions used for part manufacturing such as printing speed, temperature, etc. Hence, predictive simulation tools are required to anticipate and correct for problems like warpage or delamination prior to manufacturing of a part.

2.5.2.1 Heat Transfer

The evolution of temperature during extrusion deposition of molten material was the first phenomenon addressed due its relevance for predicting bonding between layers, solidification and the subsequent shrinkage of printed material. Yardimci and Guceri [61] were one of the first authors that investigate the heat transfer phenomena in the FFF process and that realized of the strong dependence of cooling history on the bond formed between beads in FFF. They constructed a 1-D heat transfer model considering each printed layer as one element in a mesh developed for the finite volume method. Layers were considered as closed or open loops and the heat losses varying with exposed surfaces were treated as sink terms that evolve during the solution. Open loops did consider heat losses at the ends, whereas close loops only considered heat losses from exposed surfaces. To simplify capturing the evolution of heat capacity over temperature, especially around the phase change, the problem was derived in terms of enthalpy energy. In a different publication, the same group presented the steady state analysis carried out in 2D for predicting thermal conductivities of printed components [62]. A few years later, Thomas and Rodriguez [63], developed an analytical solution for a 2-D transient heat transfer analysis assuming symmetry on the plane normal to the print direction or in other words, assuming infinitely long beads. In his model, beads of rectangular cross section were arranged in the form of a wall along the staking direction. This model was developed with the goal of predicting interfacial temperature histories to investigate the evolution of bead-to-bead properties. In another work, Li et al. [64] presented a 1-D heat transfer analysis to model the cooling process of printed beads utilizing lumped-capacity analysis which assumes that the temperature is uniform across the cross section of the printed bead. This heat transfer analysis was combined with a coalescence model to investigate the surface tension driven flow of molten material in the early stages of the material deposition. A similar lumped capacity heat transfer analysis was performed by Bellehumeur et al. [65] in order to investigate the effect of processing conditions on the neck growth between adjacent filaments. Sun et al. [66] also utilized the lumped-capacity thermal model developed by Li et al. [64] to also investigate the effect of processing conditions on neck growth. Costa et al. [67] developed an analytical solution for a 1-D transient heat transfer analysis to predict temperature evolution of a printed bead. In their analysis, conduction along the printing direction was neglected and uniform temperature across the bead was assumed. Yet, thermal contacts between beads were taken into consideration. Based on the transient solution developed for a single bead, a solution was

constructed for multiple beads deposited in a timed sequence [67]. Costa et al. [68] then generalized their previous model for three dimensions so that the deposition process is simulated by dividing a printed bead into discrete segments wherein boundary conditions are applied in a timed sequence. In a latter work of the same authors [68], the finite element method was utilized to perform a thermomechanical analysis wherein cross sections of printed beads were activated in a predefined manner to replicate the sequential deposition of printed beads. The relevance of the convective and radiative heat losses for the temperature evolution of printed beads was assessed with this 2-D FEA model. Compton et al. [69] solved a 1-D transient heat transfer model using the finite difference method. This model is for a single-bead wall, considers conduction in the vertical direction, and depicts the material deposition process by adding nodes that represent each layer at an initial temperature and in a timed manner. Temperature histories predicted with this model were in good agreement with experimental measurements carried out during the printing process of a part. Pooladvand and Furlong [70] also solved a 3-D transient heat transfer model using the finite difference method and reported good correlation between temperatures predicted with the model and experimental measurements recording during the printing process of a cylinder. Yin et al [71], also solved a 3-D transient heat transfer model using the finite element method, however, in this work the sequential deposition of material was mimicked by activating elements using the birth and death functionalities in ANSYS®.

The heat transfer models presented thus far have enabled deeper understanding of the influence of processing conditions on the final characteristics of printed objects, however, none of these have consider neither anisotropy nor are scalable to complex realistic 3-D printed geometries. One of the first 3-D transient heat transfer models that addressed these shortcomings was presented by Brenken et al. [72, 16] . In this work, the same machine code used for manufacturing a part is used to drive the progressive activation of elements in a finite element mesh, thereby virtually replicating the printing process [73]. Figure 2.16 shows an example of the temperature history predicted with this modeling approach for a vertical wall printed with 50% by weight of carbon fiber reinforced PPS [16].

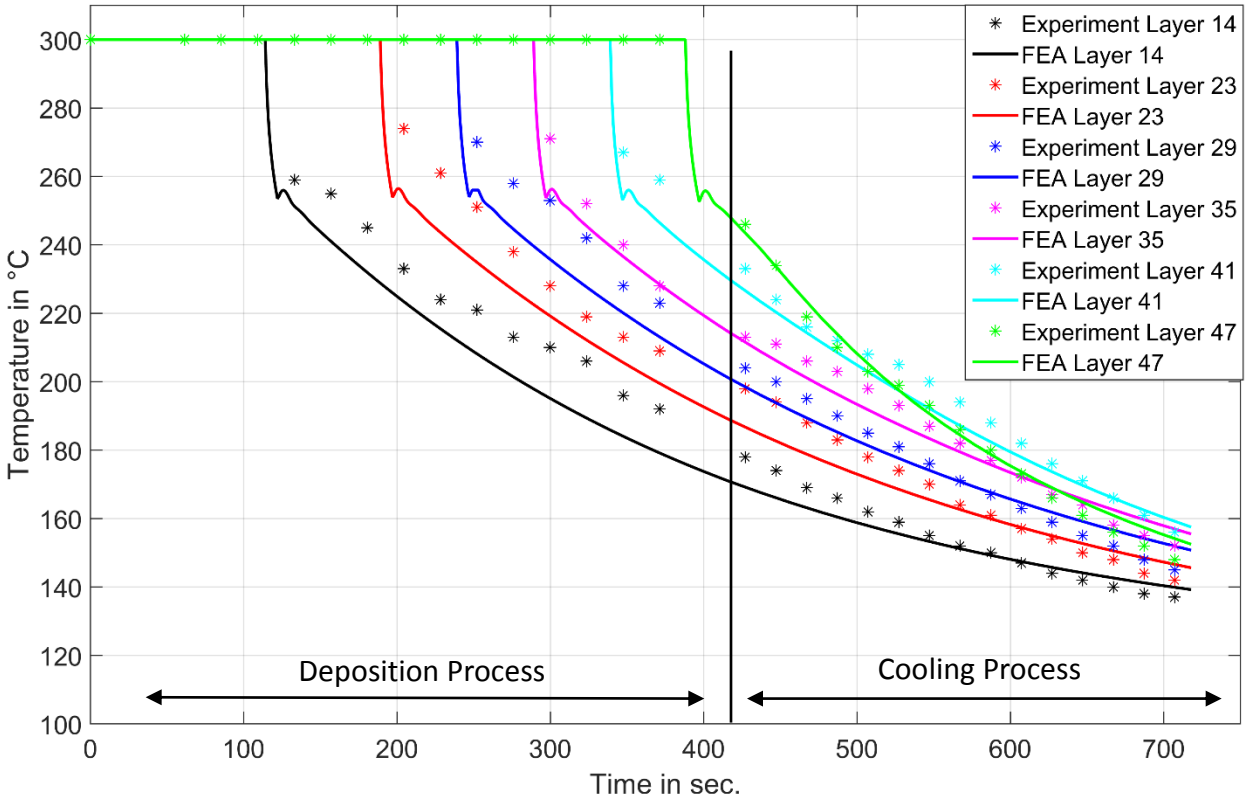

Figure 2.16 Prediction of temperature history with process modeling approach utilized by Brenken [16].

A similar simulation approach, yet for isotropic materials, was utilized by Cattenone et al. [74] to predict the temperature history of the material during the printing process of a part. More details on the structure of the last two simulation procedures are provided in Chapter 4. Although this novel process for simulating the extrusion deposition process enabled depicting the manufacturing process more accurately, elements relevant for the heat transfer process in the EDAM process like the heat losses during compaction or the locality of the convective and radiative heat losses are still missing. Hence, Chapter 5 extends the work from Brenken [16] by including local heat transfer mechanism like heat removed during material compaction, heat of crystallization and local convection conditions.

2.5.2.2 Fusion Bonding

The strong dependence of mechanical properties in the stacking direction of printed parts on the bond developed between layers has stimulated the scientific community to investigate the phenomena involved in the bonding process. The dynamics of the bonding process have been

explained with the aid of the reptation theory of polymer chains by P.G. de Gennes [30] and some of the previous work has been developed based on this contribution.

One of the first attempts to predict the bonding process as a function of the temperature history was conducted by Yardimci and Guceri [62, 61]. These authors defined a bonding potential in terms of the residence time at a given point in the material for which the temperature is above a bonding temperature weighted by the temperature difference between the material point and the bonding temperature. A more complete approach was developed by Thomas and Rodrigues [63] to predict the strength developed between filaments in the FFF process. These authors considered both the wetting process of one bead with other and the interdiffusion of polymer chains which implies that intimate contact must be stablished for the interdiffusion of polymer chains to occur. Since these two phenomena occurs simultaneously, the convolution of a function describing the interdiffusion process and a function describing the wetting distribution function is required. As a result, prediction for stress intensity factors were provided with the wetting-diffusion model developed. Although this model considered more of the phenomena involved in the bonding process, some of the assumptions made were not adequate and thus the predictions made with the model were not in good agreement with the experimental observations. Nevertheless, valuable understanding on the sensitivity to manufacturing parameters like bead dimensions and temperatures was provided. In a series of work, Li, Sun and Bellehumeur [75, 65, 64, 66] utilized a sintering model to predict the growth of the neck formed between two adjacent filaments. The sintering used in this work is based on the energy balance from the work of wetting a surface (surface tension) and the viscous dissipation of the polymer [75, 76]. These previous work also investigated the influence of post-manufacturing heat treatments on the neck developed between adjacent filaments and good correlation was found with experimental observations of neck radii. Based on the sintering model for spheres developed by Pokluda et al. [76], Guralla and Regalla [77] derived a model for sintering of cylindrical filaments. Predictions for strength in the stacking direction were made based on the averaged cross section area of the necks predicted with this model. Similar to previous work, some of the assumptions made like uniform temperature across the printed beads led to predictions of strength that deviate from experimental measurements. A more recent work by Yin et al. [71] presented a model combining the theory of reptation of polymer chains and the Flory-Huggins polymer solution theory to predict the interdiffusion of polymer chains between dissimilar materials. The convolution between this function for interdiffusion and

a function for the wetting process was carried out to predict an average strength ratio. Temperature histories extracted from a 3-D heat transfer analysis were used in the calculations of the strength ratio for simple geometries. Finally, the predictions made with this model were in excellent correlation to experimental measurements.

Previous works on predicting layer-to-layer strength during extrusion manufacturing were reviewed in this section. Although a significant amount of work has been dedicated to this subject, none of these have considered neither reinforced polymers nor semi-crystalline polymers and the analytical solutions developed are limited to simple geometries. Furthermore, the mechanisms governing wetting of adjacent beads during the EDAM process are significantly different due to the use of a compacter and solidification and melting of polymer crystals around the interface becomes important for bonding of semi-crystalline polymers. Hence, this topic is addressed in this dissertation through experimental and simulation work.

2.5.2.3 Solidification, Stress Evolution and Damage Modeling

In addition to temperature history of the printed material and bonding between printed layers, deformation, development of internal stresses and failure during manufacturing or post manufacturing are of major relevance for the EDAM process. Therefore, these topics have stimulated the scientific community as well as commercial software developers to provide solutions to reduce the empirical process of determining the right printing parameters that is commonly found in additive manufacturing. One of the first work investigating the deformation and residual stresses in parts printed with FFF was carried out by by Zhang and Chou [78]. These authors utilized a finite element model wherein the printing process was replicated by activating elements according to the printing path. The element birth and death functionalities in the finite element code ANSYS® were utilized to control the stepwise activation of elements in the coupled thermomechanical analysis. Newly added elements were exposed to convective heat losses in the heat transfer analysis while the nodes at the bottom surface of the part were fully constrained to resemble the build plate. After the simulation of the printing process by sequential element activation, additional steps were utilized for cooling of the part followed by removal of the part from the build plate. With regards to material properties utilized, temperature dependent enthalpy was utilized while the coefficient of thermal expansion and elastic modulus of the material were assumed constant. Utilizing this simulation framework, the authors investigated the effects of three

different printing toolpaths on the residual stresses and part deformation. Due to the simplifications made on the material behavior, only qualitative results were produced in this work. In a later publication of the same group [79], the effects of three manufacturing parameters, namely printing speed, layer thickness and width of the printed bead, were virtually investigated with the finite element simulation framework developed previously [78]. Their findings highlighted the sensitivity to the printing speed and bead height for part deformation whereas the bead width by itself was found nearly irrelevant for the same metric. Talagani et al. [80] described a simulation toolset developed by the company AlphaStar to predict deformation, internal stresses and delamination using Linear Elastic Fracture Mechanics (LEFM) during manufacturing by EDAM process of a part. This framework was demonstrated for the printing process of a vehicle chassis printed in the BAAM system with carbon fiber reinforced ABS. In their simulation approach, the machine code used to manufacture the part is used to drive the element activation in a stepwise manner as well as to assign local orthotropic material properties. Calibration of thermal and mechanical properties was carried out with experimental measurements from the print of a vertical wall and measurements of tensile properties in the printing and stacking direction, respectively. Only a qualitative description of the results was reported, and no validation was presented for the simulation of the Strati vehicle. Cattenone et al. [74] also utilized the machine code to control the activation of elements in the process simulation of the FFF manufacturing process. The heat transfer analysis was described previously, yet unlike the previous work that assumed elastic material behavior, incremental plasticity theory was utilized to model the behavior of the ABS. This way, the yield stress is a function of temperature with its magnitude increasing linearly below the glass transitions temperature, T_g, and its magnitude approaching zero at temperatures above T_g. As a result, the material flows at temperatures above T_g yet begins to accumulate stresses as the material is cooled below T_g, thereby capturing to some degree the viscoelastic nature of the polymer. The geometry of a bridge with multiple vertical supports was used for validating this modeling approach through measurements of deformation at prescribed test points. The model predictions were within 20% of the deformation measured experimentally. To the best of the knowledge of the author, the most complete simulation work developed for predicting stresses and deformation was developed by Brenken et al. [81, 16]. In this work, orthotropic thermoviscoelastic material behavior was used for modeling carbon fiber reinforced PPS used in the EDAM process. Validation of this simulation approach was carried out by predicting deformation of a four-layer

plate where the two layers at the bottom are oriented in the same direction and the two layers at the top are oriented at ninety degrees with respect to the bottom ones, thereby giving rise to anticlastic bending upon cooling of the printed plate to room temperature. Deformations were extracted from the printed plate along the two in-plane principal directions (X and Y) and excellent correlation was obtained between the experimental measurements and the model predictions as shown in Figure 2.17.

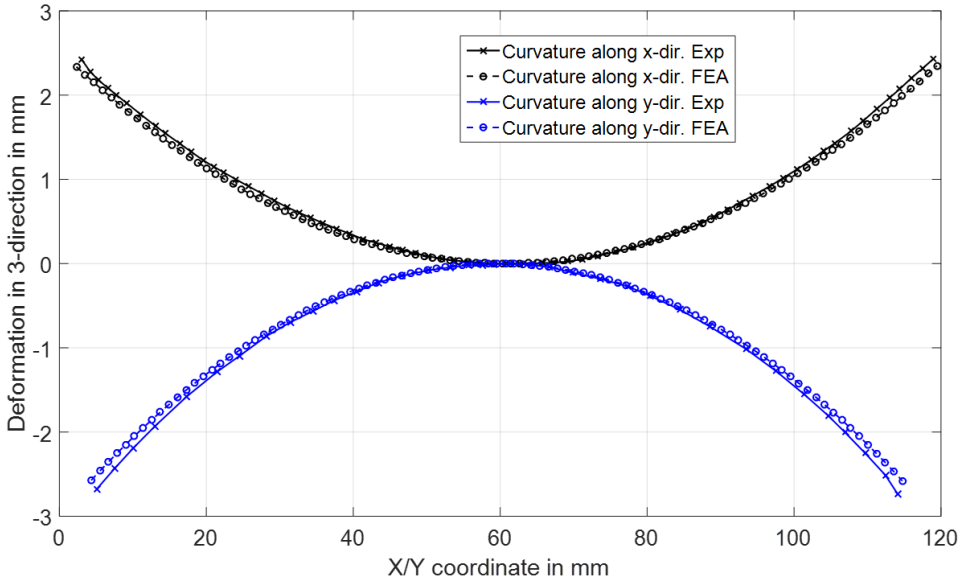

Figure 2.17 Comparison of curvatures measured experimentally and predicted with EDAM process simulation [16].

With regards to damage modeling during printing, to the best of the knowledge of the author only the work of Talagani et al. [80] claims to predict damage by delamination during printing using LEFM, yet no further details are provided by the authors. In terms of predicting the evolution of damage during testing of printed specimens, Ramirez et al. [82, 83] have developed a micromechanics model incorporating the characteristic features of the printed microstructures like fiber orientation distribution and fiber length. Hence, there is a need for predictive simulation tools for anticipating damage at both the intralayer and interlayer scales during part manufacturing. Chapter 6 focuses on predicting process-controlled interlayer properties that are used subsequently to predict damage in printed parts by delamination.

2.6 Tooling Produced with Extrusion Deposition Additive Manufacturing

Additive manufacturing provides unique design flexibility and enables manufacturing of shapes that are not possible through traditional subtractive manufacturing methods like hollow shapes. Furthermore, the arising of large-scale Extrusion Deposition Additive Manufacturing with reinforced polymers has enabled industrial applications that were not conceived before with unreinforced polymers. Examples of this applications in the composites manufacturing industry include tooling with dimensions in the scale of meters for primary operations like molding of parts at room temperature and elevated temperature, fixtures for secondary operations like trimming, assembly of multiple components or for quality inspection of composite parts. In addition to this, the low CTE attained in the printing direction due to the flow induced fiber orientation makes printing of tooling more attractive for composites manufacturing due to the potential for tailoring the CTE of the tooling.

This section focuses on the tooling applications targeted to more demanding conditions of temperature and pressure and provides examples of multiple applications demonstrated with the CAMRI system. One of the first things to consider while evaluating a material for potential use in high-temperature tooling applications is the thermomechanical behavior of the printed material. Figure 2.18-A shows the thermomechanical behavior reported in terms of the storage and loss moduli for the 50% by weight carbon fiber reinforced PPS printed with CAMRI. This thermomechanical behavior was characterized through Dynamic Mechanical Analysis (DMA) of a sample printed in the 1-direction and utilizing a double cantilever beam fixture in a Q800 DMA from TA Instruments® [84].

Since the PPS is a semi-crystalline polymer, the final printed material is composed of three phases, namely carbon fiber, a phase of crystallized polymer and a third phase of amorphous polymer. Therefore, the homogenized thermomechanical behavior is controlled by the contributions of each phase and the interactions between those. In other words, the elastic modulus of the polymer phases is strongly influenced by temperature whilst the properties of the carbon fiber do not change significantly with temperature. This results in the behavior depicted in Figure 2.18-A where two transitions occur, in the first one the material transitions from a glassy to a rubbery behavior around the T_g of the polymer while in the second one the material transitions from a rubbery to a fluid-like behavior at around the melting temperature of the polymer crystals. While the first transition occurs due to recovery of motion of the polymer chains in the amorphous

phase, the second transition occurs due to melting of the polymer crystals which removes all physical constraints in the polymer chains and thus allowing motion of these. This last transition can also be observed in the degree of crystallinity which is a relative measure of the crystallinity content in the crystalline phase. Figure 2.18-B shows the degree of crystallinity (DOC) as a function of temperature determined through Differential Scanning Calorimetry (DSC). A DSC Q2000 [85] from TA Instruments® provided the heat flow data also shown in Figure 2.18-B. The step transition in the DOC occurs over a relatively narrow temperature range which correlates to the rubbery to fluid like transition observed in the DMA for the carbon fiber PPS material.

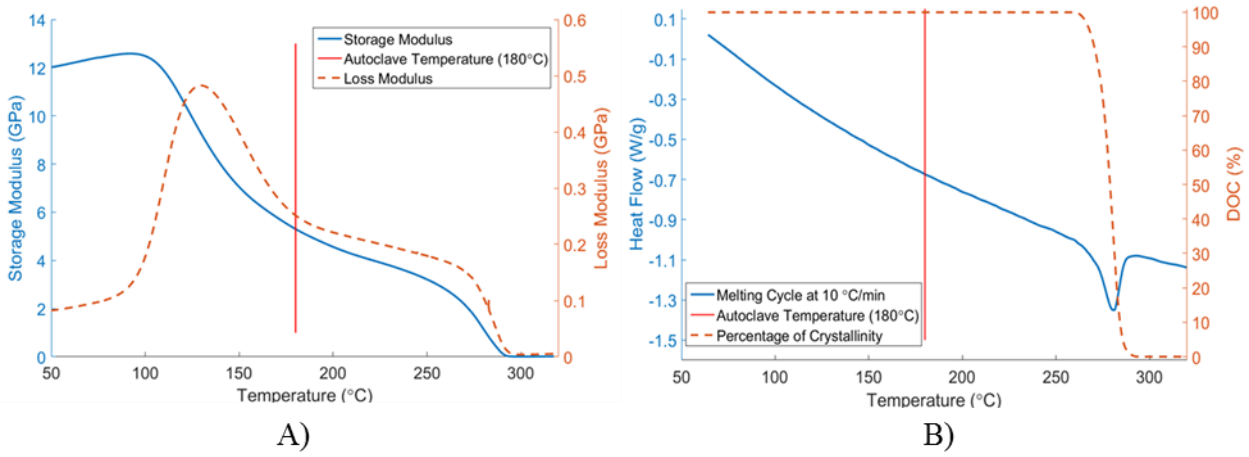

Figure 2.18 A) Storage and loss moduli as a function of temperature of the 50% by weight of carbon fiber PPS characterized with DMA. B) Degree of crystallinity as a function of temperature of the 50% by weight of carbon fiber PPS characterized with DSC.

The previous observations made on the results shown in Figure 2.18 indicate that the material should not be used in a tooling application at temperatures above $250\ °C$, otherwise the shape of the tool is susceptible to change drastically. However, printed tooling is primarily targeted for processing thermoset-based composites which are commonly processed at temperatures in the range of $180\ °C$. A vertical line in each of the plots in Figure 2.18 indicates this target process temperature for which the storage modulus is about 45% of the room temperature storage modulus and the crystallinity remains intact.

One of the first applications demonstrated with carbon fiber PPS using the CAMRI system was one-sided tooling for autoclave composites manufacturing. Figure 2.19-A shows an example of a printed tool for autoclave process manufacturing whereas Figure 2.19-B shows the part

manufactured with the printed tool at $180\ °C$ and 5.6 Bar and with aerospace grade composite material (IM7-8552). The autoclave manufacturing process begins by laying down individual plies of carbon fiber prepreg on the surface of the tooling to form a stack of layers with a predefined sequence. After the prepreg layers are stacked on the tooling surface, the tooling surfaces and the composite material are prepared for the curing process inside the autoclave. While the part is in the autoclave, vacuum, external pressure and heat is applied to assist the curing process. Consequently, the tooling surface must fulfill the following requirements to produce a high-quality part. First, the surface finish needs to be smooth and with a low roughness value, Ra, below $70\mu m$ if the tool is intended for an aerospace application [86]. Second, the surface of the tool should be free of porosity to prevent air leaks while the part is cured with vacuum and the applied external pressure. Third, the tooling surface should be durable so that multiple parts can be manufactured before replacing the tool. And the last but not the least, the thermal expansion of the part should be close to the one of the tooling and the thermal conductivity of the tool can be critical for some part geometries. However, the thermal expansion of the printed tools is highly anisotropic and can vary locally in the printed tool based on local orientation of the printed material. As a result, predictive tools are required to not only anticipate the anisotropic deformation of printed tools, but also to compensate for such a deformation. The EDAM simulation framework presented in Chapter 4 also allows for prediction and compensation of in-service deformation for printed tools.

Figure 2.19 A) One-sided tool printed with 50% by weight of carbon fiber reinforced PPS for autoclave manufacturing process. B) Part manufactured on printed tool with IM7-8552

Kunc et al. [86] and Sudbury et al. [87] also utilized the EDAM process with composites to successfully manufacture one-side tooling for autoclave and for hand-layup composites manufacturing, respectively.

The next application demonstrated with the EDAM process with composites was producing multi-cavity tooling for compression molding manufacturing. Unlike the autoclave manufacturing process, higher internal pressures are required in compression molding operations for flowing the molding material into the tool cavities. An example of a two cavities or two-sided compression molding tool for manufacturing a pin bracket is shown in Figure 2.20.

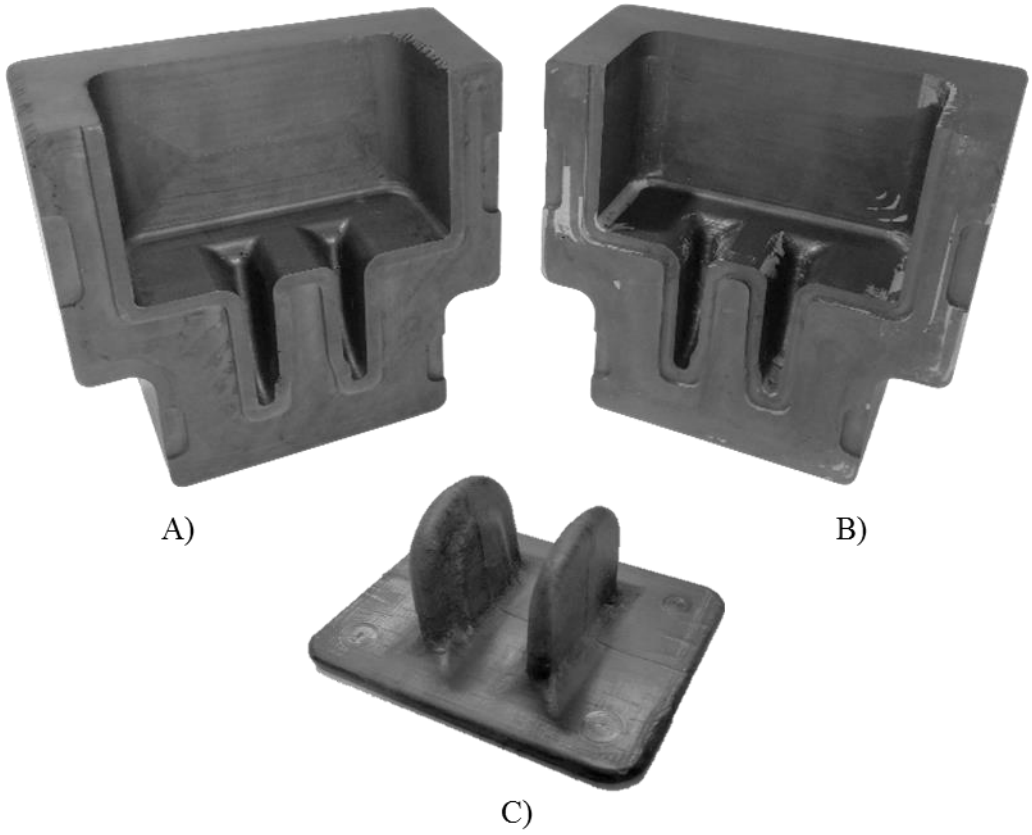

Figure 2.20 A,B) Compression molding tool printed with 50% by weight of carbon fiber reinforced PPS for manufacturing of pin bracket. C) Pin bracket manufactured by compression molding of chopped carbon fiber prepreg (IM7-8552) in a printed compression molding tool.

The pin bracket shown in Figure 2.20-C was molded with the printed tool shown in the same figure and with a molding charged prepared with carbon fiber prepreg chopped in squares of about 2.5 by 2.5 centimeters. The compression molding process with the printed tool is carried out as follows.

First, a molding charge is prepared with carbon fiber prepreg chopped in squares and either piled to fit in the upper section of the tool or arranged in a predefined and controlled configuration. Second, the two cavities of the compression molding are prepared with release agent and clamped with a metal fixture that will contain the printed tool during the compression molding process. The assembly of the cavities and the ram head as well as the molding charge is then heated in a forced convection oven to the process temperature of $180\ °C$ for about 20 minutes. Third, the preheated compression molding tool with the molding charge placed inside and the ram head installed on the top opening of the tool are then transferred to a hydraulic press. Internal pressures of up to around 69 Bar have been utilized successfully in this type of printed tools to flow and consolidate the molding charge in the molding cavity. In a final step, the metal clamp is removed, and the part can be easily removed from the compression molding tool.

Other application for EDAM with composites is tooling for hot stamping manufacturing of composites. Figure 2.21 shows an example of a two-sided tool for hot stamping manufacturing printed with 50% by weight of carbon fiber reinforced PPS in the CAMRI system. The hemisphere shape shown in Figure 2.21-C was successfully manufactured with the printed hot stamping tool following the process described next. First, both halves of the tool were preheated in a forced convection oven to the process temperature of $180\ °C$. After the tool equilibrated to the manufacturing temperature, the bottom half was transferred to a hydraulic press where a preform molding sheet was placed on top of the bottom half. Subsequently, the top halve of the tool was located on top of bottom half yet pressing partially the molding sheet. Finally, internal pressures of up to 69 Bar were applied with the hydraulic press to consolidate the molding sheet between the two halves of the printed tool.

Two additional aspects of printed tools that deserve further consideration are the durability of the tooling surface and the creep deformation of the tooling surface. A scarce number of investigations in durability of printed tooling are available in the literature due to the relatively recent industrial adoption of this technology. Nevertheless, Sudbury et al. [87] investigated the durability of the surface of printed tools prepared with multiple commercial coating systems. The tools investigated were used for manufacturing parts by hand-layup and they reported up to four parts manufactured with the best coating tested. With regards to the creep deformation in the printed tools. Kunc et al. [86] investigated the creep deformation of printed tools in autoclave manufacturing and reported deviations from the original tool shape within 0.1 mm after an

autoclave cure cycle. Similarly, Barocio et al. [88] also investigated the creep deformation of tools printed with 50% by weight of carbon fiber reinforced PPS and reported deviations from the original shape also within 0.1 mm.

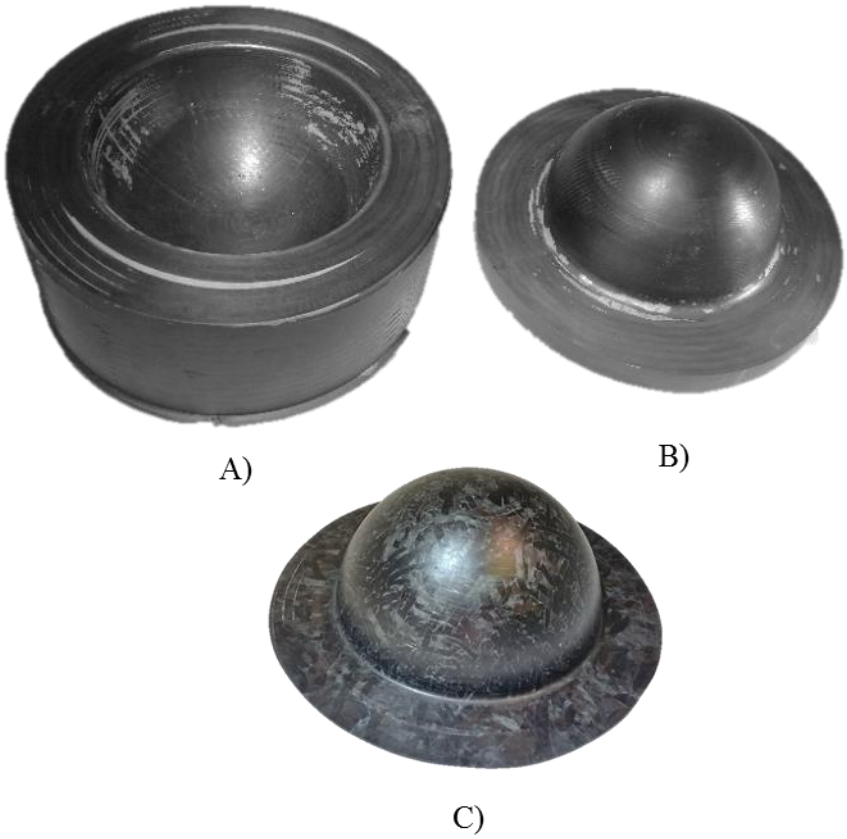

Figure 2.21 Hot stamping manufacturing tool printed with 50% by weight of carbon fiber reinforced PPS and used for manufacturing the hemisphere shape with a carbon fiber preform.

In order to provide a reference of the magnitude of the creep deformation in a printed tool after an autoclave cure cycle, the surface of the tool printed for manufacturing the air inlet duct shown in Figure 2.19 was characterized before and after the autoclave manufacturing of a part. The characterization of the surface of the tool was conducted with a FARO Edge ScanArm© HD and utilizing the laser line scanning functionality. The point cloud obtained in the characterization of the baseline was then used to reconstruct a continuous surface in the software Geomagic Wrap 2015®. Using this baseline surface, the point cloud of the second scan was automatically aligned

to the baseline surface in the software Geomagic Wrap 2015® and deviations between the point cloud and the baseline were computed. Figure 2.22 shows the surface dimensional deviations that resulted from the manufacturing of a part on the printed tool in the autoclave. The average deviations observed in Figure 2.22 are in good agreement with previous observations reported (0.1 mm), however, some outliers appeared due to defects on the surface of the tooling.

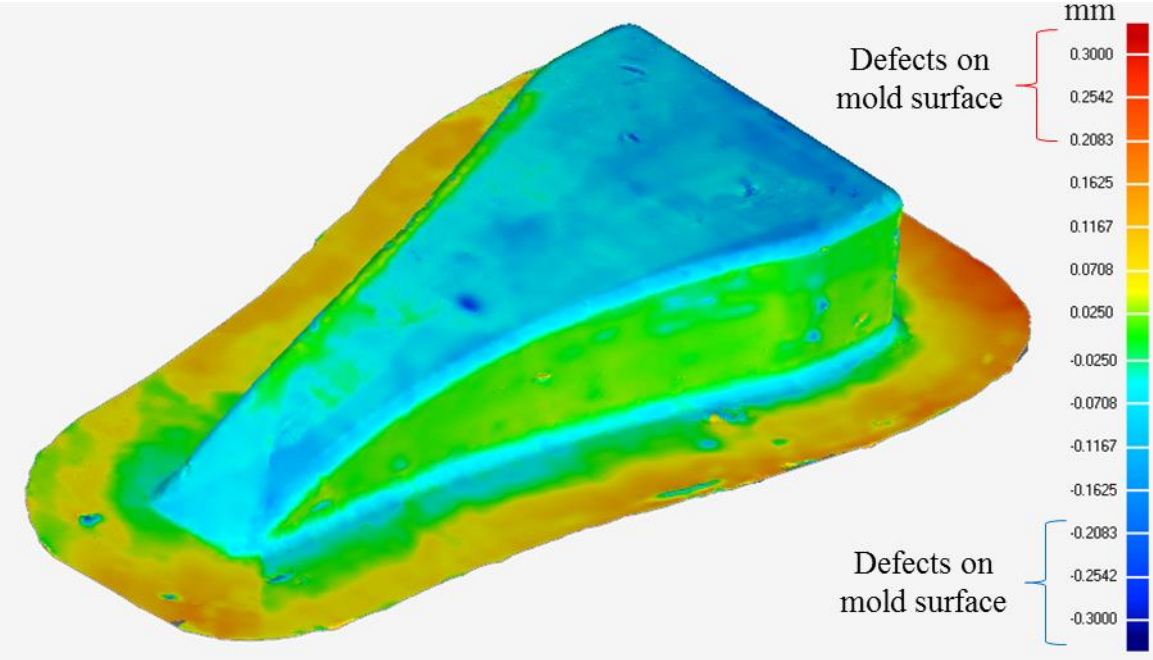

Figure 2.22 Surface dimensional deviations after using a printed tool in an autoclave manufacturing cycle.

Applications for the EDAM process with composites were demonstrated and presented in this section and challenges like anisotropic thermomechanical deformation of printed tools or creep deformation were described. Although it is not included in this dissertation, the EDAM process simulation framework presented in the chapter EDAM PROCESS SIMULATION can be utilized to predict in-service deformation of printed tools and to compensate for such deformations. Finally, a technology for printing in-situ heating elements near the surface of printed tools was developed. The reader is referred to the section Heating of 3d Printed Tooling with Circuits Printed In-Situ through Fused Filament Fabrication of chapter 7 for further details.

3. THE COMPOSITES ADDITIVE MANUFACTURING RESEARCH INSTRUMENT

The Composites Additive Manufacturing Research Instrument (CAMRI) is a medium-scale Extrusion Deposition Additive Manufacturing (EDAM) system developed at Purdue University with the aim of functioning as a research platform for investigating the phenomena involved in this manufacturing method. This chapter presents the architecture of CAMRI system in its different domains, mechanical, electronics and control systems and provides a throughout description of the process control implemented in CAMRI.

3.1 Motivation and Objectives

Efforts to transitioning the extrusion deposition technologies to manufacture parts in the scale of centimeters with FFF to the scale of meters with what today is known as EDAM started around 2013 with the pioneering work at ORNL [3]. However, by this time and for the next two years there were not EDAM systems commercially available until the BAAM® system was commercially released by CI©. By the same time circa 2014, the composites additive manufacturing group at Purdue was recently formed with the interest of printing with high-temperature polymers reinforced with high fiber content. Furthermore, the needs of our group at that time were for a research instrument of a scale smaller than BAAM and with the flexibility to vary control and process parameters rather than a commercial system with a closed control system. Hence, the first plans for developing the CAMRI system were crafted to fulfill the following objectives. The first objective was to be able to process high-temperature polymers like Polyether ether ketone (PEEK), which requires processing temperatures up to $400\ °C$, and with high content of reinforcing fibers. The second objective was to achieve a maximum deposition rate in the range of 5 to 7 kg/h of highly filled polymers, yet with the capacity for printing at lower rates. The third objective was to be able to control every aspect of the extrusion and deposition process. Since CAMRI was conceived as a research platform to conduct controlled experiments and validate simulations of the manufacturing process, the fourth objective was to enable data acquisition throughout the manufacturing process of a part. This functionality became extremely valuable later for both validating and driving simulations of the EDAM process. The last but not the least

objective defined was a target printing envelop. A cubic envelop with external dimensions of 0.5 by 0.5 by 0.5 meters was targeted for CAMRI. The CAMRI design developed to fulfill these requirements is presented in more detail in the next section.

3.2 Architecture of the CAMRI System

The objectives outlined previously for CAMRI were the starting points for sizing the components for both the extrusion system and the gantry robot used for material deposition. CAMRI is divided into two subsystems, namely the material extrusion system and the material deposition system. The motivation for choosing the architecture used in CAMRI is presented in this chapter section and the details of both subsystems are presented next.

Extrusion technology has been used extensively in the polymer processing industry for manufacturing products all the way from bags to high technology films [18]. Moreover, extrusion of fiber reinforced polymers and mechanisms leading to degradation of the fiber length during extrusion have been addressed in previous investigations [19]. Nevertheless, light weighting of extrusion equipment was never a priority since this type of equipment is commonly designed to operate continuously in a semi-permanent manufacturing setup. This prior extruder design mindset is not practical for an EDAM system with an extrusion system mounted on a gantry robot that performs movements with considerable accelerations. Improvements on extruder design for EDAM systems occurred later with the advent of the commercial systems for large scale additive manufacturing. In addition to the prohibiting weight of commercial extruders, our interest on closely monitoring the process of material deposition led to the decision of mounting the extrusion system in a stationary frame. This way, the extrusion system rests on a stationary frame while a gantry robot performs the printing trajectory for manufacturing a part layer-by-layer on top of the build plate. Additional benefits of the architecture with a stationary frame included the flexibility for mounting cameras for inspection and monitoring of the printing process as well as mounting of a volumetric feeder for conveying pellets of long discontinuous fiber into the extrusion system. Figure 3.1 shows a schematic of the CAMRI system with the principal components labeled.

There is a second fundamental difference in the operation of the extrusion system for EDAM with respect to traditional extrusion operations. Continuous production of goods by extrusion is commonly carried out in steady state conditions to minimize variability in the

manufactured goods, however, the EDAM process continuously demands changes in material flow rate to the extrusion system, thereby conditioning the steady state operation of the same.

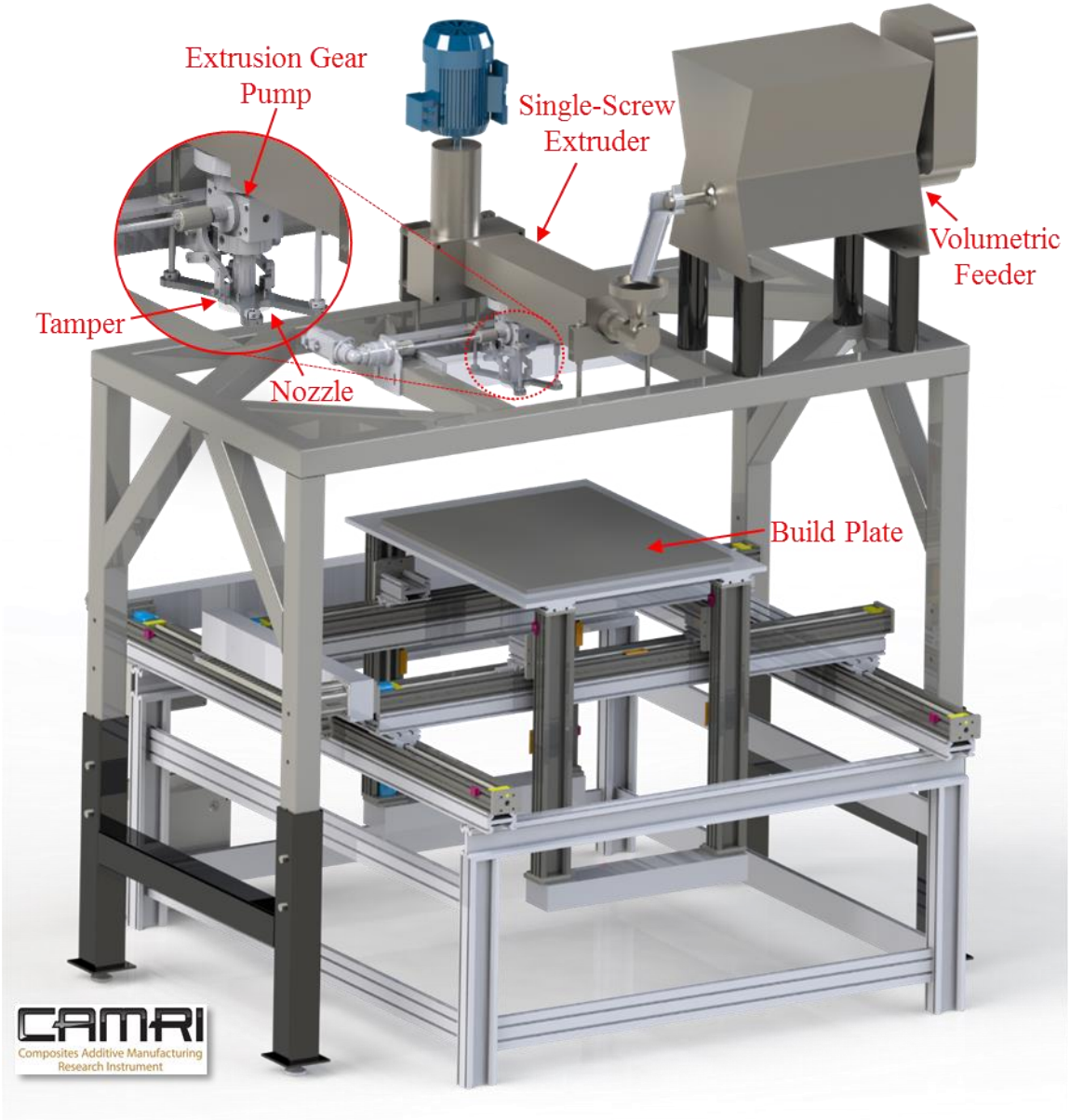

Figure 3.1 Schematic of the Composites Additive Manufacturing Research Instrument.

As a result, innovative approaches for controlling the extrusion system must be developed to achieve consistent and continuous material deposition in the EDAM process. The approach implemented in CAMRI to control the extrusion system is detailed in the section Material

Extrusion System whereas the operation of the gantry robot and other systems involved in the material deposition process like the compacter are detailed in the section Material Deposition System.

3.2.1 Material Extrusion System

The motivation for selecting the architecture of a stationary frame for mounting the extrusion system was provided before. Now the focus is on describing the components of the extrusion system and the variables involved in the process. The extrusion system used in CAMRI is composed primarily by the four elements labeled in Figure 3.2. These four elements can be described in the same sequence the feedstock material flows through the extrusion system. First, the volumetric feeder provides controlled delivery of pelletized feedstock to the single-screw extruder.

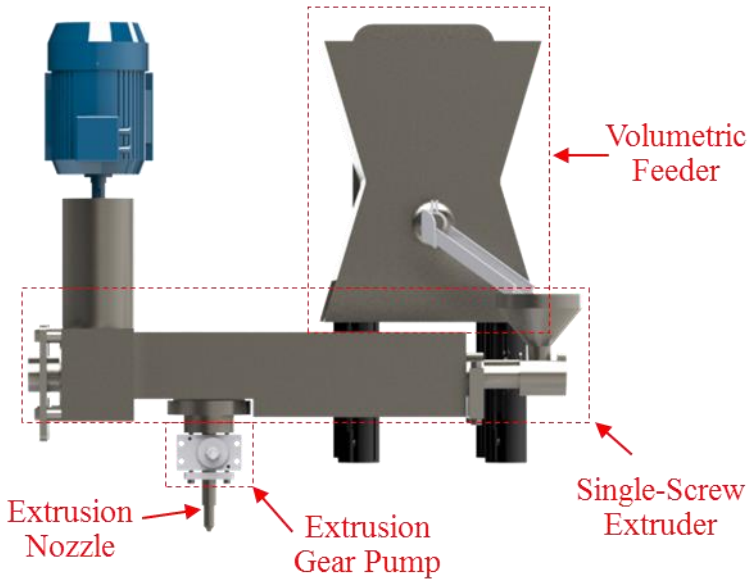

Figure 3.2 Extrusion system developed for CAMRI.

Controlling the feeding of pellets is essential to successfully process the long discontinuous fiber pellets used in this work since flood feeding of a screw with a flight depth smaller than the length of the pellets gives rise to premature damage of the pellets in the feed zone and potential clogging of the hopper. Prior to loading pelletized material to the volumetric feeder, drying of the feedstock

material is critical to remove moisture in hygroscopic materials. A volumetric feeder model FD89 and manufactured by IPM Systems is the first element in the extrusion system. This particular feeder was chosen because of its open architecture that allowed for interfacing with the rest of the control system developed for the extrusion system.

A second element of the extrusion system is the single screw extruder. The components of the $24{:}\,1$ length to diameter ratio single-screw extruder used in CAMRI are the hopper, the barrel, the $25.4\ mm$ diameter screw and the driving system comprised of a gearbox and a $3\ HP$ motor. The pellets enter the extruder through the hopper and from this point these are conveyed by the geometry and rotating action of the screw from the feeding zone through the melting zone and finally into the compression zone. A shallow and therefore long compression zone with a compression ratio of 3 pressurizes the molten material prior to entering the metering zone. Such a shallow compression zone is desired to lessen degradation of fiber length in single-screw extrusion [19]. The extruder used in CAMRI is a horizontal microtruder© provided by Randcastle© and is equipped with a Posi-Melt™ screw developed by MD Plastics©. This extruder is equipped with three heating zones equally distributed along the barrel and is capable of processing material at temperature up to $425\ °C$.

A third element in the extrusion process is the extrusion gear pump. The extrusion gear pump is in series with the single-screw extruder and provides precise volumetric flow rate control during printing. Volumetric flow rate in an extrusion gear pump behaves linearly with the rotational speed of the pump since the material displaced per revolution is defined by the geometry of the internal gears. However, a constant pressure is required at the inlet of the pump in order to achieve a consistent flow rate. The section Control of the Material Extrusion describes the approach used to achieve a constant pressure at the inlet of the pump despite all the perturbations arising from changes in flow rate during the EDAM process. The extrusion gear pump used in CAMRI is the model $12/12$ manufactured by PSI Polymer Systems® and delivers up to $6.8\ kg/h$ of molten material. Further, the extrusion gear pump is equipped with two heating zones to assure uniform temperature distribution in both the extrusion gear pump and the connector interfacing the pump with the single-screw extruder. Two pressure sensors are utilized to monitor pressure at the inlet and outlet of the extrusion gear pump, respectively.

The extrusion nozzle is the fourth element in the extrusion system. The internal design of the extrusion nozzle is critical for the final printed microstructure since it affects the fiber

orientation distribution in the extrudate leaving the nozzle. The flow phenomena controlling the evolution of fiber orientation in converging zones and in zones with constant diameter was discussed in the section Material Extrusion. In addition to influencing the fiber orientation, the nozzle design also affects the pressure drop across the nozzle. In other words, the total amount of shear deformation the material undergoes as it flows through the nozzle increases as the nozzle become longer or the diameter is reduced. Further, sudden changes in pressure like at the start or the stop conditions during printing of a part can also lead to either lack in the flow of the material or ooze of material, respectively. An approach that considers this impedance of both material and system for controlling the deposition process is also presented in one of the next sections.

Nozzles are custom made and have been manufactured with final orifice diameters of 3.175 and 4.0 mm. Additionally, the nozzle is equipped with a heating zone to maintain temperature consistency in the material delivered at the tip of the nozzle. To conclude this section on the extrusion system, the components of the extrusion system are summarized in Table 3.1.

Table 3.1 Components of the extrusion system in CAMRI.

Element of the Extrusion System	**Characteristics**
Volumetric Feeder	Model FD89 by IPM Systems
Single-Screw Extruder	Extruder: Microtruder© by Randcastle© and Screw: Posi-Melt™ by MD Plastics©
Extrusion Gear Pump	12/12 by PSI Polymer Systems®
Extrusion Nozzle	3.175 and 4.0 mm, Custom made

3.2.2 Material Deposition System

The material extrusion system described previously provides controlled delivery of extrudates for the EDAM process, the material deposition system then handles the extrudate after leaving the extrusion nozzle by performing a predefined trajectory that defines a part and by compacting the extrudate. Two primary components define the material deposition system in CAMRI, a gantry robot that moves the build plate in a three-dimensional Cartesian coordinate system and a tamper that oscillates and compacts the extruded beads. Further, the motion planning and the coordinated motion for the gantry robot is performed with a controller for numeric control machines, further details are provided towards the end of this section.

Figure 3.3 shows the gantry robot developed for the material deposition system in CAMRI. Unlike the large-scale commercial systems like BAAM or LSAM where the gantry robot carries the extrusion system, in CAMRI the extrusion system is stationary, and the gantry robot moves the build plate with the part printed on top. This gantry robot was designed and developed specifically for CAMRI utilizing modular linear motion guides BiSlide® provided by Velmex® which are depicted black in Figure 3.3. These BiSlide® modular linear guides consist of dovetail ways that house carriages equipped with PTFE bearings to provide smooth sliding motion along the linear guides.

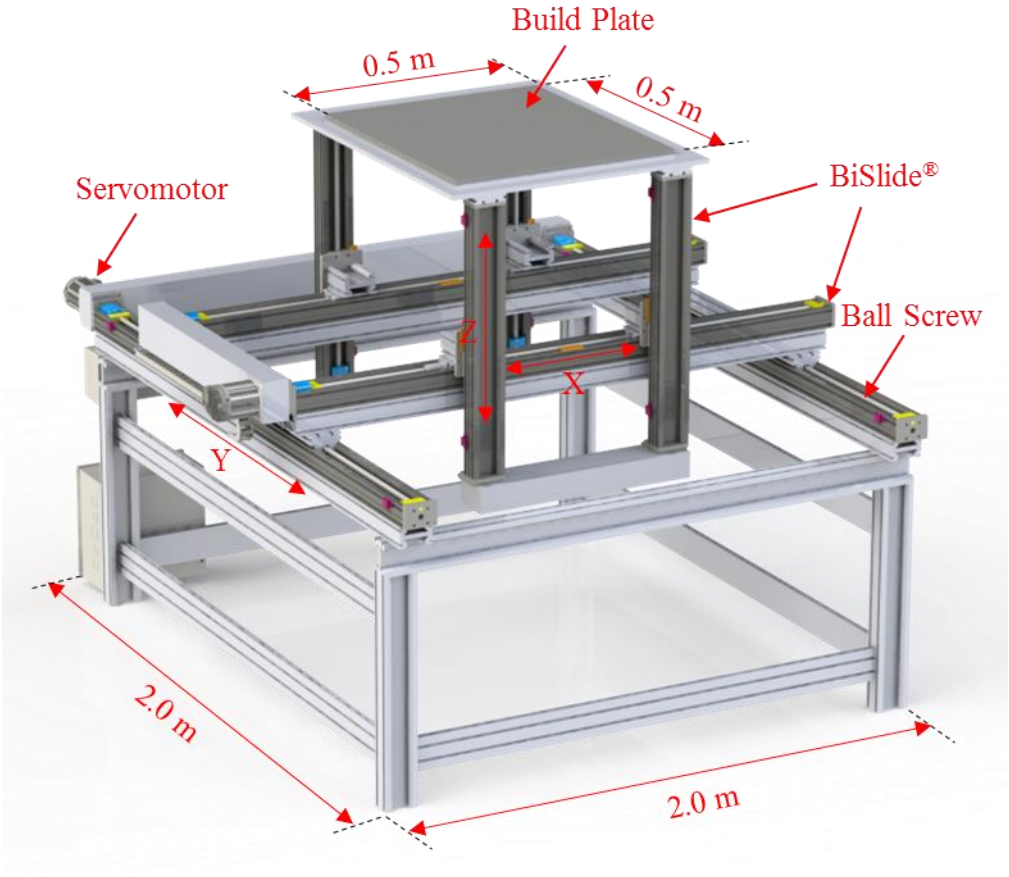

Figure 3.3 Gantry robot utilized in CAMRI.

Linear motion of the carriage is achieved through ball screws that translate rotational movement of servo motors to linear motion with minimal friction. Ball screws are both mounted parallel to the linear guides and contained within the modular BiSlide® guide. It should be noted the BiSlide® guides were originally supplied with lead screws, however, these were replaced with ball screws

to lower friction and improve the repeatability in the motion of the system. Except for the Z axis that utilizes four BiSlide® modular linear guides, the X and Y axes utilize two BiSlide® modular linear guides per axis. Synchronized movement of each pair of BiSlide® used in the X and Y axes is realized with timing belts connecting the servomotor with each of the BiSlide®. However, digital timing is used in addition to the mechanical timing to coordinate the motion of the two pairs of BiSlide® in the Z axis.

With regards to the servomotors powering the CAMRI system, direct current (DC) brushless servomotors supplied by Teknic© allowed for speeds of up to $12\ m/min$ the X-Y plane and speeds up to $3\ m/min$ the Z axis. Dynamic forces resulting from the mass of both the gantry robot and a payload assumed equal to 50% of the volume of the printing envelop filled with reinforced polymer were used to estimate the force requirements for each of axis. Additionally, frictional forces were estimated with information provided by Velmex®. Based on this force estimates, servomotors were sized to meet the needs of force with a design factor of 1.25.

One disadvantage of the architecture used for the gantry robot is that the travel distance required in the X and Y axes to travel within the build plate must be at least twice the dimensions of the build plate for the corresponding direction. Therefore, the footprint of the gantry robot is at least four times the area of the build plate.

Heating the build plate is especially beneficial for controlling the temperature history of the material printed near the build plate. Therefore, the aluminum build plate mounted on top of the gantry robot is equipped with a temperature control zone. Six strip heaters mounted underneath the build plate provide up to 1200 watts, thereby reaching maximum temperatures in the range of $250\ °C$ on the top surface of the build plate. Thermal insulation placed underneath the strip heaters and build plate protects the gantry robot from the heat of the build plate.

The second element of the deposition system is the compaction system. The tamper was the choice for the compacter mechanisms used in CAMRI owing to the simplicity of this approach for compacting extrudates in small features like corners and infill regions of a printed part. A tamper consists of an annulus placed concentric to the extrusion nozzle and with an internal diameter slightly larger than the diameter of the extrusion nozzle and an external diameter that is multiple times the width of the printed bead. During material deposition, the surface of the tamper describes reciprocating motion, thereby contacting and deforming the extrudate of molten material multiple times per second. This way, the extrudates leaving the extrusion nozzle are compacted

despite the direction traveled. Also, the flow of material in the stacking direction during compaction is prevented with the surface of the tamper that spans multiple beads at the same time. Figure 3.4-A shows a side view of the tamper utilized in CAMRI. The mechanical linkage that provides the reciprocating motion of the tamper is composed of six links which can be listed in the same order the motion propagates from the motor to the tamper as depicted in the kinematic diagram shown in Figure 3.4-B.

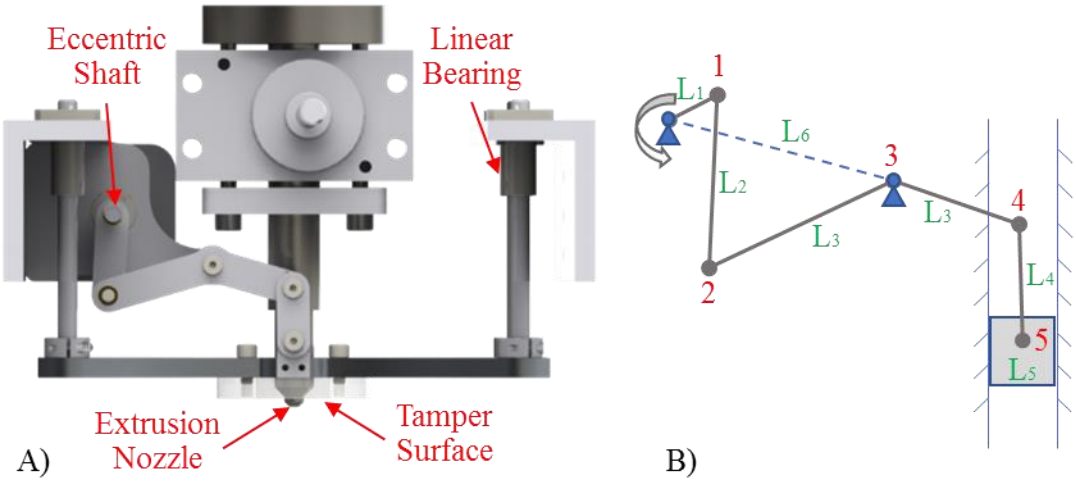

Figure 3.4 A) Section view of tamper compaction system utilized in CAMRI. B) Schematic representation of 6-bar mechanism utilized to create reciprocating motion of the tamper.

The first link, L_1, corresponds to the crank defined by the eccentric shaft attached to an electric motor on one side and to a connecting rod on the other side through the revolute joint 1. The second link, L_2, corresponds to the bar connecting the crank with a ternary link through the revolute joint 2. The ternary link, L_3, which contains revolute joints 2 through 4 is the third element in the chain. This ternary link functions as a lever that reduces the amplitude of the displacement at joint 4 with respect to the amplitude of the displacement introduced at joint 2 through the fulcrum located at the revolute joint 3. Similarly, the force applied in joint 2 is amplified at joint 4. The fourth element, L_4, of the kinematic chain is a bar that connects the ternary link at joint 4 with the slider link through the joint 5. A slider with restrained motion in the direction transverse nozzle yet with freedom to move parallel to the nozzle is the fifth element, L_5. The sixth and final element corresponds to the ground link, L_6, connecting joint 3 and the center of the motor shaft.

The kinematic equations that describe the reciprocating motion of the tamper as a function of the angular speed of the motor are provided in APPENDIX B. These set of equations were used to design the six-bar mechanism such that the target stroke of $2\ mm$ is attained and the maximum force is delivered while compacting the material. With regards to the rotational motion required as input for the tamper, a 24 VDC motor controlled with Pulse Width Modulation (PWM) delivers controlled rotation to the six-bar mechanism of the tamper.

The last consideration in the design of the tamper was to prevent adhesion of the material during compaction. Multiple materials were tested to preclude adhesion of printed material to the surface of the tamper during printing, including PTFE and ceramic coated aluminum, however, it was found the printed material would begin to stick to the surface of the tamper after reaching a critical temperature. Based on this initial observation and the approach of cooling the tamper used in the BAAM systems [5], a tamper design with active air cooling was created. The actively air-cooled tamper designed for CAMRI is manufactured out of aluminum and is equipped with internal channels for air cooling. Further, the tamper is instrumented with a thermocouple to record temperature near the surface of the tamper which enabled to investigate the effects of temperature on the adhesion of printed material to the surface of the tamper. The critical temperature for the carbon fiber reinforced PPS used in this work was found around $100\ °C$ which is in the range of the glass transition temperature of the polymer.

The last element considered as a part of the material deposition system is the motion control of the gantry robot. As mentioned before, the slicing process provides the machine code that contains the trajectory to guide the material deposition in EDAM. Printing trajectories are commonly prescribed in the form of G-code, a programing language widely used for controlling Numerical Control (NC) machines. Therefore, an NC controller is required not only to translate the G-code into trajectories but also to coordinate the motion of the axes in the gantry robot for executing the prescribed trajectories. In addition to the standard capabilities of commercial NC controllers, an open-source platform that allows for manipulation of motion parameters and with the flexibility to implement user-defined functionalities was desired for CAMRI. These requirements were met with the commercial yet at the same time open-source NC controller KFLOP© [89]. This controller is based on a Digital Signal Processor (DSP) and is equipped with a suite of libraries developed for trajectory planning, coordinated motion, G-code interpretation and geometrical corrections. Additionally, user-defined programs can be implemented and

executed in parallel to the motion calculations. This feature was critical for the implementation of the process controllers described in the following section. To interface with KFLOP©, a Human Machine Interface (HMI) hosted in a computer provides the means to load and preview machine code, however, the real time requirements of the system like motion calculations are buffered from the host computer to KFLOP©. This way, none of the critical operations related to the motion control are interfered by other processes running in the host computer. Furthermore, KMotionCNC© the HMI provided with KFLOP©, provides for ease customization to suit needs of specific applications as is the case of CAMRI. Figure 3.5 Human machine interface developed for manipulating the material deposition system used in CAMRIFigure 3.5 shows the HMI developed for CAMRI based on KMotionCNC©.

One of the particularities of the G-code programing language is the wide number of versions available due to the fact that NC machine manufacturers commonly use miscellaneous commands, also known as M codes, to control functionalities that are specific to their machines. In the case of CAMRI, multiple M codes are utilized to perform actions during printing like setting the bead dimensions, activating the tamper, recording the printing trajectory, introducing a dwell time during printing, among many other functionalities. M codes uniquely used in CAMRI to perform different operations in the printing process of a part are listed in Table B.1 of the APPENDIX B. The superior flexibility provided in KFLOP© allows for instance to trigger user defined subroutines developed in the C programming language with the M codes, thereby allowing for synchronization of user defined subroutines with the motion control. Furthermore, information of the coordinated motion, namely position, velocity, time, etc. can be accessed through user defined subroutines which enables implementing control laws that depend on the motion of the gantry robot. The reader is referred to the documentation of KFLOP© [90] for further explanation of additional functionalities available in the libraries for coordinated motion and trajectory planning.

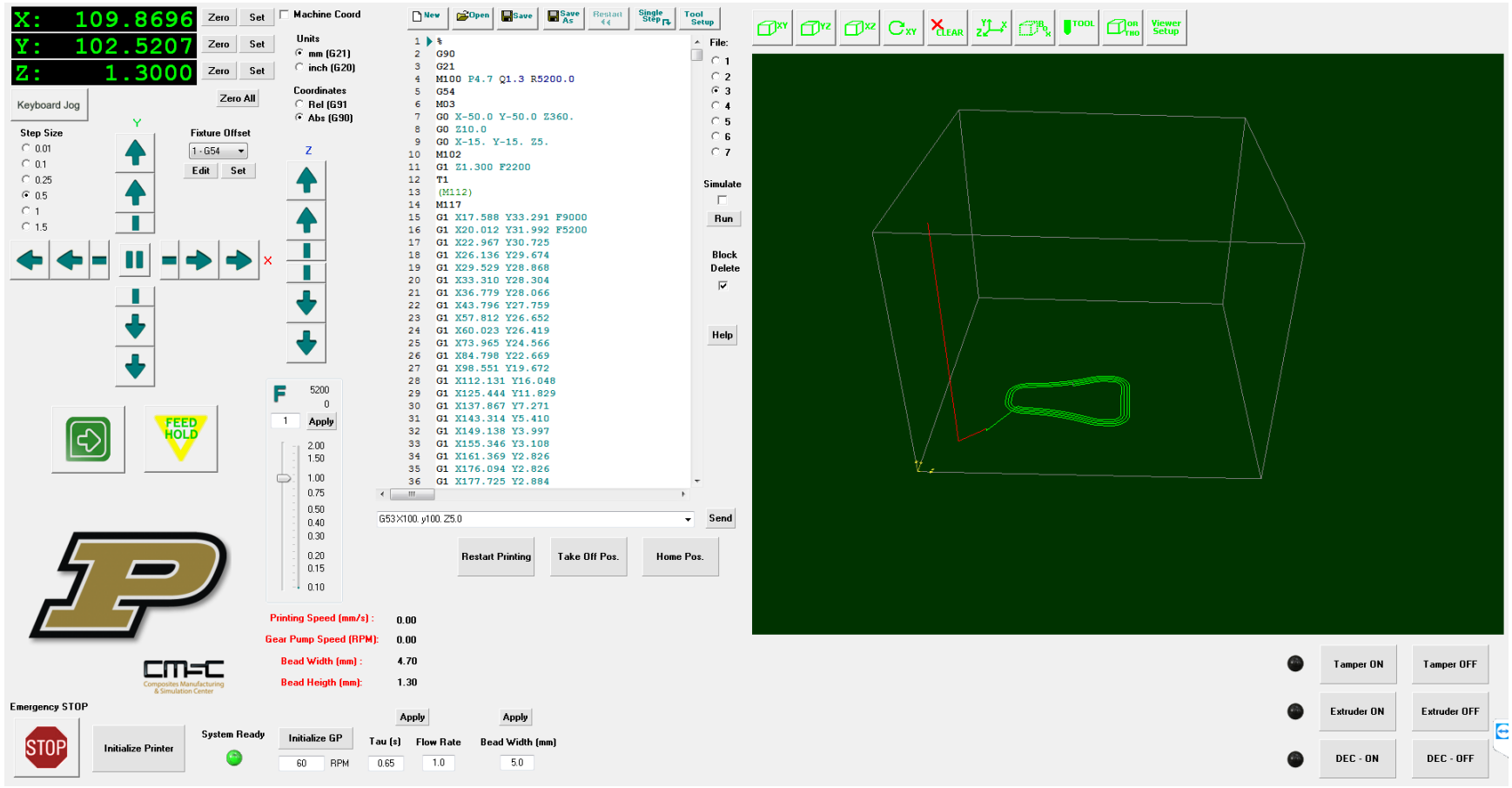

Figure 3.5 Human machine interface developed for manipulating the material deposition system used in CAMRI.

3.3 Control of the Material Extrusion System

Manufacturing of a part by extrusion deposition additive manufacturing requires precise control over consistency and dimensions of printed beads as well as on positioning of printed beads in the manufacturing process of a part. The problem of positioning printed beads during manufacturing of a part was solved with the NC controller that provides coordinated motion of the gantry robot. However, coordinating the material extrusion system with the coordinated motion of the gantry robot required the development of a novel approach to control the extrusion system. Controlling flow or pressure in steady state operation of single screw extruders has been addressed before with close loop control system, yet the variations in extrusion conditions during the EDAM process complicates reaching steady state operation of the extruder. In other words, the extruder is constantly perturbed with variations of material demand caused by changes in deposition rate during manufacturing of a part. Hence, this section presents a novel approach implemented for controlling the material extrusion system used in CAMRI which consists of a volumetric material feeder, a single screw extruder, an extrusion gear pump and an extrusion nozzle. Before describing the control approach implemented for each of these elements, the input and output conditions required at each element or the extrusion system must be understood. Figure 3.6 summarizes in a flowchart of the printing material the manipulated and controlled variables of the extrusion system. Following the flowchart of the printing material through the material extrusion system presented in Figure 3.6, the first step is feeding of the pelletized feedstock. The first process variable is the mass flow rate, $\dot{m}_p$, of pellets delivered to the single-screw extruder. This variable is manipulated through the rotational speed of the auger screw, $N_f(t)$, in the volumetric feeder. Pellets are then delivered gradually to the single screw extruder based on the material consumption rather than flooding the hopper of the extruder with material. The method used in CAMRI is known as starve feeding and results in multiple benefits compared to flood feeding like reducing fiber attrition in pellets with long discontinuous fibers, reducing pressure gradients along the extruder and improving the dynamic response of the extruder [19, 91].

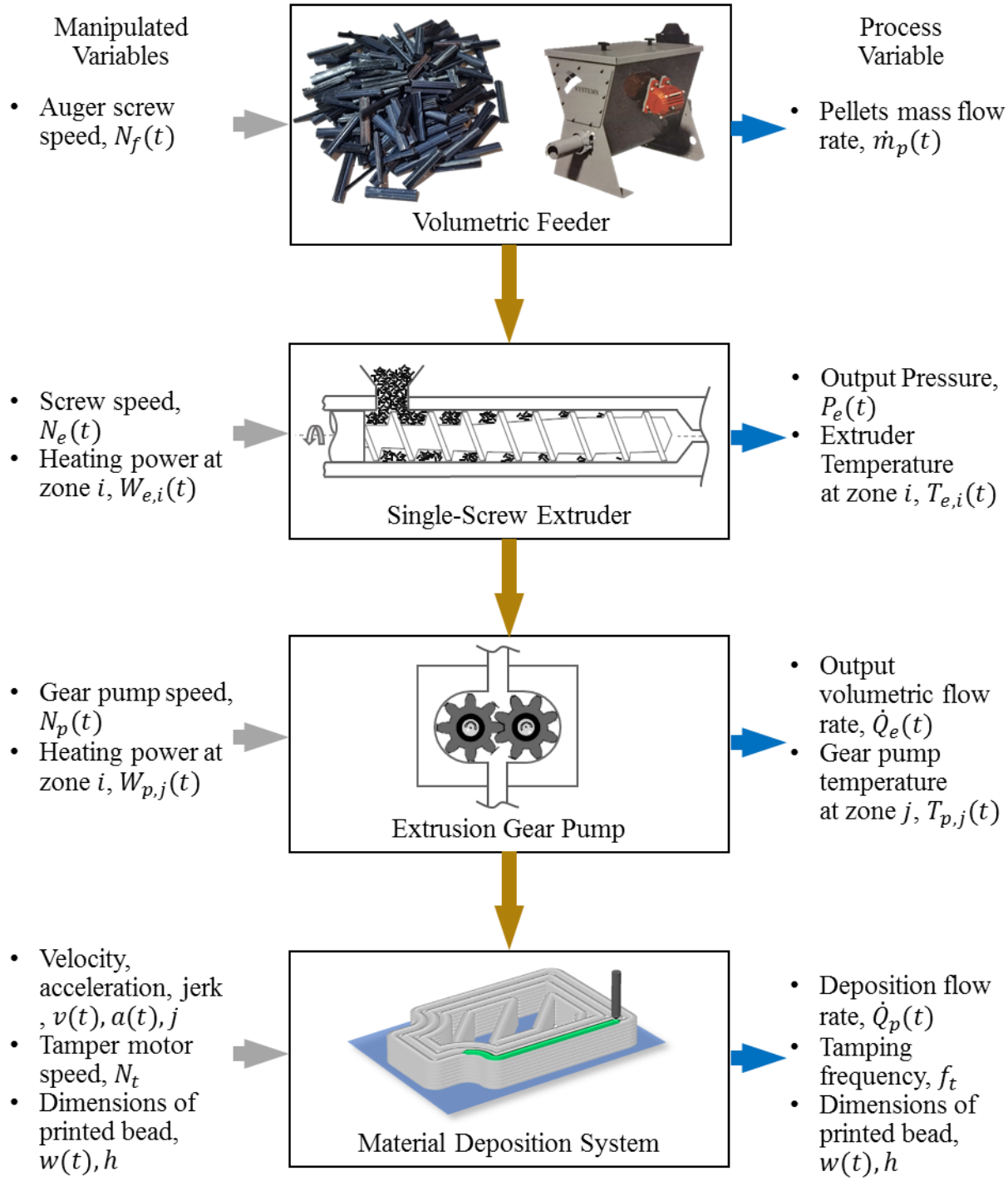

Figure 3.6 Flowchart of printing material in the extrusion system used in CAMRI and variables manipulated and controlled during the process.

The next element in the flow chart is the single-screw extruder. Temperature and pressure at the end of the extruder are the two primary variables controlled in the single-screw extruder. Controlled temperature conditions are required at three different heating zones in the single-screw extruder to assist the melting process of material. Temperature, $T_{e,i}(t)$, at each individual zone is regulated by manipulating the heating power $W_{e,i}(t)$, delivered to heating elements located in each zone. With regards to the pressure, $P_e(t)$, developed at the end of the extruder, the primary variable manipulated to control pressure is the rotational speed of the screw, $N_e(t)$. Nevertheless, temperature also influences the mechanisms to develop pressure at the end of the extruder due to the effect of temperature on the rheology of the processed material. The consequences of temperature and shear deformation of the material inside the extruder will be addressed in more details in the following section prior to discussing the close loop control system implemented for controlling $P_e(t)$. Controlling $P_e(t)$ at the inlet of the extrusion gear pump is critical to achieve consistent material delivery with this component. This is because the internal geometry of the gear pump, namely the gears and pump cavity, must be continuously filled with molten material to prevent starvation of the gears which could in turn cause a reduction in the output flow rate of the pump, $\dot{Q}_e(t)$. Alike the single-screw extruder, the temperature, $T_{p,j}(t)$, at each of the two zones in the extrusion gear pump is regulated through the heating power, $W_{p,j}(t)$, delivered through heating elements. Preserving the temperature of the molten material as it flows through the different components of the material extrusion system is critical to deliver printed beads with uniform temperature distribution.

Since extrusion gear pumps deliver controlled flow rate, the instantaneous velocity, $v(t)$, of the gantry robot and the dimensions of the cross section of the printed bead, $w(t)$ and h, can be then used to compute the flowrate, $\dot{Q}_e(t)$, required to deposit beads with such dimensions. Also, the width of the printed bead, $w(t)$, can vary during the printing process of part. The last interaction of the printing material with the processing equipment is at the extrusion nozzle which can also be influential for the control of material deposition. Flow induced phenomena inside the nozzle like fiber orientation was discussed before, however, other phenomena occurring during printing like oozing or lack of material flow at stops and starts during printing, respectively, needs to be addressed. These last two effects arise from the viscoelastic behavior of the fiber suspension of polymer melt, the compressibility of the printing material and the latency in the response of the processing equipment. Therefore, those effects should be considered in the control of the flow

rate, $\dot{Q}_e(t)$, delivered by the gear pump to achieve the desired flow rate delivered at the tip of the nozzle, $\dot{Q}_p(t)$. Additionally, a heating zone located in the extrusion nozzle provides for temperature regulation to this element of the extrusion deposition system.

In summary, there is a sequential dependence of the process variables associated to each of the elements in the material extrusion system. Again, this is better understood in terms of the flow of material through the system. The feeder supplies the mass flow rate of material demanded by the extruder to sustain the flow rate demanded by the extrusion melt pump while preserving the pressure constant. Subsequently, the extrusion melt pump delivers the volumetric flow required to deposit beads with controlled dimensions in synchrony with the movement of the gantry robot. These process control requirements resulted in the combination of open loop, feed forward and close loop control systems for controlling the process variables shown in Figure 3.6.

The diagram block in Figure 3.7 Block diagram of the control system developed for the material extrusion system used in CAMRIFigure 3.7 shows the architecture of the complete control system developed for controlling temperature, pressure, and flow rate in the material deposition system. Further explanation of the control systems implemented at each segment is presented in the next two subsections whereas the next section describes the hardware and software implementation of the control systems in CAMRI.

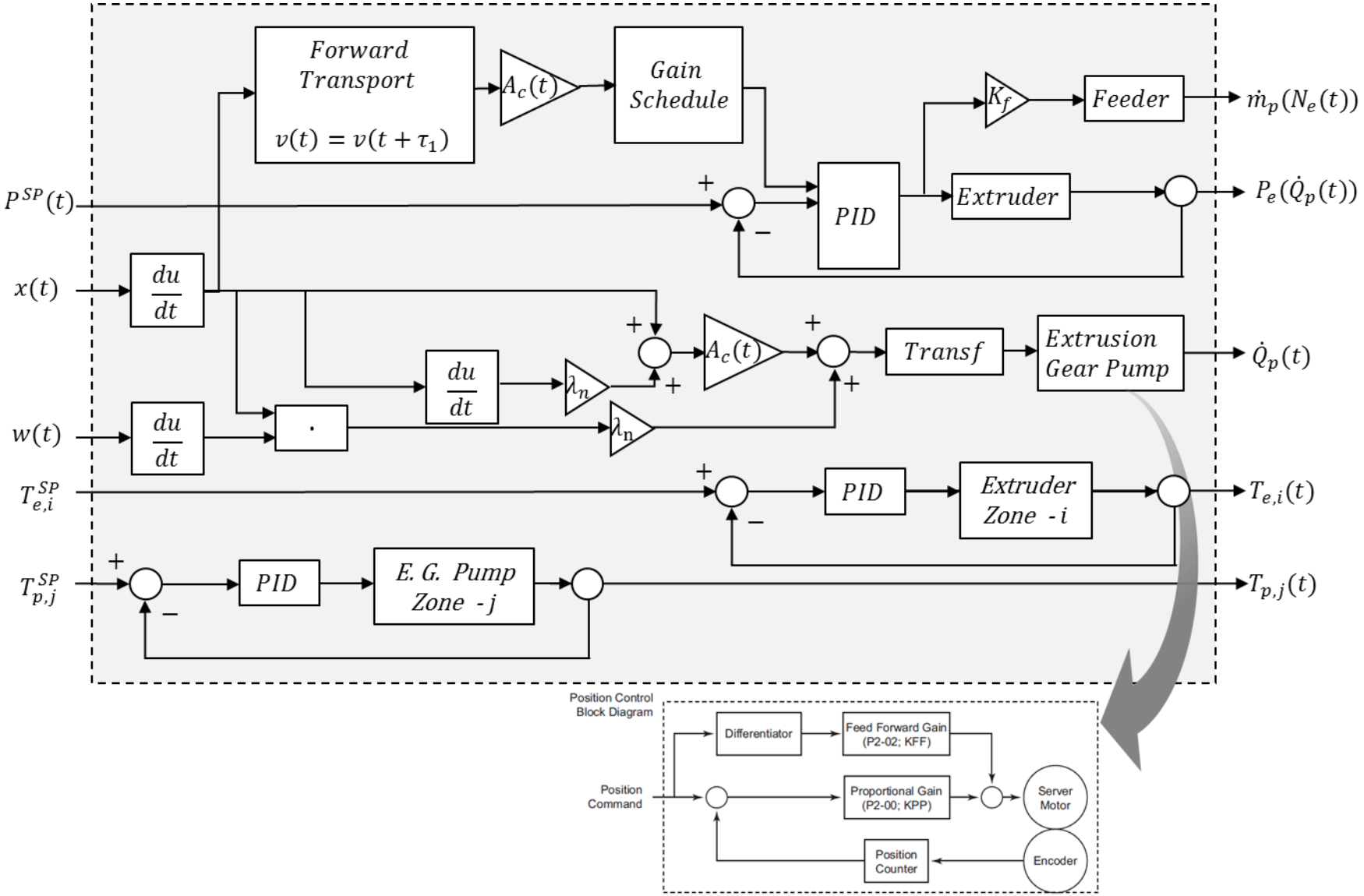

Figure 3.7 Block diagram of the control system developed for the material extrusion system used in CAMRI

3.3.1 Single-Screw Extruder

The two process variables related to the single-screw extruder, namely temperature and output pressure, were described before along with the correlation of these process variables with other elements in the material extrusion system. It was also mentioned that the primary variable manipulated to control the output pressure or flow rate of the extruder is the rotational speed of the screw, ω_e, and it was recognized the dependence of temperature on the rheological properties of the processed material. However, the effects of the rotational speed of the screw in both temperature and rheology of the material should be also considered for understanding the consequences of rapid transitions between low extrusion speeds to high extrusion speeds while operating the extruder in the EDAM process. Therefore, this section begins by providing fundamental understanding of the polymer behavior in the extrusion process with an emphasis on the consequences of changes in temperature and screw speed. This then leads to the control system utilized in the material extrusion system in CAMRI. Before continuing, it should be noted that the words printing material, polymeric material, and composite material are used interchangeably to refer to the material processed in the single-screw extruder.

Figure 3.8 shows a more accurate representation of the single-screw extrusion process used in CAMRI where the extruder is starve fed with the volumetric feeder.

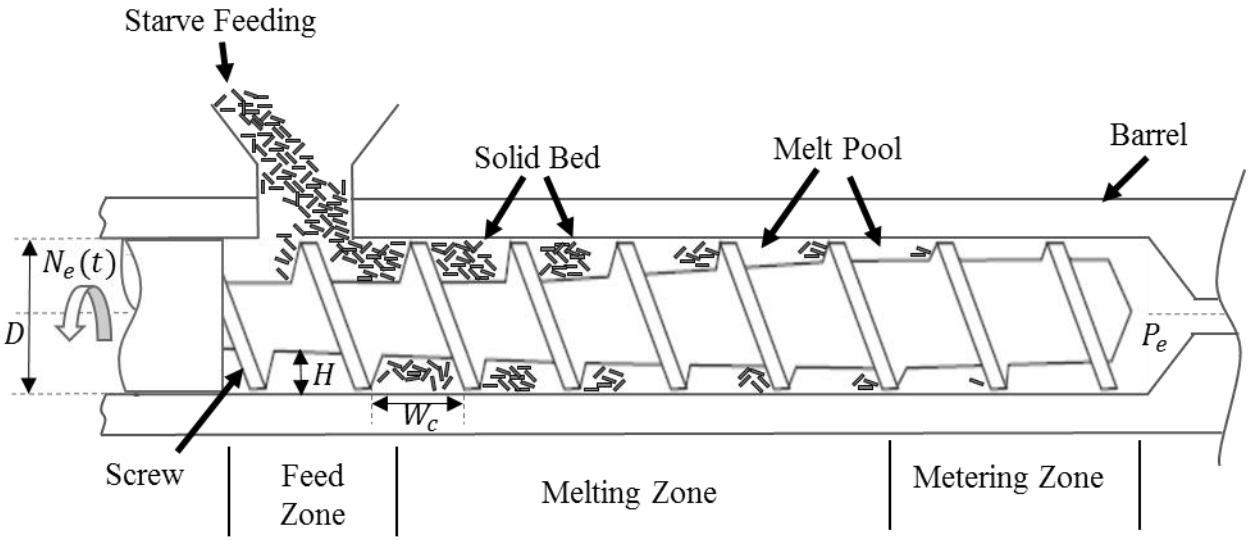

Figure 3.8 Schematic of the single-screw extruder used in CAMRI.

3.3.1.1 Principles of Single-Screw Extrusion

The temperature of the material processed with the single-screw in CAMRI is critical not only for the EDAM process but also for the operation of the extruder. Melting of the polymeric material occurs through the gradual development of a melt pool along the screw as illustrated in Figure 3.8. Two mechanisms provide the thermal energy required for melting the polymer, conduction from heating elements in the processing equipment and viscous dissipation due to constant deformation of the material. The dynamics of the first mechanism are relatively slow, in other words the time constant for heat to diffuse from the heating elements located in the barrel to the screw is a large one whereas the dynamics of the second mechanism are relatively fast. This occurs since viscous dissipation increases as a function of the rotational speed of the screw, $N_e(t)$, which can vary substantially in a relatively short period of time.

Generally, the geometry of the screws is rather complex to derive exact expressions for the viscous losses, however, simplifications made to screw geometry allows for derivation of expressions useful for understanding the contributions of processing equipment, material rheology, and processing conditions to viscous dissipation. During processing of material in single-screw extruders, complex deformation mechanisms occurs in the material flowing through extruder, yet only the shear deformation will be considered in the analysis presented next.

Viscous dissipation is defined as the product of the shear rate and the shear stress applied to the material located in the channels of the screw [91]. For a single-screw extruder, the shear rate can be approximated by the Couette shear rate [91, 18]. This method assumes the barrel moves relative to the screw at a constant tangential velocity which divided by the depth of the screw channel yields the expression shown in Equation 3.1 to approximate the shear rate, $\dot{\gamma}(t)$

$$\dot{\gamma}(t) = \frac{\pi D N_e(t)}{H} \tag{3.1}$$

where, D, is the diameter of the barrel, $N_e(t)$, is the rotational speed of the screw and H, is the depth of the screw channel as illustrated in Figure 3.8. This equation describes a linear relation between the screw rotational speed and the strain rate. Considering the decrease in H along the screw, the strain rate increases as the material moves along the screw. Moreover, the small gap between the barrel and the screw gives rise to significantly larger shear rates in the material located

in this region. Again, this provides some appreciation of the complexity in the material deformation inside the single screw extruder.

Polymer melts are well known to exhibit nonlinear behavior in the presence of a deformation rate and this nonlinear response becomes anisotropic with the presence of fibers in the polymer melt [23, 91]. Only the nonlinear behavior due to the polymer is discussed herein, but the reader is referred to the work of Pipes et al. [23, 22] for further details on the anisotropy of concentrated fiber suspensions. Polymer melts are generally considered pseudo-plastic fluids due to the reduction in the viscosity of the polymer that results from increasing shear rate. This fluid behavior is also known as shear-thinning and appears depending on the polymer at low to medium shear rates. Shear rates in the range of 1 to $10{,}000\ s^{-1}$ are typically developed in single-screw extruders [92]. Before exhibiting this shear thinning behavior, polymer melts have a linear region where the viscosity is nearly independent to the strain rate which is known as the low shear rate plateau. Similarly, a high shear rate plateau is reach after certain shear rate. Nevertheless, shear rates used commonly while processing of polymer melts are in the range of shear rates where the melt exhibits this shear thinning behavior. By inspection of the relation of viscosity or shear stress to shear rate in a logarithm scale, a straight line is realized and therefore a power law can be used to describe this fluid behavior. Equation 3.2 shows the power law describing the relation between shear stress and shear rate in a polymer melt

$$\tau(T,t) = m(T)\dot{\gamma}(t)^n \tag{3.2}$$

where $m(T)$ is the consistency index as a function of the temperature and n is the power law index given by the slope in the log-log plot of shear stress to shear rate. The effect of temperature on the rheological behavior now comes into the picture. Unlike the power law dependence of shear rate on the shear stress, temperature has a weaker influence on shear stress. Increasing the temperature in polymer melts also increases the mobility of the polymer chains in the polymer, thereby reducing the resistance to flow of the polymer melt. In other words, temperature reduces the viscosity as well as the shear stress required to deform the polymer, yet without modifying significantly the strain rate dependence [91]. As a result, $m(T)$ can simply be expressed by the product of the melt index at a reference temperature, m_o, and a function, a_T, that scales the reference melt index as a function of temperature. Different equations can be used to describe this temperature dependence

including the Williams-Landel-Ferry (WLF) equation as shown in the expression given in Equation 3.3 for the shear stress.

$$\tau(T,t) = m_o \cdot \exp\left[-\frac{C_1(T-T_r)}{C_2+(T-T_r)}\right] \cdot \dot{\gamma}(t)^n \tag{3.3}$$

The constants C_1 and C_2 are determined experimentally and attain values of about 8.86 and 101.6, respectively for amorphous polymers when the reference temperature T_r is taken 46 $°K$ above the glass transition temperature [91].

Now, using the expressions introduced in Equations 3.1 through3.3, the Equation 3.4 is constructed for estimating the viscous dissipation, $q_v(t)$, for a channel in the screw.

$$q_v(T,t) = m_o \cdot \exp\left[-\frac{C_1(T-T_r)}{C_2+(T-T_r)}\right] \cdot \left(\frac{\pi D N_e(t)}{H}\right)^{n+1} \tag{3.4}$$

Referring to Equation 3.4, a power law dependence of 1 plus the power law index n which is in the range of .5 to .9 for engineering polymers governs the viscous dissipation in single screw extrusion. In other words, there is a nearly quadratic dependence of the screw rotational speed, $N_e(T)$, on the viscous dissipation. Furthermore, self-heating of the material due to viscous dissipation occurs almost instantaneously which results in local changes in rheological behavior of the material because of both temperature and shear rate as shown in Equation 3.3. In steady state operation of the extruder, some of the thermal energy caused by viscous dissipation is removed by conduction through the processing equipment, however, the time constant for dissipating heat through conduction can be significantly larger than the time constant for self-heating of the material which is practically instantaneous. This has strong implications on the design of a control system for operating single-screw extruders in non-steady state conditions.

In order to provide some physical sense on the magnitude of the energy contributed by viscous dissipation for material melting, a single-screw extruder can operate only on the contribution of viscous dissipation and without external heating elements while operating in steady state [18, 91].

Changes in viscosity of the polymer due to both temperature and deformation rate have other consequences that are of paramount importance for controlling the single-screw extruder in CAMRI given the required non-steady operation of the extruder. Therefore, the focus is now on the conveying mechanism in single screw extruders, particularly in the ones for melt conveying. While conveying of solid pellets is governed by the combined effect of confining pellets between the screw and the barrel and the rotation of the screw, melt conveying is controlled by two flow mechanisms in the metering section, pressure and drag flow. The onset of melt conveying is considered once the material is fully molten which generally occurs at the metering zone illustrated in Figure 3.8. The two flow mechanisms are first discussed using an analytical expression derived for Newtonian and temperature independent fluids presented by Raunwendaal [91], and experimental data obtained with the extruder used in CAMRI is discussed next.

The melt conveying problem is quite complex, but it can be simplified significantly by treating the rotating system as a plate and a channel describing relative motion at an angle equal to the helix angle of the screw, ϑ. This way, the effects of screw geometry and shear rates are readily recognized and expressions for the velocity profiles of non-Newtonian fluids through the screw channel can be derived as presented by Raunwendaal [91]. Now, the velocity can be integrated over the cross section of the screw channel to obtain the expression in Equation 3.5 for the flow rate, $\dot{V}(t)$.

$$\dot{V}(t) = \left(\frac{4+n}{10}\right) P_{cz} W_c H v_{bz}(t) - \left(\frac{1}{1+2n}\right) \frac{P_{cz} W_c H^3 g_z}{4\mu(t)} \tag{3.5}$$

Where P_{cz} is the number of parallel flights in the melt conveying zone, W_c is the width of the channel illustrated in Figure 3.8 for a screw with constant pitch, H is the depth of the channel, $\mu(t)$ is the viscosity calculated at the Couette shear rate in the channel as shown in Equation 3.6,

$$\mu(t) = m\left(\frac{v_{bz}(t)}{H}\right)^{n-1} \tag{3.6}$$

g_z is the pressure gradient along the channel and finally, $v_{bz}(t)$ is the velocity parallel to the walls of the screw channel given in terms of the screw rotational speed as in Equation 3.7

$$v_{bz}(t) = \pi D N_e(t) Cos(\vartheta) \tag{3.7}$$

From the right-hand side (RHS) of Equation 3.5, the first term corresponds to the drag flow whereas the second term corresponds to the pressure flow. The drag flow contribution in Equation 3.5 includes the effect of screw geometry, screw rotational speed, and rheology of the polymer through the dimensions of the screw channel, the velocity term $v_{bz}(t)$, and the power law index, n, respectively. Further, the contribution of drag flow to the flow rate scales linearly with the rotational speed of the screw $N_e(t)$ which provides a first order estimate of the maximum pumping capacity of the screw as a function of the rotational speed. We will come back to this expression when discussing the control approach used for feeding pellets into the extruder. Also, the rotational speed of the screw is an implicit function of time since it varies constantly while operating the extruder in the EDAM process.

Pressure flow is the second contribution to the volumetric flow rate. This component becomes negative for positive pressure gradients, g_z, along the channel of the screw which is the general case for single screw extruders [91]. g_z is also equal to the shear stress gradient through the depth of the screw channel, H, ($g\_z = (\partial \tau_{yz})/\partial y$), and its magnitude can be approximated from the axial pressure gradient, g_a, ($g_z = g_a \sin(\vartheta)$). The shear thinning behavior in polymers is captured through both the viscosity and the power law index in the pressure flow term. By combining equations 3.5 through 3.7, the dependence of the pressure flow term on the rotational speed of the screw is readily recognized. If we assume a Newtonian fluid ($n = 1$), increasing the screw rotational speed will cause a linear increase in the contribution of the pressure flow to the output flow rate of the extruder. In other words, the output volumetric flow rate will decrease linearly with the screw rotational speed while processing a Newtonian fluid. The effects of temperature though not considered in Equation 3.5, will also accentuate the decrease in flow rate due to pressure driven flow in the screw. Another interesting observation from Equation 3.5 is the cubic dependence of the pressure flow on the channel depth, H, which explains the reason for shallow metering zones in single screw extruders.

The effects of the pressure flow in the flow rate was also recognized during characterization experiments of the single screw extruder used in CAMRI where a constant pellets mass flow rate, $\dot{m}_p$, was supplied at multiple constant values of N_e. During these experiments, the mass flow rate of the extruder, $\dot{m}_e$, which is simply given by the product of the density, ρ, and the volumetric

flow rate of the extruder, $\dot{V}(t)$, was characterized upon reaching steady state pressure conditions at the output of the extruder. It should be noted though, that this characterization was conducted with a nozzle attached at the end of the extruder rather than an extrusion gear pump.

Figure 3.9 shows a plot of the extruder mass flow rate, $\dot{m}_e$, resulting from varying the rotational speed of the screw, N_e, while preserving the input mass flow rate of pellets, m_p, constant.

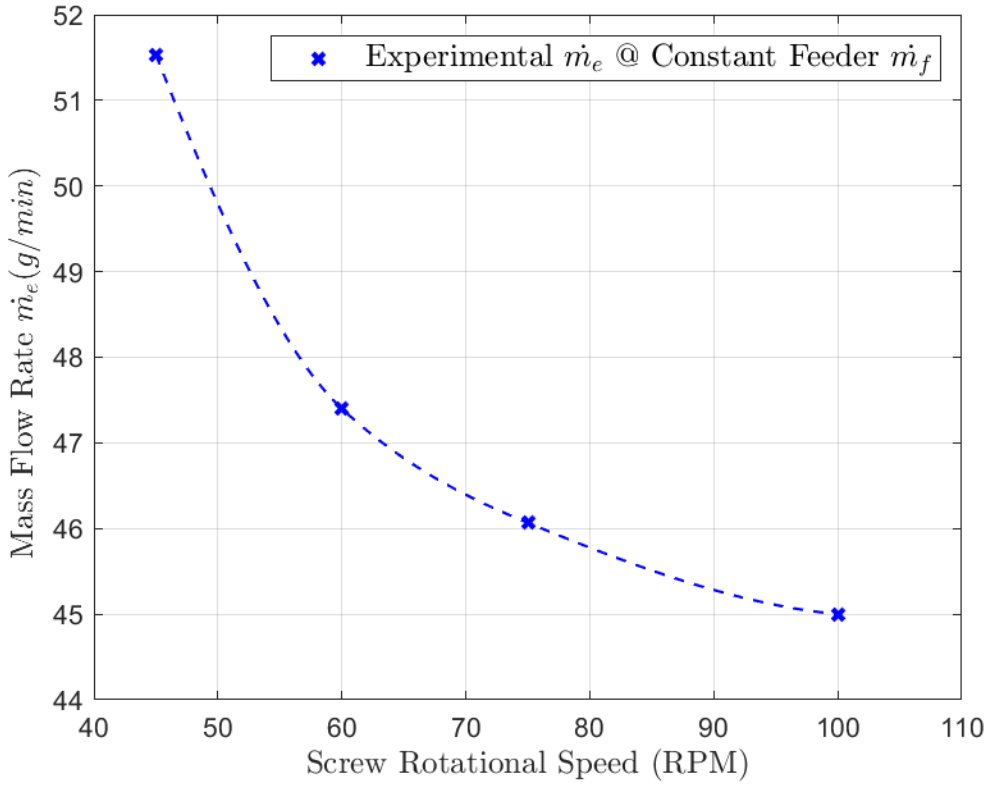

Figure 3.9 Mas flow rate of single-screw extruder used in CAMRI vs screw rotational speed at constant feeder mass flow rate.

As discussed before, the contribution of each melt conveying mechanism changes as a function of the screw rotational speed, particularly the contribution of the pressure flow. At elevated speeds, the reduction in viscosity due to both shear rate and temperature results in higher pressure driven flow which is opposed in direction to the drag flow, thereby reducing the output volumetric flow rate. Furthermore, the experimental measurements plotted in Figure 3.9 were conducted after the extruder achieved steady state which means that both pressure and temperature are in equilibrium. Following the principles presented before, it is recognized that the contribution of pressure flow

to the output volumetric flow rate becomes more significant in transients or non-steady state operation since the time constant for conducting the thermal energy resulting from viscous dissipations from the material to the barrel is significantly larger than the time constant of the material to react to changes in shear rates and temperature. Hence, the extruders instantaneous flow rate or pressure output depends not only on the combination of material behavior and screw design but also on the preceding process conditions of the extruder. In other words, the processing history influences more significantly the instantaneous response of the extruder while operating in non-steady state conditions.

3.3.1.2 Control of Single-Screw Extruder

The objective of utilizing process controllers in the single screw extruder is to maintain not only a constant output pressure but also to ensure adequate temperature conditions for material processing. While simple conventional control systems can be used to fulfill the later objective, the former objective is more complicated for the application of EDAM due to non-steady operation of the single screw extruder resulting from continuous variations of printing speed in part manufacturing. Principles of single screw extrusion were discussed in the previous section with the aim of exposing the reader to the sources of non-linear behavior in the control of single-screw extruders, especially while operating in non-steady state conditions.

The nature of this problem of manipulating the rotational speed of the screw for regulating the output pressure of the extruder despite fluctuations of flow rate advise the use of a closed loop control system. In this type of control systems, the manipulated variable is adjusted through a controller or regulator as a function of the error defined by the difference between the process variable and the target value or set point. Multiple types of controllers or compensators for single-input-single-output (SISO) systems have been developed in the framework of the classical control theory, including proportional compensators, lead compensators, lag compensator and combinations of these previous like the famous proportional, integral and derivative (PID) controller [93]. In order to utilize this type of controllers, the system to control must be not only SISO but also Linear Time Invariant (LTI). A system is linear if satisfies the principle of superposition which states that the response produced by the simultaneous application of multiple forcing functions is the sum of the multiple individual responses. And time invariance means that the system will produce the same response to the same input applied at either time t or after b

number of seconds at time $t + b$. Many real systems violate these two requirements as their dynamics undergo changes triggered by geometry, forces, weight, etc. For example, the dynamics of a car change as the weight is reduced by the consumption of the fuel. Nevertheless, classical controllers can still be successfully designed around operational points defined in linearized regions of the system [93]. This implies that even through the dynamics of the car changes as the fuel is consumed, a piecewise representation of the dynamics can be used to design classical controllers for each piece. Additionally, if information of the fuel level in the car is accessible, the control system can now be informed with the fuel level, thereby making the control system adaptive.

The problem of controlling a single screw extruder is of the same kind illustrated before for the car in terms of the non-linear behavior and the evolution of the dynamics of the system. The non-linear behavior in single screw extrusion arises from the interaction of the non-linear rheology of the processed material with the varying processing conditions used in the extrusion process. The plot of flow rate to screw rotational speed shown in Figure 3.9 renders the changes in dynamics of the single screw extruder at four different operation points. In this example, the operational point in the lower screw speed domain was less influenced by the pressure flow whereas the changes in rheology of the material caused an increase in pressure flow in the higher speed domains, thereby reducing the output flow rate of the extruder. Notice also that these points in the plot were collected at steady state pressure and temperature conditions in the extruder. The extrusion system is also time variant since the instantaneous response at a given time t is influenced by the processing conditions utilized an instant of time before t. Which results from the fact that the time constant for conducting thermal energy from the material to the processing equipment or vice versa is larger than the time constant for generating thermal energy by viscous dissipation. This scenario occurs repetitively in the extruder used for EDAM since the extruder is constantly perturbed with variations of flow rate in the manufacturing process of a part.

Hence, an adaptive closed loop control system was implemented for regulating the output pressure in the single screw extruder used for CAMRI. The type of adaptive system used for the extruder was gain scheduling due its simple implementation and the access to process variables that correlate well with the changes in the dynamics of the extruder [94]. Figure 3.10 shows the block diagram of the control system in the time domain with gain scheduling.

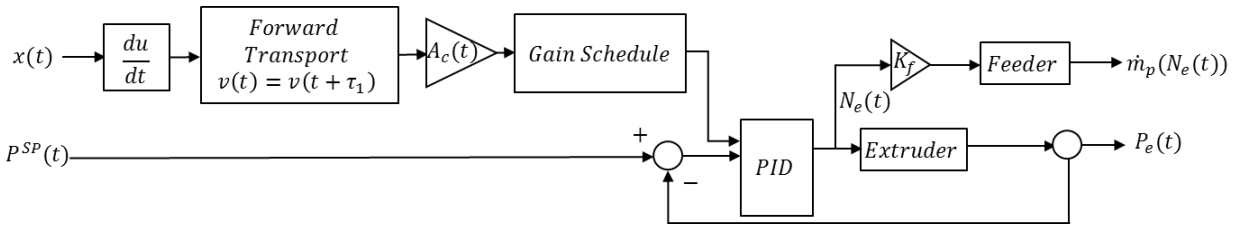

Figure 3.10 Control block diagram of gain scheduling system used for regulating pressure output in the single screw extruder used in CAMRI.

In gain scheduling, either a continuous function or a discrete tabular definition can be used to update the gains of a controller based on the value of a process variable that can be part of the same system or an external signal. This way, the gains of the controller are adapted to the changes in dynamics the system undergoes.

The architecture of a proportional integral derivative (PID) controller was utilized in the adaptive control system of the single screw extruder. Equation 3.7 provides the output, $u(t)$, in the time domain of the PID controller with gain scheduling.

$$u(t) = K_{p,m}\left(\dot{V}(t+\tau_1)\right)\left[e(t) + K_{i,m}\left(\dot{V}(t+\tau_1)\right)\int e(t)dt + K_{d,m}\left(\dot{V}(t+\tau_1)\right)\frac{dy(t)}{dt}\right] \tag{3.7}$$

The output $u(t)$ in Equation 3.73.7 is given in terms of m discrete values assigned to the proportional gain, $K_{p,m}$, the integral gain, $K_{i,m}$, and the derivative gain, $K_{d,m}$, as a function of the instantaneous volume flow rate, $\dot{V}(t+\tau_1)$, of the pump at an instant of time, τ_1, ahead of the current time, t. This means that the gains in the PID controller are assigned depending on the range of volumetric flow rate demanded by the pump. Also, gains are updated an instant of time ahead of the change in order to compensate for delays inherent to the system.

Although pressure is the process variable controlled in the single screw extruder, the variations in flow rate during manufacturing of a part correlate directly to the rotational speed of the screw as defined in the approximation for flow rate given in Equation 3.5. Further, the volumetric flow rate demanded to the extruder during manufacturing of part is defined by the instantaneous velocity of the gantry robot, $v(t)$, and the cross-section area of the printed bead,

$w(t) * h$. This is shown in the block diagram of Figure 3.10 as a gain, $A_c(t)$, equal to the cross-section area of the printed bead multiplied by the computed instantaneous velocity. Notice that the bead width can change during the manufacturing of a part, and thus it is expressed as a function of time. Further, since the controller is going to regulate the rotational speed of the screw to maintain the flow rate at the pressure specified in the set point, the instantaneous volume rate $\dot{V}(t)$ can be then used to infer the current conditions of the extruder. This information can be then utilized to schedule PID gains based on a piecewise definition of the domain of volume flow rate that is physically possible with the system.

With regards to the architecture of the PID controller utilized, the integral action utilizes the integral over time of the error, $e(t)$, defined by the difference between the set point (SP) and the process variable, $y(t)$, whereas the derivative action utilizes the derivative with respect to time of the process variable, $y(t)$. The fact that the derivate portion is not taken with respect to the error is to prevent large discontinuities in the output of the controller caused by the derivative action at changes in SP. This condition occurs constantly when the pressure set point is varied as a function of the flow rate conditions to maintain a constant pressure gradient across the extrusion gear pump. This type of adaptive PID controller provides for regulation of the transient and the steady state responses through the derivative and integral actions, respectively, and this applies at each segment of the volume flow rate domain used in gain scheduling. The upper limit of the volumetric flow rate is in the range of $1400\, mm^3/s$ and is defined by the maximum rotational speed of the extrusion gear pump and the displacement of the pump, whereas the lower operational limit is in the range of $70\, mm^3/s$. Therefore, the domain for each of the PID controllers in the adaptive control system can be made equally spaced as shown in Table 3.2. In addition to utilizing gain scheduling, the material extrusion system contains multiple delays that are inherent to both the extrusion process and the components of the extrusion system and that affect the temporal response of the extruder. Examples of these delays include the response time of the extruders drive system, the response time of the material feeder, and the residence time of the polymer. Therefore, a forward transport is applied to the gain scheduling in order to compensate for some of these delays. This way, the scheduled gains are informed to the controller an instant of time, τ_1, ahead of time to accommodate for some of the delays in the system.

Table 3.2 Regions of operation for the adaptive PID controller defined based on a piecewise definition of the domain of the output flow rate in CAMRI.

Region of Operation $(\boldsymbol{Index - m})$	**Range of** $\boldsymbol{\dot{V}}$ $(\boldsymbol{mm^3/s})$
1	$0 - 472$
2	$473 - 944$
3	$945 - 1416$

With regards to regulating the pellets mass flow rate supplied by the volumetric feeder, a simple open loop control system is used in a slave configuration with the control action applied to the extruder. Since the pressure regulator used in the extruder reacts to changes of flow rate at the end the extrusion nozzle, the same control signal output by the PID controller can be used to manipulate the mass flow rate supplied through the material feeder. This is represented in the block diagram shown in Figure 3.10 where the gain for the feeder, K_f, depends on characteristics of the screw in the extruder and the relation of rotational speed of the feeders auger to mass flow rate for a given pellet geometry. Since the output flow rate in the single screw extruder is primarily dominated by melt conveying, the drag flow component in Equation 3.5, combined with the velocity parallel to the walls of the screw channel given by Equation 3.7 can be used to approximate the gain K_f used for controlling the flow rate of the feeder as a function of the screw rotational speed.

$$K_f = \frac{4+n}{10}\pi H D P_{cz} W_c Cos(\vartheta)\rho \tag{3.8}$$

The constant K_f has units of g/rev which multiplied by the rotational speed of the screw given in units of rev/s provides the mass flow rate in units of g/s. Notice that the density used for this approximation corresponds to density of the material in molten state. This way, the mass flow rate of pellets can be controlled as a function of the screw rotational speed ensuring the extruder is never starved. However, there is a response time inherent to this approach due to the time it takes for the pellets to travel from the feeding section to the metering section of the screw. This response time varies as a function of the rotational speed of the screw and can affect the transient response of the extruder in cases where there is an abrupt increase in deposition rate. In order to lessen the effects of this response time, the same approach of using a forward transport to command the

extruder can be used to command the feeder yet with a characteristic time appropriate to the conveying of material in the extruder.

The integration of the adaptive PID controller with the open loop control of the feeder provides a solution for the problem of maintaining a relatively constant output pressure in the single extruder despite the changes in the dynamics of the system due to fluctuations in flow rate occurring during manufacturing of a part. Further, this provides also robustness to variations in properties of the feedstock material and has been used successfully to operate the extruder with different highly filled materials due to the strong dependence of the rheology of the material on the fiber content and fiber length.

The objective of this section was to present the innovations made on the process control implemented for the single-screw extruder used in CAMRI, however, the correct implementation of this control systems requires an additional set of steps including identification of the plant representing the extruder, assessment of controllability and stability of the system, and tuning of the PID parameters which were not covered herein since these are well stablished methods in the field of classic control. The particular techniques used for the implementation of this closed loop control are mentioned in the section of implementation, yet the reader is referred to the following literature for more details on these subjects [94, 93].

3.3.2 Extrusion Gear Pump

The positive displacement pump in the CAMRI system provides for precise flow rate control since flow rate is defined by combination of the geometry of the channels in the gears of the pump and the rotational speed of the gears, $N_g(t)$. This results in a linear relation between flow rate and rotational speed of the gears. However, the flow rate delivered at the tip of the extrusion nozzle may vary at transients of flow rate arising from changes in velocity or deposition conditions during manufacturing of a part. Examples of the former case include changes in velocity of the extrusion nozzle while printing around sharp corners. As the nozzle approaches a sharp corner, the motion of the gantry robot is deaccelerated to approach the corner and then accelerated to leave the corner which is made in order to reduce the inertial forces in the gantry robot due to acceleration. In the latter case, changes in deposition conditions arise with rapid movements used for translating the extrusion nozzle from one point to another without depositing material. While performing rapid movements, the flow is first stopped at the end of a printed segment and then restarted to begin

depositing material along a different segment of the print. In any case, the suspension of molten material flowing through the extrusion nozzle will tend to continue flowing or lagging to flow. We will refer to this phenomenon as the oozing effect. Using as an example the rapid movements where material is printed, at the stop of the material deposition the molten material may continue to flow or ooze out of the nozzle whereas the opposite effect may occur at the start of the deposition process. A similar effect can occur around sharp corners due to changes in flow rate. This is a complex phenomenon that can be attributed to the compressibility and viscoelastic behavior of the polymer melt and dynamic response of the extrusion gear pump.

Polymer melts exhibit both compressibility and viscoelastic behavior when subjected to stresses and deformation. The source of compressibility in polymer melts can be explained in terms of the free volume and by the compression of polymer chains [95]. Compression of polymer chains involves overcoming the secondary forces repelling the molecules in the polymer which requires pressures in the range of orders of magnitude higher than the pressures normally developed in the extrusion nozzle ($\sim 70\ Bar$) [95]. Furthermore, the compressibility of the printing material is reduced with the presence of rigid incompressible reinforcing fibers, thereby reducing the contribution of this phenomena to the oozing effect. While the response to a deformation of a solid is instantaneous, viscoelastic materials show a temporal response to applied forces or deformations which results from local flow or rearrangement of molecules in the viscoelastic material. Fiber suspensions of polymer melts behave as viscoelastic fluids and exhibit both a fluid-like and a solid-like behavior. The flow of viscoelastic fluid through the extrusion nozzle is driven by the pressure applied at the inlet of the extrusion nozzle, therefore the problem to consider inside extrusion nozzle is of creep of the viscoelastic fluid upon variations of pressure. Variations in pressure occur in the two cases described before, at starts and stops as well as at continuous changes in acceleration. While creep occurs upon application of pressure causing a delay in the response to flow of material through the nozzle, recovery occurs upon removal of the pressure giving rise to additional flow of material. Figure 2.1Figure 3.11 shows schematically the creep and recovery response of a viscoelastic fluid to a step change in stress for stress application and for stress removal, respectively. The Kelvin-Voigt model of a spring connected in parallel to a dashpot provides a viscoelastic response similar to the creep and recovery response showed schematically in Figure 3.11, therefore it could be utilized in a first attempt to model the viscoelastic behavior of the molten polymer.

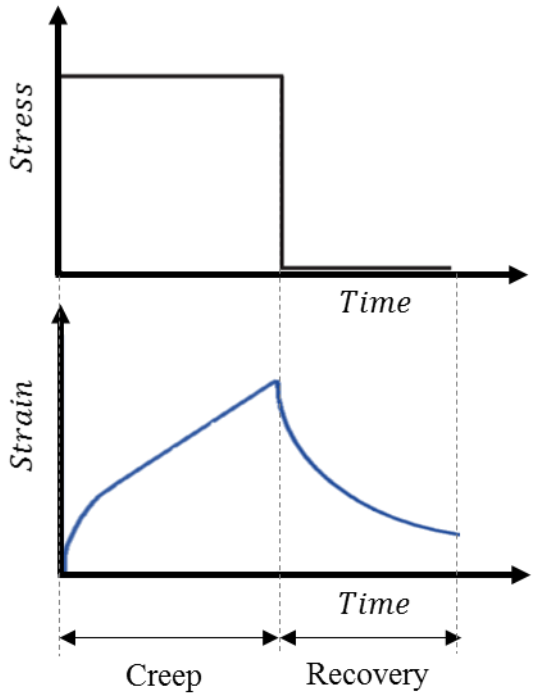

Figure 3.11 Schematic representation of creep and recovery response of a viscoelastic fluid.

The last element contributing to the oozing effect is the response time of the extrusion gear pump, this extrusion gear pump contributes primarily in step changes in flow rate due the finite time required to ramp the flow rate from zero to the desired rate. Thus far, three elements were mentioned to contribute to the oozing effect and furthermore those three effects are occurring simultaneously to consider using the material extrusion system to characterize their individual contributions. However, a lumped analysis can be carried out in terms of variables that are readily measured in the material extrusion system like pressure, flow rate and volume. Figure 3.12 shows a cross section of the extrusion nozzle used in CAMRI indicating the input flow rate and the output flow rate. In this analysis, all the sources of delay in the material response are lumped in a time constant, λ_n, which is also define by the product of two other parameters that are readily characterized utilizing the material extrusion system. Further, the objective of this lumped analysis is to determine an expression for the flow rate commanded to the extrusion gear pump, $\dot{Q}_e(t)$, that compensates for the effects mentioned before.

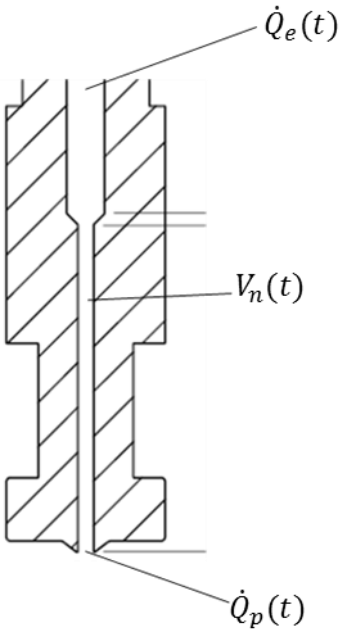

Figure 3.12 Cross section of the extrusion nozzle used in CAMRI

The lumped analysis begins by carrying out an analysis of the volume change inside the extrusion nozzle, which can be defined in terms of the input and output volumetric flow rates as shown in Equation 3.9. Notice all this analysis is carried out using exact differentials of changes around the entire internal volume, $V_n(t)$, of the nozzle which also changes as a function of time due to changes in printing conditions occurring throughout the manufacturing process of a part.

$$\frac{dV_n(t)}{dt} = d\dot{Q}(t) \tag{3.9}$$

The differential volumetric flow rate in Equation 3.9 corresponds to the difference between the output flow rate at the tip of the nozzle, $\dot{Q}_p(t)$, and the flow rate delivered by the extrusion gear pump, $\dot{Q}_e(t)$. The effects of both material behavior and nozzle-material interaction need to be captured in this analysis. A lumped compressibility, C_n, is first introduced to account for the effects of both compressibility and creep of the polymer melt in terms of a ratio of differential change in volume inside the nozzle, $dV_n(t)$, to a differential pressure, $dP(t)$, as shown in Equation 3.10. Notice a negative sign is used in Equation 3.10 to make C_n positive for reductions in volume due to pressure gradients along the length of the nozzle. Further, this parameter is characterized for

each material processed and it is also temperature dependent due to the effects of temperature to both the viscosity and the compressibility of the material. Nevertheless, we are going to neglect these effects and treat C_n as a constant value for now.

$$C_n = -\frac{dV_n(t)}{dP(t)} \tag{3.10}$$

While the parameter C_n accounts for the influence of the material to the overall response of the system, an analogy to the resistance to flow through a pipe can be used to account for the nozzle-material interaction. Therefore, the resistance to flow, R_f, can be defined as the ratio of a pressure differential, $dP(t)$, to the differential in output volumetric flow rate, $\dot{Q}_p(t)$, as shown in Equation 3.11. Further, both parameters R_f and C_n can be characterized through a couple of experiments using the material extrusion system. Similar to C_n, R_f depends on the properties of the material processed, particularly on the viscosity which is also dependent on both temperature and deformation rate. Nevertheless, this parameter is going to be treated as a constant value for now. Additionally, analytical expressions for R_f can be derived from the analysis of flow of concentrated fiber suspension through a circular channel. Analytical expressions for shear viscosities of concentrated suspensions with fibers aligned in the flow direction, which can provide a good approximation for this analysis, are provided by Pipes [23].

$$R_n = \frac{dP(t)}{d\dot{Q}_p(t)} \tag{3.11}$$

Then, by plugging Equation 3.10 and Equation 3.11 into the initial equation for the volume change inside the nozzle (Equation 3.9), the rate equation for the output flow rate given in Equation 3.12 can be obtained.

$$\frac{d\dot{Q}_p(t)}{dt} = -\frac{d\dot{Q}(t)}{R_n C_n} \tag{3.12}$$

Now, the differential flow rate term, $d\dot{Q}(t)$, in Equation 3.12 can be rewritten in terms of the flow rate entering and leaving the nozzle and it is also recognized that the two parameters can be combined into a single parameter λ_n defined as $dV_n(t)/d\dot{Q}_p(t)$. Therefore, Equation 3.12 can be written as shown in Equation 3.13.

$$\frac{d\dot{Q}_p(t)}{dt} = \frac{\dot{Q}_e(t) - \dot{Q}_p(t)}{\lambda_n} \tag{3.13}$$

As mentioned before, the output flow rate at the tip of the nozzle corresponds to the flow rate given by the product of the instantaneous speed of the gantry robot, $v(t)$, and the cross-section area of the printed bead $(w(t) \cdot h)$. Therefore, the Equation 3.13 can be written in terms of the cross-section area of the printed bead as shown in Equation 3.14.

$$\frac{d(v(t) \cdot (w(t)h))}{dt} = \frac{\dot{Q}_e(t) - v(t) \cdot (w(t)h)}{\lambda_n} \tag{3.14}$$

In addition to the changes in flow rate caused by the instantaneous velocity, $v(t)$, changes in bead width during material deposition also give rise to a change in flow rate. Therefore, Equation 3.15 is obtained by applying the chain rule to the time derivative of the left-hand side of Equation 3.14.

$$\frac{dv(t)}{dt} hw(t) + \frac{dw(t)}{dt} hv(t) = \frac{\dot{Q}_e(t) - v(t) \cdot (w(t)h)}{\lambda_n} \tag{3.15}$$

After applying the chain rule to the time derivative in Equation 3.14, another term associated with the kinematics of the gantry robot is recognized, acceleration of the gantry robot, $a(t)$, which results from the time derivative of the velocity. Since the goal is to define an expression for the volumetric flow rate, $\dot{Q}_e(t)$, commanded to the controller of the gear pump, the terms in Equation 3.15 can be rearranged to give rise to Equation 3.16.

$$\dot{Q}_e(t) = h\left[w(t)v(t) + \lambda_n w(t)a(t) + \lambda_n v(t)\frac{dw(t)}{dt}\right] \tag{3.16}$$

We are going to leave Equation 3.16 in differential form for convenience of the implementation. Now, this equation can be then implemented in the form of a feedforward control loop as depicted in the block diagram of Figure 3.13.

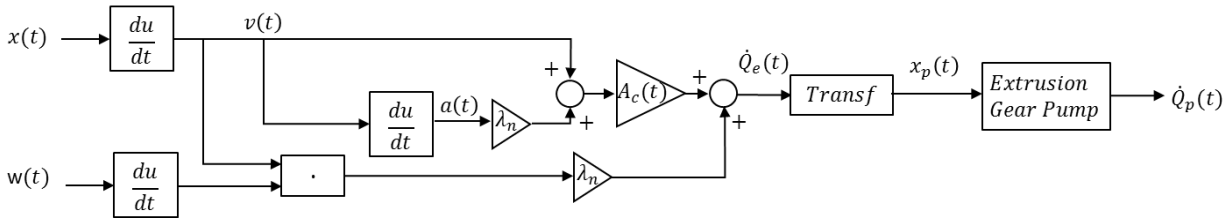

Figure 3.13 Bock diagram of the feedforward control system developed for controlling the flow rate of the extrusion gear pump in CAMRI.

After the controlling action for the extrusion gear pump is computed through the feedforward control system shown in Figure 3.13, the flow rate signal, $\dot{Q}_e(t)$, is transformed to a position commands that feeds the internal position closed loop control system of the brushless servomotor that drives the gear pump. The volumetric displacement of the pump along with the velocity and acceleration characteristics defined for the same are utilized to compute the angular position $x_p(t)$ of the shaft of the pump as a function of time. This way, the flow rate delivered by the pump is controlled with a precision in the range of less than one hundred of a degree of rotation in the shaft of the pump. The block diagram of the position close loop control used in the AC brushless servomotor driving the extrusion melt pump was included in Figure 3.7, however, the reader is referred to the user manual of the Sure Servo™ for further details [96].

3.4 Hardware and Software Architecture

This section provides an overview of the distributed control system (DCS) developed for CAMRI in terms of the elements of the hardware and pieces of software. Figure 3.14 shows the three principal hardware components used in the DCS developed for CAMRI. The first element is a Windows® based personal computer (PC) which is primarily used for the human machine interfaces (HMI) and for some of the process control systems required in CAMRI. The HMIs are the mechanism for the user to interact with CAMRI and thus it is considered the main commanding unit. The second element is the DSP-based NC controller used for planning and controlling the

coordinated motion of the three axis in the gantry robot. KFLOP© is the DSP-based NC controller utilized in CAMRI because of his multi-threading capability and the flexibility for implementing user defined programs. Further, the operative system embedded in KFLOP© not only allows for controlling up to eight motion axes but also handles the scheduling of user defined programs in a deterministic manner [89]. While operating, KFLOP© communicates with the PC through a USB port and utilizing the RS-232 protocol.

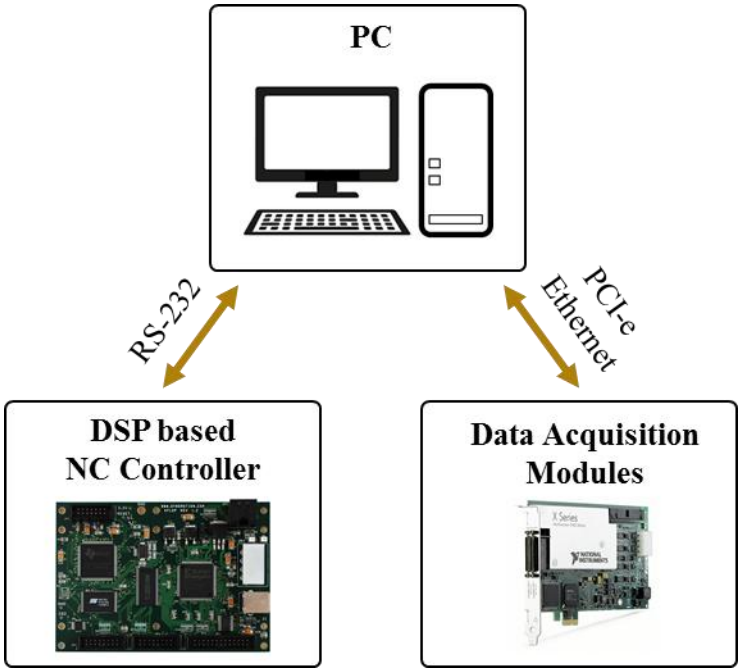

Figure 3.14 Architecture of the hardware utilized in the distributed control system developed for CAMRI.

The third element in the DCS is the hardware for data acquisition. Two data acquisition modules from National Instruments™ (NI™) are employed not only for signal acquisition of analog sensors, thermocouples, and digital signals but also for creating output digital and analog signals to command multiple actuators in CAMRI. One of the NI™ modules, the NI™-PCIe-6363, is equipped with general purpose inputs and outputs (GPIO) for both digital and analog signals and is interfaced with the PC through PCI-express. The reader is referred to the manual of this acquisition module for further details [97]. The NI™ 9214 is the second data acquisition module used in CAMRI and is exclusively utilized for acquiring temperature signals. Further, this module provides for signal conditioning of thermocouple signals that are generally in the range

of millivolts and highly susceptible to pick electromagnetic noise. This module is interfaced with the PC through Ethernet in a wired local area network. The reader is referred to the datasheet of the NI™ 9214 module for additional details on this module [98].

In addition to the primary hardware components shown in Figure 3.14, other pieces of hardware like signal conditioners, signal isolators, or power modules are used to interface signals generated in the primary hardware components with sensors and actuators. Examples worthwhile to mention of power modules used in CAMRI include the Variable Frequency Drive (VFD) used to control the AC induction motor driving the single-screw extruder, the Solid State (SS) relays used to control the power delivered by heating elements, the H-bridge circuit used to control the velocity of the DC brushed motor powering the tamper, and the electromechanical relays used to control miscellaneous pneumatic valves. The last category of hardware crucial for operation of the material extrusion system is sensors. Temperature is measured through K-type thermocouples at the different locations in the extruder, the gear pump and the extrusion nozzle whereas pressure is measured through pressure transducers at the output of the single screw extruder and at the outlet of the gear pump. On the one hand, pressure readings from the transducer located at the outlet of the extruder are used in the adaptive closed loop control system implemented for the extruder. On the other hand, pressure readings at the outlet of the gear pump are used for monitoring the deposition process and are also utilized in the safety monitors to prevent overpressures caused by clogging of the nozzle.

Alike the architecture of the hardware, the architecture of the software can be described in terms of the operations carried out at each component. Figure 3.15 summarizes the operations and functionalities performed in LabVIEW™ and KMotionCNC© at the PC, the NC controller KFLOP©, and the data acquisition modules. As mentioned before, the PC provides the means to the user for defining processing parameters, machine code, and for monitoring process variables throughout the manufacturing process of a part. This is achieved through two HMIs, one created with the software LabVIEW™ and the other created with a toolbox provided with KMotionCNC©.

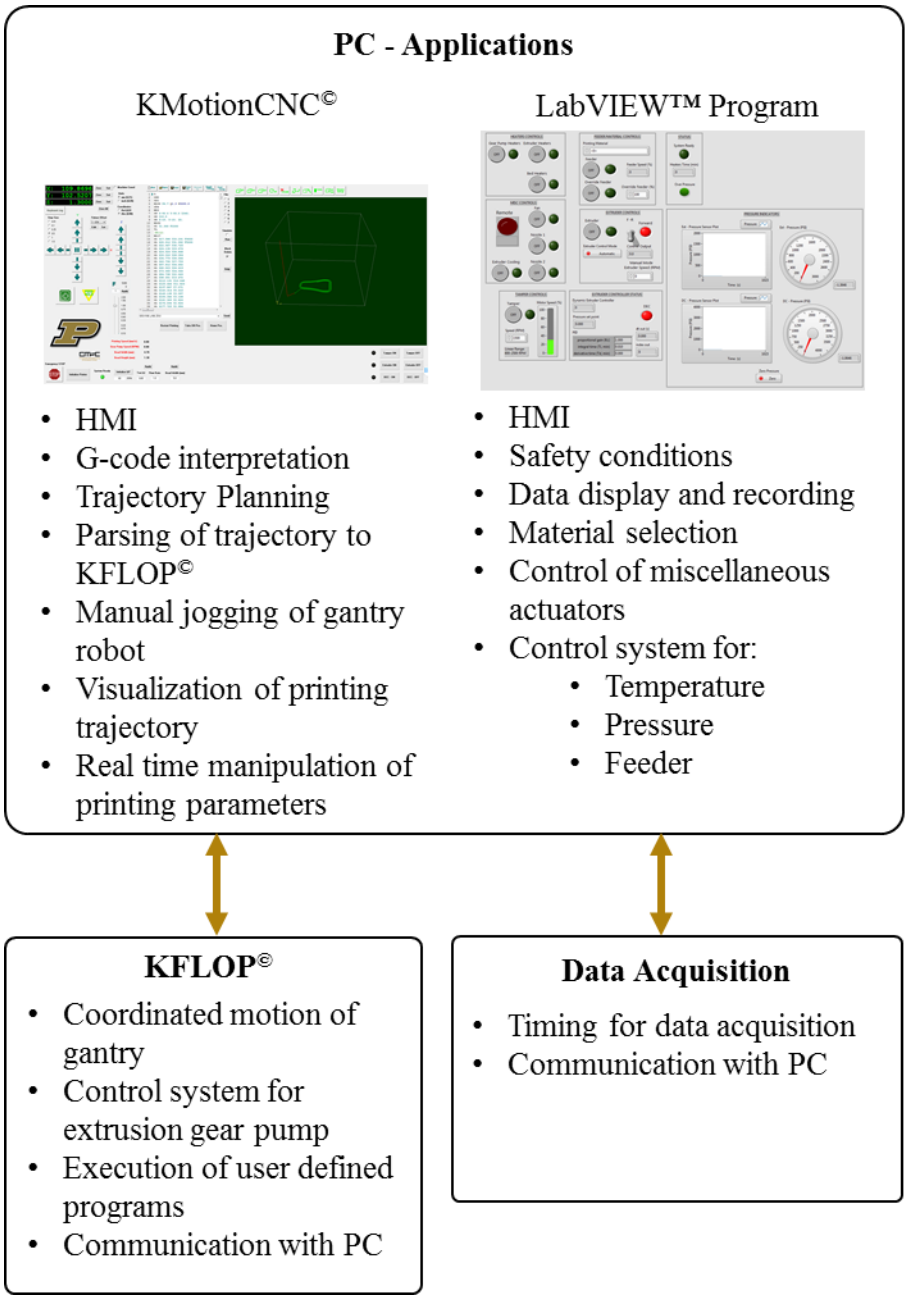

Figure 3.15 Architecture of the software in the distributed control system developed for CAMRI.

The KMotionCNC© HMI provides real time information of the coordinated motion performed during part manufacturing and allows for manipulation of process parameters like bead width, deposition speed, as well as other operation triggered through M-codes. Manual jogging of the gantry robot is also available through HMI. Figure 3.5 shows the HMI developed for KMotionCNC©. A list of M-codes used exclusively in CAMRI is provided in Table B.1 of the

APPENDIX B. In addition to provide process monitoring through the HMI, KMotionCNC© performs operations like interpreting the machine code and computing the trajectory for the gantry robot. Parsing of the precomputed printing trajectory to the NC controller KLOP© is also carried through KMotionCNC©.

The second computer program built with an HMI was developed in the programming environment of LabVIEW™ and serves multiple purposes in CAMRI. First, a redundant protection system ensures that the material extrusion system is at the appropriate operating conditions of temperature and pressure. Second, the LabVIEW™ HMI provides real time monitoring of process variables, manipulated variables and status variables of other components of CAMRI like the torque and speed of the AC servomotor coupled to the gear pump. Logging of temperature, pressure, status variables, is also possible through this HMI. Third, actuation of several other elements in CAMRI is also handled through the LabVIEW™ program, for example, the compaction frequency of the tamper, the temperature of the build plate, and the pneumatic valves for cooling of the tamper. Further, a list for selection of printing materials allows for rapid transition of different printing materials by loading automatically previously characterized process parameters. Fourth, control systems for temperature, pressure in the single screw extruder and feeder mass flow rate are also implemented in the LabVIEW™ program.

As explained in the previous section on Control of Single-Screw Extruder, the adaptive closed loop control system used for regulating the pressure in the extruder requires information from the motion of the gantry robot. Therefore, information flows not only between KFLOP© and KMotionCNC© but also between KFLOP© and LabVIEW™. The next section on implementation provides more details on how this flow of information is performed through the RS-232 protocol. Closed loop controls for the temperature of the build plate, the extrusion gear pump and the extrusion nozzle are implemented in LabVIEW™, whereas the temperature controllers for the single screw extruder are external PID controllers provided with the original single screw extruder acquired from Randcastle©. However, the individual PID controllers used in the extruder are enabled through the LabVIEW™ HMI.

Figure 3.16 shows the HMI developed in LabVIEW™ specifically for the application of CAMRI. This HMI is created in two sections, the upper section concentrates the controls for the actuators and the material extrusion system in CAMRI whereas the lower section allocates all the temperature measurements, set points for temperature controllers and data logging.

Thus far, only the operations carried out in the PC have been described, however, some of the most crucial operations in the EDAM process are performed in the NC controller KFLOP©. These include the coordinated motion of the three axes in the gantry robot, the control system for the extrusion gear pump previously introduced in the section Extrusion Gear Pump, the execution of user defined programs assisting the operation of the CAMRI system and the flow of information from KFLOP© to LabVIEW™.

The embedded operative system used in KFLOP© allows for deterministic execution of user defined programs where control systems can be implemented [90]. Additional reasons for computing the control action for the extrusion gear pump in KFLOP© instead of the PC include removing delays inherent to the communication between KFLOP© and the PC, the easy access to instantaneous velocity, acceleration and dimensions of the printed bead in KFLOP© and also due to the simplicity for creating control signals in KFLOP© for manipulating the AC servomotor used in the extrusion gear pump.

The last but not the least element in the architecture of the software is the data acquisition. In addition to digitalizing and conditioning electrical signals from the sensors in CAMRI, the acquisition modules manage the communication and delivery of data to the LabVIEW™ program. Additionally, analog and digital outputs manipulated through the LabVIEW™ program are also received by the acquisition modules, processed and translated to the intended physical signals in a timely manner.

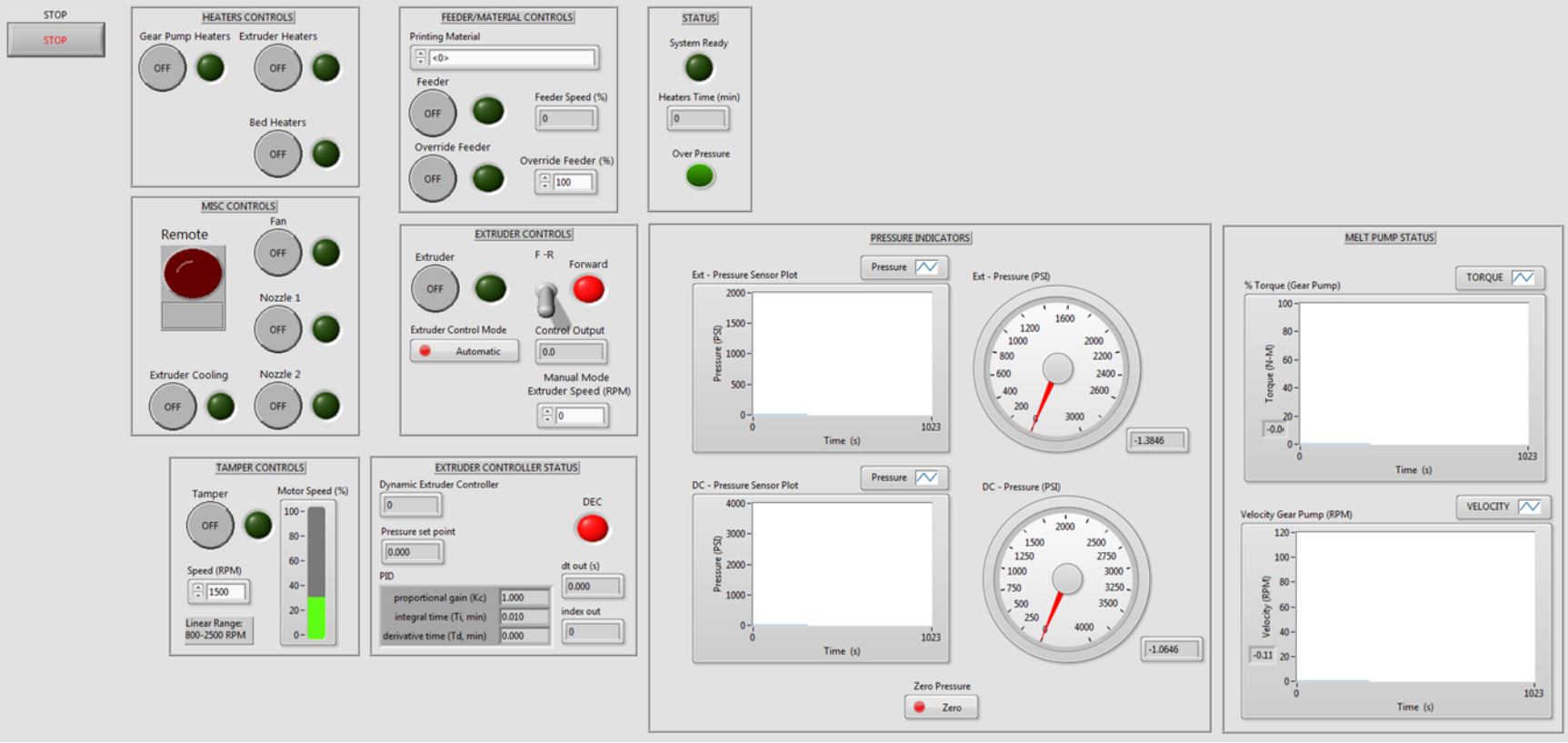

Figure 3.16 HMI developed in LabVIEW™ as part of the distributed control system used in CAMRI.

Figure 3.16 Continued

3.5 Implementation of Distributed Control System in CAMRI

The previous section described the architecture of the hardware and the software used in CAMRI and provided some insights on the distributed control system developed for coordinating the extrusion material system with the motion of the gantry robot. This section now focuses particularly on the implementation of the control systems utilized for controlling the different elements in the material extrusion system, specifically the single screw extruder, the extrusion gear pump and the volumetric feeder. The entire control system was shown for the first time in Figure 3.7 and the considerations behind the design of the distributed control system were discussed in the subsections dedicated to the single-screw extruder and the extrusion gear pump.

The flowchart in

Figure 3.18 provides the basis to explain the implementation of the multiple controllers in the DCS, however, it should be noted that only the principal functionalities are depicted in this flowchart. Different line styles are used in the blocks representing the actions in the flowchart depending on the component in the DCS that performs the action. This way, the flow of information between different elements in the DCS is rendered to some extent in the flowchart.

Now we are going to use the scenario of the printing process of a part to go through each of the actions in the flowchart. After loading the g-code to the KMotionCNC© HMI (Figure 3.5) and triggering the execution of the program by pressing the cycle start button in the HMI, a series of commands will be executed first to check if the system is ready to perform the printing operation. This assessment includes checking the status flags continuously sent from the LabVIEW™ program to the NC controller KFLOP©. These flags inform KFLOP© if the following three conditions are fulfilled in the material extrusion system. First, if the processing temperatures have been reached in the single screw extruder and gear pump. Second, if the pressure readings obtained from transducers located in the extruder and gear pump has been initialized property. Third, if the soaking time defined for the material extrusion system has been reached yet. Additionally, the status of the gantry robot is assessed to make sure all emergency signals are clear as well as to confirm the system has been successfully initialized. If one of these conditions is not satisfied, a warning message will appear to inform the user the system is not ready yet. After clearing these check points, two sequences of operations begin simultaneously at the NC controller KFLOP© and at the LabVIEW™ program, respectively. Shown at the left side of the flowchart in

Figure 3.18, the first operation is performed at KMotionCNC© and consists of interpreting the G-code, calculating the trajectory for the gantry robot and parsing this trajectory to KFLOP©. In order to achieve real time and uninterrupted execution of the trajectory at KFLOP©, trajectory points equivalent to multiple seconds of the g-code execution are buffered to KFLOP©.

From this point on, the manipulation and execution of position commands is performed in the KFLOP© controller. Using forward transports to compensate for the delays inherent to the distributed control system were discussed previously, yet this entails knowing the trajectory to be performed in the future. More specifically, the trajectory must be known in the future at forward transport times,τ_i, with respect to the current execution time. This functionality is implemented through a circular buffer created inside KFLOP© where position commands are stored at the beginning of the program execution for a predefined time, τ_{max}, and updated as the program execution progresses. Figure 3.17 shows a schematic representation of the circular buffer implemented in KFLOP©. Once the k slots in the buffer are filled with position commands at the beginning of the program execution, the pointer, P_1, arrives to the position where it started filling the buffer. At this point the buffer is said to be rewinded and the position command in the first memory slot of the buffer is sent to motion execution prior to store a new position command in the same memory slot. Then, the execution pointer, P_1, is moved to the next memory slot and the same procedure is repeated while marching through the buffer as illustrated in

Figure 3.18Figure 3.17. Following the same logic, multiple pointers, P_i, can be used to gather information on the forthcoming trajectory of the gantry robot. Since the time between the slots in the buffer is constant, the number of slots, n_i, to look ahead from P_1 can be determined simply by the ratio of the required forward transport, τ_i, to the sampling period dt, ($n_i = \tau_i/dt$). Hence, the predefined time, τ_{max}, is defined by the largest forward transport, τ_i, required in the system. Also notice the buffer is composed of a series of sequential memory locations accessed through pointers, therefore the term rewinding is used to indicate the address in the pointers is updated to the address where the buffer begins.

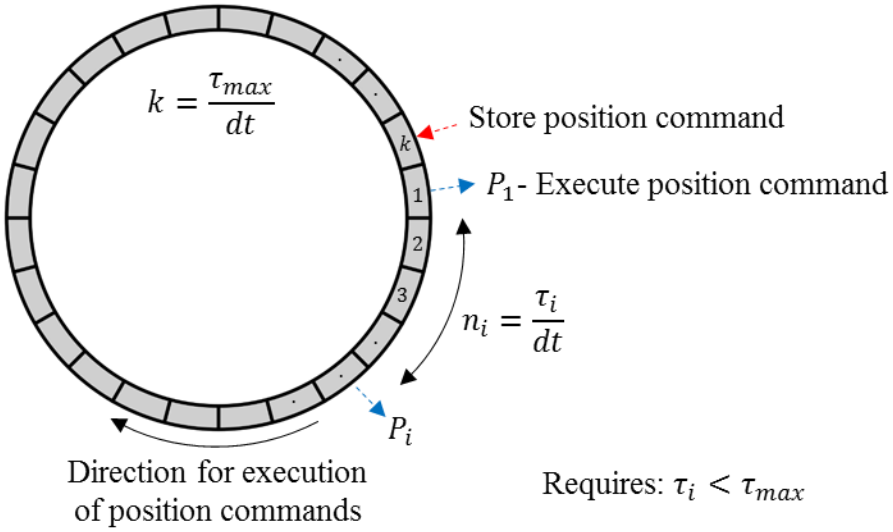

Figure 3.17 Schematic representation of circular buffer implemented in KFLOP© to achieve forward transport, τ_i.

Continuing with the flowchart in Figure 3.18, the step after filling the circular buffer is to perform the coordinated motion of the axes in the gantry robot. By sending the motion commands to execution inside KFLOP©, the movement required at each axis in the gantry robot is resolved through the inverse kinematics of the robot and converted to a train of digital pulses that command each servomotor. This protocol for communicating the motors with the NC controller is simply known as pulse and direction and is an open loop scheme since the NC controller does not receive feedback on the position of the gantry. Nevertheless, the servomotors are equipped internally with a position closed loop control system that ensures accurate angular positioning of the motor shaft. With this communication protocol, an electronic gear ratio provides the relation of pulses to linear motion of the axis whereas the frequency of pulse train defines the linear velocity of the axis.

In parallel to sending the motion commands to execution, the flow rate for the extrusion gear pump is computed inside KFLOP© utilizing Equation 3.16. The computed flow rate is then transformed to an angular velocity utilizing the volumetric displacement of the pump (mm^3/rev). Since the same protocol of pulse and direction is used to command the AC servomotor driving the gear pump, a motion axis in KFLOP© is dedicated to the gear pump in order to generate a pulse train through commands of angular velocity.

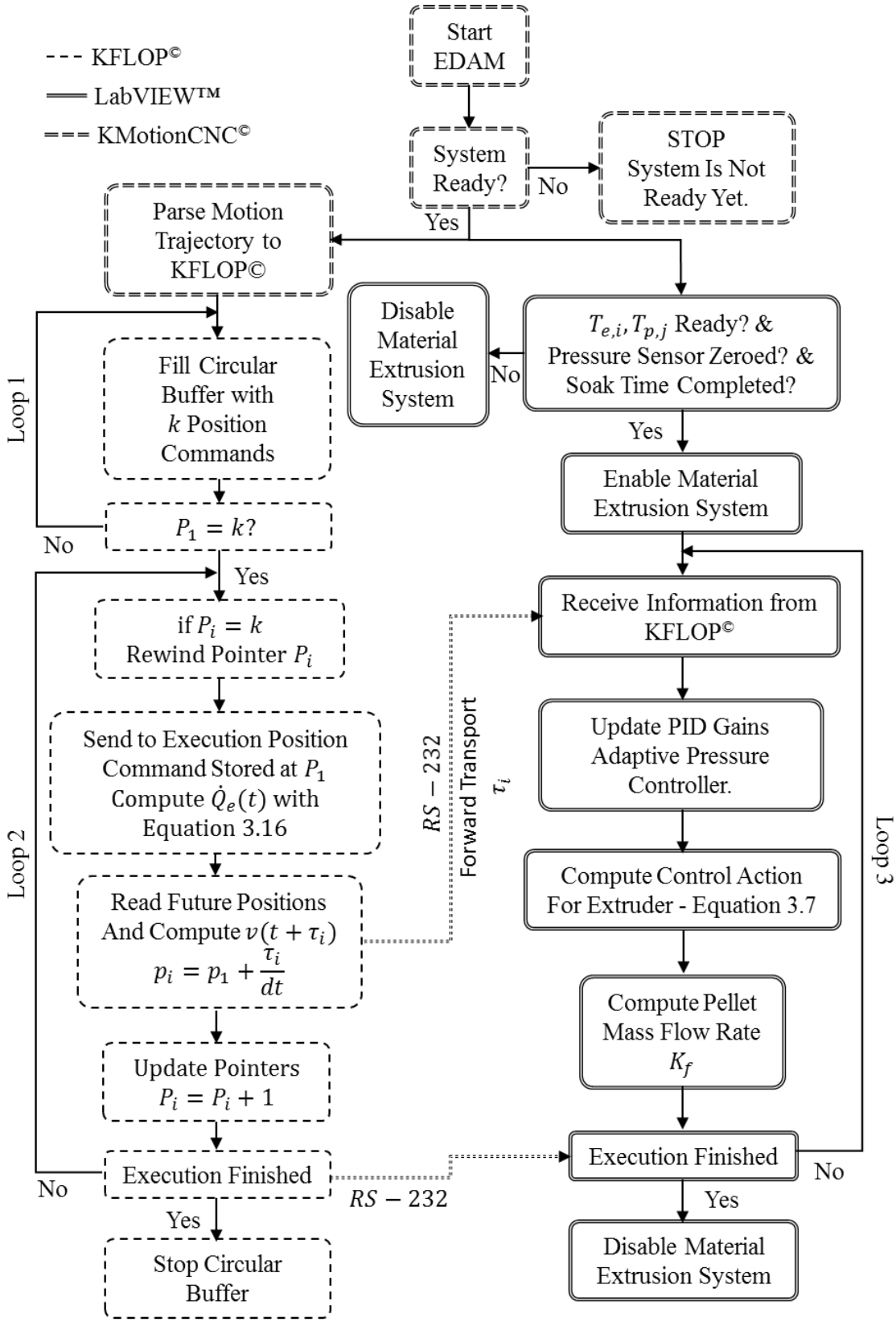

Figure 3.18 Operation flowchart of the distributed control system implemented in CAMRI.

Table 3.3 provides the parameter λ_n characterized for a 3.175 mm nozzle and the 50% by weight carbon fiber reinforced PPS used in this work. Additional details on the procedure for characterizing λ_n are provided towards the end of this section.

Table 3.3 Parameter λ_n characterized for a 3.175 mm nozzle and with 50%wt. carbon fiber PPS.

Material	**Nozzle Geometry**	$\boldsymbol{\lambda_n}$ $(\boldsymbol{s})$
Celstran® PPS-CF50-01	Ø 3.175 mm x 75.0 mm	0.0521

Utilizing the trajectory information stored in the circular buffer (Figure 3.17), the instantaneous velocity that will be performed at an instant of time, τ_i, in the future can be computed and sent to LabVIEW™ to inform the adaptive control system used for the single screw extruder. The same approach can be extended to inform other control systems that would benefit from forward transports like the volumetric feeder. Another application that leverages this functionality is printing with the product of coextruding multiple materials as described in the provisional patent application included in the section 7.2 of chapter 7.

The last step before cycling trough this loop is updating the addresses of the pointers, P_i, used for reading information from the circular buffer. This loop repeats throughout the manufacturing process of a part and it is automatically stopped upon reaching the end of the printing process. It should be noted though, the loop drawn around the operations concerned with the calculation of the flow rate for the pump is executed a slower rate than the loop used for updating the circular buffer. However, synchronization of both loops is handled by the scheduler in KFLOP©.

Now we are going to divert our attention to the processes depicted on the right side of the flowchart in

Figure 3.18 which occur primarily in LabVIEW™. The first process occurring in LabVIEW™ after starting the EDAM process is concerned with the status of the material extrusion system. As mentioned previously, temperature, pressure and soak time conditions must be satisfied in order to operate the material extrusion system. Otherwise, significant damage in the extrusion equipment can occur from operating the extrusion system while is still cold. By enabling the material extrusion system, the pump will be prepared to execute commands provided by KFLOP©, the feeder will supply the material demanded by the extruder and the single screw extruder will perform the control action of the adaptive PID controller.

In the next block, the instantaneous velocity of the gantry robot is received with a forward transport, τ_1. Using this information, the flow rate that is going to be demanded an instant of time, τ_1, in the future can be estimated to guide the selection of controller gains that are more suitable for the upcoming change in operation conditions. Additional details on the characterization of these parameters are provided towards the end of this section.

Table 3.4 lists the regions of operation used in the adaptive PID controller based on the flow rate demanded during material deposition. Furthermore, the proportional, derivative and integral gains used in the adaptive PID controller are provided at each region of operation in the same table. Additional details on the characterization of these parameters are provided towards the end of this section.

Table 3.4 Gains used in adaptive PID control based on region of operation defined by the flow rate demand.

Region of Operation $(\boldsymbol{Index - m})$	**Range of** $\boldsymbol{\dot{V}}$ $(\boldsymbol{mm^3/s})$	$\boldsymbol{K_{p,m}}$	$\boldsymbol{K_{i,m}}$ **(s)**	$\boldsymbol{K_{d,m}}$ **(s)**
1	$0 - 472$	0.024	0.54	0.66
2	$473 - 944$	0.025	0.60	0.72
3	$945 - 1416$	0.025	0.64	0.88

After updating the gains of the PID controller with the received information on the motion of the gantry robot, the control action of the adaptive PID controller is computed with a discrete version of the function given in Equation 3.7. Since discrete signals are used in the entire control system, the integral an derivatives of the error in Equation 3.7 are approximate using the trapezoidal rule and numerical differentiation, respectively [99]. Also, the output of the PID controller is bounded with an upper limit of 120 RPM and a lower limit of 0 RPM to prevent operating the extruder beyond its physical limits.

Subsequent to implementing the control action for the extruder, the mass flow rate commanded to the feeder is computed with the rotational speed of the single screw extruder, $N_e(t)$, and the gain K_f. Equation 3.8 provided a good first order estimate for K_f, however, this equation overestimates the value of this constant since it does not consider neither the pressure flow in the extruder nor the influence of a Saxton mixer located in the metering section of the screw. This type

of distributive mixers improves the uniformity of the melt but introduces additional fiber attrition and mechanical energy to the material [19]. Therefore, experimental calibration of K_f was required in order to prevent overfilling the extruder with material. Table 3.5 lists the gain K_f characterized for the 50% by weight carbon fiber reinforced PPS with Equation 3.8 and after experimental calibration. All the parameters required for Equation 3.8 and 3.5 are listed in Table A.14 of APPENDIX A, yet it should be noted that some of these parameters were calibrated to match experimental data obtained with the single screw extruder.

Table 3.5 Feeder gain K_f for the 50%wt. carbon fiber PPS.

Material	**Gain K_f (Equation 3.8)**	**Gain K_f (Adjusted)**
Celstran® PPS-CF50-01	1.124	0.98

After computing the mass flow rate of the feeder, the status of the printing process in informed to LabVIEW™ and the material extrusion system is disabled if the EDAM process has terminated, otherwise the loop starts again by receiving operation conditions from KFLOP©.

Thus far, only three loops were described in the operation of the DCS developed for CAMRI, however, there is a fourth loop cycle used for the temperature controllers. From the loops indicated in the flowchart of

Figure 3.18, the loop used for the circular buffer utilizes the highest sampling rate of 11.11 KHz whereas the loops 2 and 3 are operating at 20 Hz. With regards to the temperature controllers, a sampling rate of 1 Hz is utilized.

The last topic to cover as part of implementation of the distributed control system is the determination of parameters used in the control of the extrusion gear pump and in the PID used in the extruder.

Determination of the parameter λ_n used in the feed forward control of the extrusion gear pump is achieved through a couple of experiments conducted with the material extrusion system. As described in the section Extrusion Gear Pump, the parameter λ_n is given by the product of the resistance to flow, R_f, and the lumped compressibility, C_n, defined in Equation 3.11 and Equation 3.10, respectively. Both R_f and C_n are dependent on the rheological behavior of the processed material and therefore these are temperature dependent, however, in highly filled fiber suspensions like the ones used in this work, the shear viscosity is strongly influence by the fibers, thereby

lessening the impact of temperature on the viscosity. This is strictly true for small changes in temperature around the processing temperature of the polymer melt. Based on these observations a single value was characterized for the nozzle and material listed in Table 3.3. Characterizing the resistance to flow, R_f, is carried out simply by measuring the steady-state output flow rate at two different processing conditions that somewhat represent the operational conditions used in CAMRI. Output mass flow rate is characterized by collecting samples of material extruded at a constant gear pump speed and at fixed periods of time. After weighing the samples collected at a fixed period, the mass flow rate is computed from the weight measured and the period used for collecting the sample. Volumetric mass flow rate is then estimated by dividing the mass flow rate by the density of the material at room temperature. Additionally, the pressure at the outlet of the gear pump which corresponds to the pressure at the inlet of the extrusion nozzle is recorded. By taking differentials of pressure and volumetric flow rate at the two operation points, R_f can be estimated from the ratio of the two differentials as shown in Equation 3.11. Table 3.6 shows the R_f characterized with a first operation point taken at the operation region 1 and a second operation point taken at the operation region 2 according to Table 3.2. A flow rate of around $318\ mm^3/s$ was used in the first operation point whereas a flow rate of around $697\ mm^3/s$ was used in the second. Experimentally measured pressure and volumetric flow rates used for estimating R_f are listed in Table A.15 of the APPENDIX B.

Table 3.6 Parameters R_f and C_n characterized for 50%wt carbon fiber PPS with the CAMRI system.

Material	**Nozzle Geometry**	**Process Temperature** $(°\boldsymbol{C})$	$\boldsymbol{R_f}\ \left(\frac{\boldsymbol{N}}{\boldsymbol{mm^5}}\cdot\boldsymbol{s}\right)$	$\boldsymbol{C_n}\ \left(\frac{\boldsymbol{mm^5}}{\boldsymbol{N}}\right)$
Celstran® PPS-CF50-01	$Ø, 3.175\ mm$ $L, 75.0\ mm$	305	$7.115 \cdot 10^{-3}$	7.324

The next parameter to characterize is the lumped compressibility given by Equation 3.10. Since this parameter accounts for multiple phenomena occurring simultaneously as described before in the section Extrusion Gear Pump, experimental measurements are performed with the material extrusion system rather than quantifying the contribution of each phenomena to this parameter. As a result, an experiment is carefully conducted to measure the volume of material oozed out from

the tip of the nozzle after instructing a step change in extrusion speed to the gear pump. A video recording system mounted near the tip of the nozzle provides image frames that can be utilized to estimate the distance, dl, the extrudate oozes after the pump goes from a constant speed to zero. The sensitivity of this experiment is then increased as the magnitude of speed change in the gear pump increases, however, increasing the extrusion speed also increases the shear strain rate developed in the extrusion nozzle which ultimately reduces the viscosity of melt. Ideally, C_n, should be characterized for multiple rates of speed change in the gear pump, yet the sensitivity of this method decreases as the rate of speed change in reduced, thereby complicating the measurement of dl at the tip of the nozzle. Hence, an operation point corresponding to a printing speed commonly used in CAMRI was selected to characterize C_n.

While the pressure differential, dP, is readily determined from the difference between the pressure at the outlet of the extrusion nozzle, which is atmospheric pressure, and the pressure and the inlet of the extrusion nozzle, the volume differential, dV, is approximated from the oozing resulting from a step change in the speed of the gear pump. The oozed distance, dl, is determined from recorded frames and multiplied by the cross section of the extrudate to determine dV. The extrusion condition utilized for characterizing C_n is in the region 2 of the operation conditions defined in Table 3.2 and corresponds specifically to a volumetric flow rate of around $697\ mm^3/s$. Table 3.6 lists the value characterized for C_n through the method described before and with the conditions outlined above. Experimentally measured pressure differentials dP, oozed distance dl and cross-sectional area of the extrudate are provided in Table A.16 of APPENDIX A.

Now with regards to tuning of the PID parameters used in the adaptive PID controller, finding optimal gains for the PID can be challenging in the absence of transfer functions that describe the dynamics of each region of operation in the single screw extruder. Multiple methods for identifying the dynamics of each region in the extruder are available in the literature, then traditional control design can be applied to identify optimal controller gains for each region [93, 94]. In addition to this approach, automatic PID tuning algorithms can be utilized without knowing the dynamics of the system to determine a set of gains adequate for the system. The latter approach was used to determine the gains required at each region of operation in the adaptive PID controller utilizing a PID tuning algorithm based on relay feedback and the Ziegler-Nichols method implemented in LabVIEW™ [100]. The basic idea behind this method is the observation that many systems reach limit cycle oscillations under relay feedback [94]. Therefore, the objective of the

tuning procedure is to find the frequency of the square wave used in the relay feedback that reaches the limit cycle oscillation of the system. Then, the period of the square wave that reached the limit cycle oscillation is extracted along with the ultimate gain used to reach this condition. These two parameters are then used in the heuristic method of Ziegler-Nichols to estimate PID gains that will produce an acceptable response. Subsequently, fine tuning of the PID gains was performed for each operation region to improve the transient response of the system.

In order to perform the experiments required for tuning the PID gains at each region of operation in the extruder, a constant flow rate equal to the mean flow rate of a particular region was commanded to the gear pump in the tuning process of such a region. At the same time, a square wave resulting from the relay action is introduced at the setpoint, in this case in terms of pressure set point. Then the procedure described before is performed to tune the gains of the PID controller. The gains after the fine tuning are listed in Table 3.4 for each of the regions of operation of the single screw extruder.

Finally, the last step is to demonstrate the functionality of the distributed control system implemented in CAMRI which is presented in the next section.

3.6 Performance of Distributed Control System Implemented in CAMRI

The previous sections described challenges with controlling pressure in single screw extruders and the effects occurring in the material and flow that lead to the so-called oozing effect, then a distributed control system was introduced to address these issues and to coordinate the material extrusions system with the motion of the gantry robot. Now the objective is to demonstrate the functionality of the distributed control system developed for CAMRI. The first clear example of the functionality of the distributed control system is the printed tools presented in the section Tooling Produced with Extrusion Deposition Additive Manufacturing where each of those was manufactured utilizing CAMRI. However, a simple scenario is presented to assess the control systems developed for the material extrusion system.

The objective of the assessment presented herein is to investigate the robustness of the distributed control system to deposit material at varying conditions that require transitioning between regions of operation of flow rate (Table 3.2). In other words, the ability to print over a broad range of speeds is assessed along with the ability of the system to respond to rapid changes in flow rate. Hence, a hollow square was designed with a wall thickness equal to three printed

beads and with external dimensions of 254.0 by 254.0 mm, with the purpose of introducing transitions in printing conditions at each corner of the square. This way, two sides can be printed at a deposition rate representing the range of operation 1 whereas the other two sides can be printed at deposition rate representing the range of operation 2, thereby assessing the ability to print not only over a representative range of speeds but also with continuous changes in deposition conditions. Figure 3.19 shows the test geometry used for testing the consistency in material deposition at different printing speeds.

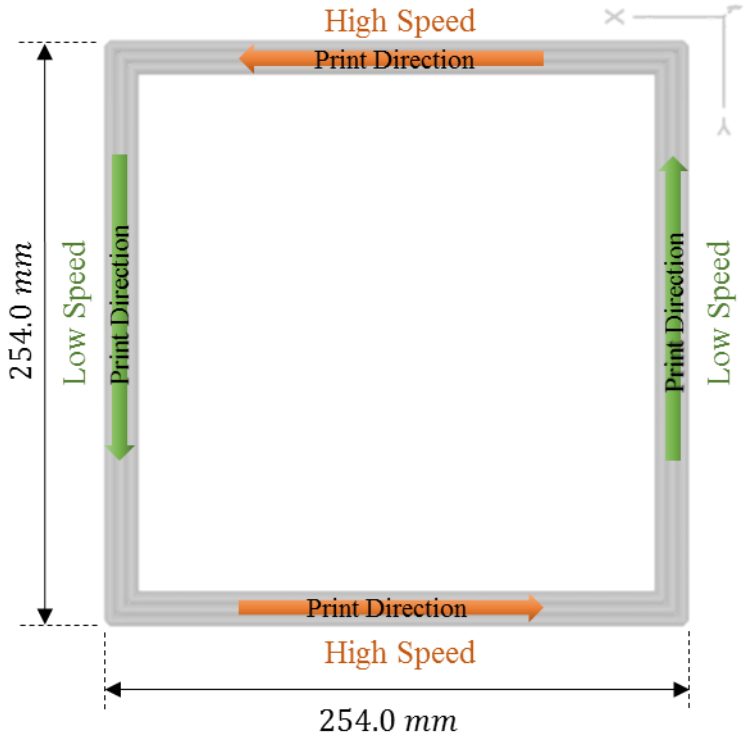

Figure 3.19 Test geometry used for assessing consistency in material deposition at different printing speeds.

Only qualitative measures were used to assess the consistency near the corners of the test square since accurate measurements are not possible due to the scalloped printed surface. The thickness of the printed section near the corner was inspected on both the low printing speed side and the high printing speed side near the corners. These regions were chosen for obvious reasons, transitions in print speed occurs in these regions and thus making these more susceptible to variations in flow rate.

Printing speeds were chosen such that the material extrusion system transitions from the operating region 1 to 2 and vice versa. Table 3.7 lists the printing speeds and extrusion conditions used while printing the square test geometry.

Table 3.7 Processing conditions use for printing test geometry.

Processing Variable	**Value**
Build Plate Temperature (K)	393.15
High Printing Speed (mm/s)	91.67
Low Printing Speed (mm/s)	33.3
Extrusion Temperature (K)	573.15

The transient evolution of printing speed, pressure at the outlet of the extrusion gear pump and pressure at the outlet of the single screw extruder were recorded during the printing process of the test geometry. Figure 3.20 shows the transient behavior of these variables during the manufacturing of the square geometry. Transitions in printing speed during part manufacturing are plotted with red solid lines whereas the pressure response at the outlet of the extrusion gear pump is plotted with dashed blue lines. The sharp increase in pressure in the extrusion gear pump is a consequence of the steep changes in flow rate demanded to the gear pump during part manufacturing. The flow rate commanded to the servomotor driving the gear pump is proportional to the printing speed and acceleration as given by Equation 3.16.

A constant pressure setpoint of $400\ psi$ at the outlet of the single screw extruder was used during these experiments. The adaptive closed loop control system implemented for controlling the single screw extruder maintained the pressure at the outlet of the single screw extruder well bounded within 600 and $300\ psi$ despite the fluctuation in material demand during part manufacturing. This pressure component is shown with blue solid lines in Figure 3.20. Such fluctuations in pressure at the inlet of the gear pump (outlet of the single screw extruder) are acceptable for the internal lubrication of the extrusion gear pump according to the manufacturer of the extrusion gear pump but more importantly, these do not compromise the output flow rate.

Hence, this demonstrates the effectiveness of the adaptive control system implemented in the material extrusion system to maintain the pressure at the output of the single screw extruder bounded despite the steep and continuous fluctuation in flow rate.

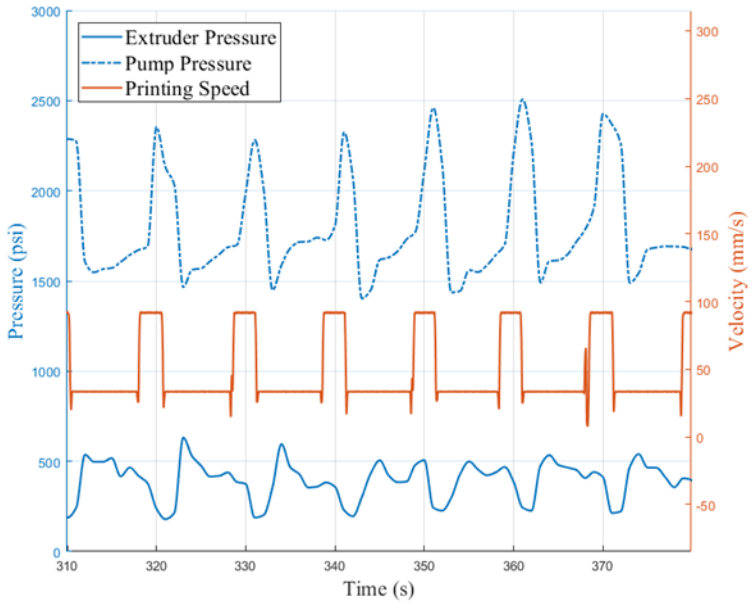

Figure 3.20 Processing variables recorded during manufacturing of test geometry. Pressure at the outlet of the extrusion gear pump, pressure at the outlet of the single screw extruder and printing speed.

Figure 3.21 shows examples of the consistency in material deposition achieved in the regions near the corner where steep transitions in printing speed were introduced. It should be noted that gaps between the beads shown around the corner in the picture on the right side correspond to geometrical gaps in the machine code and no to gaps due to the lack of flow. Overall, good consistency in printed quality was attained around the all the corners where steep changes in flow rate occurred.

Measurements of the width in the straight sections printed before and after the corner were taken with a caliper and maximum differences in the range of $0.4\ mm$ were observed between both sides. Again, these measurements are not accurate due to the scalloped surface of the printed wall but provide an indicator of the ability to print consistently despite steep changes in printing speed.

The second indicator is the spacing between beads after undergoing a change in deposition speed, particularly, after transitioning from a low printing speed to a high printing speed. A problem that would arise if the single screw extruder is not capable of responding to such a change in flow rate is that the gear pump will be starved and the beads printed immediately after the transition will be skinny. In the opposite case of transitioning from a high printing speed to a low

printing speed, the pressure can overshoot and trigger one of the overpressure safety mechanism if the pressure controller does not react rapidly to those changes. Nevertheless, the adaptive control system implemented in CAMRI is responsive to accommodate these fluctuations as demonstrated in the pressure history shown previously in Figure 3.20.

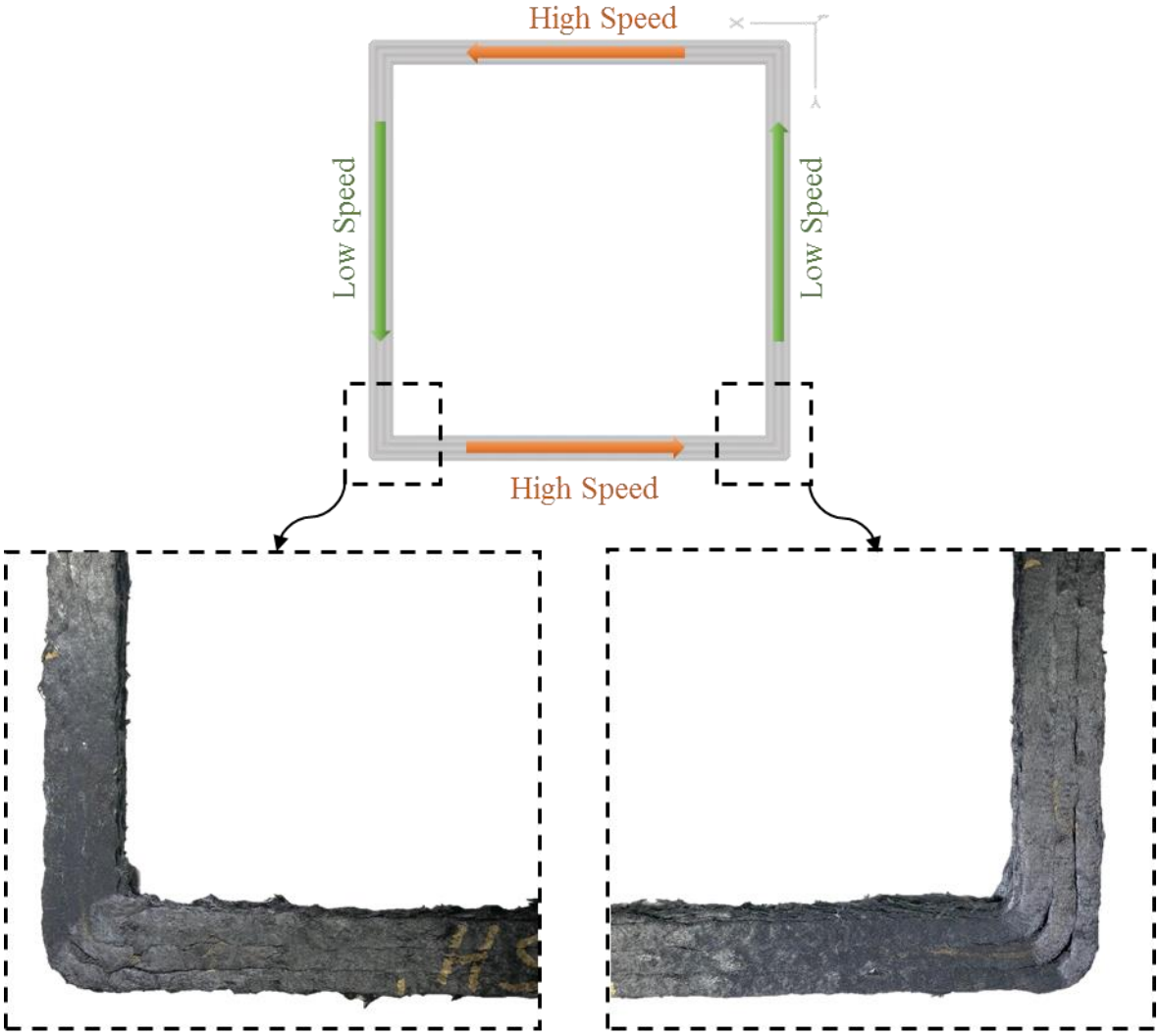

Figure 3.21 Corners of the printed test geometry where transitions occur.

Future improvements to the CAMRI system include implementing an algorithm in the CAMRI's controller that identifies corners within the instructions in the machine code that will leave a gap at the corners. Having identified the corners with a gap, the geometrical space left in those corners can be predicted and the flow rate corrected to fill the gaps

4. EDAM PROCESS SIMULATION

Previous work on modeling of the Extrusion Deposition Additive Manufacturing (EDAM) process has been reviewed in the section Process Simulation with the emphasis on three areas, heat transfer, fusion bonding, and solidification, stress evolution and damage modeling. Now this chapter introduces the framework used in this dissertation for simulating heat transfer, fusion bonding of semi-crystalline polymers and delamination during the EDAM process utilizing Abaqus© 2017 [101]. With this simulation framework, the actual process of depositing beads of molten material in a layer by layer basis is replicated by activating elements in a finite element mesh. The following sections describe in great detail the simulation framework in order to prepare the reader for the subsequent chapters presenting simulations of heat transfer, fusion bonding and damage modeling.

4.1 EDAM Process Simulation Framework

The basic idea of activating elements in a finite element mesh for replicating the continuous material deposition has been utilized in different simulation applications previously, for example for simulating welding processes as well as for additive manufacturing [78, 79]. However, these simulations were initially developed in commercial finite element (FE) software with the technology of birth and death element where the addition of finite elements involved reformulating the finite element problem to consider the change in element count. With this approach, the stiffness matrix of the finite element problem needs to be resized upon addition of new elements which can consume a significant portion of the solution time in a relatively large analysis. The second challenge in simulating additive manufacturing processes is tracking of the free surfaces as the manufacturing process of a part evolves. Identifying exposed surfaces throughout the simulation of an additive manufacturing process is fundamental for the correct simulation of the heat transfer. Furthermore, the ability to communicate external information for driving the activation process of elements was in general limited in commercial FE software.

With the advent of process simulations for additive manufacturing, four crucial functionalities were deployed in Abaqus© 2017 to facilitate simulating additive manufacturing processes. The first functionality was the UEPActivationVol user subroutine that enabled the addition or removal of finite elements to simulate the additive manufacturing process. Unlike the

precursor approach of model change, in this approach the size of the finite element problem (stiffness matrix) in defined based on a part unspecific mesh defined at the beginning of the analysis. Therefore, the stiffness matrix is only populated with new entries as elements are activated instead of reformulating the problem every time the elements count changes. This way, elements status can be modified at each time increment of a given step in the finite element analysis [101].

The second functionality released in Abaqus© 2017 was the automatic detection of free surfaces upon activation of elements. This is available for convection and radiation heat losses through the keywords FFS and RFS, respectively. A tool-path mesh intersection module consisting of multiple utility subroutines was the third functionality released in Abaqus© 2017. Utilizing these utility subroutines, algorithms can be implemented for controlling the activation of finite elements based on the printing history used for manufacturing of a part. We will refer to this printing history as the event series and corresponds to a spatial and temporal description of the printing conditions, namely time, position, mass flow rate, type of feature printed, etc. The snippet shown in Figure 4.1 provides an example of the event series used to communicate the printing trajectory to the EDAM process simulations performed in Abaqus©.

Time (s)	Position X (mm)	Position Y (mm)	Position Z (mm)	Extrusion (On/Off)	Type of printed feature
0.201	11.79	3.41	0	1	3
0.301	17.65	3.41	0	1	3
0.402	23.51	3.41	0	1	3
0.502	29.37	3.41	0	1	3
0.602	35.23	3.41	0	1	3
0.703	41.09	3.41	0	1	3
0.803	46.95	3.41	0	1	3
0.904	52.8	3.41	0	1	3
1.004	58.66	3.41	0	1	3
1.105	64.52	3.41	0	1	3

Figure 4.1 Example of event series utilized to drive the EDAM process simulations.

While the first four columns in the event series provide the temporal and spatial description of the position of the extrusion nozzle, the fifth and sixth columns are used to inform the extrusion condition and the type of feature printed, respectively. Currently, the extrusion condition only takes the on and off states representing whether the extruder is depositing material or not, however, more advance options can be developed based on a flow rate command which allows for variations in bead dimensions. With regards to the sixth column, the type of feature printed, namely external walls, solid sections, infills, etc. are communicated to the process simulation for applying the correct boundary conditions in the heat transfer analysis.

The last but not the least important functionality deployed in Abaqus© 2017 was the concept of property and parameter tables which facilitates communicating external information to the user subroutines. For example, the event series is communicated to the user subroutines in Abaqus© through a table collection. As we will see later, information for other subroutines is passed in through table collections.In order to perform process simulations of the EDAM process with composite materials, a framework utilizing suit of subroutines including some of the ones mentioned previously was implemented by Favaloro et al. [73] to drive the activation process of finite elements using the event series. Additionally, local material orientations are computed based on the printed trajectories contained in the event series in order to assign orthotropic material properties in the multiple material models used. This contribution was crucial for enabling physics based simulations of the EDAM process in the work presented in this dissertation as well as in the dissertation from Brenken [16]. Further details on the algorithm used for determining local material orientation and activation times developed by Favaloro et al. [73] is provided in the section Activation Time and Local Material Orientations.Since multiple subroutines are used to perform the process simulation in Abaqus©, it is essential to understand the execution order, the interconnectivity of subroutines and the operations performed at each subroutine. The flow diagram shown in Figure 4.2 illustrates the execution order of the subroutines primarily used for simulating the EDAM process. The first call to subroutines occurs at the start of the analysis and the first subroutine called is UEXTERNALDB© [101]. This subroutine is used for initializing a global array that can be shared among all threads in a parallel solution procedure and that serves the purpose of communicating the local material orientation, activation time and the type of feature printed across all the subroutines.

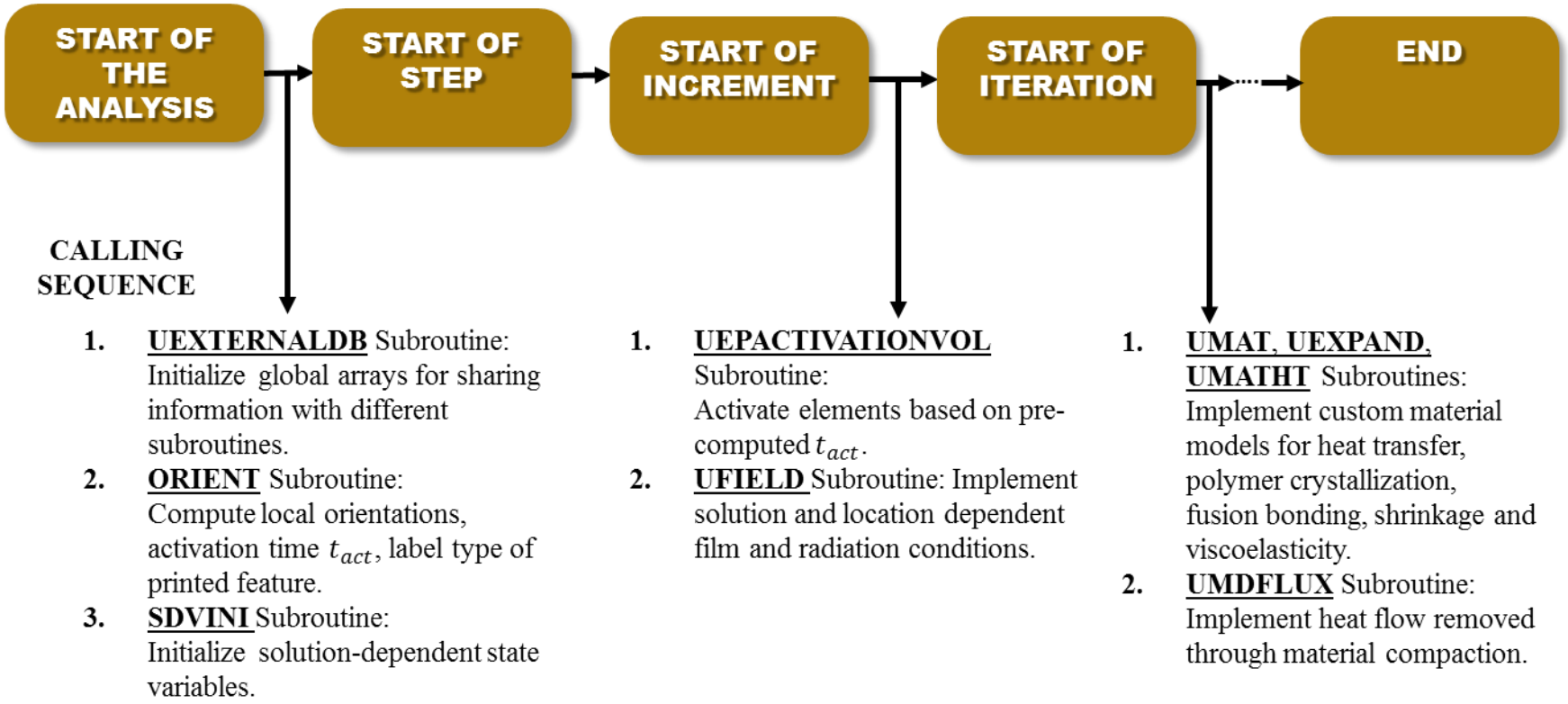

Figure 4.2 Execution order of subroutines utilized in the EDAM process simulation.

The set of utility subroutines SMAFloatArrayXXXXXX is used to create, access and modify the global arrays [101]. The "X" symbols at the end of the subroutine name indicate multiple subroutines of the same family used for the purposes mentioned before.

After creating global arrays in UEXTERNALDB© for sharing information across all the other user subroutines, the ORIENT© subroutine is called next. This subroutine is used to compute the local material orientation, the activation time, t_{act}, and to label the type of printed feature for each individual element based on the information provided in the event series. The algorithm developed by Favaloro et al. [73] was implemented by the author in a ORIENT© subroutine to determine the activation time, t_{act}, and the local material orientation at each integration point of the element. This way, orthotropic material properties are readily assigned in the heat transfer analysis presented later. The utility subroutines from the toolpath-mesh intersection module released in Abaqus© 2017 are also used inside the ORIENT© subroutine to identify the segments of the event series intersecting a particular element. The ORIENT© is called at each integration point of the element, however, the fact that multiple elements are used to represent a printed bead allows assuming the same orientation in all the integration points of an element. Further, local orientation is determined using information of the centroid of the element and thus the same orientation is obtained regardless of the integration point considered in the calculation. Therefore, the orientation needs to be computed only once for each element. Finally, elements are also labeled in the ORIENT© subroutine based on the printed feature these belong to. The third and last subroutine called at the start of the analysis is SDVINI©. Utilizing the SDVINI© user subroutine, the activation times, t_{act}, already stored in data arrays for each element are assigned to each of the integration points in the element. In addition to serve for element activation, the activation time, t_{act}, is used in material models implemented in other user subroutines to calculate for instance evolution of crystallinity and degree of bonding as shown in previous work of Brenken [16] and Barocio et al. [102]. The next call to user subroutines occurring in the flow diagram of Figure 4.2 occurs at the start of an increment. Upon starting an increment, calls to the UEPATIVATIONVOL© subroutine are made to activate elements with activation times within the time increment in consideration. This way, elements are activated based on the printing trajectory input through the event series. Currently, the element progressive activation functionality in Abaqus© 2017 only supports fully active or inactive elements. Yet, future releases might allow for partial element activation, thereby making possible some simplifications to the process simulation

like capturing multiple layers in a single element. The suite of subroutines described thus far, namely UEXTERNALDB©, ORIENT©, SDVINI©, UEPATIVATIONVOL©, and the utility subroutines from the toolpath-mesh intersection module are concerned only with the activation of elements based on the event series. Nevertheless, the subroutines described next are related to material models and complex boundary conditions.

Calls to the UFIELD© subroutines also occur at the start of an increment. The UFIELD© subroutine is used to prescribe predefined field variables at the element nodes. The UFIELD© subroutine is used to implement position and temperature dependent film coefficients. Further details on the implementation of this subroutine are provided in Chapter 5. Since this subroutine is called at the start of an increment, the material models implemented through this subroutine is used in an explicit solution scheme. In other words, the material properties used in a given increment are not influenced by the results obtained at the end of the increment.

The next step in the solution process of the FEA where subroutines are called is at the start of each iteration performed in the iterative solution procedure. The flow diagram of the subroutine execution process in Figure 4.2 lists the multiple user defined subroutines utilized for implementing material models for heat transfer, polymer crystallization, fusion bonding, anisotropic material shrinkage and viscoelasticity. Table 4.1 lists the material models implemented in each subroutine. The implementation of the models for heat transfer and fusion bonding are found in this dissertation whereas the implementation of polymer crystallization and melting, shrinkage and Thermoviscoelasticity are covered in the PhD dissertation from Brenken [16].

Table 4.1 Material models implemented through user subroutines in Abaqus© including the work from Brenken [16].

Material Model	**User Subroutine**
Orthotropic Heat Transfer Polymer Crystallization and Melting Fusion Bonding	UMATHT©
Anisotropic Shrinkage Crystallization Shrinkage	UEXPAND©
Thermoviscoelasticity	UMAT©

In addition to the user subroutines utilized for implementing material models, the user subroutine UMDFLUX© was utilized to capture the heat losses from the compaction process carried out with

either a roller or a tamper. Unlike the user subroutines listed in Table 4.1 which are called at each integration point, the UMDFLUX© user subroutine is called only once per element to compute the heat flow removed during a time increment. The following chapter on heat transfer presents the implementation of a heat flux function that moves along with the extrusion nozzle replicating the effect of a tamper or a roller. Utility subroutines provided with the toolpath-mesh intersection module are also used within the UMDFLUX© to access information of the event series required for computing the heat removed from the surface of an element.

4.2 Activation Time and Local Material Orientations

The framework for simulating the extrusion deposition additive manufacturing process with composites was presented in the previous section. The use of new functionalities deployed in Abaqus© 2017 was mentioned before as one of the primary contributors for this simulation framework, however, the algorithm implemented with these functionalities is one of the most important pieces to be able to simulate the EDAM process in Abaqus©. Therefore, the algorithm for determining the activation times, local material orientation and labeling elements based on the type of feature printed is presented in this section. This algorithm was originally developed and implemented by Anthony Favaloro [73] for determining material orientation and activation times and it has been also described in the dissertation from Brenken [16]. A small addition was made in this work to the original algorithm in order to label elements based on the type of feature printed.

The algorithm used to determine activation times, local material orientation and to label nodes based on the printed feature is performed in the ORIENT© subroutine which provides information like nodal location, nodal number, element number, etc. In addition to this information, the global stacking direction, x_i^S, the width, w, and height, h, of the printed bead and the event series are required to determine the parameters mentioned before for the process simulation of a part utilizing a part unspecific mesh. At this stage, printed beads with rectangular cross section are considered, yet this algorithm can be readily extended to other bead shapes.

The first step is to find segments in the event series that pass within a radial distance from the centroid of the element equal to the minimum radius, r, required to contain the cross section of a bead. Provided the nodal locations, x_i^n, in the ORIENT© subroutine, the location of the element centroid, x_i^C is computed first. Then, Equation 4.1 can be used to determine the minimum

radius, r, required to contain the cross section of the bead. A calibration factor, r_s, is included to provide fine adjustments to the searching process of event series.

$$r = (1 + r_s)\sqrt{w^2 + h^2} \tag{4.1}$$

The radius, r, the location of the centroid, x_i^c, and the event series are passed to the utility subroutine getEventSeriesTimeIntervalLGLocationPath© to efficiently perform a search of segments in the event series that intersect a sphere centered at x_i^c and with a radius equal to r. The search performed by the utility subroutine returns the number of segments, $nSeg$, in the event series that intersected the searching sphere. The following information is returned for each of the $nSeg$ segments that intercepted the sphere: the start location, x_i^A, the end location, x_i^B, the time at the start location, t^A, the time at the end location, t^B, the extrusion condition at the start and end locations and an ID indicating the type of feature printed at the start and at the end of the segment. An initially defined array is used to store this data for the next step which consists of interrogating each of the $nSeg$ segments in a loop with the same number of iterations than segments. The first step in screening the segments consists on interrogating the extrusion condition at the start of the segment. If the extrusion condition is 0, the segment is discarded, otherwise the length of the segment, L^{AB}, is computed using the start and end locations of the segment as shown in Equation 4.2.

$$L^{AB} = \left\| x_i^B - x_i^A \right\| \tag{4.2}$$

After computing the length of the segment, a local coordinate system can be defined for the segment knowing the stacking direction x_i^S. The principal direction X_i^1 is determined from the two points in the segment whereas the other two principal directions, X_i^2 and X_i^3 can be then defined through the cross products in Equation 4.3 indicated through the permutation symbol ε_{ijk}.

$$X_i^1 = \frac{x_i^B - x_i^A}{\left\| x_i^B - x_i^A \right\|} \tag{4.3}$$

$$X_i^2 = \frac{\varepsilon_{ijk} x_j^S X_k^1}{\left\| \varepsilon_{ijk} x_j^S X_k^1 \right\|}$$

$$X_i^3 = \varepsilon_{ijk} X_j^1 X_k^2$$

These principal directions now correspond to a coordinate system with origin in x_i^A. We then compute the location of the centroid of the element with respect to the coordinate system with origin in x_i^A and define the coordinates x^1, x^2, x^3 for the centroid.

$$\begin{aligned} x^1 &= \left(x_i^C - x_i^a\right) \cdot X_i^1 \\ x^2 &= \left(x_i^C - x_i^a\right) \cdot X_i^2 \\ x^3 &= \left(x_i^C - x_i^a\right) \cdot X_i^3 \end{aligned} \tag{4.3}$$

We can now use the coordinates of the centroid in the new coordinate system to continue screening the segments. The first condition to check is if x^1 in negative which means the centroid of the element is behind the start point of the event series which causes to disregard this segment. Yet, if the segment is larger than zero and smaller or equal to the length of the segment L^{AB} is further considered. At this point, the activation time, t_{act}, can be computed assuming constant velocity within the segment with Equation 4.4.

$$t_{act} = t^A + \frac{x^1}{L^{AB}} (t^B - t^A) \tag{4.4}$$

The next check to make is with the coordinate x^2 obtained with Equation 4.3. If the magnitude of this coordinate is smaller or equal to half of the bead width, $w/2$, it means the centroid is within the bead in the 2-direction. The same check is performed to the coordinate x^3 obtained with Equation 4.3, and the segment is further considered if x^3 is within zero and the height of the bead,

h. Satisfying all the previous checks indicates the element is within the width and the height of the bead and an activation time was determined for this segment. The objective at the end is to utilize the orientations computed with the segment that yields the smallest activation time. Therefore, as the loop is performed for each of the $nSeg$ segments returned by the utility subroutine, the orientations X_i^1, X_i^2 and X_i^3 for the smallest activation time are tracked and used to define the local material orientation and activation time, t_{act}, respectively.

However, another conditions should be considered to capture elements that might be missed at corners when there is change in printing direction. This occurs due to the linear wise description of the trajectory given by the event series and the approach described before to screen the segments based only on a rectangular box as illustrated in Figure 4.3.

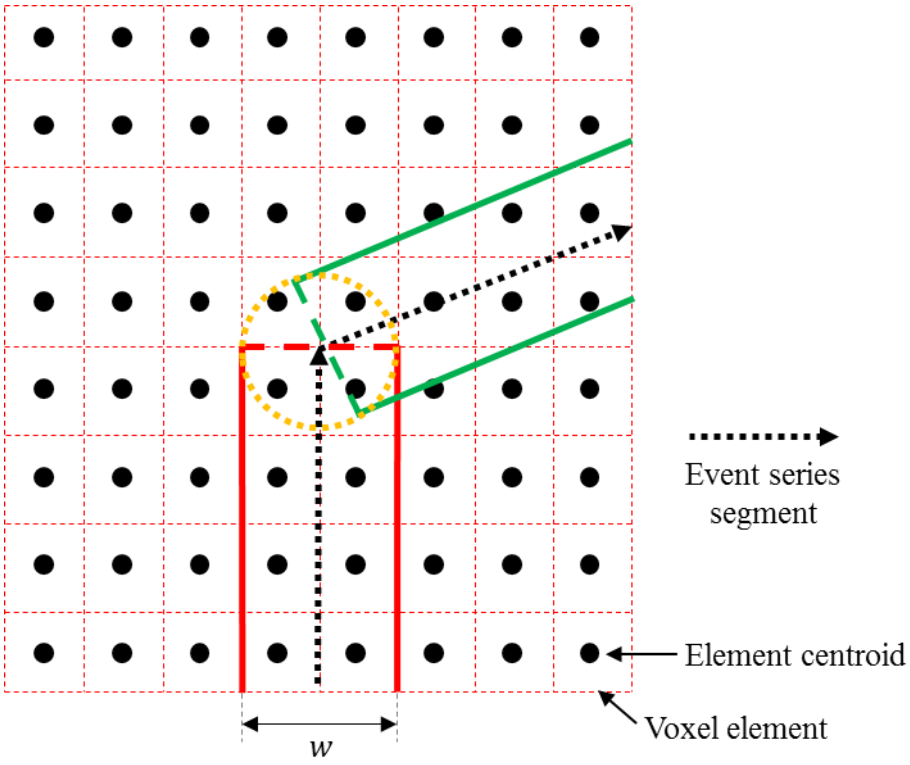

Figure 4.3 Illustration of elements missed when capping circle is not considered in the rectangular bounding activation box [73].

The green and red rectangular sections in Figure 4.3 represent from a top view of a voxel mesh the approach described so far, however, the circle cap in yellow can be included at the end of the rectangular bounding boxes used in the screening process of segments. This can be considered as

a complementary case in the screening performed with the coordinate x^1 for the cases where x^1 is larger than the length of the segment L^{AB} yet smaller than L^{AB} plus half the bead width, $w/2$. In addition to this, extrusion condition at the end of the segment must be one. If these two previous conditions are satisfied, the checks using the coordinate x^2 are again performed yet now with respect to the width of the cap, w^{cap}, given in Equation 4.5.

$$w^{cap} = \sqrt{w^2 - 4(x^1 - L^{AB})} \tag{4.5}$$

The same check performed with coordinate x^3 $(0 < x^3 < h)$ is carried out for the segment captured with the rectangular bounding boxes equipped with the capping circle, $(L^{AB} < x^1 < L^{AB} + w/2)$. Finally, the activation time and orientations are defined based on the segment that passed all the checks described before and that yielded the smallest activation time, t_{act}.

After identifying this segment, the ID used to communicate the type of feature printed in the event series is read at the start of the segment or at the end of the segment depending on the type of bounding box used to find the smallest activation time, t_{act}. The ID at the start of the segment is used if the rectangular bounding box was used whereas the ID at the end of the segment is used if the bounding box with the capping circle was used. Table 4.2 lists the IDs used to identify the different regions in the printed part which is going to be used for assigning section dependent film and radiation conditions in the heat transfer analysis.

Table 4.2 Types of printed features and their corresponding ID used in the event series.

Feature Type	**ID**
Infill Section	1
Internal Wall	2
External Wall	3
Solid Section	4

Although this approach does not require a part specific mesh, the preprocessing carried out in the ORIENT© can be reduced by utilizing a mesh that only contains the elements that are going to be activated during the process simulation. Therefore, the same algorithm described above can be used to generate a voxel mesh that only contains the elements used in the process simulation,

thereby reducing not only the preprocessing time but also the size of the output file since field variables area also recorded for the inactive elements.

Figure 4.4 shows the correct local material orientation computed with the algorithm described before at different instants of time in the simulation of the printing process. The blue arrows correspond to the principal direction X_i^1 whereas the yellow arrows correspond to the principal direction X_i^2 computed with Equation 4.3. The principal direction X_i^3 which also corresponds to the stacking direction was hidden in Figure 4.4 Figure 4.3to improve visualization. Notice the material orientation in the hoop and radial direction of the bell are determined correctly as expected with the algorithm presented before.

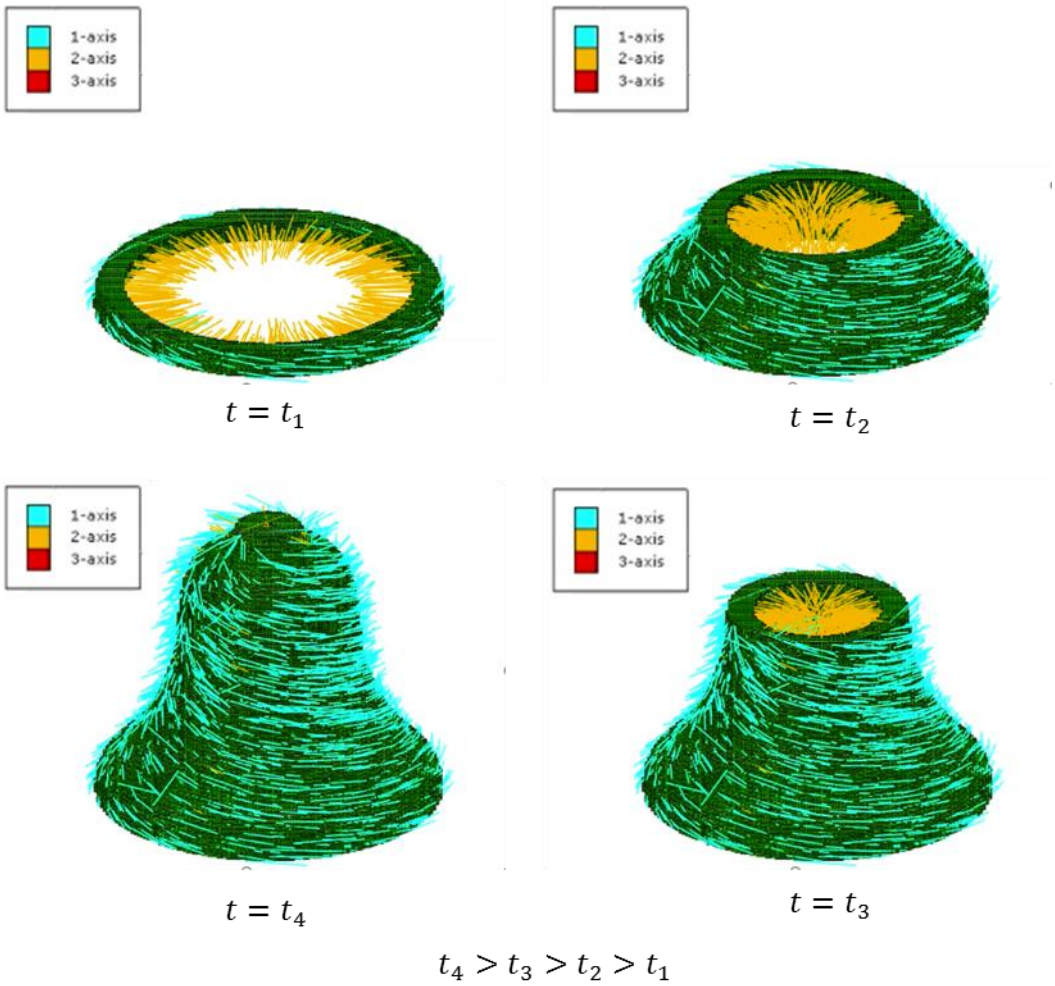

Figure 4.4 Example of local material orientation computed based on the printing trajectory at different instants of time in the simulation of the printing process of a bell.

4.3 EDAM Process Simulation in Abaqus©

The framework for simulating the EDAM process and the algorithm used to activate elements based on the machine code were described thoroughly in the last two sections. We will now focus on the procedure in which this framework is used to perform the thermomechanical simulation of the EDAM process. Further, the same framework can be also utilized to analyze the post-manufacturing performance of printed parts. Figure 4.5 shows the flowchart of the process and performance simulation carried out using the framework described previously.

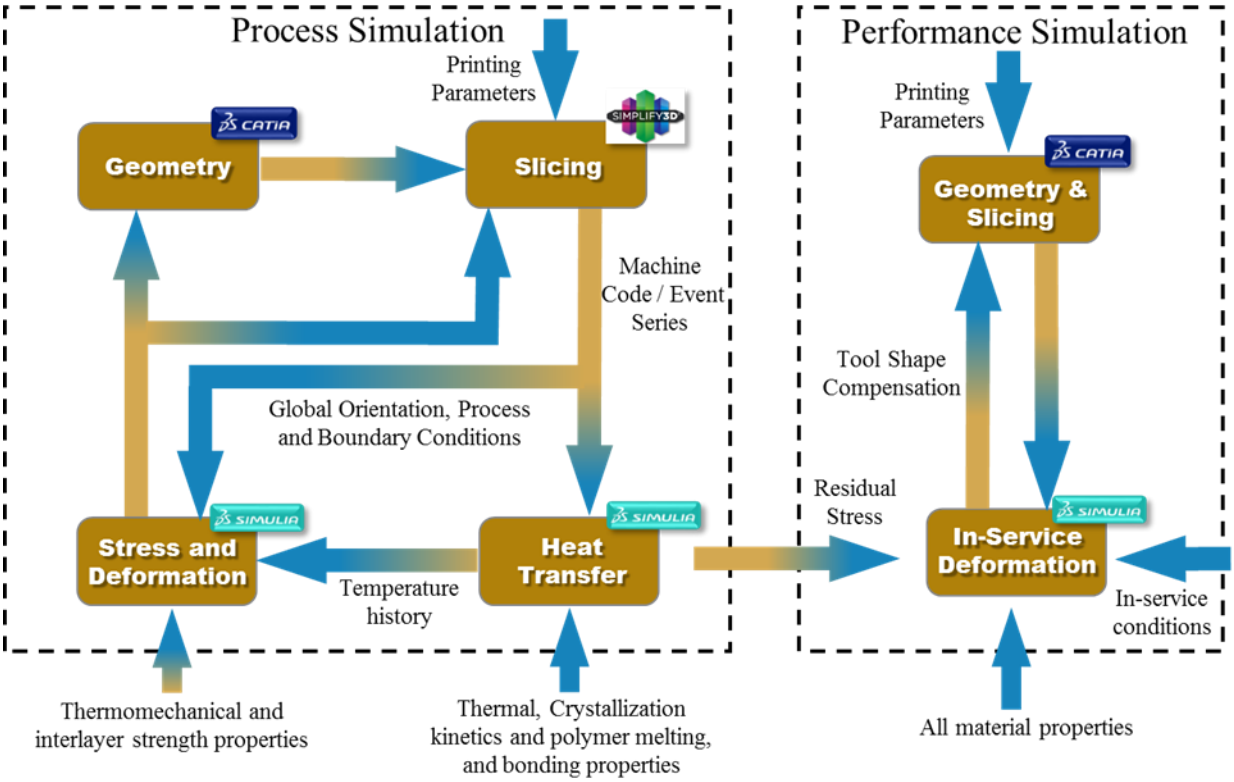

Figure 4.5 Flowchart of the process and performance simulation carried out in the simulation framework for the EDAM process.

Alike the real printing process of a part, the process simulation begins with the geometry definition. The geometry of the printed shape is used in this step rather than the geometry of the final shape. The next step is the slicing of the geometry for which we need to define slicing parameter such as infill percentage, number of outer perimeters, angle of the infill, number of solid layers, etc. Upon slicing of the geometry, the machine code that contains the printing trajectories is generated in the

language of G-code. The machine code contains only position commands and thus none of the dynamics of the EDAM system are captured in the G-code. In order to transform the G-code to the events series used in the process simulation, either the position commands can be interpreted as movements performed at a constant speed or the same kinematic equations used for the motion of the material deposition system can be used to create the event series. The later approach is used for generating the ES of the EDAM process performed in CAMRI. More specifically, the motion of the gantry robot in CAMRI is recorded while performing the position commands in the G-code, thereby capturing all the details of the actual deposition process. This functionality for recording the event series is implemented in CAMRI through a user defined program in the NC controller KFLOP©.

Following the creation of the event series, a sequentially coupled thermomechanical analysis is performed. This type of analysis is appropriate for most of the phenomena occurring in the EDAM process since the temperature history can be computed without information from the deformation and stress fields. Nevertheless, this is not necessarily true if delamination or any other form of damage occurs during the process simulation since temperature fields are precomputed and therefore remain unaffected if large thermal resistances developed between adjacent layers upon delamination. A strongly coupled thermomechanical analysis would be required to capture these changes in heat transfer conditions caused by material discontinuities developed upon damage of the printed material. However, the element progressive activation functionality in Abaqus© does not support yet strongly coupled thermomechanical analysis.

In order to perform the sequentially coupled thermomechanical analysis of the printing process, a heat transfer analysis is carried out first utilizing multiple user subroutines for material models along with the suite of subroutines for activating elements based on the event series. From the flowchart presented in Figure 4.2, the UFIELD©, the UMATHT© and the UMDFLUX© subroutines are used specifically to capture phenomena like convection, radiation, tamper heat losses, orthotropic heat transfer, latent heat of crystallization, etc. The following chapter on HEAT TRANSFER IN addresses these phenomena and presents the implementation of these subroutines. Other material models are coupled with the heat transfer analysis to predict for instance the degree of crystallinity in the polymer and the degree of bonding between adjacent layers. Details on the phenomenological model implemented for polymer crystallization and melting can be found in the chapter of FUSION BONDING OF SEMI-CRYSTALLINE POLYMERS IN THE EDAM

PROCESS, yet the implementation and characterization was presented in the dissertation from Brenken [16]. With regards to the material model for predicting bonding between adjacent layers, the chapter 6 presents the details on the material model, implementation and characterization of the fusion model developed in this work. The degree of bonding obtained in the heat transfer analysis shows already the variation of interlayer adhesion based on printing history, yet the real use of this model is for predicting delamination of printed parts. As a result of the heat transfer analysis, the temperature history is obtained for each element printed virtually.

The temperature history output by the heat transfer analysis is then used in a stress analysis along with the suite of subroutines for element activation based on event series. This way, the material shrinkage and the stress evolution in the printed part is coupled with the temperature evolution precomputed in the heat transfer analysis. The thermoviscoelastic behavior and the orthotropic material shrinkage of the printed CF reinforced PPS was analyzed and implemented by Brenken [16] through UMAT© and UEXPAND© subroutines, respectively. Chapter 6 introduces the material model for fusion bonding utilized in this work for predicting the adhesion between layers in the EDAM process with semi-crystalline polymers.

As a result of the stress analysis, the residual stresses and residual deformation of the printed part is obtained which can subsequently drive the decision to change either the geometry or the slicing parameters as shown schematically in Figure 4.5 to meet certain distortions or stress limits. Moreover, the same approach of modifying geometry or slicing parameters can be used if failure of the part by debonding of adjacent layers is predicted using the fusion bonding model and cohesive zone model.

After performing the process simulation of the EDAM, the residual stress state and deformation in the printed part can be carried over to a performance analysis to investigate the response of the printed part to thermal or mechanical loads. Since the primary application for EDAM with composites at this stage is tooling for parts manufacturing, the performance in this context is concerned with the tool shape change at the processing conditions where the tool is used. Nevertheless, structural analysis of semi-structural printed components can be also performed in the same framework. Although not included in this dissertation, examples of simulation-informed tool design performed with the simulation framework introduced in this chapter have been presented at multiple conferences including SAMPE and Abaqus© users meetings [88].

5. HEAT TRANSFER IN EXTRUSION DEPOSITION ADDITIVE MANUFACTURING

Extrusion deposition additive manufacturing (EDAM) is a unique manufacturing method in the sense that polymer-based materials used in this method undergo temperature changes from the melt temperature to room temperature after leaving the polymer processing equipment. Multiple heat transfer phenomena occurring simultaneously contribute to cooling and solidify the beads of printed material after leaving the extrusion nozzle. Mechanical and thermomechanical properties of polymers, particularly the elastic moduli and coefficient of thermal expansion, are generally highly sensitive to temperature and govern the evolution of stresses and deformation in a printed part. Further, temperature governs the diffusion properties of polymer which is relevant for interlayer bonding. Also, the evolution of crystallinity in semi-crystalline polymers is influenced by the cooling rate of the printed material. Hence, it is of paramount importance to accurately model the temperature evolution of the printed material in order to predict the adhesion between layers as well as the evolution of stress and deformation in the printing process of a part.

This chapter is dedicated to the heat transfer analysis in the EDAM process and begins by describing the heat transfer phenomena participating in the EDAM process. Then, each of these phenomena is investigated and methods for capturing those in the process simulation of the EDAM are developed. In a subsequent section, the implementation of these methods in the process simulations performed with Abaqus© is presented. Finally, experimental validation of temperature predictions for the printed material in the EDAM process is presented.

5.1 Heat Transfer Mechanisms in Extrusion Deposition Additive Manufacturing

Part manufacturing through EDAM is performed by continuously depositing beads of molten material on top of either a build plate or on top of previously deposited material. In the former case the temperature of the build plate can remain constant while in the latter case the substrate formed by the previously deposited material is likely at a temperature lower than the melt. Therefore, significant temperature gradients arise as this process of depositing molten material on top of previously cooled down material evolves during part manufacturing.

Hence, a brief description of the phenomena participating in the cooling process of the material upon deposition is provided in this section before describing the approaches used to include the multiple heat transfer phenomena in the process simulation of EDAM.

We will know start to consider from the moment the material leaves the extrusion nozzle. At this point, the temperature across the diameter of the extrudate can be considered homogenous for our material of interest, carbon fiber reinforced PPS, and for the relatively small nozzle diameter used in CAMRI. This is because carbon fibers enhance the thermal conductivity of the printing material and the diameter of the extrusion nozzle is sufficiently small to prevent developing temperature gradients across the diameter of the extrudate. However, this assumption should be reconsidered if extrusion nozzles with large orifice diameters are used. After the extrudate of molten material leaves the extrusion nozzle, the extrudate undergoes a ninety degree turn while the nozzle moves along the printing direction to lay onto the surface of previously deposited material as illustrated in Figure 5.1.

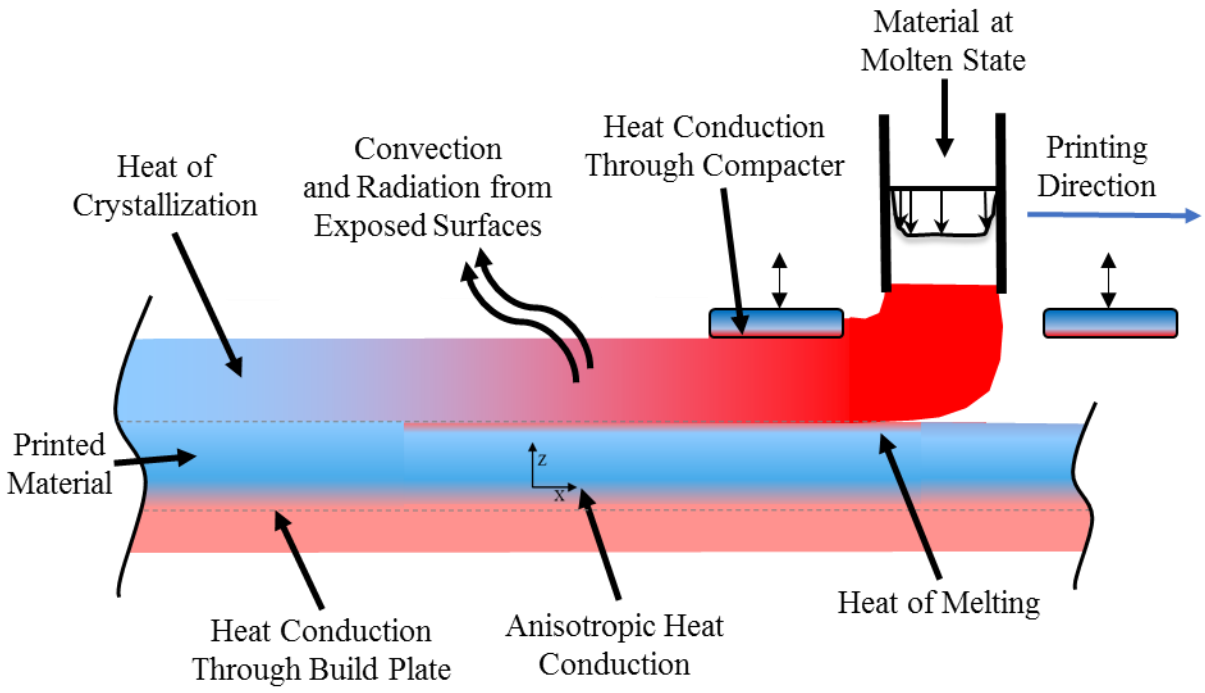

Figure 5.1 Heat transfer phenomena occurring simultaneously during material deposition in the EDAM process.

As previously described in the introduction, fibers suspended in the polymer melt are flow aligned along the extrusion direction which introduces anisotropy in the thermal conductivities of the printed material. Immediately after leaving the extrusion nozzle, the extrudate of molten material is compacted by the mechanical action of a reciprocating tamper or a rolling action of a compaction roller. In either case, the surface of the compaction system is actively cooled to prevent adhesion of printed material. In the case of CAMRI, the tamper is cooled by circulating compressed air through internal channels located near the surface of the tamper, thereby effectively removing the thermal energy harvested during material compaction. Multiple benefits arise by compacting the beads like improved surface wetting, yet a side effect is the heat removed by conduction when the surface of the tamper is in contact with the molten material. Figure 5.1 illustrates the tamping of an extrudate as it leaves the extrusion nozzle. Heat losses during material compaction vary with position and time during the EDAM process, thus this can be modeled as a moving heat source as explained in the following section Heat Losses in Material Compaction. Characterization of the compaction heat losses is also provided in the same section.

During material compaction, the newly deposited bead is squeezed against previously printed beads which aid wetting the surface of the substrate with the molten material and thus decreasing the thermal resistance. This way, thermal energy diffuses more effectively from the newly deposited bead which is at the processing temperature to the relatively cooler printed material as depicted in Figure 5.1. Heat diffuses in a similar way when the first layer is deposited on top of the build plate which is commonly maintained at a temperature lower than the material processing temperature. Further, the heat diffusion is not even in all directions due to the anisotropic thermal conductivity of the printed material and thus the subsequent section addresses anisotropic heat conduction.

Because of the diffusion of thermal energy from newly deposited to previously deposited material, local remelting of polymer crystals can occur around the interface between the two beads as depicted in Figure 5.1. Melting and crystallization of semi-crystalline polymers occur in the EDAM and involve endothermic and exothermic processes, respectively. Polymer crystallization and remelting is important in fusion bonding of semi-crystalline polymers and these phenomena are also coupled with heat transfer due to the heat associated with the physical reaction of the polymer. A physical reaction differs from a chemical reaction by the fact that the former is reversible and the latter not.

Two additional heat transfer phenomena occur at the exposed surfaces of the printed material. On the one hand, convection arises due to heat conduction from the hot surface of the printed material to the air surrounding the part which in turn gives rise to local changes in air density. Buoyancy driven flow arises from these changes in density, thereby giving rise to a hydrodynamic and a thermal boundary which act together to remove thermal energy from the surface through the movement of air. Therefore, convection is highly dependent on the geometry and the local temperature of the exposed surfaces as well as on the characteristics of the surrounding like the temperature of the air and the ability of the air to circulate. The section Convection in Extrusion Deposition Additive Manufacturing is dedicated to convection and methods to model this local mechanism of heat transfer in the EDAM process simulation.

On the other hand, heat losses through radiation from exposed surfaces are also important in the EDAM process, particularly at elevated temperatures. Radiation can be attributed to the activity in the electron configuration of the constituent materials [28]. Unlike convection that requires a medium to transport energy, thermal energy in radiation does not require a medium since energy is transported through electromagnetic waves or photons. Radiation from surrounding surfaces like the hot build plate or the processing equipment may also incident on the surface of the printed material. Therefore, the radiation problem is not only concerned with the temperature and property of the material but also with the surrounding surfaces. The section Radiation in Extrusion Deposition Additive Manufacturing describes the approach used to model radiation during the EDAM as well as the characterization of the emissivity for our material of interest.

5.2 Heat Conduction in Extrusion Deposition Additive Manufacturing

The principal objective of analyzing heat conduction is to determine the temperature history of the printed material in combination with the different boundary conditions mentioned before. Anisotropic heat conduction occurs in the printed material due to the presence of fibers with relatively higher thermal conductivity than the surrounding polymer inside printed beads. However, the scale considered in the heat transfer analysis is at the bead level which allows treating printed beads as an orthotropic continuum medium with principal directions, 1,2 and 3. The 1-direction corresponds to the orientation along the dominant fiber orientation which coincides with the printing direction. The 2-direction corresponds to the transverse in-plane direction and finally the 3-direction is given by the cross product of the previous two which coincides with the stacking

direction. A graphical representation of this local material orientation was provided previously in Figure 2.11. Then, by applying the principles of energy conservation and the Fourier's conduction law to an infinitesimal volume taken from a quiescent orthotropic medium, the transient heat conduction can be derived in a Cartesian coordinate system equation as shown in Equation 5.1 [28, 103]. Also, a heat generation term $\dot{q}(T,t)$ was considered in the heat conduction equation.

$$\nabla \cdot (K_i(T) \cdot \nabla T) + \dot{q}(T,t) = \rho C_p(T) \frac{\partial T}{\partial t} \tag{5.1}$$

The transient heat conduction equation also known as heat equation is given in vector notation where ∇ is the vector differential operator, $\nabla = \hat{\imath}(\partial/\partial x_1) + \hat{\jmath}(\partial/\partial x_2) + \hat{k}(\partial/\partial x_3)$, ρ is the density which is assumed constant and $C_p(T)$ is the heat capacity as a function of temperature and at a constant pressure. Further, the thermal conductivities in the principal directions, $K_i(T), i = 1,2,3$, are temperature dependent since the heat transfer analysis is performed over a broad temperature range defined from the material processing temperature to room temperature. Noticeable changes occur to the thermal conductivities as a function of temperature primarily due to changes in the conduction mechanisms occurring at the molecular level in the polymer as a function of temperature [103]. Thus, changes in thermal conductivity are more noticeable in material directions governed by the polymer, namely the 2 and 3 directions. Thermal conductivities as a function of temperature can be either predicted through micromechanics techniques [104, 105], or characterized experimentally with representative samples of the orthotropic medium. The latter approach was utilized in this work for the material of interest, PPS-CF50, and the following subsection provides more details on the characterization method.

The heat generation term, $\dot{q}(T,t)$, in Equation 5.1 accounts for the heat generated or the heat absorbed during crystallization of polymer or melting of previously crystallized polymer, respectively. Polymer crystallization and melting are described in more detail in the chapter FUSION BONDING OF SEMI-CRYSTALLINE POLYMERS IN THE EDAM PROCESS as well as in the dissertation from Brenken [16]. Nevertheless, we will state for now that crystallization kinetics and crystal melting are strongly dependent on temperature. Therefore, the polymer crystallization is strongly coupled with the heat transfer analysis since temperature drives the evolution of crystallinity, $\chi_v(T)$, while the latent heat, H^*, associated with the phase change

affects the temperature field at the same time. The heat generation, $\dot{q}(T)$, can be then expressed as shown in Equation 5.2 by the product of the density, ρ, the latent heat involved in the phase change, H^*, and the rate of change in crystallinity.

$$\dot{q}(T) = \rho H^* \frac{d\chi_v(T)}{dt} \tag{5.2}$$

The rate of change of crystallinity is positive when polymer crystallizes and becomes negative when melting occurs, thereby defining the sign of the heat generation due to the exothermic or endothermic physical reaction, respectively. The development of crystallinity in the polymer has other implications like additional shrinkage, change in viscosity, and improvement in mechanical properties of the polymer.

Now with regards to the boundary conditions in the EDAM process. Either the role of the build plate can be considered in the heat transfer analysis or not, in the former case the thermal resistance developed due to the roughness of the surfaces in contact, namely the build plate and the printed material, could be considered whereas in the latter case a boundary condition of the first kind is simply assumed on the same surface [103]. The build plate in CAMRI provides controlled temperature conditions and the compaction actions significantly improves the thermal contact of the printed material with the build plate which leads to the assumption of a boundary condition of the first kind at the bottom surface (bs) of the printed part as given in Equation 5.3.

$$T|_{bs} = T_{bp} \tag{5.3}$$

Heat losses due to material compaction can be modeled as a moving heat flux, $q_c''(x,t)$, that moves along the same trajectory the extrusion nozzle travels during part manufacturing. Thus, the moving heat flux defines a boundary condition of the second kind at the surface of the printed bead (pbs),

$$-K\frac{\partial T}{\partial n}|_{pbs} = q_c''(x,t) \tag{5.4}$$

where K is the thermal conductivity in the direction normal, n, to the surface where the heat flux, q_c'', is applied. While the surface heat flux resulting from material compaction with a tamper can be modeled as a circular shaped distribution, the surface heat flux distribution from the roller might be captured adequately through a rectangular shaped distribution. The specific treatment made for this boundary condition is explained in the subsequent section on Heat Losses in Material Compaction.

Convection and radiation boundary conditions are also applied to the exposed surfaces (es) of the printed material. Convection is considered a boundary condition of the third kind since it involves the partial derivative of the temperature field along the outward-drawn normal, n, to the surface and a linear relation of the temperature field at the surface [103].

$$-K\frac{\partial T}{\partial n}|_{es} = h(x,T)\cdot(T|_{es} - T_{\infty,f}) \tag{5.5}$$

The convection boundary condition depends on the film coefficient, $h(x,T)$, which is a function of the temperature and the position of the surface within a printed part and depends also on the ambient fluid temperature $T_{\infty,f}$. An analysis has been performed to determine correlation equation for $h(x,T)$ that capture the local nature of this coefficient and is presented in the next section Convection in Extrusion Deposition Additive Manufacturing. The last boundary condition considered on the exposed surfaces (es) of the printed material is radiation

$$-K\frac{\partial T}{\partial n}|_{es} = \varepsilon\sigma(T^4|_{es} - T_{\infty,s}^4) \tag{5.6}$$

where ε is the emissivity of the material, σ is the Stephan-Boltzmann constant, and $T_{\infty,s}$ is an equivalent radiation ambient temperature. The expression for radiation given in Equation 5.6 assumes a grey surface which implies that the emissivity, ε, of the material is equal to the absorptivity of the material, α_r. The representation of the radiation phenomenon through this boundary condition, Equation 5.6, can be improved by including view factors, F_{ij}, to consider the geometry in the calculation of the irradiation absorbed at the surface of the printed material caused by emission from hot surfaces surrounding a printed part. Examples of surrounding hot surfaces

in CAMRI include the heated build plate and the material extrusion system. Nevertheless, the complexity of tracking view factors in process simulation increases rapidly as the complexity of printed geometries increases which becomes impractical for the gains in accuracy. A section of this chapter is dedicated to radiation and the characterization of the emissivity of the 50%wt. carbon fiber reinforced PPS.

5.2.1 Characterization of Thermophysical Properties

The thermophysical properties required for the heat conduction analysis were shown in Equation 5.1 and these include the thermal conductivities in the three principal orientations as a function of temperature, the density and the heat capacity as a function of temperature. These thermophysical properties were characterized by an external entity contracted to perform these measurements, the Thermophysical Properties Research Laboratory, and these were reported and used previously in the work from Brenken [16]. However, the methods for characterizing the properties are describe herein for the sake of providing a complete description of the heat transfer analysis and the properties can be found in the APPENDIX A.

Thermal conductivities were characterized indirectly utilizing measurements of thermal diffusivity, $\alpha_{T,i}$, as shown in Equation 5.7. Thermal diffusivities, $\alpha_{T,i}$, were characterized from samples representative of the three principal directions, $i = 1,2,3$, and utilizing the flash method [106]. In this method, a thin sample prepared for each of the planes normal to the principal material orientations is subjected on one face to a short laser burst in a carefully controlled environment [107]. The temperature rise on the opposite face of the specimen is recorded and analyzed at different temperature conditions to determine $\alpha_{T,i}(T)$. The same experiment is repeated for each of the three samples representing the three principal directions. In addition to the thermal diffusivity, the density, ρ, and the heat capacity, $C_p(T)$, are required to determine the thermal conductivities K_i.

$$K_i(T) = \alpha_{T,i}(T) \cdot C_p(T) \cdot \rho \tag{5.7}$$

Heat capacity is determined as a function of temperature utilizing a differential scanning calorimeter (DSC) with sapphire as a reference material [108]. In this method, the sample and the sapphire reference are heated in a controlled environment inside the cell of the DSC and the

differential heat flow required to heat both samples at a constant rate is recorded. The recorded signals for heat flow, temperature and the known specific heat of the sapphire are then employed to compute the specific heat of the 50%wt. carbon fiber PPS. Unlike the thermal conductivities, the specific heat is a property that does not depend on the fiber orientation.

As mentioned in the previous section, density is assumed constant and therefore it was determined from geometrical measurements of the square samples provided for charactering thermal conductivities and the mass of the sample [107]. The density, thermal diffusivities, specific heat and thermal conductivities characterized by the Thermophysical Properties Research Laboratory are provided in the same order in Table A.3 to Table A.6.

The latent heat of crystallization was also characterized through non-isothermal crystallization experiments performed in a DSC Q2000 from TA Instruments© [85]. This type of experiments consists of heating a small sample of material typically in the range of 5 to 10 mg to the processing temperature of the material, 310 $°C$ as is the case of the 50%wt. carbon fiber PPS. A dwell time of 10 minutes at this temperature follows in order to achieve uniform temperature distribution and to ensure that polymer crystals in the sample are fully molten. Then, the specimen is cooled down to room temperature at a constant rate while the differential heat flow is recorded. Since the sample is encapsulated in a small aluminum pan, the differential heat flow is measured with respect to an empty pan. This way the contribution of the thermal mass of the pan to the heat flow signal is removed. Figure 5.2 shows the heat flow signal recorded during a non-isothermal crystallization experiment where the 50%wt. carbon fiber PPS was cooled from the melt temperature to room temperature at a constant cooling rate of 25 $°C/min$. The exothermic peak shown in the heat flow signal, dash-dot blue line in Figure 5.2, is the result of the crystallization process occurring while the sample is cooled down. Further, the sensitive heat associated with the reduction in temperature of the sample needs to be removed from the heat flow signal before integrating the heat flow to estimate the energy released during crystallization. Assuming the heat capacity of the material does not change significantly as it crystallizes, a straight baseline can be drawn connecting the inflexion point in the heat flow signal at the onset of crystallization with the last inflexion point in the heat flow signal corresponding to the end of the crystallization. This baseline is sketched with a red dashed line whereas the onset and end of crystallization are marked with black "+" symbols in Figure 5.2.

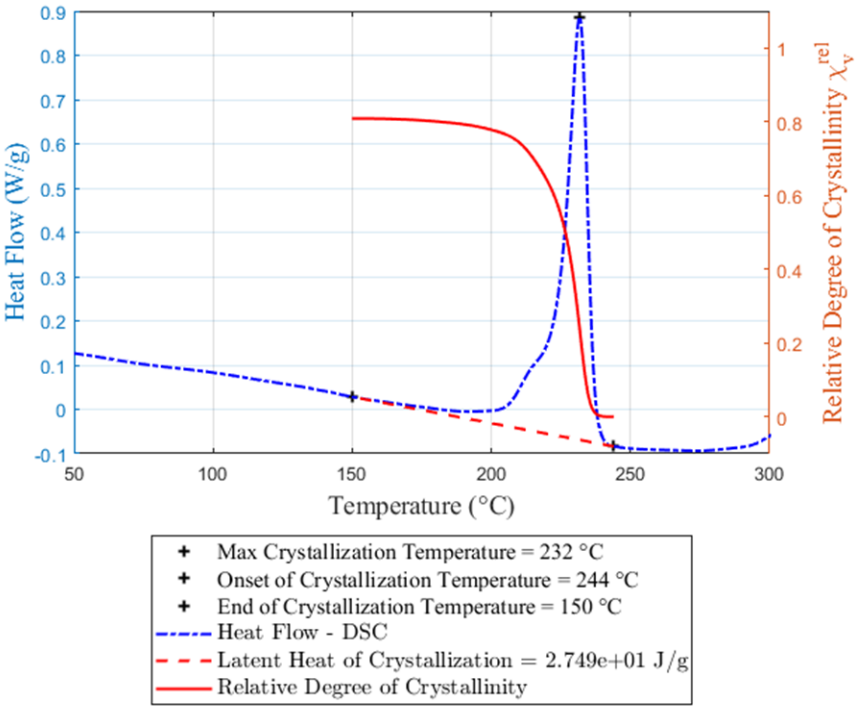

Figure 5.2 Non-isothermal crystallization of 50%wt. CF/PPS cooled from the melt at $25\ °C/min$.

Since the kinetics of polymer crystallization is the result of crystal nucleation and crystal growth which are controlled by the degree of undercooling and diffusion, respectively, the crystallization kinetics and the maximum crystallinity developed among other aspects are affected by the cooling rate, a, [33, 109]. Using the exothermic peak in the heat flow signal, the relative degree of crystallinity at any time t can be estimated by dividing the integral of heat flow computed from the onset of crystallization to any time t by the total heat of crystallization, $H^*|_a$, given by the integral of heat flow computed from the onset to the end of crystallization as shown in Equation 5.8.

$$\chi_v^{rel} = \frac{\int_{t_{onset}}^{t} \dot{q}_{DSC} - \dot{q}_{baseline}\, d\tau}{\int_{t_{onset}}^{t_{end}} \dot{q}_{DSC} - \dot{q}_{baseline}\, d\tau} \tag{5.8}$$

$\dot{q}_{DSC}$ is the heat flow measured with the DSC which corresponds to the dash-dot blue line in Figure 5.2, whereas the $\dot{q}_{baseline}$ accounts for the sensitive heat of cooling the material and corresponds

to the red dashed line in Figure 5.2. The relative degree of crystallinity, χ_v^{rel}, given by Equation 5.8 corresponds to the red solid line in Figure 5.2. A script developed in Matlab© analyzes the heat flow obtained from the DSC and integrates numerically the heat flow due to crystallization as shown in Figure 5.2 to estimate the latent heat of crystallization. This script can be found in Table B.2 of the APPENDIX B.

Equation 5.8 provides relative values for the degree of crystallinity, however, absolute values of crystallinity are required in Equation 5.2 to capture the effect of cooling rate on the amount of energy released by crystallization. Absolute values of crystallinity are obtained by dividing the integral in the numerator of Equation 5.8 by the latent heat of fusion of a perfect crystal which might be only achievable by crystalizing in a polymer solution [110]. However, values in the range of $77.5\ J/g$ have been reported previously in the literature for PPS [111]. Since the material system in consideration is a composite with 50% by weight of carbon fiber where only the polymer crystallizes, a simple rule of mixtures provides a good estimate for H^*.

The effects of cooling rate on the crystallization kinetics and the amount of crystallinity developed in the printed material are captured with the crystallization kinetics model developed by Velisaris and Seferis [112] which was used by Brenken et al. [16, 72] to model the crystallization kinetics of the 50%wt. carbon fiber reinforced PPS. More details on this model are presented in chapter 6 and also in the thesis of Brenken [16]. While characterizing the coefficients of this model, the authors assumed a value for H^* equal to $38\ J/g$ which is also used herein to compute the latent heat of crystallization.

Figure 5.3 shows the evolution of the degree of crystallinity, χ_v, obtained from non-isothermal crystallization experiments conducted at different cooling rates. The maximum value of crystallinity obtained in these experiments was around 0.83 at a cooling rate of $5\ °C/min$ whereas the minimum value of crystallinity obtained in these experiments was around 0.7 at a cooling rate of $40\ °C/min$.

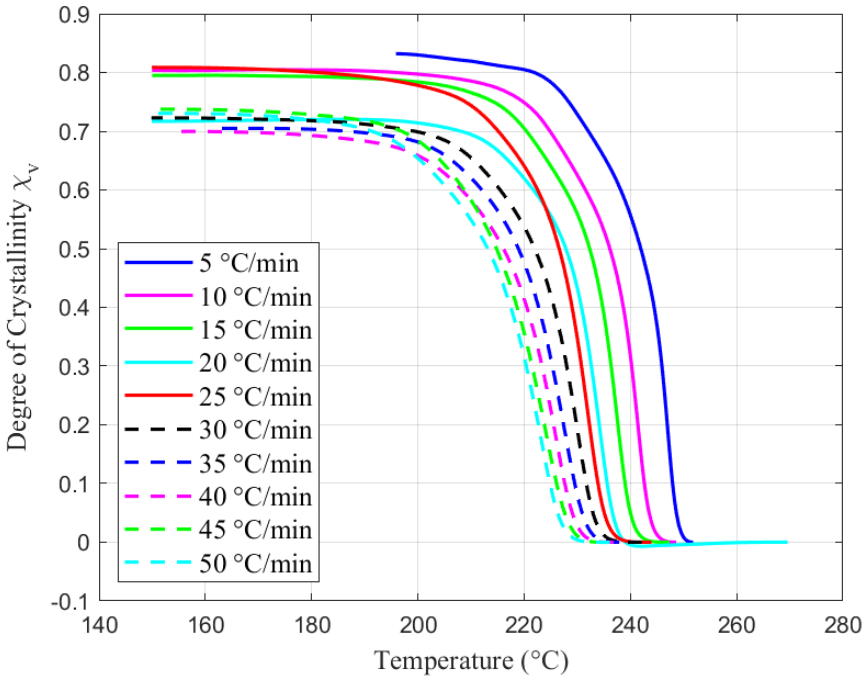

Figure 5.3 Non-isothermal crystallization of 50%wt. CF/PPS at different cooling rates.

Although the maximum crystallinity reached does not change significantly with the cooling rates shown in Figure 5.3, quenching will inhibit crystallization in polymers like PPS [109]. Finally, Table 5.1 shows the value for H^* utilized to compute the internal heat generation in the heat conduction equation as well as the maximum absolute crystallinity possible for this material.

Table 5.1 Maximum crystallinity and heat of crystallization for 50%wt. CF-PPS.

Material	$H^*\ (J/g)$	χ_v^{max}
Celstran® PPS-CF50-01	38.0	0.83

5.3 Convection in Extrusion Deposition Additive Manufacturing

Convective heat losses are inherent to the EDAM process and are one of the principal mechanisms contributing to the cooling process of a part during manufacturing and post-manufacturing. The mechanism of heat convection originates near the hot surface of printed parts by local heating of the air surrounding the surfaces. As the air is heated locally, density gradients develop which combined with the gravitational acceleration gives rise to buoyancy driven flow. This way, thermal

energy is conducted from the surface to the air and subsequently conveyed away through buoyancy driven flow. This results in the development of a hydrodynamic and a thermal boundary layer that governs natural convection developed over surfaces that are at temperatures higher than the surrounding fluid medium. Now in the context of EDAM, continuous changes in geometry and temperature gradients developed during part manufacturing also introduce a transient behavior in the evolution of the thermal and the hydrodynamic boundary layers. In other words, there is a characteristic time for diffusion of thermal energy from the surface of a newly deposited bead to the surrounding air. The convection coefficient, $h(x,T)$, is a local quantity that depends not only on the surface temperature but also on the geometry of the surface, the properties of the fluid surrounding the part and the movement of the part [113]. Although temperature is not indicated explicitly in the convection coefficient, $h(x,T)$, analytical determination of this coefficient requires knowledge of the temperature distribution in the medium flowing over the surface. Air is the surrounding medium in the case of the EDAM process. By applying the Newton's law of cooling and the Fourier's law of conduction to the medium flowing over the surface, this statement becomes clearer as shown in Equation 5.9

$$h(x,T) = -K_f \frac{\frac{\partial T_f}{\partial n}|_s}{(T_s - T_{\infty,f})} \tag{5.9}$$

where T_s is the surface temperature, $T_{\infty,f}$ is the ambient temperature of the air, K_f is the thermal conductivity of the fluid and $\partial T/\partial n$ is the temperature gradient in the fluid at the interface between the fluid and the surface and in the direction normal to the surface (s). Again, this enforces the fact that $h(x,T)$ is not a material property like thermal conductivity, yet rather a local quantity that depends on the factors mentioned above.

Since EDAM is generally carried out in an uncontrolled environment compared to the controlled temperature conditions used in heated chambers like in FDM, convective heat losses are more significant in EDAM due to larger temperature differences between the surface of printed parts and the ambient air. Describing the local convection conditions accurately during part manufacturing is complex due to the continuous change in geometry arising by the continuous deposition of new layers as well as due to the geometrical complexity of some of the parts produced with this manufacturing method. Different approaches have been used in the past for modeling this

boundary condition in simulations of extrusion-based additive manufacturing. For example, Costa et al. [67, 68, 114] used a constant and relatively high convection coefficient ($\sim 70\ W/m^{2}°C$), to account for both convection and radiation from exposed surfaces. Brenken [16] used the convection coefficient to calibrate the temperature predictions obtained with his process simulation to experimentally measured temperature history from the printing process of a wall. A range of convection coefficients typical for natural convection was suggested by this author. Compton et al. [69] utilized a correlation equation derived for vertical walls suspended in an infinitely large medium to estimate the average convection coefficient used in his 1-D heat transfer analysis. Overall, a good correlation between model predictions and experimental temperature measurements has been reported with these calibrated approaches for vertical walls. However, these approaches are limited to wall structures which represent only a small fraction of the geometries of interest in EDAM. Furthermore, more realistic and intricate geometries may consist of both internal and external geometries which can lead to significantly different convection conditions and therefore material cooling histories. For example, Figure 5.4 shows different regions in the sliced geometry of one half of the pin bracket compression molding tool presented before, where convection conditions will develop differently depending on the interaction with the surrounding air. External walls in this case interact more directly with the air surrounding the part than the internal walls where there is not a natural path for the surrounding air to flow through that region and remove thermal energy. However, capturing the physical phenomena involved in convection in the simulation of the printing process of a real part is not feasible with existing simulation tools.

Hence, this section presents a set of empirical correlation equations that provide an estimate of the local convection coefficients in simulations of part manufacturing and for each type of printed features labeled in Figure 5.4. This way, a better representation than a calibrated constant convection coefficient is utilized in printing simulations of geometries more complex than a wall and without the expense of solving the strongly coupled thermal and hydrodynamic problems involved in natural convection.

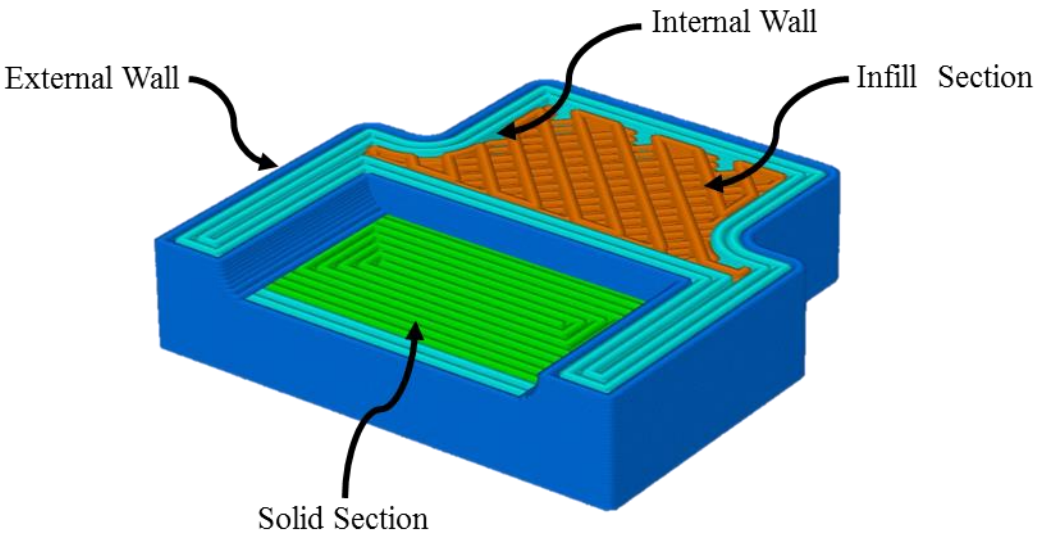

Figure 5.4 Examples of regions subjected to different convective heat losses in a printed part.

A review of existing correlation expressions is provided in the next section followed by the analysis carried out to derive a correlation expression with the aim of investigating the sensitivity of utilizing the local convection coefficients instead of an average convection coefficient in simulations of the printing process of a part. Although this correlation expression was derived for the specific case of a vertical wall, this correlation expression provides overall a better approximation for the local convection coefficients than existing correlation expressions due to the appropriate boundary conditions used herein. Finally, correlation equations suggested for each region labeled in Figure 5.4 are provided in the last subsection.

5.3.1 Correlation Equations for Natural Convection

Numerous correlation expressions have been developed in the past for different fundamental geometries utilizing experimental measurements of boundary layers or from analytical and numerical solutions obtained for the boundary layer problem [28, 113]. These expressions provide approximations in steady state for average and local convective coefficients of geometries like vertical walls, horizontal plates, cylinders and spheres suspended in a medium, etc. Therefore, some of these expressions may be useful to model the convection coefficient in the regions shown in Figure 5.4.

Before proceeding any further with correlation equations, we should state two primary assumptions made in order to utilize correlation equation for natural convection in process

simulations. Further, same assumptions are carried over while developing new correlation expressions for natural convection in EDAM. The first assumption is that the boundary layers developed at each of these regions do not interact with each other. In other words, the boundary layer developed in an external wall does not affect the boundary layer developed in a solid section surrounded by external walls. The severity of this assumption on the predicted local convection coefficient will vary depending on the geometry of a part. The second assumption is that natural convection occurs instantaneously during EDAM, thereby allowing to utilize correlation expressions describing natural convection in steady state to represent the transient convection mechanism developed in EDAM.

Correlation expressions are generally given in terms of the dimensionless numbers for natural convection, specifically in terms of the Grashof number and the Prandtl number. The Grashof number, Gr_x, is given in Equation 5.10 and corresponds to the ratio of buoyancy forces to viscous forces in natural convection whereas the Prandtl number, Pr, is a fluid property that represents the ratio of the momentum to the thermal diffusivities [28]. Prandtl numbers for common fluids are readily available in tables.

$$Gr_x = \frac{g\beta\left(T_s - T_{\infty,f}\right)x^3}{\nu^2} \qquad Pr = \frac{C_p\mu}{K_f} = \frac{\nu}{\alpha} \tag{5.10}$$

Gravitational acceleration is denoted by g, β is the volumetric thermal expansion, x is the characteristic dimension of the body, ν is the kinematic viscosity of the fluid. With regards to the Prandtl number, C_p is the heat capacity at constant pressure and μ is the dynamic viscosity of the fluid and K_f is the thermal conductivity. For ideal gases, β can be approximated with the inverse of the film temperature, $\beta = 1/T_{film}$, with T_{film} being the average of the surface temperature, T_s, and the ambient temperature, $T_{\infty,f}$. It should be noted that all the other temperature dependent material properties are evaluated at the film temperature. Then the Rayleigh number, Ra_x, is given by the product of the Gr_x and the Pr numbers as given in Equation 5.11.

$$Ra_x = Gr_x Pr = \frac{g\beta(T_s - T_{\infty,f})x^3}{\nu\alpha} \tag{5.11}$$

The connection between these two dimensionless numbers and the local convection coefficient, $h(x,T)$, is given through the Nusselt number, Nu_x, which represents a ratio of the convection to the conduction heat transfer as shown in Equation 5.12 [28]. Thus, the objective is to determine correlation equations for the Nusselt number, Nu_x, that provide local convective coefficients through Equation 5.12.

$$Nu_x = \frac{xh}{K_f} \tag{5.12}$$

Analytical similarity solutions obtained for the laminar boundary layer problem of an isothermal vertical wall provides the expression for the local Nusselt number, Nu_x, given in Equation 5.13 in terms of Gr_x and a function that depends on the Prandtl number, $f(Pr)$ [28].

$$Nu_x = \left(\frac{Gr_x}{4}\right)^{\frac{1}{4}} \cdot f(Pr) \tag{5.13}$$

Recognizing the functional form of Equation 5.13 and the definition of Ra_x, we can anticipate that correlation expressions for the Nu_x will have a form similar to Equation 5.14 with constant A, B, and n parameters.

$$Nu_x = A + (B \cdot Ra_x)^n \cdot f(Pr) \tag{5.14}$$

After declaring the major assumptions made, correlations expressions that may be applicable to the regions of a printed part shown in Figure 5.4 are reviewed. Then, only the ones developed with boundary conditions appropriate for describing convection in EDAM will be adopted. Further, new expressions are derived utilizing results from numerical analysis of the laminar boundary layer problem. Based on the regions labeled in Figure 5.4, the following analogies can be made. The external walls in Figure 5.4 can be treated as vertical plates mounted on top of an infinitely

long heated surface, which corresponds to the heated build plate used in CAMRI. Further, a similar treatment can be applied to internal walls in the presence of infills with large openings as depicted in Figure 5.5-B, otherwise these will be treated similarly to infill sections. With regards to solid sections labeled in Figure 5.4, these can be treated as horizontal plates immersed in a medium with infinite extent. Nevertheless, the condition illustrated in Figure 5.4 of a solid section surrounded by vertical walls is one where the assumptions of non-interacting correlation equations may not be adequate especially near the edges where the two features intersect.

Infill regions are also illustrated in Figure 5.4. Multiple designs for infill structures are possible with slicers nowadays, including cells with rectangular, honeycomb and triangular shapes. Examples of rectangular shaped cells with different relative dimensions are provided in Figure 5.5.

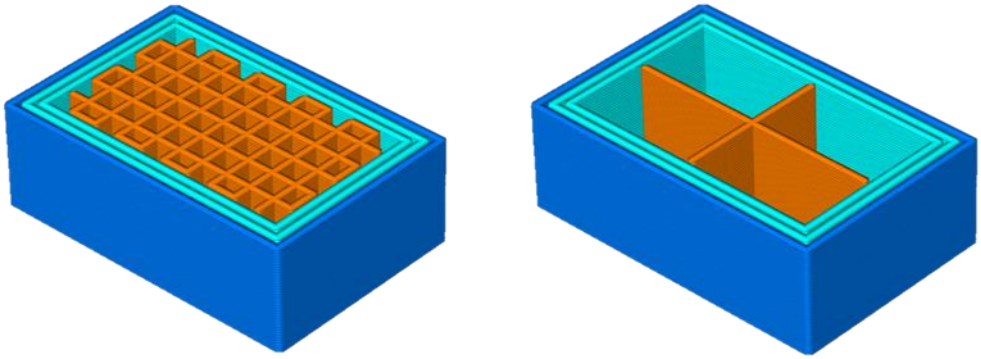

Figure 5.5 A) Example of dense infill where correlation equations for channels is more appropriate for infill. B) Example of sparse infill where correlation equations for external walls is more appropriate for infill.

Natural convection developed inside cells of the infill depends not only on the geometry but also on the non-isothermal temperature distribution along the height of the walls of the infill cell. Further, the heated build plate provides a bottom surface with constant temperature to the infill cell, thereby making the upper uncovered face of the cell the only passage to exchange thermal energy with the surrounding air. Thus far, this description of the infill cells reassembles a vented cavity, however, infill regions are in some cases covered with solid layers. As a result, the problem of natural convection from the cell is transformed to a problem of internal convection inside a close cell. The same conditions also apply to internal walls in the presence of a dense infill as

illustrated in Figure 5.5-A. While infill cells can vary from dimensions in the range of a centimeter as the one illustrated in Figure 5.5-A, infills can also have dimensions close to the external dimensions of the part as illustrated in Figure 5.5-B. Therefore, treating the infill as vented cavities is adequate in the former case whereas treating the infill as external walls is more adequate for the latter case.

We will now focus on reviewing correlation expressions available in the literature for each of the analogies made above for external walls, solid regions and infill regions, respectively. Correlation equations to determine the local Nusselt number, Nu_x, in vertical plates have been developed in the past based on experimental, analytical and numerical investigations of the thermal boundary layer developed under three principal boundary conditions, namely constant surface temperature, constant heat flux applied on the surface, and predefined temperature profiles on the surface. Churchill and others have developed correlation expressions for semi-infinite vertical plates under isothermal and constant heat flux conditions for both natural and forced convection [115, 116, 117, 118, 28]. Also, the effect of inclination on the Nusselt number was initially considered by Vliet [119] for inclined plates with constant heat flux. He concluded that the same correlation expressions could be used in vertical plates angled less than $60°$ with respect to the vertical when the contribution of gravity parallel to the surface was used in the calculation of the Rayleigh number. The case of assisting convection where both natural convection and forced convection coexist has been considered also as the sum of some arbitrary power of individual correlation equations for natural and forced convection [116]. Vertical plates with multiple temperature profiles were also investigated through numerical solution of the equations governing natural convection by Na [120]. However, there is a major difference in the natural convection problem analyzed while deriving these previous correlation expressions and the one encountered in EDAM which is illustrated in Figure 5.6. All these previous correlations have been developed for vertical plates immersed in a fluid of infinite extent with boundary conditions that allows for the development of a vertical stream of air that starts at the bottom edge of the plate and continues flowing along the surface of the plate. On the contrary, the heated build plate used in the EDAM introduces a boundary condition at the bottom of the plate that precludes the circulation of air from the infinite fluid domain near the build plate, thereby reducing effectively the amount of thermal energy removed through natural convection in the regions near the build plate. Nevertheless, the regions far from the build plate may be well represented through existing correlation equations.

Hence, there is a need for a correlation expression derived from experiments considering the appropriate boundary conditions imposed by the build plate in both the thermal and the flow problems. Subsequent sections in this chapter address this problem for a part geometry printed in CAMRI with the goal of investigating the relevance of utilizing local convection coefficients in simulations of part manufacturing.

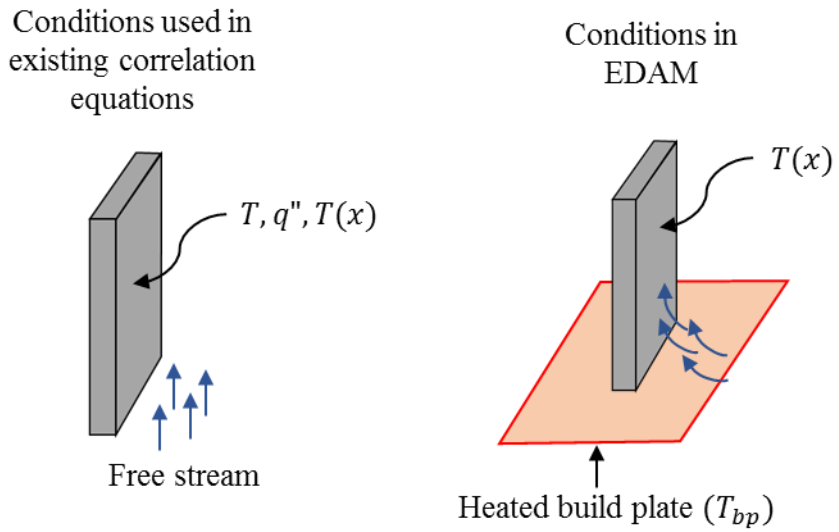

Figure 5.6 Major differences in boundary conditions used in existing correlation expressions for vertical walls and the conditions for a printed wall in EDAM.

As stated previously, convection in printed solid sections will be treated as natural convection developed in horizontal plates. Numerous correlation expressions with functional form of the type $Nu_{L^*} = A \cdot Ra_{L^*}^{C}$ have been developed for natural convection from horizontal plates with different shapes and aspect ratios, yet all for isothermal plate conditions [121, 122, 123, 124, 28]. Although this is not truly the case in EDAM where solid sections are highly non-isothermal immediately after printing, temperature gradients on printed solid sections are reduced relatively quick due to thermal conduction with the surrounding material. Therefore, we will accept the approximation provided by the correlation expressions given in Equation 5.15. Although numerous correlation expressions for natural convection from horizontal plates are available in the literature, the one given in Equation 5.15 has being validated for multiple fluids and for a wide range of Rayleigh numbers [28, 113]. This correlation equation provides an average Nusselt coefficient, $\overline{Nu_{L^*}}$, for flat regions with characteristic length, L^*, which was proposed by Goldstein et al. [121] to be the

ratio of the area to the perimeter of the flat plate ($L^* = A/p$). Further, this correlation applies not only for rectangular sections but also for triangular and circular regions [122]. Individual correlation expressions are given for both cases of laminar ($10^4 \leq Ra_{L^*} \leq 10^7$) and turbulent flow ($10^7 \leq Ra_{L^*} \leq 10^{11}$) [28]. An average film coefficient, $\bar{h}(T)$, is then determined using Equations 5.11 and 5.12 but substituting the local position, x, by the characteristic length, L^*.

$$\overline{Nu_{L^*}} = 0.54 Ra_{L^*}^{1/4} \; (10^4 \leq Ra_{L^*} \leq 10^7)$$
$$\overline{Nu_{L^*}} = 0.15 Ra_{L^*}^{1/3} \; (10^7 \leq Ra_{L^*} \leq 10^{11}) \tag{5.15}$$

Unlike the well-defined hydrodynamic and thermal boundary layers formed along the surface of vertical walls, natural convection from horizontal surfaces is characterized by parcels of fluid departing from the hot surface. This complicates the development of general correlation equations for local Nusselt numbers in non-isothermal horizontal plates since parcels of fluid departing from the surface will be influenced by temperature gradients in this case. Hence, this area deserves further research in the future.

The last printed region to consider is infills. Two different treatments for the convection coefficient were previously mentioned to be appropriate for infill regions based on the relative dimensions of the cells. But before describing those conditions, we will define a cell as a closed profile extruded along the print direction and covered at the bottom with the build plate. The first case of infill cells is such where the cross-sectional area of the cell is in the range of a couple tens of square centimeters (Figure 5.5-A), thereby resembling a small vented cavity. Further, infills of this scale are commonly used as scaffolds to support subsequent solid layers. Covering this type of infill cells would then transform the problem from convention from vented cavities to one of internal convection. Convection in vented cavities has been investigated in the past for applications of solar receivers for different geometries including cylindrical, cubic and hemispherical shapes [125, 126, 127]. However, the open cavities addressed in these previous works are angled such that thermal and hydrodynamic boundary layers develop around the walls of a cavity which does not occur effectively in the small vertical infill cells of our interest. Different and less effective natural convection mechanisms develop in vertical infill cells since there is not a natural path for the air to flow into the cell and convey away thermal energy. This leads to the assumption of

neglecting convective heat losses in infill regions smaller than a critical length that is going to be defined later with the aid of numerical solutions of the appropriate natural convection problem. The second treatment is applied to infill cells with cell dimensions larger than the critical length and these regions will be treated similarly to external walls. These two treatments provide the upper and the lower bounds for possible convection coefficients inside infill cells, however, the spectrum of infill sizes that are neither small to neglect convection nor large for being treated as external wall deserves further research.

5.3.2 Numerical Investigation of Natural Convection from a Vertical Surface

In the previous section, the fact that existing correlation equations for vertical plates represent a problem with different boundary conditions than the ones imposed in EDAM was identified. While existing correlation equations are derived from investigations of the thermal boundary layer developed parallel to a vertical surface suspended in an infinite medium, the problem of our interest is of a vertical surface placed on top of an infinitely long surface with a heated section which represents better the conditions encountered in CAMRI as well as in other large-scale additive manufacturing systems. This scenario was investigated for a vertical surface informed with temperature profiles developed during the printing process of a part that contains a vertical wall with similar dimensions. Clearly, these temperature profiles do not represent all the possible cases of geometry and processing conditions in EDAM yet this investigation provides further understanding on local convection mechanisms. The final goal of this investigation is to derive a correlation expression that is more appropriate for the aforementioned problem, however, we should not forget that this is not a general representation of the convection mechanism in EDAM since it does not capture any effects of geometry.

The assumption that natural convection occurs instantaneously was stated before in order to utilize temperature results from simulations of the manufacturing process of a part to inform the numerical analysis of natural convection presented herein. Natural convection has been investigated widely through numerical and analytical solutions of the laws governing buoyancy driven flow especially in scenarios where experimental procedures are not feasible like internal cavities. For instance, Bilgen and coworkers [128, 126] investigated the mechanism of natural convection in open square cavities at different orientations utilizing numerical solutions obtained with their own implementation based on the finite difference method. Similarly, Prakash et al.

[125] performed a numerical study in Ansys® Fluent® of natural convection from cavities with different geometries and aspects ratios. Another work that investigated numerically natural convection combined with radiation for cavities was presented by Gonzalez et al. [129].

The mechanism of natural convection is investigated herein through the coupled numerical solutions of the three fundamental laws governing the fluid motion, namely conservation of mass, conservation of momentum and conservation of energy. The commercial finite volume-based software Ansys® Fluent® (Ansys® Release Version 16.2) was used to analyze this natural convection problem in the laminar regime and at steady state. For the problem in consideration, the general equations in the spatial description solved in Fluent® are the following [130]. Equation 5.16 provides the equation for mass conservation in steady state.

$$\nabla \cdot \rho\vec{V} = 0 \tag{5.16}$$

This steady state form of the mass conservation or continuity equation is also called the divergence-free velocity field, where the density ρ and the velocity $\vec{V}$ are operator ∇ denoting the vector differential operator [131]. The conservation of momentum in steady state is then given by Equation 5.17 [130].

$$\nabla \cdot \left(\rho\vec{V}\vec{V}\right) = -\nabla p + \nabla(\bar{\bar{\tau}}) + \rho\vec{g} \tag{5.17}$$

Where p is the static pressure, the term $\rho\vec{g}$ is the gravitational force, and $\bar{\bar{\tau}}$ is the stress tensor given by $\bar{\bar{\tau}} = \mu\left[\left(\nabla\vec{V} + \nabla\vec{V}^T\right) - 2/3(\nabla \cdot \vec{V}I)\right]$, where μ is the viscosity, I is the identity tensor and the last group corresponds to the volumetric dilation. External forces are neglected in Equation 5.17 since flow is only driven by buoyancy force which is captured with the gravitational force term. Finally, conservation of energy in steady state neglecting viscous dissipation and internal heat generation is given by Equation 5.18 [130].

$$\nabla \cdot \left(\vec{V}(\rho E + p)\right) = \nabla \cdot (K\nabla T) \tag{5.18}$$

Where the left-hand side captures the kinetic energy and the pressure work whereas the right-hand side accounts for conduction in the laminar regime. A common approximation made in the analysis of natural convection is to only account for density changes in the Equation 5.17 for linear momentum and neglect density changes in the other two governing equations. However, this approximation known as the Boussinesq approximation is only valid for small temperature changes [113, 130]. Instead of using the Boussinesq approximation, a fully coupled solution scheme was utilized in Fluent® with the pressure-based solver. Steady state solutions of the equations governing the natural convection problem were obtained using a pseudo-transient analysis with default explicit relaxation factors provided in Fluent®. Ideal gas behavior was assumed for the fluid domain and the operating density specified in Fluent® was set equal to zero to ensure that the hydrostatic pressure in the fluid at rest is equal to zero [130].

Material properties defined for the air include the heat capacity, C_p, thermal conductivity, K_f, viscosity, μ_f, and the molecular weight, Mw. A piecewise polynomial description of the first three material properties was provided as a function of the temperature while a constant molecular weight was used. Temperature dependent properties utilized to construct the piecewise polynomial description of the air were obtained from the website Engineering Toolbox [132] and can be found in Figure A.2 to Figure A.4 of the APPENDIX A whereas other material properties used for the air can be found in Table A.17 of the same appendix. Also, since this investigation is in the laminar regime, the Rayleigh number, Ra_x, is checked to confirm that this stays below the critical value of 10^9 [28]. It should be noted that from this point on the units used for temperature are in the Kelvin temperature scale.

Figure 5.7 shows schematically the fluid domain used for analyzing the problem of interest. The dimensions of the fluid domain are large enough to avoid interference of the walls with the hydrodynamic boundary layer developed along the vertical plate and around the build plate. Also, a domain size sensitive study was performed to define the final dimensions of the fluid domain shown in Figure 5.7. Hexahedral elements (eight nodes element) were used to discretize the fluid domain and the boundary conditions are as follow. Faces A, B, C and F in Figure 5.7 are treated as walls with non-slip conditions and with constant ambient temperature equal to $T_{\infty,f}$. Symmetry is enforced in Face D since the vertical wall is modeled as a surface with zero thickness. A pressure output boundary condition is assigned to Face E, therefore velocity gradients are zero at this boundary condition as well. A gauge pressure equal to zero is used in the output boundary

condition and backflow is defined normal to this surface with temperature equal to $T_{\infty,f}$. This way thermal energy conveyed with the air can leave the problem domain and air at $T_{\infty,f}$ can reenter the problem domain [130].

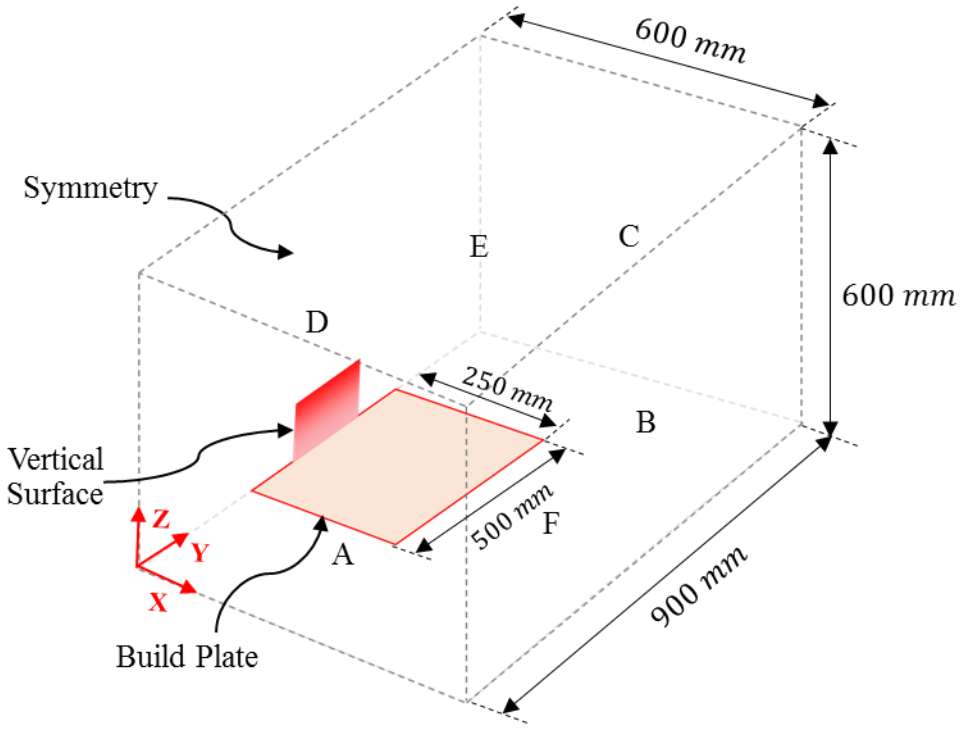

Figure 5.7 Schematic of the geometry of the fluid domain used in investigation of natural convection from non-isothermal vertical surface.

Non-slip wall conditions were also assumed in both the build plate and the vertical plate shown in Figure 5.7 but with the difference that a constant temperature, T_{bp}, is used at the build plate and a temperature profile is introduced along the vertical plate.

The latter is meant to represent temperature profiles developed during part manufacturing along the height of vertical printed sections. Nevertheless, obtaining such a general temperature profiles is not possible in EDAM since the temperature history of a part depends not only on the geometry and printing history but also on the printing conditions such as the temperature at the build plate and the deposition temperature of the material. Hence, the primary purpose of this investigation is to explore the impact of utilizing local convective coefficients on the temperature predicted through the transient heat transfer analysis of the printing process of a part. Given this

purpose, the geometry of the stringer tool shown in Figure 5.8 will be used as a benchmark to investigate the different mechanisms of heat transfer addressed throughout this chapter.

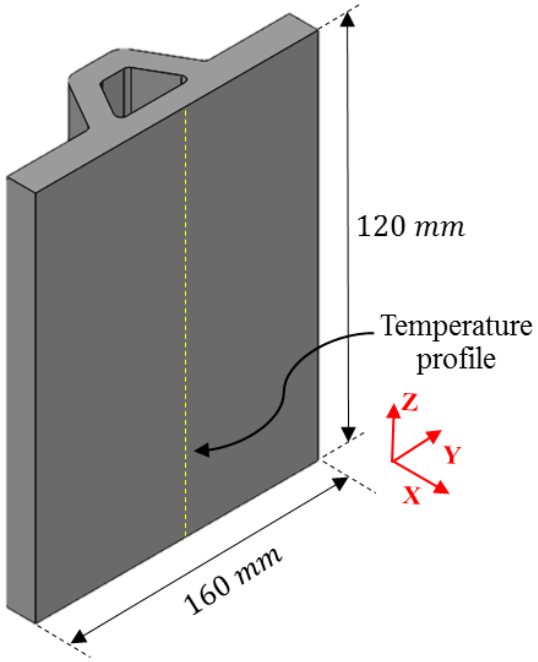

Figure 5.8 Geometry of stringer tool utilized to obtain temperature profiles used in natural convection analysis.

The dimensions of the vertical surface illustrated in Figure 5.7 are defined based on the geometry of the stringer tool shown in Figure 5.8 whereas the dimensions of the build plate are based on the heated build plate used in CAMRI. Furthermore, the printed part and the build plate move relative to the nozzle in CAMRI which continuously perturbs the thermal and hydrodynamic boundary layers developed parallel to the vertical surface. Such an effect was not considered herein due to the complexity of describing the movement of the part in the simulations and it is not considered to cause a drastic difference in the convection mechanism since the velocities of the build plate are relatively low. The scenario modeled though, is closer to printing conditions used in commercial large scale printers like BAAM and LSAM where the part is stationary while the deposition head moves relative to the part as well as to the cooling process of a part after printing in CAMRI.

5.3.2.1 Mesh Sensitivity Analysis

Prior to utilizing the simulation setup to investigate natural convection on the vertical plate with different process conditions, a mesh sensitivity analysis was conducted to assure the results obtained with the model are not influenced by the discretization of the fluid domain. To perform the sensitivity analysis, a temperature profile developed during part manufacturing was extracted along the yellow dashed line illustrated in Figure 5.8. Such a profile can be obtained from experimental temperature measurements during part manufacturing or from temperature predictions from transient heat transfer simulations of the part printing process. The latter approach was used herein but experimental temperature measurements are also provided in the validation section.

The sensitivity of two field variables was monitored as the density of the mesh was increased, the total power removed from the vertical wall and the average convection coefficient, $\bar{h}$. The first one is obtained by integrating the heat flux at each element face located on the vertical wall whereas the second one is obtained from the area weighted average of the local convection coefficient, h. Table 5.2 lists the five element sizes assessed in the mesh sensitivity analysis.

Table 5.2 Results of mesh sensitivity analysis.

Element Size $(\boldsymbol{mm})$	**Power Removed from Wall** $(\boldsymbol{W})$	$\boldsymbol{\bar{h} = \frac{1}{A}\sum_{i=1}^{n} h_i A_i}$
10	15.184	5.180
5	26.121	8.936
4	25.163	9.380
3	26.962	9.380
1.5	24.343	8.983

In order to capture more accurately the temperature and velocity fields near the vertical surface and the build plate, the element size listed in Table 5.2 was enforced in both the vertical surface and the heated build plate. Further, the mesh density was then reduced in the regions far from the heated surfaces by biasing the element size from a minimum size of $3\ mm$ near the region of interest to $12\ mm$. Based on the results of the mesh sensitivity analysis summarized in Table 5.2, an element size of $4\ mm$ was chosen for subsequent investigations. Such an element size gave rise to a total number of elements of around four hundred thousand in the fluid domain. Figure 5.9

shows the mesh used for a vertical surface with a heights of 113.1 mm, a cutout was made in the mesh to illustrate the variation in mesh density through the fluid domain. Although vertical surfaces with different heights were used in the subsequent section to investigate natural convection, the mesh size and density distribution resulting from the meshing control parameters mentioned above did not change significantly.

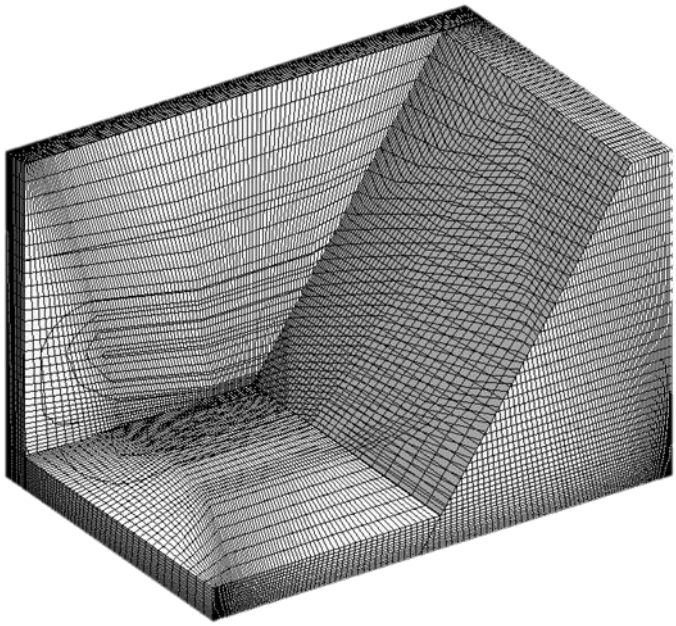

Figure 5.9 Mesh utilized in the natural convection analysis with cutout to illustrate mesh density distribution.

5.3.2.2 Numerical Investigation of Natural Convection Informed with Temperature Gradients from Extrusion Deposition Additive Manufacturing

A simulation setup was presented previously for investigating the mechanism of natural convection on a vertical surface placed on top of a horizontal plate maintained at a constant temperature. A mesh sensitivity analysis was also performed to select a mesh density appropriate for this problem. Now we will utilize this simulation setup to investigate the mechanism of natural convection on a vertical surface representing the vertical face of the stringer tool shown in Figure 5.8. Notice the words wall, and vertical surface and vertical plate are used interchangeably throughout this section to refer to the vertical surface illustrated in Figure 5.7.

The objective of this investigation is to obtain local Nusselt numbers, Nu_z, as a function of the height of the wall with temperature profiles informed from results of precomputed transient

heat transfer simulations of the printing process of this part. Then, the obtained local Nusselt numbers, Nu_z, are used to fit a proposed correlation equation that can be used in the process simulation of this part. Again, this is possible under the assumption made previously that natural convection occurs instantaneously and therefore only depends on the instantaneous temperature distribution.

The framework for simulating the EDAM process in Abaqus© with composite materials was already presented in chapter 4, yet specific details of the transient heat transfer analysis are provided throughout this chapter. For the sake of this investigation, the printing simulation of the stringer tool considered orthotropic heat conduction, heat losses due to material compaction as well as heat losses through radiation and convection with a calibrated constant convection coefficient. The material used in the simulation of the printing process was PPS reinforced with 50% by weight of carbon fiber and the dimensions of the printed bead used in this simulation were 1.3 by 4.7 mm along with a constant printing speed of 91.67 mm/s. Thermophysical properties provided in the previous section were used in the simulation of the printing process of the part.

Additionally, the effect of the build plate temperature on the local convection coefficient was investigated with this simulation setup. For this, the printing process of the stringer tool was performed at three different build plate temperatures, 393.15 K, 443.15 K and 493.15K, which represent build plate temperature typically used in the CAMRI system. Temperature profiles were then extracted along the yellow dashed line shown in Figure 5.8 at five different instants of time that correspond to the wall heights listed in Table 5.3. The same information was extracted at each of three build plate temperatures investigated. Table 5.3 lists the total of 15 conditions investigated through simulation. It is worthwhile mentioning that investigating these conditions experimentally is highly complicated and, even impossible in some cases, therefore simulation approaches like the one presented herein are preferred.

It should be also noted that temperature profiles are extracted at the middle section of the surface despite the existence of temperature gradients along the width direction of the stringer geometry. This was made in order to simplify the mapping of temperature between the different meshes utilized in the process simulations performed in Abaqus© and the one used in the simulation of natural convection in Fluent®.

Table 5.3 List of temperature profiles investigated through simulations of natural convection.

Identifier	**Wall Height - W_h (mm)**	**Build Plate Temperature - T_{bp} (K)**
$W_h1 - T_{bp}1$	9.1	393.15
$W_h2 - T_{bp}1$	35.2	393.15
$W_h3 - T_{bp}1$	61.1	393.15
$W_h4 - T_{bp}1$	87.1	393.15
$W_h5 - T_{bp}1$	113.1	393.15
$W_h1 - T_{bp}2$	9.1	443.15
$W_h2 - T_{bp}2$	35.2	443.15
$W_h3 - T_{bp}2$	61.1	443.15
$W_h4 - T_{bp}2$	87.1	443.15
$W_h5 - T_{bp}2$	113.1	443.15
$W_h1 - T_{bp}3$	9.1	493.15
$W_h2 - T_{bp}3$	35.2	493.15
$W_h3 - T_{bp}3$	61.1	493.15
$W_h4 - T_{bp}3$	87.1	493.15
$W_h5 - T_{bp}3$	113.1	493.15

Two scripts were implemented for this purpose, one Python script outputs temperature profiles along a path defined in Abaqus at predefined instants of time and a script developed in Matlab® reads temperature profiles output by Abaqus© and create temperature profiles appropriate for Fluent®. The script for creating temperature profiles for Fluent® is rather simple but it is included in Table B.3 of the APPENDIX B. After creating the input temperature profiles, these are mapped to the vertical wall in Fluent® in which the temperature profile is uniform along the width of the wall.

Figure 5.10 shows the fifteen temperature profiles extracted from printing simulations of the stringer tool. Temperature profiles are color coded based on the build plate temperature as follow, black corresponds to $T_{bp} = 393.15\,K$, blue to $T_{bp} = 443.15\,K$ and magenta to $T_{bp} = 493.15\,K$. The same color code is employed in the rest of plots included in this section.

Figure 5.10 clearly shows the influence of the boundary condition of the first kind imposed by the build plate temperature on the temperature profiles developed along the stacking direction of the par. Despite the low thermal conductivity of the printed material in the stacking direction, the temperature of the build plate impacts the temperature history of the printed material up to a distance of around 40 mm from the build plate. This represents around 30 layers with the bead

height of 1.3 mm considered in these printing simulations. However, as the printing front progresses beyond this distance where conduction dominates the temperature history of the printed material, the convective and radiative heat losses dominate the transient cooling history of the printed material.

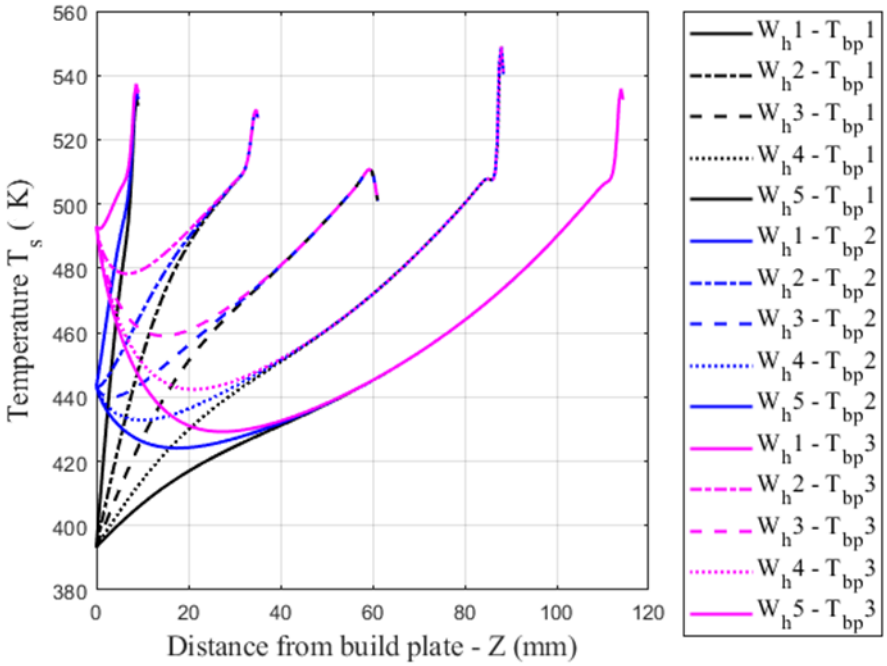

Figure 5.10 Temperature profiles extracted from simulations of the printing process of the stringer tool and used in numerical investigation of natural convection.

5.3.2.3 Results

After introducing temperature profiles, a steady state solution was computed for each of the fifteen conditions investigated. Convergence of the solution was judged based on the recommendation of a minimum reduction of three orders of magnitude of the scaled residuals provided in the manual of Fluent® [130]. Both velocity and temperature fields are solved and therefore information of the thermal and hydrodynamic boundary layers is available. Also, the local Rayleigh number, Ra_x, is confirmed to be below the critical number for a vertical wall.

Since our objective is to investigate both the evolution of the convection coefficient along the height of the wall and the effects of the build plate temperature on the distribution of the convection coefficient, we can start by inspecting the thermal boundary layer. As stated before in

Equation 5.9, the local convection coefficient is obtained by applying Newton's law of cooling and Fourier's law to the fluid at the interface. The denominator in Equation 5.9 is constant exclusively for isothermal walls, however, in our case, the temperature profile mapped to the surface defines the behavior of the denominator. The distance over which this temperature gradient develops corresponds to the thickness of the thermal boundary layer. Therefore, a thick boundary layer decreases the temperature gradient and thus reducing the local convection coefficient whereas as thin thermal boundary layer increases the temperature gradient, thereby increasing the convection coefficient. Figure 5.11 shows a cut in the XZ plane of the thermal boundary layer developed parallel to the vertical surface for three of the conditions investigated, namely the highest vertical surface at each of the build plate temperatures investigated: $W_h5 - T_{bp}1$, $W_h5 - T_{bp}2$, $W_h5 - T_{bp}3$. This cut was made at the middle of the vertical surface. Therefore, the inverted "T" shape depicted in Figure 5.11 corresponds at the bottom to the temperature field developed on top of the heated build plate whereas the vertical temperature field corresponds to the boundary layer developed parallel the non-isothermal vertical surface. Also notice the temperature field was mirrored with respect to the symmetric boundary condition stated in the definition of the problem and also shown schematically in Figure 5.7. Although only a cross sectional view of the thermal boundary layer is shown in Figure 5.11, the thermal boundary layer is three dimensional due to the effects of the relative position of the vertical surface with respect to the build plate as well as the influence of the local convection on the build plate.

By inspecting the thermal boundary layers depicted in Figure 5.11, a relative increase in the thickness of the thermal boundary layer is clearly noticed as the temperature of the build plate is increased from $393.15\ K$ to $493.15\ K$ in the cross sectional cut shown for the conditions $W_h5 - T_{bp}1$ and $W_h5 - T_{bp}3$, respectively. Further, the change in thickness in the thermal boundary layer occurs primarily near the build plate. Hence, we can anticipate a reduction in the local convection coefficient in the regions of the vertical surface located near the build plate as well as exchange of thermal energy between the vertical wall and the heated build plate in this region.
Figure 5.11 gives brief insights into the distribution of the convection coefficient along the height of the vertical surface given the different build plate temperatures, but we can now appreciate the three-dimensional nature of the boundary layer by examining the local convection coefficient on the vertical surface.

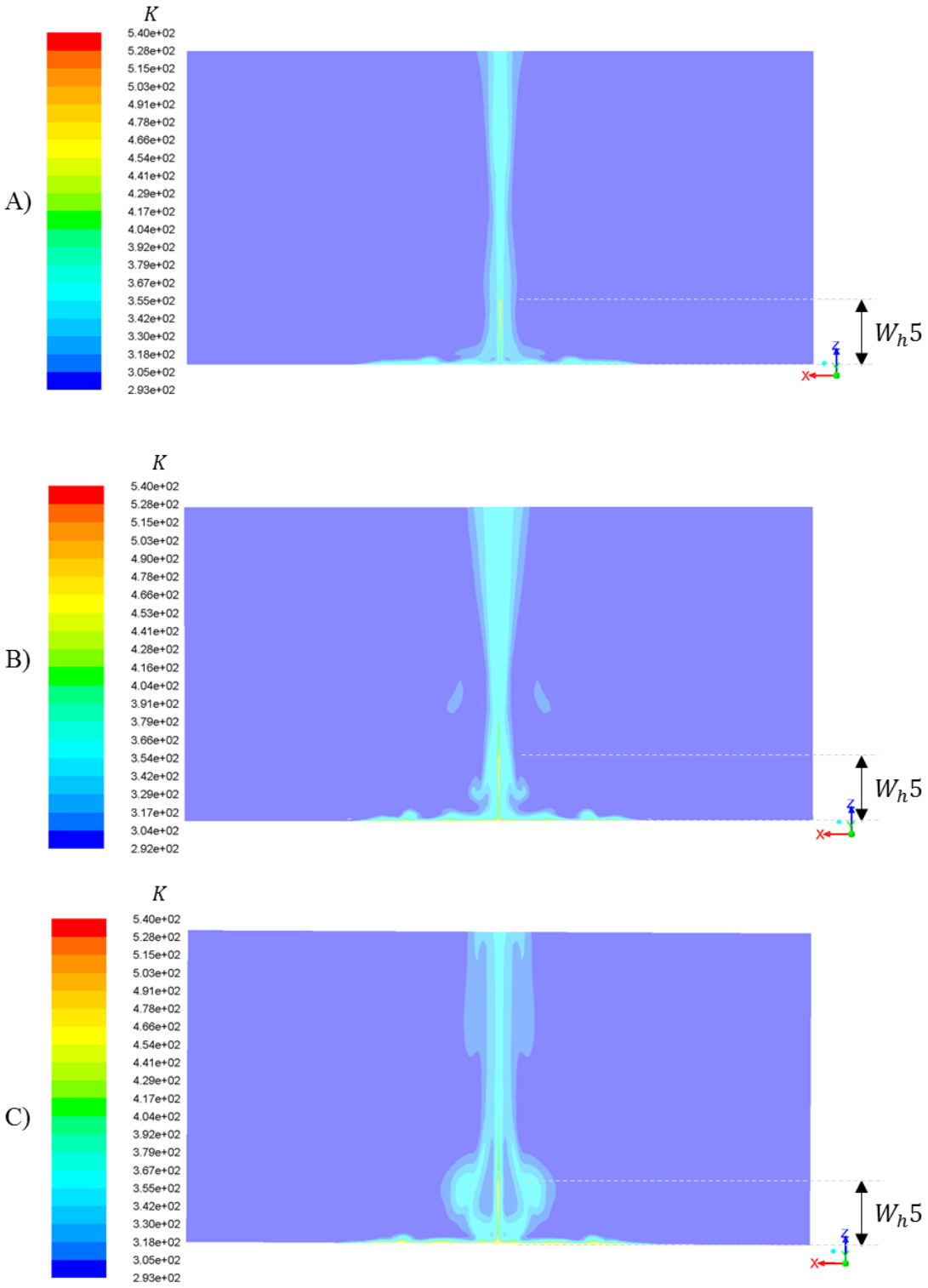

Figure 5.11 Cut in the XZ plane of thermal boundary layer developed parallel to the highest vertical surface investigated and for the three build plate temperatures considered. A) $W_h5 - T_{bp}1$. B) $W_h5 - T_{bp}2$. C) $W_h5 - T_{bp}3$.

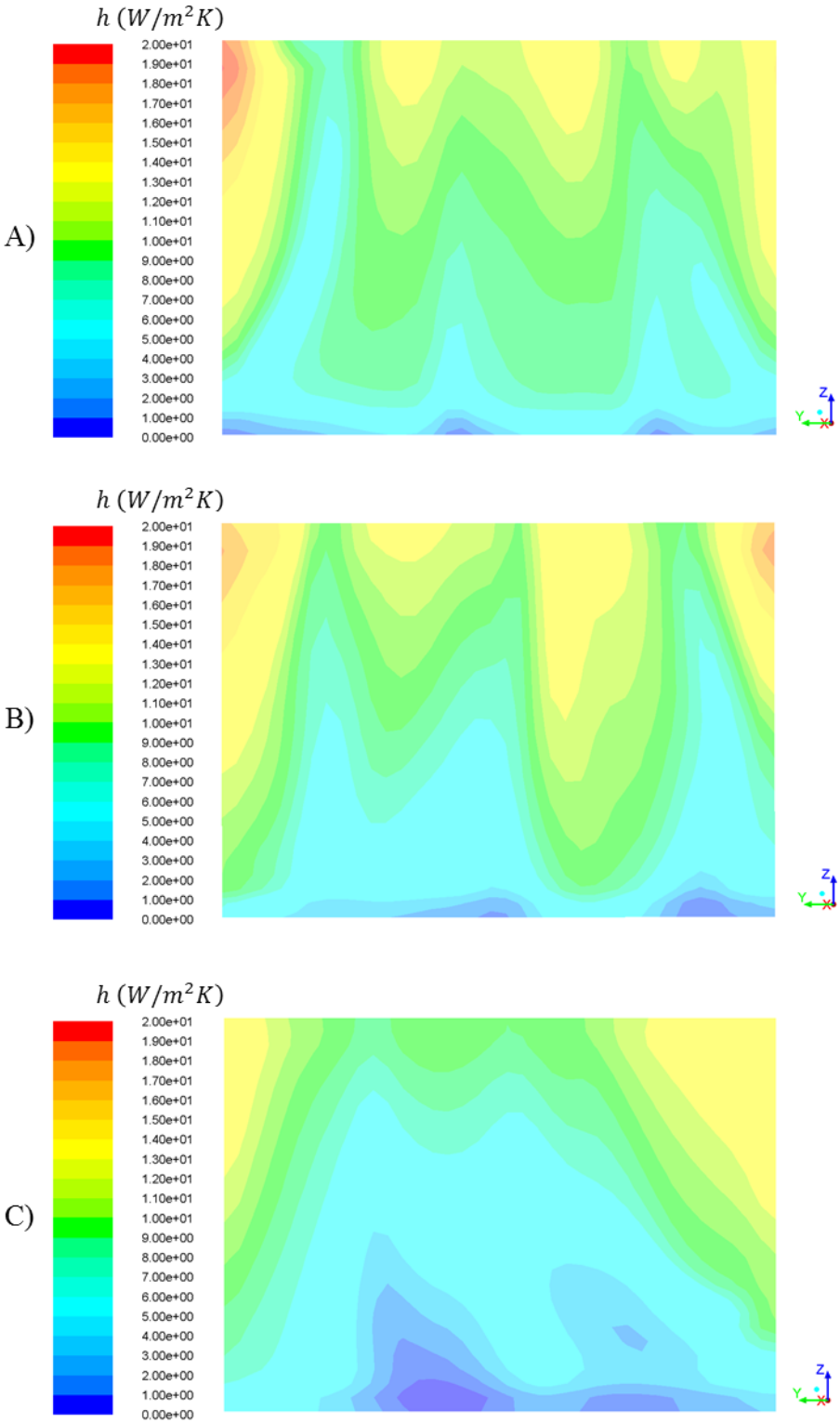

Figure 5.12 Local convection coefficient, h, developed on the highest vertical surface investigated and for the three build plate temperatures considered. A) $W_h5 - T_{bp}1$. B) $W_h5 - T_{bp}2$. C) $W_h5 - T_{bp}3$.

Figure 5.12 shows the local convection coefficient, h, for the same three conditions shown in Figure 5.11. Since the three plots are in the same scale, we can appreciate the relative increase in dominance of the blue regions as the build plate temperature is decreased from $493.15\ K$ in Figure 5.12-A to $393.15\ K$ in Figure 5.12-B.

Since the objective of this study is to describe the local convection only as a function of the distance from the build plate, Z, the local convection coefficient, h, shown in Figure 5.12 was averaged over the width of the vertical surface and weighted with the area of the element. Edge effects observed near the boundaries of the vertical surface were also considered in this area-weighted average. From this point on, we will refer to the area-weighted average convection coefficient simply as the local convection coefficient, h_z. Figure 5.13 shows the local convection coefficient, h_z, as a function of the distance, Z, from the build plate for each of the fifteen conditions investigated and listed in Table 5.3.

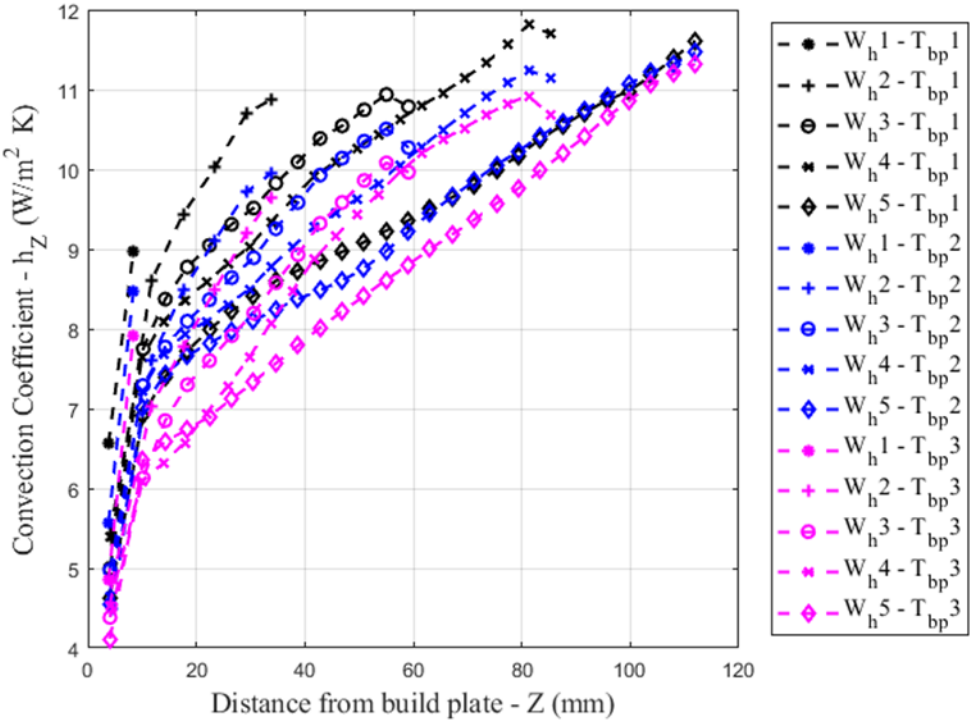

Figure 5.13 Convection coefficient as a function of the distance, Z, from the build plate for each of the conditions considered. (Area-weighted average convection coefficient over the width of the vertical surface).

The influence of the build plate temperature now becomes clearer from the area-weighted average convection coefficient shown in Figure 5.13. The plot in Figure 5.13 shows that overall the local convection coefficient, h_z, increases for the same height of the vertical surface as the temperature of the build plate decreases. Notice also the local convection coefficient is not affected significantly ($< 0.5\, W/m^2K$) after a certain distance, Z, from the build plate in the range of $70\, mm$. Another observation is that despite the effect of build plate on the convection coefficient, the shape of the curve describing the convection coefficient as a function of the distance, Z, from the build plate is not affected significantly. Instead, the curves seem to be shifted in the vertical direction as the build plate temperature decreases.

Since our objective is to create a correlation equation that captures the behavior of the convection coefficient as a function of both the build plate temperature and the distance from the build plate, the next step is to transform the convection coefficient to Nusselt numbers. Utilizing Equation 5.12, the local convection coefficient and the distance, Z, from the build plate, the local Nusselt number, Nu_z, can be estimated. Figure 5.14 shows Nu_z as a function of the distance, Z, from the build plate for all the conditions investigated herein.

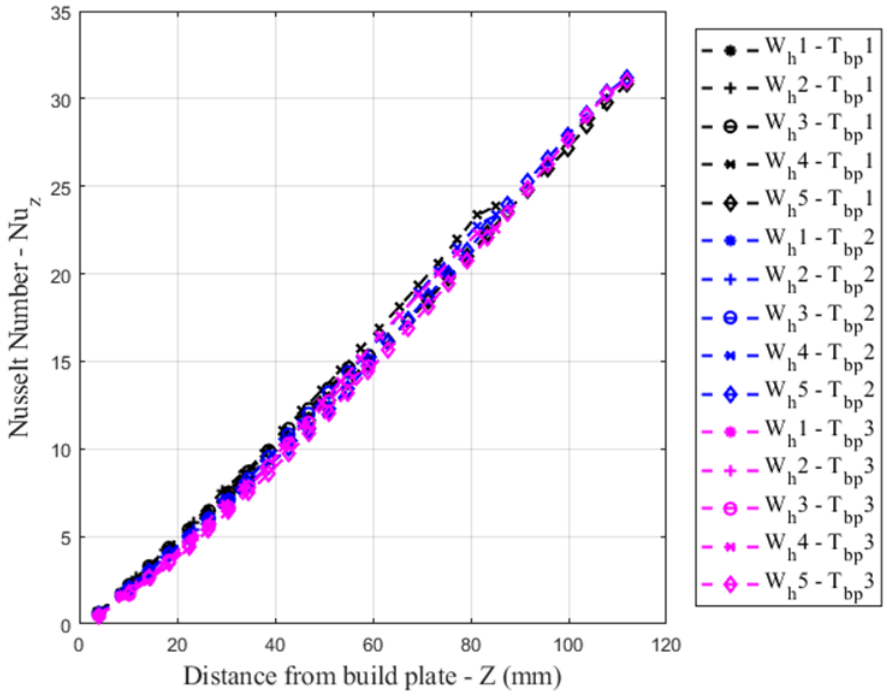

Figure 5.14 Local Nusselt number, Nu_z, as a function of the distance, Z, from the build plate for each of the conditions considered.

Now from the plot of the local Nusselt number, Nu_z, the dependence of the build plate temperature is still noticeable but rather weak. Moreover, the behavior observed previously in the curves of h_z as a function of the distance Z is still observable in the Nusselt number. In other words, the curve of Nu_z for a given wall height seems to be shifted up as the build plate temperature decreases from $493.15\ K$ to $393.15\ K$. Hence, the effect of the build plate temperature may be readily captured with a shift factor in the correlation equation that depends on the build plate temperature.

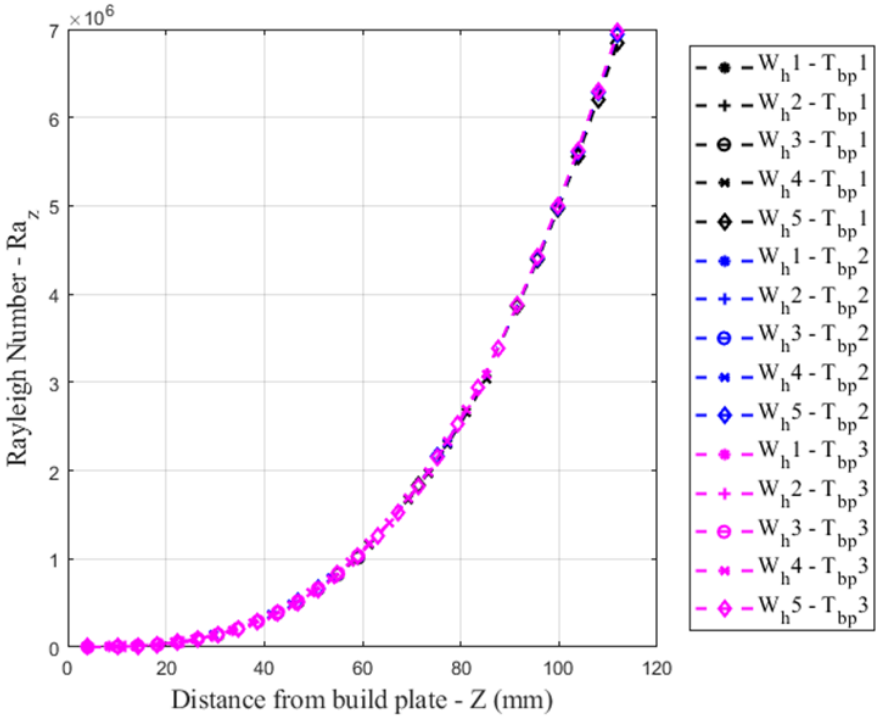

Figure 5.15 Local Rayleigh number, Ra_z, as a function of the distance, Z, from the build plate for each of the conditions considered.

The second dimensionless number important for natural convection is the local Rayleigh number, Ra_z, which is given by Equation 5.11. The Rayleigh number is analogous to the Reynolds number in forced convection and it should be checked to identify the regime of operation. The laminar regime for convection from vertical surfaces is defined below a critical Rayleigh number of 10^9 [28]. Further, Ra_z is a function of the local Grashof number, Gr_z, and the Prandtl number, Pr, as given by Equation 5.11. The local Rayleigh number can be then estimated for each of conditions considered herein utilizing properties of the air evaluated at the film temperature which is defined

by the average of the temperature at the surface and the ambient temperature of the air ($T_{film} = (T_S + T_{\infty,f})/2$). The thermophysical properties of the air utilized for estimating Gr_z are provided in Figure A.2 through Figure A.4 as well as in Table A.17 of the APPENDIX A.

Figure 5.15 shows the local Rayleigh number, Ra_z, as a function of the distance Z from the build plate for each of the fifteen conditions investigated. Two important observations should be made with regards to the curves of the local Rayleigh number. First, the maximum value estimated for Ra_z is around three orders or magnitude below the critical Rayleigh number (10^9), thereby confirming the results are within the laminar regime. Second, the influence of the different temperature profiles (shown in Figure 5.10) does not have a significant influence on the Ra_z which result obvious from the dependence of Ra_z on the distance Z to the third power. In other words, the ratio of the buoyancy forces to viscous forces has a stronger dependence on the distance from the build plate than on the temperature gradients developed along this direction. The images of the numerical analysis of natural convection were used by courtesy of Ansys®.

5.3.2.4 Correlation Equation Developed Based on Numerical Results

After computing the dimensionless numbers important to describe natural convection, we can start to shape the form of the correlation equation based on our previous observations and the form of analytical solution of the thermal boundary layer. It was recognized since the beginning of this section that correlations expressions to describe natural convection parallel to a vertical surface may look somehow alike Equation 5.14. Further, it was recognized while analyzing the Nusselt number that a vertical offset in the correlation equation may suffice to account for the vertical shift in the behavior of the Nusselt number for different build plate temperatures. Therefore Equation 5.19 was proposed to correlate the Rayleigh number, the Prandtl number, and the temperature of the build plate with the local Nusselt number.

$$Nu_z = A \cdot T_{bp} + B \cdot Ra_z^n \cdot Pr^m \tag{5.19}$$

A, B and the exponents m and n are constant values that can be characterized with the Nusselt number obtained with the numerical investigation of natural convection and the other dimensionless numbers shown previously. The function lsqcurvefit in Matlab® provided the nonlinear least-squares solver utilized to characterize the four coefficients in Equation 5.19.

The same script developed in Matlab® for creating input temperature profiles for Fluent® includes a section dedicated to import and organize temperature, local heat flux, and local convection coefficient extracted from Fluent® as a function of the distance from the build plate. With all this information, the Nusselt and Rayleigh numbers are computed and then passed to the lsqcurvefit function to characterize the coefficients in the correlation equation in a least-square sense. This script can be found in Table B.4 from the APPENDIX B. Table 5.4 lists the parameters characterized for the correlation equation utilizing the results from the numerical analysis of natural convection.

Table 5.4 Parameters characterized for correlation equation (Equation 5.19)

Parameter	**Value**
A	$-1.0169 \cdot 10^{-3}$
B	0.1059
n	0.3665
m	0.2

We can now compare predictions made with the correlation equation in Equation 5.19 to the numerical results obtained previously. The local Nusselt number predicted with this equation is then used with Equation 5.12 to calculate the local convection coefficient, h_z. Figure 5.16 presents three plots that compare the numerical results used to fit the correlation expression to the predictions made with Equation 5.19. Conditions used to evaluate the correlation equation are the same used in the numerical investigation, namely temperature profile, location and thermophysical properties of the air. Overall the predictions made with the correlation equation are in great agreement with the numerical results. While the closest prediction is made for the build plate temperature of 443.15 K, the largest deviation from the numerical results was observed at the lowest temperature investigated (393.15 K).

This correlation equation captures well the behavior predicted through the simulations of natural convection and under the assumptions stated before, therefore it can be used to provide a better description of the convection coefficient than a constant convection coefficient in simulations of the EDAM process.

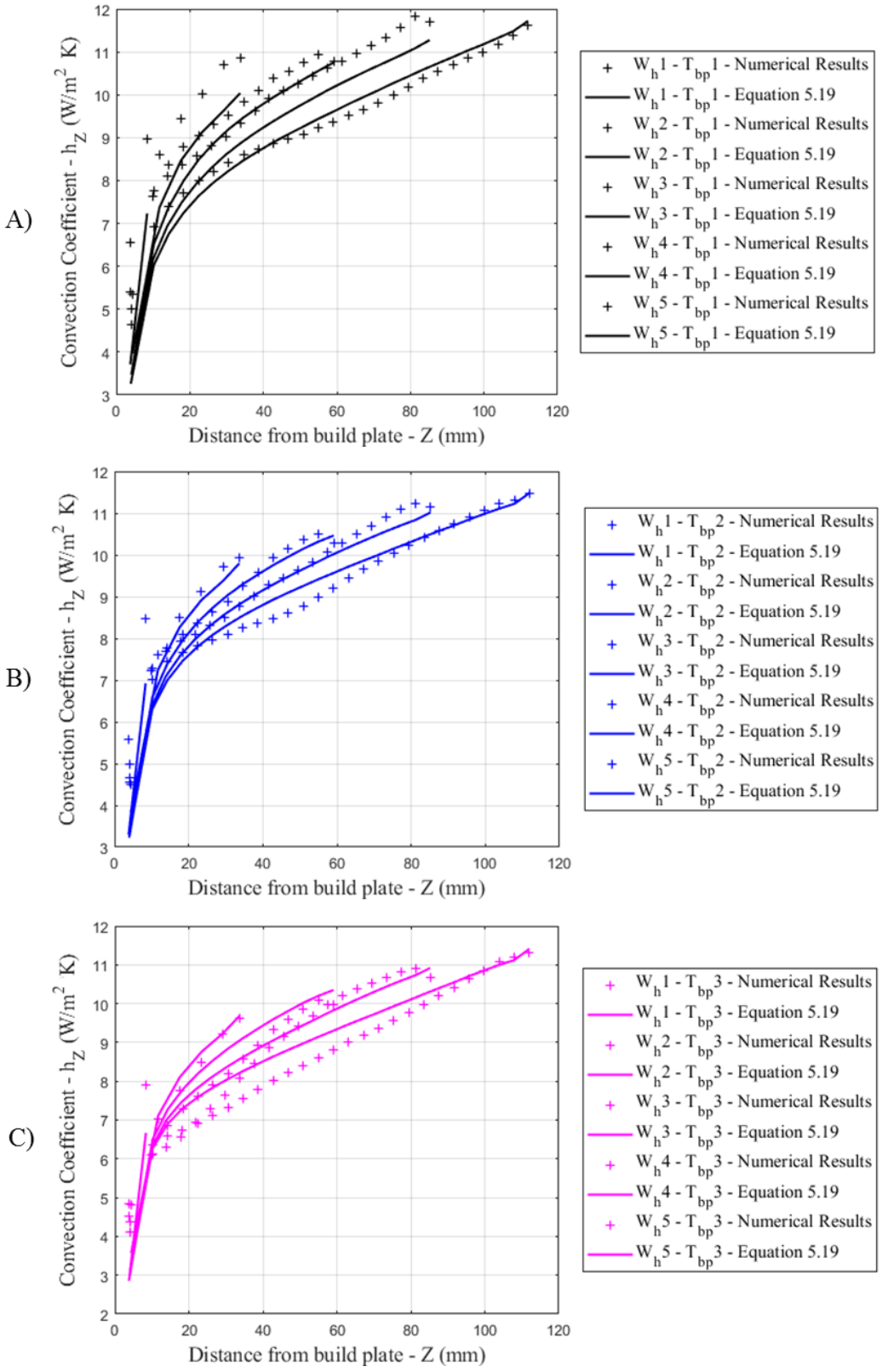

Figure 5.16 Comparison of local convection coefficient, h_z, obtained in numerical analysis and predicted with correlation equation (Equation 5.19).

The relevance of capturing details of the convection mechanism through the correlation equation presented before is addressed in the last section of this chapter where both formulations, constant convection coefficient and position dependent convection are compared.

The original purpose of investigating the mechanism of convection was to assess the relevance of local convection coefficients in the temperature history predicted in transient heat transfer simulations of EDAM, for which a specific geometry that contains a vertical surface was chosen and used to drive these investigations. Therefore, the correlation equation derived is strictly speaking representative of only flat vertical surfaces since it does not capture any geometric aspect of a printed geometry.

In order to explore the behavior of this correlation expression in vertical surfaces longer than the $120\,mm$ of the stringer tool, three different temperature gradients were defined considering a temperature range from $443.15\,K$ to $580.15\,K$ and assuming three different wall heights, 200, 400 and $600\,mm$, respectively. The build plate temperature considered was the lower bound in this temperature range. Rayleigh numbers resulting from these conditions were assessed to confirm that these temperature profiles are still within the laminar regime ($Ra_z < 10^9$). Figure 5.17 shows the convection coefficient predicted with Equation 5.19 for three different temperature profiles.

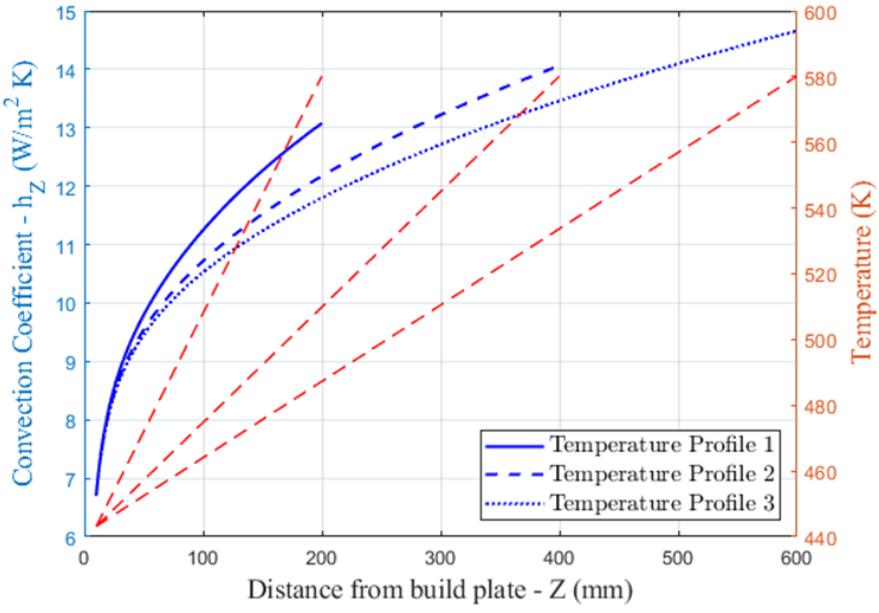

Figure 5.17 Investigation of convection coefficient predicted with correlation equation for different temperature profiles.

The three temperature profiles in Figure 5.17 illustrate the dependence of the convection coefficient on the temperature gradient developed along the height of the vertical surface. While the smallest temperature gradient shown for the Temperature Profile 3 yields the shallowest asymptotic response for the convection coefficient, the largest temperature gradient shown for Temperature Profile 1 yields the steepest asymptotic response for the convection coefficient. Such changes in the asymptotic response of the convection coefficient result from the fact that coefficients in Equation 5.19 were characterized with temperature gradients developed during part manufacturing which are not truly constant as the ones used in Figure 5.17. Nevertheless, these examples serve for demonstrating the behavior of Equation 5.19 at wall heights higher than the ones investigated herein. Predictions made with this equation far beyond the range considered in the numerical analysis ($Z > \sim 200mm$) deserve further investigation since changes in temperature gradients at higher distances from the build plate could influence the mechanism of local convection. Also, the convection mechanism is modified drastically at the onset of turbulence which for this case occurs at wall heights in the range of $700\,mm$. Finally, the fact that the movement of the build plate and part in CAMRI was not considered leads to the conclusion that Equation 5.19 slightly underpredicts the actual convection conditions in CAMRI but captures properly the convection conditions in systems with a stationary build plate.

5.4 Radiation in Extrusion Deposition Additive Manufacturing

Heat losses through radiation are also important to consider in the process simulation of the EDAM since printed material is deposited in the molten state. Radiative heat losses are significant at elevated temperature since their contribution scales with the fourth power of the temperature at the surface as shown previously in Equation 5.6.

Unlike convection that develops through the air medium surrounding a surface, radiation does not require a medium since thermal energy is emitted from the surface in the form of electromagnetic waves [28]. All forms or matter emit radiation above the absolute zero temperature and this has both directional and spectral distributions depending on the conductive nature of the emitter. Further, thermal energy is not only emitted from a surface but also irradiated onto a surface by emission of all other surrounding surfaces. Other material properties relevant to radiation in an opaque material like the composite in consideration here includes the reflectivity, $\rho_{\lambda,\theta}$, and the absorptivity, $\alpha_{\lambda,\theta}$, that determine the fraction of irradiation reflected from the surface

and the fraction of the irradiation absorbed at the surface, respectively. Notice that subscripts λ and θ correspond to specific wavelengths and direction [28]. Furthermore, in the context of EDAM, some of the hot surfaces emitting radiation like the processing equipment move relative to the printed part, which further complicates describing radiation in process simulations. Hence, modeling radiation with such level of details is complex due to the directionality dependence arising from the geometry of printed objects and the directional distribution of the emitted radiation as well as the interactions with surrounding surfaces that also emits radiation.

Since accounting for all these factors in the process simulation of a real printed part is not practical, a similar approach to utilizing different convection conditions based on the printed feature can be used for radiation. Before describing the specific radiative conditions used in each printed region, we will state the assumptions made in the radiation boundary conditions applied at exposed surfaces. First, the surface of the printed material is assumed to behave as a grey surface which requires the emission and the absorption characteristics of the material to be diffuse and independent of the wavelength, λ, [28]. A diffuse surface is such that there is not directionality dependence on the emission and absorption behavior. Under these assumptions it can then be stated that $\varepsilon_\lambda = \alpha_\lambda$ in the spectrum where emission and irradiation occur. Second, the irradiation from other surfaces surrounding the surface of the printed material is also going to be assumed diffuse. And third, radiation is only considered between surfaces of solids.

Before considering radiation across different regions within the part, we should recognize all printed beads lose heat through radiation immediately after these are deposited and despite the region those belong to. This is due to fact that radiation occurs instantaneously and does not require a medium to transport energy like convection does. Furthermore, heat losses through radiation are more significant than heat loses through natural convection at temperatures near the deposition temperature therefore we cannot simply disable radiation in infill regions. Therefore, the same radiation condition is applied to all exposed surfaces for now yet suggestions for future improvement are provided in the section Implementation of Surface Boundary Conditions.

All the exposed surfaces in a printed are treated as gray surfaces that emit and absorb radiation in a diffuse manner. Additionally, all surface surrounding the part are also assumed to emit thermal energy in a diffuse manner. Under this assumption, the emissivity and the absorptivity are the same and therefore radiation heat fluxes can be estimated with Equation 5.20.

$$q_r'' = \sigma\varepsilon(T_s^4 - T_{\infty,r}^4) \quad (5.20)$$

Where σ is the Stephan-Boltzmann constant, ε, is the emissivity of the material, T_s, is the surface temperature of the printed material and, $T_{\infty,r}$ is the radiation ambient temperature. $T_{\infty,r}$ is calibrated to account for energy absorbed at the surface of the printed material and emitted by the hot surrounding surfaces. For the case of CAMRI, there are multiple hot surfaces surrounding a printed part including the printed build plate, the cover of the single screw-extruder, and the melt pump. Each of these components operates at different temperatures and therefore contributes to different extent. Calibration of this temperature is performed with experimental temperature measurements and simulation of the same printed geometry. In this case, the geometry of the stringer tool was used to calibrate the radiation ambient temperature.

The only parameter left out in Equation 5.20 is the emissivity, ε, which is a material property that can be characterized utilizing a printed geometry as it will be described in the following subsection.

5.4.1 Emissivity Characterization

The emissivity of the printed 50% by weight of carbon fiber PPS was characterized experimentally utilizing a pre-calibrated FLIR® A655sc thermal camera and an isothermal blackbody cavity. The characterization was performed at different temperatures in order to investigate the effects of temperature on the emissivity of the printed material. To create a blackbody cavity with our material of interest, the geometry of half an ovoid was additively manufacturing in CAMRI. The half ovoid was printed hollow with one bead through the thickness of the wall and with four solid layers printed through the thickness in the plane of cut, in other words, the printed ovoid was printed hollow and fully closed. Figure 5.18 shows the printed half ovoid equipped with thermocouples to monitor temperature distribution during the characterization experiment.

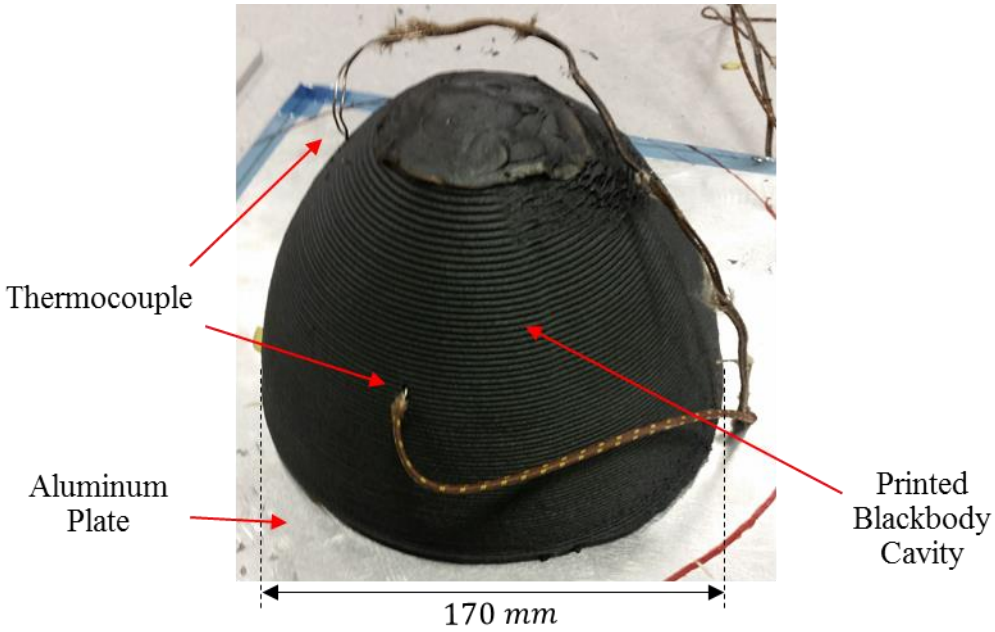

Figure 5.18 Printed blackbody cavity utilized for characterizing the emissivity of the 50% by weigh of carbon fiber PPS.

A circular orifice with diameter of 38.1 mm was made on the face of the plane of cut in order to create the diffuse emission required for the characterization of the emissivity. The face on the plane of cut was then attached with mechanical fasteners to a square aluminum plate with an orifice of about 50.8 mm centered at the middle of the plate. Two small orifices were made in opposite sides of the printed cavity to insert thermocouples as shown in Figure 5.18. The aluminum plate served for attaching the printed blackbody cavity to an oven that provided the thermal energy for heating the blackbody cavity. While the aluminum plate was exposed on the face mating with the printed blackbody cavity, the side of the aluminum plate facing the exterior was covered with ceramic fiber insulation to lessen heat losses from the oven and to ensure a more uniform temperature in the printed blackbody cavity. An additional thermocouple was placed on top of the ceramic insulation to monitor the temperature at the front face. The thermal camera was located normal to the opening of the blackbody cavity and at a distance of 1 m as shown in Figure 5.19. The camera was then focused to the interior of the black body cavity.

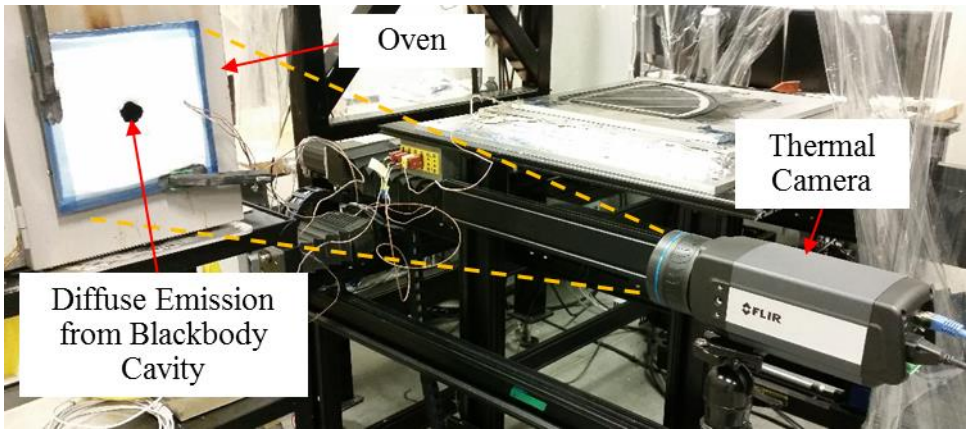

Figure 5.19 Experimental setup used for characterizing emissivity.

The following procedure was conducted to characterize the emissivity of the material at five different temperatures within the range of 403.15 K to 523.15 K and with increments of about 24 K. This temperature range was chosen for two reasons, the lower bound was defined based on the lower limit of the calibration range provided with the thermal camera whereas the upper bound was defined to prevent melting of the crystalline phase in the PPS.

The first step in the characterization was to set the temperature in the oven to about 30 K above the target temperature in order to account for temperature gradients developed inside the oven, however, the thermocouples attached to the blackbody cavity provided precise temperature readings of the cavity. The oven with the printed cavity reached steady state in about one hour. Once the temperature is uniform inside the blackbody cavity, inspection of the diffuse emitter is performed with the thermal camera utilizing the software ResearchIR© provided by FLIR® systems. Since the thermal camera senses radiance over the angular aperture of the camera (24°), the emission from surrounding surfaces should be accounted for in the measurements of the emissivity. The thermocouple placed on the frontal face of the aluminum plate provides temperature measurements of this surface which is the second highest temperature in the experimental setup. ResearchIR© provides for compensation of reflected temperatures in which the temperature measured from the front plate is used to estimate the radiance from the ambient [133]. Then, the emissivity used in the thermal imager is adjusted until the temperature reported by the camera matches the temperature sensed with the thermocouples located inside the blackbody cavity. Figure 5.20 shows an example of the temperature map provided by the thermal camera at the orifice of the blackbody.

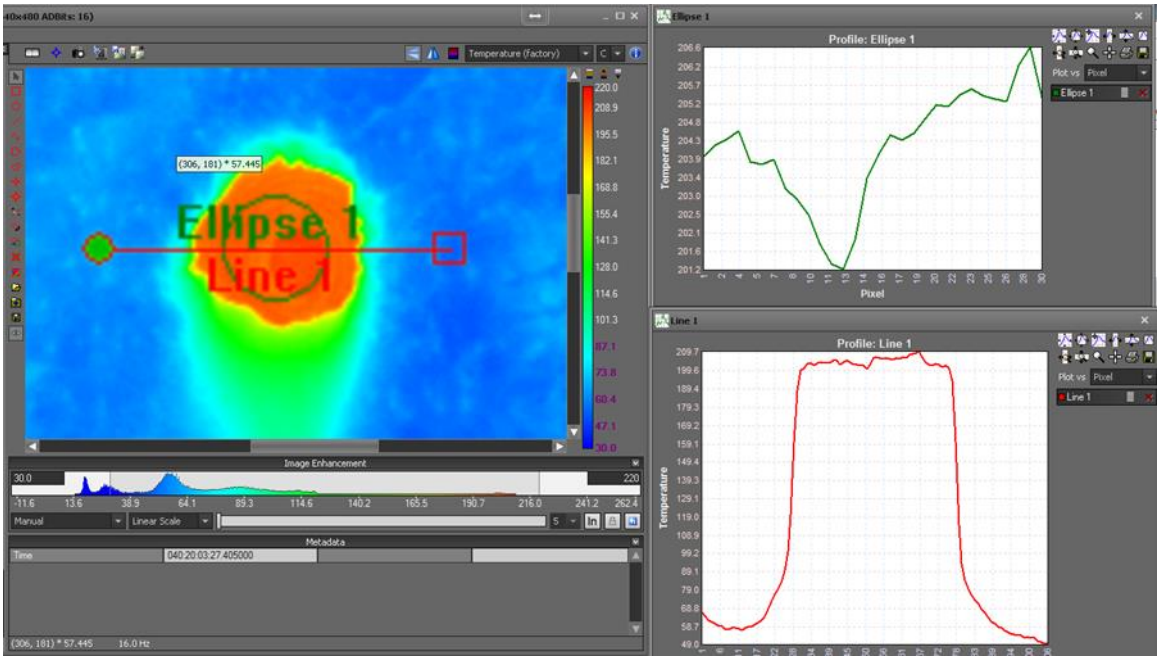

Figure 5.20 Example of temperature at the orifice of the blackbody cavity sensed with thermal camera (Temperature recorded in $°C$).

Since the temperature recorded with the thermocouples varied within $5\ K$, the average of the two measurements was used as the reference in the iterative process of finding the emissivity of the material. Similarly, the temperature measured with the thermal camera was average along the green ellipse shown in Figure 5.20. This procedure was repeated for each of the five isothermal conditions investigated. Table 5.5 summarizes the emissivity characterized at different temperatures as well as the temperatures used to account for the radiance of the ambient which was given by the thermocouple placed on the surface of the ceramic insulation.

Table 5.5 Emissivity characterized as a function of temperature.

Temperature Blackbody Cavity (K)	**Ambient Temperature (K)**	**Emissivity**
404.05	313.45	0.93
429.9	318.35	0.933
448.55	324.15	0.93
476.25	325.45	0.936
523.15	333.86	0.941

The characterized emissivity shows a slight increase with temperature after around $448.55\ K$. It should be noted the spectra range of the infrared camera is from 7.5 to $14.0\ \mu m$ and thus only the emission within this spectrum is captured with the thermal camera. The spectral distribution for this material is not known, however, these measurements can be used for engineering purposes of modeling radiation in process simulations of the EDAM. We should be also aware of other sources of error in these measurements like temperature gradients in the blackbody cavity as well as on the front cover insulated with ceramic material. Further, the calculation of emissivity can be performed using a regression algorithm if the factory calibration of the thermal camera were available [134].

5.5 Heat Losses in Material Compaction

Two primarily mechanism for material compaction have been adopted in EDAM systems, rollers and vibrating plates also referred to as tampers. During part manufacturing, the surface of the compaction mechanism contacts and deforms an extruded bead of molten material from an initially circular shape to a rectangular shape with rounded corners. This way, previously printed material is rapidly wetted with molten material of the newly deposited beads and thus improving thermal conduction as well as adhesion between layers.

Regardless of using a tamper or a roller for compacting beads of molten material, the temperature difference between the surface of the compaction mechanism and the molten material will give rise to conduction of thermal energy from the molten material to the compaction system. While printing material is extruded at the melt temperature of the polymer, the surface of the compaction system is maintained below a certain temperature in order to prevent adhesion of the printed material. Further, in the case of utilizing a roller, the surface of the roller contacts continuously the molten material as the extrusion head lays down beads whereas in the case of a tamper, the surface of the tamper contacts segments of an extruded bead multiple times per second in a discrete manner. Since the surface of the roller or the tamper spans beyond the width of a single printed bead, thermal energy is also removed to some degree from previously printed material surrounding a newly deposited bead. Hence, the heat removed during material compaction can be modeled as a surface heat flux describing the same movement of the printing nozzle.

The heat flux removed with the surface of the compacter also has a spatial distribution in the plane of material deposition (XY) due to factors controlling heat conduction between the printed material and the surface of the compacter. These include for instance the temperature

difference between the surface of the compacter and the surface contacted, changes in contacted area during bead compaction and thermal resistance between the surface of the compacter and printed material. Since these parameters change continuously during the printing process of a part, it is neither feasible nor practical to characterize a heat flux distribution. Thus, a constant heat flux distribution was preferred to model heat removal during material compaction.

A radially symmetric Gaussian distribution was chosen for modeling the heat flux removed with the tamper whereas a double Gaussian distribution was chosen for the heat flux removed with the roller. In the former case the radially symmetric Gaussian distribution is centered on the axis of the tamper whereas in the latter case one Gaussian distribution is centered at the middle of the length of the roller and the second one is centered at the middle of the width of the roller. Figure 5.21 illustrates in 2D the distribution of heat flux across the diameter of the tamper and along the length and diameter of the roller. Distribution functions were selected based on the assumption that the surface of the compacter rapidly develops better thermal contact with the surface of molten material than with the surface of already printed material. And also based on the observation that the newly deposited bead is generally contacted in the central area of the compacter.

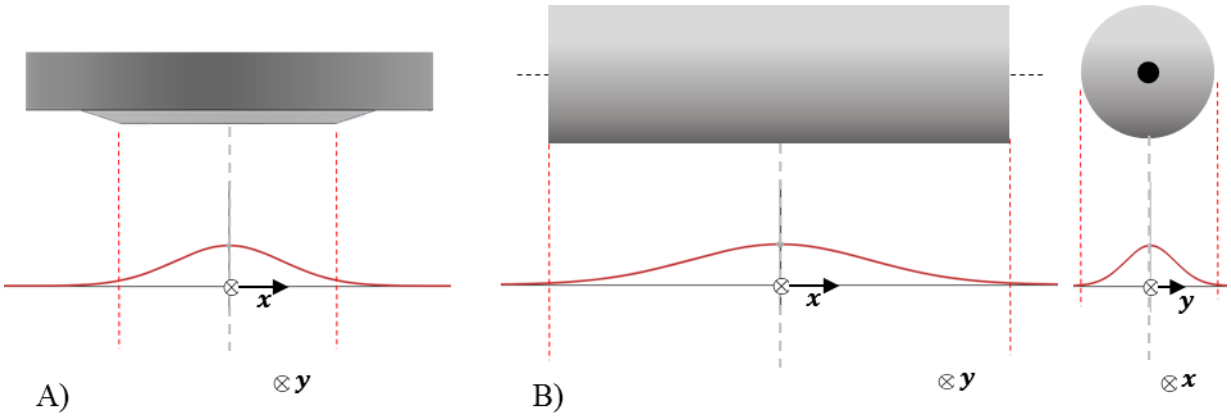

Figure 5.21 2D schematic representation of heat flux distribution on the surface of compacter. A) Radially symmetric Gaussian distribution utilized to model the tamper. B) Two-dimensional Gaussian distribution utilized to model the roller.

Therefore the 2-dimensional Gaussian distributed heat flux moving in the xy plane is described by Equation 5.21. This heat flux distribution is centered at $x = 0$ and $y = 0$ which corresponds to the geometrical center of the surfaces of the roller and the tamper as illustrated in Figure 5.21.

$$q''(x,y,t) = q_0'' e^{-A(x+v_x t)^2} e^{-B(y+v_y t)^2} \tag{5.21}$$

q_0'' corresponds to the heat flux concentrated at the center of the distribution, A and B are the concentration parameters that control the shape of the Gaussian distribution in the x and y directions, respectively. v_x and v_y are the printing velocities in the x and y directions, respectively. Similar heat flux distributions have been used in the past for modeling welding and laser heat sources. The best example perhaps is the work of Goldak et al. [135] where they developed a double ellipsoid model to simulate 3D welding heat sources using finite element. Equation 5.21 represents a particular case of the model presented by these authors with the subtle difference that the through thickness distribution is not used in the compacter. Moreover, the conditions used to estimate the concentration factors were inspired by their work.

Equation 5.21 describes a double Gaussian heat flux distribution that is appropriate to model either the tamper of the roller with the difference that $A = B$ for the tamper and $A \neq B$ for the roller. Therefore, this general form is implemented in a UMDFLUX© subroutine in Abaqus© to model both compaction mechanisms and the details on the implementation are given in a subsequent section.

In order to satisfy the conservation of energy, the heat flux distribution integrated over the area of the compacter must equal the total heat flow, Q^C. The total heat flow, Q^C, removed with the tamper has been characterized for the CAMRI system utilizing a simple methodology presented in the next subsection. The total heat flow is then obtained by integrating the heat flux distribution over the entire domain as shown in Equation 5.22.

$$Q^C = \iint_{-\infty}^{\infty} q_0'' e^{-A(x+v_x t)^2} e^{-B(y+v_y t)^2} dx dy \tag{5.22}$$

After performing the double integral, the heat flow, Q, is given by Equation 5.23

$$Q^C = \frac{\pi q_0''}{\sqrt{AB}} \tag{5.23}$$

Since our objective is to obtain an expression for $q_0"$ as a function of the heat flow, Q^C, the previous equation is rearranged to give rise to Equation 5.24.

$$q_0" = \frac{Q^C\sqrt{AB}}{\pi} \tag{5.24}$$

The next step is to determine the concentration parameters *A* and *B* based on the dimensions of the tamper and the roller. This is achieved by imposing the condition that the heat flux, $q"(x, y, t)$, decays to only five percent of the heat flux concentrated at the center of the distribution, $q_0"$, at the edges of the compacter. The respective edges are the radius of the tamper, r_t, for the tamper and half the length of the roller, $l_r/2$ and the radius of the roller, r_r, for the roller. Utilizing the tamper as example, the concentration parameter A can be determined utilizing the condition stated previously which is shown in Equation 5.25.

$$q"(r_t, 0,0) = (0.05)q_0" = q_0"e^{-A(r_t)^2} \tag{5.25}$$

After solving for A in Equation 5.25, the expression in Equation 5.26 is obtained.

$$A = \frac{\ln(20)}{r_t^2} \approx \frac{3}{r_t^2} \tag{5.26}$$

For the case of the tamper, we only need to solve for either *A* or *B* due to the symmetry of the distribution whereas for the case of the roller *A* and *B* are evaluated at half the length of the roller and at the radius of the roller, respectively.

Now we can plug Equations 5.26 and 5.24 into Equation 5.21 to get the final expression given by Equation 5.27 for the radially symmetric Gaussian distributed heat flux removed with the tamper during material compaction.

$$q"(x, y, t) = \frac{3Q^C}{\pi r_t^2} e^{-\frac{3(x+v_x t)^2}{r_t^2}} e^{-\frac{3(y+v_y t)^2}{r_t^2}} \tag{5.27}$$

Similarly, the double Gaussian distributed heat flux used for the roller can be obtained by plugging the appropriate concentration factors obtained with Equation 5.26 in Equation 5.21. Given the length of the roller, $l_r/2$ and the radius of the roller, r_r, Equation 5.28 provides the expression for the heat flux removed with the roller.

$$q''(x,y,t) = \frac{6Q^C}{\pi\sqrt{r_r^2 l_r^2}} e^{-\frac{12(x+v_x t)^2}{l_r^2}} e^{-\frac{3(y+v_y t)^2}{r_r^2}} \tag{5.28}$$

Lastly, the radially symmetric Gaussian distributed heat flux utilized to model the heat losses due to tamper compaction does not consider the fact that the tamper is an annulus rather than a circle. In CAMRI, the external diameter of the annulus contacting material is around $44\ mm$ whereas the internal diameter is around $7\ mm$ which represents around 2.5% of the surface area of the tamper. Therefore, the proposed Gaussian distribution is considered appropriate.

5.5.1 Characterization of Heat Losses in Material Compaction

The compaction system used in CAMRI was presented previously in chapter 3. Since it is critical to maintain the temperature at the surface of the tamper below a critical temperature, the tamper developed for CAMRI is equipped with an internal circuit for circulating compressed air. A critical temperature of around $120\ °C$ was found experimentally in CAMRI for 50% by weight carbon fiber PPS. Moreover, the tamper is made from aluminum to improve conduction from the surface contacting the molten material to the circuit of cooling channels. This way thermal energy is effectively removed from the tamper while compacting beads of molten material in the EDAM process. Figure 5.22 shows a side view of the tamper developed for CAMRI with the process variables, air mass flow rate $\dot{m}$, input air temperature, T_{in}, and output air temperature, T_{out}, required to characterize the heat flow removed during material compaction.

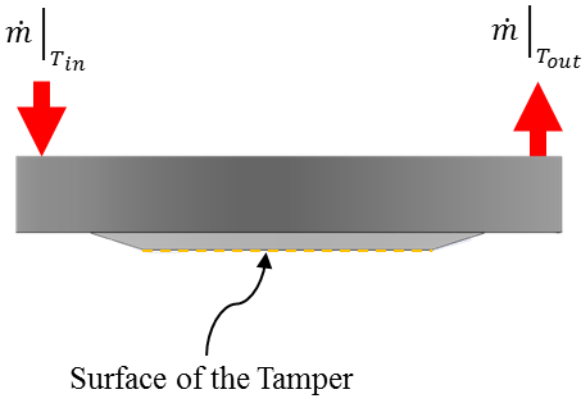

Figure 5.22 Side view of the tamper implemented in CAMRI indicating the process variables used to characterize the heat flow removed with the tamper.

We know consider the tamper in steady state and carry out an energy balance around the body of the tamper. While operating, the tamper receives thermal energy not only from compaction of beads of molten material but also from the equipment surrounding the tamper, especially the extrusion nozzle that passes through the middle of the tamper. Therefore, the heat flow, Q^S, contributed by the equipment surrounding the tamper and the heat flow, Q^C, removed during material compaction enter the control volume. The air mass flow rate entering the tamper introduces a heat flow Q_{in}^a that is equal to the product of the mass flow rate, $\dot{m}$, the heat capacity at constant pressure, C_p, and the temperature of the air at the inlet, T_{in} ($Q_{in}^a = \dot{m}C_pT_{in}$). Similarly, the air mass flow rate leaving the tamper removes a heat flow Q_{out}^a, equal to the product of $\dot{m}, C_p$ and temperature of the air leaving the tamper, T_{out}. Recognizing the mass flow rate is conserved within the tamper, the energy balance can be written as shown in Equation 5.29.

$$\dot{m}C_p(T_{out} - T_{in}) = Q^C + Q^S \tag{5.29}$$

As indicated by Equation 5.29, we need to know the heat flow contributed by the surrounding to the tamper. The heat flow Q^S is characterized without printing yet while the system is operating in steady state at the operating temperature. This means that the tamper is operating at a constant number of strikes per second (SPS) and it is exposed to local convection and radiation from the extrusion nozzle and the melt pump as well as to heat conduction with the rest of the compaction mechanism. This way, the heat flow contribution from material compaction is removed from

Equation 5.29, and the heat flow Q^S is determined with the temperature T_{out}^s characterized without printing as given by Equation 5.30

$$Q^S = \dot{m}C_p(T_{out}^S - T_{in}) \tag{5.30}$$

If the same air mass flow rate, $\dot{m}$, and air input temperature, T_{in}, are used to characterize both Q^S and Q^C, Equation 5.30 can be plugged into Equation 5.29 to yield Equation 5.31.

$$Q^C = \dot{m}C_p(T_{out} - T_{out}^S) \tag{5.31}$$

In order to characterize first Q^S and then Q^C, a setup consisting of a volumetric flow rate regulator model H2051B-580 (originally designed for MIG and TIG welding applications), and a custom-made air connection instrumented with a temperature sensor were employed to control the flow rate and to monitor the output temperature of the cooling air, respectively. The instrumented air connection was thermally insulated with ceramic fiber insulation and equipped with a thermocouple suspended at the center of the air channel inside the air connection to record the temperature of the air leaving the tamper. Such an instrumented air connection was located within 10 cm from the air connections of the tamper to minimize heat losses by through the air lines. The volumetric flow rate regulator delivers controlled flow rate at a constant output pressure of 334.74 kPa (50 PSI) and the pneumatic system inside and around the tamper is perfectly sealed so that mass is conserved. In order to perform measurements under controlled conditions of pressure, flow rate and with a known ideal gas, argon was supplied to the tamper at a volumetric flow rate of 314.66 cm^3/s, (40 CFH).

To determine the mass flow rate, $\dot{m}$, at the thermodynamic conditions of the supplied volumetric flow rate, the instrumented air connection was placed next to the pressure regulator to measure the temperature of the air supplied from the argon cylinder. The pressure at this point is constant and equal to 334.74 kPa, then utilizing the ideal gas law and recognizing that the mass, m, is equal to the number of moles, n, multiplied by the molar mass of the Argon, M_{Ar}, the density of the argon can be determined with Equation 5.32.

$$\rho|_{T,P} = \frac{PM_{Ar}}{RT} \tag{5.32}$$

Then, the mass flow rate, $\dot{m}$, is given by the product of the volumetric flow rate, $\dot{V}$, and the density of the argon obtained with Equation 5.32. Using the same mass flow rate and air input temperature utilized to characterize Q^S, the heat flow Q^C can be characterized with measurements of the air output temperature at steady state during the printing process of a part.

While printing a part, the area of the tamper interacting with the printed material changes based on the design of the printing pattern, thick walls and flat regions are common areas in a printed part where a significant portion of the tamper's surface interacts at the same time with the printed material. As a result, measurements of the process variables mentioned above were recorded while printing both the stringer tool shown previously in Figure 5.8 and flat plates with dimensions of about 150 by 200 mm and with eight layers in the thickness direction. The former geometry is used throughout this chapter to present the different heat transfer mechanisms whereas the latter geometry is used in the next chapter on fusion bonding to prepare double cantilever beam specimens. The temperature of the air leaving the tamper, T_{out}, is recorded once the system reaches steady state, which takes about three minutes after the printing process starts. Table 5.6 lists the operating conditions used while characterizing Q^C in the CAMRI system. These conditions are reported since the heat flow will vary based on the printing conditions utilized, especially if printing speed is change significantly while preserving the same tamper speed. Also, varying the tamping ratio will change the instant of time the molten material is in contact with the surface of the tamper and thus the heat flow Q^C.

Table 5.6 Operating conditions utilized in CAMRI while characterizing the heat flow Q^C.

Process Variable	**Value**
Temperature Nozzle (K)	573.15
Temperature Gear Pump (K)	573.15
Tamper Speed (SPS)	25
Printing Speed (mm/s)	91.67
Dimensions of printed bead - w, h (mm)	4.7, 1.3
Orifice of Extrusion Nozzle (mm)	3.175

For example, reducing the printing speed while preserving the other conditions the same will reduce the magnitude of the total heat flow removed from the tamper Q^C, which is realized by the fact that the length of the segment of extrudate that is compacted in a single strike of the tamper is reduced. However, these differences become notorious only at significantly different printing speeds.

Finally, the heat flow Q^C is estimated utilizing Equation 5.31, the thermophysical properties of the argon, and the measurements performed in the two scenarios described previously. Notice the second entry used in the superscript denotes the condition for which the parameter was characterized, $Strngr$, denotes the stringer whereas, Plt, denotes the plate. The values for Q^C are reported in Table 5.7 as well as the parameters characterized in each of the experiments. Thermophysical properties used for the argon were obtained from the website The Engineering ToolBox [132] and are listed in Table A.18 of the APPENDIX A.

Table 5.7 Parameters characterized to estimate the heat flow, Q^C, removed with the tamper used in CAMRI.

Parameter Characterized	**Parameter Value**
$Q^{C,Strngr}\ (W)$	51.84
$T_{out}^{Strngr}\ (K)$	381.65
$Q^{C,Plt}\ (W)$	49.05
$T_{out}^{Strngr}\ (K)$	378.65
$T_{out}^{S,Strngr} = T_{out}^{S,Plt}\ (K)$	326.05
$T_{in}^{Strngr} = T_{in}^{Plt}\ (K)$	292.35
$P\ (kPa)$	334.74
$\dot{V}\ (cm^3/s)$	314.67

The difference in heat flow characterized with the stringer geometry and the plate is only around 5.3%. Although a detailed transient heat transfer analysis could be performed to approximate the heat removed during compaction of a single bead of molten material, the approach presented herein was preferred since the measurements performed capture the primary mechanisms of heat transfer occurring simultaneously around the tamper. Hence, the highest value for Q^C listed in Table 5.7 provides a good estimate for the heat removed by the tamper and that can be used in the Gaussian distributed heat flux.

5.6 Numerical Implementation of Transient Heat Transfer Analysis

The transient heat transfer analysis carried out to determine the temperature history of printed material during the EDAM process is performed in Abaqus© Standard which employs an implicit integration scheme. Again, this is implemented within the framework for simulation of the EDAM process presented in chapter 4. Therefore, this section presents the implementation of the orthotropic heat conduction, the latent heat of crystallization, the surface boundary conditions and the moving heat flux used to model the compacter used in CAMRI.

As recognized previously, the anisotropic heat conduction occurring in the printed composite material can be simplified to heat conduction in an orthotropic medium. Orthotropic heat conduction is implemented in a UMATHT© subroutine in Abaqus©, the implementation of orthotropic heat conduction for the process simulations was performed previously by Brenken [16], however, the strong coupling of polymer crystallization and heat transfer was added herein by including the latent heat of crystallization or melting in the heat transfer analysis. The UMATHT© subroutine is called at the integration points of the element and provides the freedom to implement user defined material behavior [136]. Calculations inside this subroutine are performed in the local orientation. A brief overview of the implementation of orthotropic heat conduction is presented for the sake of completeness in this chapter.

The UMATHT© is called at the beginning of each iteration performed in the solution of the non-linear thermal energy problem solved using Newton's method [136]. The non-linear behavior arises from the dependence of the thermal conductivity on the temperature field as well as from the change in internal energy due to heat generation or absorption during polymer crystallization and melting, respectively. Field variables like temperature are provided within the subroutine at the beginning and at the end of each increment. Utilizing the thermophysical properties and the field variables provided within the UMATHT© subroutine, variables like internal energy and heat fluxes must be defined within the subroutine as described next.

The first step in the subroutine is to read in the thermal conductivities from the user defined thermal material model in Abaqus©. Two out of the three thermal conductivities, $K_i(T), i = 1,2$, and the heat capacity, $C_p(T)$, are defined as linear functions of temperature whereas the conductivity K_3 is a constant value. Such linear functions were constructed by Brenken [16] with the thermophysical properties of the 50% by weight carbon fiber reinforced PPS given in the APPENDIX A. The temperature dependent thermal conductivities and the heat capacity are

evaluated with the temperature at the end of the increment. Also, any change in crystallinity, $\Delta\chi_v$, during the increment is also required. The evolution of crystallinity is described with a crystallization kinetics model coupled through a temperature condition with a melting model. The original implementation and characterization of these models for our material of interest was conducted by Brenken et al. [72, 16] and the implementation was modified latter to the temperature based coupling by Barocio et al. [137]. Further details on the evolution of crystallization are provided in the chapter 6. Nevertheless, for the sake of the heat transfer analysis, we are only interested in the change in crystallinity, $\Delta\chi_v$. Once the heat capacity and change in crystallinity are determined, the internal thermal energy at a integration point is given by Equation 5.33

$$U = U(T) - H^*\Delta\chi_v \tag{5.33}$$

where $U(T)$ is the internal thermal energy as a function of the temperature and per unit of mass, and H^* is the heat of crystallization corresponding to 100% transformation of CF-PPS which was given in Table 5.1. Internal energy, U, is also updated at the end of the increment in the UMATHT©. We then define the change in internal energy as a function of temperature. Since the problem considered herein neglects changes in internal energy associated with external forces and volume changes, the change in internal energy with respect to the temperature is simply equal to the heat capacity at constant pressure, C_p, as given by Equation 5.34.

$$\frac{\partial U}{\partial T} = C_p \tag{5.34}$$

The next variable to define is the heat flux in each of the principal directions which is denoted by f_i , $i = 1,2,3$ within the UMATHT©. The heat flux f_i is then given by Equation 5.35.

$$f_i = -K_i \frac{\partial T}{\partial x_i}, i = 1,2,3 \tag{5.35}$$

The temperature gradient, $\partial T/\partial x_i$, is provided within UMATHT©. Next, the change in heat flux with respect to the temperature is computed as given by Equation 5.36. Notice that this term is

zero in the 3-direction since the thermal conductivity is a constant value in this direction. Otherwise, the derivative of the K_i with respect to temperature is simply the slope of the linear function describing temperature dependent conductivity.

$$\frac{\partial f_i}{\partial T} = -\left(\frac{\partial K_i}{\partial T}\right)\frac{\partial T}{\partial x_i}, i = 1,2,3 \tag{5.36}$$

The last variable to defined within the UMATHT© is the variation of the heat flux, f_i, with respect to the temperature gradient, $\partial T/\partial x_i$. This term is simply equal to minus the thermal conductivity in the direction x_i as given by Equation 5.37

$$\frac{\partial f_i}{\partial\left(\frac{\partial T}{\partial x_i}\right)} = -k_i, i = 1,2,3 \tag{5.37}$$

Finally, variables described in Equations 5.33 through 5.37 are updated at each iteration carried out in the Newton's method utilized in Abaqus© to solved this non-linear problem. The reader is referred to the Abaqus© documentation for further details on this subroutine [136].

5.6.1 Implementation of Surface Boundary Conditions

The boundary conditions applied to exposed surfaces in the simulation of the EDAM process were described in two of the previous sections of this chapter. Convection and radiation boundary conditions share the challenge that exposed surfaces change dynamically as the simulation of the printing process evolves. However, this challenge was overcome with the release of the options FFS and RFS in the keywords used in Abaqus© for applying convection and radiation, respectively. With these new functionalities, constant radiation and constant convection conditions are automatically applied to all exposed surfaces of elements that have been activated during the simulation of the printing process, thereby providing a solution for tracking exposed surfaces at each time increment in the solution. Radiation is currently applied to all exposed surfaces utilizing the RFS option in the keyword Radiate used in Abaqus© to apply radiation boundary conditions [136]. However, this approach does not allow for direct application of neither solution dependent boundary conditions nor feature dependent boundary conditions as require for the correlation

equations utilized to describe natural convection. Hence, a user subroutine UFIELD© was employed to implement solution and feature dependent convection boundary conditions in the simulation of the EDAM process.

To leverage the existing functionality for tracking exposed surfaces in Abaqus, a user defined field variable, $FV1$, is utilized in a Film Property table to define a solution dependent convection coefficient. Then, the Film Property table is passed to the keyword for applying convection boundary conditions in Abaqus©, *FILM, and the option FFS is also specified to track exposed surfaces during the solution. This procedure is performed as follows. First, the UFIELD subroutine is called at the beginning of an increment and at the nodal locations. Inside the subroutine, the field variable is updated using other field variables from the previously converged increment. This way, the convection coefficient specified at the nodal values is interpolated by Abaqus© to apply the solution and feature dependent convection coefficient computed at the beginning of each increment. It should be noted that this is an explicit approach since the convection coefficient is only computed at the beginning of an increment and it does not change during the iterations performed within an increment. However, the error introduced this way become notorious for large time increments.

After having described the execution procedure for this implementation in Abaqus©, we will focus on the implementation of the subroutine. The first step in the subroutine is to identify the type of feature the node in consideration belongs to. Specific IDs were previously assigned in Table 4.2 to each of the four different types of features categorized for a printed part. This ID is stored in a global array to each node in the ORIENT© subroutine as previously presented in the section Activation Time and Local Material Orientations. Then, the ID is read from the global array and one of the following four conditions will be executed.

- $ID = 1 \,\&\, 2$

This corresponds to an infill regions and internal walls for which convection is neglected if the ratio of cross sectional area to perimeter of the cell is smaller than around $2\ mm$. Therefore, the $FV1$ will be equal to zero in this case. If the infill is large enough to be treated as an external wall, then the same conditions as ID=3 are applied. A refined criterion should be created for cells where there is some degree of convective heat losses.

- $ID = 3$

This ID is used for the external walls where convection can be described using the correlation equation determined previously for vertical surfaces. The following procedure is performed inside the subroutine to determine the local convection coefficient, h_Z, given by Equation 5.19. First the film temperature, T_{film}, is determined by computing the average between the ambient temperature for convection, $T_{\infty,f}$, and the mid-point temperature at the node. The mid-point temperature is simply the average between the temperature at the beginning and at the end of the increment provided by the subroutine.

The next step is to compute the Grashof number as given by Equation 5.10. The volumetric expansion, β, is approximated as $1/T_{film}$ whereas a polynomial function for the kinematic viscosity, ν, is evaluated at the film temperature. The polynomial function for ν is provided in Figure A.5 of the APPENDIX A. Then, utilizing the coordinates of the node, x_i^n, provided in the subroutine, a predefined stacking vector, S_i, for the print, and the origin of the build plate, x_i^{bp}, the distance, Z, of the node with respect to the build plate is computed as given by Equation 5.38

$$Z = \left\|(x_i^n - x_i^{bp})S_i\right\| \tag{5.38}$$

After computing the Gr_z number, the local Rayleigh number, Ra_z, is computed as the product of the Gr_z and the Pr number as given by Equation 5.11. The Pr number can be assumed constant and equal to 0.702 for the case of air.

The next step is to compute the local Nusselt number, Nu_z, utilizing the correlation equation given in Equation 5.19 and with the coefficients listed in Table 5.4. Then, the local convection coefficient, h_z, is determined from Equation 5.12 and using the distance, Z, for the node as well as the thermal conductivity, K_f, evaluated at the film temperature. A polynomial function for K_f is provided in Figure A.3 of the APPENDIX A.

- $ID = 4$

The last condition is for solid and flat regions. Both convection and radiation are considered in this case. While the radiative heat flux is described by Equation 5.20, the convective heat flux now depends on the convection coefficient provided by the correlation equation given by Equation 5.15. Unlike the position dependent film coefficient used in vertical wall, an average convection coefficient, $\overline{h_{L^*}}$, is computed with the local temperature at the nodes labeled with ID equal to 4.

The same procedure used for the vertical walls is repeated here, but with the subtle difference that the distance, Z, is replaced by a constant characteristic length, L^*, while calculating the Rayleigh number and the $\overline{h_{L^*}}$ coefficient. L^* is given by the ratio of the area to the perimeter of the flat region ($L^* = A/p$). Since neither of these two quantities are provided in the UFIELD© subroutine, the user needs to provide an estimate for L^*. This parameter is readily estimated for geometries with a single flat region, however, in geometries with multiple flat regions the area-weighed average L^* given by Equation 5.395.395.39 may provide a better estimate for a global $\overline{L^*}$.

$$\overline{L^*} = \frac{1}{A_T}\sum_{i=1}^{n} A_i L_i^* \tag{5.39}$$

Then, based on the magnitude of the computed Ra_{L^*}, the appropriated correlation equation given by Equation 5.15 is used to compute the Nusselt number, Nu_{L^*}. And finally, the average convection coefficient $\overline{h_{L^*}}$ is obtained using Equation 5.12 and L^* as characteristic distance.

It was recognized previously that all printed beads lose heat through radiation immediately after these are deposited and despite the region those belong to. On the other hand, interior surfaces of an infill cell located far below the deposition front will become closer to a blackbody cavity. This indicates that radiation heat losses from the surface of a small infill cell should neither be neglected nor assumed similar to the exterior surfaces. A better approach can be to only consider radiation above certain surface temperature above which radiation is relevant at the interior of the infill cells. A second approach can be tracking the deposition front and defining a characteristic depth measured above which radiation is significant to be considered. In either case, further investigation of the radiation mechanism inside infill regions would be required. Again, these approaches are suggested since these can be readily implemented in the UFIELD subroutine as follows. First, the convective and radiative heat fluxes can be grouped into a single heat flux. The total heat flux can be implemented as convection with a coefficient that yields the total surface heat flux when evaluated in the *FILM command in Abaqus© with the surface temperature, T_s, and the convection ambient temperature, $T_{\infty,f}$. This is readily achieved by converting the radiative heat flux into an equivalent convective heat flux. By setting a convective heat flux equal to a radiative heat flux, an equivalent convection coefficient, h^*, can be determine as shown in Equation 5.40.

$$FV1 = h_z + \frac{\sigma\varepsilon(T_s^4 - T_{\infty,r}^4)}{(T_s - T_{\infty,f})} = h_z + h^* \tag{5.40}$$

The sum of the local convection coefficient and the equivalent convection coefficient can be then passed to the $FV1$ used in the film property table. This way, convection and radiation could assigned locally and selectively to exposed surfaces in the simulation of the EDAM process.

5.6.2 Implementation of Moving Heat Flux

In the previous section Heat Losses in Material Compaction, the heat flux removed by a tamper or a roller during material compaction was described as a function of a double Gaussian distributed heat flux. Particular forms of the distributed heat flux considered for the tamper and the roller were given in Equation 5.27 and Equation 5.28, respectively. However, the general form given by Equation 5.41 obtained by plugging in Equation 5.24 into Equation 5.21 was implemented in a UMDFLUX© user subroutine in Abaqus©.

$$q''(x, y, t) = \frac{Q^C\sqrt{AB}}{\pi} e^{-A(x+v_x t)^2} e^{-B(y+v_y t)^2} \tag{5.41}$$

This user subroutine allows for implementation of moving or stationary heat fluxes and is it called once for each element and at each iteration [136]. Heat fluxes are then applied within this subroutine as point heat sources and multiple heat events are possible. We will use the concept of heat event later as we describe the implementation.

In order to implement this double Gaussian distributed heat flux moving along with the deposition nozzle in printing simulations, we need to integrate this heat flux over the time the compacter touches the surface of an element as well as over the surface of the element to determine the amount of energy removed during a time increment, Δt. Now, since the element is fixed in space and the compacter moves relative to the element, we will replace the positions x and y in the original heat flux distribution by the distance l_1 and l_2 measured from the center of the compacter to the centroid of an element, respectively ($l_i = x_i^A - x_i^c, i = 1,2$). Furthermore, we will now define the compacter's heat flux in the local coordinate system with the 1-direction defined parallel to the trajectory of the nozzle and the 2-direction transverse to the trajectory. After

rewriting Equation 5.41, we can start by integrating the heat flux over the surface of the element Ω_e as given by Equation 5.42.

$$q_e(l,t,\Omega_e) = \int_{\Omega_e} \frac{Q^C\sqrt{AB}}{\pi} e^{-A(l_1+v_1t)^2} e^{-B(l_2+v_2t)^2} d\Omega \tag{5.42}$$

Under the assumption that the area of the element, Ω_e, is relatively small compared to the area of the compacter, we can approximate the heat flow, $q_e(l,t,\Omega_e)$, resulting from integrating the heat flux over the area of the element as given by Equation 5.43.

$$q_e(l,t,\Omega_e) \approx \frac{Q^C\sqrt{AB}}{\pi} e^{-A(l_1+v_1t)^2} e^{-B(l_2+v_2t)^2} \Omega_e \tag{5.43}$$

The next step is to calculate the thermal energy, E_e, removed from the surface of the element while the surface of the compacter moves relative to the surface of an element. This thermal energy corresponds to the heat flow removed over a period of time equal to Δt. Therefore, we integrate the heat flow $q_e(l,t,\Omega_e)$ over a time increment Δt as given by Equation 5.44.

$$E_e(l,t,\Omega_e) = \Omega_e \int^{\Delta t} \frac{Q^C\sqrt{AB}}{\pi} e^{-A(l_1+v_1t)^2} e^{-B(l_2+v_2t)^2}\, dt \tag{5.44}$$

After performing this integral analytically, the thermal energy removed while the compacter moves relative to the surface of the element in an increment of time Δt is given by Equation 5.45

$$E_e(l,t,\Omega_e) = \frac{Q^C\sqrt{AB}}{2\sqrt{\pi}\sqrt{Av_1^2+Bv_2^2}} e^{-\frac{AB(l_2v_1-l_1v_2)^2}{Av_1^2+Bv_2^2}} \left(Erf\left[\frac{\Delta t(Av_1^2+Bv_2^2)+Al_1v_1+Bl_2v_2}{\sqrt{Av_1^2+Bv_2^2}}\right] - Erf\left[\frac{Al_1v_1+Bl_2v_2}{\sqrt{Av_1^2+Bv_2^2}}\right]\right)\Omega_e \tag{5.45}$$

Equation 5.45 is now in a form we can implement in the UMDFLUX© to integrate the heat flux over the surface of an element at discrete time increments. Therefore we will know focus on describing the implementation.

The first step in the UMDFLUX© subroutine is to read in the activation time computed at the beginning of the finite element analysis in the ORIENT© subroutine. The activation time t_{act} is accessed from the global arrays employed to share this parameter across the subroutines. If t_{act} is smaller than the time at the end of the increment, t_1, the execution proceeds, otherwise this element is not active yet and the execution of the subroutine ends here.

The second step is to read in the parameters for the compacter. These are passed into the subroutine through a parameter table and include the type of compacter, two definitions for radius r_1 and r_2 and the heat flow, Q^C, removed during material compaction.

In a third step, the utility subroutine getEventSeriesTimeIntervalLGLocationPath© is employed to find the segments in the event series that intersect a sphere yet only within the time window of the increment, t_0 to t_1. Where t_0 is the time at the beginning of the increment and t_1 is the time at the end of the increment. The center of the sphere is provided by the centroid of the element, x_i^c, which is computed with the nodal positions of the element. And the radius of the sphere, r_s, is computed as given by Equation 5.46.

$$r_s = (1 + b)\sqrt{r_c^2 + h^2} \tag{5.46}$$

Where b is a calibration factor to modify the sensitivity for detecting segments in the event series, and it is currently set to 0.1. r_c is either the radius of the tamper or half the length of the roller, depending on the compacter selected and h is the height of the printed bead. This utility subroutine returns the n_{seg} segments of the event series that intercepted the sphere defined previously. The following information relevant to this implementation is provided for each of the n_{seg} segments, the position at the start of the segment, x_i^A, the position at the end of the segment x_i^B, the time at the start of the segment, t^A, the time at the end of the segment, t^B, the deposition status at the start of the segment, d_s^A, and the deposition status at the end of the segment, d_s^B.

The fourth step consist of screening the n_{seg} to find the segments or fractions of segments that correspond to a heat event in which the compacter removes thermal energy from the surface

of an element. A loop is performed to check each of the n_{seg} segments returned by the utility subroutine and to compute the heat flow for the ones that truly represent a heat event. Inside the loop, the following steps are performed.

The status flag is check at the start of the segment and if enabled, the execution proceeds, otherwise we move to the next segment. The next set of calculations are to determine the exact period of time, Δt, the tamper contacts the upper face of an element located at the top of a printed bead. Δt is given as $t_1^{he} - t_0^{he}$. Since the compacter's heat flux only removes thermal energy at the upper surface of a printed bead, only elements located at the top of a bead are of interest.

The segments of the event series are specified at the bottom of printed bead and thus we introduce a check position offset from the positions x_3^A and x_3^B. For a voxel mesh with N_{el}^h number of elements through the thickness of the bead and with equal height, h_{el}, the new positions to check $x_3^{A^*}$ and $x_3^{B^*}$ are given by Equation 5.47. These positions correspond to the bottom face of an element located at the top of a bead.

$$x_3^{A^*} = x_3^A + \left(N_{el}^h - 1\right)h_{el}$$
$$x_3^{B^*} = x_3^B + \left(N_{el}^h - 1\right)h_{el} \tag{5.47}$$

Using these positions offset from the event series, we now check if the combination of new segment positions and element centroid location required for an element located at the top of a bead are satisfied. Additionally, we need to compute the correct t_1^{he} and t_0^{he} times since the times at the beginning and at the end of a segment (t^A and t^B) do not necessarily coincide with the times at the beginning and end of an increment (t_1 and t_0) and more importantly, this is required to make the implementation insensitive to the time increment utilized in the FEA analysis. This is illustrated in Figure 5.23 for two segments of the event series.

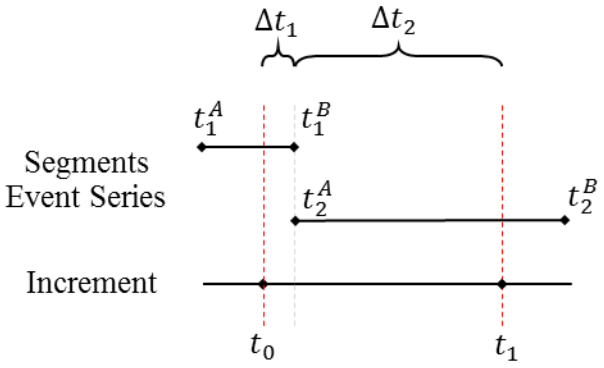

Figure 5.23 Time diagram with increment and segments of event series.

The following three conditions are checked sequentially and if one the condition is met, the times for the heat event (Δt) are determined based on the time diagram shown in Figure 5.23.

The first condition checked is illustrated in Figure 5.24-A and requires the centroid of the element, x_3^c, to be above the positions $x_3^{A^*}$ and $x_3^{B^*}$. If this condition is met, the smallest value between t_1 and t^B is assigned to t_1^{he} whereas the largest value between t_0 and t^A is assigned to t_0^{he}. See time diagram in Figure 5.23 for further clarification.

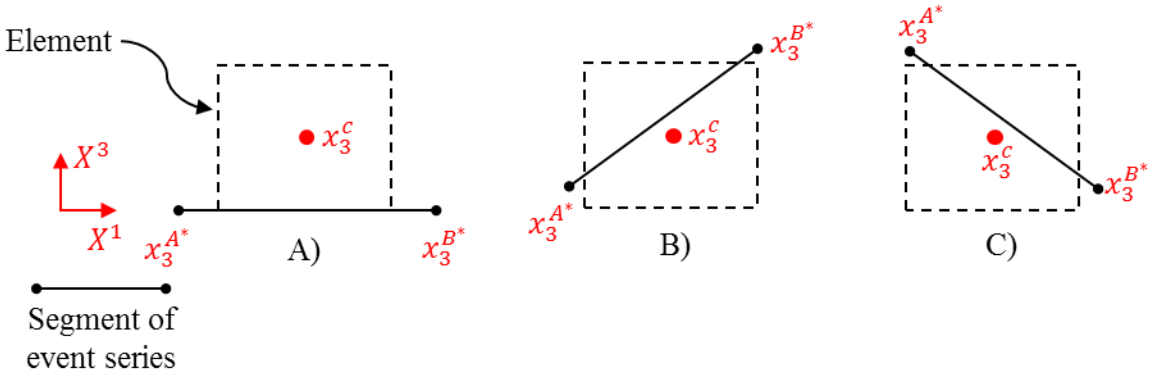

Figure 5.24 Schematic representation of conditions required for an element and a segment of the event series to be considered in a heat event.

If the first condition is not met, the second condition checked is illustrated in Figure 5.24-B and requires x_3^c to be above $x_3^{A^*}$ but below $x_3^{B^*}$. This condition can occur while transitioning from one layer to another. If this condition is met, the smallest value between t^B and t_u is assigned to t_1^{he},

where the time t_u is the time after moving from $x_3^{A^*}$ to x_3^c. t_u is interpolated as given by Equation 5.48. The largest time value between t_0 and t^A is assigned to t_0^{he}.

$$t_u = t^A + (x_3^c - x_3^{A^*}) \frac{t^B - t^A}{x_3^{B^*} - x_3^{A^*}} \tag{5.48}$$

If the previous condition is not met, a third condition is checked. Figure 5.24-C illustrates the situation where x_3^c is below $x_3^{A^*}$ but above $x_3^{B^*}$. Although it is unlikely to move the printing head downwards during the printing process, this conditions is still considered to capture cases where this may occur. If this condition is satisfied, the smallest value between t_1 and t^B is assigned to t_1^{he} whereas the largest value between t^A and t_d is assigned to t_0^{he}. t_d is the time at which the compacter crossed the centroid of the element and it is interpolated as given by Equation 5.49.

$$t_d = t^B - (x_3^c - x_3^{B^*}) \frac{t^B - t^A}{x_3^{B^*} - x_3^{A^*}} \tag{5.49}$$

If none of the previous checks is met, the segment is dismissed. On the contrary, the period of time, Δt, is computed as $t_1^{he} - t_0^{he}$. This difference must be positive to be considered a heat event. In the case that we have a heat event, we move forward and compute the area of the element using the position of the nodes.

Once we have the correct start time, t_0^{he}, and end time, t_1^{he}, for a heat event, we need to compute the correct start position, x_i^S, and end position, x_i^E, for the heat event. We defined both positions with respect to the position at the start of the segment, x_i^A. Equation 5.50 provides the correct start position and end position for the heat event.

$$\begin{aligned} x_i^S &= x_i^A + (t_0^{he} - t^A) \frac{x_i^B - x_i^A}{t^B - t^A} \\ x_i^E &= x_i^A + (t_1^{he} - t^A) \frac{x_i^B - x_i^A}{t^B - t^A} \end{aligned} \tag{5.50}$$

At this point we have the start and end positions of the heat event in the global coordinate system. We know calculate the in-plane distances l_x and l_y defined from the start of the segment to the centroid of the element as given y Equation 5.51. This is readily extended to 3D if the compacter is used in printing with multiple axis.

$$l_x = x_1^S - x_1^c$$
$$l_y = x_2^S - x_2^c \tag{5.51}$$

Similarly, the velocities can be computed as given by Equation 5.52.

$$v_x = \frac{x_1^E - x_1^S}{t_1^{he} - t_0^{he}}$$
$$v_y = \frac{x_2^E - x_2^S}{t_1^{he} - t_0^{he}} \tag{5.52}$$

Now we need to transform these variables given in the global coordinate system to a local coordinate system with the 1-direction oriented parallel to the print direction and the 2-direciton perpendicular to the print direction. The distances and velocities in the local coordinate system are simply obtained by transforming the coordinate system as given by Equation 5.53.

$$l'_i = \lambda_{ij} l_j$$
$$v'_i = \lambda_{ij} v_j \tag{5.53}$$

Where the transformation matrix, λ_{ij}, is given by Equation 5.54.

$$\lambda_{ij} = \begin{bmatrix} \cos(\theta) & \sin(\theta) \\ -\sin(\theta) & \cos(\theta) \end{bmatrix} \tag{5.54}$$

The last component required to evaluate the thermal energy removed from the element is the concentration parameters A and B. These are evaluated as given by Equation 5.26, however, we should not forget that for the case of the tamper $A = B$ whereas for the roller A is computed with the radius of the roller and B with the width of the roller.

We have computed the distances, l_1, l_2, the velocities, v_1, v_2, the period of the heat event, Δt, and the area of the element, Ω_e, therefore we can compute the energy removed from the surface of the element utilizing Equation 5.45. This thermal energy, E_e, is finally divided by the length of the increment, $(t_1 - t_0)$, to determine the heat flow for this heat event, q_e^k, that Abaqus© will apply during the increment. Further, the location to apply the heat event within the element is specified using isoparametric coordinates which in our case are $(0,0,1)$ to indicate the heat flow is removed from the top surface of the element.

This procedure is repeated for the n_{seg} segments of the event series returned by the utility subroutine to finally determine the k number of heat events that occur during a time increment.

5.6.2.1 Validation of Moving Heat Flux Implementation

In order to validate the correct implementation of the moving heat flux, a couple of tests were performed to assess the implementation presented before in the UMDFLUX© subroutine. Since the area of the element was approximated numerically, the impact of the ratio of the element surface area to compacter surface area on the total thermal energy removed was investigated. Furthermore, the insensitivity to the time increment used in the FEA analysis is also confirmed here.

An event series describing the movement of the deposition head at constant speed along a straight line for 1.407 seconds was used. Utilizing this event series and the script described in chapter four for generating voxel meshes, the voxel mesh for the strip shown in Figure 5.25 was generated with three elements distributed through a thickness of $1.3\,mm$. Thermophysical properties for the 50% by weight carbon fiber reinforced PPS were used in this model. Further, the model is perfectly adiabatic in order to quantify only the energy removed by the compacter. A tamper removing a heat flow, Q^C, equal to $50\,W$ was utilized as compacter for all the validation cases. Given the heat flow, Q^C, and the time the compacter moved along the path, the energy removed over such a period of time can be estimated analytically by integrating the heat flow from zero to the $1.4\,s$ of duration of the heat flux to yield a total of $70.0\,J$. This implies the surface of

the tamper must be in full contact with the mesh all the time. This estimation though, does not consider the fact that at time zero the tamper is located on the left edge of the mesh geometry in Figure 5.25 and therefore half of the tamper diameter is missed at the beginning.

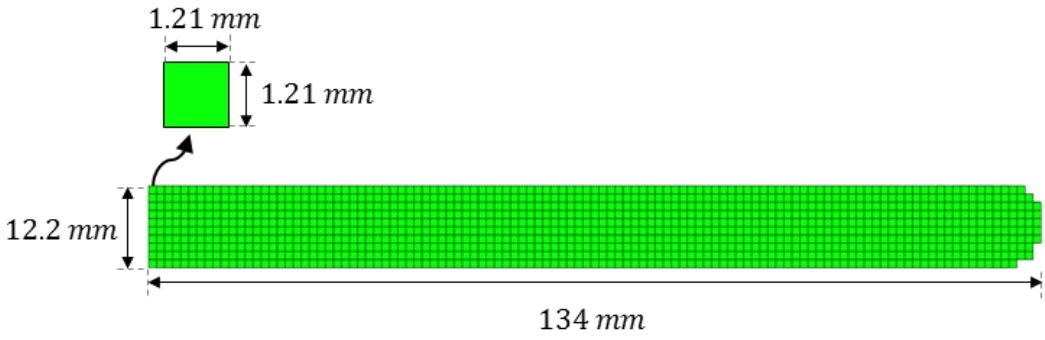

Figure 5.25 Mesh of the strip used for validating implementation of moving heat flux.

The first validation performed was for time increments, since the times for a heat event are computed precisely despite changes in time increment of the analysis, we should not expect any significant difference in the thermal energy removed with the tamper. In this investigation, all the elements are active from the beginning of the analysis, otherwise, the energy calculations will also depend on the number of inactive elements intercepted by the tamper. This implies $t_{act} = 0$ for all elements.

Since the thermal energy is preserved within the domain of the analysis, the energy removed by the compacter can be obtained from the difference in thermal energy at the beginning and at the end of the analysis. The method used herein to integrate the thermal energy over the entire domain consists of extracting the thermal energy, U, computed inside the UMATHT© subroutine at each integration point which is given in units of energy per unit of mass. For each integration point, the thermal energy is obtained by the product of U and the mass of the integration point. Then, the energy is integrated over the domain of the geometry considered.

First, four analyses were carried out with different time increments to confirm the insensitivity of the energy removed with the compacter to the time increment used in the analysis. A tamper with radius of 5 mm was utilized in these analyses. Since the variations in thermal energy removed with the tamper across the different time increments assessed is six orders of magnitude smaller than the total energy removed, the difference in removed thermal energy with respect to

the smallest time increment, ($0.01\ s$) is reported in Table 5.8. Such differences are six orders of magnitude smaller than the total energy removed, thereby confirming the implementation is insensitive to time increments.

Table 5.8 Validation of insensitivity to time increment used in the FEA analysis with $68.8\ J$ of total thermal energy removed.

Time Increment, Δt^*, Used in FEA (s)	**Difference in Thermal Energy Removed with Tamper with Respect to $\Delta t^* = 0.01$ (μJ)**
0.01	0.0
0.1	0.239
1.0	3.24
10.0	4.40

An approximation was made in this implementation for the integral of the heat flux over the area of an element since the area of the element is generally a small fraction of the area of the compacter. Therefore, the influence of area fractions in the range of 5% to 1.3% of element surface area to tamper surface area on the thermal energy removed with the tamper was also assessed. These analyses were performed with the same mesh shown in Figure 5.25 and utilizing a time increment of $1\ s$ in the solution of the FEA. The same conditions used before for the compacter were used and the same procedure for computing the thermal energy removed was carried out. Since these investigations were conducted on a mesh with a fixed element size, the radius of the tamper was modified to vary the area fraction. Differences in thermal energy removed in the FEA and the analytical approximation were calculated for the four area fractions assessed. Such differences are reported in Table 5.9 along with the area fraction employed.

Table 5.9 Sensitivity of removed thermal energy to ratio of element surface area to tamper surface area.

Tamper Radius (mm)	**% Difference FEA and Analytical ($70.0\ J$)**	**% Area Fraction (A_e/A_{tamper})**
3	1.69	5.19
4	2.84	2.92
5	2.28	1.87
6	2.14	1.30

The results shown in Table 5.9 for tamper radii greater than $4\ mm$ show the expected decrease in error between the analytical approximation and the numerical prediction as the percentage in area fraction decreases. The fact that the smallest error was obtained with the largest area fraction is simply due to the stronger dependence on the mesh size that in this particular case resulted beneficial.

On the other hand, the conditions generally used for simulating the printing process performed in CAMRI consists of element sizes in the range of 1.8 by 1.8 mm and with a tamper radius of $22\ mm$ which gives rise to an area fraction of approximately 0.21%. Which further reduces the sensitivity of the mesh size to the calculations of the thermal energy removed.

Now to illustrate the functionality of the moving heat flux discussed throughout this section, Figure 5.26 shows an example of the transient distribution of heat flux, q_3'', developed at different instants of time as the tamper moves over the surface of the material strip used for validation. The time increment used here was $0.01\ s$ and the tamper radius was $5\ mm$. Notice the heat flux tail developed behind the tamper. This arises due to heat conduction from the material underneath the surface where the heat flux was removed. This becomes clearer in the temperature field shown in the next figure.

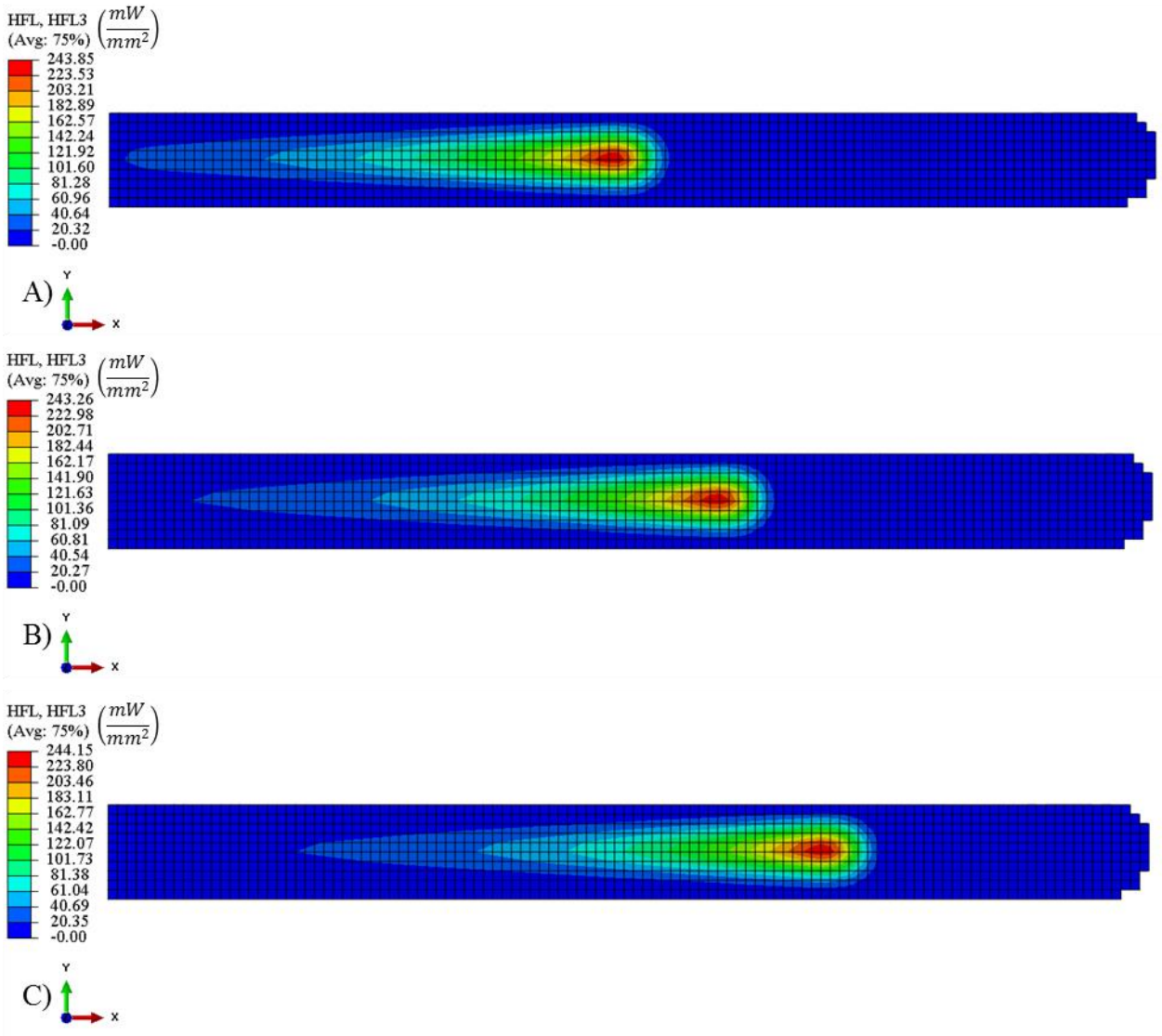

Figure 5.26 Example of the heat flux, q_3'', field developed with the double Gaussian heat flux distribution utilized to model a tamper moving over a strip of material. A) $t = 0.45\ s$. B) $t = 0.75\ s$. C) $t = 1.05\ s$.

Figure 5.27 shows an example of the transient temperature field developed as the tamper moves over the surface of the strip of material. Temperature fields shown in this figure correspond to the same instants of time shown for the heat flux fields. Notice the temperature at the surface drops significantly around the current locations of the tamper shown in these figures, however, heat conduction from the material surrounding the surface occurs and thus heating the surface back.

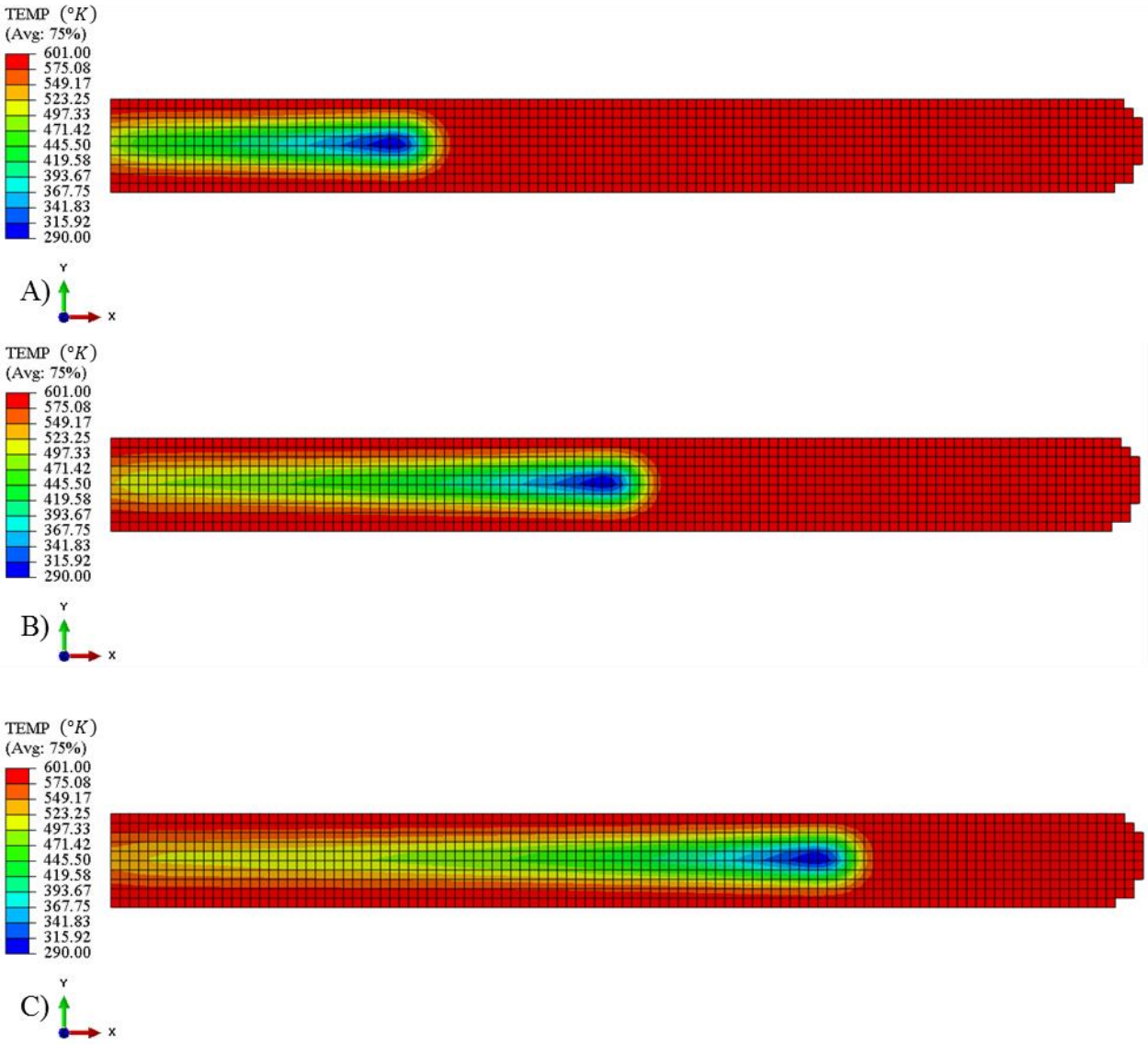

Figure 5.27 Example of temperature field developed as the tamper moves over a strip of material. A) $t = 0.45\ s$. B) $t = 0.75\ s$. C) $t = 1.05\ s$.

5.7 Predictions of Temperature in Extrusion Deposition Additive Manufacturing

The primary mechanisms of heat transfer participating in extrusion deposition additive manufacturing were presented throughout this chapter and models for capturing these in the simulation of the printing process were presented. Implementation of these models through user subroutines in Abaqus© was also presented and developed to work in the context of the framework for simulating the EDAM process. Therefore, we now utilize this physics-based simulation framework to predict the evolution of temperature during the printing process of the stringer tool.

Figure 5.28 shows the geometry of the stringer tool after the slicing process carried out for converting the three dimensional solid into a set of printed layers. The slicing was performed with a layer height of 1.3 mm which yields a total of 92 layers.

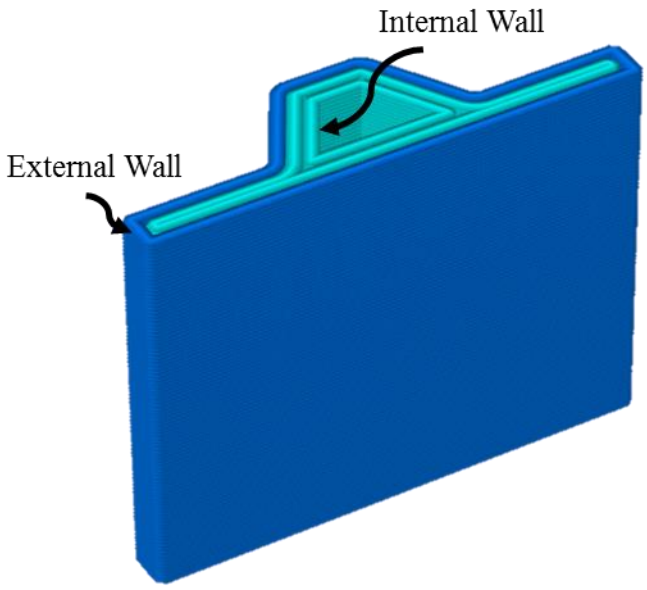

Figure 5.28 Geometry of the stringer tool after slicing process.

These predictions are validated against experimental temperature measurements recorded during the printing process of stringer tool in CAMRI. This section presents first the experimental setup used for recording the temperature and it is followed by the predictions made through simulation.

5.7.1 Experimental Temperature Measurements in EDAM

The experimental setup implemented for recording temperatures during the printing process of the stringer tool was implemented in the CAMRI system and consisted of a thermal camera FLIR® A655sc calibrated in a temperature range of 373.15 to 873.15 K, and three thermocouples for monitoring the temperature of the build plate. Further, a lens with a field of view of 20° was used in the thermal camera. The thermal camera was positioned on the build plate pointing normal to the vertical flat surface of the stringer tool and at a distance of 0.55 m from the surface of the stringer tool. Figure 5.29 shows the setup implemented in CAMRI to perform these measurements.

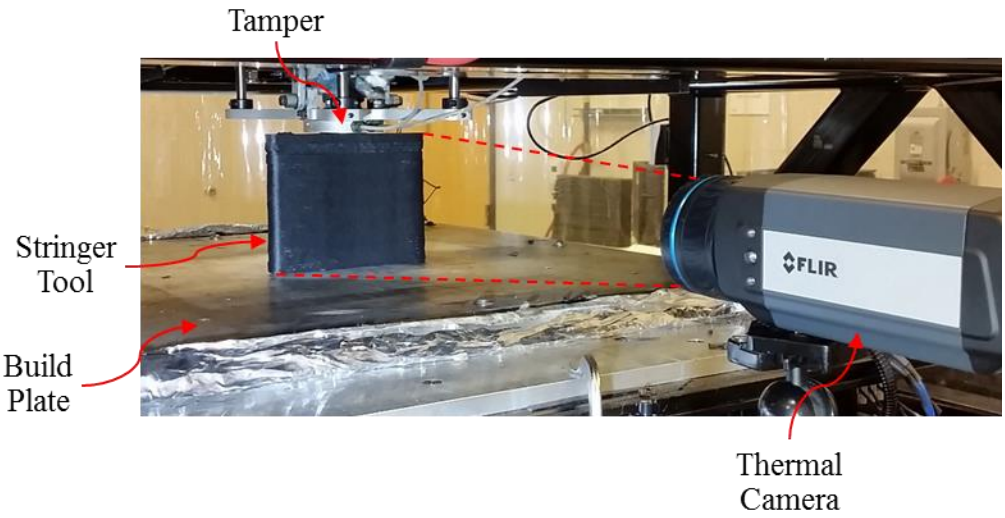

Figure 5.29 Experimental setup implemented in CAMRI to record temperature during printing process of the stringer tool.

Prior to conduct temperature measurements during the printing process of a part, the camera was calibrated to account for the radiation from other surrounding hot surfaces like the build plate or the polymer processing equipment. To calibrate the camera, a printed stringer tool was instrumented with three thermocouples equally distributed along the height of the part and located near the center of the geometry. Thermocouples were tight fit into shallow and small orifices drilled on the surface of the stringer tool. The instrumented stringer tool was then placed on top of the build plate and at the location where the stringer tool will be printed. At this point, the build plate and the polymer processing equipment is enabled and set to the processing temperatures used during part manufacturing. Upon reaching steady state, a temperature gradient is stablished along the height of the stringer tool and the thermocouples provide temperature readings at those three particular locations. Now on the side of the thermal camera controls, an average of the emissivity previously characterized for the carbon fiber reinforced PPS and reported in Table 5.5 as well as the distance from the surface of the stringer tool to the lens of the camera were provided to the ResearchIR© software that controls the camera. The next step was to iteratively find the reflected temperature that makes coincide the temperature readings from the thermocouples with the temperature readings provided by the thermal camera. A reflected temperature of $413.15\,K$ provided a good match between the temperatures sensed with the thermal camera and the ones

measured with the thermocouples. Table 5.10 summarizes the parameters used in ResearchIR© to record temperatures during the printing process of the stringer tool.

Table 5.10 Parameters utilized in thermal camera FLIR® A655sc for temperature acquisition during printing.

Parameter	Value
ε	0.934
$Distance\ from\ object\ (m)$	0.58
$Reflected\ Temperature\ (K)$	413.15

This calibration step was crucial to lessen the influence of the radiation from the surrounding surfaces on the recorded temperatures. The conditions used for printing the stringer tool with 50% by weight carbon fiber reinforced PPS were as follows: the dimensions of the printed bead were 4.7 by 1.3 mm, the printing speed was 91.67 mm/s, the temperature of the extrudate leaving the nozzle was 573.15 K, the temperature measured at the top of the build plate was 443.15 K, and the speed of the tamper was 1500 SPM. It should be noted the temperature reported for the build plate is the temperature measured at the top surface and not the temperature set point used for the controller. A temperature gradient of around 30 K developed between the top surface of the build plate and the bottom where the thermocouple used by the temperature controller is located. Also, the temperature of the extrudate reported corresponds to the temperature of the melt measured through a thermocouple located at the tip of one of the pressure sensors that is in direct contact with the melt. Table 5.11 reports all the process parameters used in CAMRI for printing the stringer tool. It should be noted that process conditions like the extrusion temperature varies within ± 3 K during the printing process of a part due to fluctuation in printing speed.

Table 5.11 Process conditions in CAMRI used for printing stringer tool.

Process Variable	Value
Bead Dimensions - $w, h\ (mm)$	4.7, 1.3
Orifice of Extrusion Nozzle (mm)	3.175
Extrusion Temperature (K)	573.15
Temperature Build Plate (K)	443.15
Printing Speed (mm/s)	91.67
Tamper Speed (SPS)	25
Temperature Nozzle (K)	573.15

Table 5.11 continued

Temperature Gear Pump (K)	573.15
Temperature Upstream Connector (K)	573.15
Temperature Extruder Zone 1 (K)	572.0
Temperature Extruder Zone 2 (K)	561.0
Temperature Extruder Zone 3 (K)	561.0

Prior to start printing the part in CAMRI, a thin layer of contact cement is applied to the surface of the build plate to improve adhesion of the printed part to the build plate. A sacrificial bead is also printed around the perimeter of the stringer tool for the purpose of priming some material prior to print the actual part. The printing process of the stringer tool took around $18\ min$ and required about 480 grams of 50% by weight of carbon fiber reinforced PPS. Figure 5.30 shows the stringer tool after printing.

Figure 5.30 Stringer tool printed in CAMRI with 50% by weight of carbon fiber reinforced PPS (scale in mm).

Figure 5.31 shows an example of the temperature field developed along the vertical surface of the stringer tool during the printing process of this part. The thermal image shown in Figure 5.31 was captured while the outermost bead was deposited (hottest region at the top of the vertical surface). Additionally, the rapid cooling of newly deposited material is shown by the last bead printed at the top of the stringer tool. This thermal image also shows the strong influence of the build plate

temperature on the temperature of the first layers printed and located at the bottom of the stringer tool.

A total of around thirty thousand frames like the one shown in Figure 5.31 were captured during the printing process of the part at a rate of 20 frames per second. These temperature frames are used later for extracting the temperature evolution at multiple locations within the part.

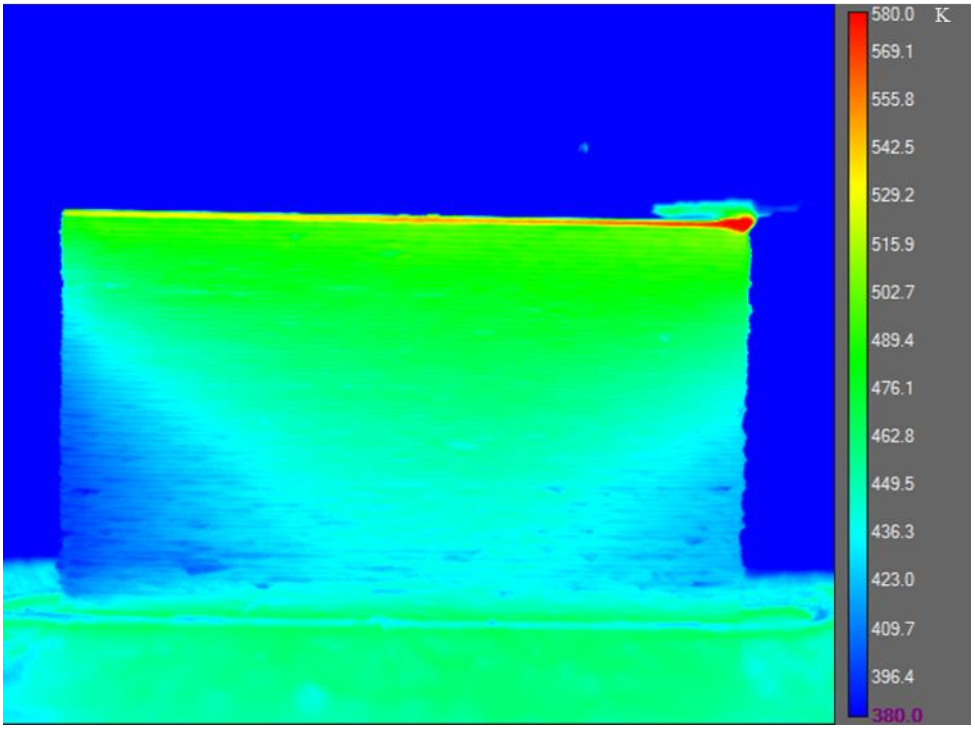

Figure 5.31 Temperature distribution captured with the FLIR® A655sc thermal camera during the printing process of the stringer tool.

5.7.2 EDAM Process Simulation of the Stringer Tool

In order to simulate the printing process of the stringer tool shown in Figure 5.30, an event series that contains the trajectory and the status conditions required for the process simulation as a function of time must be generated. Given the machine code used for part manufacturing, a user defined program implemented inside the controller KMotionCNC© generates the event series for simulating the printing process of a part including all the dynamics of the CAMRI system.

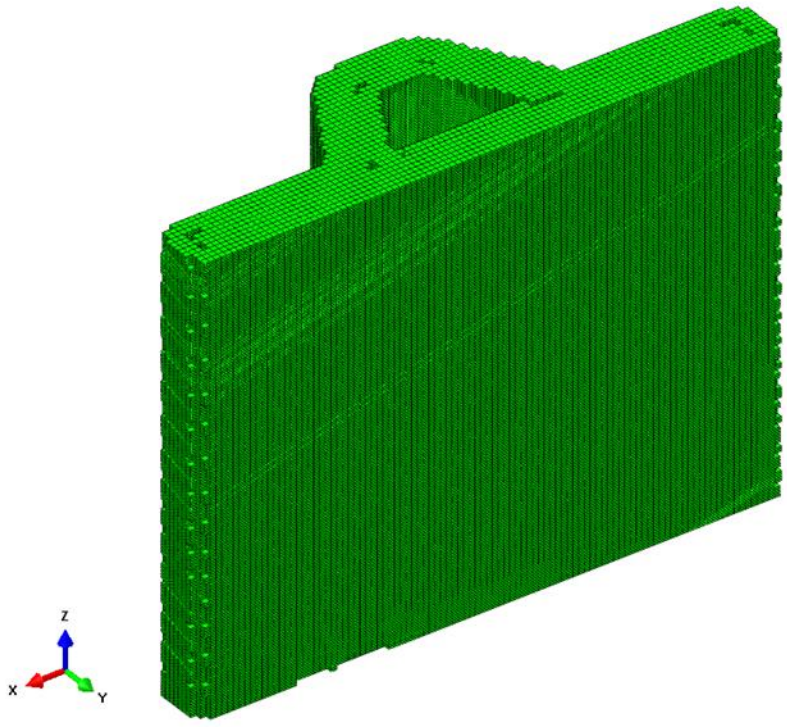

Figure 5.32 Voxel mesh used in EDAM process simulation of the stringer tool.

A voxel mesh of the stringer tool was created utilizing the script described in the chapter 4 for generating voxel meshes from event series. Three linear solid elements type DC3D8 were used to represent a printed bead in both the height and width directions. This resulted in the mesh shown in Figure 5.32 which contains 410,310 voxel elements with dimensions of 1.58 by 1.58 by 0.43 mm.

In the same process of generating the mesh for the process simulation, node sets containing the nodes of the bottommost elements are generated based on the elements that will be activated at each time increment concerned with the printing of the first layer. This way, the temperature boundary condition imposed by the build plate is applied only to the nodes belonging to elements in the first layer that have been activated. In addition to create the mesh for the process simulations, material input files and subroutines are automatically filled with the appropriate element count and process information utilizing the same script for mesh generation. Therefore, we will refer to this script as the input file generation script. Figure 4.2 provided already an overview of the user subroutines utilized in the process simulation including the ones described in this chapter.

This relatively fine mesh of the stringer tool was designed on purpose to capture with a high level of detail the temperature gradients developed during part manufacturing. Nevertheless, previous mesh sensitivity studies carried out with this simulation framework have shown that printed beads with the same dimensions can be represented with only two by two elements and still capture the temperature gradients relevant for predicting stresses and deformation [16].

Three steps in the solution finite element solution of the transient heat transfer problem are generally considered in EDAM process simulations. In a first step, the material deposition process is simulated. The second and third steps are for simulating the cooling process after printing of a part and while this is on top of the build plate and after the part is removed from the build plate, respectively. For now, we will only consider the temperature evolution of the material during printing which is the most relevant for fusion bonding which is covered in the next chapter of this dissertation.

In addition to the mesh, we need to define the process conditions used in the simulation, namely deposition temperature, ambient temperature for convection and radiation, power removed with the compacter as well as the build plate temperature. The process conditions used in the process simulation were the same used in the printing process of the stringer tool, namely deposition temperature, temperature at the build plate, etc. Table 5.12 summarizes the process conditions utilized in the EDAM process simulation of the stringer tool.

Table 5.12 EDAM process conditions used in simulation of part manufacturing.

Process Variable	**Value**
Temperature Build Plate (K)	443.15
Ambient Temperature Convection (K)	295.15
Ambient Temperature Radiation (K)	423.15
Heat Flow Removed by Tamper (W)	51.8
Emissivity - ε	0.934

Now with regards to the boundary conditions used. Convection boundary conditions were considered only at the external walls shown in Figure 5.28 whereas convection was assumed negligible at the internal walls. The correlation equation (Equation 5.19) derived previously for vertical surfaces and informed with temperature gradients extracted from this part provides the local convection coefficient. Table 5.4 provides the coefficients for the correlation equation. The ambient temperature used for convection was the ambient temperature measured within the

envelope of CAMRI. Since CAMRI sits behind a fume hood with plastic curtains, these were fully open while printing the stringer tool in order to preclude effects of the fume hood on the convective conditions.

On the other hand, radiation was assumed in both internal and external walls. Since the emissivity does not change significantly with temperature, an average of the emissivity previously reported in Table 5.5 was used. The ambient temperature for radiation was found empirically by comparing temperature evolution at different locations extracted from the thermal video with temperature predictions at the same locations obtained in the process simulation. Recommendations for the radiation ambient temperature are given at the end of the validation section.

The tamper used in CAMRI uses a compaction surface with an external diameter of $22\ mm$ and it was modeled as a moving heat source with the distribution given by Equation 5.27. Heat flow removed during material compaction, Q^C, through the tamper was characterized for this geometry and it is given in Table 5.7.

Temperature dependent thermal conductivities and heat capacity used in the simulation are also reported in the APPENDIX A whereas the latent heat of crystallization considered in the simulation is reported in Table 5.1. Finally, the framework for process simulation presented in chapter 4 was used to simulate the material deposition process, assign local material orientation and identify features within the printing part for proper application of convection boundary conditions.

The transient heat transfer analysis of the printing process of the stringer tool was solved in Abaqus© Standard 2017. This EDAM process simulation was conducted in the high performance computing cluster Halstead at Purdue University and utilizing 60 cores (6 Xeon-E5 processors). Computing the solution for this problem took around two hours and fifty minutes.

5.7.3 Results EDAM Process Simulation

Once the transient heat transfer problem is solved, field variables are available for each increment material is deposited in the EDAM process simulation. Figure 5.33 shows the evolution of the temperature field at four different stages of the printing process of the stringer.

Notice from these four temperature fields the dominance of the temperature boundary condition on the temperature evolution of the first printed layers. Figure 5.33-A shows in specific how the three first printed layers rapidly reached the temperature of the build plate.

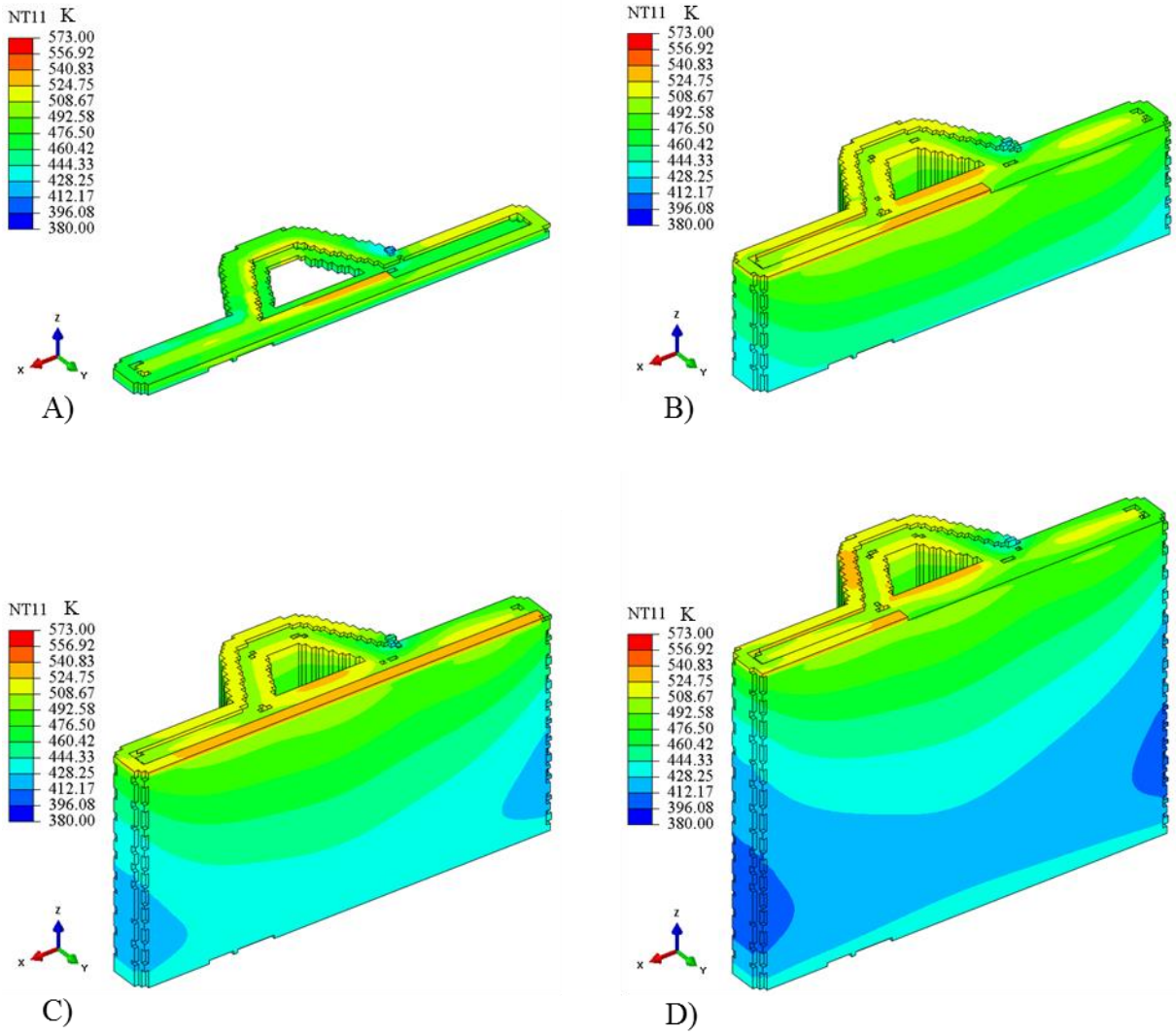

Figure 5.33 Evolution of temperature predicted during the printing process of the stringer tool. A) Temperature field after 3 layers. B) Temperature field after 32 layers. C) Temperature field after 61 layers. D) Temperature field after 90 layers.

However, as the deposition front progresses in the stacking direction, the influence of the build plate rapidly decays due to the low thermal conductivity of the printed material in this direction and therefore, convection and radiation heat losses become dominant in the temperature evolution

of the printed material. Furthermore, the temperature at the surface of the printed bead also decays rapidly upon deposition primarily due to the thermal energy removed with the tamper and the radiation heat losses that are significant at the deposition temperature.

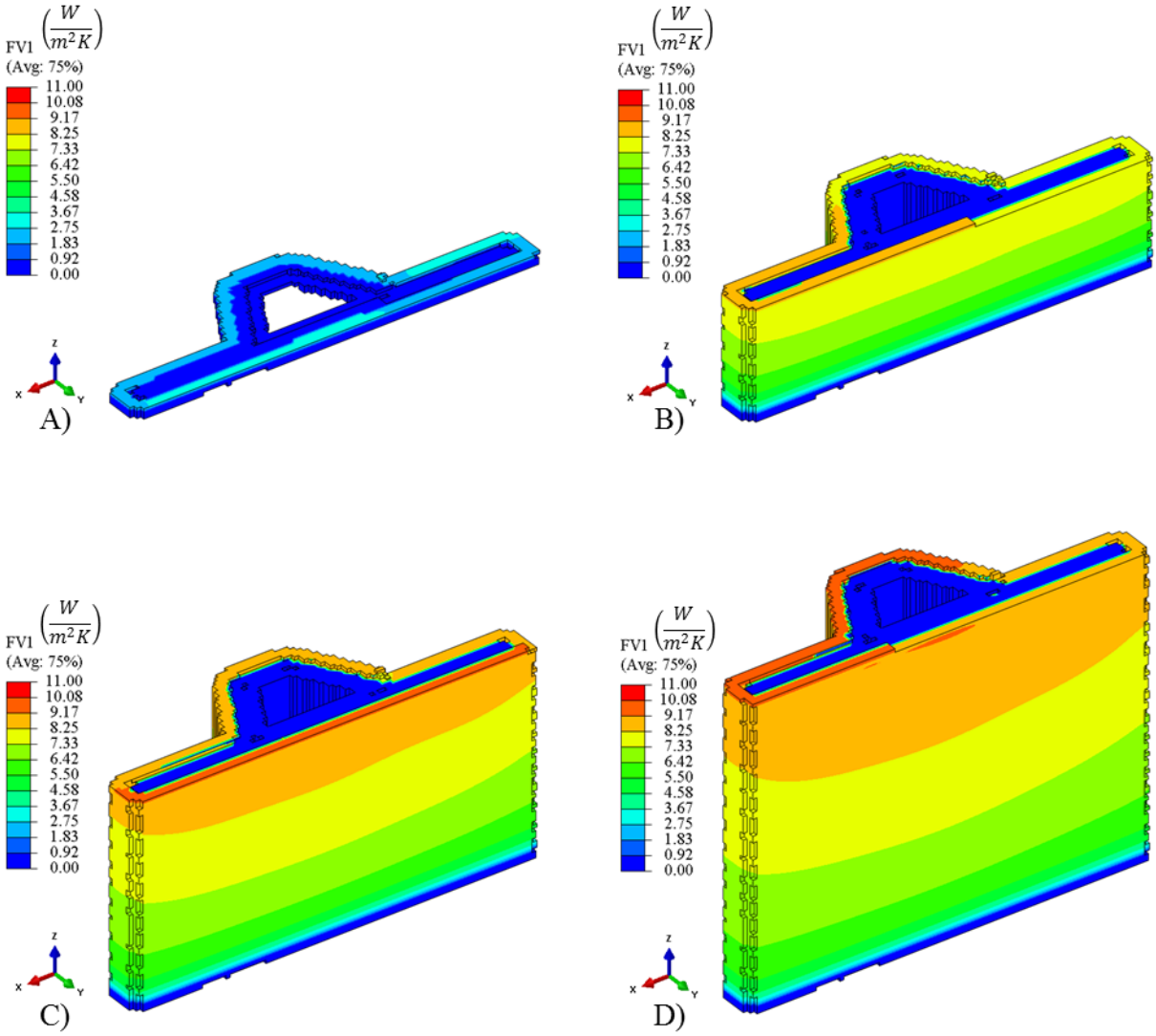

Figure 5.34 Evolution of local convection coefficient, h_z, during the printing process of the stringer tool. A) Convection coefficient after 3 layers. B) Convection coefficient after 32 layers. C) Convection coefficient after 61 layers. D) Convection coefficient after 90 layers.

The other field variable of interest for now is the local convection coefficient. Figure 5.34 shows the evolution of local convection coefficient, h_z, during manufacturing of the stringer tool.

In the early stages of the printing process, the short distance from the build plate and the rapid cooling of the printed layers by heat conduction reduces near to zero the convection coefficient. However, as the deposition front progresses along the stacking direction, the convection coefficient increases gradually with both temperature and distance from the build plate. Notice also the convection coefficient inside the stringer tool is zero since convection was neglected for internal walls. The importance of implementing local convection coefficients as opposed to utilizing an average convection coefficient is addressed in a sensitivity analysis presented at the end of this chapter.

5.7.4 Validation of Temperature Predictions

Results of the transient heat transfer simulation were presented previously and thus we will now focus on validating these temperature predictions against experimental measurements. The experimental setup described at the beginning of this section was utilized to record frames of temperature fields during the printing process of the stringer tool. Using these experimental measurements, a qualitative validation of the temperature field is presented first and it is followed by a quantitative validation of the transient temperature evolution predicted at different layer locations along the height of the part.

Figure 5.35 shows a qualitative comparison between the temperature field captured with the thermal camera and the temperature field predicted in the process simulations at three different stages of the printing process, namely after printing 30 layers, 50 layers and 70 layers. Experimental temperature fields are shown on the left side of Figure 5.35 whereas the numerical predictions are shown on the right side. Further, the scales in both temperature fields are linear and are in the same temperature range to be able to compare side-to-side the experimental and predicted temperature fields. Overall, a really close correspondence between the temperature fields characterized experimentally and predicted through the EDAM process simulations is observed in Figure 5.35. Figure 5.35

Additional facts that should be noted with regards to the experimentally measured temperature fields include: First, a fraction of the build plate is shown for the three cases at the bottom end of the stringer tool.

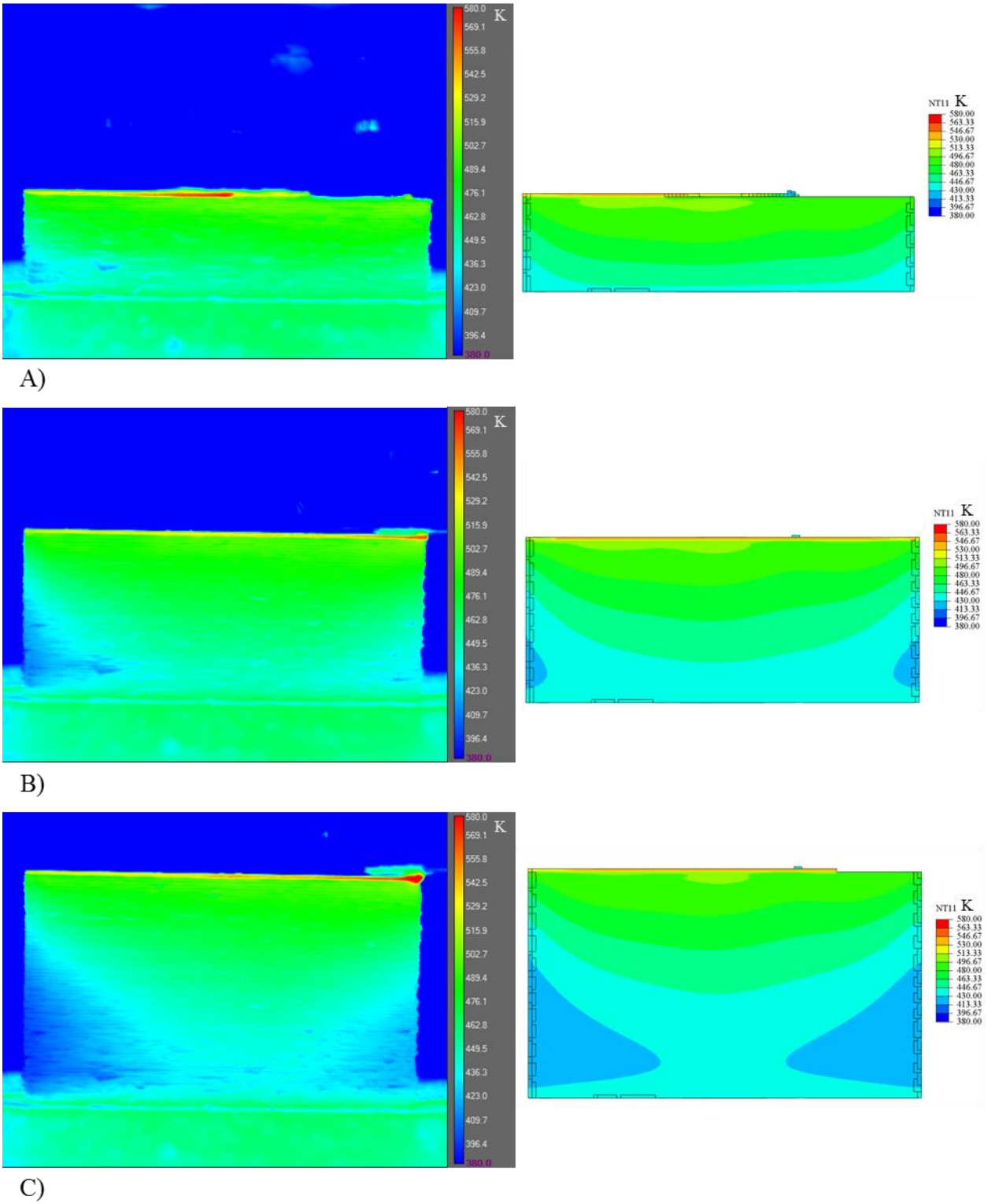

Figure 5.35 Qualitative validation of temperature fields characterized experimentally (left) and predicted (right) in the EDAM process simulation of the stringer tool. A) Temperature field at layer 30. B) Temperature field at layer 50. C) Temperature field at layer 70.

Second, the build plate not only radiates thermal energy but also reflects radiation emitted from the stringer tool which is more significant when the deposition front is closer to the build plate. This is caused by changes in geometry and intensity of the radiation emitted from the surface as the part cools down. As a result, it is complicated to obtain accurate temperature measurements near the build plate.

To provide a quantitative comparison of the temperature predictions and the experimental measurements, the transient temperature evolution during the printing process of the stringer was extracted at different layer locations. Twelve layer locations were chosen starting at the layer number 26 and increasing in an interval of four until layer 70. The transient temperature evolution was extracted at the middle of a printed bead and along the center of the flat vertical surface of the stringer tool. Figure 5.36 shows approximately the twelve layer locations from which transient temperature evolution was extracted.

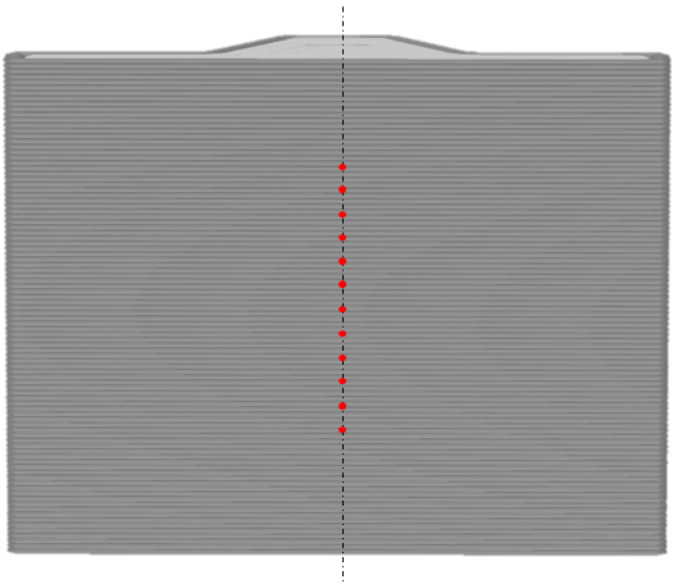

Figure 5.36 Approximate layer locations for extracting transient temperature evolution.

Locations below the lowest layer position shown in Figure 5.36 were avoided because of significant reflections from the build plate especially at the early stages of the printing process. Further, noise introduced due to the movement of the camera with the build plate was removed from the experimental data utilizing a moving average filter with a span of $5\ K$. Experimental data was processed and filtered with a script developed in Matlab©.

Figure 5.37 shows the experimental and predicted transient temperature evolution at the twelve layer locations. As shown by this plot, predictions of the transient temperature evolution are in great agreement with the experimental measurements, thereby demonstrating that the relevant heat transfer mechanisms are captured in the EDAM process simulation. The only parameter calibrated here was the radiation ambient temperature which is applied to all exposed surfaces. A discussion of the individual heat transfer mechanisms follows and it also covers the relevance of radiative heat losses in the cooling process of the printed material.

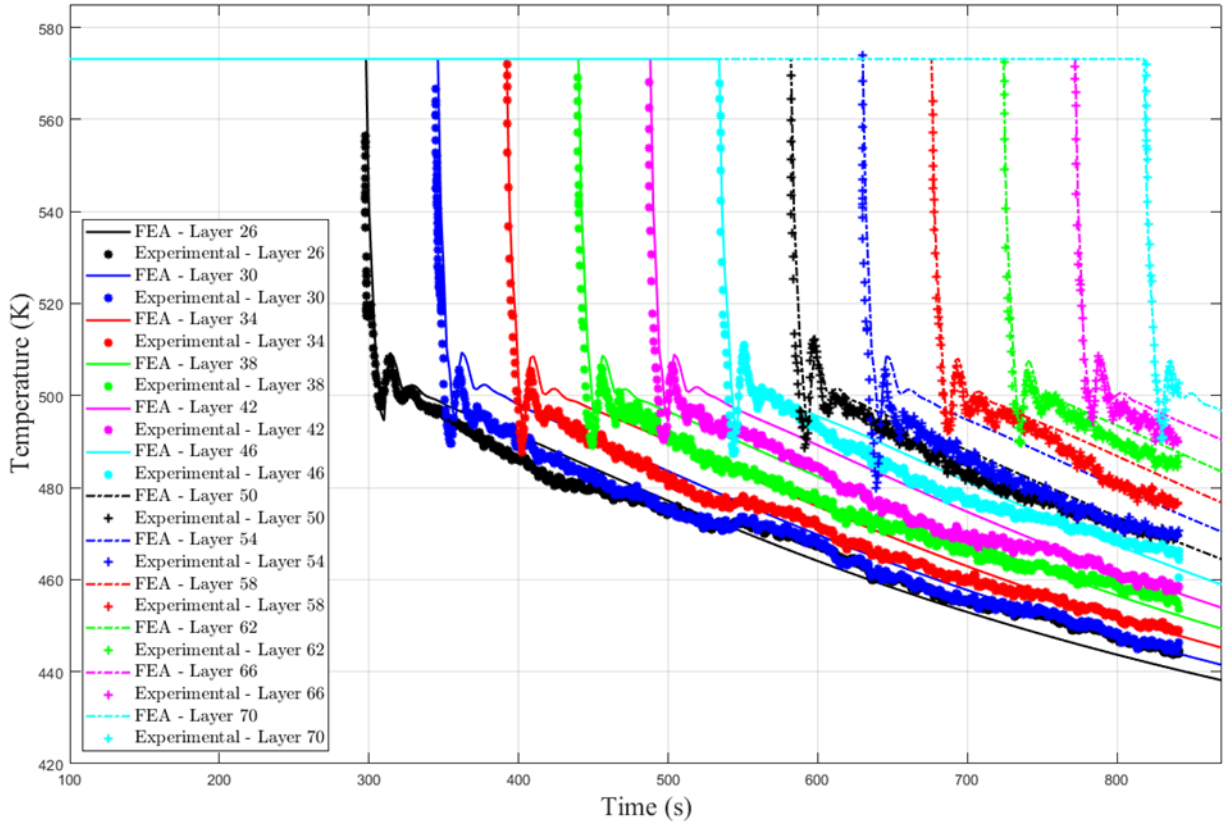

Figure 5.37 Transient evolution of temperature during part manufacturing at multiple layer locations measured experimentally and predicted in the EDAM process simulation of the stringer tool.

5.8 Contribution of Individual Heat Transfer Mechanisms

Three primary advancements were made to the transient heat transfer analysis, namely the inclusion of the latent heat of crystallization, the implementation of a moving heat source to model thermal energy removed during material compaction and the implementation of local convection coefficients. Further, predictions made with this simulation framework have been validated against experimental measurements. The only parameter calibrated in the model was the radiation ambient temperature. Now that we have a validated model, we can remove systematically each of the heat transfer mechanisms added in this work to investigate its relevance in the prediction of the transient temperature evolution of the printed material.

The relevance of radiation primarily at elevated temperatures has been mentioned throughout this chapter, however, quantitative information has not been provided yet. In order to investigate the relevance of radiative heat losses, the transient temperature evolution predicted in the EDAM process simulation of the stringer tool was extracted at the location of layer 26. Utilizing this temperature evolution, the convective and radiative heat fluxes were computed. While the radiative heat losses were calculated with Equation 5.20, the convective heat losses were computed with Equation 5.9 and utilizing the local convection coefficient predicted with the Equation 5.19.

Figure 5.38 shows the temperature evolution predicted for layer 26 and the convective and radiative heat fluxes resulting from the transient surface temperature. This plot shows that as soon as the material is deposited, the radiative heat losses dominate over the convective heat losses until the surface of the material is cooled down to about $490.0\ K$. While at the deposition temperature the radiative heat losses are around 170% larger than the convective heat losses, this ratio is inverted at temperatures about $460.0\ K$. Hence, the transient cooling process transitions from radiation dominated to convection dominated at temperatures in the range of 490.0 to $500.0\ K$. In order to investigate the relevance of utilizing local convection coefficients in the EDAM process simulation, an analysis was carried out with a constant convection coefficient of 9 (W/m^2K) to compare predictions of temperature evolution during part manufacturing. This convection coefficient corresponds to the local convection coefficient averaged along the height of the vertical wall which also coincides with the recommendations provided by Brenken [16] for the EDAM process simulation of walls with heights in the range of $100\ mm$. Transient evolution of

temperature was extracted at six layer locations starting at layer 26 and increasing in multiples of eight until layer 66. Only this layers were reported for improving data visualization.

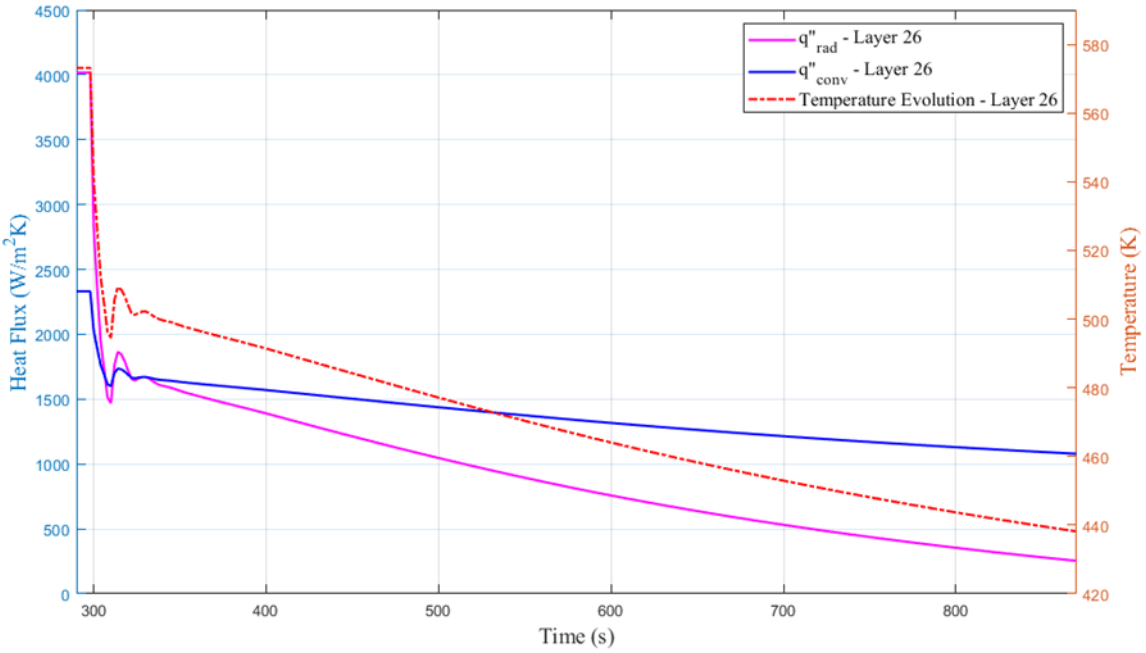

Figure 5.38 Contributions of convective and radiative heat losses to the cooling process of the printed material.

Figure 5.39 shows the transient evolution of temperature predicted with the analysis that utilizes the local convection coefficient, h_z, and with the analysis where a constant convection coefficient was assumed. The initial temperature drop occurring during the deposition of the layer is still capture accurately since radiation governs this transient behavior as discussed previously. However, the cooling rate in the region dominated by convection is definitely overestimated using an average convection coefficient. Hence, capturing more details of the convection mechanism in process simulations improve temperature predictions in the temperature range dominated by convection ($< 500K$) and this results also confirmed the assumptions made for implementing the local convection coefficient in this particular geometry were appropriate.

To investigate the relevance of accounting for the thermal energy removed through the compaction of the molten material, the moving heat flux used to model the tamper in the EDAM process simulations was disabled. This way, the already validated transient temperature evolution was compared to the temperature evolution predicted with the analysis that neglects the effects of

the tamper. Temperature evolutions were compared at the same six layer locations utilized in the comparison of the convection coefficient.

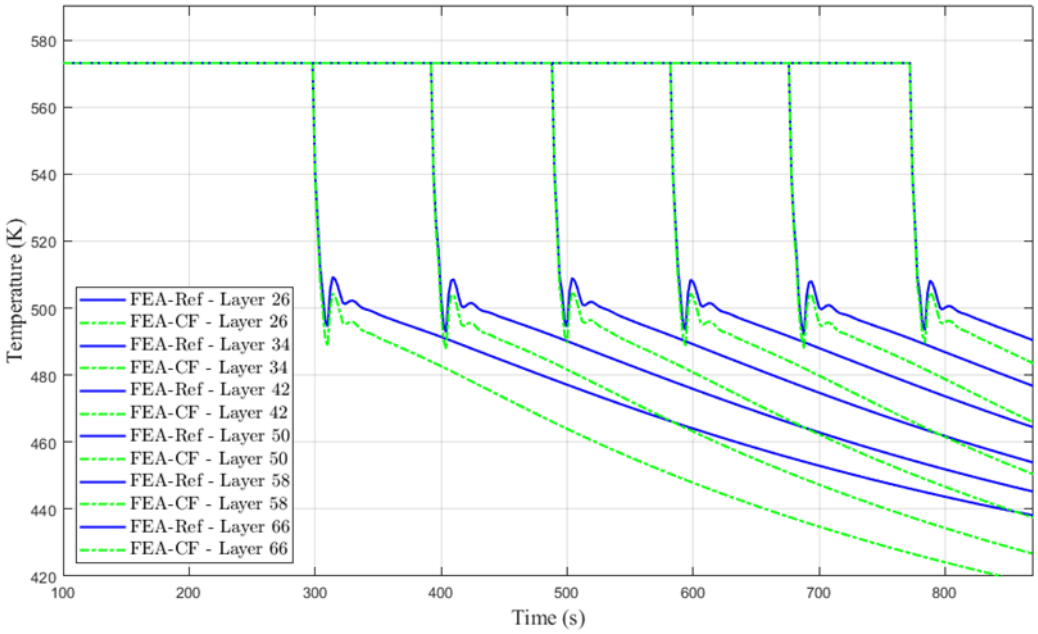

Figure 5.39 Comparison of transient evolution of temperature predicted using local convection coefficients (FEA-Ref) and a constant average convection coefficient (FEA-CF).

Figure 5.40 compares the transient evolution of temperature predicted by considering the heat losses from the compacter (FEA-Ref) with the temperature evolution predicted neglecting the compacter (FEA-NT). By neglecting the heat losses from the compacter, a temperature difference of around $20.0\,K$ develops between the temperature curves obtained with both approaches. Furthermore, since the first temperature drop is underestimated by neglecting the tamper heat losses, the subsequent ripples are also damped due to the lower difference in temperature between this layer and the one deposited above. Since the tamper only removes heat as it passes through the surface of the printed material (represented by elements in this case), the contribution of this heat transfer mechanisms is primarily at the early stages of the material deposition. As a result, the temperature range dominated by natural convection remained almost unaffected upon removal of the tamper. The plots in Figure 5.40 clearly showed the contribution of the heat removed through the compacter to the prediction of the transient evolution of temperature. It is also recognized that for this geometry in particular which has a small layer time ($\sim 12\,s$), the compacter heat losses

might be captured by calibrating the radiation heat losses. Nevertheless, calibrating this heat losses through the radiation coefficient will not be appropriate for parts with longer layer times and with beads printed parallel to each other since the tamper also interacts with the surfaces of adjacent beads. Hence, capturing heat losses from material compaction in the EDAM process simulations is important not only to accurately predict temperature evolution upon material deposition but also the local temperature evolution in printed beads that are touched multiple times with the compacter. Additional experimental validation should be performed in the future to support these conclusions.

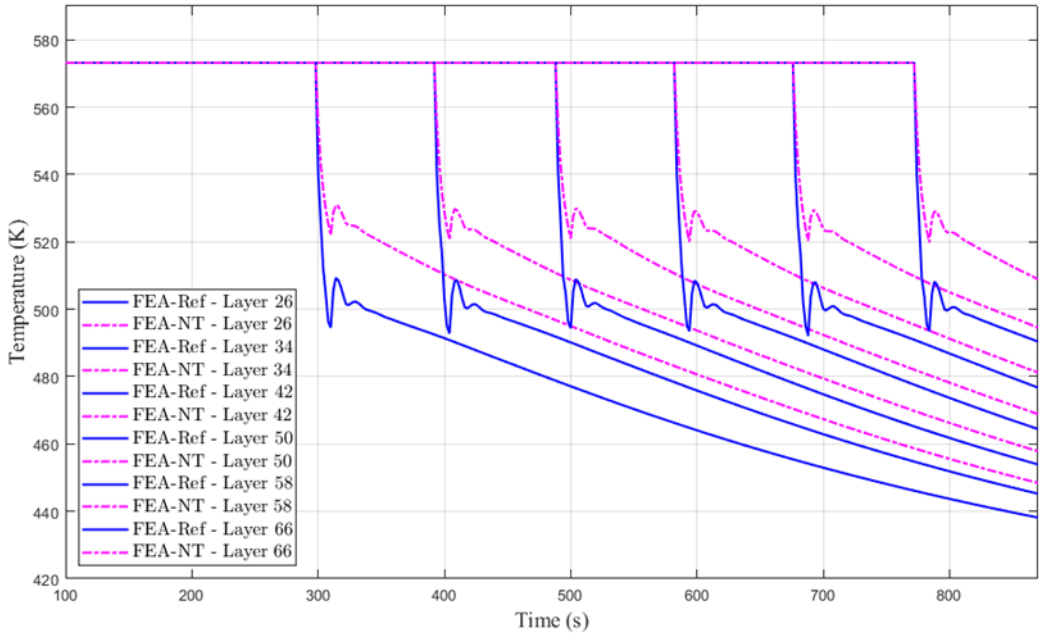

Figure 5.40 Comparison of transient evolution of temperature predicted considering the tamper (FEA-Ref) and neglecting the heat removed through the tamper (FEA-NT).

A final study was performed to assess the influence of capturing the heat for crystallization on the predictions of transient temperature evolution. The EDAM process simulation of the stringer tool was carried out neglecting heat of crystallization and temperature evolution was extracted at the same six layer locations used above.

Figure 5.41 shows the transient evolution of temperature predicted while considering and neglecting the heat of crystallization in the FEA-Ref and FEA-NC curves, respectively. The initial temperature drop remains unaffected since crystallization initiates at lower temperatures at cooling rates like this ($\sim 400 K/min$). However, a difference of temperature in the range of $5.0\ K$ arises

gradually as the polymer begins to crystallize. Although this difference in temperature is not significant, capturing the heat of crystallization in sections with large cross-sectional areas will make a larger difference since thermal energy is maintained longer due to the low thermal conductivity of the printed materials.

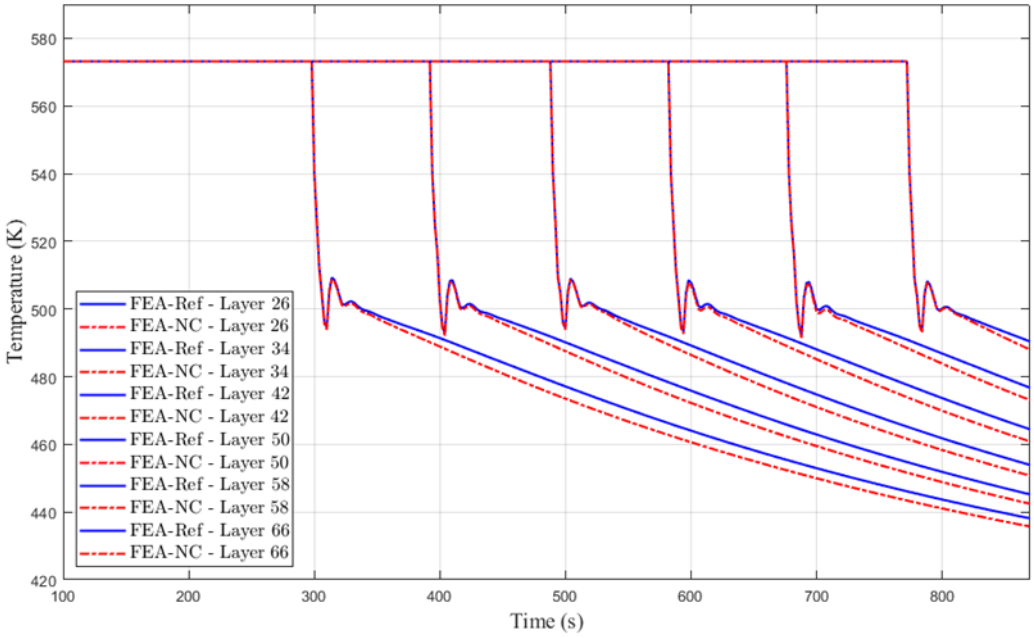

Figure 5.41 Comparison of transient evolution of temperature predicted considering the heat of crystallization (FEA-Ref) and neglecting the heat of crystallization (FEA-NC).

Since radiation ambient temperature is the only process parameter calibrated in the transient heat transfer analysis, a simple suggestion to estimate the radiation ambient temperature is provided. A first order estimate of the radiation temperature can be obtained by taking an area weighted average of the temperatures at the surfaces enclosing in a cube the part under consideration. In the case of CAMRI, one should consider the build plate, the surface of the extrusion equipment that is stationary and above the build plate, and the external ambient.

6. FUSION BONDING OF SEMI-CRYSTALLINE POLYMERS IN THE EDAM PROCESS

As described previously in the introduction of this dissertation, the interlayer strength in extrusion deposition additive manufacturing with fiber reinforced composites is primarily governed by the bond developed with the polymer matrix at the interface between two adjacent layers. This results from the in-plane preferred orientation of the reinforcing fibers. The final orientation distribution within a printed bead results from the flow-induced fiber orientation and bead compaction. Hence, the evolution of interlayer strength is described by fusion bonding of polymer at the interface formed by two adjacent printed layers.

This chapter begins by describing the phenomena participating in the process of fusion bonding of semi-crystalline reinforced polymers under the highly non-isothermal conditions developed in EDAM. The importance of polymer crystallization to diffusion and to the interfacial strength evolution described in terms of the degree of bonding is discussed as well. The degree of bonding is computed from the ratio of G_{IC} developed with a given temperature and crystallization histories to the maximum value for $G_{IC,\infty}$ achieved in a perfectly bonded joint. Then, a process-simulation informed method for characterizing welding times under the highly non-isothermal conditions of EDAM is presented. A subsequent section presents the numerical implementation of this bonding model in a UMATHT© subroutine in Abaqus©. Finally, predictions of the degree of bonding made with this model are verified against experimental measurements of the degree of bonding. It should be noted that some of this work has been published previously [102, 137].

6.1 Phenomena Involved in Fusion Bonding of Semi-Crystalline Polymers

Fusion bonding of two polymeric interfaces involves multiple steps that include surface rearrangement, surface approach, wetting, interdiffusion and randomization of polymer chains and crystallization in the case of semi-crystalline polymers [138, 29, 139, 140].

We now describe these steps in the contexts of the extrusion deposition additive manufacturing process. In EDAM, surface arrangement is concerned with changes to the conformation state of the polymer chains that may occur while the suspension of fibers in molten polymer flows through the printing nozzle. Stretching of polymer chains near the surface of the

extrudate is the primary change in conformation state that will arise from the shear flow developed inside the extrusion nozzle. Stretching of polymer chains near the surface can have effects not only on the morphology of the crystalline structure developed near the interface but also on the crystallization kinetics since stretching the chains lowers its entropy, thereby facilitating crystallization [141, 142]. The next two steps of surface approach and wetting are concerned with stablishing physical contact between the two surfaces that will be bonded. In the case of CAMRI, a tamper is used for compacting an initially circular extrudate of molten material to a rectangular bead with rounded edges. Since this process of compacting an extrudate occurs while the printed material is still in the molten state, physical contact with the surface of previously printed material is achieved instantaneously. Further, if we consider that the surface tension of the melt is not significantly lower than the surface tension of the layer underneath printed with the same material, perfect wetting is achieved. This leads to the first assumption made herein that instantaneous wetting is achieved upon bead compaction. Furthermore, the assumption of instantaneous wetting is also considered for different compaction ratios. Figure 6.1 shows schematically the phenomena involved in fusion bonding during EDAM and depicts the compaction of the extrudate after it leaves the extrusion nozzle.

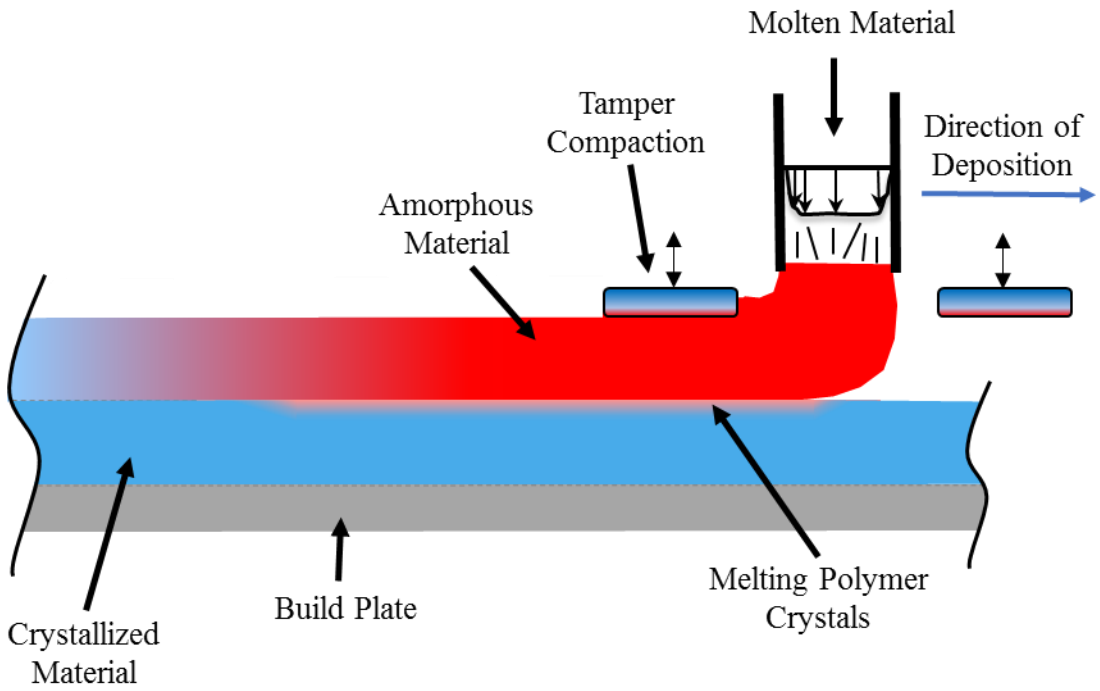

Figure 6.1 Schematic representation of phenomena involved in fusion bonding during EDAM.

Once the surfaces are in close physical contact, which is also referred to as establishment of intimate contact, and in the absence of factors restraining the mobility of polymer chains, diffusion of polymer chains will occur across the interface. Factors that restrain mobility of polymer chains include fixed obstacles and crystallization. We will revisit the role of crystallization after explaining the diffusion of polymer chains.

Figure 6.2 shows the microstructure of two full beads from a section of 4 by 3 beads printed in CAMRI with 50% by weight carbon fiber reinforced PPS. Figure 6.2-C shows a closer look to the interface formed between bead 1 and 2 where no signs of a physical interface can be distinguished.

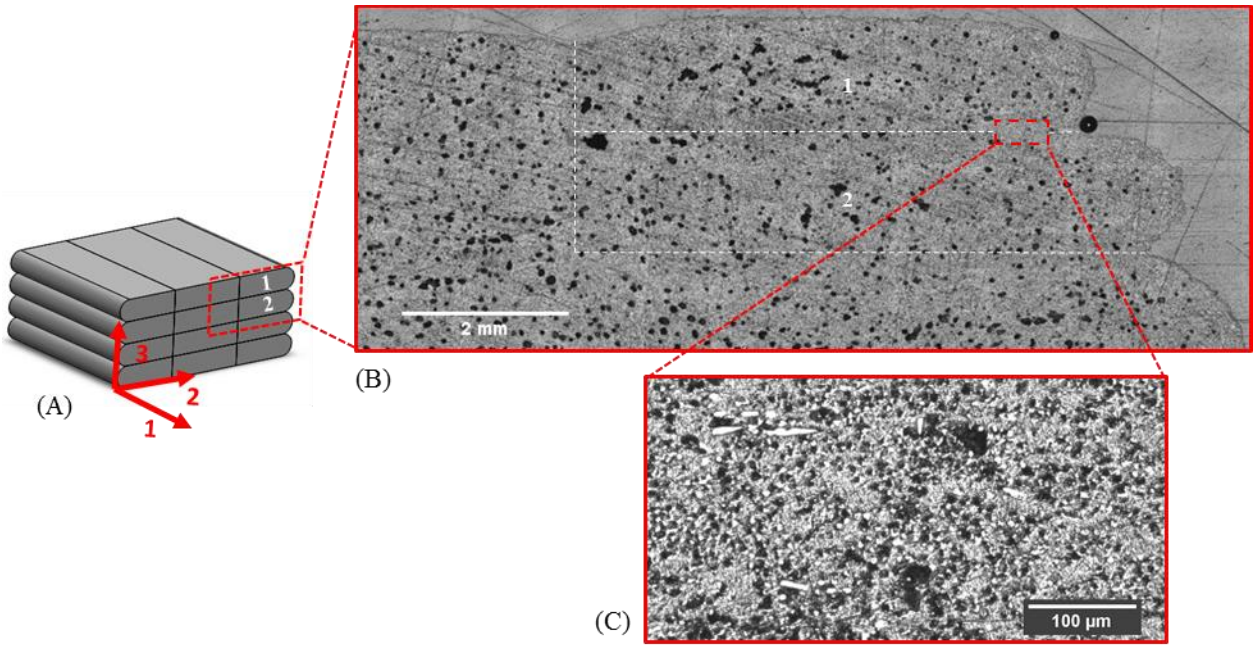

Figure 6.2 A) Schematic representation of printed section with 4 by 3 beads. B) Microstructure of section printed with 50% by weight carbon fiber reinforced PPS. C) Detailed microstructure around the interface between two adjacent beads showing no physical signs of an interface.

Randomization of polymer chains at the interface is reached if the conditions at the interface are such that chains can diffuse for a period of time close to the reptation time, t_r. Figure 6.3 shows schematically chains after instantaneous wetting and after randomization is attained across the interface. The term autohesion is used to refer to the process of diffusion occurring until randomization is reached. After the autohesion process is completed, the initially visible interface

between the bonding surfaces vanishes and mechanical and fracture properties close to the bulk material are achieved.

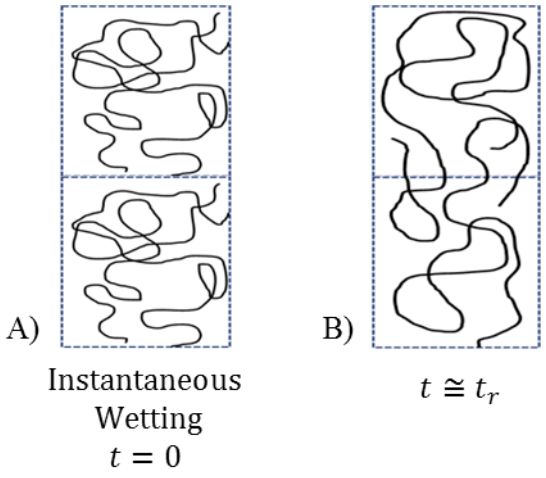

Figure 6.3 Schematic representation of polymer chains after: A) Instantaneous wetting and B) Randomization of polymer chains.

The time evolution of the autohesion process has been described before through the reptation theory of polymer dynamics developed by De Gennes [143, 30]. Reptation theory defines the reptation time, t_r, as the time required for a polymer chain to escape from a confining tube formed by topological constraints surrounding the polymer chain. Such topological constraints are imposed by entanglements between neighboring polymer chains as well as by rigid constraints like reinforcing fibers and particles. In De Gennes' reptation model for polymer melts, an entangled chain (confined chain) diffuses along its own confining tube in a way similar to the motion of a snake. Figure 6.4 shows a schematic representation of the reptation movement of a polymer chain in an entangled melt.

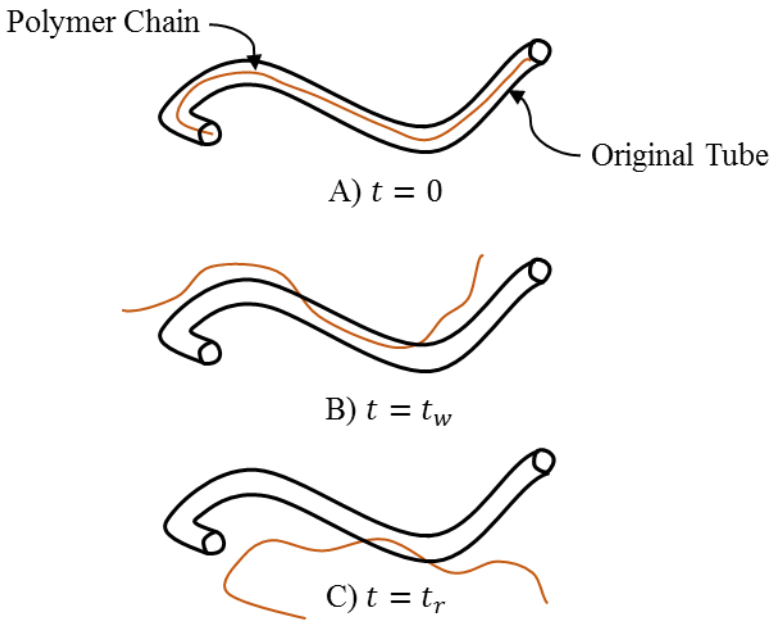

Figure 6.4 Schematic representation of the reptation movement of a polymer chain in an entangled melt.

Based on the reinterpretation of the reptation theory given by Rubinstein and Colby [92], the curvilinear motion of the polymer chain around the topological constraints can be described in terms of the curvilinear diffusion coefficient, D_c, given by Equation 6.1

$$D_c = \frac{KT}{N\xi} \tag{6.1}$$

where ξ is the Rouse friction coefficient, K the Boltzmann's constant, T the absolute temperature, and N the average number degree of polymerization. The average length of the tube can be then represented as the average contour length, $\langle L \rangle$, which can be approximated as given by Equation 6.2.

$$\langle L \rangle \approx a\frac{N}{N_e} \approx \frac{b^2 N}{a} \approx \frac{bN}{\sqrt{N_e}} \tag{6.2}$$

Where a is the entanglement strand length, N, is the number of Kuhn monomers in the chain, N_e, the number of Kuhn monomers in an entanglement strand and b is the length of a Kuhn monomer. Therefore, Equation 6.2 shows that the average contour length is shorter than the contour length of the chain, bN, by the factor $\sqrt{N_e}$. Since the reptation time corresponds to the time it takes for the polymer chain to escape from its confining tube of length equal to $\langle L \rangle$, t_r can be approximated as given by Equation 6.3.

$$t_r \approx \frac{\langle L \rangle^2}{D_c} \approx \frac{\xi b^2}{KT}\frac{N^3}{N_e} = \frac{\xi b^2}{KT} N_e^2 \left(\frac{N}{N_e}\right)^3 \tag{6.3}$$

Notice from Equation 6.3 the reptation time scales with the cube of the molecular weight ($t_r \sim M^3$), however, the experimentally measured scaling exponent is 3.4 [92]. This discrepancy results in part due to the assumption of treating the neighboring polymer chains as fixed obstacles rather than polymer chains performing the same snake like motion. One way to determine t_r experimentally is through stress relaxation or oscillatory shear experiments of polymer melts, however, such experiments are complicated to perform in the presence of fibers due to the effects of fibers and fiber orientation on the local deformation mechanisms. Equation 6.3 also shows that t_r decreases asymptotically with the temperature, T.

Utilizing the concepts of the reptation theory, Prager and Tirrel [144] derived an expression for the time evolution of the density of polymer chains crossing an interface with the aim of predicting the evolution of fracture toughness. This type of relationships between polymer dynamics and the time evolution of interfacial properties during autohesion have been derived by Prager and Tirrel and others [144, 138, 145]. These relationships attain the form given by Equation 6.46.1 for the evolution of strength, $\sigma(t)$, and critical energy release rate, $G_{IC}(t)$, respectively. Multiple authors have confirmed experimentally the time dependence predicted with the reptation theory on the evolution of interfacial properties using healing experiments [32, 146, 147, 148]. An example of a healing experiment based on measurements of Mode-I critical energy release rate, G_{IC}, consist first on extending a crack in a self-similar manner in a double cantilever beam (DCB) specimen. In a second step, the cracked DCB specimen is heated at the desired temperature and for a controlled period of time. In a third step, the recovered strength is measured by mechanically

testing the healed portion of the DCB. This way, relationships for recovered G_{IC} are obtained as a function of time and temperature.

$$\frac{\sigma(t)}{\sigma_\infty} = \left(\frac{t}{t_r}\right)^{\frac{1}{4}}$$
$$\frac{G_{IC}(t)}{G_{IC\infty}} = \left(\frac{t}{t_r}\right)^{1/2} \tag{6.4}$$

Multiple examples can be found in the literature where expressions like the ones given by Equation 6.4 have been extended to model the evolution of the degree of autohesion in the processing of composite laminates [149, 140, 150, 151, 152].

While these previous investigations were carried out with amorphous polymers, the mechanisms governing the evolution of interfacial properties in semi-crystalline polymers also involve diffusion of polymer chains yet the failure mechanism become more complicated due to the formation of polymer crystals. Further, the mobility of polymer chains is rapidly inhibited upon the start of the crystallization process.

Development of crystallinity across an interface between two polymeric surfaces has been identified as crucial for developing interfacial strength in bonds with semi-crystalline polymers [153]. Non-isothermal bonding in semi-crystalline polymers has been investigated experimentally by Smith et al. [154], Zanetto et al. [139], Bournan el al. [140] and Plummer et al. [155]. Investigations carried out by these authors have revealed a faster recovery of interfacial strenght under non-isothermal conditions than under isothermal crystallization. Furthermore, their experimental resutls showed the importance of melting the polymer at the interface on the cooler side during non-isothermal bonding. This way, polymer crystals can develop across the interface. On the contrary, polymer crystals will nucleate at the interface and grow into each side of the bonding surface with structures controlled by the cooling history.

Based on these previous observations, the following three situations have been identified in the highly non-isothermal EDAM process with semi-crystalline polymers.

The first situation occurs when a printed bead underneath a newly deposited bead has not developed crystallinity. In this case, diffusion of polymer chains across the interface will occur as

soon as the surfaces are in intimate contact and it will proceed until crystallinity develops across the interface. If the time comprised from the point when material was deposited to the point before crystallization starts is similar or longer than the reptation time, randomization of polymer chains across the interface is attained. Once the polymer starts to crystallize, the crystallization front will progress in the same direction temperature gradients develop during part manufacturing. This way, the polymer chains already randomized at the interface are involved in the formation of polymer crystals at the same interface.

The second situation occurs when the previously deposited bead is already crystallized but it has not cooled down significantly below the onset temperature of crystal melting. If this condition is encountered, local remelting can occur upon deposition of a new bead, thereby allowing for diffusion of polymer chains across the interface to some extent before crystallization occurs. Again, crystallization will developed in the same direction temperature gradients develop during the printing process, progressing from the low temperature regions to the high temperature regions. The first and second scenarios where crystallinity is developed across layer-to-layer interfaces are depicted in Figure 6.5-A.

The third situation occurs when the printed substrate is already crystallized and cooled down significantly so that melting cannot not occur near the surface of the substrate. In this case, diffusion of polymer chains is not possible across the interface. Further, the large degree of supercooling in the polymer located at the bottom of a newly deposited bead will lead to nucleation of polymer crystals that will likely grow from the interface into the volume of the newly deposited bead. Figure 6.5-B depicts this condition where polymer crystals are not formed across the interface but rather nucleated on the surface of a cool substrate. A similar effect of crystal nucleation and growth at polymeric interfaces was observed in fusion boding experiments of polypropylene performed by Smith et al. [154].

As described in Equation 6.4, the reptation time only provides a relative measure of the change in interfacial strength or critical energy release rate as a function of time and temperature, therefore calibration experiments are generality performed to make quantitative predictions of these fracture properties. Although the complexity of the failure mechanisms at an interface are not captured with this expression derived from scaling arguments of polymer dynamics, this can provide useful relations to inform other models (like cohesive zone models) that allow capturing more details of the damage mechanisms occurring while separating fusion bonded layers.

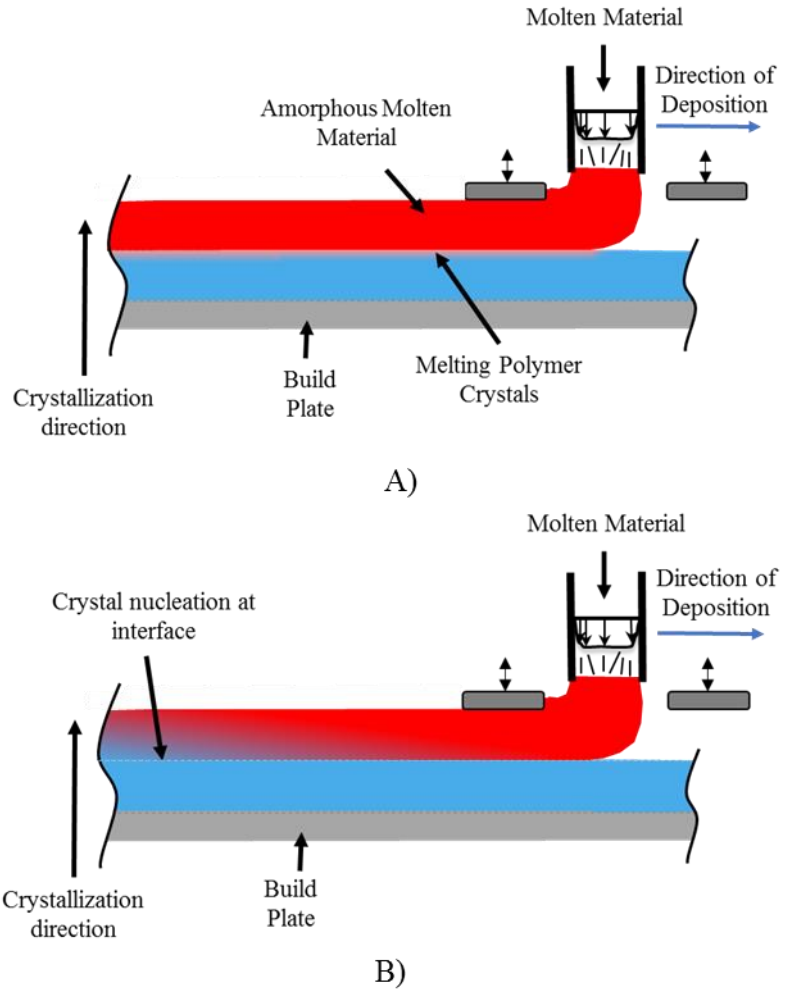

Figure 6.5 Scenarios for fusion bonding of semi-crystalline polymers in the EDAM process. A) Polymer crystals developed across the interface between two beads. B) Polymer crystals nucleate at the surface of previously deposited beads.

It was previously recognized that polymer diffusion is rapidly precluded upon the onset of crystallization which is simply explained by the entrapment of polymer chains in rapidly growing polymer crystals. Further, the compacter used in EDAM for consolidating printed beads provides instantaneous wetting of previously printed material.

Based on these previous observations and assumptions, a non-isothermal autohesion model based on theory of polymer reptation was coupled with the evolution of crystallinity to predict the evolution of interlayer properties in EDAM. This approach assumes that the amount of diffusion achieved at the interface controls the crystalline structure developed at the interface and thus the

resulting interfacial fracture properties. Nevertheless, the effects of crystallinity on the interlayer fracture properties are neglected. The evolution of crystallinity is controlled with two phenomenological models, one for crystallization kinetics and other for melting of polymer crystals. These two phenomena, polymer diffusion and crystallization, are coupled with the heat transfer analysis presented in chapter 5 to capture the effects of temperature and cooling rate on the evolution of the interfacial properties and the crystallization behavior, respectively.

The following two subsections present phenomenological models utilized to capture polymer diffusion and the evolution of crystallinity in the EDAM process simulations. A coupling between polymer diffusion and the evolution of crystallinity is introduce by disabling the diffusion model at crystallinity volume fractions higher than a critical degree of crystallinity. This simple coupling is introduced to capture the rapid reduction in the curvilinear diffusion coefficient caused by the polymer crystallization.

6.1.1 Polymer Diffusion

Diffusion of polymer chains through an interface between two adjacent layers of non-crystallized material in the EDAM process is carried out under highly non-isothermal conditions. Thus, the non-isothermal autohesion model developed by Yang and Pitchumani [149] was used to model the evolution of the mode-I Critical Energy Release Rate (CERR), $G_{IC}(t)$. Since instantaneous wetting is assumed, we defined the degree of autohesion predicted with this model as the degree of bonding, D_b, which represents a fraction developed of the mode-I CERR with respect to a perfectly bonded joint (G_{IC}/G_{IC_∞}). A perfectly bonded joint will be defined more precisely while presenting the characterization of the welding times.

In order to generalize equations for autohesion (Equation 6.4) which are valid particularly for polymers with low molecular weight ($M_c < M < 8M_c$), the reptation time t_r was replaced by a welding time t_w since the interpenetration length required to develop interfacial properties is smaller than the average contour length for a high molecular weight polymer as shown schematically in Figure 6.4-B [153, 149]. Therefore, for a polymer with molecular weight, M greater than around eight times the critical molecular weight, M_c, t_w is shorter than t_r [153].

Yang and Pitchumani [149] derived their non-isothermal autohesion model using the polymer reptation theory as follow. Utilizing the solution of a transient diffusion equation, they represented the probability density function of finding a particular segment of the polymer chain

at some position, s, along the curvilinear coordinate of the tube confining the polymer chain, and at a time t. By solving the diffusion equation, the mean square displacement of the polymer chain, l^2, at a given time is obtained as a function of the reptation diffusion coefficient, D_r. Then, an expression similar to Equation 6.3 was obtained by the authors. Finally, the ratio of the mean square displacement of the polymer chain to the average minimum length of the tube for welding, $\langle L_w \rangle$, provided the integral equation given by Equation 6.5.

To include the effect of crystallization on the diffusion properties in this non-isothermal autohesion model, either the welding time, t_w, can be a function of the crystallinity or the upper integration limit of the integral expression in Equation 6.5 can be defined as a function of the evolution of crystallinity. The latter approach was used herein for convenience of the model implementation. The time to crystallize, t_c, is defined as the time such that the degree of crystallinity, X_{vc}, is below a critical value, X_{vc}^{crit}, as given by Equation 6.5.

$$D_b(t) = \frac{G_{IC}(t)}{G_{IC_\infty}} = \left[\int_0^{t_c} \frac{1}{t_w\big(T(\tau)\big)} d\tau\right]^{\frac{1}{2}}, t_c \in \{t \ \ s.t. \ \ X_{vc} < X_{vc}^{crit}\} \tag{6.5}$$

The X_{vc}^{crit} can be estimated from rheology experiments with unfilled polymer. An alternative method is to assume a small degree of crystallinity, ($< 5\%$), will hinder the diffusion of polymer chains due to the steep decrease in diffusivity with the onset of crystallization. Equation 6.5 can be also utilized to predict interlayer strength by replacing the power with $1/4$ [149]. Since the welding time, t_w, has a strong dependence on temperature, an Arrhenius equation can be used to describe t_w as given by Equation 6.6.

$$t_w(T) = A \cdot exp\left(\frac{E_A}{RT}\right) \tag{6.6}$$

Where A is a pre-exponential factor, E_A, an activation energy and R is the gas constant. Multiple techniques can be used for characterizing, t_w, as a function of temperature including bonding experiments, small angle oscillatory shear rheology, stress relaxation experiments and healing experiments. The first technique was preferred herein due to the presence of fibers and the non-isothermal conditions in the EDAM process. The subsequent section Characterization of Non-

Isothermal Welding Time presents the characterization method developed to determine t_w combining experimental measurements and temperature predictions performed with the EDAM process simulation.

6.1.2 Evolution of Crystallinity

The evolution of the degree of crystallinity, X_{vc}, in semi-crystalline polymers is controlled by both polymer crystallization and melting. Especially in the EDAM process where molten material is continuously deposited on top of previously deposited material which can be already crystallized. This section presents the models used for capturing polymer crystallization and melting as well as the coupling between these two.

6.1.2.1 Polymer Crystallization

Crystallization is a physical transformation that occurs while the polymer is cooled from the melt to room temperature and consists of two processes: crystal nucleation and crystal growth. The former is a prerequisite for the latter. During this transformation, polymer chains are ordered into crystalline structures developed based on the cooling conditions. A penalty in entropy and enthalpy occurs due to the ordering of polymer chains in a crystalline structure which is manifested as additional shrinkage and release of thermal energy.

Homogenous and heterogeneous nucleation occurs in semi-crystalline polymer after overcoming a free energy barrier. While in the former case nuclei develop in the bulk of a supercooled polymer, in the latter case nucleation occurs on the surface of impurities or heterogeneities [33]. If we consider a parallelepiped nucleus with dimensions l, m and n, for heterogeneous nucleation, the free energy for formation of a nucleus is given by the difference in Gibb's free energy of a crystal and the melt ($\Delta G = G_c - G_m$) which can be expressed in terms of the surface energies as given by Equation 6.7.

$$\begin{gathered} \Delta G = -\Delta g lmn + 2\gamma_e mn + 2\gamma_s lm + \Delta\gamma nl \\ \Delta\gamma = \gamma_s + \gamma_{hn} - \gamma_{hm} \end{gathered} \tag{6.7}$$

Where γ_e and γ_s are the end and lateral surface energies, respectively. The surface energy γ_{hn} correspond to the surface free energy between the heterogeneity and the nucleus whereas γ_{hm} is

the surface free energy between the heterogeneity and the melt. In our case, m, is oriented normal to the interface between the nucleus and the heterogeneity. Δg is the free energy of fusion given by Equation 6.8 in which Δh is the enthalpy of fusion and ΔT is the degree of supercooling that corresponds to the temperature difference with respect to the equilibrium melting temperature, T_m°, ($\Delta T = T - T_m^\circ$) [33].

$$\Delta g = \frac{\Delta h \Delta T}{T_m^\circ} \tag{6.8}$$

In order to form a stable nucleus, a critical nucleus size must be developed at which the free energy given by Equation 6.7 for the formation of a nucleus is equal or less than zero. Only two energies in Equation 6.7 favor nucleation, the free energy of fusion, Δg, and the surface free energy between the heterogeneity and the melt, γ_{hm}. The contribution of the former increases as the degree of supercooling, ΔT, increases whereas the latter one depends on the nature of the heterogeneity. In homogenous nucleation, only Δg, favors nucleation. As a result, the energy barrier in heterogeneous nucleation is overcome at temperatures closer to the melt than in homogenous nucleation.

For carbon fiber reinforced semi-crystalline polymers, the surface of the carbon fibers act as nucleation sites for crystallization, thereby favoring the development of crystallinity as the suspension of fibers in molten polymer is cooled from the melt. Once a nucleus reaches a critical size to become stable, polymer crystals continue to grow. However, a secondary nucleation mechanism can occur by homogenous nucleation in polymer rich regions inside a fiber filled system. We will revisit the secondary nucleation shortly.

After crystals nucleate, the subsequent crystal growth is a complex process controlled primarily by diffusion and the conditions surrounding a growing polymer crystal. For example, crystals nucleated on the surface of fibers will tend to grow in an epitaxial manner whereas crystals nucleated in the bulk polymer will tend to grow in a spherulitic manner [33]. In the former case, polymer chains will be folded either along the surface of a heterogeneity or normal to the surface. In the latter case, crystals will grow radially from the nucleus and in the form of lamellar structures.

These two forms of crystal growth have been observed in our material of interest, which is Polyphenylene sulfide (PPS) reinforced with 50% by weight of carbon fiber. Figure 6.6 shows two

different crystalline microstructures developed with the PPS in a polymer rich region (Figure 6.6-A) and a near the surface of a carbon fiber (Figure 6.6-B). These microstructures were captured from a fracture surface sputter coated with gold and using a back-scattered electrons detector in a Nova Nano Scanning Electron Microscope (SEM).

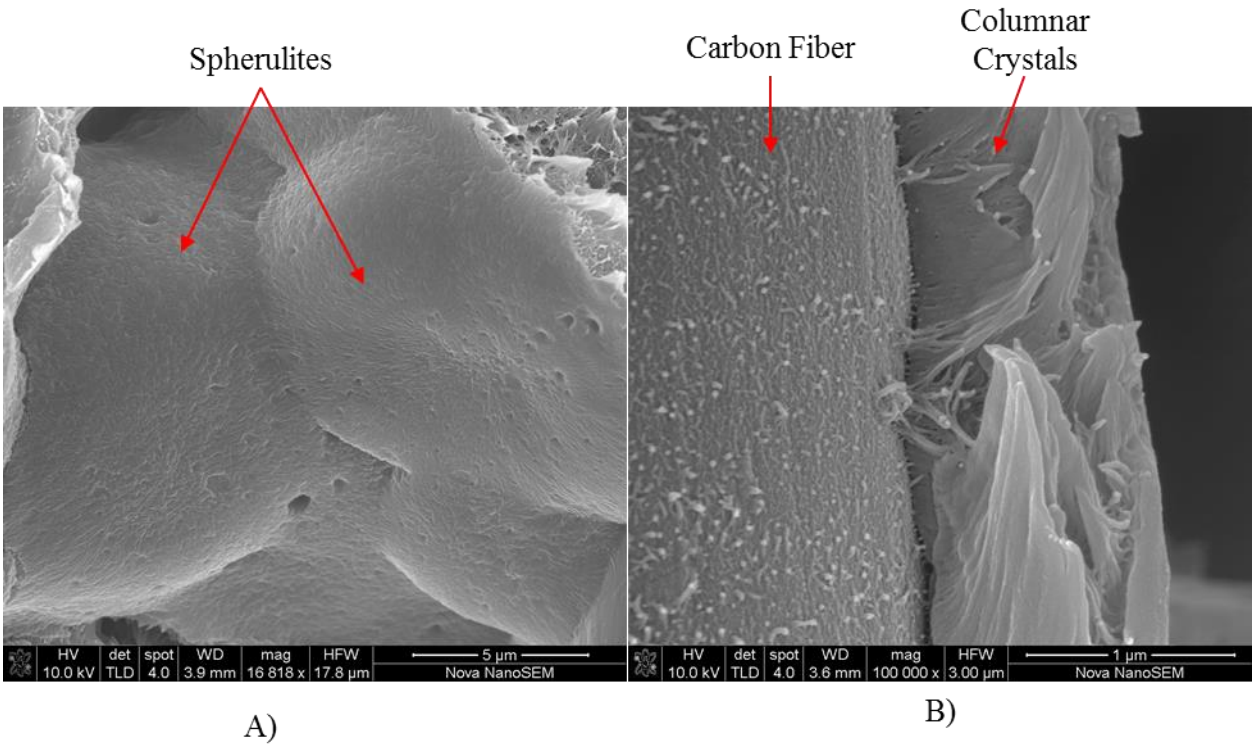

Figure 6.6 SEM image of crystalline structures developed in PPS reinforced with 50% by weight carbon fiber. A) Spherulitic crystal growth in polymer rich region. B) Columnar crystal growth on the surface of the fibers.

The kinetics of polymer crystallization will be then controlled by both: the rate of crystal nucleation and the rate of crystal growth. While the nucleation rate increases as the degree of supercooling increases, the diffusion controlled growth rate decreases with the degree of supercooling. Figure 6.7 shows schematically the rate of nucleation and growth as a function of the temperature. The equilibrium melting temperature is at the far right side of the temperature axis and thus the degree of supercooling increases in the direction opposite to the temperature as illustrated in Figure 6.7. Furthermore, the cooling rate will also influence the rate of transformation and the morphology of the developed crystalline structures.

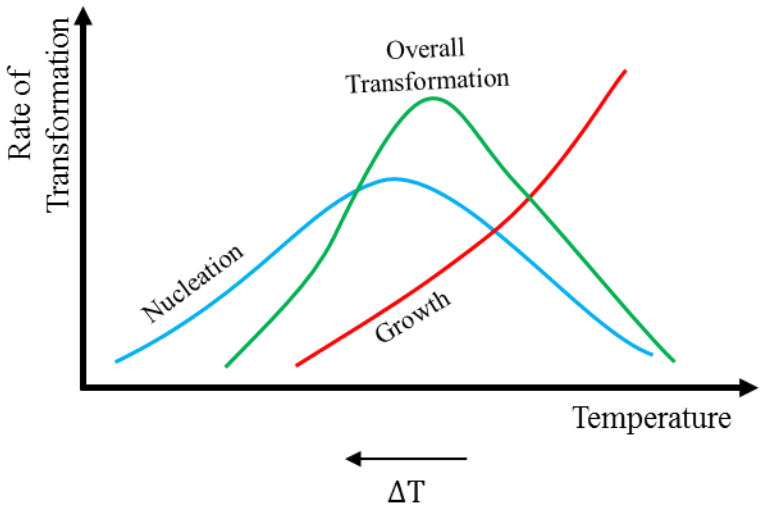

Figure 6.7 Schematic representation of the rate of transformation in polymer crystallization.

Since our objective is to predict the evolution of crystallinity in the highly non-isothermal conditions of EDAM, a phenomenological model was used to capture the kinetics resulting from the two crystallization mechanisms described with Figure 6.6. Velisaris and Seferis [112] developed a phenomenological model to capture the two nucleation and growth processes occurring while reinforced semi-crystalline polymers are cooled from the melt. The kinetics of each mechanism is considered through a function, $F_{vc_i}, i = 1,2$, and the contribution of each mechanism to the overall crystallization rate is weighted by the factors, $w_i, i = 1,2$, as given by Equation 6.9. The product of the weighted sum of the two crystallization mechanisms and the maximum degree of crystallinity X_{vc_∞} yields the degree of crystallinity.

$$X_{vc}(T) = X_{vc\infty}\left(w_1 F_{vc_1} + w_2 F_{vc_2}\right) \tag{6.9}$$

The weight factors satisfy the condition that their sum is always equal to unity. Each function F_{vc_i} describing a crystallization mechanism contributing to the crystallization rate is described by the integral expression given by Equation 6.10

$$F_{vc_i} = 1 - exp\left\{-C_{1_i}\int_0^t T \cdot exp\left[\frac{-C_{2_i}}{\left(T - T_g + T_{c_i}\right)} - \frac{C_{3_i}}{\left(T\left(T_{m_i} - T\right)^2\right)}\right] n_i \tau^{n_i - 1} d\tau\right\} \quad (6.10)$$

$$i = 1,2$$

where the parameters C_{1_i} capture the temperature dependence on the crystallization rate, and C_{2_i} describe the temperature dependence on the crystal growth for each mechanism. Similarly, C_{3_i} is related to the enthalpy of nucleation in each mechanism. The temperatures T, T_g, T_{c_i} and T_{m_i} used in this model represent the temperature of the process, the glass transition temperature of the polymer, the melting temperature of the polymer, and an empirically determined temperature limiting the diffusion term in Equation 6.10, respectively. n_i is the Avrami coefficient of each of the crystallization mechanisms which is characterized from isothermal crystallization experiments. Characterizing all the coefficients in Equation 6.10 requires of both isothermal and non-isothermal crystallization experiments. While the isothermal crystallization experiments are performed at temperature near the melting temperature, non-isothermal experiments are carried out at multiple cooling rates representative of the manufacturing conditions. Crystallization experiments can be performed using Differential Scanning Calorimetry (DSC) where the heat released during the melting or crystallization is measured as a function of time. The kinetics of the crystallization process is then inferred from the heat signal of the exothermal process occurring during crystallization.

Using crystallization kinetics data obtained through isothermal and non-isothermal DSC experiments of the 50% by weight carbon fiber reinforced PPS, Brenken [16] characterized the coefficients in Equation 6.10 using a genetic algorithm. A glass transition temperature, T_g, equal to 373.15 K was utilized for fitting the experimental data to the crystallization kinetics model. Table 6.1 lists the coefficients reported by Brenken and used to predict the evolution of crystallinity in EDAM process simulations. Brenken et al. [72] utilized the Velisaris and Seferis model and the parameters characterized for the 50% by weight carbon fiber reinforced PPS to predict the evolution of the degree of crystallinity in process simulation of the EDAM process.

Table 6.1 Parameters of the Velisaris and Seferis crystallization kinetics model for 50% by weight of carbon fiber reinforced PPS [16].

Parameter	**Crystallization Mechanism** $(\boldsymbol{F_{vc_1}})$	**Crystallization Mechanism** $(\boldsymbol{F_{vc_2}})$
w_i	0.765	0.235
n_i	3	2
$C_{1_i}\ (s^{-n}K^{-1})$	$1.16 \cdot 10^{11}$	$4.733 \cdot 10^{13}$
$C_{2_i}\ (K)$	$1.19 \cdot 10^{4}$	$1.045 \cdot 10^{3}$
$C_{3_i}\ (K^3)$	$3.27 \cdot 10^{7}$	$2.387 \cdot 10^{8}$
$T_{c_i}\ (K)$	218.7	1.07
$T_{m_i}\ (K)$	577.51	599.74

6.1.2.2 Melting of Semi-Crystalline Polymer

Melting of polymer crystals is essentially the reverse of crystallization. The melting behavior of polymer crystals depends upon the crystallization history of the semi-crystalline polymer [156]. While fine crystals developed under rapid cooling rates will melt at relatively low temperatures, large crystals formed under a slow cooling process will melt at temperatures closer to the equilibrium melting temperature, T_m°. Therefore, we can expect melting to occur over a range of temperatures defined by the distribution of crystal sizes formed. This is readily shown through the thermodynamics of melting. If we assumed a lamellar crystal as a parallelepiped crystal with dimensions $l, x,$ and y. The change in free energy, ΔG, is given by Equation 6.11.

$$\Delta G = -\Delta g l x y + 2\gamma_e x y + 2l\gamma_s(x + y) \tag{6.11}$$

Where Δg is the free energy of fusion given by Equation 6.8, γ_e and γ_s are the surface energy at the ends and sides of the crystal, respectively. In a lamellar crystal, the sides will be much smaller than the top and bottom ends of the crystal, thus we can neglect the contribution of the sides to the change in free energy [156]. Further, the change in free energy at melting is equal to zero. Thus, we combine Equation 6.11 and Equation 6.8 given the free energy conditions at melting to obtain the expression for the melting temperature as a function of the lamellar thickness, l, given by Equation 6.12.

$$T_m = T_m^\circ - \frac{2\gamma_e T_m^\circ}{l\Delta h} \tag{6.12}$$

As predicted from thermodynamics, the melting temperature of a crystal will approach the equilibrium melting temperature as the lamellar thickness increases. Which agrees with the statement made previously on the dependence of the melting temperature on the crystal size.

Since predicting the crystal size distribution developed at each location in the EDAM process simulations is unfeasible, a phenomenological model that assumes a fixed distribution of lamellar thicknesses was used. But this distribution function must be representative of the crystalline structure developed during the EDAM process. The model developed by Greco and Maffezzoli [31] given by Equation 6.13 assumes a distribution of crystal lamellar thickness with a sharpness factor, k_{mb}, and a distribution factor, d.

$$\frac{dX_{vc}}{dT} = k_{mb}\{exp[-k_{mb}(T - T_c)]\} \cdot (1 + (d-1)\, exp[-k_{mb}(T - T_c)])^{\frac{d}{1-d}} \tag{6.13}$$

The temperature T_C corresponds to the peak in the heat flow signal characterized in DSC experiments. In order to characterize the coefficients in Equation 6.13, melting experiments at heating rates of up to 110.0 K/min on samples cooled from the melt at a cooling rate inverse to the heating rate were performed in a DSC by Brenken [16]. This way, the distribution of lamellar thickness developed over a wide range of cooling rates was considered in the characterization of the distribution function used in Equation 6.13.

Table 6.2 Parameters of the Greco and Maffezzoli melting model for 50% by weight of carbon fiber reinforced PPS [16].

Parameter	**Value**
k_{mb}	0.2701
d	1.7031
$T_c\ (K)$	548.55

The experimentally measured melting behavior of the carbon fiber reinforced PPS showed a negligible dependence on the heating rate, thereby confirming that the model proposed by Greco

and Maffezzoli is appropriate for capturing the melting behavior of this material. This model was also used in publication of Brenken et al. [72] to predict the evolution of crystallinity in simulations of the EDAM process.

6.1.2.3 Coupling between Crystallization and Melting Models

To satisfy the thermodynamics of melting presented above, the condition given by Equation 6.14 was used for coupling the crystallization kinetics model with the crystal melting model.

$$X_{vc}(T) = \begin{cases} T > T_m^*, & X_{vc}(T) - Melting \ \rightarrow Equation\ 6.13 \\ T \leq T_m^*, & X_{vc}(T) - Crystallization \ \rightarrow Equation\ 6.9 \end{cases} \qquad (6.14)$$
$$X_{vc} \in [0\ 1]$$

Where T_m^* is the temperature at the onset of melting which for the carbon fiber PPS of our interest occurs at $523.15\ K$. This coupling is different from the consideration from Brenken [16] where the melting model controls the evolution of crystallinity when the temperature increases ($dT > 0$). Which prevents capturing cold crystallization that can occur by reheating partially crystallized material at temperatures above T_g.

6.2 Characterization of Non-Isothermal Welding Time

The welding time as a function of temperature given by Equation 6.6 was characterized from non-isothermal bonding experiments. Bonding experiments provide measures of the degree of bonding, D_b, which corresponds to the ratio of $G_{IC}(t)$ developed over the maximum $G_{IC\infty}$ that can be developed in a perfectly bonded joint of the same material system. However, these bonding experiments do not provide a direct measure of the welding time. The temperature and time history of the bonding process is also required in order to determine the welding time as a function of temperature. Hence, the following method was developed to characterize the welding time from highly non-isothermal bonding experiments.

First, double cantilever beam (DCB) specimens were printed with different processing conditions, namely varying the temperature of the build plate and the dwell time between the layers defining the plane of crack propagation. Then, utilizing the EDAM process simulation capabilities presented in chapter 5, the temperature history predicted numerically at the interface of crack

propagation was extracted until the onset of crystallization, t_c. In a final step, the welding time described by Equation 6.6 was plugged into Equation 6.5 which predicts the degree of bonding. Given the numerically predicted temperature history, the activation energy E_A and the pre-exponential factor A used in Equation 6.6 were fitted with the experimentally measured degree of bonding and the temperature history in a least square manner. The following three sections present in more details the experimental and simulation procedures utilized for characterizing the welding times as a function of temperature and under highly non-isothermal conditions.

6.2.1 Experimental Characterization of the Degree of Bonding

The degree of bonding is defined here in terms of a ratio of mode-I Critical Energy Release Rates, G_{IC},thus DCB specimens were used to measure this fracture property from specimens fabricated with different degree of bonding. Different degrees of bonding were introduced in printed DCB specimens by varying two printing parameters, namely the temperature of the build plate and a dwell time introduced between the layers defining the interface along the plane of crack propagation. Table 6.3 lists seven printing conditions utilized to characterize the welding time from bonding experiments. The choice of these two printing parameters was in order to introduce different temperature histories at the interface that defines the plane for crack propagation in the DCB

Table 6.3 Printing parameters varied to introduce different degrees of bonding in printed panels used for preparing DCB specimens.

Condition – ID	**Build Plate Temperature** $(\boldsymbol{K})$	**Dwell Time** $(\boldsymbol{s})$
DCB – 488 – 5	488.15	5
DCB – 488 – 10	488.15	10
DCB – 488 – 20	488.15	20
DCB – 488 – 40	488.15	40
DCB – 393 – 10	393.15	10
DCB – 413 – 10	413.15	10
DCB – 523 – 10*	523.15	10
DCB – 523 – 10* – HT	523.15	10

In order to prepare DCB specimens, rectangular panels with dimensions of 100 by 180 mm and with six beads in the thickness direction were printed in CAMRI. Printed beads with dimensions

of 4.7 by 1.3 mm (w, h) were used for preparing these panels. Further, panels were printed with beads oriented in the direction of the longest dimension (180 mm). The printing process of each panel takes around 285 s plus the dwell time listed in Table 6.3.

Three DCB specimens were made from each panel and with dimensions of approximately 25 by 7.8 by 150 mm which are based on the recommendations provided in the ASTM D5528 standard for mode-I Interlaminar fracture toughness [157]. Dimensions and initial crack lengths for each of the 21 DCBs prepared can be found in Table A.19 of the APPENDIX A. The label "Sx" is added at the end of the conditions ID listed in Table 6.3 to identify each specimen by substituting "x" by the number of specimen (1-3). An exception in the dimensions of the printed panel was made for the condition marked with "*" for which six panels with dimensions of 50 by 180 mm were printed. One DCB with the same dimensions was cut out of each panel. These panels were made smaller and printed with the highest build plate temperature to introduce a high degree of bonding. Three out of the six DCB were heat treated after printing at 573.15 K and for approximately 15 min and which are labeled as DCB – 523 – 10* – HT. We will revisit these additional samples while determining the degree of bonding from the values of G_{IC} characterized with the DCBs.

Table 6.4 lists the values of the process variables defined in CAMRI for printing the panels utilized in the characterization of the welding time.

Table 6.4 Process conditions used in CAMRI for printing panels used for preparing DCB specimens.

Process Variable	**Value**
Bead Dimensions - w, h (mm)	4.7, 1.3
Orifice of Extrusion Nozzle (mm)	3.175
Extrusion Temperature (K)	583.15
Printing Speed (mm/s)	91.67
Tamper Speed (SPS)	25
Temperature Nozzle (K)	583.15
Temperature Gear Pump (K)	583.15
Temperature Upstream Connector (K)	573.15
Temperature Extruder Zone 1 (K)	572.0
Temperature Extruder Zone 2 (K)	561.0
Temperature Extruder Zone 3 (K)	561.0

The initial crack required in the DCB specimens was introduced during printing of the panels and between the third and fourth printed layers (middle of the panel thickness). A timed paused equal to the dwell times listed in Table 6.3 was introduced after printing the third layer of a panel. Then, the gantry robot in CAMRI was programed to automatically move to a predefined safe position where a piece of polyimide film was precisely located with the aid of a fixture on top of the third printed layer. A precise location of the polyimide film was crucial to ensure the front of the crack tip is normal to the direction of crack propagation. The polyimide film utilized is manufactured by UPILEX® with an average thickness of 25 μm. The printing process was automatically resumed once the dwell time was reached and three additional layers were printed on top of the previously printed layer. Once the printing process finished, the plates were cooled down for five minutes on top of the build plate. Upon removal, the printed plates were cooled down under natural convection on top of the frame of the CAMRI system. Figure 6.8 shows an example of a printed panel before and after introducing the polyimide film for creating an initial crack.

Figure 6.8 Process for introducing initial crack with a polyimide film during printing of panels utilized in the preparation of DCB specimens.

Prior to cut individual DCB specimens out of the printed plates, steel piano hinges were adhesively bonded at the end with the initial crack. Urethane adhesive (Lord-7542) was utilized for bonding the piano hinges to the printed composite. The surface of the printed plate was cleaned with acetone prior bonding whereas the surface of the hinges was sanded with 320 grit and cleaned with acetone. The plates with bonded piano hinges were precisely cut in a CNC controlled waterjet cutting

system. Figure 6.9 shows one of the DCB specimens utilized in the characterization of the welding time.

Figure 6.9 Example of printed DCB specimen prepared with piano hinges.

DCB specimens were dried in a polymer pellet dryer for 24 hours at $335.15\ K$ to remove moisture before performing the fracture tests. The initial crack length, a_0, was measured from the front of the crack tip defined by the polyimide film to the center of the pin in the piano hinge. The average width, b, and beam thickness, h, of each DCB was computed from three measurements taken along the length of the DCB. The average width, b, thickness, h, and initial crack length, a_0, for the 21 specimens tested are reported in Table A.19 of the APPENDIX A.

Testing of the DCBs was conducted in a universal testing machine MTS®-810 equipped with a 5 KN load cell and under fixed grip conditions to attain stable crack propagation. Per recommendation of the ASTM-D5528 standard [157], a loading rate of $2\ mm/min$ was used for opening the DCB whereas an unloading rate of $10\ mm/min$ was used for closing the DCB. Figure 6.10 shows the setup used in the DCB fracture tested performed in the universal testing machine. Load and displacement were recorded during both loading and unloading at a rate of $10\ Hz$.

A traveling optical microscope (Leica S6D) equipped with a camera (PixeLINK Model PL-B776) was employed to monitor the extension of the crack tip during the fracture test. Frames were recorded at intervals of $0.75\ s$ and throughout the entire fracture test. In order to track the location of the crack tip, a sticker with a printed millimetric scale was attached to the edge of the DCB. This way, the frames recorded with the traveling microscope can be used to track the evolution of the crack tip during the fracture test.

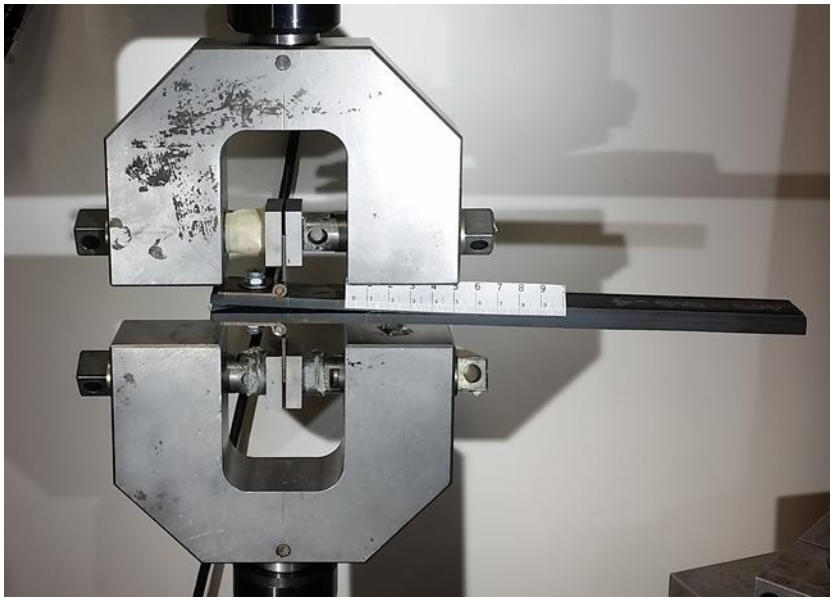

Figure 6.10 Setup used for testing DCB specimens in Universal Testing Machine.

In order obtain multiple measurements from a single specimen, three loading cycles were performed after extending the crack for about 15 mm in each loading cycle. Four crack extensions were estimated using the frames recorded during the fracture test of the DCB including the visual onset of crack extension.

Three methods were utilized to compute the energy release rate, G_I, from the DCB fracture test, namely the Compliance Calibration (CC) method, the Modified Beam Theory (MBT) method and the Modified Compliance Calibration (MCC) method [157, 158]. The approach that yielded the most conservative values of critical energy release rate, G_{IC}, was adopted at the end.
Utilizing the load, P, and the displacement at the load point, δ, recorded during the fracture test, the energy release rate G_I can be estimated with the CC method as given by Equation 6.15.

$$G_1 = \frac{nP\delta}{2ba} \tag{6.15}$$

Where n is a calibration parameter obtained by fitting a straight line in a double logarithm plot of the inverse of the compliance, C, versus the crack length [158]. The compliance is defined as $C = \delta/P$. Additionally, b is the width of the sample and a is the crack length. G_{IC} is obtained with the same expression but at the critical load and displacement associated with each crack length, a.

The second approach used to compute G_{1C} was the MBT method given by Equation 6.16.

$$G_1 = \frac{3P\delta}{2b(a + |\Delta|)} \tag{6.16}$$

In this method, a parameter Δ is added to the prediction made through beam theory in order to account for rotation of the crack tip that is neglected in the beam theory approach. Δ can be obtained experimentally by generating a least squares plot of the cube root of the compliance, $C^{1/3}$, as a function of the crack length, a, [157]. The distance from the origin to the intercept of the least squares plot with the origin determines the correction parameter Δ.

The inverse problem of predicting the flexural modulus of the beam is readily achieved with this approach as given by Equation 6.17.

$$E_f = \frac{64(a + |\Delta|)^3 P}{\delta b h^3} \tag{6.17}$$

Where h is the thickness of the DCB specimen. The flexural modulus estimated with this expression should be independent of the crack length, however, fiber bridging in composites with continuous fibers can lead to an increase in E_f as a function of the crack length, a.

MCC was the last method utilized in the calculation of G_{1C} and it is given by Equation 6.18.

$$G_1 = \frac{3P^2 C^{2/3}}{2A^1 bh} \tag{6.18}$$

The parameter A^1 used in the MCC approach is determined by creating a plot of the crack length normalized by the thickness of the DCB, a/h, as a function of the cube root of the compliance, $C^{1/3}$, [157]. The slope of the line fitted along the experimental data points corresponds to A'. Detailed results are presented herein only for one of the specimens, however, the same analysis and plots were generated for all the specimens and those are provided in Figure A.6 of the APPENDIX A.

Figure 6.11 shows the load-displacement curve for the three cycles utilized in the fracture tests of the printed DCBs. The plots presented next correspond to the data characterized from the DCB – 488 – 5 – S1 specimen. Points of initiation of delamination during the fracture test of the DCB are marked with blue asterisks in Figure 6.11. Similarly, points in the load-displacement curve were a crack was extended are marked with black asterisk.

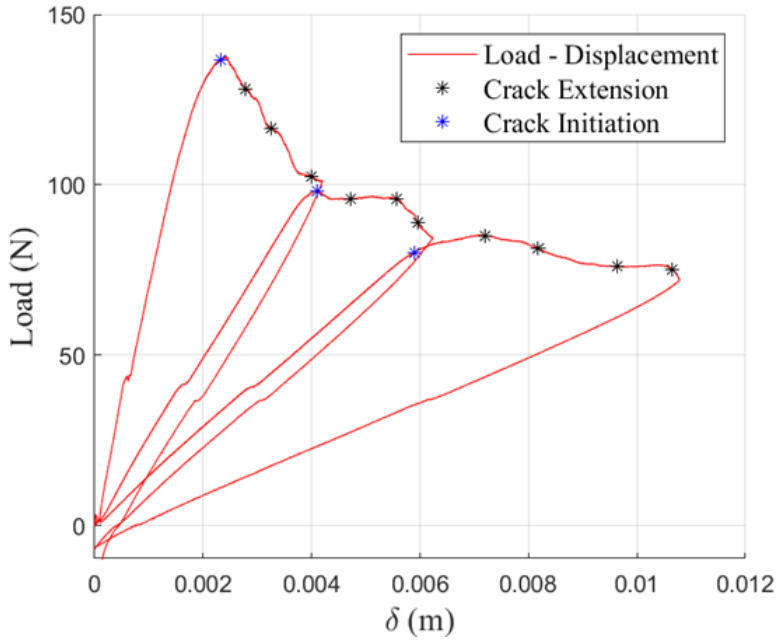

Figure 6.11 Load-displacement curve with three loading cycles
(Data from specimen DCB – 488 – 5 – S1)

In order to utilize the CC method to determine G_{1C} at the points of crack initiation and extension, the parameter n was determined from the slope of the line shown in Figure 6.12.

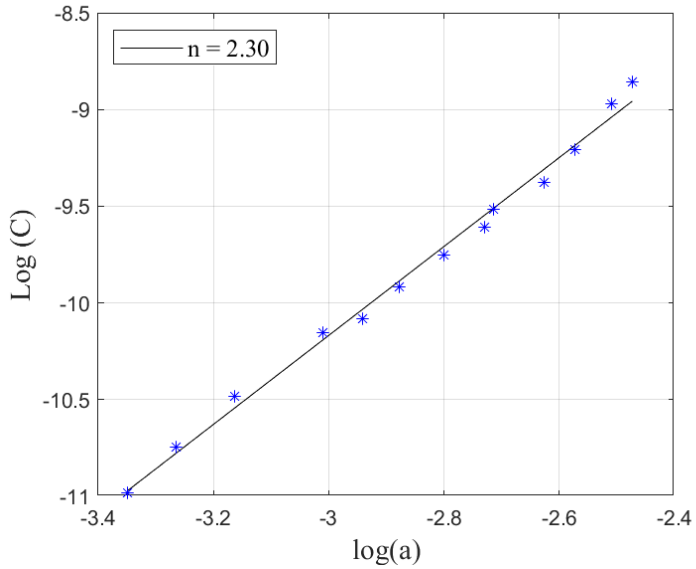

Figure 6.12 Determination of n parameter utilized in compliance calibration method (Data from specimen DCB – 488 – 5 – S1).

Predicting G_{IC} with the MBT method requires the determination of the parameter Δ. Figure 6.13 shows the plot of the cubic root of the compliance to the crack length used in the determination of the parameter Δ.

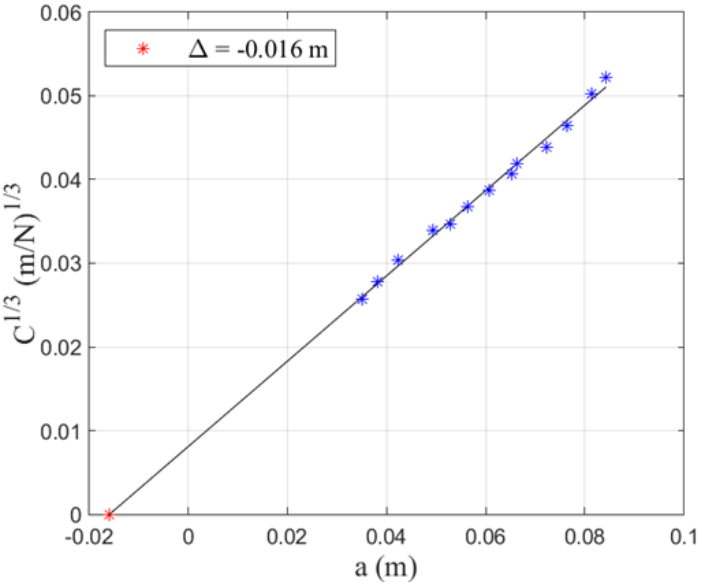

Figure 6.13 Determination of Δ parameter utilized in the modified beam theory method (specimen DCB – 488 – 5 – S1).

Now to estimate G_{IC} using the MCC method, the parameter A^1 was determined from the slope of the linear fit shown in Figure 6.14.

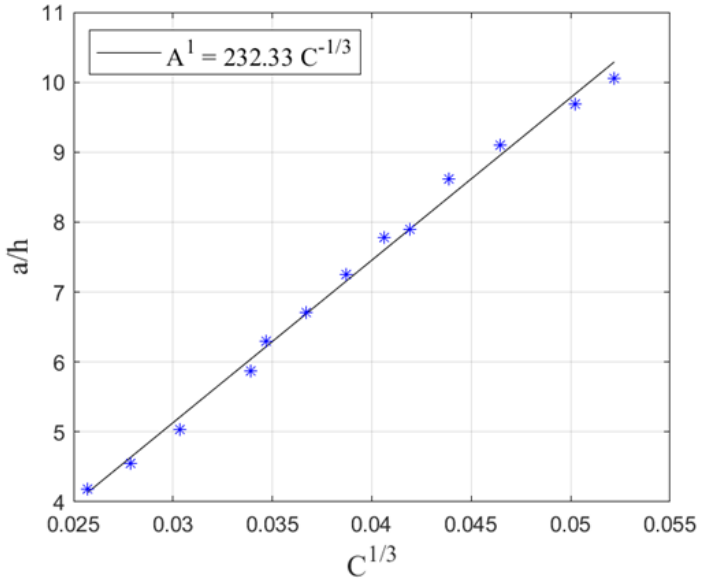

Figure 6.14 Determination of A^1 parameter utilized in the modified compliance calibration method (specimen DCB – 488 – 5 – S1).

After determining the coefficients required for estimating G_{IC} using the aforementioned methods, a delamination resistance curve that shows G_{IC} as a function of the crack length was generated. Since G_{IC} is a material property, it should not change with the crack length. However, slight fluctuations in G_{IC} occurred during crack extension in printed DCBs due to roughness on the plane of crack propagation. Figure 6.15 shows the delamination resistance curve created with the G_{IC} estimated with each of the three aforementioned methods.

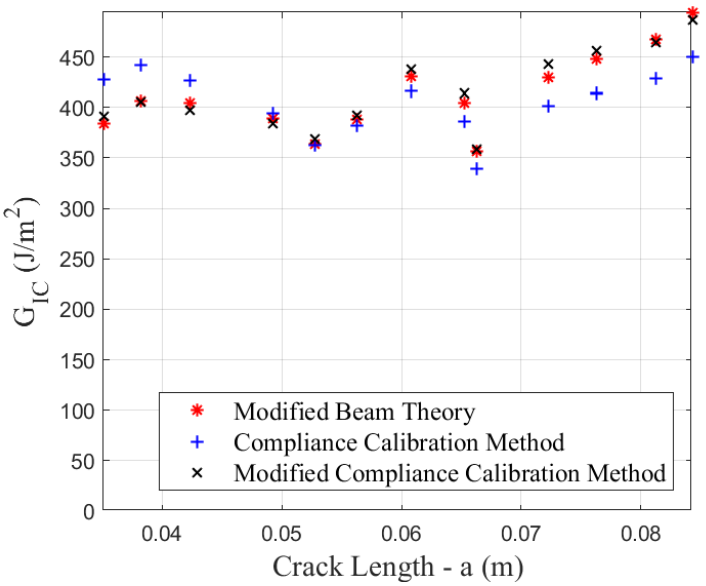

Figure 6.15 Delamination resistance curve from DCB test of specimen DCB – 488 – 5 – S1.

For all the specimens tested, the CC method yielded the most conservative mean values of G_{IC} as well as the smallest standard deviations (SD). Therefore, the estimates of G_{IC} obtained with this method were used. Values for the mean and the standard deviation of the experimentally determined G_{IC} were computed for each of the conditions investigated and considering the results of all the specimens tested.

Table 6.5 Summary of G_{IC} characterized from each set of DCB bonding experiments.

Condition – ID	**Mean** G_{IC} (J/m^2)	**SD** G_{IC} (J/m^2)
DCB – 488 – 5	455	71
DCB – 488 – 10	450	49
DCB – 488 – 20	433	40
DCB – 488 – 40	392	33
DCB – 393 – 10	58	17
DCB – 413 – 10	211	60
DCB – 523 – 10*	502	45
DCB – 523 – 10* – HT	498	60

It was mentioned at the beginning of this section that three additional specimens were printed with the same conditions as DCB – 523 – 10* and heat treated after printing (DCB – 523 – 10* – HT).

The mean G_{IC} characterized from those samples was practically the same than the one reported here for the DCB – 523 – 10*. Therefore, the mean value reported for DCB – 523 – 10* is considered the maximum that can be achieved for this material system and under the printing conditions used in CAMRI. The degree of bonding, D_b, is then determined with respect to this value.

6.2.2 Temperature History Informed from EDAM Process Simulations

The previous section presented the mechanical characterization of G_{IC} performed with DCBs prepared with different processing conditions. However, the temperature history that led to the G_{IC} characterized experimentally is still required in order to be able to characterize the welding time, $t_w(T)$, given by Equation 6.6 for our material of interest.

In order to estimate the transient temperature evolution at the interface formed between layers three and four of the plates printed for preparing DCB specimens, a transient heat transfer analysis of the printing process was carried out with our capabilities for EDAM process simulation. Details on the heat transfer analysis were already provided in chapter 5. It should be noted that this method was preferred against attempting to measure the temperature at the interface experimentally which is not feasible.

The EDAM process simulation is driven with the event series of the printing process. Such an event series was generated in CAMRI with a user defined program as explained before. A voxel mesh of the printed plates was created utilizing the script described in the chapter 4 for generating voxel meshes from event series. Three and four linear solid elements type DC3D8 was used to represent a printed bead in the height and width directions, respectively. This resulted in the mesh shown in Figure 6.16 which contains 227,138 voxel elements with dimensions of 1.18 by 1.18 by 0.43 mm.

The same conditions used for printing the plates in CAMRI which are listed in Table 6.4 were used for the EDAM process simulation. Additionally, the process conditions listed in Table 6.6 were used for convection, radiation and heat losses through the tamper. While the different build plate temperature conditions used for printing the plates were specified directly in the EDAM process simulations, the dwell times were explicitly introduced in the event series. Therefore, a different event series was created for each of the dwell time conditions. A total of six simulations

of the printing process of the plate were performed since only the temperature histories of the plates that yielded a value for G_{IC} lower than the one assumed perfectly bonded are required.

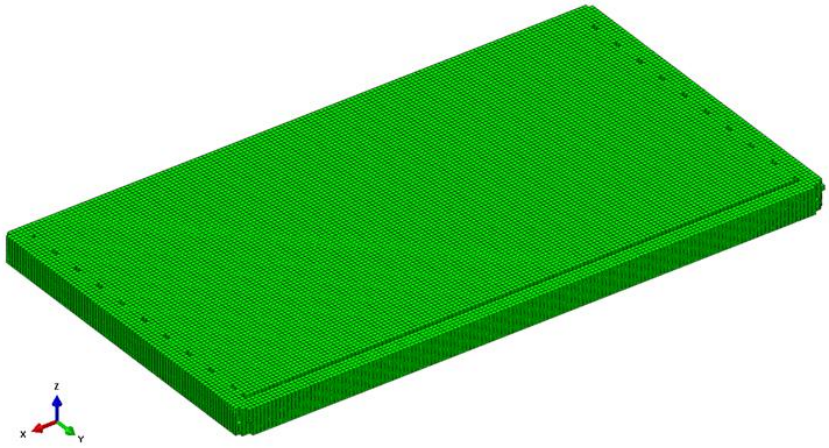

Figure 6.16 Voxel mesh used in EDAM process simulation of plates used for preparing DCB specimens.

In order to obtain an estimate of the temperature near the interface, the temperature and crystallinity histories were extracted at the integration point of a representative element located at the bottom of the fourth layer. Since the temperature history extracted from the element's integration point is used to calibrate the welding times, the estimates of degree of bonding at the interface become non-local and thus these become relevant only at the same geometrical locations. Such a location is $0.215\ mm$ above the interface between two adjacent layers. A better approach would be to use local quantities (temperature measured at the nodes), however, this was chosen due the implementation of the bonding model which also computes the degree of bonding in a non-local sense. Further details and suggestions for better local implementations are provided in the section Mesh Implications.

Table 6.6 EDAM process conditions used in simulation of the printing process of the plates.

Process Variable	**Value**
Ambient Temperature Convection (K)	303.15
Ambient Temperature Radiation (K)	423.15
Material Deposition Temperature (K)	583.15
Heat Flow Removed by Tamper (W)	49.0

Table 6.7 continued

Build Plate Temperature (K)	Given in Table 6.3

The evolution of crystallinity was computed with the approach presented above and the model parameters characterized by Brenken [16]. Figure 6.17 shows four stages in the simulation of the printing process of the plate used for preparing the DCB – 413 – 10 specimens.

Since the temperature history across our plane of interest in the printed plate did not change significantly except for the regions near the edges, the temperature history was inferred from an element located at the middle of the plate.

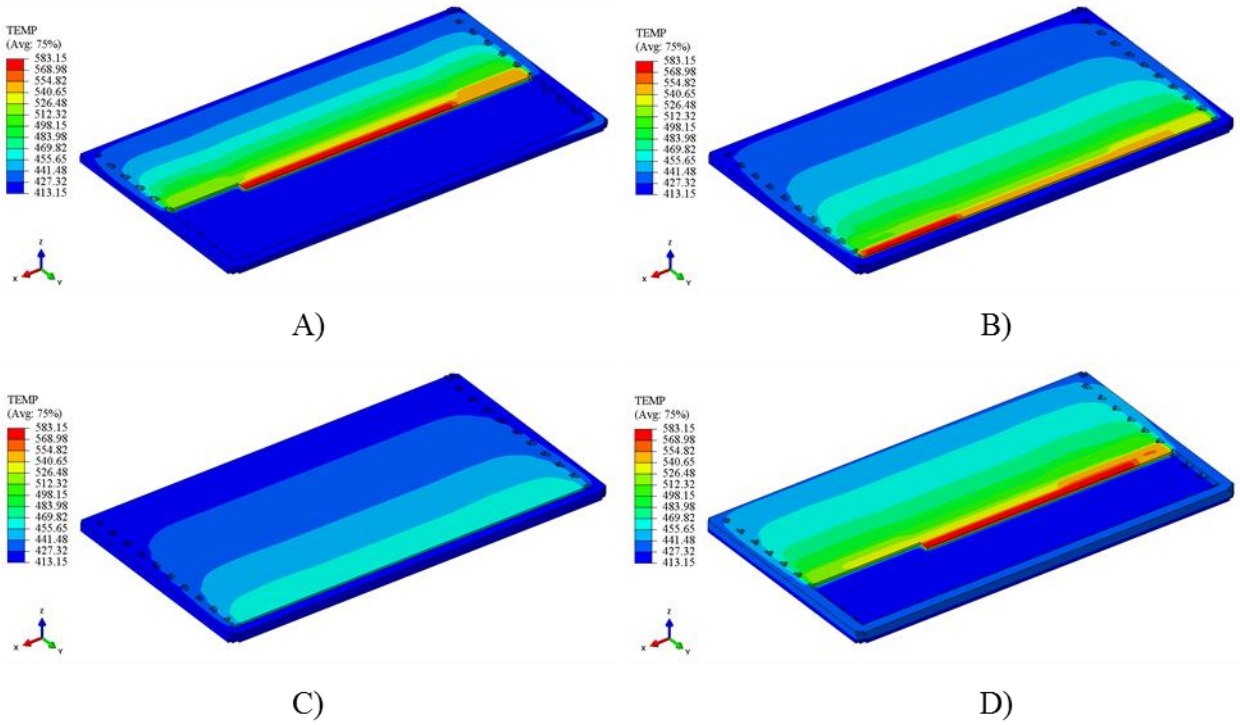

Figure 6.17 Different stages in the printing process of plate with conditions for DCB – 413 – 10 specimens. A) Printing second layer. B) End of printing of third layer. C) End of dwell time between third and fourth layers. D) Printing fourth layer after dwell time.

The temperature history required to characterize, t_w, only comprises until the time at the onset of crystallization, t_c, thus temperature was extracted until the crystallinity reached a critical value, X_{vc}^{crit}, equal to 0.05. This is due to the fact that crystallization hinders the mobility of polymer

chains, thereby rapidly increasing the welding time and precluding the progression of the degree of bonding.

Figure 6.18 shows the temperature histories estimated at the interface between the third and fourth layers for each of the plates printed for DCB preparation and until the time, t_c, the degree of crystallinity reached the critical value, X_{vc}^{crit}. Since the plates are relatively thin, only around 7.8 mm, heat conduction dominates the cooling process of the first three layers constituting one half of the DCB specimen whereas the heat losses through radiation and convection occurring during the dwell time have a weaker influence.

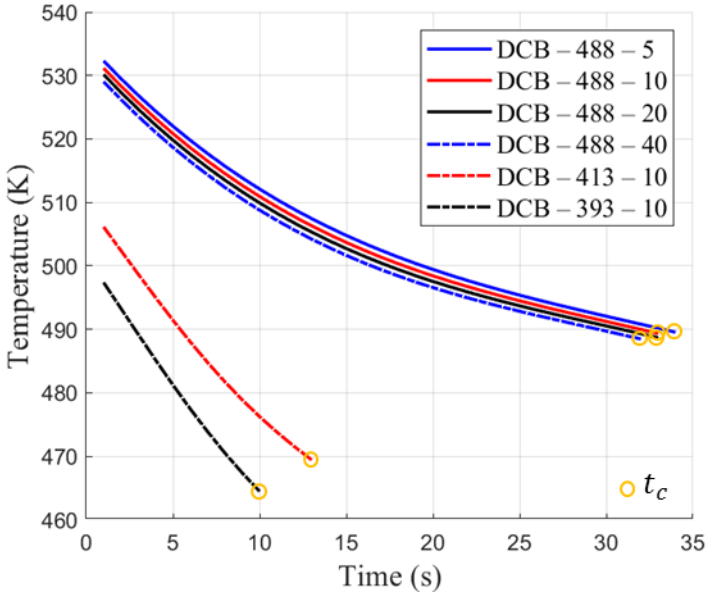

Figure 6.18 Temperature histories estimated near the interface between the third and fourth layers.

6.2.3 Calibration of Welding Time

Values for fracture property G_{IC} were experimentally characterized from plates printed with different processing conditions and the temperature histories at the interface corresponding to the plane of crack propagation were estimated from simulations of the printing process of the plate. We now take the ratios of G_{IC} to $G_{IC\infty}$ to determine the degree of bonding as given by Equation 6.5. Table 6.8 lists the degree of bonding estimated for each of the conditions used for preparing DCB specimens.

Table 6.8 Summary of D_b determined from experimental measurements of G_{IC}.

Condition – ID	**Mean** $\boldsymbol{D_b}$	**SD** $\boldsymbol{D_b}$
DCB – 488 – 5	0.91	0.14
DCB – 488 – 10	0.90	0.09
DCB – 488 – 20	0.86	0.08
DCB – 488 – 40	0.78	0.06
DCB – 393 – 10	0.12	0.03
DCB – 413 – 10	0.42	0.12
DCB – 523 – 10*	1.0	0.08

The degree of bonding here is interpreted as the result of the combination of diffusion of polymer chains and crystallinity developed across the interface. In other words, it is assumed that the amount of diffusion achieved at the interface controls the crystalline structure developed at the interface and thus the resulting interfacial fracture properties. Hence, the welding time can be estimated as a function of temperature utilizing the experimentally measured degree of bonding and predicted temperature histories. By plugging in Equation 6.6 into Equation 6.5, the expression given by Equation 6.19 is obtained.

$$D_b(t) = \left[\int_0^{t_c} \frac{1}{A \cdot exp\left(\frac{E_A}{RT(\tau)}\right)} d\tau \right]^{\frac{1}{2}}, t_c \in \{t \ \ s.t. \ \ X_{vc} < X_{vc}^{crit}\} \tag{6.19}$$

Then, given the degree of bonding attained with different temperature histories, $T(t)$, the activation energy, E_A, and the pre-exponential factor, A, can be determined by minimizing the square of the error defined by the difference between the left hand side of Equation 6.19 and the right hand side of the same Equation. The non-linear least squares data fitting tool lsqcurvefit available in Matlab® was used to find the optimal values for E_A and A considering the six conditions listed in Table 6.8 and the six temperature histories given in Figure 6.18. Since lsqcurvefit utilizes a vector-valued function, fourth order polynomials were used to fit the temperature profiles shown in Figure 6.18. The fitted temperature profiles were then used inside the integral function given by Equation 6.19. Table 6.9 lists the values obtained for the activation energy, E_A, and the pre-exponential factor, A.

Table 6.9 Parameters determined for the welding time defined with Arrhenius equation.

Parameter	Value
$E_A\ (J/mol)$	$6.803 \cdot 10^4$
A	$4.258 \cdot 10^{-6}$

6.3 Numerical Implementation of Fusion Bonding Model for EDAM Process Simulations

The fusion bonding model was implemented in a UMATHT® subroutine for predicting the degree of bonding in the framework of EDAM process simulations. The implementation presented here has been presented before but it is provided here as well for completeness of this chapter [102]. This subroutine is called at each material point and at every global iteration. The information passed into the subroutine is used to compute the increment of the degree of bonding and evolution of crystallinity at each increment of the finite element solution. The flowchart in Figure 6.19 summarizes the implementation performed inside the UMATHT® subroutine to compute the degree of bonding considering the evolution of temperature and crystallinity.

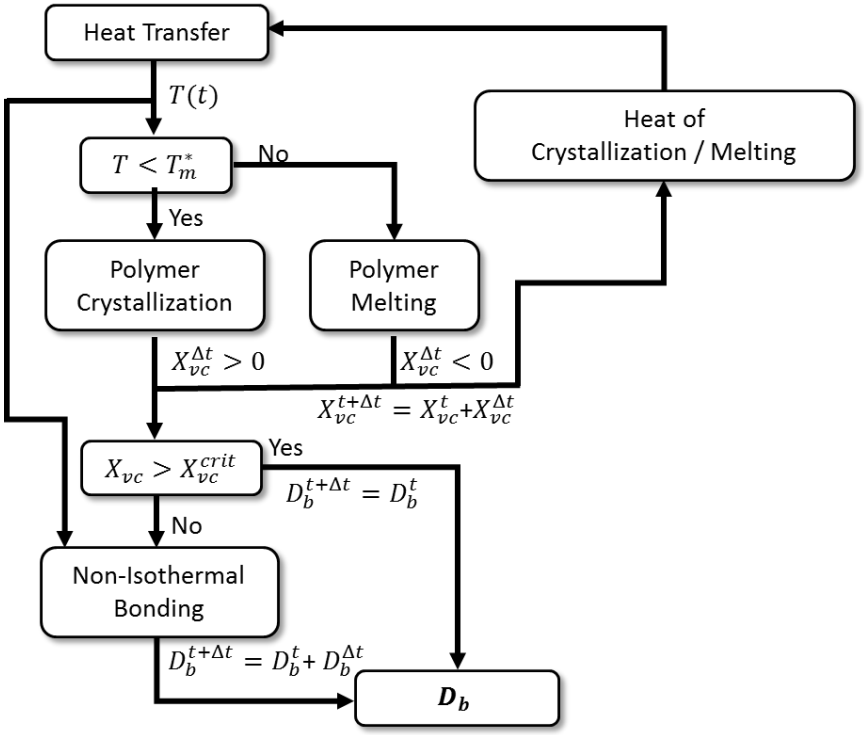

Figure 6.19 Flowchart of fusion bonding model implemented in a UMATHT® subroutine to predict the degree of bonding.

The first condition checked after a call to the UMATHT® subroutine is the activation time, t_{act}. If the time at the beginning of an increment is greater than the activation time, the execution sequence given in the flowchart of Figure 6.19 is performed, otherwise no action is taken. If the time increment, Δt, at which the loop in Figure 6.19 is executed is small enough, the order of the sequence used for computing the evolution of crystallinity and the degree of bonding becomes irrelevant. In the case the time at the beginning of an increment is greater than the activation time, the first condition checked determines whether the crystallization kinetics model or the polymer melting model control the evolution of crystallinity. The crystallization kinetics model and the polymer melting model are given by Equation 6.9 and Equation 6.13 , respectively. The implementation of the models for crystallization kinetics and for polymer melting was performed by Brenken et al [72], however, the coupling between these two models was change here. After the evolution of crystallinity is computed, a condition that the crystallinity is not greater than a critical degree of crystallinity equal to five percent is checked. If this is not true, the degree of bonding is computed utilizing Equation 6.5. The integral inside this equation is approximated numerically utilizing the Simpson's 3/8 rule with a step size h as given by Equation 6.20. The limits of the analytical integral in the left-hand side (LHS) are defined from the time the element is activated in the process simulation t_{act}, to the time crystallization reaches the critical limit, t_c. The numerical integration on the right-hand side (RHS) is carried out at each time increment Δt.

$$\int_{t_{act}}^{t_c} \frac{1}{t_w\big(T(\tau)\big)}\, d\tau \approx \sum_{i=1}^{t_c/\Delta t} \frac{3h}{8}\big(f(\tau_0) + 3f(\tau_1) + 3f(\tau_2) + f(\tau_3)\big) \tag{6.20}$$

The functions $f(\tau_n)$ are replaced by the inverse of the welding time evaluated at time increments of h as given by Equation 6.21. The temperature T_n used at each of the time increments h is linearly interpolated from the temperature passed into the UMATHT® at the beginning and at the end of a time increment Δt. It should be noted that $h \ll \Delta t$.

$$f(\tau_n) = \frac{1}{t_w\big(T_n(\tau_n)\big)} \quad n = 0{,}1 \ldots 3 \tag{6.21}$$

The welding time, t_w, is calculated with the Arrhenius expression given by Equation 6.6 and utilizing the parameters provided in Table 6.9. In the case of utilizing long time increments in the solution of the finite element problem, the approximation of the time integral in Equation 6.20 is improved by splitting the time increment, Δt, into smaller sub-increments Δt_{sub}. The final expression for the degree of bonding is given by Equation 6.22.

$$D_b(t) = \left[\sum_{i=1}^{t_c/\Delta t} \frac{3h}{8} \left(f(\tau_0) + 3f(\tau_1) + 3f(\tau_2) + f(\tau_3) \right) \right]^{\frac{1}{2}} \tag{6.22}$$

The evolution of both the degree of crystallinity and the degree of bonding are tracked utilizing solution-dependent state variables in Abaqus© which are updated at the end of the increment in the UMATHT® subroutine.

6.3.1 Mesh Implications

The implementation for the degree of bonding presented above provides estimates of the degree of bonding at the interface in a non-local sense. This results from the fact that calculations of the degree of bonding are performed at the integration points of an element and not at the nodes located at the interface between two layers. The latter approach will be more accurate for capturing the local bonding process at the interface between two adjacent layers. This implementation is possible in Abaqus© but requires tracking elements that share nodes across an interface between adjacent layers. This way, two activation times, one from an element below the interface and other from an element above the interface, will provide the right times to compute the evolution of crystallinity and degree of bonding. However, such an implementation is left for future improvements in the bonding predictions.

Owing to the same implication of computing the degree of bonding in a non-local sense, temperature profiles used in the calibration of the welding times were also extracted at locations near the interface between adjacent layers. Such a location can be either at the integration point or at the centroid of the element located above the interface since the degree of bonding is computed from the time an element is enabled, t_{act}. As a result, the predictions of the degree of bonding will be accurate only at elements located at the bottom of a bead and at the location used for extracting

temperatures for calibrating the welding time. Hence, the sensitivity of this approach to different mesh densities is given by the interpolation from the integration points to the location used for extracting the temperature profiles utilized in the calibration of the welding time. In the current case, the temperature profiles were extracted from a position located 0.215 mm above the interface between two layers.

In order to assess the interpolation of the degree of bonding at this location, the printing process of the plate shown in Figure 6.17 was performed with three additional mesh densities. The degree of bonding was extracted along two lines defined on a XY plane located $0.215\ mm$ above the interface between the layers three and four. These lines were oriented along the length and width of the plate, X and Y directions, respectively, and centered at the middle in each direction. The degree of bonding was interpolated at 20 points equally spaced along each of these lines. A mean value for the degree of bonding was computed along both directions utilizing the interpolated degree of bonding.

Table 6.10 Average degree of bonding obtained with different number of elements through the thickness of the bead.

Element Size - mm (h_e, w_e)	**Number of Elements per Bead (h_n, w_n)**	**D_b averaged over the X direction**	**D_b averaged over the Y direction**
$0.65, 1.567$	$2\ , 3$	0.343	0.368
$0.43, 1.567$	$3\ , 3$	0.383	0.399
$0.325, 1.567$	$4\ , 3$	0.399	0.401
$0.26, 1.567$	$5\ , 3$	0.414	0.411

The average results in Table 6.10 show that for a mesh density equal or finer than the mesh size used for calibrating the welding times (3 by 3 elements per bead), the predictions made vary by less than 8% with respect to the mean D_b measured experimentally (Table 6.8). The D_b interpolated in the mesh with only two elements was under predicted by around 10%. Therefore, a minimum of three elements through the thickness is recommended.

6.4 Verification of Degree of Bonding Predictions

In order to verify the degree of bonding predicted with the simulation approach presented throughout this chapter, the printing process of the plates used for preparing DCB specimens was

simulated. Event series created in the first place for predicting the temperature evolution near the interface where bonding occurs were utilized again. The implementation of the bonding model presented in the flowchart of Figure 6.19 was utilized with the parameters calibrated for the welding time given in Table 6.9. Also, the parameters for the crystallization kinetics and melting model given in Table 6.1 and Table 6.2, respectively, were utilized. Further, the temperature condition given by Equation 6.14 was used to define the coupling between the crystallization kinetics model and the polymer melting model.

Figure 6.16 shows the voxel mesh used in the simulation of the printing process of the plates and which contains $227{,}138$ voxel elements with dimensions of 1.18 by 1.18 by $0.43\ mm$. The conditions utilized in the EDAM process simulation are summarized in Table 6.11.

Table 6.11 Process conditions utilized in EDAM process simulation of printed plates used for validating prediction of D_b.

Process Variable	**Value**
Ambient Temperature Convection (K)	303.15
Ambient Temperature Radiation (K)	423.15
Material Deposition Temperature (K)	583.15
Heat Flow Removed by Tamper (W)	49.0
Build Plate Temperature (K)	Given in Table 6.3

The degree of bonding was extracted along two lines defined on a XY plane located $0.215\ mm$ above the interface between the layers three and four. These lines were oriented along the length and width of the plate, X and Y directions, respectively, and centered at the middle in each direction. The degree of bonding was interpolated at 20 points equally spaced along each of these lines. A mean value for the degree of bonding was computed along both directions utilizing the interpolated degree of bonding. Figure 6.20 shows the degree of bonding developed at the XY plane mentioned above.

As shown by Figure 6.20, the degree of bonding estimated at the plane of interest is fairly uniform. The small local fluctuations are caused by the discrete activation by segments of bead (multiple elements at a time), however, improvements can be made in the future to remove these effects. We can now compare the experimentally determined D_b reported in Table 6.5 to the average values obtained in the EDAM process simulation of the plate. Figure 6.21 compares the average degree of bonding predicted in the EDAM process simulation to the experimentally

determined D_b. The blue error bars in the experimental data indicate one standard deviation from the mean value.

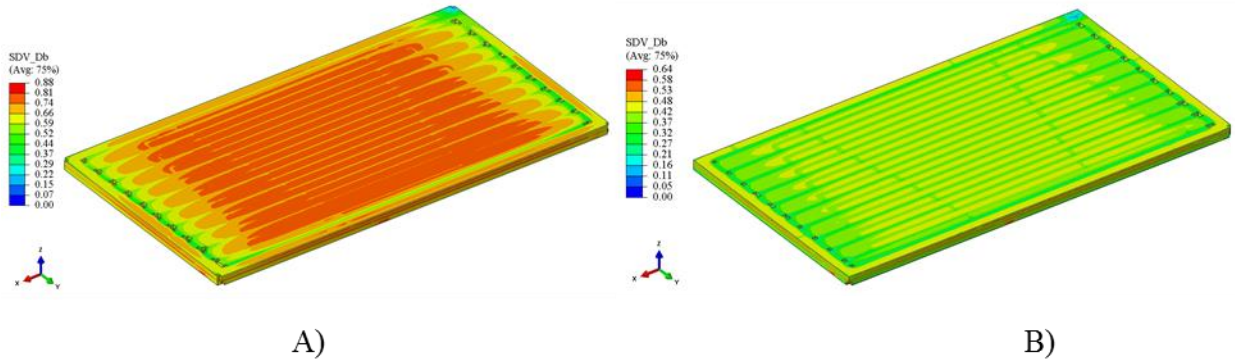

Figure 6.20 Examples of degree of bonding predicted in printed plates.
A) Condition DCB – 488 – 10. B) Condition DCB – 413 – 10.

Great correlation between experimental and predicted degrees of bonding was obtained for five of the conditions as shown in Figure 6.21 whereas the prediction for the condition DCB – 413 – 10 was significantly overestimated.

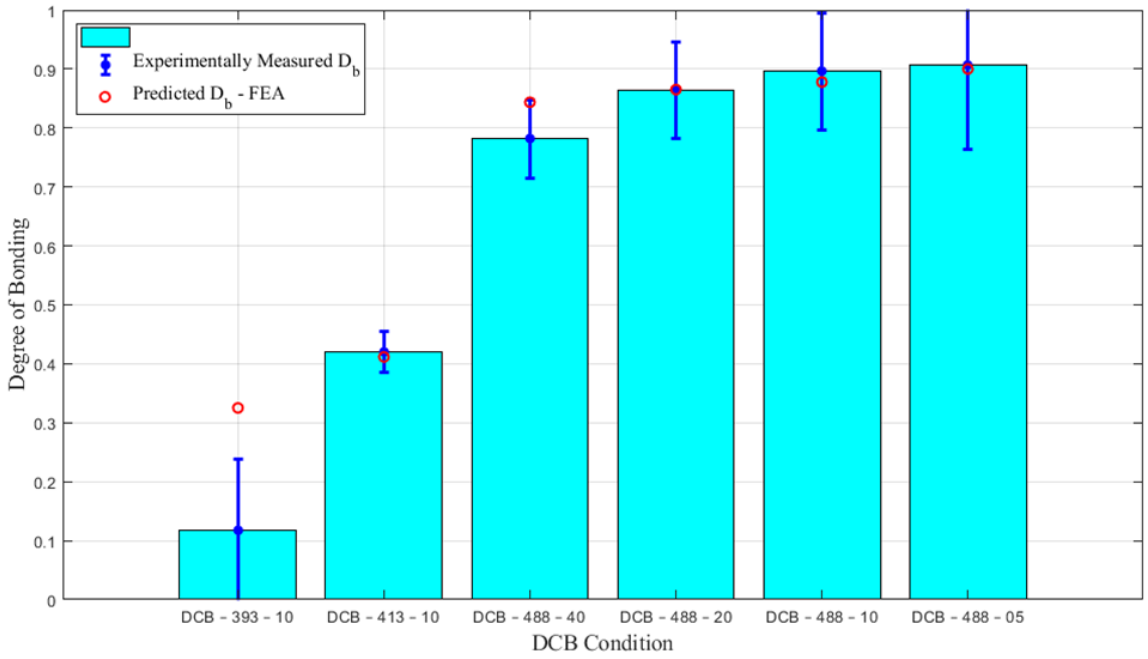

Figure 6.21 Comparison of experimentally characterized and predicted D_b.

Notice also the large standard deviation in this experimental condition for the low mean value. This suggests that fusion bonding which requires melting and crystallization through the interface, did not occurred here and only secondary bonding, namely mechanical interlocking through the roughness of the printed surface and nucleation at the interface, provided such a residual resistance. This also shows that this type of conditions is not captured with the non-local approach implemented here. A local approach needs to be used to precisely capture if melting occurs at an interface. As a result, predictions made within the range of calibration can be used with confidence whereas degrees of bonding predicted below 0.4 should be considered bonding by secondary mechanisms. Additional experimental results would be required to define this limit more precisely. The following section shows additional experimental results to support the conclusion that no fusion bonding occurred under the conditions used to prepare the DCB – 413 – 10 specimens.

6.4.1 Inspection of Crack Propagation Path

To provide more physical evidence of the difference in fracture behavior of the different conditions used for preparing DCB specimens, the crack propagation path of two conditions were inspected. Conditions that yielded the highest and lowest degree of bonding, DCB – 488 – 5 and DCB – 393 – 10, respectively, were investigated. Ideally, the crystalline microstructure formed across the plane of crack propagation should be investigated in an optical transmission microscope under cross polarized light. However, the high carbon fiber content precludes the transmission of light even through a thin section of a sample. Multiple attempts were made to prepare samples by cutting thin slices from a plane perpendicular to the plane of crack propagation and normal to the beam direction which was mounted on epoxy resin to allow for polishing. Nevertheless, the crystalline microstructure was altered perhaps due to friction heating during polishing and thus erasing the crystalline microstructure.

After this attempt, a second approach consisted of preparing samples for optical microscopy cut from the edge of a DCB near the crack tip. Such a preparation involved polishing the section extracted from the edge of the DCB to obtain a mirror like finish. The surfaces prepared for each DCB condition were scanned along the region of crack propagation in a reflected light microscope (Leica DMI5000M). Nevertheless, only small differences along the path of crack propagation were observed with the 50X objective used for capturing these images.

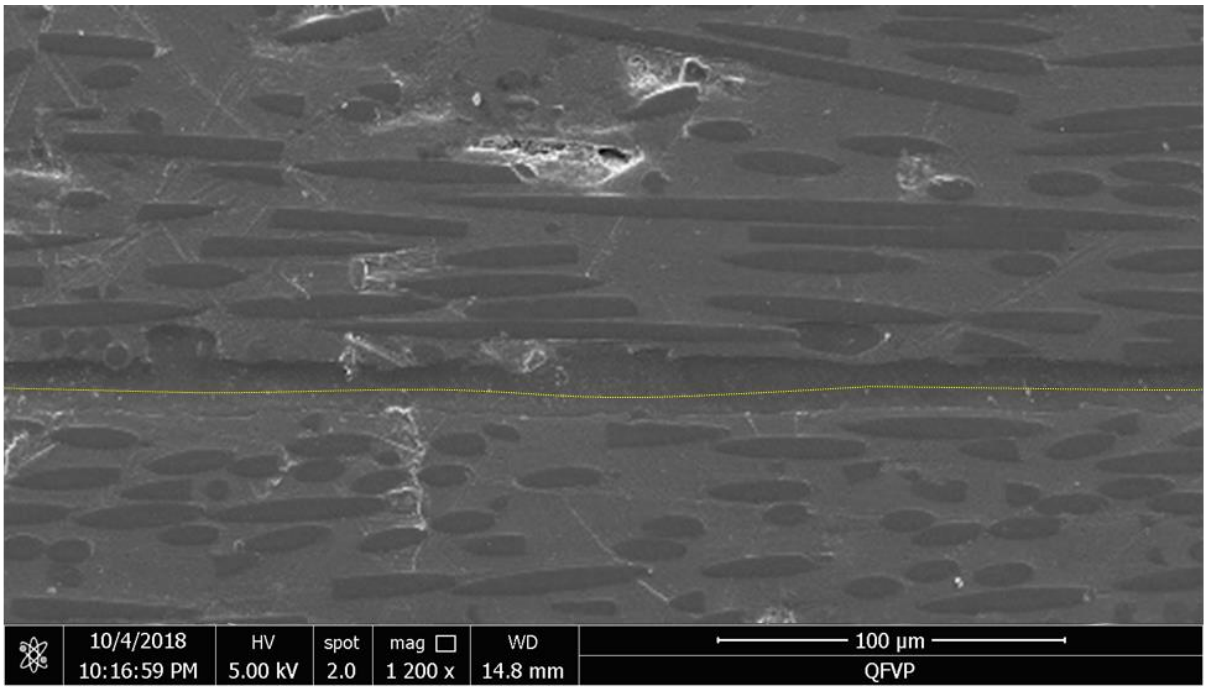

A)

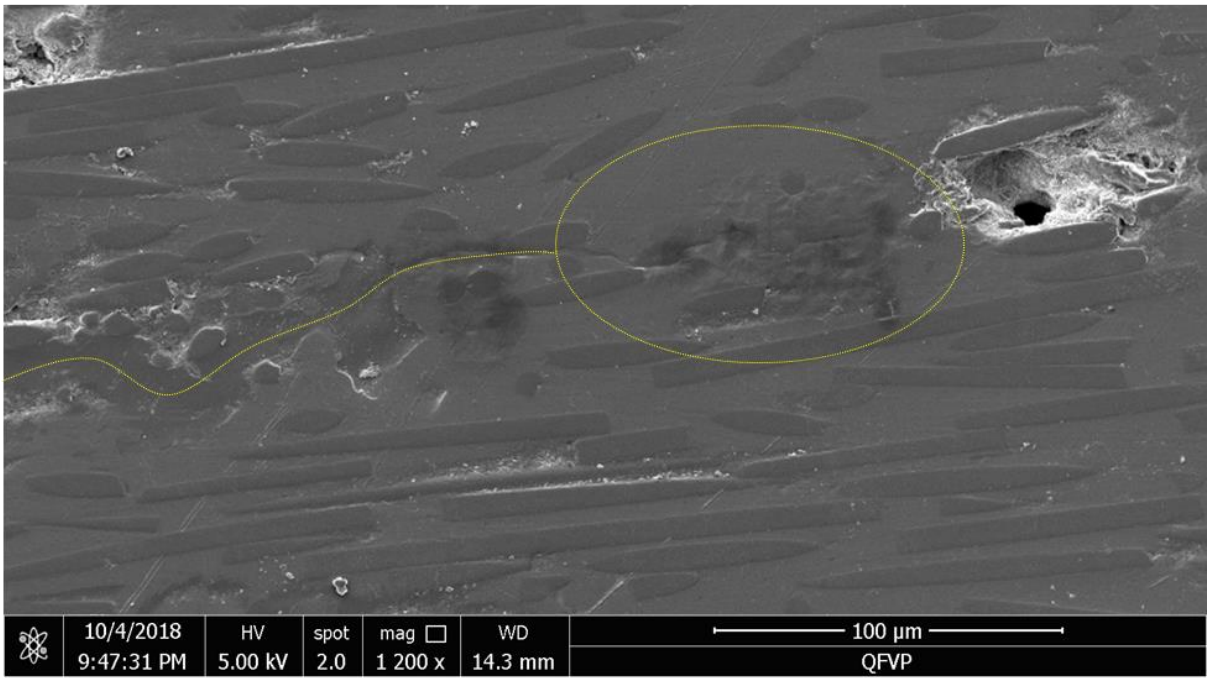

B)

Figure 6.22 SEM micrographs taken from the edge of DCB specimens and highlighting the path of crack propagation. A) DCB – 393 – 10 – S1. B) DCB – 488 – 5 – S2.

In a third investigation, the same specimens were investigated under a Scanning Electron Microscope (SEM). The already polished surfaces were sputter coated with a thin film of gold/palladium to make the surface of the specimens electrically conductive. Figure 6.22 shows the microstructures captured from the edge of a specimen of the types DCB – 488 – 5 and DCB – 393 – 10, respectively. These SEM microstructures were captured with a back-scattered electrons detector in a SEM model Quanta 650 FEG. The path of crack propagation is indicated with a yellow dotted line in both figures. Figure 6.22-A does not show a crack tip since the specimen DCB – 393 – 10 – S1 was fully opened after the fracture test. A smooth and continuous crack path is observed for the specimen of the family DCB – 393 – 10, which suggest that crystallization did not occur across the interface. Instead, polymer crystals likely nucleated from the surface of the printed substrate due to the large degree of supercooling [154].

On the other hand, multiple spherulitic structures were found along the path of crack propagation in the specimen of the family DCB – 488 – 5. Figure 6.23 provides a closer view to the crack tip circled in Figure 6.22-B.

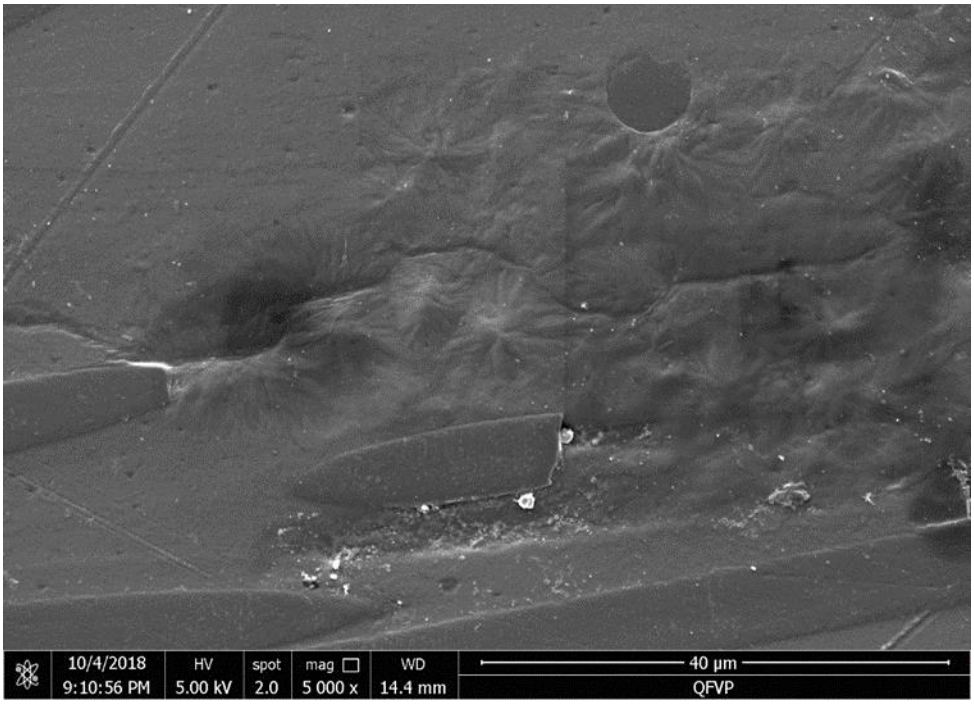

Figure 6.23 Closer view to region around crack tip in DCB – 488 – 5 – S2.

Unlike the flat path of crack propagation developed with the other set of processing conditions, a more complex undulant path was developed in the specimen that developed crystallinity across the interface. From the closer view around the crack tip in Figure 6.23, it seems like the crack found the least resistance path to propagate across the impingement of two adjacent spherulitic structures. Which is suggested to be the cause for the undulant path of crack propagation.

6.5 Demonstration of Degree of Bonding Predicted in EDAM Process Simulations

In order to illustrate variations in degree of bonding that can be developed within a printed part due to variations in temperature and crystallization histories, the simulation of the printing process of a bell is presented. The geometry of a bell was chosen due to the changes in layer time arising while printing this geometry with a constant speed. Figure 6.24 shows the geometry of a bell printed with 50% by weight carbon fiber reinforced PPS and the voxel mesh used to simulate the EDAM process.

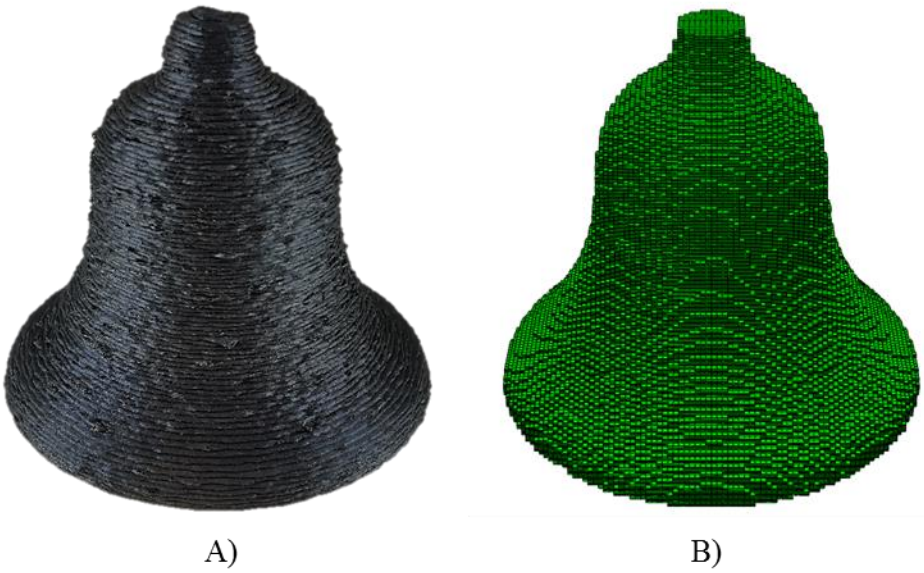

Figure 6.24 Geometry of additively manufactured bell shape. A) Bell printed in CAMRI with 50% by weight of CF-PPS. B) Voxel mesh of the bell used in the EDAM process simulation.

This bell shape was printed in the CAMRI system at a relatively low printing speed ($33\ mm/s$) in order to allow the printed material to cool down and to develop enough stiffness to support

subsequent layers. Otherwise, the geometry may collapse under its own weight and with the action of the tamper. Despite these considerations, sagging is still noticeable in the region around the tip of the bell.

The event series required for the EDAM process simulation of the bell was generated using the user defined program executed in CAMRI. Utilizing this event series, the voxel mesh shown in Figure 6.24-B was created and in which a printed bead is represented with three and four elements through the thickness and width, respectively.

The transient heat transfer analysis presented in chapter 5 was performed for the printing process of the bell. A relatively low build plate temperature of 393.15 K was used to rapidly cool down and solidify the initial layers with the goal of rapidly develop stiffness to support subsequent layers. Since a relatively low build plate temperature was used in the printing process of the bell, the ambient temperature for radiation, $T_{\infty,r}$, is also lower than in previous examples. The ambient radiation temperature was estimated following the recommendations provided in chapter 5. The thermal energy removed during material compaction was also reduced compared to previous examples due to a significant reduction in printing speed with respect to the conditions used to characterize compaction heat losses. Characterizing the tamper heat losses for different printing speeds is left for future work. Furthermore, the exposed surface area undergoing convection and radiation heat losses is overestimated with the voxel mesh used to model the bell which is caused by the scalloped representation of the curved shape of the geometry attained with the voxel elements. Future improvements to the implementation of the heat transfer analysis include accounting for the overexposed area in curved regions of a part. This results in overestimating the cooling behavior predicted for the bell and thus this is only presented to illustrate the variations in degree of bonding that can be developed within a part. Table 6.12 lists the process parameters utilized in the transient heat transfer analysis carried out in the EDAM process simulation of the bell.

Table 6.12 Process parameters used in the EDAM process simulation of the bell.

Process Variable	**Value**
Ambient Temperature Convection (K)	303.15
Ambient Temperature Radiation (K)	423.15
Material Deposition Temperature (K)	573.15
Heat Flow Removed by Tamper (W)	20.0

Table 6.13 Continued

Build Plate Temperature (K)	393.15
Printing Speed (mm/s)	33

The model for fusion bonding implemented in the UMATHT© subroutine provided predictions of the degree of bonding in the EDAM process simulation of the bell. The fusion bonding model is illustrated in the flowchart shown in Figure 6.19 whereas the autohesion model, the polymer crystallization model and the polymer melting model are given by Equation 6.5, Equation 6.9 and Equation 6.13, respectively.

Figure 6.25 shows on the left the evolution of the degree of bonding, D_b, and on the right the evolution of the degree of crystallinity, X_{vc}, predicted in the EDAM process simulation of the bell for the following instants of time: A) after $320\ s$, B) after $640\ s$, C) at the end of the printing process of the bell and D) $90\ s$ after the printing process of the bell was concluded. This set of figures illustrates the fusion bonding scenarios of the first and second kind described previously and illustrated in Figure 6.5-A where polymer crystals develop across an interface between adjacent layers. In this scenario, polymer chains can diffuse across an interface until the crystallization front reaches the interface, thereby creating polymer crystals that involve polymer chains from the two layers involved in the interface. A condition of the third kind where crystallinity is not developed across an interface also occurs in the first layers of the bell. This is due to the rapid cooling and therefore the rapid initiation of crystallization in the first layers which is caused by the relatively low build plate temperature used in the printing process of the bell. The low degree of bonding developed across the initial layer has been experienced while detaching printed bells from the build plate wherein the first one or two layers are readily detached from the rest of the printed part.

The crystallization front evolving in the same direction temperature gradients develop is also illustrated in Figure 6.25 wherein crystallization initiates near the build plate and progresses along the height of the bell. Also, the crystallization front lags behind the material deposition front in this example which is ideal for fusion bonding since it allows for polymer diffusion across the interface. The rapid cooling of the first layers due to the relatively low build plate temperature condition precluded developing the maximum crystallinity in the first layer which corresponds to a degree of crystallinity of 0.84.

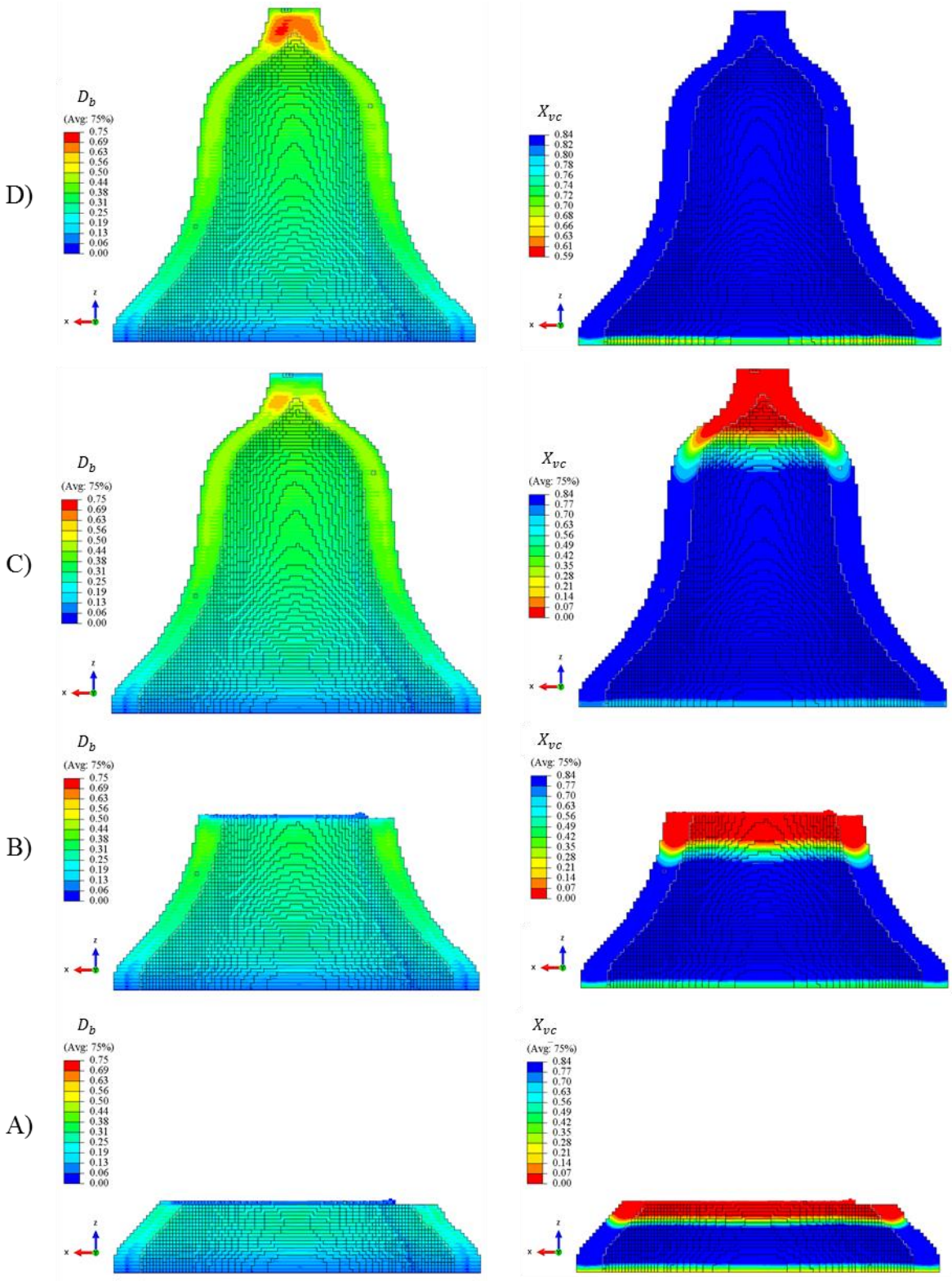

Figure 6.25 Evolution of the degree of bonding, D_b, and the degree of crystallinity, X_{vc}, predicted in the EDAM process simulation of the bell.

The example of the bell provided in Figure 6.25 demonstrated the variations in degree of bonding that can occur through a part due to different cooling and crystallization histories. Hence, the fusion model presented herein stablished a relation between processing conditions used for part manufacturing and the interlayer fracture properties in a printed part.

Utilizing this fusion bonding model, investigations can be carried out to address questions like the dependence of the dimensions of the printed bead on the minimum layer time to develop acceptable bonding between layers printed with semi-crystalline polymeric materials. Such a dependence results from the following physical observations. As the dimensions of the bead are increased, the ratio of the volume to the exposed surface increases and thus the thermal energy lost through convection and radiation with respect to the thermal mass deposited in a unit length of the printed bead is reduced. Therefore, a large bead will cool down slower than a small bead and therefore increasing the minimum layer time required to develop an acceptable degree of bonding between adjacent layers.

7. INVENTIONS

This chapter includes two white papers prepared for disclosing inventions to the office of technology commercialization at Purdue University. A non-provisional patent application has been filed for an invention related to embedding heating circuits in articles made through EDAM. A provisional patent application has been filed for a second invention related to additive manufacturing by coextruding continuous multifunctional materials.

7.1 Heating of 3d Printed Tooling with Circuits Printed In-Situ through Fused Filament Fabrication

A non-provisional patent application has been filed for this invention and the inventors are listed as follow:

- Eduardo Barocio
- R. Byron Pipes
- Bastian Brenken
- Anthony Favaloro
- Nicholas M. DeNardo

This non-provisional patent application was published under the name Methods and Apparatus for Embedding Heating Circuits into Articles Made by Additive Manufacturing and Articles Made Therefrom. And the publication number given to this patent is US 2018/0281279 [159].

7.1.1 Introduction

During the last twenty years, Additive Manufacturing (AM) techniques have evolved from rapid prototyping methods to a potential manufacturing method for in-service parts and tooling. Fused Filament Fabrication (FFF) is one of the most commonly used techniques. In its extrusion based process, feedstock material in either a pellet or filament form is molten and deposited on a printing bed. By following a predefined machine path, the printer controls the history of deposition, and a part is built layer by layer. A reinforcing material such as discontinuous carbon fiber can be utilized by changing the feedstock. By combining carbon fiber with high temperature thermoplastics such as PPS or PEI, the thermomechanical properties required by high performance tooling are achieved. Additionally, the progressive buildup of structure allows for novel heating element insertion not

available in traditionally tooling methods. The method presented here is an enabling technology for the effective use of composite AM tooling in applications requiring temperature controlled tools.

7.1.1.1 Process Description

The FFF process begins with a CAD file like the one shown in Figure 7.1. For the production of tooling, two CAD geometries are created. The first is the desired net shape of the part. The second is a slightly modified geometry so that printed bead centers aligned with the surface of the net shape part.

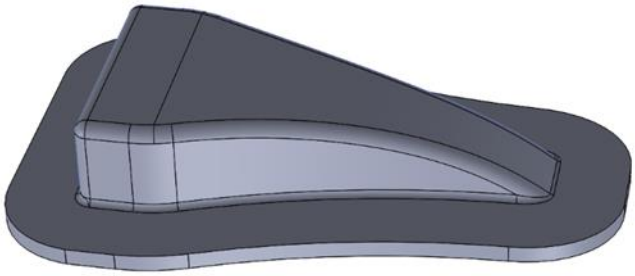

Figure 7.1 CAD geometry to be printed.

Following geometry creation, a slicing tool is used to determine the machine path for the printer that will be used to build the part layer by layer as seen in Figure 7.2. Many open source slicing software packages such as Slic3r or ReplicatorG as well as commercial software such as Simplify3D are available. Slicing can be performed with certain types and amounts of infill allowing a structure to be built that is not necessarily fully solidified. Infilled structures allow significant material savings to produce equivalent final shapes.

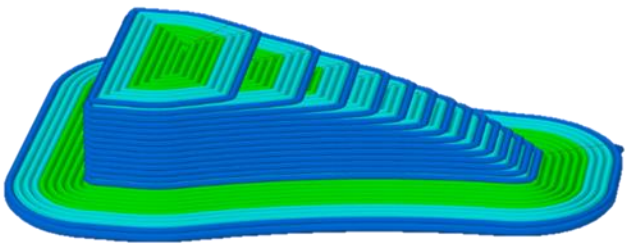

Figure 7.2 Slicing process that translates CAD files to layers and machine code

Parts produced via FFF, like the part shown in Figure 7.3, have surface finishes prescribed by the resolution and dimensions of the printed bead. Therefore, when a large-scale printer with greater bead diameter and thickness is utilized, printed parts will have a very rough surface finish. Furthermore, it becomes more difficult to represent part curvatures appropriately.

Figure 7.3: Part printed with FFF

As previously mentioned, in order to compensate for rough surface finishes, post processing is used to take a printed geometry from near net shape to net shape. Figure 7.4 shows a part after the machining process used for smoothing the printed surface.

Figure 7.4 Printed part after finishing process

7.1.1.2 Additive Manufacturing With Carbon Fiber Reinforced Polymers

A limiting factor of polymer AM on the size of printed parts via FFF is excessive distortion which can result in failed prints. In order to print large parts, this distortion must be suppressed. The root cause of the distortion is the addition of hot materials onto previously cooled materials. The newly added hot material contracts as it cools developing tensile stresses while inducing compressive stresses in the previously cooled material. As no additional mechanical forces are applied while

printing, these stresses can relax in the form of deformation causing the warping of the neat ABS (white) beam seen in Figure 7.5. Love et al. [2] identified carbon fiber filler as an enabling technology for large scale additive manufacturing. The carbon fiber serves a dual purpose in reducing warpage. First, the low Coefficient of Thermal Expansion (CTE) of the fibers in their longitudinal direction results in reduced overall CTEs of the printed composite material. This reduction of CTE however, is primarily in the bead direction due to fiber alignment induced by convergence and shear in the extrusion nozzle. Second, the fibers result in significant increase in modulus in the bead direction. Therefore, lower strains developed by the temperature gradients and the warping is reduced as it can be seen for the carbon fiber filled ABS (black) beam illustrated in Figure 7.5. As mentioned, the reduction of CTE and increase in stiffness is primarily in the bead direction; therefore, the beneficial effects of the addition of carbon fibers are primarily seen in thin walled structures. A wider printed part will still see detrimental warping as the transverse CTE and stiffness are not affected significantly by the addition of fibers.

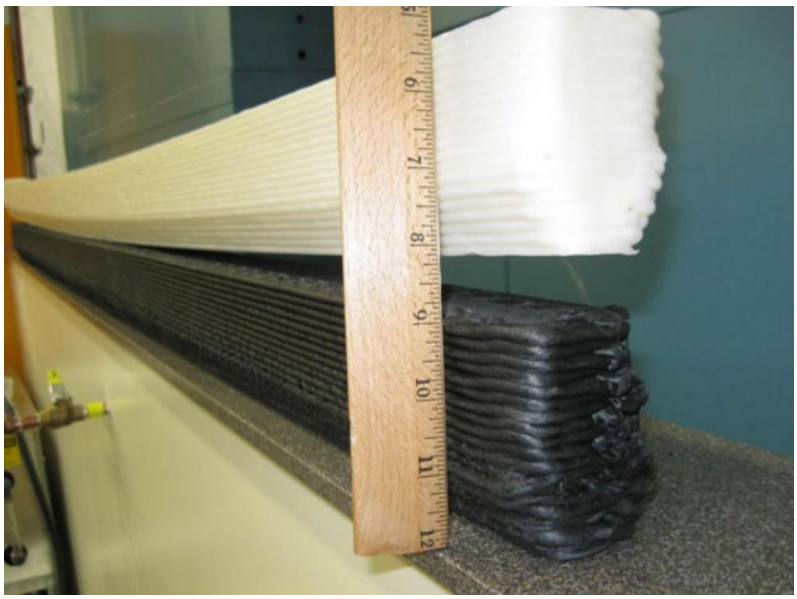

Figure 7.5 Warping of ABS vs CF-ABS in Large Scale FFF [2].

Parts manufactured by FFF characteristically have orthotropic properties due to printing direction, bead morphology, and inter-bead voids. However, with an isotropic feedstock, the degree of anisotropy is dependent on machine parameters potentially being negligible in a design stage. The introduction of carbon fibers to the printed bead, while resulting in reduced warping magnitudes,

introduces significant anisotropy into printed parts. Traditional composite intuition can assist in preliminary design. For example, a square printed by tracing the perimeter will behave similarly to a 0/90 laminate with carbon fiber increasing the stiffness and decreasing the CTEs in the 0 and 90 degree in plane directions. However, with the FFF process, the morphology of the printed structure with respect to the stacking direction is fixed. Layers are deposited in their entirety and then the next higher layer is built. In this way, the process is similar to laminate stacking without 3D weaves. Therefore, the thermomechanical behavior in the stacking direction is fixed and is similar to that of the neat polymer. The severity of distortion in the stacking direction can be reduced through the use of an infill structure rather than fully densified as a reduction in thermal mass (material) results in a lower warpage.

In addition to the CTEs and the mechanical properties, heat conduction within the printed part is also governed by an anisotropic relationship. Instead of one conduction parameter as for isotropic materials, a second order conduction tensor has to be utilized. Specifically, the heat diffusion parallel to the bead direction is about an order of magnitude larger compared to the directions transverse to it. This is due to the fact that the neat polymer has the properties of a heat insulator with a very low conductivity, while carbon fibers are good heat conductors. With the shear alignment of the fibers parallel to the bead direction, the fibers increase the conduction in this direction significantly. For the application of heating a composite 3D printed tools, this has to be considered while designing the topology of the heating elements. As a consequence, the design can be a challenge since the heat analysis is more complicated than for an isotropic material, however, it also enables the tailored design of a printed tool to optimize for external heat technology implementation. Since the neat polymer is a heat insulator, achieving sufficient tool surface temperatures for a curing process could result in local melting of the polymeric material in the vicinity of the heaters. Here, another large benefit of adding carbon fibers becomes apparent as they help to distribute the heat towards the regions of the tool where it is needed for curing.

7.1.1.3 Composite FFF For Tool Production

The design, manufacturing, and testing of tooling for a variety of applications (trimming/machining, wet layup composites, out of autoclave composites, autoclave composites, compression molding, stamping) is one of the most expensive and time consuming portions of a product development cycle that often requires multiple iterations. Specifically, tooling for the

production of composite parts must have relatively low CTEs preferably matching that of the part being produced, in process thermal management capability to ensure that the composite is kept at temperatures appropriate for curing, smooth surface finishes as the tool surface finish directly affects the part surface finish, vacuum integrity, and thermal stability (sufficient mechanical properties at elevated temperatures).

With these requirements considered, AM via FFF with carbon fiber filled high a temperature polymer such as PPS and PEI is a promising method for composite tool production. As previously mentioned, carbon fiber filled beads have CTE properties similar to that of composite materials and in-plane properties can be designed to resemble the in-plane properties of laminates. However, the stacking direction CTEs will remain large and must be accounted for in design so that the appropriate shape is attained by the tool when at curing temperature. Appropriate surface finish and vacuum integrity are attained by machining tools from near net shape to net shape and applying a final coating. Thermal stability is one of the most important concerns. A tool must be able to maintain significant mechanical stiffness while at elevated temperatures. Therefore, an appropriate printing material must be chosen. In our work, we have utilized 50wt% carbon fiber filled PPS. Figure 7.6 and Figure 7.7 show example results of our material system from both Dynamic Mechanical Analysis (DMA) and Differential Scanning Calorimetry (DSC). The DMA results show that even at 180°C, our material still possesses significant modulus only reduced by about a factor of 2 versus the room temperature modulus.

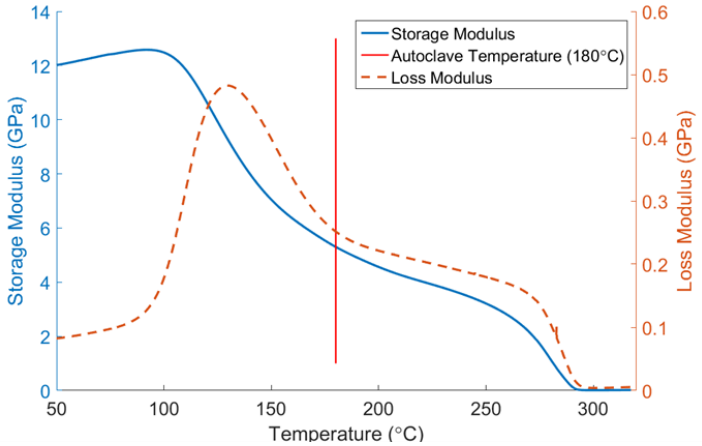

Figure 7.6 Effect of temperature on the storage modulus characterized through DMA

On the other hand, the DSC results show that melting of the crystalline regions of the printed PPS do not happen until around 270°C corresponding to the same temperature point at which rapid loss of modulus is seen in the DMA results.

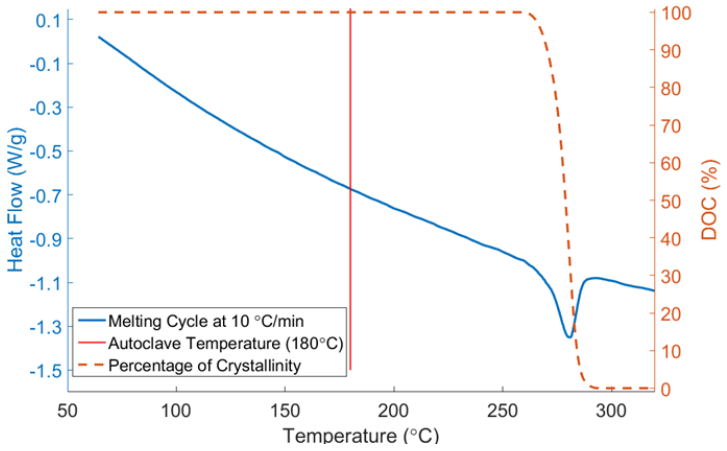

Figure 7.7 Phase transition of the polymer characterized using DSC

The remainder of this report will be concerned with the remaining feature required for many composite tooling application: in process thermal management. Specifically, the issues involved with the application of traditional heating technologies will be discussed and a novel in print heating element insertion technique will be detailed.

7.1.2 Existing Tool-Heating Technologies

Different technologies have been developed over the last years for heating tools used in polymer and composites processing. Tools are traditionally made from high-thermal conductive materials like steel or aluminum alloys but in some cases, materials like carbon fiber composites or glass fiber composites are preferred due their low CTE. Depending on the processing technique used for producing a part, the tool is self-heated or heated by external ways, namely forced or natural convection. Autoclave-cure processes use forced convection for heating the tool while Resin Transfer Molding (RTM), Vacuum Assisted Resin Transfer Molding (VARTM), and Injection Molding (IM) tools are heated through heating elements embedded inside the tooling. The technologies preferred for tool heating include the use of cartridge heaters embedded in the tool, mat heaters attached to the back side of the tool surface, and heat-transfer fluids pumped through channels built into the tool. Determining which of these technologies is more adequate for a giving

application depends mostly on the thermal conductivity of the tooling material and the tool design. Cartridge heaters are preferred in tools made from high-thermal conductive materials, while mat heaters are preferred on tooling surfaces composed of thin sections of good thermal conductors. On the other hand, pumping heat transfer fluids is preferred in applications where tools are made from not only good thermal conductors, but also from materials that withstand the pressures developed inside the channels.

This section investigates the use of the different heating technologies in 3-D printed tools made with carbon fiber reinforced polymers. As mentioned before, the orthotropic thermal conductivity of the printed material facilitates heat diffusion in the direction where the fibers are oriented, while hindering heat diffusion in the direction transverse to the fibers at the same time. This non-isotropic behavior brings additional challenges in tool heating that are not encountered in traditional tooling materials. As a result of the limitations found by using traditional heating technologies in printed tools, a novel localized heating technology was developed. This invention enables using printed molds in high temperature applications and allows local temperature control on tooling surfaces through heating circuits placed in-situ during the printing process.

The performance of existing technologies for heating printed molds was assessed by comparing temperature gradients developed on a representative tooling geometry, as shown in Figure 7.8. In simulations, this was equipped with each of these technologies. Large temperature gradients during molding processes could give rise to defects and residual deformations on the molded part, and thus the importance of uniform tool temperature. The steady-state temperature distribution at the surface of the representative tool was determined through a 3D-Heat Transfer (HT) analysis carried out using a commercial finite element tool (Abaqus). For these analyses, the actual printed mesostructure was included in the HT analysis to capture the local variations of thermal conductivity introduced by the presence of the inter-bead voids. Orthotropic thermal conductivity was introduced based on the coordinate system defining orientations in Figure 7.8. The printing orientation, which is the Z direction according to Figure 7.8, has the highest thermal conductivity (assumed $k\_Z = 3$ $(W/m^{2}°C)$, while the transverse orientations (X and Y) are the ones with the lowest thermal conductivity (assumed $k\_X = k\_Y = 1$ $(W/m^{2}°C)$. Owing to the symmetry of the printed geometry, the two planes in Figure 7.8 split the geometry into four identical quadrants, thereby simplifying the HT analysis. As a result, just one of these quadrants was modeled.

During RTM or VART processes, heated tools are subjected to heat losses by convection and radiation with the surroundings as well as by conduction through the foundation used for supporting the tool. Nevertheless, for the current analysis only convective losses from the surface and the sides of the tool are considered. The tool surface, which is covered with the material to be processed plus release films and other miscellaneous plies, was treated as a surface subjected to natural convection with a constant film coefficient of 10 W/°C. This conservative assumption was made since these additional layers of material provide significant thermal insulation, reducing the convective losses. On the other hand, higher convective losses from the sides of the tool, which are completely exposed to the surroundings, were treated with a film coefficient of 15 W/ °C. Finally, the bottom tool surface was assumed to be perfectly insulated for all the cases except the mat heaters.

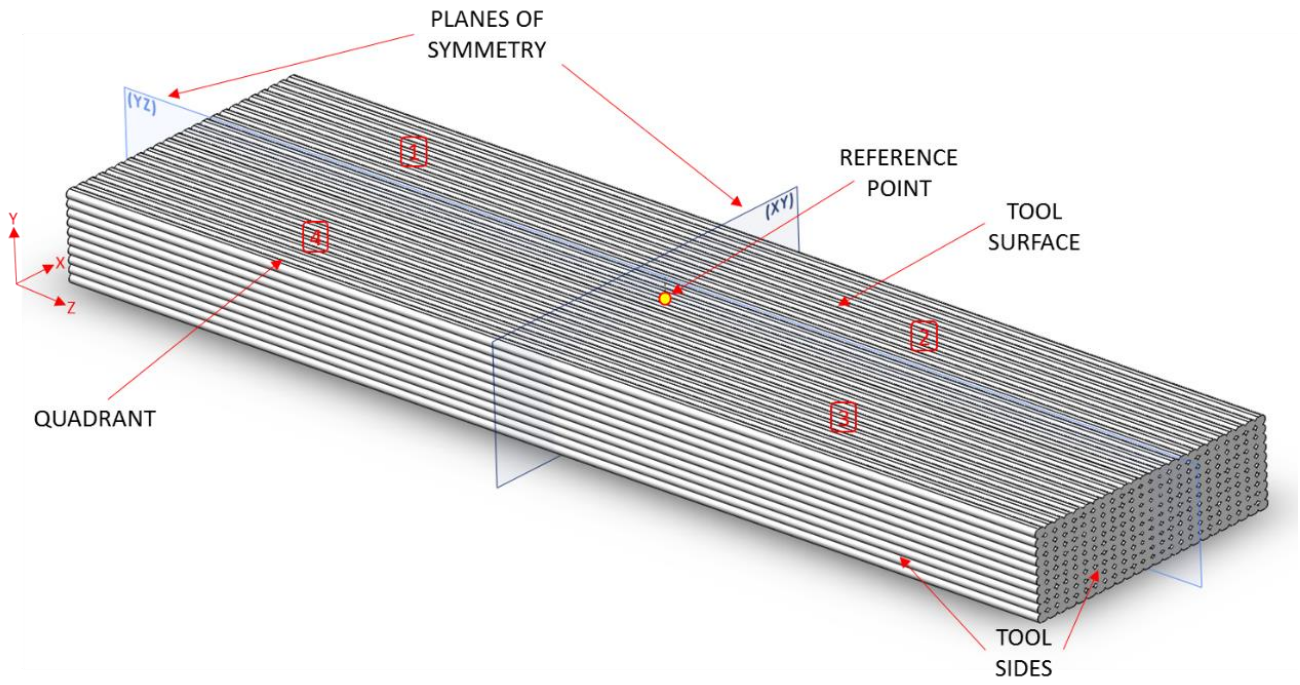

Figure 7.8 Representative tool geometry used in heat transfer analyses for different heating technologies

In addition to comparing the temperature gradients on the tooling surface, the maximum temperature developed around the heat sources was examined for the different heating technologies. A reference point, located at the intersection between the two planes of symmetry and the tooling surface, functioned as control point throughout the analyses with the different

technologies. For each case, two analysis were carried out aiming to achieve 150° C and 180° C at the control point, respectively. By doing so, temperatures around heat sources were compared under similar operational conditions. Excessive temperature could cause local melting of the printed material thereby compromising the stiffness of the material in that region and distorting the tooling surface. Further, an additional analysis explores the temperature limits of the tool with the different technologies by bounding the maximum allowable temperature near the heat source. The following section details the treatments made for modeling the different heating technologies.

7.1.2.1 Printed Tool Equipped With Cartridge Heaters

Cartridge Heaters (CH) are one of the preferred choices for heating metallic tools due to their low cost and easy implementation. CHs impose a constant heat flux, $q"$, that is simply defined by the ratio between the input electrical power and the surface area of the cartridge heater ($q" = W/m^2$). The printed tool modeled in this analysis was equipped with three commercially available cartridge heaters equally spaced along the mid-plane of the tool. The CH, delivering a maximum heating power of 45W, were inserted transversely to the orientation with highest thermal conductivity. With this setup, the higher conductivity in the z-direction aids in distributing the heat parallel to the beads reducing the temperature gradients in this direction. Figure 7.9 shows the temperature distribution on the tooling when the control temperature was set to 180° C at the control point. It is worthwhile mentioning that due to the linearity of the heat transfer analysis the temperature distribution on the tooling surface is linearly scaled with the control temperature. Thus, only the results for a control temperature of 180° are included.

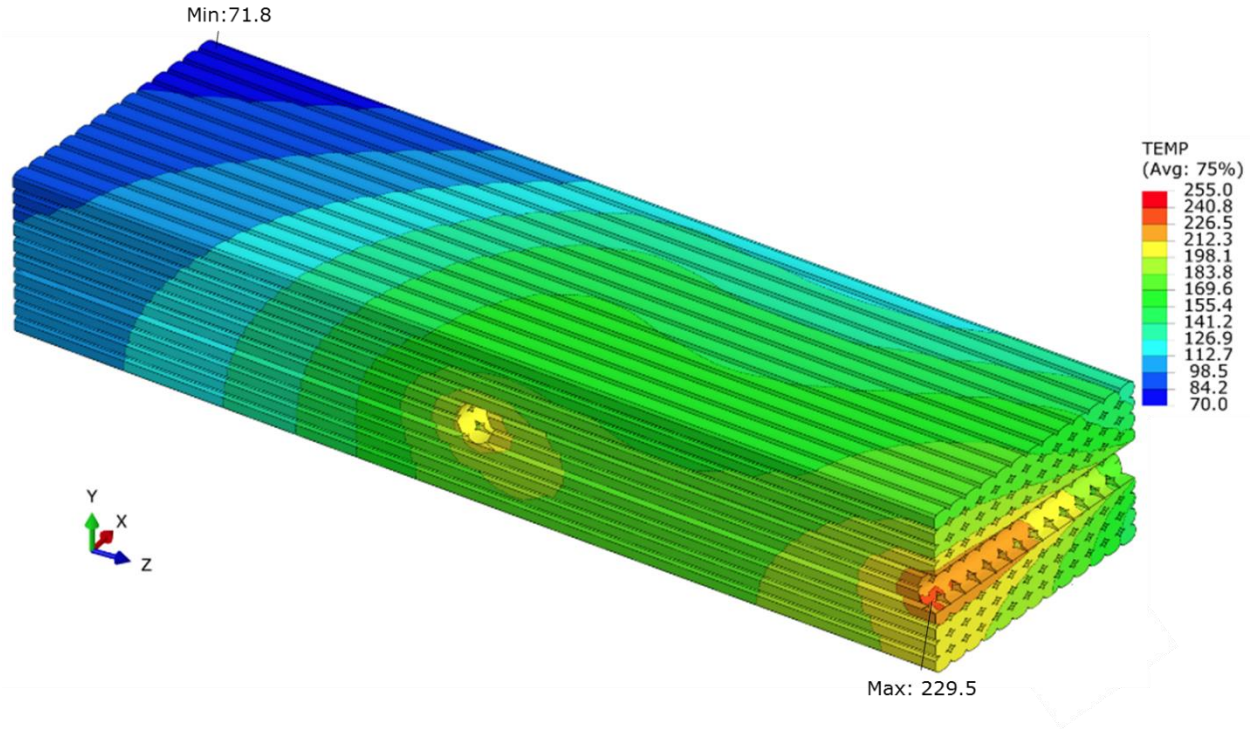

Figure 7.9 Temperature distribution of tool equipped with cartridge heaters obtained by setting the temperature at the reference point to 180° C.

Reaching 180°C at the control point with CH, introduced temperatures up to 229.5°C around the heat source as shown in Figure 7.9, which compromises the integrity of the structure in this zone. Hence, the maximum temperature that can be achieved with CH at the control point was 157.6° C based on a maximum temperature of 200°C, which is recommended for this material.

7.1.2.2 Printed Tool Equipped With Channels For Heat Transfer Fluid

Although pumping Heat Transfer Fluids (HTF) through channels built into tools is costly and difficult to scale, this technology has been widely used in tooling applications due to its capacity for providing not only controlled heating but also active cooling. Conventionally, HTF is pumped through either channels machined in the tooling or tubing attached to the back side of the tooling. Further, this technology requires more complex pressure and temperature control loops to achieve a constant temperature along the channel and thus on the tooling surface. Even though fluid channels can be readily build during the 3D printing process, there are two main limitations for the adoption of this technology. First, the porous structure inherent to the bead-by-bead manufacturing process would cause pressure drops and fluid leakage. Second, excessive forces

due to the internal pressure could deform the tooling surface and cause local damage in the structure.

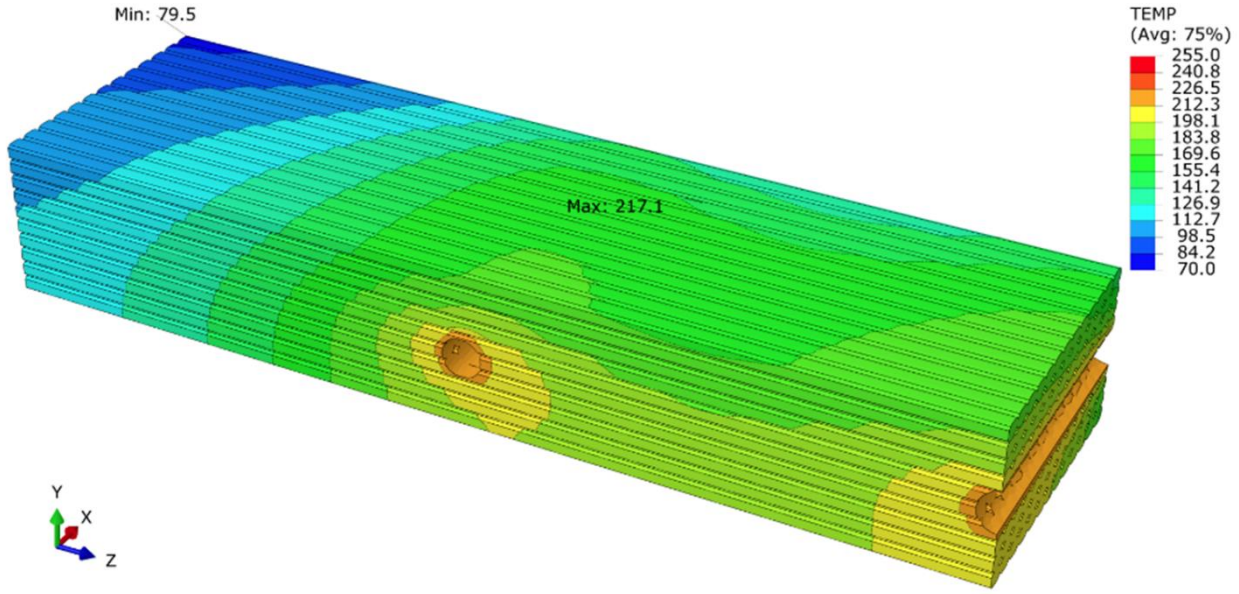

Figure 7.10 Temperature distribution of printed tool equipped with channels for heat transfer fluid obtained by setting the temperature at the reference point to 180° C.

Modeling the use of HTF for heating a tooling required the following assumptions. First, it was considered that the thermal boundary layer in the channel is fully developed and thus imposing a constant temperature condition from the fluid entrance. Second, a constant temperature condition was assumed along the full length of the channel which implies that the HTF has infinity heat capacity, however, this condition can be satisfied at low L/D ratios and using advanced pressure and temperature controls. The HTF channels were located again perpendicular to the orientation with the highest thermal conductivity. Since the orientation of the channels is also symmetric with respect to the planes shown in Figure 7.8, both planes of symmetry were used in the heat transfer analysis for the tool equipped HTF channels.

Figure 7.10 shows that the temperature of the HTF must be higher than the temperature recommended for this material (200C) to achieve the desired temperature, 180 °C, at the control point. Thus, the maximum temperature that can be achieved without compromising the structural integrity of the material was determined to be 166.1° C.

7.1.2.3 Printed Tool Equipped With Mat Heater

Heating tools with Mat Heaters (MH) is the preferred choice for achieving uniform tooling temperatures when the tool is made from thin sections of materials with high thermal conductivity. Since MH are semi-flexible, those are conventionally bonded to the back side of tooling surfaces and provide a constant heat flux that is controlled to achieve a uniform temperature on the tooling surface. Typical construction of MH consists of heating ribbons embedded in silicone rubbers or polyamide which are characterized by their low thermal conductivity. Such an insulation limits the maximum temperature that can be achieve with MH.

For the heat transfer analysis, a constant heat flux provided by the MH was applied through the bottom side of the tool neglecting the thermal resistance between the MH and the tool. This last assumption is appropriate for the analysis as long as the bottom surface is finished and the mat heater is perfectly bonded to the surface. Figure 7.11 shows the temperature distribution in a tool equipped with a mat heater at the bottom surface of the tool.

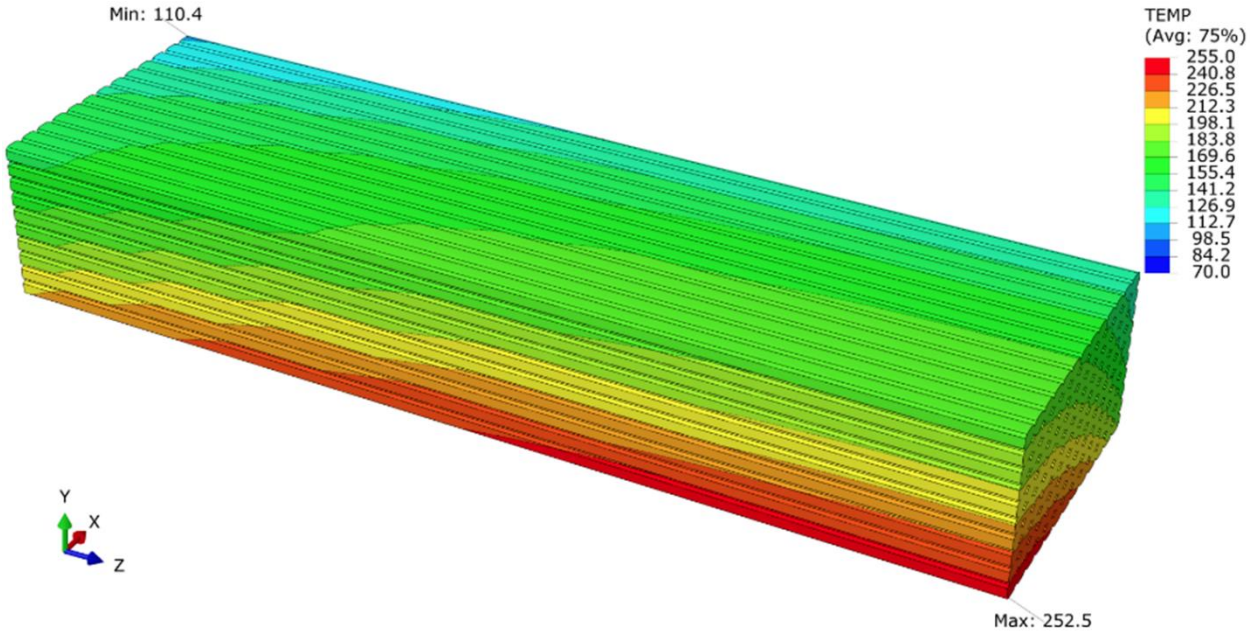

Figure 7.11 Temperature distribution of printed tool equipped with mat heaters obtained by setting the temperature at the reference point to 180° C.

While a uniform temperature distribution on the tool surface is achieved with MH, temperatures above the maximum recommended temperature, 200 °C, develop on the surface where the MH is

bonded. Thus, the max temperature that can be achieved at the reference point without deteriorating the performance of the tool was 144.3° C.

7.1.2.4 Printed Tool Equipped With Heating Circuit

The previous analyses have shown that the limiting factors for adopting existing heating technologies on printed tools are both the low thermal conductivity and low melting temperature of the polymeric material. Hence, the concept of embedding Heating Circuits (HC) during the printing process of the tool was developed to enable higher temperature and better temperature control on the tooling surface. By embedding HC near the tooling surface, the heat is not only distributed more evenly on the surface, but also diffused more rapidly to the surface. Wire density in the HC can also be varied depending on the heating requirements of the tool. Further, the orthotropic thermal conductivity can turn favorable for heating with this method by designing the path of the heating wire based on the local material orientation. Multiple HC can be embedded and controlled by zones depending on the heating requirements of a tool.

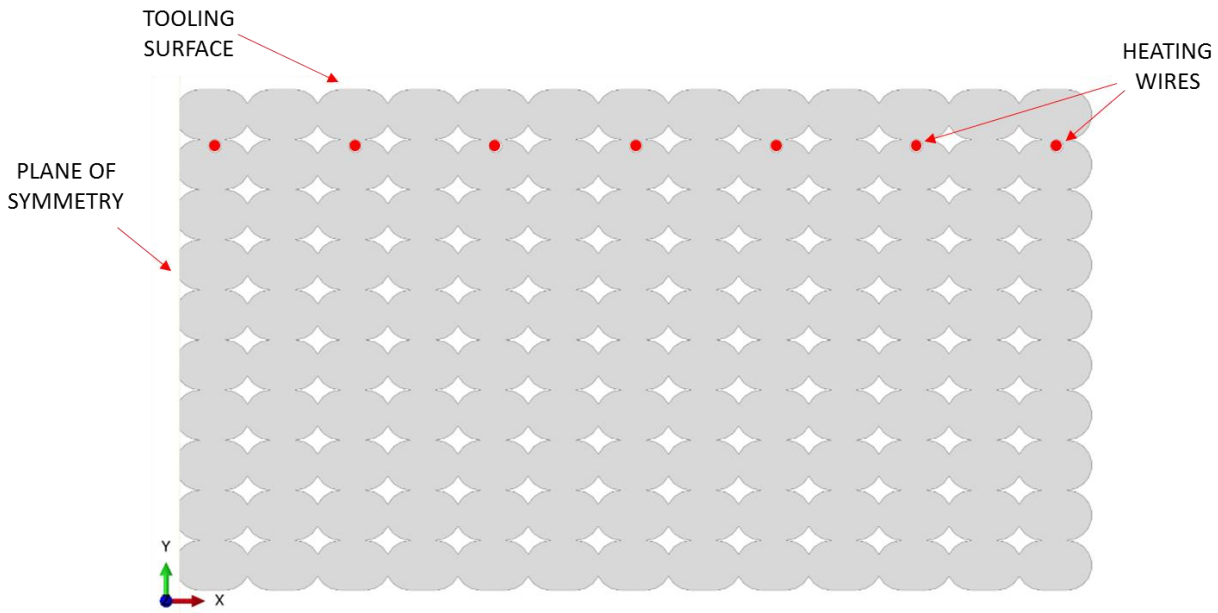

Figure 7.12 Cross-sectional view of printed tool equipped with heating circuit.

For the case study presented in this work, the heat generated by the circuits is purely governed by the joule heating phenomenon caused when either AC or DC current flows through a conductive wire, however, the same technology of printing heating circuits can be directly applied to tools

heated through induction heating of ferromagnetic wires. Figure 7.12 shows the cross section of the tool equipped with HC used in the heat transfer simulation.

By comparing the temperature distribution shown in Figure 7.13 of a tool equipped with HC with the temperature distribution of other existing technologies three main things can be pointed out. First, the temperature gradients on the tool surface are significantly reduced compared to the HTF and CH technologies. Second, the maximum temperature achieved near the heat source was significantly reduced compared to the other three heating technologies, thereby enabling temperatures on the tool surface above 180° C, namely up to 194.5°C. Third, even though a similar temperature distribution on the tooling surface was achieved with the MH, HC significantly reduced the temperature gradients across the thickness of the tool which reduces the thermal stresses and deformations in the tool.

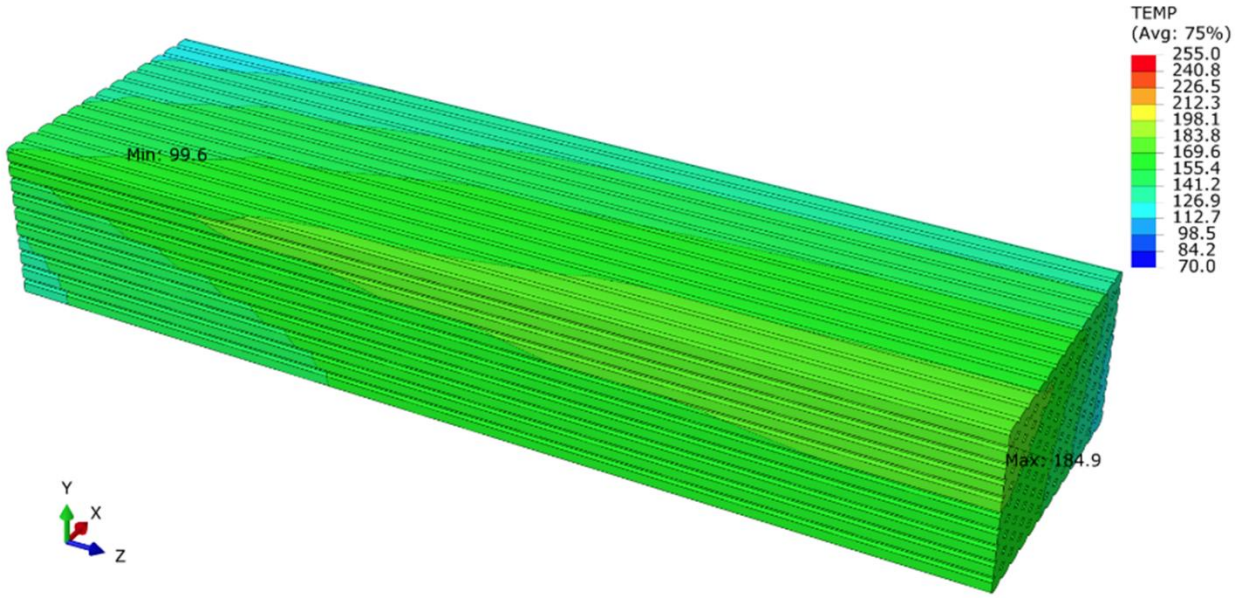

Figure 7.13 Temperature distribution of printed tool equipped with heating circuits obtained by setting the temperature at the reference point to 180° C.

7.1.2.5 Comparison Of Technologies Used For Heating Tools

Previous heat transfer analyses carried out for a printed tool equipped with different heating technologies confirmed the improvement achieved with the HC by reducing the temperature gradients on the tooling surface. This section compares quantitatively temperature profiles developed on the tooling surface along the X,Y and Z axes of the tool. Temperature profiles were

extracted from the edge formed by the intersection of both planes of symmetry, as depicted in Figure 7.14, and the intersections between the planes of symmetry and the tooling surface.

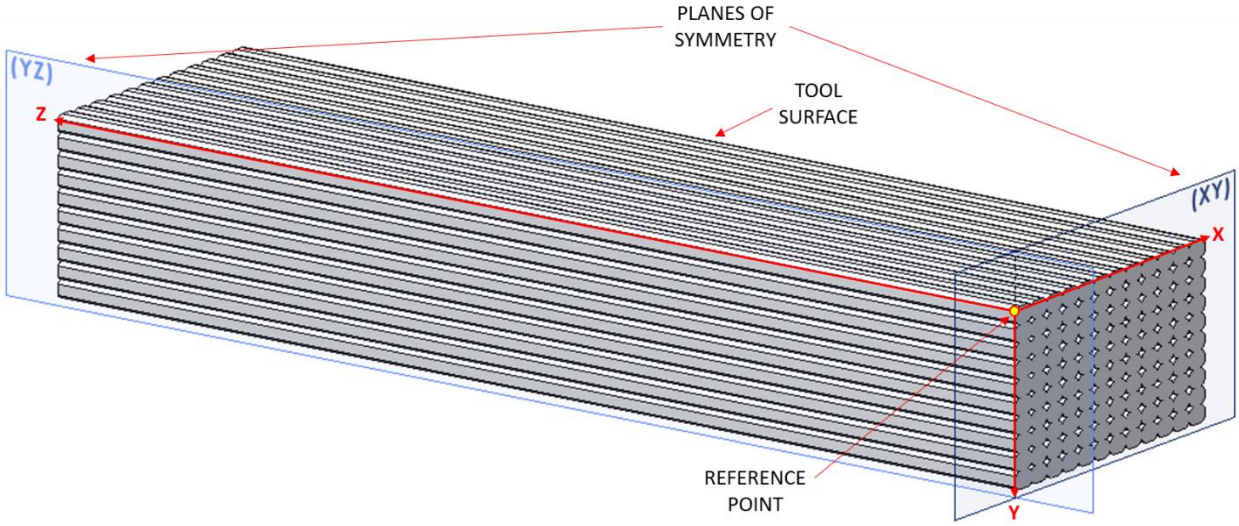

Figure 7.14 Locations where temperature profiles were extracted.

Figure 7.15 shows a significant reduction in temperature gradients along the Z direction achieved with the HC when compared to the other traditional technologies. The temperature profile obtained using MH follows closely the one obtained with the HC, however, the temperature profiles in a more intricate tool shape will be strongly influenced by the variations in the thermal diffusion distance. In other words, changes in thickness will introduce temperature gradients simply due to the increase in heat diffusion distance.

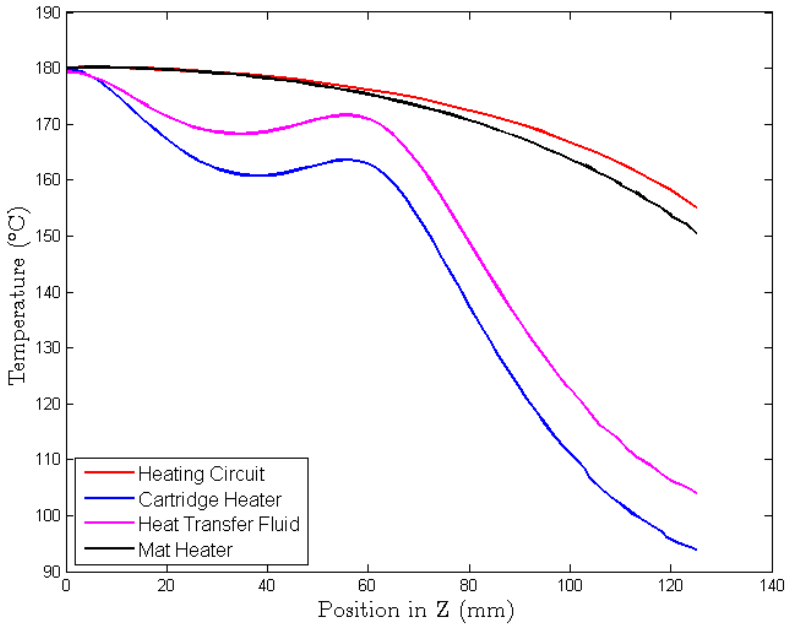

Figure 7.15 Temperature profile developed in the Z direction at the tooling surface.

Figure 7.16 depicts the temperature profiles in the X direction. The HC undergoes a more rapid increase in temperature gradient as we move away from the reference point compared to the other technologies, but this response is readily improved with a denser heating circuit.

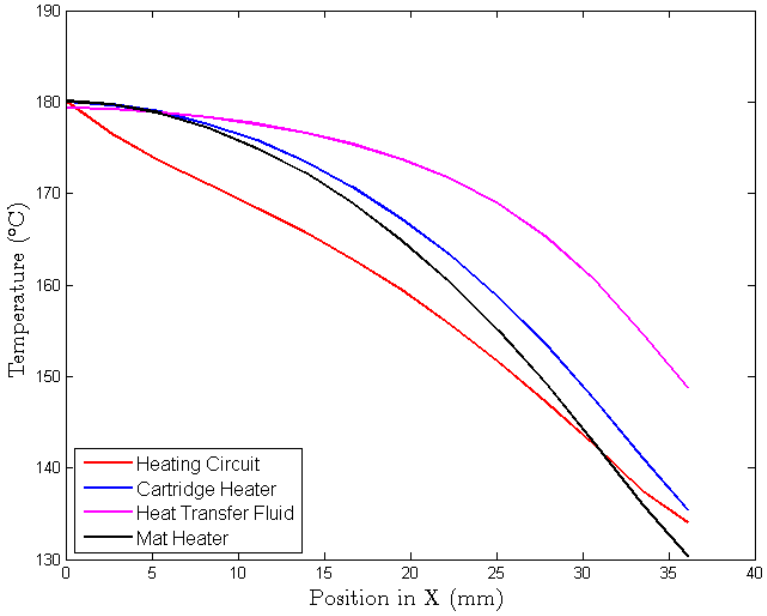

Figure 7.16 Temperature profile developed in the X direction at the tooling surface.

Although both HC and MH developed similar temperature profiles on the tooling surface, the HC significantly reduced the temperature gradients in the Y axis. Figure 7.17 compares the temperate profiles developed through the thickness of the tool with the different heating technologies. This plot also captures the maximum temperature developed inside the tool, which as expected was maximal for the mat heaters. Though the location of the CH or HTF channels can be optimized for reducing the temperature gradients on the tooling surface, the effective use of this technologies in printed tools is still limited by the low-thermal conductivity of the printed composite material.

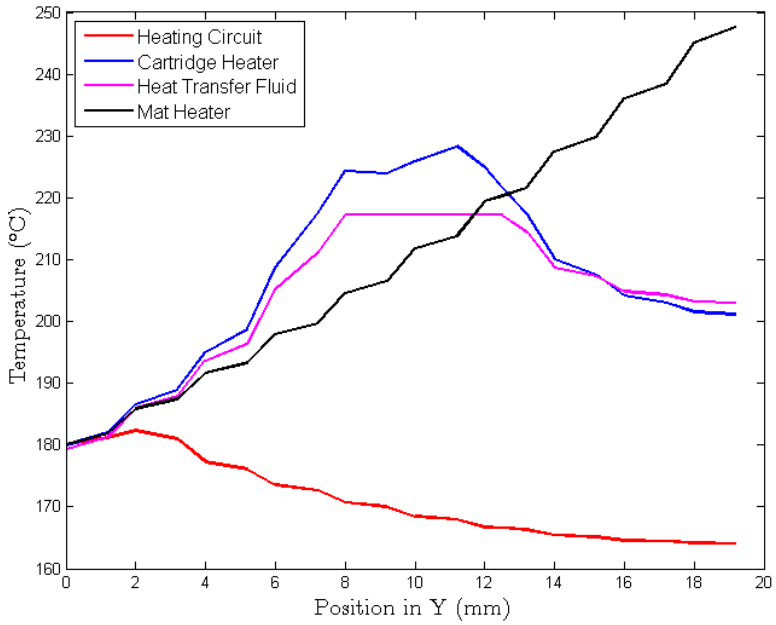

Figure 7.17 Temperature profile developed through the thickness of the printed tool.

An additional advantage of using HC is that CH and HTF require fully densified structures for containing the heating element or the fluid, respectively. Hence, the use of heating wires enables printing more complex tooling surfaces without needing fully densified support structures, thereby reducing cost, printing time and heat losses through the foundation of the tool.

The following section describes different processes for depositing the HC during the printing process and points out additional benefits of using this development compared to traditional technologies.

7.1.3 In-Situ Printing Of Heating Circuits

Heating circuits have demonstrated superior performance reducing temperature gradients on printed tool surfaces compared to traditional heating technologies. Since the heating circuits are build-up at the same time the part is printed, minimal post-processing steps are required to use the heating circuits. On the other hand, MH and CH require finished surfaces to achieved good thermal contact, while the HTF requires further preparation for connecting the pumping system to the tool. Embedding HC during printing can be achieved through different ways, namely coextruding the wire with the printing material, placing pre-shaped circuits between layers, or using the Automatic Wire Dispensing System (AWDS) that was conceptually developed for this purpose. HC require good thermal contact with the printing material and in some applications interconnections, these aspects are addressed below for each deposition method.

Co-extrusion is widely used in industrial applications going from processing toothpaste to isolating electrical wires with thermoplastic polymers. However, for embedding heating wires, the traditional co-extrusion must be complemented with a compacting mechanism that consolidates the co-extruded wire as it leaves the nozzle. This consolidation step is essential for preserving the co-extruded wire at the desired position and to achieve good thermal contact between the printed layers. Such a compaction step can be achieved with a roller following the deposition path or with a mechanical tamper surrounding the co-extrusion nozzle. Pressure developed inside the co-extrusion nozzle can be used to fully wet the surface of the wire and achieve good thermal contact, but the wire needs to be heated before entering the nozzle to prevent rapid solidification around the wire. Additionally, a simple shear cutting tool is required at the end of the co-extrusion nozzle to cut off the wire at the ends of the circuit. The combination of the co-extrusion system, the compacting step, and the cutting tool will enable scaling the use of heating circuits to more complex tool geometries where circuits need to be placed on different planes and sections.

Although pre-shaping HC is only practical for flat-shape tools, a brief description of the process is included. Since the FFF process is carried out layer by layer, HC can be embedded in the printed part pausing the printing process at desired locations. Subsequently, HC are manually located and embedded into the previously-printed layer at particular points with the aid of an external heat source. Then, the printing process continuous and the newly extruded material covers the heating circuit.

The last method discussed here for embedding HC during printing is using the AWDS. This system combines both, the capability of the co-extrusion nozzle to deliver heating wire embedded into the extruded material, and the flexibility of the manual method to orient the heating circuits at any direction in the part. The AWDS consists of a rotating platform mounted around the deposition nozzle as depicted in Figure 7.18.

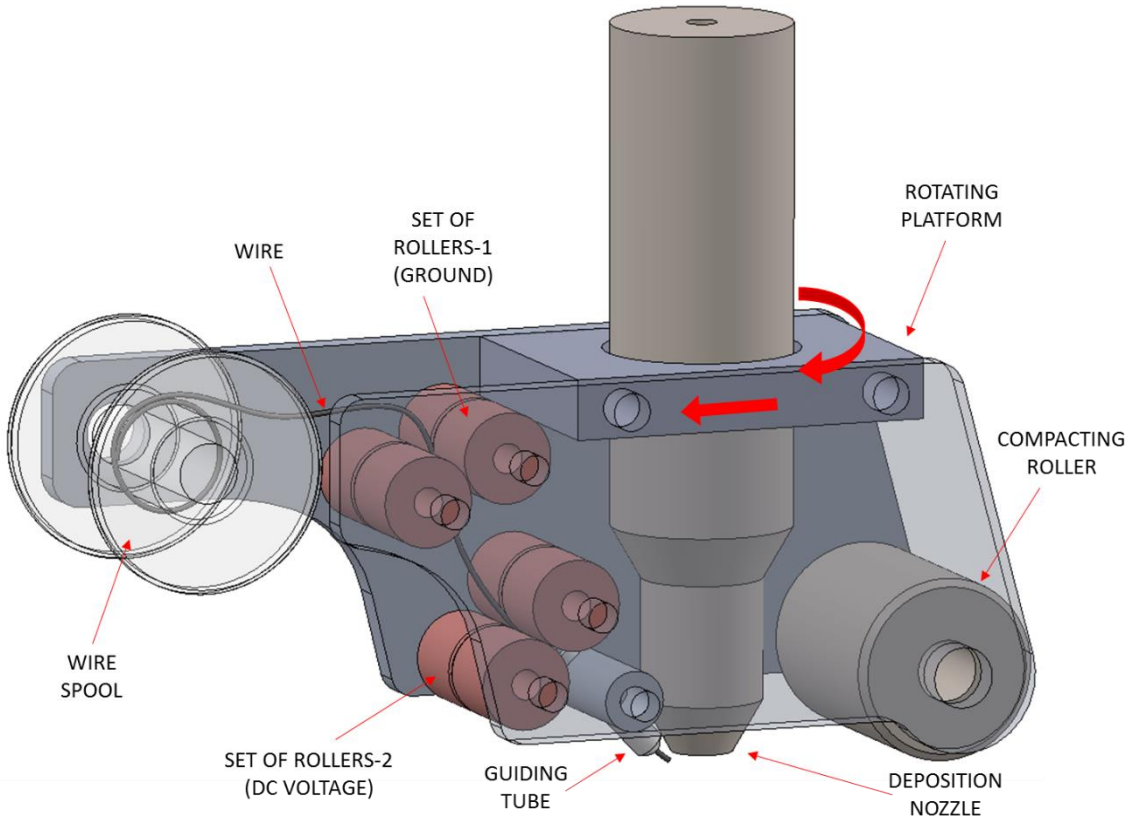

Figure 7.18 Automatic Wire Dispensing System (AWDS)

This platform can be configured to either follow the printing path or to follow a preprogrammed path without extruding material. A spool of heating wire mounted on the moving platform supplies wire to a first set or rollers that guides the wire coming from the spool and provides electrical ground. A second set of rollers pulls the wire and supplies a controlled DC voltage that creates a current in the wire as it moves between the two set of rollers, thereby heating the wire by joule effect. When following the printing path, wire is heated and then guided right next to the extrusion nozzle through a ceramic guiding tube. Then, the wire is laid down and covered with extruded material that is subsequently compacted with a roller mounted on the same platform. Pre-heating

the wire is necessary during this process to fully wet the wire with the printing material, otherwise the material might solidify rapidly around the cold wire leading to a poor thermal contact. After finalizing a heating circuit, the wire is cut with the shear cutter included after the second set of rollers.

The AWDS can be also utilized for inserting heating circuits between printing layers without extruding material. This feature is especially useful when HC need to be oriented differently than the printing orientation. To achieve this, the printing process is paused at the layer where the heating circuit needs to be collocated, which gives time to this layer for solidifying. Embedding the heating wire on an already solidified substrate requires, first to move the AWDS closer to the surface where the wire will be placed so that the compacting roller can be used for pressing the wire into the substrate, and second to heat up the wire at higher temperatures so that it can locally melt the region where is laid down. Posterior to laying down the heating circuit, the printing process is resumed and continues until another heating circuit needs to be laid down in this manner.

Both methods for placing HC, the co-extrusion nozzle and the AWDS, enable the use of HC in complicated tooling shapes. For instance, concave tooling will require installing heating circuits on different planes during the printing process, which is readily accomplished with one of these two methods. Furthermore, tailoring the orientation of the heating circuits based on the local material properties and heating requirements becomes possible with the AWDS.

7.1.3.1 Demonstration of Heating Circuits Technology

A first prototype was tested on August 23th, 2016 to prove the functionality of the HC on a printed tool. A C-shaped structure was printed in the CAMRI (Composites Additive Manufacturing Research Instrument) system developed at Purdue University using 50% by weight of carbon fiber reinforced Polyphenylene Sulfide (PPS). A single heating circuit was embedded between two adjacent layers during the printing process of the prototype, specifically between the second and third layers located from top to bottom as shown in Figure 7.19. The HC consists of continuous and equally spaced loops of heating wire (Ni-Cr 80/20 alloy). The space between loops was set to around 5 mm which is the equivalent to the width of approximately one and a half printed beads.

The heating circuit is controlled with a PID controller which uses the temperature read from a thermocouple embedded at the middle of the part and between the last two upper layers of

the printed part. A variable-voltage AC source is used to power the heating circuit and allows to scale the heating power simply by varying the voltage of the source. Yet, DC sources can also be used seamlessly with the heating circuits.

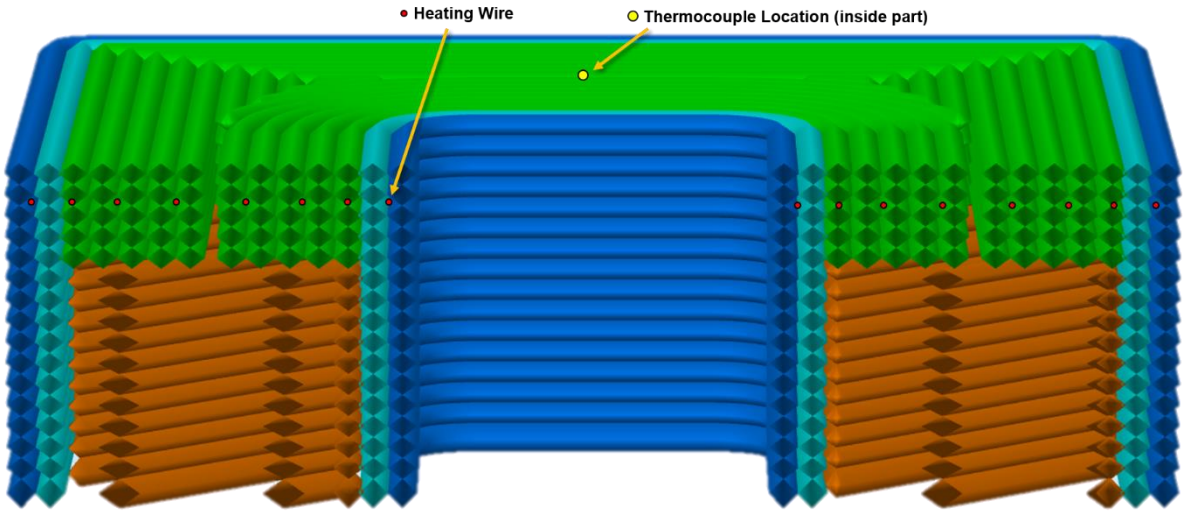

Figure 7.19 Section view of a printed tool equipped with a heating circuit and a thermocouple. Green: Solid layer, Orange: Partially filled layer, Blue: Perimeters

Figure 7.20 shows the setup used for testing the printed tool equipped with a heating circuit. A variable voltage AC power supply was employed to power the circuit, and a fixed voltage of 30 VAC RMS was used for this test.

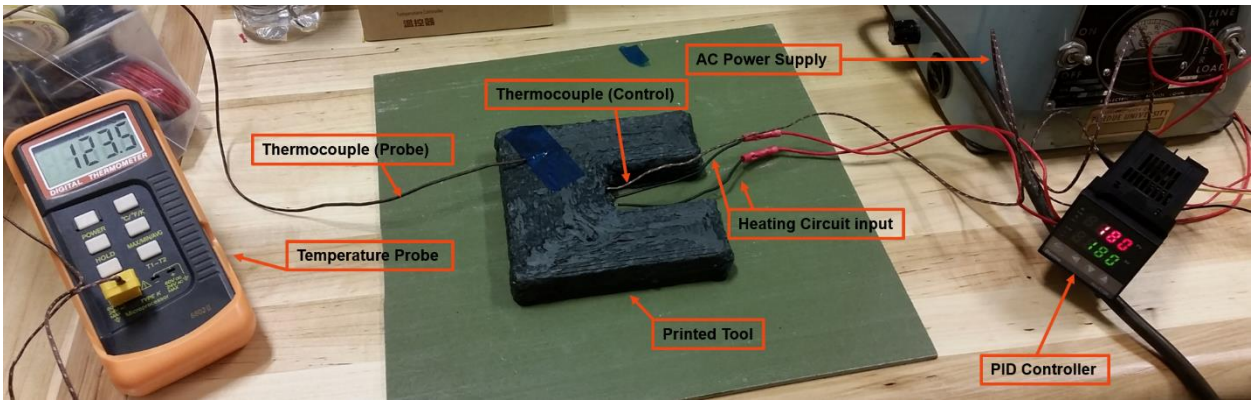

Figure 7.20: Setup used to test printed mold equipped with a heating circuit

The measured resistance of the heating circuit was 14 ohms which combined with the input voltage of 30 VAC delivered a maximum power of 65 W. The temperature was set to 180 °C in the PID controller and the system took around 15 minutes to achieve the desired temperature.

Nevertheless, the temperature at the tool surface, measured with an external temperature probe, differed by approximately 57 °C from the set pointed temperature. Such a difference is caused by the combination of the following two factors: first, due to the low thermal conductivity of the printed material in the transverse direction, and second, because the thermocouple is located between the heating elements and the upper surface. Although this temperature gradients across the part are unavoidable, placing the thermocouple of the control system on the tool surface will ensure that the set pointed temperature is achieved.

A thermo-imaged captured during the heating test (Figure 7.21) demonstrates qualitatively that there are no significant temperature gradients developed on the surface of the printed tool equipped with heating circuits. The absolute temperature scale shown in Figure 7.21 differs from the actual temperature readings due to the lack of calibration available for the thermal-camera used in this experiment (SEEK CompactXR).

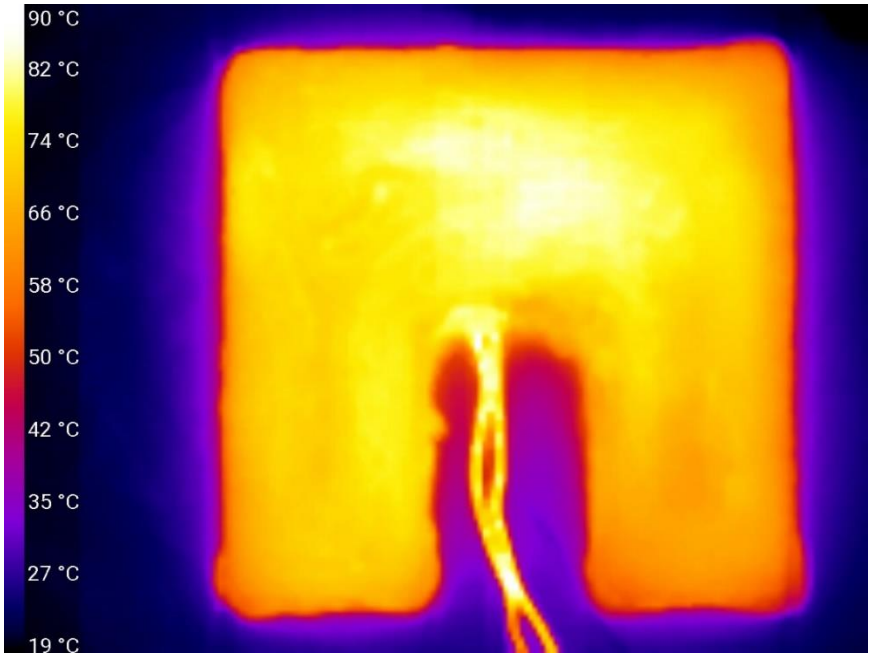

Figure 7.21 Qualitative inspection of temperature gradients developed at the surface of the printed tool.

7.1.4 Conclusions and Future Work

In order to overcome the limitations of using traditional heating technologies in printed tools, a technology using Heating Circuits (HC) printed in-situ during the tool manufacturing process was developed. Heat transfer analyses of a representative tool equipped with existing tool heating technologies confirmed the superior performance of HC in reducing temperature gradients. HC embedded in a printed tool enables precise temperature control of the tool by zones, which is not readily achievable with traditional technologies. The so-called heating circuits can be also combined with contactless technologies for tool heating, namely induction heating. Other potential application where the embedded circuit can be utilized simultaneously is for sensing temperature inside the tool based on changes in resistance of the circuit.

Additionally, a novel system for laying down HC called AWDS was conceptually developed. The AWDS' rotating platform allows introducing heating circuits in the two following manners. First, AWDS can deposit HC simultaneously with the printing process following the printing trajectory. Second, AWDS can lay down HC on a layer-by-layer basis without extruding material, thereby enabling wire orientations that are different from the printing path and HC with varying densities. Finally, the HC technology was reduced to practice by testing the temperature gradients developed on a printed tool surface equipped with a heating circuit.

7.2 Methods and Apparatus to Additively Manufacture by Coextruding Continuous Multifunctional Composite Materials

A provisional patent application has been filed for this invention and the inventors are listed as follow:

- Eduardo Barocio
- Jorge A. Ramirez
- Miguel A. Ramirez
- Bastian Brenken
- R. Byron Pipes

The provisional patent application for this invention has been filed under the title Methods and Apparatus for Additive Manufacturing of Articles by Co-Extruding Continuous Multifunctional Composite Materials, and Articles Made Thereof.

7.2.1 Introduction

The technology of Extrusion Deposition Additive Manufacturing (EDAM) consists of manufacturing three-dimensional geometries by depositing beads of molten material in a layer-by-layer basis. EDAM is a screw extruder-based process that has enabled processing high-temperature and highly reinforced polymer composites that otherwise could not be processed with traditional filament-based processes due to the high viscosity of the reinforced polymer. Further, printing structures of the large scale size (meters) has become feasible due to advancements in the printing materials and the EDAM technology. Specifically, due to both the reduction in coefficient of thermal expansion (CTE) and the increase in stiffness gained by reinforcing printing polymers with discontinuous fibers as described by Love et. al [2]. Work at the Composites Manufacturing and Simulation Center (CMSC) at Purdue has focused on printing with carbon fiber reinforced Polyphenylene Sulfide (PPS), which is a semi-crystalline high-temperature polymer processed at 310 °C. Fiber contents of up to 50% by weight have been processed with the Composites Additive Manufacturing Research Instrument (CAMRI) developed at the CMSC. Extrusion deposition additive systems developed by Thermwood and Cincinnati Inc. are commercially available screw-based EDAM systems.

The EDAM process of polymer composites utilizes pelletized composite material that contains discontinuous fibers impregnated with polymer. The pelletized material can take the form

of Long Discontinuous Fiber (LDF) or compounded composite with the primary difference in the initial fiber length where LDF lengths are in the range of 10,000 microns, whereas fiber length in compounded material is typically below 500 microns. The pelletized material is fed into a single-screw extrusion system that melts and applies pressure to the printing material. Two primary sources of heat drive the melting process of the polymer in a screw-based extrusion system. The first one is the heat supplied externally from heaters and the second is the viscous dissipation (shear heating) in the polymer. This mechanism requires substantial mechanical energy that results in fiber fracture and thereby, fiber length attrition. After flowing through the extruder, the molten polymer composite enters the printing nozzle where converging zones cause the fibers to orient in the print direction, thereby introducing anisotropy in the mechanical, diffusion and flow properties of the extrudate. Upon leaving the nozzle, the composite material is first deposited on an actively heated build plate and in subsequent passes it is deposited on previously deposited material substrate layers. Finally, the deposited extrudate is compacted with a tamping in order to reduce extrudate thickness and to consolidate the extrudate with adjacent deposited layers.

Fiber attrition in the extrusion process of the polymer composite additive manufacturing reduces limits the strength in a printed component. Therefore, current applications for EDAM with composites have been limited to non-structural applications. Tooling, molds, jigs and fixtures used in autoclave and compression molding composites manufacturing are examples of the current applications for this technology. Furthermore, applications demanding temperatures and pressures in excess of 180 °C and 35 Bar, respectively, have been demonstrated with the technology developed. Hence, motivated by the need for improved strength of elements fabricated with the state-of-the-art of EDAM technology, a technology has been developed to continuously and/or selectively print with hybrid materials comprising of at least two phases.

One phase can be comprised of a polymeric material either unreinforced or reinforced with discontinuous fibers or other fillers. A second phase can comprise of continuous elements impregnated with a polymeric matrix that could provide not only structural properties but also include sensing, heating, cooling, or microelectronic elements. The word “phase” in the context of this document is used to refer to the multiple material forms used with the co-extrusion additive manufacturing process, rather than the individual phases inside a material form. The polymeric material that can be used in each phase includes, but is not limited to thermoplastics, thermosets or elastomers. Furthermore, the options of fillers or discontinuous fibers reinforcing one of the

phases include, but are not limited to organic fillers, mineral fillers, carbon fiber, glass fiber, aramid fiber, or natural fiber. With regards to the phase comprising continuous elements embedded in a polymeric material, these can include, but are not limited to carbon fibers, glass fibers, aramid fibers, heating wires, sensing wires, microelectronics, or a combination of multiple of them. As a result of the wide variety of combinations that become possible with continuous elements, the name of Continuous Multifunctional Composite (CMC) was coined to refer to the phase of continuous elements fully impregnated with a polymeric material. A more detailed description of the manufacturing process of the CMCs is provided in the methods section. The phrase "second phase" refers to the CMCs in the context of this document. Nevertheless, this invention is not limited to two phases only.

In order to integrate the new material form in the existing EDAM process, a system that embodies a custom designed co-extrusion head, a custom developed control algorithm, and a custom developed feeding mechanism was developed. The word co-extrusion head and co-extrusion nozzle are used interchangeably in the context of this document. The integration of such a system in an EDAM machine enables selectively printing of hybrid material consisting of at least two phases without interrupting the printing process. This is achieved by co-extruding multiple phases of material through the co-extrusion head. During the printing process with multiple phases, the co-extrusion head is actively heated and fed with at least one of the polymer phases in molten state. A second or even multiple other phases enter the co-extrusion head and merge with the flow of the molten phase. Coextruding multiple phases has at least two advantages that differentiate this technique from existing systems for printing with continuous fiber systems. First, multiple phases can be heated and melted or not as these are conveyed with the molten second polymer phase, thereby allowing deposition of material at higher rates. Second, the pressure developed inside the co-extrusion head improves the wetting of the solid phases with the molten phase which in turn improves the thermal diffusion from the molten phase into the solid phases. As an additional consequence of the improved wetting, the diffusion properties and loads are transferred more effectively across the multiple phases in an extruded bead.

The methods section introduces the heat transfer analysis carried out to develop the co-extrusion head and describes in more detail the control algorithm and feeding mechanism developed for this technology. An overview of the prior art found for this technology is included in the next section.

7.2.1.1 Prior Art of Technologies for Printing with Continuous Fibers

The system and material form developed for printing with continuous elements presented in this work overcomes three main limitations that can be found in state-of-the-art technologies for printing with continuous fibers. First, the deficient impregnation of fibers with polymer inside that phase, and the deficient impregnation of the continuous phase with the surrounding phases. The second deficiency is the low deposition rate limited by the diffusion-controlled mechanism of heating and melting the polymeric material in a filament-based printing system. Third, the need for interrupting the printing process to deposit a continuous filament. In addition to mitigating these issues, the described technology of CMC combined with the system or apparatus presented herein enables printing with multi-phase and/or multifunctional materials including but not limited to reinforcing fibers, heating wires, cooling elements, sensing elements and microelectronics. Prior art of printing with continuous elements has been identified from two institutions, namely the company Markforged and the University of Texas at El Paso (UTEP), and a brief overview or their inventions is included.

Markforged claims a void-free carbon fiber reinforced composite filament used as the feedstock material in their 3D printing process [160, 161, 162]. Markforged's technology is based on the common fused deposition modeling or fused filament fabrication technique. Thus, their filament material system is limited to only thermoplastic resins. Their emphasis is on the core material which consists of continuous carbon fiber material or semi-continuous. Their method for printing with the filament material consists of feeding the reinforced filament into a heated extrusion nozzle that melts the thermoplastic resin by heat conduction from the tip of the nozzle. The filament is then extruded through the nozzle by applying pressure. The description of their filament material is limited to an outer diameter greater than or equal to 0.006 inches and less than or equal to 0.030 inches. The claims regarding Markforged additive manufacturing system includes a movable build platen for the support of the printed part. A heated print head capable of melting the thermoplastic material. The systems that drives the print head to move spatially in the x-y direction. A cutting mechanism is employed to reduce the continuous strand into a discontinuous strand depending on the layer requirement, it is positioned adjacent to the ironing tip.

UTEP has filed a patent covering the handling and embedding process of a wire on a 3D printed or additively manufactured substrate [163]. The process described in this patent requires

of both an embedding head and an embedding surface. The embedding head is fixed on an automation motion system, the wire embedding head begins and terminates an embedded wire pattern on a surface of a three-dimensional part in order to automatically create an embedded wire pattern. A sensor tracks the distance between the direct wire embedding head and the embedding surface. The embedding head's position can be adjusted using the sensor's feedback. The embedded wire pattern comprises interconnections between electronic components, an electromagnetic device, a heating element, a heat dissipation element, and/or mechanical reinforcement.

A second patent filed by UTEP covers the systems or methods for embedding a filament or filament mesh in a three-dimensional structure, structural component or structural electronic, electromagnetic or electromechanical component/device [164]. Some of the mentioned technologies include the use of ultrasonic horns, joule heating, among others to accomplish the embedding process.

7.2.2 Methods

Printing with Continuous Multifunctional Composites (CMC) begins with the material form containing continuous elements embedded in a polymeric matrix. The CMC can be made out of reinforcing fibers, microelectronics, sensing elements, heating elements, cooling elements or a combination of multiple of these. The next step in the process of printing with CMC is coextruding the fully impregnated continuous strand with molten polymeric material within the co-extrusion head. As the CMC enters the co-extrusion head, heat begins to diffuse from the molten material to the CMC, thereby heating and melting if applicable the polymeric phase. Melting of the polymer phase allows the continuous fibers or elements to slip relative to one another and thus the system can be bent in a sharp radius during deposition. The following subsections describe first, the method used for producing the CMC. Second, the heat transfer analysis carried out to ensure that the polymeric phase in the CMC is fully molten at the exit of the co-extrusion head. Third, the system or apparatus developed for printing selectively and continuously with CMC is described.

7.2.2.1 Production of Continuous Multifunctional Composites Preform

To manufacture Continuous Multifunctional Composites (CMC), a pultrusion system was implemented to impregnate strands of continuous elements with polymeric materials. The process

for impregnating continuous fibers with polymeric materials is described in early patents by Imperial Chemical Industries [165]. Figure 7.22 outlines the primary steps in the pultrusion system implemented. This system has been utilized to produce CMC with continuous carbon fiber impregnated with Polyphenylene Sulfide (PPS).

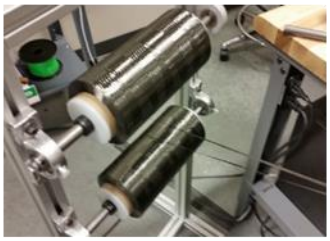

Spools of continuous elements

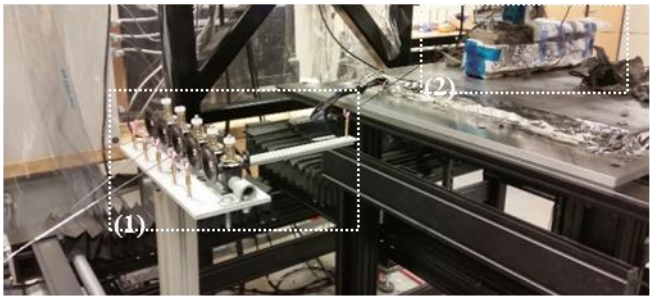

(1) Tensioners and converging pin. (2) Impregnation bath

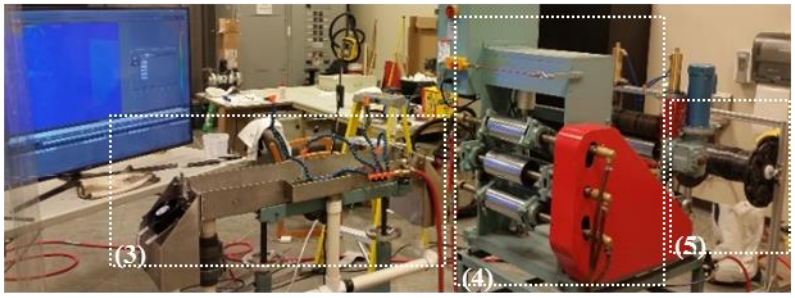

(3) Cooling bath. (4) Pulling system. (5) CNC Pick up system

Figure 7.22 Pultrusion system developed for producing CMCs

The pultrusion process begins with spools of bare, coated or sized continuous elements. Spools of carbon fiber in the example shown in Figure 7.22-A are mounted on rollers and kept fixed in place by a stationary frame (i.e., the spools are free to rotate but not translate in space). The strands of carbon fiber pass through a set of tensioners, by which an initial tension is applied to maintain the strands from loosening. Afterwards, the strands of carbon fibers are gathered with a converging pin. The converged strand then passes through a pulley located just before the inlet of the resin bath to establish the first contact angle. The contact angles are important to develop the impregnation pressure driving the polymer into the strand of continuous elements. The words “impregnated strand” and “CMC” are used interchangeably in the context of this document.

As the strand of continuous elements enters the impregnation bath consisting of a pool of liquid or molten polymer, a lubrication layer of polymer is drawn with the continuous strand. Inside

the impregnation bath, a set of fixed pins submerged in the liquid polymer guides the continuous strand through the bath. While the strand travels through the pins, pressure develops between the continuous strand and the stationary pins, thereby squeezing the liquid polymer into the strand of continuous elements. After sliding through the stationary pins, the impregnated strand travels through a converging die which also introduce a pressure gradient contributing to impregnate the strand. Further, the converging die shapes the final dimensions of the CMC. After leaving the impregnation bath, the impregnated strand is cooled down through natural convection in air and forced convection in water. In a final step, the pulling system, which drives the continuous strand through the impregnation bath, feeds the CMC pickup system. As a result of the careful design and control of the pultrusion process, the microstructure shown in Figure 7.23 is obtained. It should be noted that the continuous strand is greatly impregnated with the system shown above. Hence, the high level of impregnation obtained through this process used for producing the CMC mitigates the deficient impregnation attained with existing technologies for printing with continuous fibers.

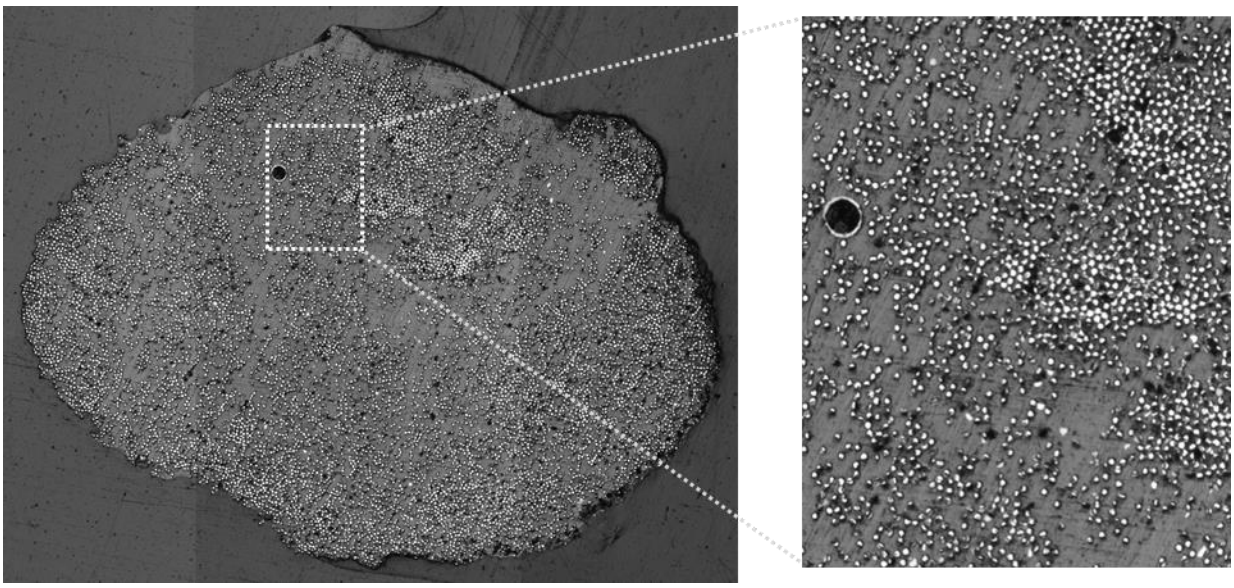

Figure 7.23 Microstructure of CMC made from continuous carbon fiber (shown in white) and PPS (shown in grey).

7.2.2.2 Heat Transfer Analysis of the Co-extrusion Process

Printing with multi-phase materials can be accomplished by a co-extrusion process where the CMC is fed into a co-extrusion nozzle conveying a phase of molten material. The molten phase can be either a reinforced or non-reinforced thermoplastic, thermoset or elastomer. As the CMC enters

the co-extrusion nozzle, the CMC is combined with molten polymeric material. The pressure built inside the nozzle aids wetting the surface of the CMC with the molten polymer, thereby reducing the thermal resistance to diffuse heat from the molten phase into the second or multiple phases. As the CMC and the molten phase flow along the co-extrusion nozzle, heat continues to diffuse into the continuous phase while additional heat is supplied by the body of the co-extrusion nozzle. Since thermal conductivity in polymeric materials is relatively low, the process of heat diffusion is slow and therefore there is a critical co-extrusion distance needed to fully melt the polymer in the second phase. Further, the critical co-extrusion distance is strongly dependent on the co-extrusion speed.

As a consequence of the small bending radius before failure of the CMC in the solid state, an essential consideration for printing with this material system is to melt the polymeric matrix in the CMC to a large extend so that the continuous strand can bend in a tight radius at the exit of the nozzle. Otherwise, excessive stresses can develop inside the CMC which could rupture the continuous elements in the CMC. To fulfill this condition with the design of the co-extrusion nozzle, a transient heat transfer analysis was carried out to estimate the temperature evolution of the material. The heat equation given by Equation 7.1 was derived by carrying out an energy balance around an infinitesimal element considered inside the co-extrusion nozzle. To capture the energy conveyed with the fluid flow, the advection term, $(\rho C_p v_z \partial T/\partial z)$, was included in the heat equation. The velocity of the flow v_z which represents the coextrusion speed is defined in the Z direction due to the Cartesian coordinate system used for deriving this expression. The density ρ and the heat capacity C_p come into play in the advection term as well.

$$\frac{\partial}{\partial x}\left(k_x \frac{\partial T}{\partial x}\right) + \frac{\partial}{\partial y}\left(k_y \frac{\partial T}{\partial y}\right) + \frac{\partial}{\partial z}\left(k_z \frac{\partial T}{\partial z}\right) - \rho C_p v_z \frac{\partial T}{\partial z} + \dot{q} = \rho C_p \frac{\partial T}{\partial t} \tag{7.1}$$

The heat diffusing in the three directions is described through the three thermal conductivities $k_i, i = x, y, z$. In addition to the diffusion and advection terms, an external heat source $\dot{q}$ is included to account for the latent heat of crystallization either absorbed in the event of melting of polymer crystals or released in the event of polymer crystallization. As stated before, the material used for producing the first batch of CMCs consist of a semi-crystalline polymeric matrix, namely Polyphenylene Sulfide. With regards to initial and boundary conditions for the

crystallinity in both phases, a fully crystallized initial condition is assumed for the CMC while a fully molten initial condition is assumed for the coextruding material. Two models, one describing polymer crystallization and other describing polymer melting, were used to describe the evolution of crystallinity in each regime. The crystallization process is temperature and time dependent and thus the model proposed by Velisaris and Seferis was used [112]. This model describes the evolution of crystallinity as a function of two mechanisms described by integral expressions $F_{vc_i}, i = 1{,}2$ and weighted through the weighting factors $w_i, i = 1{,}2$. The maximum fraction of crystallinity $X_{vc\infty}$ multiplies the sum of the two weighted integral expressions that vary from zero to one to define the degree of crystallinity as given by Equation 7.2.

$$X_{vc}(T,t) = X_{vc\infty}(w_1 F_{vc_1} + w_2 F_{vc_2}) \tag{7.2}$$

Similarly, the melting process of the crystalline regions in the polymer are described using the model developed by Greco and Maffezzoli [31]. This model assumes a statistical distribution of lamellar thickness and thus the melting process is only temperature dependent. The melting of polymer crystals is then given by Equation 7.3.

$$\frac{dX_{vc}}{dT} = k_{mb}\{\exp[-k_{mb}(T - T_c)]\} \cdot (1 + (d-1)\exp[-k_{mb}(T - T_c)])^{\frac{d}{1-d}} \tag{7.3}$$

Where k_{mb} and d capture the sharpness and the shape factor of the distribution of lamellar thickness, respectively. T_c Is the temperature recorded at the energy peak of the exothermic reaction recorded in DSC experiments. Due to the consistent distribution of lamellar thickness formed at different cooling rates, the transition between the crystallization and melting models is defined by the temperature condition given by Equation 7.4.

$$X_{vc} = X_{vc} + \Delta X_{vc}; \quad \Delta X_{vc} = \begin{cases} \Delta X_{vc}(T,t) > 0, & T < T_{om} \\ \Delta X_{vc}(T) < 0, & T \geq T_{om} \end{cases} \tag{7.4}$$

$$X_{vc} \in [0\ 1]$$

Where T_{om} is the average onset temperature of melting. Similar to the heat transfer analysis, the effect of the material flow must be considered in the evolution of crystallinity during the co-extrusion process. Therefore, the material derivative of the degree of crystallinity is carried out and rearrange in the form given by Equation 7.5 to describe the evolution of the crystallinity in an Eulerian frame of reference.

$$\frac{\partial X_{vc}}{\partial t} = \frac{DX_{vc}}{Dt} - \frac{\partial X_{vc}}{\partial z} v_z \tag{7.5}$$

The analysis described above was implemented in a UMATHT user subroutine and solved numerically using the commercial FEA package ABAQUS [166]. Initial conditions for crystallinity and temperature were imposed in the heat transfer analysis as well as the respective temperature boundary conditions at the inlet and body of the nozzle.

Initial and boundary conditions at the inlet of the coextrusion nozzle for the CMC were assumed at constant room temperature. Similarly, the PPS processing temperature (300 °C) was used for the initial and boundary conditions at the inlet of the coextrusion nozzle of the second phase since this enters the co-extrusion nozzle while is molten.

A constant temperature boundary condition was used for the nozzle. Figure 7.24-A sketches the geometry used in the heat transfer analysis. The materials utilized for this analysis comprise the previously produced CMC for the continuous phase and PPS reinforced with 50% by weight of discontinuous carbon fiber for the fully molten phase. Input material properties were estimated using micromechanics and characterized experimentally for the continuous and discontinuous phases, respectively.

The process for designing the co-extrusion nozzle involved first defining a target volume fraction of CMC. Based on CMC produced for testing this technology and a conservative initial trial volume fraction, a target of 10% was defined. Using the average diameter of the produced CMC (1.26 mm), a nozzle diameter of 4 mm was determined to fulfill the required volume fraction. A maximum extrusion speed of around 3500 mm/min was determined based on the nozzle diameter and the throughput of around 10 lb/hour given by the extrusion system. Upon defining these processing conditions, an iterative process followed to determine the nozzle length that will ensure the material get fully molten as is delivered at the end of the nozzle. After multiple iterations

a nozzle length of 70 mm was considered. Nevertheless, the length of the nozzle was extended by 2.5mm due to geometric constraints imposed by the existing CAMRI system which made a total nozzle length of 72.5 mm.

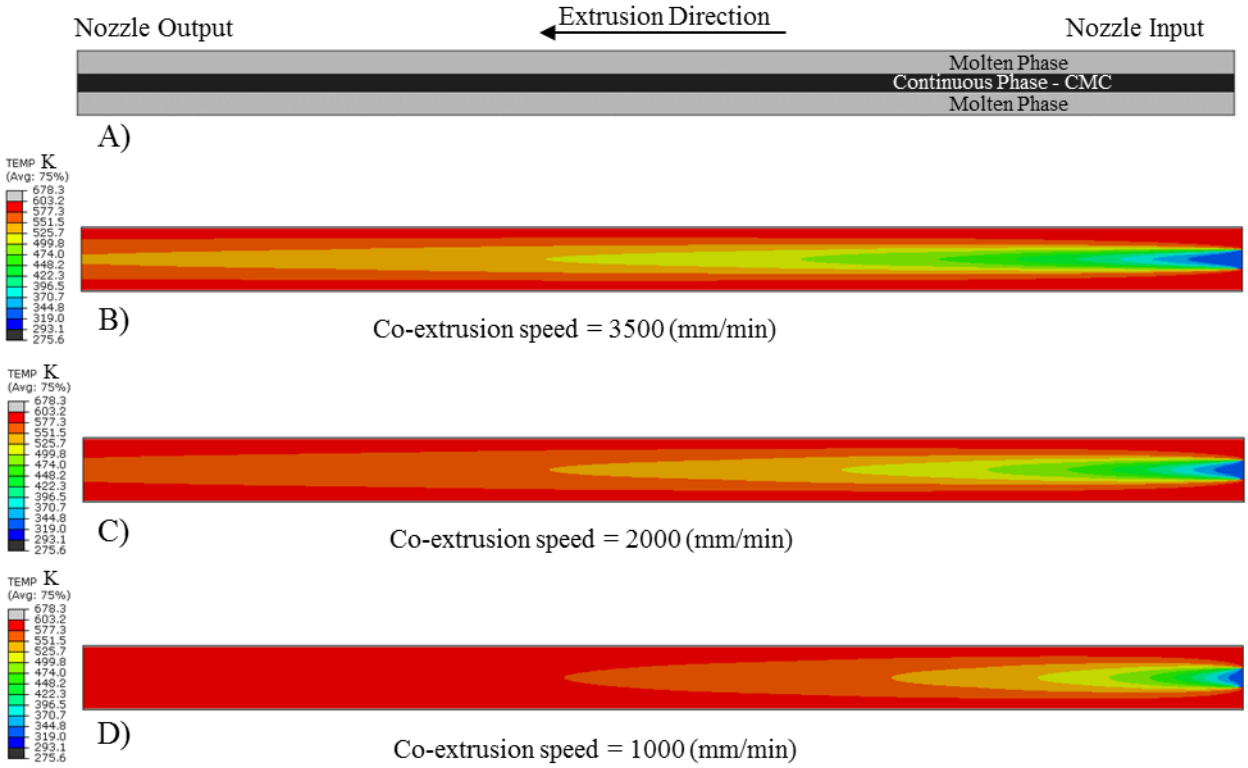

Figure 7.24 Temperature distribution inside the co-extrusion nozzle in steady state at different co-extrusion speeds. A) Sketch of the extrudate inside the co-extrusion nozzle. B) Steady state temperature distribution of the extrudate at co-extrusion speed of 3500 mm/min. C) Steady state temperature distribution of the extrudate at co-extrusion speed of 2000 mm/min. B) Steady state temperature distribution of the extrudate at co-extrusion speed of 1000 mm/min.

The set of pictures in Figure 7.24 compares the temperature distribution in steady state inside the co-extrusion nozzle at three different deposition speeds including the maximum extrusion speed. Similarly, Figure 7.25 compares the distribution of crystallinity in steady state inside the co-extrusion nozzle for the same set of printing speeds. The red regions in Figure 7.25 correspond to the material that is fully molten while the blue regions indicate fully crystallized material. Furthermore, the influence of the processing speed on the melting front is depicted in Figure 7.25

where the crystallization front moves closer to the end of the nozzle as the extrusion speed increases.

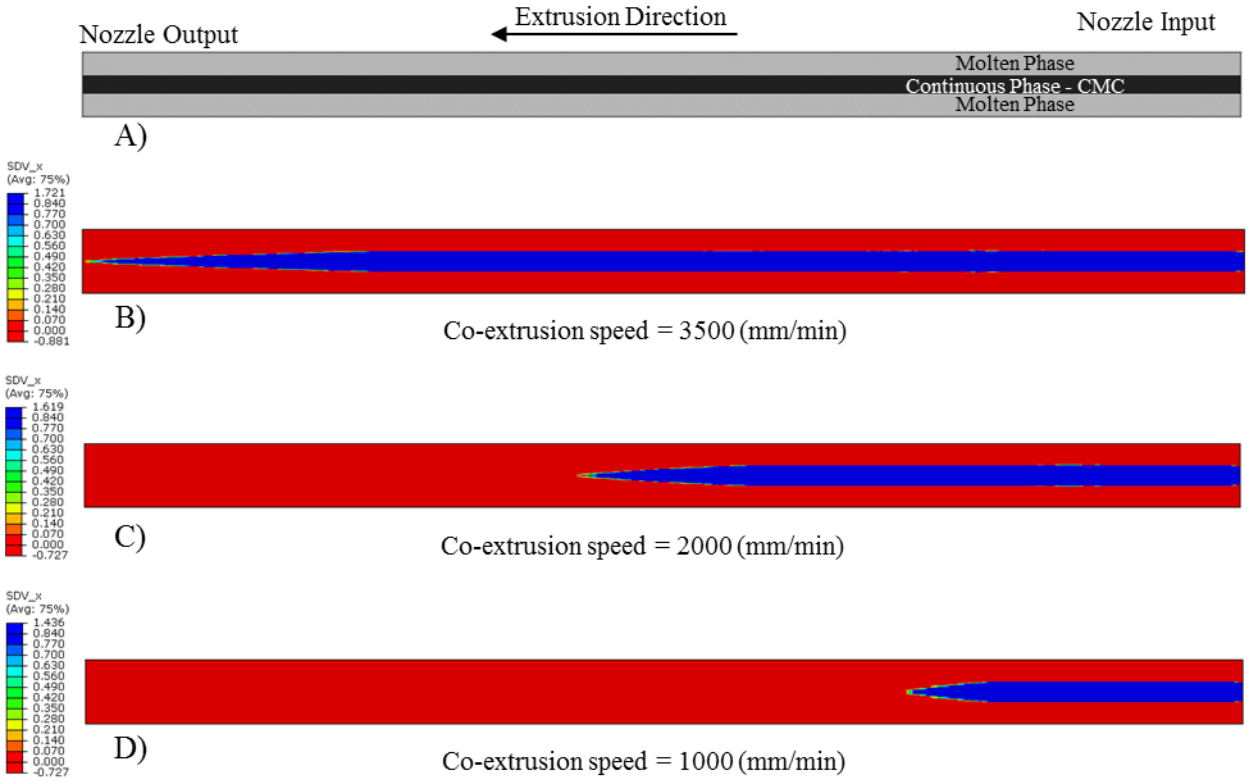

Figure 7.25 Distribution of crystallinity in the co-extrusion nozzle in steady state at different deposition speeds. A) Sketch of the extrudate inside the co-extrusion nozzle. B) Steady state distribution of crystallinity in the extrudate at co-extrusion speed of 3500 mm/min. C) Steady state distribution of crystallinity in the extrudate at co-extrusion speed of 2000 mm/min. B) Steady state distribution of crystallinity in the extrudate at co-extrusion speed of 1000 mm/min.

7.2.2.3 Co-extrusion System for Printing with CMC

The co-extrusion system or apparatus developed for printing with multiple phases was designed as a supplementary component that can be integrated in other EDAM systems by replacing the regular extrusion nozzle with this co-extrusion system. The render of the co-extrusion nozzle in Figure 7.26 shows three of the principal components of the co-extrusion system: 1) The feeding system, 2) the cutting system and 3) the co-extrusion head. In addition to the co-extrusion system, the structure of the control algorithm for printing with CMC is described in this subsection.

First, the feeding system comprises one or multiple pairs of rollers which drive the CMC strand. The rollers are design to accommodate CMC strands with a wide variety of diameters. The rollers can be driven by any type of electric motor. Further, a constant pressure is maintained between each pair of rollers to maintain contact between the CMC and the rollers and to improve traction.

Second, the cutting system (Figure 7.26) consists of a sharp blade which is pressed against the CMC when cutting, thereby enabling to cut the CMC at any time during the printing process. This way, CMC can be printed selectively. The cutting blade can be actuated via electric, pneumatic, hydraulic, or other type of actuators.

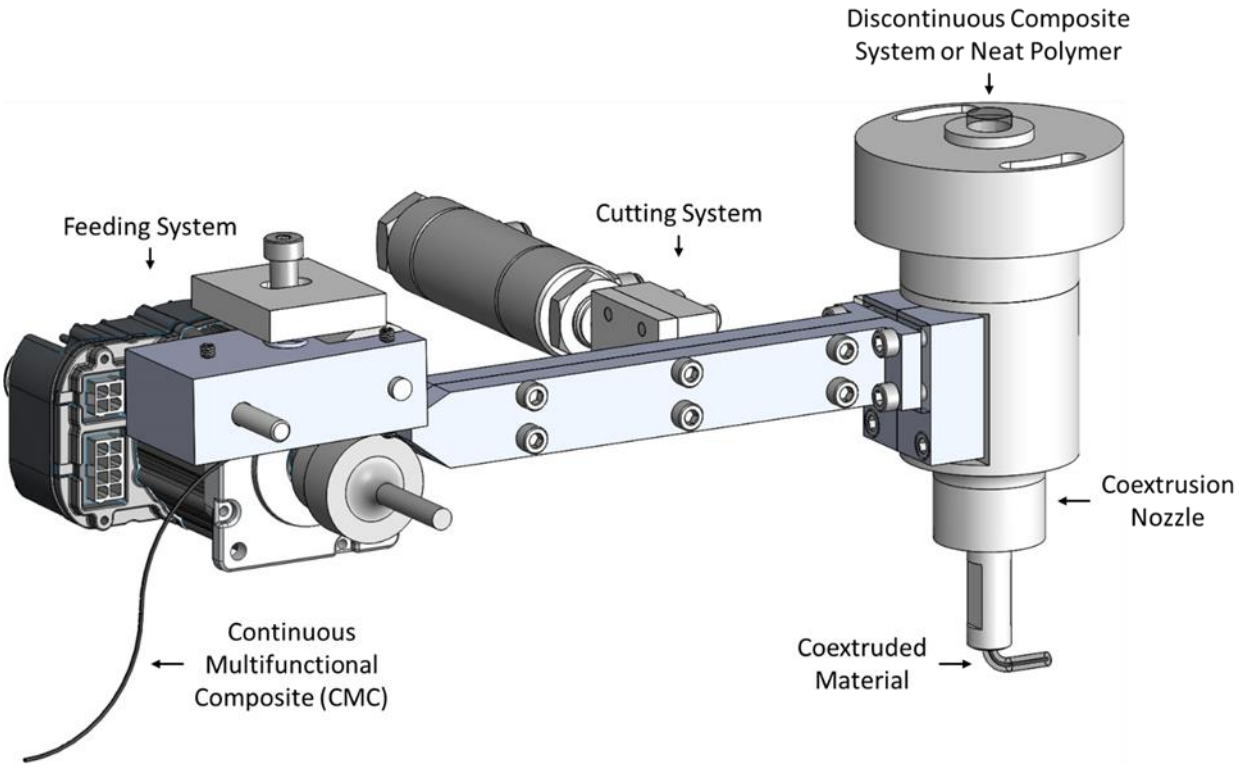

Figure 7.26 Co-extrusion system for printing with two phases (CMC and molten polymeric material).

Third, the co-extrusion nozzle (Figure 7.26) is where the CMC strand is combined with molten fluid. The fluid may be a reinforced or non-reinforced polymer composite. The CMC and molten fluid are pressurized, driven out of the co-extrusion nozzle and deposited. The CMC strand is guided to enter the co-extrusion nozzle tangent to the flow of molten material. This design permits

easy alignment of the CMC strand with the incoming material and prevents sharp bending of the CMC which could cause its rupture. A cross-section view of the co-extrusion system shown in Figure 7.27 renders the trajectory the CMC follows from the feeding system until the end of the nozzle.

Coextruding technology has been in industry for a long time, however, the existing control systems are not suitable for utilizing this technology in the context of additive manufacturing. As a result, a novel control approach for continuously and selectively dispensing a continuous strand of CMC was developed. Further, this control approach can be readily extended to accommodate feeding multiple phases simultaneously. The structure of the control system is summarized as follows.

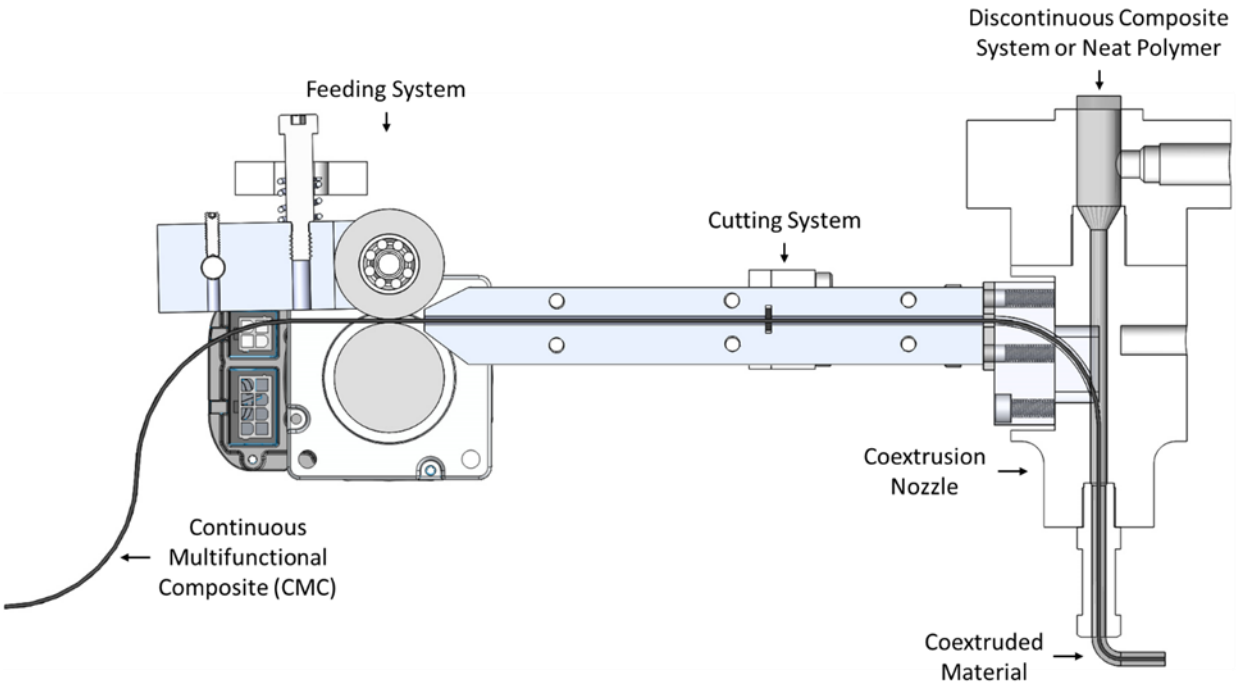

Figure 7.27 Cross-section view of co-extrusion system.

To start printing with CMC, an event either included in the machine code or manually introduced by the user triggers the feeding system. In the event of activating the feeding system, the control algorithm determines the right time and speed to start feeding CMC into the co-extrusion nozzle such that the CMC is delivered at the desired time and position in the printing process. In the event of disabling the CMC while printing, the control algorithm estimates the right time to stop feeding

CMC and trigger the cutting mechanism. It is noteworthy to mention that other conditions like feeding CMC at different rates than the co-extrusion material are possible with this control system.

7.2.3 Preliminary Results

Many benefits and a wide range of new possibilities are readily recognized by printing CMCs with the apparatus or system described above. However, the benefit of printing with CMCs specifically designed for improving the mechanical properties, namely stiffness and strength, has been investigated through analytical tools. It should be noted that a structural CMC has been already produced at the CMSC with carbon fiber and PPS with the pultrusion process described in the methods section. An engineering analysis using micromechanics was carried out to determine the improvement in stiffness achieved by introducing the structural CMC in discontinuous carbon fiber reinforced PPS.

The elastic modulus of the composite is greatly influenced by the fiber volume fraction, however, the strength of the composite is greatly influenced by the fiber length rather than the fiber volume fraction [167]. As a result, the contribution of the structural CMC to the strength of the printed materials is expected to be more significant than the increase in elastic modulus. Predicting strength requires further understanding of the microstructure developed after the co-extrusion process of the CMC as well as the failure mechanisms governing the strength of the composite, therefore predictions are limited to stiffness thus far.

The method of finite elements was used to conduct the micromechanical analysis of an mesostructure containing three phases as shown in Figure 7.28. The phase shown in blue depicts the discontinuous fibers in the molten phase used in the co-extrusion process, whereas the phase in red corresponds to the continuous fibers in the CMC. The third phase which correspond to the clear regions in the Representative Volume Element (RVE) represents the polymeric matrix. The following assumptions were made for the sake of this initial predictions of the elastic modulus.

- Continuous fibers are assumed to be dispersed across the RVE while the orientation was enforced in the print direction.
- The matrix is assumed to be isotropic and the fibers transversely isotropic. Both materials behave linearly elastic.
- The fibers are assumed to be cylindrical with constant diameter.
- A perfectly bonded assumption is made at the fiber-matrix interface

- The orientation of the fibers in the phase with discontinuous fibers disregards the effect of the continuous fibers.

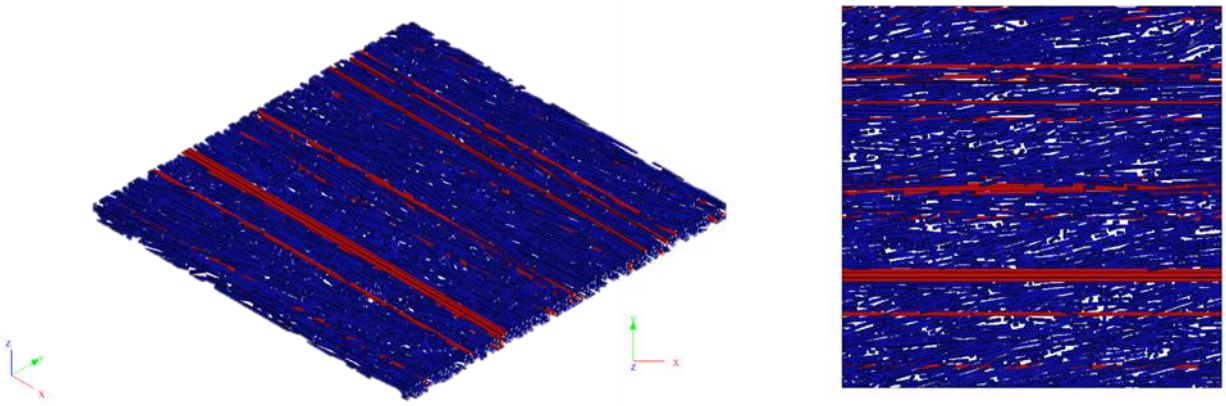

Figure 7.28 Representative volume element of the double phase material system. Red: Fibers of the continuous phase. Blue: Fibers of the discontinuous phase.

Table 7.1 lists the properties of the constituent materials used in the prediction of the elastic modulus for the hybrid material [168].

Table 7.1 Properties of constituent materials used in micromechanics analysis

Polyphenylene Sulfide (PPS)	
$E\ (GPa)$	3.5
ν	0.3
AS4 Carbon Fiber	
$E_1(GPa)$	235.0
$E_2 = E_3\ (GPa)$	14.0
$\nu_{12} = \nu_{13}$	0.2
ν_{23}	0.25
$G_{12} = G_{13}(GPa)$	28.0
$G_{23}(GPa)$	5.5

As mentioned before, a volume fraction of 10% of continuous phase was chosen as initial testing condition, which was also used for determining the critical nozzle length. The fiber volume fraction inside the continuous phase is 40% whereas the fiber volume fraction in the phase with discontinuous fiber is 40%. Therefore, the fiber volume fraction of 40% is preserved in the final hybrid material. With regards to the fiber orientation, the second order orientation tensor $[A]_{cf}$

and $[A]_{df}$ given by Equation 7.6 describes the orientation state in the phase with continuous and discontinuous fibers, respectively.

$$[A]_{df} = \begin{bmatrix} 0.8 & 0 & 0 \\ 0 & 0.15 & 0 \\ 0 & 0 & 0.05 \end{bmatrix}$$

$$[A]_{cf} = \begin{bmatrix} 1.0 & 0 & 0 \\ 0 & 0 & 0 \\ 0 & 0 & 0 \end{bmatrix} \tag{7.6}$$

The elastic modulus in the 1-direction predicted for the system of discontinuous fiber and 10% of CMC and the discontinuous fiber system is reported in Table 7.2. The value of the discontinuous fiber system agrees with experimental results obtained for the same material system which provides confidence in the predictions made through micromechanics for the material system including CMC.

Table 7.2: Prediction of elastic moduli for material system reinforced with CMC and without CMC

Property	$V_{df} = 100$	$V_{df} = 90, V_{cf} = 10$
$E_1(GPa)$	26.4	36.2

An improvement of around 37% in the elastic modulus (E_1) can be gained by inserting 10% of CMC in the carbon fiber reinforced PPS used for printing. Furthermore, a significant improvement in the strength of the printed composite is expected for the material system including CMCs. These two significant improvements in the mechanical properties of printed composites can enable printing structural components that only required in-plane properties. Nevertheless, this system or apparatus for printing CMC can be readily extended for 3-D printing with multiple axis.

7.2.4 Conclusions and Ongoing Work

Both the CMC and the apparatus or system for printing with multiple phases was introduced throughout this paper. Engineering heat transfer analysis of the co-extrusion process was carried out to determine processing conditions needed to melt a CMC continuously. The results from the heat transfer analysis guided the design process of the extrusion head described herein. A control

scheme developed for printing with continuous fibers was outlined. Preliminary results obtained through micromechanical analysis of the target mesostructure reveals the improvements gained in stiffness due to the addition of continuous fibers. Ongoing work includes physical testing of the co-extrusion system and characterization of the multi-phase material system analyzed through micromechanics. Subsequently, multifunctional CMC will be produced with the already developed pultrusion system at Purdue and experimentally tested in a printed component.

In addition to reinforcing printed composites, applications that will leverage the versatility of the CMC include, but are not limited to reinforced components with health monitoring for industries producing parts for the automotive, aerospace or sporting equipment. In addition to the inclusion of this technology on existing products, the tooling industry which is undergoing a revolution with the arrival of the additive manufacturing technologies could leverage other features of the CMC like active heating or cooling in tools for compression molding, injection molding, resin transfer molding or any other polymer or composite processing tool.

8. CONCLUSIONS AND RECOMMENDATIONS

This final chapter starts by providing a brief overview of the topics covered in each chapter. Following the overview, conclusions and final remarks are provided for each chapter. Finally, general recommendations for future work and improvements to current work are provided at the end of this chapter.

Chapter 2

A throughout review on the state of the art in EDAM process equipment and EDAM process simulations was provided in this chapter. The EDAM process was described in terms of all the physical phenomena participating in this manufacturing process.

Literature reviewed on experimental characterization of printed composites showed significant progress done recently on improving mechanical properties of printed parts with the addition of continuous reinforcing fibers. However, these approaches developed for desktop scale additive manufacturing are not readily scalable for medium to large part manufacturing. This problem was identified earlier and a technology was developed and protected for coextruding a pre-impregnated filament with continuous fibers which can overcome the limits in deposition rate of the filament-based methods. Details on this technology are provided in Chapter 8. The last section of this chapter addressed the application of EDAM with composites for applications of printed tooling. An experimental investigation on the creep deformation in a printed tool after an autoclave cycle was presented here. Permanent deformations in the range of $0.1\ mm$ were quantified. Further, recommendations for assessing materials for specific tool applications were provided.

Chapter 3

A medium scale EDAM system was developed with the goal of investigating the phenomena involve in this manufacturing process. A distributed control system was developed and implemented to simultaneously control the single-screw extrusion of high-temperature fiber reinforced polymers and the material deposition. An adaptive closed control system provides regulation for the pressure output by the single-screw extruder whereas a feedforward control system compensates for the viscoelastic behavior of the molten polymer, the compressibility of the polymer and the response time inherent to the system during material deposition. The following conclusions are drawn based on the work presented in this chapter.

- The feedforward control system corrects for oozing and lack of flow at changes in deposition speed, for example at starts and stops in the printing process of a part, thereby reducing material accumulation and empty regions when these events occur. Material and equipment parameters required for this control system are characterized with simple experiments that can be performed with the same system as presented in this chapter.
- The adaptive closed loop control system implemented for the single-screw extruder provides a well bounded pressure despite fluctuations in flow rate that occur during printing. Which is a requirement for the proper operation of the extrusion gear pump used in CAMRI. The printing process of a part with large changes in printing speed demonstrated this functionality.
- The largest contribution made by developing this system was providing our group with a research tool to investigate the EDAM process. The custom developed distributed control system provided unparalleled flexibility for custom experiments as well as for investigating the influence of process and control parameters on the material deposition process. Further, the data and process acquisition capabilities in CAMRI simplified validation of predictions made in the EDAM process simulation.

Chapter 4

The phenomenon of bonding and the multiple mechanisms of heat conduction presented in this dissertation were implemented in the context of an existing framework for simulating the EDAM process. In this EDAM process simulation framework, the process of depositing beads of molten material is replicated virtually by activating elements in a part unspecific mesh and utilizing the machine code used for part manufacturing. This chapter describes in detail the simulation framework implemented by Favaloro et al. [73] in Abaqus© utilizing a suite of user-defined subroutines. An addition was made to his implementation in order to track the type of features printed within a part which was used in chapter five to apply feature dependent convection conditions. Finally, this chapter provides an overview of all the material models currently used in this simulation framework including the work presented in this dissertation and work presented in the dissertation from Brenken [16].

Chapter 5

This chapter presented in great detail the mechanisms of heat transfer participating in the EDAM process. Predicting the material temperature evolution is of paramount importance in EDAM since

the thermoelastic, the thermophysical, the diffusion and the mechanical properties of polymeric materials change significantly as these cool down from the deposition temperature to room temperature. Hence, previous work on this subject was extended significantly to improve the predictive capabilities in the EDAM process simulation. The primary four additions made include: First, the evolution of crystallinity was strongly coupled with the heat transfer analysis to account for heat of crystallization which was characterized from DSC experiments. This was implemented in a UMATHT© user subroutine.

Second, feature dependent convection conditions were enabled in order to implement convection conditions depending on the type of feature printed, namely external walls, internal walls, infill regions or solid sections. A correlation expression for external walls was derived from numerical analysis of natural convection from a vertical surface with temperature gradients commonly developed during part manufacturing. Although this correlation expression is not general since it does not capture the influence of the part geometry, it provides a better description of the mechanism of natural convection. A correlation expression found in the literature was used to describe convection from solid sections. These correlation expressions were implemented in a UFIELD© user subroutine.

Third, the heat removed during material compaction was modeled as a moving heat flux with a double Gaussian distribution. The heat removed with the tamper in CAMRI during part manufacturing was characterized experimentally. The implementation of the moving heat flux was performed in a UMDFLUX© subroutine.

Fourth, the emissivity of the printed material was characterized experimentally as a function of temperature. The radiation ambient temperature was the only parameter calibrated in the process simulation. Recommendations for first order estimates of the ambient radiation temperature were provided.

A validation case was presented in which a great correlation was obtained between the predicted and the experimental temperature history recorded during the printing process of a stringer tool. The following conclusions are drawn based on an investigation presented on the contribution of each heat transfer mechanisms to the temperature predictions.

- Radiative heat losses were found to dominate cooling from exposed surfaces on the vertical wall of the stringer tool at temperatures in the range from the deposition temperature to above $500\ K$ whereas convective heat losses dominate below this temperature.

- The latent heat of crystallization had a minor effect on the temperature predictions, however, it is recommended to consider heat of crystallization in parts with thick printed sections.
- Utilizing a constant average convection coefficient instead of a local convection coefficient significantly overestimates the cooling process dominated by convection at temperatures below $500\,K$. Therefore, utilizing the correlation expression derived from numerical analysis of natural convection is recommended. Although this expression is not general since it does not capture geometry effects, it provides a better physical description of the convection mechanism than a constant average convection coefficient.
- Capturing the thermal energy removed during material compaction was found to have a strong impact on the temperature predictions at the early stages of the material deposition. Also, subsequent interactions of the compacter with already printed material are captured with the model implemented for the compacter.

Chapter 6

A phenomenological model for predicting the evolution of interlayer fracture properties, namely G_{IC}, was presented in this chapter. Interlayer properties in fusion bonded semi-crystalline polymers is strongly influenced by the crystalline microstructure formed across an interface which in this case was assumed to be controlled by the amount of polymer chain diffusion occurring across an interface between adjacent layers and prior to development of crystallinity. Since polymer diffusion is precluded upon crystallization, a coupling was made between a phenomenological model describing polymer diffusion and phenomenological models describing the evolution of crystallinity. Further, the assumption of instantaneous wetting was made based on the material compaction provided with the tamper. The welding time required for the fusion bonding model was characterized combining experimental measurements of the degree of bonding and predictions of temperature histories obtained with the EDAM process simulations. The degree of bonding was determined from values of G_{IC} characterized through double cantilever beam fracture experiments of specimens printed with different processing conditions. The evolution of crystallinity was controlled by a polymer crystallization model coupled with a polymer melting model previously implemented by Brenken et al. [72]. The implementation of the fusion bonding model was performed in a UMATHT© subroutine. This fusion bonding model enabled predicting G_{IC} developed between layers based on the temperature and the crystallization histories.

Predictions of the degree of bonding were confirmed by simulating the printing process of plates used for preparing DCB specimens used in fracture tests. Based on the results presented in this chapter the following conclusions are drawn.

- The fusion bonding model presented here stablished a relation between processing conditions and interlayer fracture properties which is extremely valuable for anticipating weak interlayer bonding prior to part manufacturing. With this information, the printing process of part can be designed to mitigate weak interlayer bonding, thereby bridging the empirical gap of finding processing conditions that would lead to crack-free printed parts.
- Predictions of the degree of bonding, D_b, in the range of 1 to 0.4 are confirmed against experimental results. A degree of bonding of 1 corresponds to the interlayer fracture property G_{IC} of a perfectly bonded joint.
- Predictions of degrees of bonding below 0.4 suggest secondary bonding where polymer crystals nucleate at the surface of previously deposited layers. A more accurate definition of this limit requires additional experimental data. Additionally, a non-local implementation of this fusion bonding model can provide a more precise description of the local fusion bonding process. Suggestions for future implementations are provided in chapter 5.
- The interlayer fracture properties predicted with the fusion bonding model can be integrated in failure models to predict delamination during the printing process of a part or during service of a part.

Chapter 7

Two inventions were presented in this chapter, one concerned with in-situ printing of heating elements for high-temperature tooling applications and a second one concerned with methods for printing with multiphase materials. While the first invention overcomes limitations of existing tool heating technologies to provide uniform temperature distribution on the surface of printed tools, the second invention provides a method to scale up the deposition rates currently available for printing with continuous fibers. Also, the method developed in this invention overcomes the problem of marginal impregnation of fibers with polymeric matrix attained in existing methods for printing with continuous fibers.

8.1 Recommendations for Future Work

Significant progress on the field of Extrusion Deposition Additive Manufacturing of semi-crystalline polymer composites was presented in this dissertation and the dissertation from Bastian Brenken [16]. Nevertheless, a list of problems and phenomena that still need to be addressed from the side of process modeling and from the side of the EDAM technology is provided below.

- Modeling intra-bead failure and the combination of both: intra-bead failure and interlayer failure during part manufacturing. Situations where a crack initiates at an edge and propagates into adjacent beads has been encountered during part manufacturing in large-scale EDAM systems.
- Investigate mechanism strengthening the interface between in-plane adjacent beads. While the interlayer strength between adjacent layers is governed by fusion bonding, other mechanism strengthening an interface between two in-plane adjacent beads may develop including the presence of fibers across the interface.
- The thermoviscoelastic behavior of the molten material for predicting sagging during material compaction and due to gravity deserves further research and work on modeling.
- Develop reduced models that could be used in the process control of large-scale EDAM systems as well as to aid in the phase of part design for EDAM.
- Predict interlayer fusion bonding in amorphous polymers. While the model for fusion bonding presented herein is for semi-crystalline polymers, the same model yet without considering crystallization can be used to predict diffusion-controlled interlayer fracture properties of amorphous polymers.
- With regards to the EDAM technology, methods to provide controlled fiber orientation will allow reducing the anisotropy in the printed bead and thus the stresses caused by local changes in bead orientation within a printed part.
- Methods to promote fibers across the interlayer interface should be developed to enhance the interlayer fracture properties.

APPENDIX A. MATERIAL PROPERTIES AND PARAMETERS

Table A.1 Elastic constants of the 50% by weight carbon fiber reinforced PPS [16].

Property	**Value**
$E_1\ (GPa)$	28.08
$E_2\ (GPa)$	5.23
$E_3\ (GPa)$	4.50
ν_{12}	0.29
ν_{13}	0.40
ν_{23}	0.42
$G_{12}\ (GPa)$	3.15
$G_{13}\ (GPa)$	2.51
$G_{23}\ (GPa)$	1.50

Table A.2 Temperature dependent coefficients of thermal expansion in the three principal directions of printed 50% by weight carbon fiber reinforced PPS [16].

Temperature Range	$\boldsymbol{\alpha_1}\ \boldsymbol{(1/K)}$	$\boldsymbol{\alpha_2}\ \boldsymbol{(1/K)}$	$\boldsymbol{\alpha_3}\ \boldsymbol{(1/K)}$
$T < T_g$	$2 \cdot 10^{-6}$	$26.8 \cdot 10^{-6}$	$43.0 \cdot 10^{-6}$
$T_g < T < T_C$	$2 \cdot 10^{-6}$	$1.85 \cdot 10^{-7} \cdot T - 3.18 \cdot 10^{-5}$	$7.32 \cdot 10^{-7} \cdot T - 2.01 \cdot 10^{-4}$
$T_C < T$	$2 \cdot 10^{-6}$	$2.36 \cdot 10^{-7} \cdot T - 1.01 \cdot 10^{-4}$	$7.78 \cdot 10^{-7} \cdot T - 3.49 \cdot 10^{-4}$

Table A.3 Sample dimensions, masses, density values [107]. Sample A-1 corresponds to sample of Material in the 1-Direction, Sample A-2 corresponds to sample of Material in the 2-Direction, Sample A-3 corresponds to sample of Material in the 3-Direction.

Sample Description	Thickness (cm)	Diameter (cm)	Mass (gm)	Density $(\mathrm{gm}/\mathrm{cm}^3)$
SAMPLE A-1	0.2311	1.2687	0.36897	1.262
SAMPLE A-2	0.2527	1.2699	0.40756	1.272
SAMPLE A-3	0.2536	1.2698	0.40654	1.265

Table A.4 Results for the specific heat [107].

Sample Description	Temperature (°C)	Specific Heat ($W \cdot sec / gm \cdot K$)
Sample A	23.0	0.9215
	25.0	0.9264
	30.0	0.9364
	35.0	0.9461
	40.0	0.9555
	45.0	0.9650
	50.0	0.9746
	55.0	0.9848
	60.0	0.9954
	65.0	1.0071
	70.0	1.0199
	75.0	1.0341
	80.0	1.0502
	85.0	1.0674
	90.0	1.0868
	95.0	1.1078
	100.0	1.1285
	105.0	1.1459
	110.0	1.1593
	115.0	1.1731
	120.0	1.1881
	125.0	1.2024
	130.0	1.2168
	135.0	1.2313
	140.0	1.2452
	145.0	1.2589
	150.0	1.2726
	155.0	1.2871
	160.0	1.3007
	165.0	1.3143
	170.0	1.3288
	175.0	1.3425
	180.0	1.3564
	185.0	1.3702
	190.0	1.3832
	195.0	1.3985
	200.0	1.4120
	205.0	1.4265

Table A.4 Continue

Sample Description	Temperature (°C)	Specific Heat ($W \cdot sec/gm \cdot K$)
Sample A	210.0	1.4393
	215.0	1.4539
	220.0	1.4675
	225.0	1.4799
	230.0	1.4923
	235.0	1.5048
	240.0	1.5182
	245.0	1.5299
	250.0	1.5401

Table A.5 Thermal diffusivity results [107]. Sample A-1 corresponds to sample of Material in the 1-Direction, Sample A-2 corresponds to sample of Material in the 2-Direction, Sample A-3 corresponds to sample of Material in the 3-Direction.

Temperature (°C)	SAMPLE A-1 (cm^2/sec)	SAMPLE A-2 (cm^2/sec)	SAMPLE A-3 (cm^2/sec)
23.0	0.01689	0.00611	0.00332
50.0	0.01602	0.00582	0.00319
100.0	0.01533	0.00546	0.00267
150.0	0.01502	0.00530	0.00219
200.0	0.01466	0.00498	0.00207
250.0	0.01465	0.00482	0.00194

Table A.6 Thermal conductivity calculations [107]. Sample A-1 corresponds to sample of Material in the 1-Direction, Sample A-2 corresponds to sample of Material in the 2-Direction, Sample A-3 corresponds to sample of Material in the 3-Direction.

Sample Description	Temperature (°C)	Temperature (°F)	Density (gm/cm^3)	Specific Heat ($W \cdot sec/gm \cdot K$)	Diffusivity (cm^2/sec)	Thermal ($W/cm \cdot K$)	Conductivity ($BTU \cdot in/hr \cdot ft^2 \cdot F$)
SAMPLE A-1	23.0	73.4	1.2623	0.9215	0.01689	0.01964	13.6236
	50.0	122.0	1.2623	0.9746	0.01602	0.01971	13.6665
	100.0	212.0	1.2623	1.1285	0.01533	0.02184	15.1432
	150.0	302.0	1.2623	1.2726	0.01502	0.02413	16.7314
	200.0	392.0	1.2623	1.4120	0.01466	0.02613	18.1194
	250.0	482.0	1.2623	1.5401	0.01465	0.02848	19.7495
SAMPLE A-2	23.0	73.4	1.2726	0.9215	0.00611	0.00716	4.9685
	50.0	122.0	1.2726	0.9746	0.00582	0.00721	5.0054
	100.0	212.0	1.2726	1.1285	0.00546	0.00784	5.4373
	150.0	302.0	1.2726	1.2726	0.00530	0.00858	5.9519
	200.0	392.0	1.2726	1.4120	0.00498	0.00894	6.2052
	250.0	482.0	1.2726	1.5401	0.00482	0.00944	6.5507
SAMPLE A-3	23.0	73.4	1.2651	0.9215	0.00332	0.00387	2.6838
	50.0	122.0	1.2651	0.9746	0.00319	0.00393	2.7273
	100.0	212.0	1.2651	1.1285	0.00267	0.00381	2.6432
	150.0	302.0	1.2651	1.2726	0.00219	0.00352	2.4449
	200.0	392.0	1.2651	1.4120	0.00207	0.00369	2.5641
	250.0	482.0	1.2651	1.5401	0.00194	0.00378	2.6210

Table A.7 Principal components of the fiber orientation tensor characterized from bead printed in CAMRI [16].

Tensor Component	Value
a_{11}	0.763
a_{22}	0.178
a_{33}	0.059

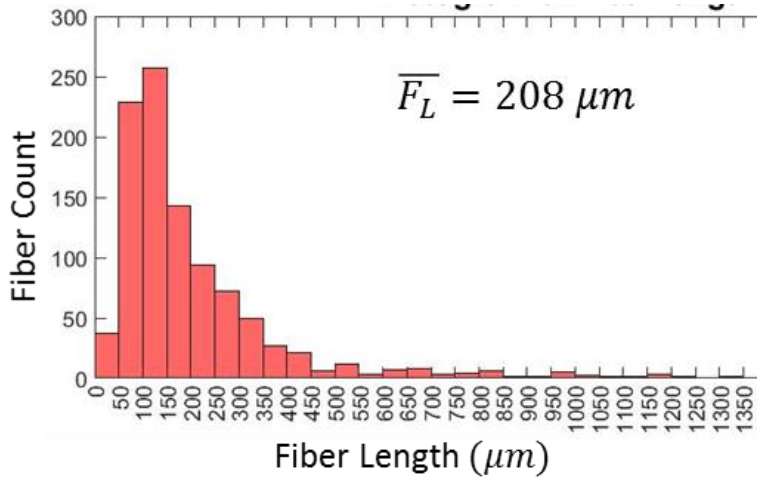

Figure A.1 Fiber length distribution after processing pellets of PPS reinforced with long discontinuous fibers in CAMRI.

Table A.8 Summary of mechanical properties in the 1-direction reported in the literature for different printed materials.

Source	**Material**	**Tensile Modulus** ($\boldsymbol{GPa}$)	**Tensile Strength** ($\boldsymbol{MPa}$)
Tekinalp et al. [25]	ABS/CF 10wt.%	7.7	52
	ABS/CF 20wt.%	11.5	60
	ABS/CF 30wt.%	13.8	62
	ABS/CF 40wt.%	13.7	67
Love et al. [2]	ABS/CF 13vol.%	8.91	70.69
Ning et al. [169]	ABS/CF 3wt.%	2.1	40.8
	ABS/CF 5wt.%	2.45	42
	ABS/CF 7.5wt.%	2.5	41.5
	ABS/CF 10wt.%	2.15	33.8
	ABS/CF 15wt.%	2.25	35
Hill et al. [38]	ABS/CF 20wt.%	8.4	66.8
Duty et al. [36]	ABS/CF 20wt.%	11.9	65.7
	ABS/GF 20wt.%	5.7	54.3
	ABS/GF 40wt.%	10.8	51.2
Compton and Lewis [42]	Epoxy/SiC/CF 10wt.%	24.5	66.2
DeNardo [15]	PPS/CF 50wt.%	26.4	92.2
Gardner et al. [41]	PEI/CNT 4.7wt.%	3	125.3
Shofner et al. [170]	ABS/VGCF 10wt.%	0.8	37.4
Shofner et al. [171]	ABS/VGCF 5wt.%	1.27	27
	ABS/5wt.% SWNT	1.74	32.5
Perez et al. [172]	ABS/Jute fiber 5wt.%	1.54	25.9
Bahajan et al. [43]	Epoxy/CF 15wt.%	4.05	66.3

Table A.9 Continued

Duty et al. [37]	ABS/chopped CF 20wt.%	10.87	47.7
	ABS/CF 15wt.%	11.88	61.9
	PEI/CF 20wt.%	8.36	61.1
Ferreira et al. [45]	PLA/CF 15wt.%	7.54	53.4
Hill et al. [39]	PA6/CF 20wt% / Prop 25wt%	16.11	146.9
	PA6/CF 30wt% / Prop 20wt%	17.33	128.2
Spoerk et al. [44]	PP/CF 10 vol%	2.981	42.835
	PP/CF 15 vol%	3.946	48.89
	PP/CF 20 vol%	4.7354	57.25
Ferreira et al. [45]	PETG/CF 20%wt	3.3	29.8

Table A.10 Summary of mechanical properties in the 2-direction reported in the literature for different printed materials.

Source	**Material**	**Tensile Modulus** ($\boldsymbol{GPa}$)	**Tensile Strength** ($\boldsymbol{MPa}$)
Love et al. [2]	ABS/CF 13vol.%	1.52	7
Hill et al. [38]	ABS/CF 20wt.%	2.6	12.8
Duty et al. [36]	ABS/CF 20wt.%	2.1	10.3
	ABS/GF 20wt.%	2.5	15.3
Compton and Lewis [42]	Epoxy/SiC/CF 10wt.%	8.06	43.9
DeNardo [15]	PPS/CF 50wt.%	2.6	9.72
Mahajan et al. [43]	Epoxy/CF 15wt.%	2.84	46
Duty et al. [37]	ABS/chopped CF 20wt.%	1.98	6.8
	ABS/CF 15wt.%	1.83	5.8
	PEI/CF 20wt.%	1.1	4.3
Ferreira et al. [45]	PLA/CF 15wt.%	3.92	35.4

Table A.11 Summary of mechanical properties in the fiber direction reported in the literature for continuous fiber reinforced materials.

Source	**Impregnation Method**	**Material**	**Tensile Modulus** ($\boldsymbol{GPa}$)	**Tensile Strength** ($\boldsymbol{MPa}$)
Matsuzaki et al. [46]	In-situ impregnation	PLA/CF 6.6vol%	19.5	185.2
		PLA/Jute fiber 6.1vol%	5.11	57.1

Table A.12 Continued

Van der Klift et al. [57]	Pre-impregnated filament	Nylon/CF 6vol.%*	14	140
		Nylon/CF 18vol.%*	35.7	464.4
Li et al. [47]	In-situ impregnation	PLA/CF 34vol.%	23.8	91
Melenka et al. [59]	Pre-impregnated filament	Nylon/AF 4vol.%	1.77	31
		Nylon/AF 8vol.%	6.92	60
		Nylon/AF 10vol.%	9	84
Tian et al. [48]	In-situ impregnation	PLA/CF 10wt.%	20.6	256
Bettini et al. [49]	In-situ impregnation	PLA/AF 8.6vol.%	9.34	203
Dickson et al. [56]	Pre-impregnated filament	Nylon/CF 11vol.%	8.46	198
		Nylon/AF 8vol.%	4.23	110
		Nylon/GF 8vol.%	3.29	156
		Nylon/AF 10vol.%	4.76	161
		Nylon/GF 10vol.%	4.91	212
Yang et al. [50]	In-situ impregnation	ABS/CF 10wt.%	4.19	147
Goh et al. [54]	Pre-impregnated filament	Nylon/CF 41%	13	600
		Nylon/GF 35%	20	450
Gonzalez-Estrada et al. [55]	Pre-impregnated filament	Nylon/CF	4.431	104
Hao et al. [51]	In-situ impregnation	Epoxy/ CF	164.4	792.8
Liu et al. [52]	In-situ impregnation	PA6/CF 35%vol	Flexural - 34.12	Flexural - 417.19
		PA6/CF 41%vol	Flexural - 46.9	Flexural - 491.12
		PA6/CF 42.5%vol	Flexural - 48.52	Flexural - 504.21
		PA6/CF 43.98%vol	Flexural - 66.73	Flexural - 564.045

Table A.13 Continued

		PA6/CF 47.78%vol	Flexural - 70.705	Flexural - 520.56
Blok et al. [58]	Pre-impregnated filament	Nylon/CF 27%vol	62.5	968

Table A.14 Operation and geometry parameters of single screw extruder

Parameter	**Value**	**Method Obtained**
P_c	1	Calibrated
$W_c\ (mm)$	25.4	Measured
$H\ (mm)$	1.267	Measured
$D(mm)$	25.4	Measured
$g_z\ (N/mm)$	$4 \cdot 10^{-3}$	Calibrated
$\vartheta(deg)$	30	Measured
$m\ (N \cdot s/(mm^2\ ))$	$1 \cdot 10^{-3}$	Calibrated
n	0.6	Calibrated
$\rho(g/(mm^3\ ))$	0.0012	Calibrated

Table A.15 Experimental measurements at operation points used to determine R_f

Operation Point	**Pressure** $(\boldsymbol{N/mm^2})$	**Gear Pump Speed** $(\boldsymbol{RPM})$	**Mass Flow Rate** $(\boldsymbol{g/min})$	**Volumetric Flow Rate** $(\boldsymbol{mm^3/s})$
1	3.654	20.4	24.3	318.89
2	6.343	44.4	53.1	696.85

Table A.12 Continued

$\boldsymbol{dP}\ (\boldsymbol{N/mm^2})$	$\boldsymbol{d\dot{Q}_p}\ (\boldsymbol{mm^3/s})$
2.689	377.95

Table A.16 Experimental measurements used to determine C_n

Volumetric Flow Rate $(\boldsymbol{mm^3/s})$	**Gear Pump Speed** $(\boldsymbol{RPM})$	$\boldsymbol{dP}$ $(\boldsymbol{N/mm^2})$	$\boldsymbol{dl}$ $(\boldsymbol{mm})$	**Extrudate Cross Sectional Area** $(\boldsymbol{mm^2})$	$\boldsymbol{dv}$ $(\boldsymbol{mm^3})$
696.85	44.4	-6.3429	5.6	8.296	46.457

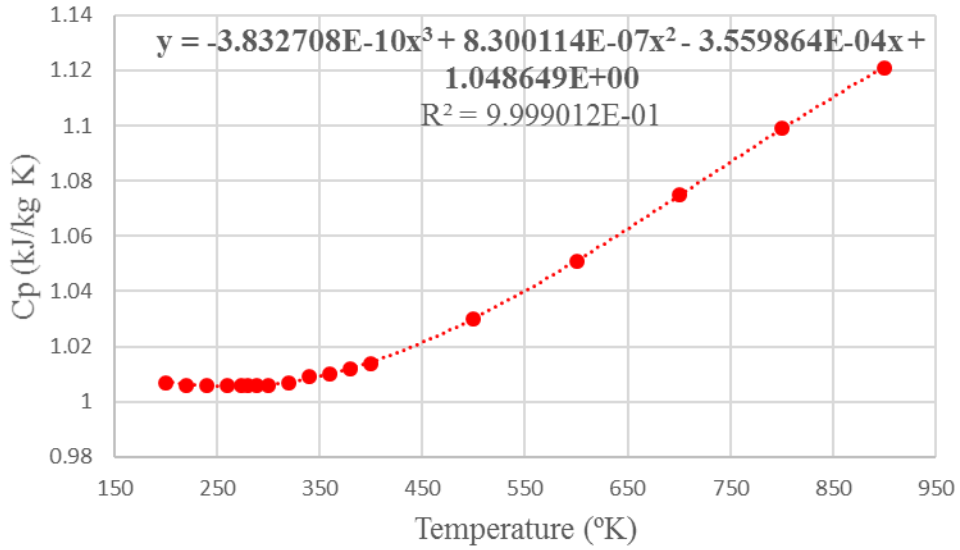

Figure A.2 Piecewise polynomial description of the heat capacity, C_p, of air as a function of temperature.

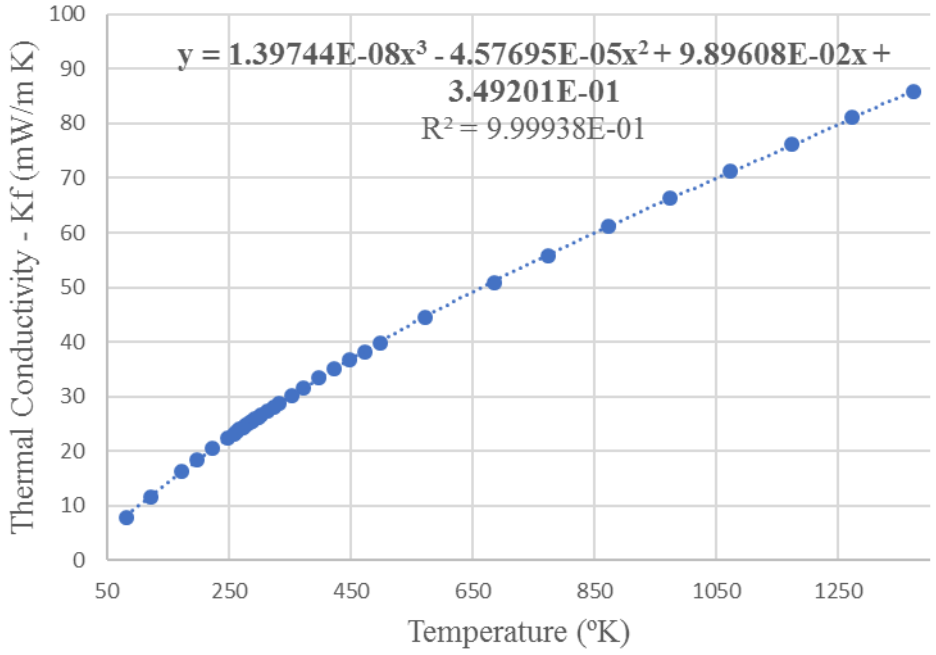

Figure A.3 Piecewise polynomial description of the thermal conductivity, K_f, of air as a function of temperature.

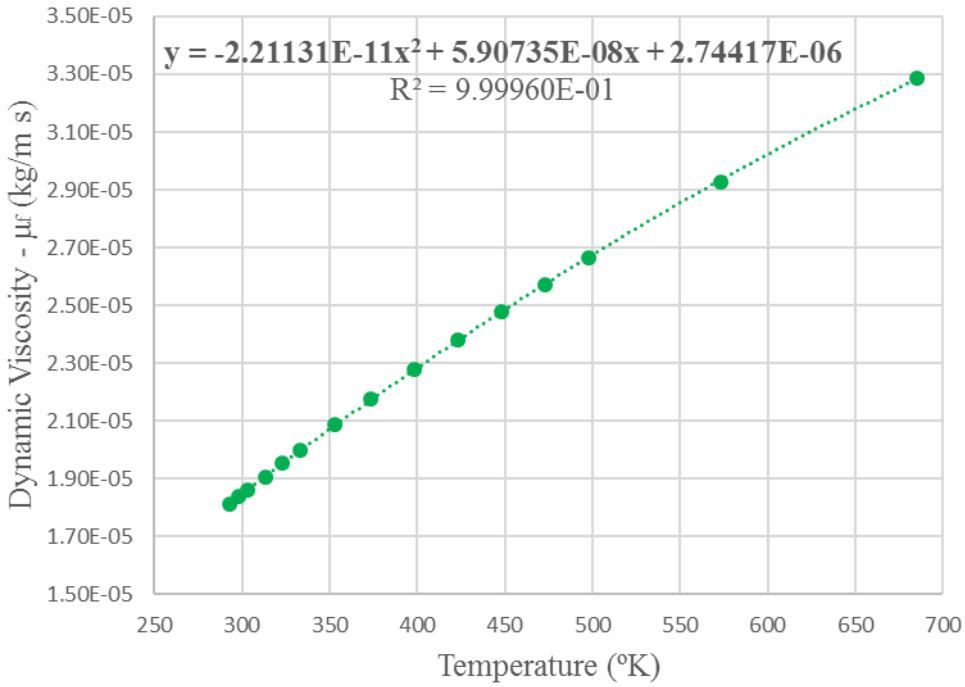

Figure A.4 Piecewise polynomial description of the dynamic viscosity, μ_f, of air as a function of temperature.

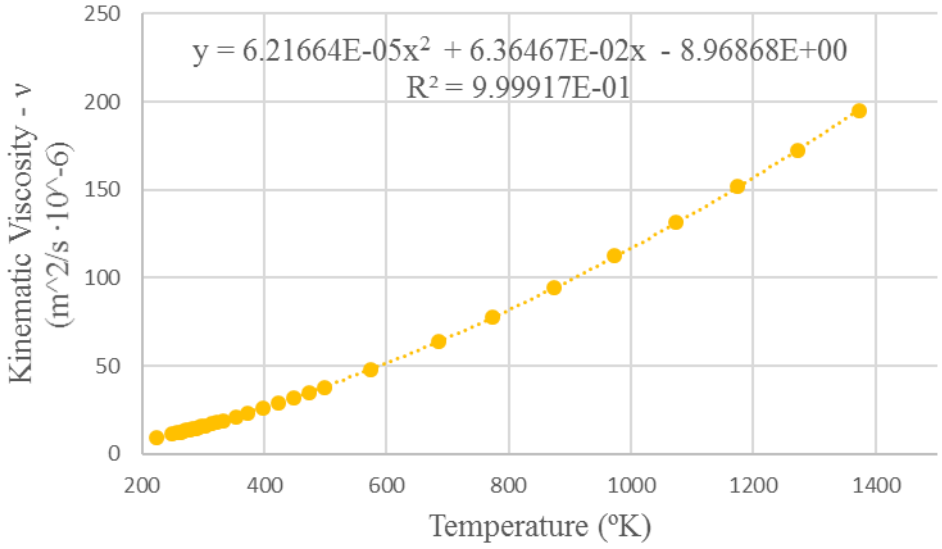

Figure A.5 Piecewise polynomial description of the kinematic viscosity, ν, of air as a function of temperature.

Table A.17 Additional material properties of the air used in natural convection analysis.

Property	**Value**
Molecular Weight - M_w $(kg/m\,s)$	28.966
Density - ρ (kg/m^3)	Ideal Gas

Table A.18 Thermophysical properties of Argon considered in the characterization of Q^C

Property	**Value**
M_{Ar} $(kg/kMol)$	39.948
C_P $(kJ/kg\,°K)$	0.523
ρ (kg/m^3) Computed with Eq. 5.32	5.666

Table A.19 Dimensions of DCB specimens used for characterizing welding time.

Specimen	**Average Width** $\boldsymbol{b}$ $\boldsymbol{(mm)}$	**Average Thickness** $\boldsymbol{h}$ $\boldsymbol{(mm)}$	**Initial Crack Length** $\boldsymbol{a_0}$ $\boldsymbol{(mm)}$
DCB – 488 – 5 – S1	24.19	8.39	34.29
DCB – 488 – 5 – S2	24.25	8.14	34.48
DCB – 488 – 5 – S3	24.12	8.09	34.26
DCB – 488 – 10 – S1	24.18	8.17	34.29
DCB – 488 – 10 – S2	24.25	8.16	34.14
DCB – 488 – 10 – S3	24.20	8.32	34.46
DCB – 488 – 20 – S1	24.14	8.34	33.43
DCB – 488 – 20 – S2	24.19	8.35	33.61
DCB – 488 – 20 – S3	24.15	8.59	33.03
DCB – 488 – 40 – S1	24.09	8.31	32.47
DCB – 488 – 40 – S2	24.19	8.41	32.08
DCB – 488 – 40 – S3	24.20	8.56	31.69
DCB – 393 – 10 – S1	24.08	8.14	33.33
DCB – 393 – 10 – S2	24.63	7.44	31.25
DCB – 393 – 10 – S3	24.38	7.35	30.41
DCB – 413 – 10 – S1	23.67	7.80	34.33
DCB – 413 – 10 – S2	24.15	7.31	32.66
DCB – 413 – 10 – S3	24.02	7.11	32.18
DCB – 523 – 10*– S1	24.58	7.30	33.22
DCB – 523 – 10*– S2	24.64	7.42	31.89
DCB – 523 – 10*– S3	24.21	7.95	32.65

Figure A.6 Data reduction of DCB fracture tests for all the conditions investigated.

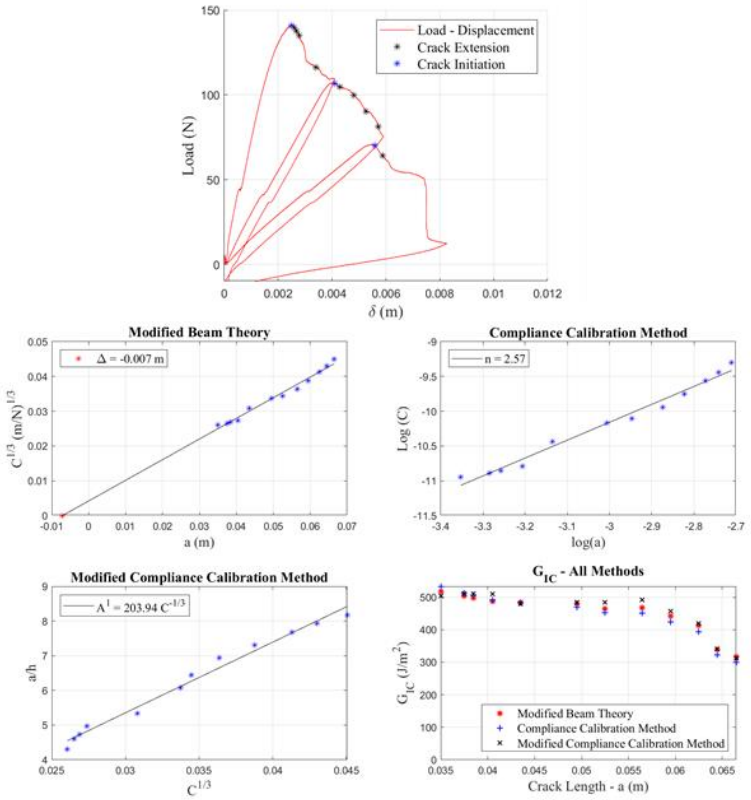

DCB – 488 – 5 – S2

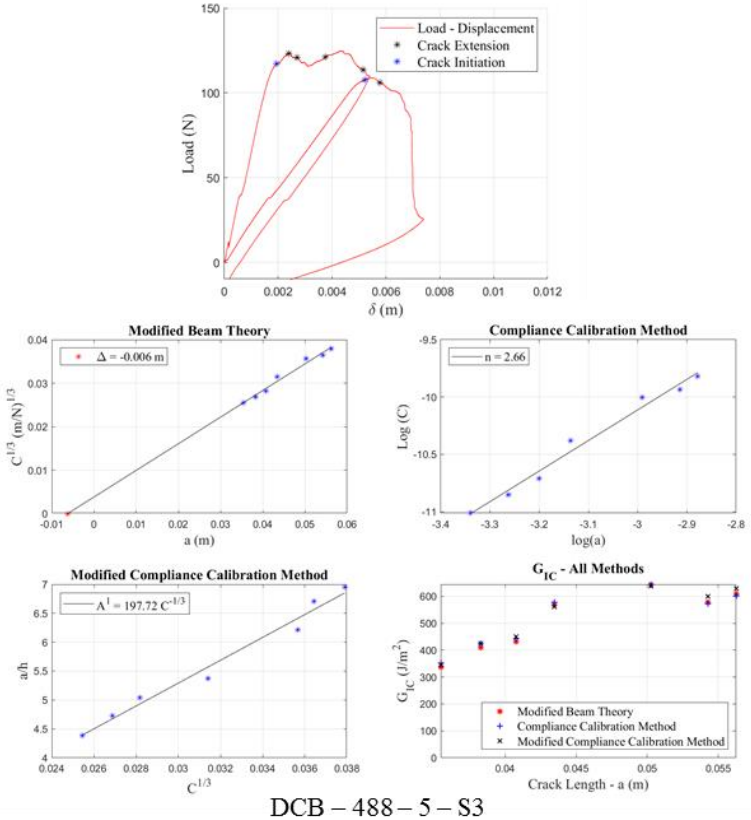

DCB – 488 – 5 – S3

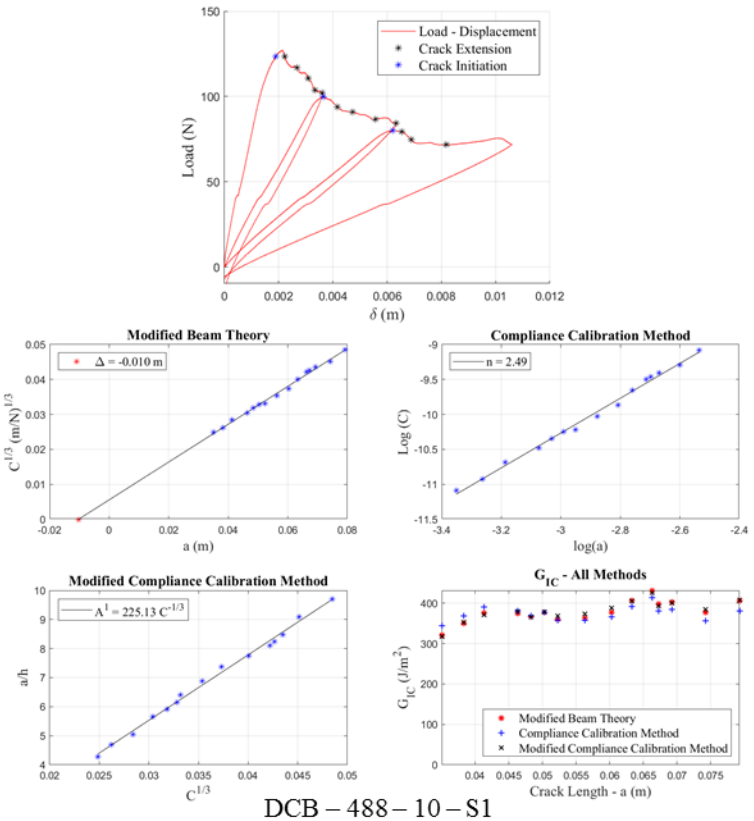

DCB – 488 – 10 – S1

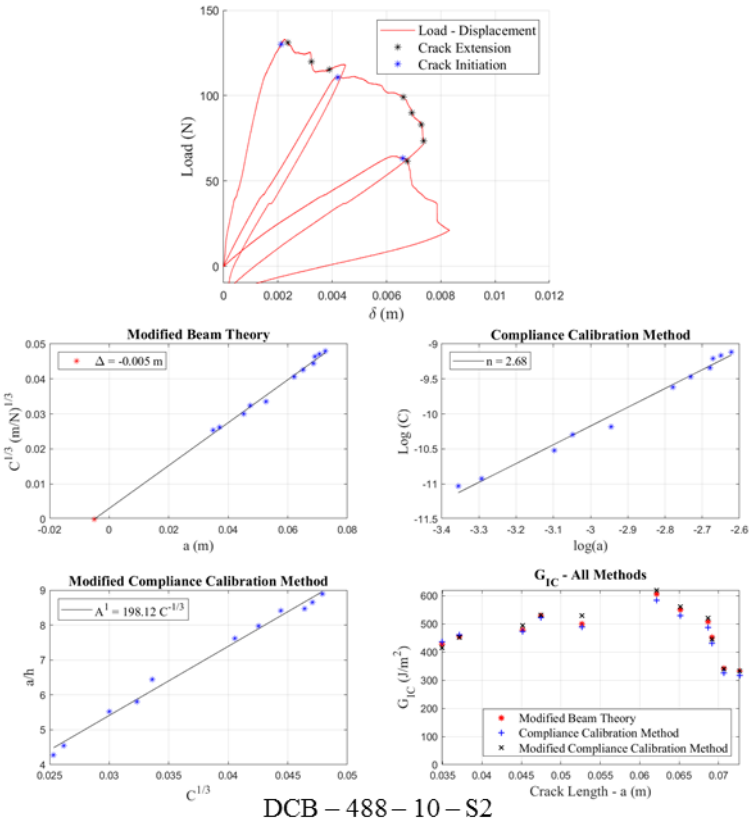

DCB – 488 – 10 – S2

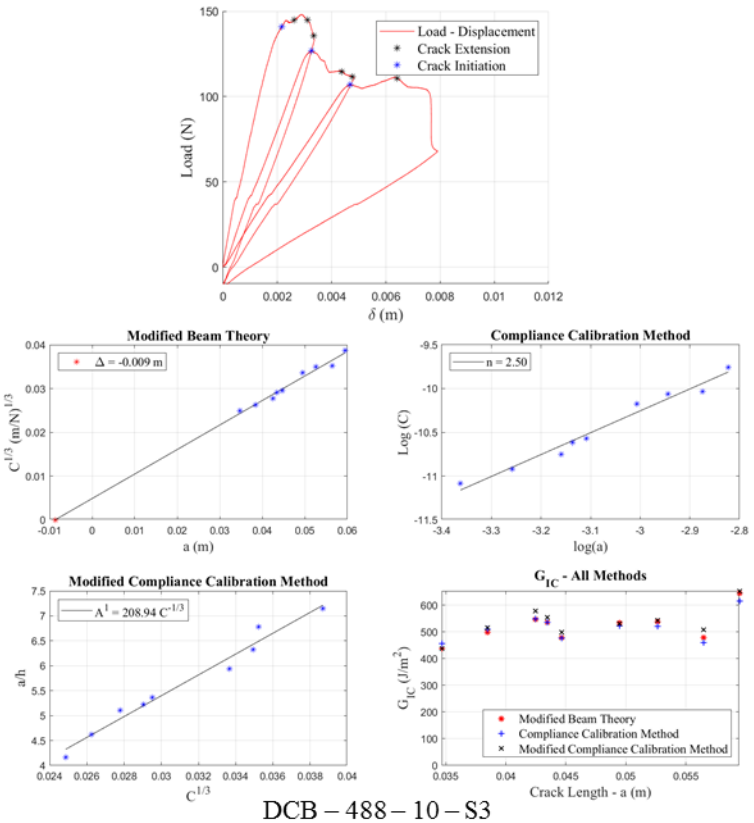

DCB – 488 – 10 – S3

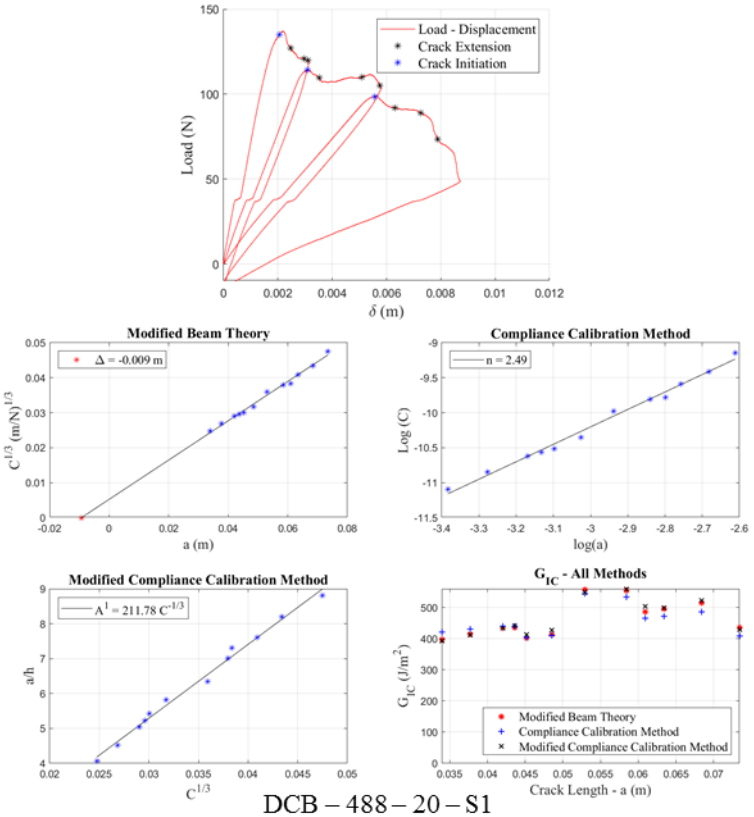

DCB – 488 – 20 – S1

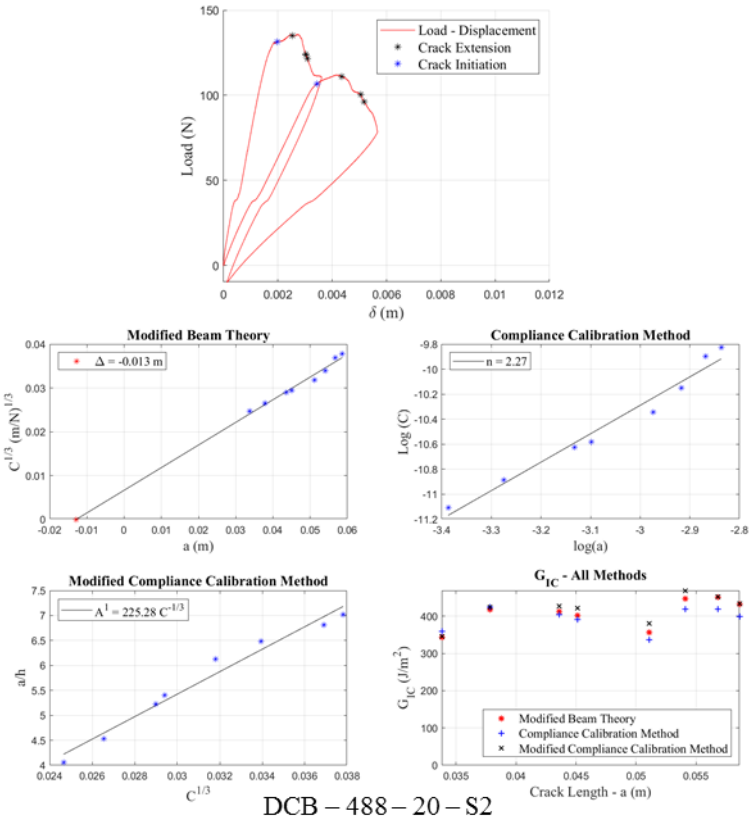

DCB – 488 – 20 – S2

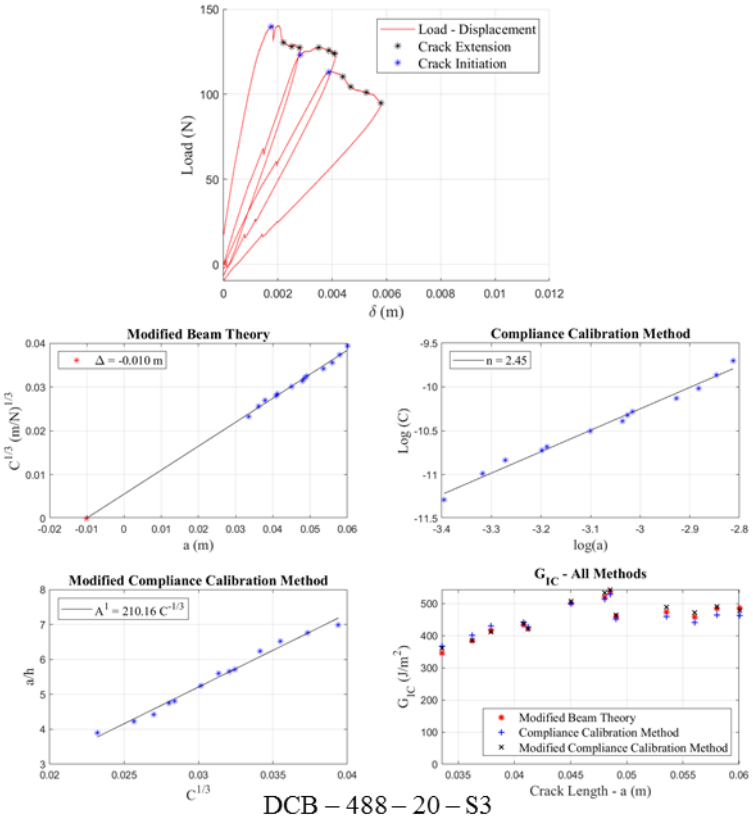

DCB – 488 – 20 – S3

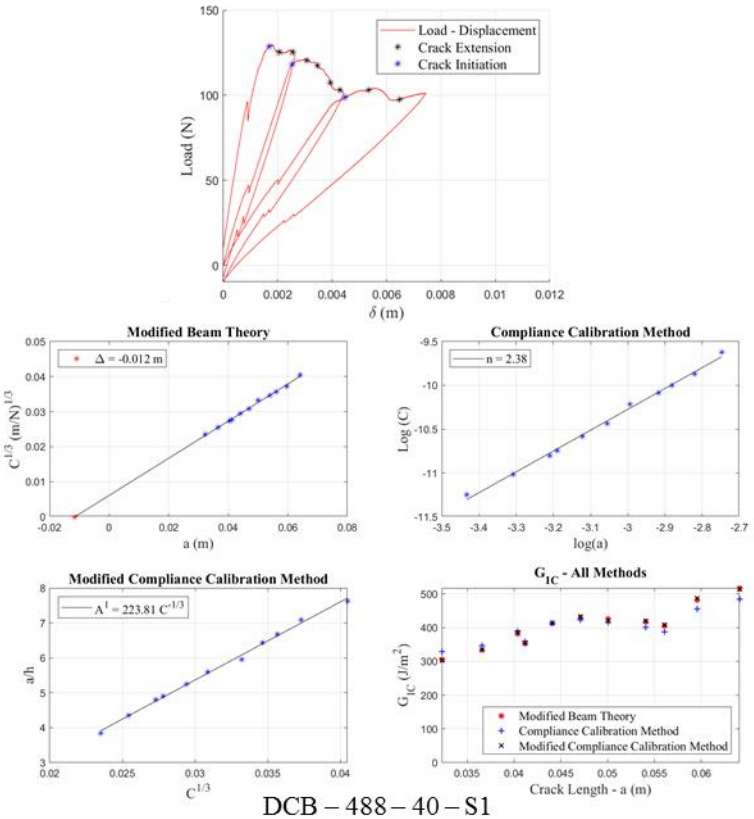

DCB – 488 – 40 – S1

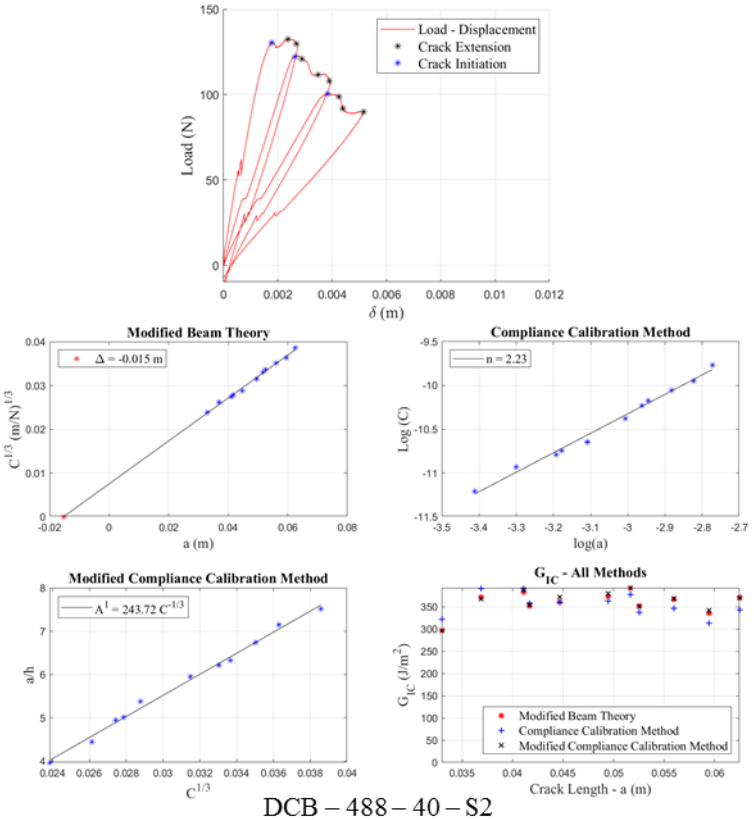

DCB – 488 – 40 – S2

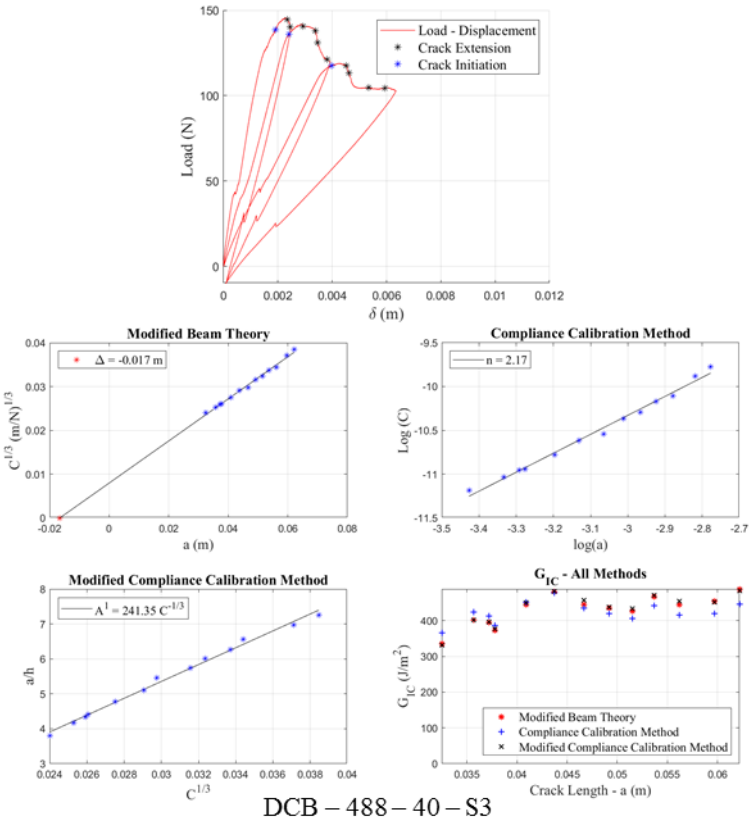

DCB – 488 – 40 – S3

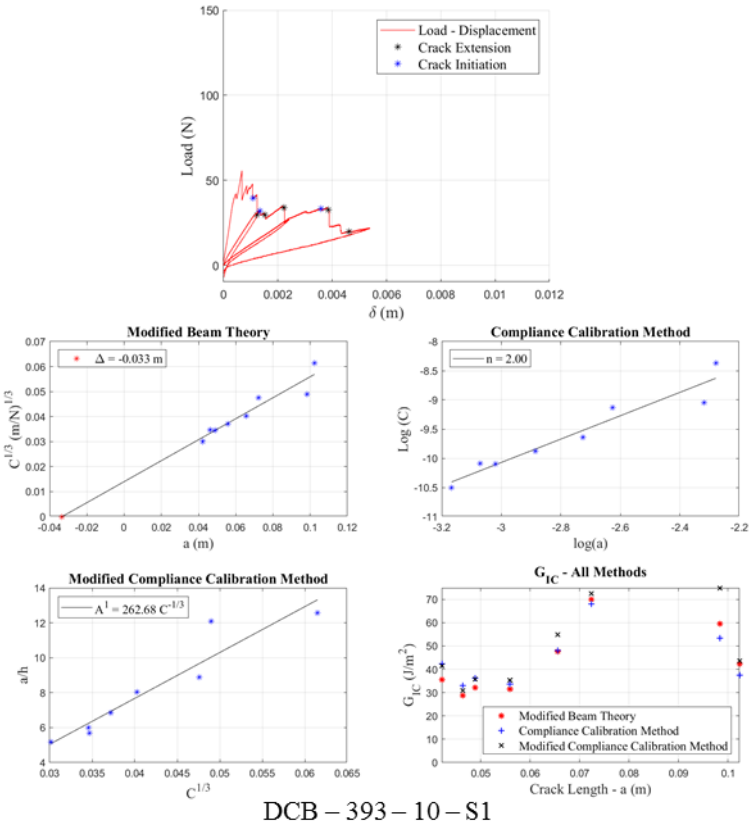

DCB – 393 – 10 – S1

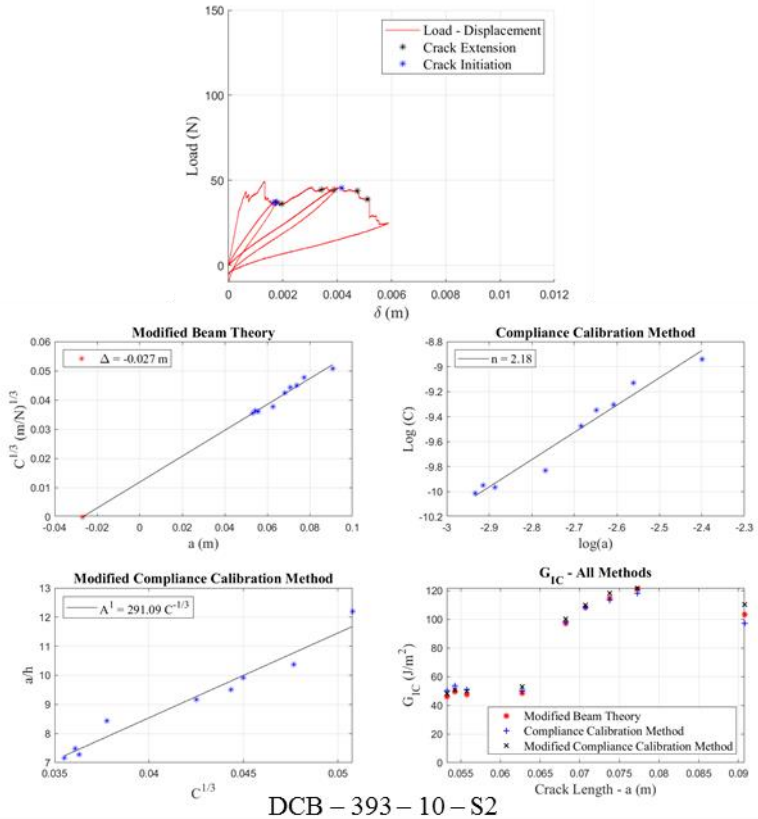

DCB – 393 – 10 – S2

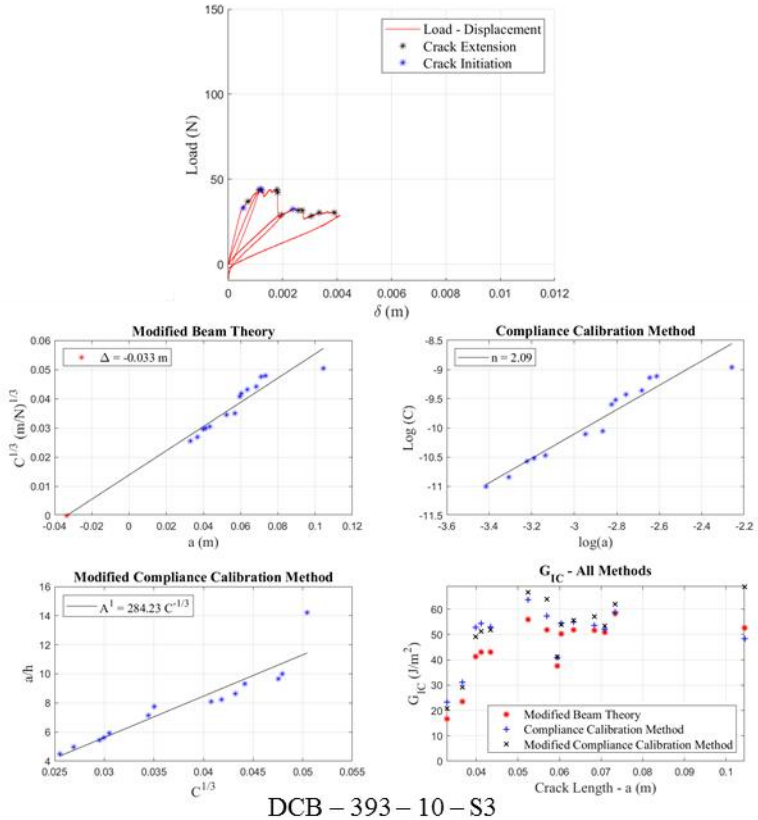

DCB – 393 – 10 – S3

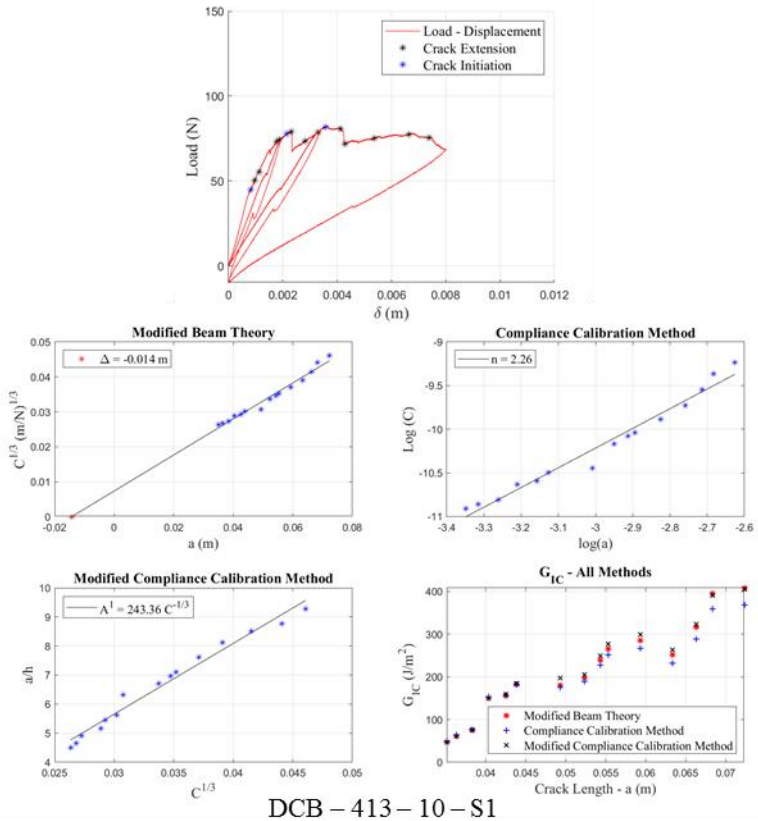

DCB – 413 – 10 – S1

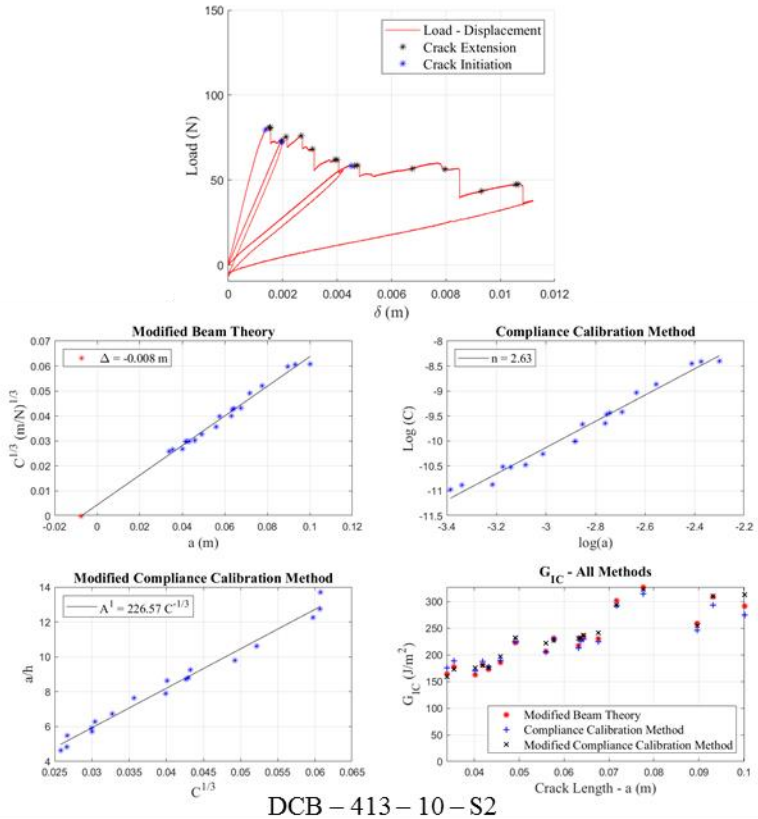

DCB – 413 – 10 – S2

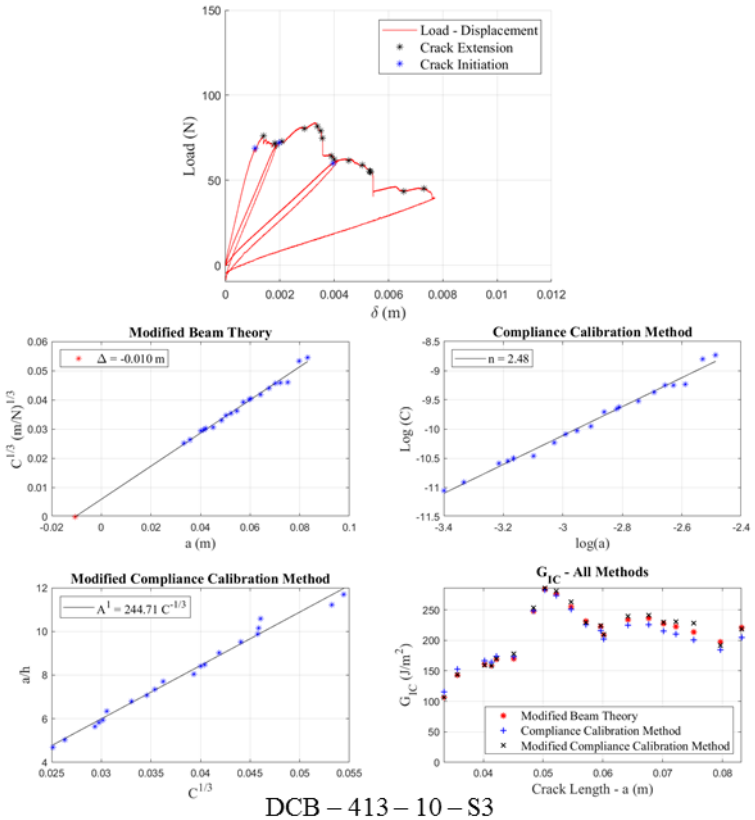

DCB – 413 – 10 – S3

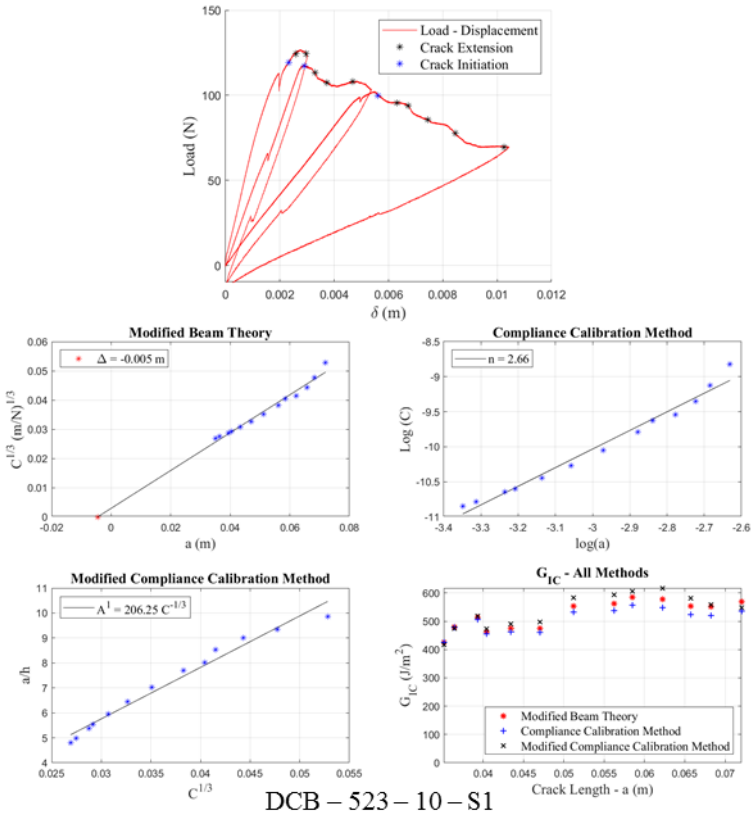

DCB – 523 – 10 – S1

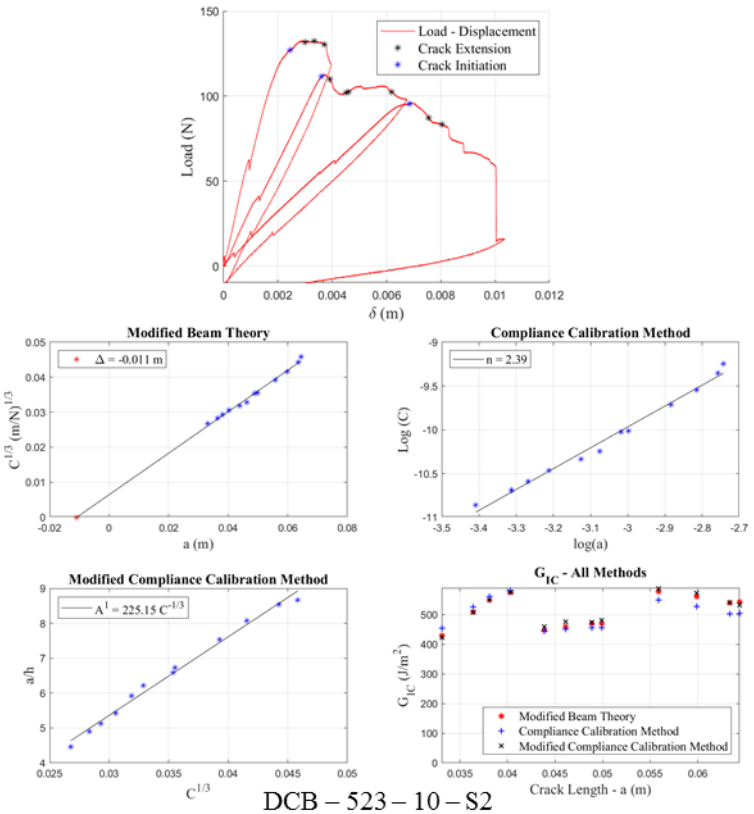

DCB – 523 – 10 – S2

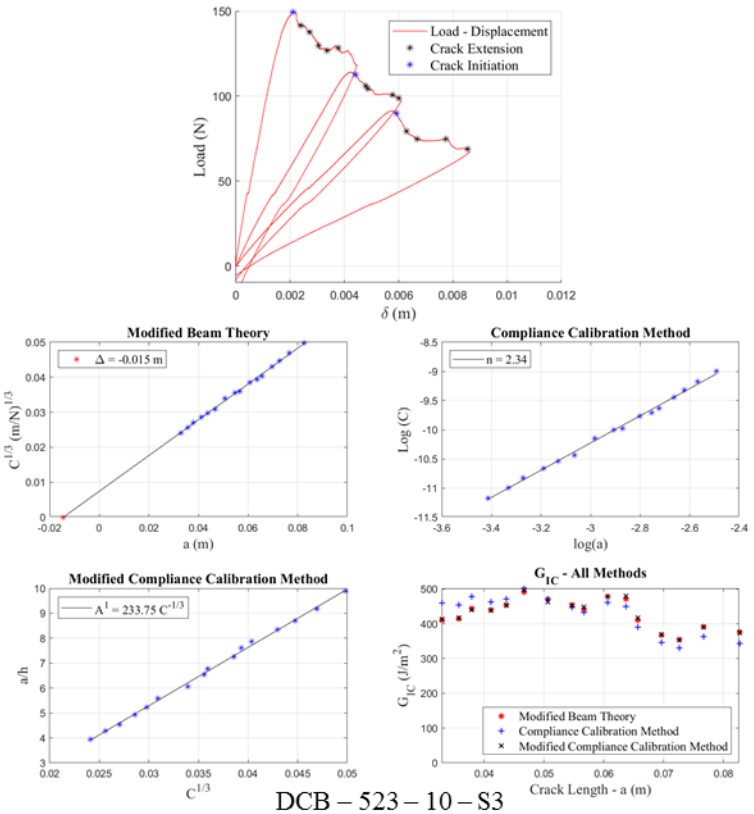

DCB – 523 – 10 – S3

APPENDIX B. SCRIPTS AND ADDITIONAL EQUATIONS

Table B.1 List of M-codes used in CAMRI

M-code	Function
M05	Disable material extrusion system
M03	Enable material extrusions system
M08	Enable fan for active cooling
M09	Disable fan for active cooling
M100, ‘P’,‘Q’, ‘R’	Enable adaptive control system, pass bead width ‘P’, bead height ‘Q’, and nominal printing speed ‘R’.
M101	Disable adaptive control system
M102	Enable tamper
M103	Disable tamper
M104, ‘P’,‘Q’, ‘R’	Update bead dimensions or nominal printing speed, pass bead width ‘P’, bead height ‘Q’, and nominal printing speed ‘R’.

M-code	Function
M105	Enable air cooling for tamper
M106	Disable air cooling for tamper
M109	Enable printing with continuous fibers
M110	Disable printing with continuous fibers
M112	Record event series during part printing process
M113	Stop recording event series
M114, ‘P’	Pause printing process for ‘P’ millisecond
M115	Enable miscellaneous functions
M116	Disable miscellaneous functions

Table B.2 Matlab® Script for computing degree of crystallinity and latent heat of crystallization from heat flow obtained with DSC

```
% Analysis of DSC Thermograms for Crystallization From the Melt under
% Non-isothermal Conditions
% Code Developed by Eduardo Barocio
% Composites Manufacturing and Simulation Center - Purdue University
clc
clear all
close all
% Control Switch
    % Switch = 1 for enabling plots of individual cooling rates
    % Switch = 0 for disabling plots of individual cooling rates
Switch=1;
% Select Data set (1 = Dataset 1; 2 = Dataset 2)
DataSet=1;
% Select the individual experiment to generate plot of degree of
% crystallinity and heat flow (cooling rate)
Plot_Exp=25;
% Import Excel data files
if DataSet==1
    T_rate=[3; 5; 10; 15; 20; 25; 30; 35; 40; 45; 50 ];
elseif DataSet==2
    T_rate=[10; 20; 30; 40; 50; 60; 70; 80; 90];
end
% Max Crystallization Temperature
Crystal_M_Temp=zeros(3,1);
```

```
% Onset of Crystallization Temperature
Crystal_O_Temp=zeros(3,1);
%%************************************************************************%%
%%************************************************************************%%
%   Read Data from XLSX files
%%************************************************************************%%
%%************************************************************************%%
if DataSet==1
% Files data set 1
 files=['50%CF  PPS  -  CM-03c-min.xlsx';'50%CF  PPS  -  CM-05c-min.xlsx';'50%CF  PPS  -  CM-10c-
min.xlsx';...
       '50%CF  PPS  -  CM-15c-min.xlsx';'50%CF  PPS  -  CM-20c-min.xlsx';'50%CF  PPS  -  CM-25c-
mi2.xlsx';...
       '50%CF  PPS  -  CM-30c-min.xlsx';'50%CF  PPS  -  CM-35c-min.xlsx';'50%CF  PPS  -  CM-40c-
min.xlsx';...
       '50%CF PPS - CM-45c-min.xlsx';'50%CF PPS - CM-50c-min.xlsx'];
elseif DataSet==2
% Files data set 2
 files=['50%CF PPS - CM-10c-min-T2.xlsx';...
   '50%CF PPS - CM-20c-min-T2.xlsx';...
   '50%CF PPS - CM-30c-min-T2.xlsx';...
   '50%CF PPS - CM-40c-min-T2.xlsx';...
   '50%CF PPS - CM-50c-min-T2.xlsx';...
   '50%CF PPS - CM-60c-min-T2.xlsx';...
   '50%CF PPS - CM-70c-min-T2.xlsx';...
   '50%CF PPS - CM-80c-min-T2.xlsx';...
   '50%CF PPS - CM-90c-min-T2.xlsx'];
end
W_sample=zeros(7,1);
L=length(T_rate);
for i=1:L
 index=sprintf('Rate%d',i);
 % Read data from excel file
 Data=xlsread(files(i,:), 1, 'A:E');
 % Get sample size mg
 W_sample(i,1)=Data(14,2);
 % Transform data into seconds
 time.(index)=Data(65:end,1).*60;
 % normalize Heat flow
 HF.(index)=Data(65:end,3)./W_sample(i,1);
 % Temperature
 Temp.(index)=Data(65:end,2);
 % Calculate Temperature rate
 d_T=[0.001; diff(Temp.(index))];
 d_t=[0.001; diff(time.(index))];
 % Cooling rate
 T_Rate=d_T./d_t;
 % Calculate heat capacity dh/
 Cp.(index)=[0; -diff(HF.(index))]./T_Rate(:,1);
 Cp.(index)=HF.(index)./T_Rate(:,1);
 % Calculate Enthalpy H=(dq/dt)*(dt)
 Enthalpy.(index)(:,1)=HF.(index).*[diff(time.(index));.3];
 int_ent=length(Enthalpy.(index)(:,1));
 %%************************************************************************%%
 %%************************************************************************%%
 %  Find onse of Crystallization Temp, Max Crys. Temperature and end of
 %  crystallization
 %%************************************************************************%%
 %%************************************************************************%%
 % Find the Max Temp during Crystallization and both ends of the
 % crystallization peak. Then integrate over time from peak to peak.
 if DataSet ==1
    H_T=find(Temp.(index)<=270,1);
    L_T=find(Temp.(index)<=180,1);
 elseif DataSet==2
 % Use different segments depending on the cooling rate
    if T_rate(i,1)>30
        H_T=find(Temp.(index)<=230,1);
        L_T=find(Temp.(index)<=170,1);
    else
        H_T=find(Temp.(index)<=240,1);
```

```
        L_T=find(Temp.(index)<=195,1);
    end
 end
 % Find the Max Crystallization Temp.
 Max_CT=find(HF.(index)(:,1)>=max(HF.(index)(H_T:L_T,1)),1);
 Crystal_M_Temp(i,1)=Temp.(index)(Max_CT,1);
 % % Calculate derivate (up to 300C) for finding peak cristallization Temperature.
 d_F_HF.(index)=diff(HF.(index)(H_T:L_T,1),1);
 % Find the onset Temperature of the crystallization
 H_CT=(find(d_F_HF.(index)(:,1)>=1e-4,1))+H_T;
 Crystal_O_Temp(i,1)=Temp.(index)(H_CT,1);
 % Find the end of crystallization process
 L_CT=find(abs(d_F_HF.(index)(:,1))>=4.5e-5,1,'last');
 % Temp.(index)(L_CT+H_T,1)
 % Sum 30 C to be out of the peak
 T_Final=find(Temp.(index)<=Temp.(index)(L_CT+H_T,1)-30,1);
 % Create bottom line to integrate
 time_bottom=time.(index)(H_CT:T_Final,1);
 temp_bottom=Temp.(index)(H_CT:T_Final,1);
 % Heat Flux bottom line
 HF_bottom=linspace(HF.(index)(H_CT,1),HF.(index)(T_Final,1),(T_Final-H_CT+1))';
 %%*************************************************************************%%
 %%*************************************************************************%%
 % Calculate heat of crystallization and Degree of crystallinity
 %%*************************************************************************%%
 %%*************************************************************************%%
 % Integrate the curves
 % Substract the baseline from the heat flow curve
 Y_HF=HF.(index)(H_CT:T_Final,1)-HF_bottom(:,1);
 t_integrate=time.(index)(H_CT:T_Final,1);
 % Calculate total heat of crystallization
 L_H_C.(index)=trapz(t_integrate(:,1),Y_HF(:,1));
 LHeatCrystallization(i,1)=L_H_C.(index);
 %Latent heat of crystallization of a pure crystal
 L_H_PC=34;
 % Calculate the evolution of the crystallization
 int_period=length(Y_HF);
 dt_DOC=diff(t_integrate);
 % Initial degree of crystallinity
 DOC_t.(index)(1,1)=0;
 % Create array with crystallization temp
 Temp_C.(index)=Temp.(index)(H_CT:T_Final,1);
 for i2=1:(int_period-1)
 % DOC calculated with latent heat of crystallization of a pure crystal
DOC_t.(index)(i2+1,1)=DOC_t.(index)(i2,1)+((dt_DOC(i2,1)*((Y_HF(i2,1)+Y_HF(i2+1,1))/2))/L_H_PC)
;
 end
 %%*************************************************************************%%
 % Plot integration area and heat flow curves
 %%*************************************************************************%%
 %%
 % Generate Plot of degree and crystallinity vs heat flow signal
 if Plot_Exp==T_rate(i,1)
    figure (30)
    grid on
    yyaxis left
    plot(Temp.(index)(Max_CT,1),HF.(index)(Max_CT,1),'k+',...     %Max Crys Temp
     Temp.(index)(H_CT,1),HF.(index)(H_CT,1),'k+',...           %Onset of C.T
     Temp.(index)(T_Final,1),HF.(index)(T_Final,1),'k+',...     %End of C
     Temp.(index)(:,1), HF.(index)(:,1),'-.b',...
     temp_bottom(:,1),HF_bottom(:,1),'--r','linewidth',1.50);        %bottom integration line
    xlabel('Temperature (\circC)','fontsize',14,'FontName','Times New Roman');
    ylabel('Heat Flow (W/g)','fontsize',14,'FontName','Times New Roman');
    hold on
    yyaxis right
    plot(Temp.(index)(H_CT:T_Final,1),DOC_t.(index)(:,1),'r','linewidth',1.50);
    ylabel('Relative Degree of Crystallinity \chi^r^e^l_v','fontsize',14,'FontName','Times New
Roman');
    axis([50 300 -0.1 1.1]);
    lgd=legend(sprintf('Max                    Crystallization                    Temperature
= %d %cC',round(Temp.(index)(Max_CT,1)),char(176)),...
```

```
     sprintf('Onset                of                Crystallization                Temperature
= %d %cC',round(Temp.(index)(H_CT,1)),char(176)),...
     sprintf('End                  of                Crystallization                Temperature
= %d %cC',round(Temp.(index)(T_Final,1)),char(176)),...
     sprintf('Heat Flow - DSC'),...
     sprintf('Latent Heat of Crystallization = %2.3d J/g',L_H_C.(index)),...
     sprintf('Relative Degree of Crystallinity'));
    set(lgd, 'interpreter','latex');
    set(lgd, 'FontSize', 12);
    set(lgd, 'FontName', 'Times New Roman');
    set(lgd, 'Location', 'southoutside');
    saveas(gcf,'HeatOfCrystallization.png');
 end
%%
% Plot the curve with the integration area and max temperatures
 if Switch==1
    figure (i);
    subplot(1,2,1)
    plot(Temp.(index)(Max_CT,1),HF.(index)(Max_CT,1),'k*',...    %Max Crys Temp
     Temp.(index)(H_CT,1),HF.(index)(H_CT,1),'k*',...          %Onset of C.T
     Temp.(index)(T_Final,1),HF.(index)(T_Final,1),'k*',...    %End of C
     temp_bottom(:,1),HF_bottom(:,1),'--r',...              %bottom integration line
     Temp.(index)(:,1), HF.(index)(:,1),'b');
    xlabel('Temperature (C)');
    ylabel('Heat Flow (W/g)');
    title(sprintf('Crystallization from Melt at %d C/min',T_rate(i,1)));
    lgd=legend(sprintf('Max Crystallization T = %d C',round(Temp.(index)(Max_CT,1))),...
     sprintf('Onset of Crystallization T = %d C',round(Temp.(index)(H_CT,1))),...
     sprintf('End of Crystallization T = %d C',round(Temp.(index)(T_Final,1))),...
     sprintf('Latent Heat of Crystallizatio = %d J/g',L_H_C.(index)));
    set(lgd, 'interpreter','latex');
    set(lgd, 'FontSize', 12);
    set(lgd, 'FontName', 'Times New Roman');
    set(lgd, 'Location', 'southwest');
    subplot(1,2,2)
    plot(time.(index)(Max_CT,1),HF.(index)(Max_CT,1),'k*',...    %Max Crys Temp
     time.(index)(H_CT,1),HF.(index)(H_CT,1),'k*',...          %Onset of C.T
     time.(index)(T_Final,1),HF.(index)(T_Final,1),'k*',...    %End of C
     time_bottom(:,1),HF_bottom(:,1),'--r',...              %bottom integration line
     time.(index)(:,1), HF.(index)(:,1),'b');
    xlabel('Time (s)');
    ylabel('Heat Flow (W/g)');
    title(sprintf('Crystallization from Melt at %d C/min',T_rate(i,1)));
    lgd=legend(sprintf('Max Crystallization time= %d s',round(time.(index)(Max_CT,1))),...
     sprintf('Onset of Crystallization = %d s',round(time.(index)(H_CT,1))),...
     sprintf('End of Crystallization = %d s',round(time.(index)(T_Final,1))),...
     sprintf('Crystallization      time      =      %d      s',round(time.(index)(T_Final,1)-
time.(index)(H_CT,1))));
    set(lgd, 'interpreter','latex');
    set(lgd, 'FontSize', 12);
    set(lgd, 'FontName', 'Times New Roman');
    set(lgd, 'Location', 'southwest');
%%*********************************************************************%%
% Plot degree of Crystallinity as a function of t and T
%%*********************************************************************%%
    figure(L+i)
    subplot(1,2,1)
    plot(time.(index)(H_CT:T_Final,1),DOC_t.(index)(:,1),'b');
    xlabel('Time (s)');
    ylabel('Degree of Crystallinity');
    title(sprintf('Crystallization from Melt at %d C/min',T_rate(i,1)));
    subplot(1,2,2)
    plot(Temp.(index)(H_CT:T_Final,1),DOC_t.(index)(:,1),'b');
    xlabel('Temperature (C)');
    ylabel('Degree of Crystallinity');
    title(sprintf('Crystallization from Melt at %d C/min',T_rate(i,1)));
 end
end
```

Table B.3 Script developed in Matlab® to create temperature profiles used in Fluent® and utilizing temperature profiles extracted from transient heat transfer analysis performed in Abaqus©.

```
% Script to read in temperature profiles extracted from Abaqus and to create
% temperature profiles used in ANSYS Fluent.
% Script developed by Eduardo Barocio
% Composites Manufacturing and Simulation Center - Purdue University
clc
clear all
close all
%%
% Controls
% Enable to create input profile for ansys
Profile=1;
% Define number of temperature profiles to create
num_conditions=18;
% Define locations in X and Y to define temperature profile
x_pos=0.0;
y_pos=0.3;
%% Import data FEA and create profiles for Ansys
FID = fopen('TempData_TempProfile_TBL_BPT_493.15.rpt');
header = textscan(FID,'%s',1,'Delimiter','\n');
for i = 1:num_conditions
  Save_file=sprintf('Condition_%d',i);
  header = textscan(FID,'%s',2,'Delimiter','\n');
  data1 = textscan(FID,'%f %f');
  DataFEA.(Save_file).temp_K = data1{1,2};
  DataFEA.(Save_file).pos_mm = data1{1,1};
  DataFEA.(Save_file).pos_m = data1{1,1}/1000;
  Wall_height(i,1)=max(DataFEA.(Save_file).pos_m);
  num_dataPoints=length(DataFEA.(Save_file).pos_m);
  %% Write file for Ansys with temperature gradient
  if Profile==1
%   Write file preparation
    Output_file=sprintf('TBL_493K_Condition_%d_%f_m.prof',i,Wall_height(i,1) );
    fileID =fopen((Output_file),'w');
    fprintf(fileID, '((printedwall-p%d point %d)\n',i, num_dataPoints );
%   for x
    fprintf(fileID, '(x\n');
    for j=1:num_dataPoints
        fprintf(fileID, '%f\n', x_pos);
    end
    fprintf(fileID, ')\n');
%   For y
    fprintf(fileID, '(y\n');
    for j=1:num_dataPoints
        fprintf(fileID, '%f\n', y_pos);
    end
    fprintf(fileID, ')\n');
%   For Z
    fprintf(fileID, '(z\n');
    for j=1:num_dataPoints
        fprintf(fileID, '%f\n', DataFEA.(Save_file).pos_m(j,1));
    end
    fprintf(fileID, ')\n');
%   For Temperature
    fprintf(fileID, '(wall-temperature\n');
    for j=1:num_dataPoints
        fprintf(fileID, '%f\n', DataFEA.(Save_file).temp_K(j,1));
    end
    fprintf(fileID, ')\n');
    fprintf(fileID, ')\n');
    fclose(fileID);
  end
end
fclose(FID);
```

Table B.4 Script developed in Matlab® to process local convection coefficients extracted from Fluent® and used to fit correlation equation for natural convection from a vertical surface.

```
% Script developed to process local convection coefficient extracted
% from numerical analysis of natural convection in Fluent.
% This scrips also fits the correlation equation for natural convection
% from a vertical surface utilizing a non-linear least squares solver.
% Script developed by Eduardo Barocio
% Composites Manufacturing and Simulation Center - Purdue University
clc
clear all
close all
%% Controls
% Enable to create input profile for ansys
% Define parameters to be used in the calculation of the TBL
 % Infinity Temperature (K)
T_inf= 298.15;
 % Coefficients for thermal conductivity (T)
Coeff_K_f=[3.49201E-04;...
           9.89608E-05;...
           -4.57695E-08;...
           1.39744E-11];
K_f_T=@(T)(Coeff_K_f(1)+...
           Coeff_K_f(2)*(T)+...
           Coeff_K_f(3)*(T^2)+...
           Coeff_K_f(4)*(T^3));
Sol_Cond_num=['_1_T_393.15.txt ';...
              '_5_T_393.15.txt ';...
              '_9_T_393.15.txt ';...
              '_13_T_393.15.txt';...
              '_17_T_393.15.txt';...
              '_1_T_443.15.txt ';...
              '_5_T_443.15.txt ';...
              '_9_T_443.15.txt ';...
              '_13_T_443.15.txt';...
              '_17_T_443.15.txt';...
              '_1_T_493.15.txt ';...
              '_5_T_493.15.txt ';...
              '_9_T_493.15.txt ';...
              '_13_T_493.15.txt';...
              '_17_T_493.15.txt'];
Number_conditions_Analyzed=length(Sol_Cond_num(:,1));
BuildPlate_Temperatures=[393.15;393.15;393.15;393.15;393.15;...
                         443.15;443.15;443.15;443.15;443.15;...
                         493.15;493.15;493.15;493.15;493.15];
% Preallocate arrays
x_pos=[];
y_temp=[];
z_Film=[];
z_nuss=[];
x_Rayl=[];
y_Pr=[];
weigths=[];
z_nuss_Avg=[];
x_Rayl_Avg=[];
y_Pr_Avg=[];
weigths_Avg=[];
temp=[];
Pos_mm=[];
BPT=[];
Wall_height_mm=zeros(Number_conditions_Analyzed,1);
%% Settings for generating plots
    color_list = {'k','k','k','k','k','b','b','b','b','b','m','m','m','m','m','g','c','c'};
    style_list_FEA    =    {'-','-.','--',':','-','-','-.','--',':','-','-','-.','--',':','-','-
','-.','--',':','-'};
    style_list_EXP    =    {'--*','--+','--o','--x','--d','--*','--+','--o','--x','--d','--*','--
+','--o','--x','--d'};
%% Read in file output from Fluent - Multiple conditions
for i=1:Number_conditions_Analyzed
% Read in temperature data from Fluent
```

```
    Open_File=sprintf("Temp_C"+Sol_Cond_num(i,:));
    FID_2 = fopen(Open_File);
    header = textscan(FID_2,'%s',4,'Delimiter','\n');
    Save_file=sprintf("C"+Sol_Cond_num(i,1:8));
    data1 = textscan(FID_2,'%f %f');
    cast_var=data1{1,1};
    DataTBL.(Save_file).Pos_Z_mm = cast_var(:,1).*1000;
    length_dataTBL=length(DataTBL.(Save_file).Pos_Z_mm);
    Wall_height_mm(i,1)=max(DataTBL.(Save_file).Pos_Z_mm);
    cast_var=data1{1,2};
    DataTBL.(Save_file).Temp = cast_var(:,1);
    fclose(FID_2);
% Read in Convection coefficients extracted from Fluent
    Open_File=sprintf("Film_C"+Sol_Cond_num(i,:));
    FID_2 = fopen(Open_File);
    header = textscan(FID_2,'%s',4,'Delimiter','\n');
    data1 = textscan(FID_2,'%f %f');
    cast_var=data1{1,2};
    DataTBL.(Save_file).film = cast_var(:,1);
    fclose(FID_2);
% Read in Nusselt number extracted from Fluent
    Open_File=sprintf("Nusselt_C"+Sol_Cond_num(i,:));
    FID_2 = fopen(Open_File);
    header = textscan(FID_2,'%s',4,'Delimiter','\n');
    data1 = textscan(FID_2,'%f %f');
    cast_var=data1{1,2};
    DataTBL.(Save_file).nuss = cast_var(:,1);
    fclose(FID_2);
%   Averaging over width of the wall
%   Index to filter
    z_search=5.0;
    average_index(1,i)=1;
    count=1;
    k=1;
%   Averaging over width of the wall - Uniform element surface area
%   Define thresshold for search
    thresshold=3.0;
    while k<length_dataTBL
        if (DataTBL.(Save_file).Pos_Z_mm(k,1)>z_search+thresshold)
           count=count+1;
           average_index(count,i)=k;
           z_search=DataTBL.(Save_file).Pos_Z_mm(k,1);
           DataTBL.(Save_file).Avg_Pos_Z_mm(count-
1,1)=mean(DataTBL.(Save_file).Pos_Z_mm(average_index(count-1,i):average_index(count,i)-1,1));
           DataTBL.(Save_file).Avg_Film(count-
1,1)=mean(DataTBL.(Save_file).film(average_index(count-1,i):average_index(count,i)-1,1));
           DataTBL.(Save_file).Avg_Nuss(count-
1,1)=mean(DataTBL.(Save_file).nuss(average_index(count-1,i):average_index(count,i)-1,1));
           DataTBL.(Save_file).Avg_Temp(count-
1,1)=mean(DataTBL.(Save_file).Temp(average_index(count-1,i):average_index(count,i)-1,1));
        end
        k=k+1;
    end
    average_index(count+1,i)=length_dataTBL;
DataTBL.(Save_file).Avg_Pos_Z_mm(count,1)=mean(DataTBL.(Save_file).Pos_Z_mm(average_index(count
,i):average_index(count+1,i)-1,1));
DataTBL.(Save_file).Avg_Film(count,1)=mean(DataTBL.(Save_file).film(average_index(count,i):aver
age_index(count+1,i)-1,1));
DataTBL.(Save_file).Avg_Nuss(count,1)=mean(DataTBL.(Save_file).nuss(average_index(count,i):aver
age_index(count+1,i)-1,1));
DataTBL.(Save_file).Avg_Temp(count,1)=mean(DataTBL.(Save_file).Temp(average_index(count,i):aver
age_index(count+1,i)-1,1));
% ************************************************
%% Compute Dimensionless Numbers
% ************************************************
% ****** Non-averaged Values *********
% Dimensionless position
DataTBL.(Save_file).Dmsnlss_Pos_Z_mm=DataTBL.(Save_file).Pos_Z_mm./max(DataTBL.(Save_file).Pos_
Z_mm(:,1));
% Compute Rayleigh Number
```

```
    [DataTBL.(Save_file).Ra_x,
DataTBL.(Save_file).Pr_x,DataTBL.(Save_file).weigths,DataTBL.(Save_file).kVisco]= ...
                                        Rayleigh_T_x(DataTBL.(Save_file).Pos_Z_mm,...
                                                     DataTBL.(Save_file).Temp,...
                                                     T_inf );
% Compute Thermal Conductivity of the fluid
    DataTBL.(Save_file).K_f=arrayfun(K_f_T, ((DataTBL.(Save_file).Temp+T_inf)/2));
% Compute Nusselt Number from the convection coefficient
    DataTBL.(Save_file).Nusselt=DataTBL.(Save_file).film.*DataTBL.(Save_file).Pos_Z_mm./...
                                (DataTBL.(Save_file).K_f.*1000);
    DataLength=length(DataTBL.(Save_file).Nusselt);
% Create Array with build plate temperature
    DataTBL.(Save_file).BPT(1:DataLength,1)= BuildPlate_Temperatures(i,1);
% ****** Averaged Values **************
% Dimensionless position
DataTBL.(Save_file).Avg_Dmsnlss_Pos_Z_mm=DataTBL.(Save_file).Avg_Pos_Z_mm./max(DataTBL.(Save_fi
le).Avg_Pos_Z_mm(:,1));
% Compute Rayleigh Number
    [DataTBL.(Save_file).Avg_Ra_x,
DataTBL.(Save_file).Avg_Pr_x,DataTBL.(Save_file).Avg_weigths,DataTBL.(Save_file).Avg_kVisco]= .
..
                                        Rayleigh_T_x(DataTBL.(Save_file).Avg_Pos_Z_mm,...
                                                     DataTBL.(Save_file).Avg_Temp,...
                                                     T_inf );
% Compute Thermal Conductivity of the fluid
    DataTBL.(Save_file).Avg_K_f=arrayfun(K_f_T, DataTBL.(Save_file).Avg_Temp);
% Compute Nusselt Number from the convection coefficient
DataTBL.(Save_file).Avg_Nusselt=DataTBL.(Save_file).Avg_Film.*DataTBL.(Save_file).Avg_Pos_Z_mm.
/...
                                (DataTBL.(Save_file).Avg_K_f.*1000);
    DataLength=length(DataTBL.(Save_file).Avg_Nusselt);
% Create Array with build plate temperature
    DataTBL.(Save_file).Avg_BPT(1:DataLength,1)= BuildPlate_Temperatures(i,1);
%% Generate plots
    legend_list_Temp{i} = {...
    sprintf('W_h%d - T_b_p1',1),...
    sprintf('W_h%d - T_b_p1',2),...
    sprintf('W_h%d - T_b_p1',3),....
    sprintf('W_h%d - T_b_p1',4),...
    sprintf('W_h%d - T_b_p1',5),...
    sprintf('W_h%d - T_b_p2',1),...
    sprintf('W_h%d - T_b_p2',2),...
    sprintf('W_h%d - T_b_p2',3),....
    sprintf('W_h%d - T_b_p2',4),...
    sprintf('W_h%d - T_b_p2',5),...
    sprintf('W_h%d - T_b_p3',1),...
    sprintf('W_h%d - T_b_p3',2),...
    sprintf('W_h%d - T_b_p3',3),....
    sprintf('W_h%d - T_b_p3',4),...
    sprintf('W_h%d - T_b_p3',5),...
    };
% Plot temperature vs distance from build plate
    figure(1)
plot(DataTBL.(Save_file).Pos_Z_mm(:,1),DataTBL.(Save_file).Temp(:,1),style_list_FEA{i},'color',
color_list{i},'linewidth',1.5);
    xlabel('Distance from build plate - Z (mm)','fontsize',14,'FontName','Times New Roman');
    ylabel('Temperature T_s (\circK)','fontsize',14,'FontName','Times New Roman');
    lgd=legend(legend_list_Temp{i});
    grid on
    set(lgd, 'FontSize', 12);
    set(lgd, 'FontName', 'Times New Roman');
    set(lgd, 'Location', 'eastoutside');
    hold on
% Plot average convection coefficient vs distance from build plate
    figure(5)
plot(DataTBL.(Save_file).Avg_Pos_Z_mm(:,1),DataTBL.(Save_file).Avg_Film(:,1),style_list_EXP{i},
'color',color_list{i},'linewidth',1.5);
    xlabel('Distance from build plate - Z (mm)','fontsize',16,'FontName','Times New Roman');
    ylabel('Convection Coefficient - h_Z (W/m^2\circK)','fontsize',16,'FontName','Times New
Roman');
    lgd=legend(legend_list_Temp{i});
```

```
    grid on
    set(lgd, 'FontSize', 16);
    set(lgd, 'FontName', 'Times New Roman');
    set(lgd, 'Location', 'eastoutside');
    hold on
% Plot average Rayleigh number vs distance from build plate
    figure(7)
plot(DataTBL.(Save_file).Avg_Pos_Z_mm(:,1),DataTBL.(Save_file).Avg_Ra_x(:,1),style_list_EXP{i},
'color',color_list{i},'linewidth',1.5);
    xlabel('Distance from build plate - Z (mm)','fontsize',14,'FontName','Times New Roman');
    ylabel('Rayleigh Number - Ra_z','fontsize',14,'FontName','Times New Roman');
    lgd=legend(legend_list_Temp{i});
    grid on
    set(lgd, 'FontSize', 12);
    set(lgd, 'FontName', 'Times New Roman');
    set(lgd, 'Location', 'eastoutside');
    hold on
% Plot average Nusselt number vs distance from build plate
    figure(8)
plot(DataTBL.(Save_file).Avg_Pos_Z_mm(:,1),DataTBL.(Save_file).Avg_Nusselt(:,1),style_list_EXP{
i},'color',color_list{i},'linewidth',1.5);
    xlabel('Distance from build plate - Z (mm)','fontsize',14,'FontName','Times New Roman');
    ylabel('Nusselt Number - Nu_z','fontsize',14,'FontName','Times New Roman');
    lgd=legend(legend_list_Temp{i});
    grid on
    set(lgd, 'FontSize', 12);
    set(lgd, 'FontName', 'Times New Roman');
    set(lgd, 'Location', 'eastoutside');
    hold on
% Generate Data structures used for fitting Correlation equation
    x_pos=[x_pos;DataTBL.(Save_file).Dmsnlss_Pos_Z_mm(:,1)];
    y_temp=[y_temp;DataTBL.(Save_file).Avg_Temp(:,1)];
    z_Film=[z_Film; DataTBL.(Save_file).Avg_Film(:,1)];
    z_nuss_Avg=[z_nuss_Avg; DataTBL.(Save_file).Avg_Nusselt(:,1)];
    x_Rayl_Avg=[x_Rayl_Avg; DataTBL.(Save_file).Avg_Ra_x(:,1)];
    y_Pr_Avg  =[y_Pr_Avg; DataTBL.(Save_file).Avg_Pr_x(:,1)];
    weigths_Avg=[weigths_Avg; DataTBL.(Save_file).Avg_weigths];
    z_nuss=[z_nuss; DataTBL.(Save_file).Nusselt(:,1)];
    x_Rayl=[x_Rayl; DataTBL.(Save_file).Ra_x(:,1)];
    y_Pr  =[y_Pr; DataTBL.(Save_file).Pr_x(:,1)];
    weigths=[weigths; DataTBL.(Save_file).weigths];
    temp =[temp; DataTBL.(Save_file).Temp];
    Pos_mm=[Pos_mm;DataTBL.(Save_file).Pos_Z_mm];
    BPT = [BPT; DataTBL.(Save_file).BPT];
end
%% Fit correlation expression for the Nusselt number
% Create structure used to fit data
F_Data.Nusselt=z_nuss;
F_Data.Rayleigh=x_Rayl;
F_Data.Prandl = y_Pr;
F_Data.Weights=weigths;
F_Data.Temp=temp;
F_Data.Pos=Pos_mm./1000;
F_Data.BPT=BPT;
% Options - Non-linear least squares solver
options      =      optimoptions('lsqcurvefit','FiniteDifferenceType','central','MaxFunEvals',
1000000,'MaxIter',350,'TolX',1e-25,'TolFun',1e-25,'TolPCG',1e-
30,'PlotFcn',@optimplotfval,'PlotFcn', @optimplotresnorm );
% ************** Correlation Equation - Equation 5.19 ***********************************
model        =        @(x,F_Data)                (F_Data.Weights.*(x(1).*F_Data.BPT        +
(x(2).*(F_Data.Rayleigh.^x(3)).*(F_Data.Prandl.^x(4)))));
% Initial guess
x_o=[-0.010, 0.1, 0.2, 0.2];
% Upper and lower bounds
x_Min = [-10.0, 0.0, 0.0, 0.2];
x_Max = [10.0, 3.0, 0.5, 0.5];
% X and Y data
xdat=F_Data;
ydat=F_Data.Nusselt(:,1).* F_Data.Weights;
[C_2,resnorm_2,residual_2,exitflag_2,output_2,lambda_2,jacobian_2]=lsqcurvefit(model,x_o,xdat,y
dat,x_Min,x_Max,options);
```

```
%% Plot correlation expression vs existing correlation expressions
% Define condition to be plotted
condition=15;
Save_file=sprintf("C"+Sol_Cond_num(condition,1:8));
model_Val_2              =              @(x,F_Data)              (x(1).*F_Data.BPT              +
(x(2).*(F_Data.Rayleigh.^x(3)).*(F_Data.Prandl.^x(4))));
val_Data.Rayleigh=DataTBL.(Save_file).Avg_Ra_x;
val_Data.Prandl=DataTBL.(Save_file).Avg_Pr_x;
val_Data.Temp=DataTBL.(Save_file).Avg_Temp;
val_Data.Pos=DataTBL.(Save_file).Avg_Pos_Z_mm./1000;
val_Data.BPT=DataTBL.(Save_file).Avg_BPT;
Correlation_2.Nusselt_Wall=feval(model_Val_2,C_2,val_Data);
% ******************
% From Churchill and Ozoe 1973-1972 for wall with uniform temperature (WUT)
CandO_WUT.Nusselt                                                                    =
0.503.*(DataTBL.(Save_file).Avg_Ra_x(:,1).^(1/4))./((1+(0.492./DataTBL.(Save_file).Avg_Pr_x(:,1
)).^(9/16)).^(4/9));
CandO_WUT.Film                                                                       =
CandO_WUT.Nusselt(:,1).*DataTBL.(Save_file).Avg_K_f./(DataTBL.(Save_file).Avg_Pos_Z_mm(:,1)./10
00);
% ******************
% ******************
% From Churchill and Ozoe 1973-1972 for wall with uniform heat flux  (WUHF)
CandO_WUHF.Nusselt                                                                   =
0.563.*(DataTBL.(Save_file).Avg_Ra_x(:,1).^(1/4))./((1+(0.437./DataTBL.(Save_file).Avg_Pr_x(:,1
)).^(9/16)).^(4/9));
CandO_WUHF.Film                                                                      =
CandO_WUHF.Nusselt(:,1).*DataTBL.(Save_file).Avg_K_f./(DataTBL.(Save_file).Avg_Pos_Z_mm(:,1)./1
000);
% From Churchill for assisted convection (AC)
% Velocity of the printing plate (m/s)
fluid_vel=0.05;
% Compute the Nusselt number for "natural convection"
val_Data.Nusselt_N_AC=0.563.*(val_Data.Rayleigh.^(1/4))./((1+(0.437./val_Data.Prandl).^(9/16)).
^(4/9));
% Compute the Reynolds Number
val_Data.Reynolds=fluid_vel.*DataTBL.(Save_file).Avg_Pos_Z_mm(:,1)./(1000.*DataTBL.(Save_file).
Avg_kVisco(:,1));
val_Data.Nusselt_F_AC=0.464.*(val_Data.Reynolds(:,1).^(1/2)).*(val_Data.Prandl(:,1).^(1/3))./..
.
                            ((1+(0.0205./val_Data.Prandl(:,1)).^(2/3)).^(1/4));
val_Data.Nusselt_AC = ((val_Data.Nusselt_N_AC.^3)+( val_Data.Nusselt_F_AC.^3)).^(1/3);
% ******************
% Determine film coefficient
Correlation_2.Film=Correlation_2.Nusselt_Wall.*DataTBL.(Save_file).Avg_K_f./(DataTBL.(Save_file
).Avg_Pos_Z_mm(:,1)./1000);
val_Data.Film_AC(:,1)=val_Data.Nusselt_AC(:,1).*DataTBL.(Save_file).Avg_K_f./(DataTBL.(Save_fil
e).Avg_Pos_Z_mm(:,1)./1000);
% Plot Nusselt number predicted with different correlation Equations
figure( 'Name', 'Correlation Equations' )
    plot(DataTBL.(Save_file).Avg_Pos_Z_mm(:,1),DataTBL.(Save_file).Avg_Nusselt(:,1),'*b',...
    DataTBL.(Save_file).Avg_Pos_Z_mm(:,1),Correlation_2.Nusselt_Wall(:,1),'m',...
    DataTBL.(Save_file).Avg_Pos_Z_mm(:,1),CandO_WUT.Nusselt(:,1),'k',...
    DataTBL.(Save_file).Avg_Pos_Z_mm(:,1),CandO_WUHF.Nusselt(:,1),'--b',...
    DataTBL.(Save_file).Avg_Pos_Z_mm(:,1),val_Data.Nusselt_AC(:,1),'k','linewidth',2);
    xlabel('Wall position (mm)','fontsize',14);
    ylabel('Nusselt Number','fontsize',14);
    legend('Solution Thermal Boundary Layer FEA',...
       'Correlation Equation_1',...
       'Correlation Equation_2',...
       'Correlation Equation_3',...
       'Correlation Equation_WUT',...
       'Correlation Equation_WUHF',...
       'Assisting Convection','Location','southeast');
% Plot Convection Coefficient predicted with different correlation
% equations
figure('Name', 'Predictions Film Coefficient')
plot(DataTBL.(Save_file).Avg_Pos_Z_mm(:,1),DataTBL.(Save_file).Avg_Film(:,1),'+b',...
     DataTBL.(Save_file).Avg_Pos_Z_mm(:,1),Correlation_2.Film(:,1),'m',...
     DataTBL.(Save_file).Avg_Pos_Z_mm(:,1),CandO_WUT.Film(:,1),'k',...
     DataTBL.(Save_file).Avg_Pos_Z_mm(:,1),CandO_WUHF.Film(:,1),'--b',...
```

```
     DataTBL.(Save_file).Avg_Pos_Z_mm(:,1),val_Data.Film_AC(:,1),'--r','linewidth',1.5);
    xlabel('Wall position (mm)','fontsize',14);
    ylabel('Nusselt Number','fontsize',14);
    legend('Solution Thermal Boundary Layer FEA',...
       'Correlation Equation_1',...
       'Correlation Equation_2',...
       'Correlation Equation_3',...
       'Correlation Equation_WUT',...
       'Correlation Equation_WUHF',...
       'Correlation Equation_4',...
       'Assisting Convection','Location','southeast');
%% Create plots to compare predictions made with correlation equation
% to values obtained in numerical analysis of natural convection.
% This section is repeated for each of the three build plate temperatures
% considered, however, only one is included here for reference.
Plot_Cond_num=['_1_T_443.15.txt ';...
               '_5_T_443.15.txt ';...
               '_9_T_443.15.txt ';...
               '_13_T_443.15.txt';...
               '_17_T_443.15.txt'];
N_PlotCond=length(Plot_Cond_num(:,1));
color_list = {'b','b','b','b','b','b','b','b','b','b','m','m','m','m','m','g','c','c'};
style_list_VAL = {'+','-','*','*','*','+','+','+','+','+','o','o','o','o','o'};
for j=1:N_PlotCond
    Save_file=sprintf("C"+Plot_Cond_num(j,1:8));
    val_Data.Rayleigh=DataTBL.(Save_file).Avg_Ra_x;
    val_Data.Prandl=DataTBL.(Save_file).Avg_Pr_x;
    val_Data.Temp=DataTBL.(Save_file).Avg_Temp;
    val_Data.Pos=DataTBL.(Save_file).Avg_Pos_Z_mm./1000;
    val_Data.BPT=DataTBL.(Save_file).Avg_BPT;
% Correlation Equation
    model_Val_2             =             @(x,F_Data)             (x(1).*F_Data.BPT             +
x(2).*F_Data.Rayleigh.^x(3).*F_Data.Prandl.^x(4));
% Compute Nusselt number and convection coefficient
    Correlation_Pw.Nusselt_Wall=feval(model_Val_2,C_2,val_Data);
Correlation_Pw.Film=Correlation_Pw.Nusselt_Wall.*DataTBL.(Save_file).Avg_K_f./(DataTBL.(Save_fi
le).Avg_Pos_Z_mm(:,1)./1000);
% Create list of labels for plots
    legend_list_Temp{j} = {...
    sprintf('W_h%d - T_b_p2 - Numerical Results',1),...
    sprintf('W_h%d - T_b_p2 - Equation 5.19',1),...
    sprintf('W_h%d - T_b_p2 - Numerical Results',2),...
    sprintf('W_h%d - T_b_p2 - Equation 5.19',2),...
    sprintf('W_h%d - T_b_p2 - Numerical Results',3),....
    sprintf('W_h%d - T_b_p2 - Equation 5.19',3),...
    sprintf('W_h%d - T_b_p2 - Numerical Results',4),...
    sprintf('W_h%d - T_b_p2 - Equation 5.19',4),...
    sprintf('W_h%d - T_b_p2 - Numerical Results',5),...
    sprintf('W_h%d - T_b_p2 - Equation 5.19',5),....
    sprintf('W_h%d - T_b_p2',4),...
    sprintf('W_h%d - T_b_p2',5),...
    sprintf('W_h%d - T_b_p3',1),...
    sprintf('W_h%d - T_b_p3',2),...
    sprintf('W_h%d - T_b_p3',3),....
    sprintf('W_h%d - T_b_p3',4),...
    sprintf('W_h%d - T_b_p3',5),...
    };
% Plot Nusselt Number as a function of the distance from the build plate
% (Z)
    figure(17)
plot(DataTBL.(Save_file).Avg_Pos_Z_mm(:,1),DataTBL.(Save_file).Avg_Nusselt(:,1),style_list_VAL{
1},'color',color_list{j},'linewidth',1.0);
    xlabel('Distance from build plate - Z (mm)','fontsize',14,'FontName','Times New Roman');
    ylabel('Nusselt Number - Nu_z','fontsize',14,'FontName','Times New Roman');
    lgd=legend(legend_list_Temp{j});
    hold on
plot(DataTBL.(Save_file).Avg_Pos_Z_mm(:,1),Correlation_Pw.Nusselt_Wall(:,1),style_list_VAL{2},'
color',color_list{j},'linewidth',1.5);
    xlabel('Distance from build plate - Z (mm)','fontsize',14,'FontName','Times New Roman');
    ylabel('Nusselt Number - Nu_z','fontsize',14,'FontName','Times New Roman');
    lgd=legend(legend_list_Temp{j});
```

```
    hold on
    grid on
    set(lgd, 'FontSize', 12);
    set(lgd, 'FontName', 'Times New Roman');
    set(lgd, 'Location', 'eastoutside');
% Plot Convection coefficient as a function of the distance from the build
% plate
    figure(18)
plot(DataTBL.(Save_file).Avg_Pos_Z_mm(:,1),DataTBL.(Save_file).Avg_Film(:,1),style_list_VAL{1},
'color',color_list{j},'linewidth',1.0);
    xlabel('Distance from build plate - Z (mm)','fontsize',14,'FontName','Times New Roman');
    ylabel('Convection  Coefficient  -  h_Z  (W/m^2\circK)','fontsize',14,'FontName','Times  New
Roman');
    lgd=legend(legend_list_Temp{j});
    hold on
plot(DataTBL.(Save_file).Avg_Pos_Z_mm(:,1),Correlation_Pw.Film(:,1),style_list_VAL{2},'color',c
olor_list{j},'linewidth',1.5);
    xlabel('Distance from build plate - Z (mm)','fontsize',14,'FontName','Times New Roman');
    ylabel('Convection  Coefficient  -  h_Z  (W/m^2\circK)','fontsize',14,'FontName','Times  New
Roman');
    lgd=legend(legend_list_Temp{j});
    hold on
    grid on
    set(lgd, 'FontSize', 12);
    set(lgd, 'FontName', 'Times New Roman');
    set(lgd, 'Location', 'eastoutside');
end
%% Investigate predictions with correlation expression within laminar regime
val_Test.Pos=linspace(10,600,200)';
val_Test.Temp=linspace(443.15,580.15,200)';
val_Test.BPT=393.15*(ones(200,1));
% Compute Rayleigh Number - Equation 5.11
[val_Test.Rayleigh, val_Test.Prandl,val_Test.Weigths,val_Test.kVisco]= ...
                                        Rayleigh_T_x(val_Test.Pos,...
                                                     val_Test.Temp,...
                                                     T_inf );
% Compute Thermal Conductivity of the fluid
val_Test.K_f=arrayfun(K_f_T, (val_Test.Temp + T_inf)/2);
% Define function for Correlation Equation
model_Val_2             =             @(x,F_Data)             (x(1).*val_Test.BPT             +
x(2).*val_Test.Rayleigh.^x(3).*val_Test.Prandl.^x(4));
% Compute Nusselt number and convection coefficient with correlation
% equation
val_Test.Nusselt=feval(model_Val_2,C_2,val_Test);
val_Test.Film=val_Test.Nusselt.*val_Test.K_f./(val_Test.Pos(:,1)./1000);
% Plot convection coefficient as a function of the distance from the build plate
figure(24)
grid on
% Convection coefficient
yyaxis left
plot(val_Test.Pos(:,1),val_Test.Film(:,1),'b','linewidth',1.50);
xlabel('Distance from build plate - Z (mm)','fontsize',14,'FontName','Times New Roman');
ylabel('Convection Coefficient - h_Z (W/m^2 K)','fontsize',14,'FontName','Times New Roman');
lgd=legend(legend_list_Temp{j});
hold on
% Temperature profile
yyaxis right
plot(val_Test.Pos(:,1),val_Test.Temp(:,1),'--r','linewidth',1.0);
xlabel('Distance from build plate - Z (mm)','fontsize',14,'FontName','Times New Roman');
ylabel('Temperature (K)','fontsize',14,'FontName','Times New Roman');
lgd=legend(sprintf('Temperature Profile 1'),...
           sprintf('Temperature Profile 2'),...
           sprintf('Temperature Profile 3'));
set(lgd, 'interpreter','latex');
set(lgd, 'FontSize', 12);
set(lgd, 'FontName', 'Times New Roman');
set(lgd, 'Location', 'southeast');
```

REFERENCES

[1] I. Standard, *17296-2, 2015" Additive manufacturing: Overview of process categories and feedstock", Geneva, Switzerland.*

[2] L. J. Love, V. Kunc, O. Rios, C. E. Duty, A. M. Elliott, B. K. Post, R. J. Smith and C. A. Blue, "The importance of carbon fiber to polymer additive manufacturing," *Journal of Materials Research*, vol. 29, pp. 1893-1898, 2014.

[3] C. Holshouser, C. Newell, S. Palas, L. J. Love, V. Kunc, R. F. Lind, P. D. Lloyd, J. C. Rowe, C. A. Blue, C. E. Duty and others, "Out of bounds additive manufacturing," *Advanced Materials and Processes*, vol. 171, no. 3, 2013.

[4] P. Novikov and S. Jokić, "Mataerial," [Online]. Available: http://www.mataerial.com/#5thPage. [Accessed 3 October 2018].

[5] C. I. "CI and ORNL advancing large-part additive manufacturing," March 2014. [Online]. Available: http://wwwassets.e-ci.com/PDF/Press-Releases/CI-and-ORNL-Advancing-Large-Part-Additive-Manufacturing_Mar-2014.pdf. [Accessed 3 October 2018].

[6] I. M. T. S. "IMTS History - Highlights from IMTS 2014," 2014. [Online]. Available: https://www.imts.com/show/history2014.html. [Accessed 3 October 2018].

[7] C. I. "BAAM fact sheet," [Online]. Available: https://www.e-ci.com/baam/. [Accessed 3 October 2018].

[8] A. C. Roschli, "Dynamic Extruder Control for Polymer Printing in Big Area Additive Manufacturing," 2016.

[9] T. "LSAM - Large Scale Additive Manufacturing," [Online]. Available: http://www.thermwood.com/lsam_home.htm. [Accessed 3 October 2018].

[10] T. "LSAM Specifications," 2017. [Online]. Available: http://thermwood.com/lsam/lsam_specifications.htm. [Accessed 3 October 2018].

[11] D. M. S. "Hybrid Additive/Subtractive," 2018. [Online]. Available: http://www.dmscncrouters.com/additive_manufacturing/. [Accessed 3 October 2018].

[12] A. S. "Additive Manufacturing," October 2016. [Online]. Available: https://www.additivemanufacturing.media/products/-ingersoll-introduces-wide-and-high-additive-manufacturing-wham-machines. [Accessed 3 October 2018].

[13] R. S. Bay and C. L. Tucker, "Stereological measurement and error estimates for three-dimensional fiber orientation," *Polymer Engineering \& Science,* vol. 32, pp. 240-253, 1992.

[14] "Celanese Product Data," Celanese Corporation, [Online]. Available: https://www.celanese.com/engineered-materials/products/Celstran-LFRT/product-data.aspx. [Accessed 6 October 2018].

[15] N. M. DeNardo, "Additive Manufacturing of Carbon Fiber-Reinforced Thermoplastic Composites," 2016.

[16] B. Brenken, Extrusion Deposition Additive Manufacturing of Fiber Reinforced Semi-crystalline Polymers, Ph.D. Dissertation, 2017.

[17] S. G. Advani and C. L. Tucker, "The Use of Tensors to Describe and Predict Fiber Orientation in Short Fiber Composites," *Journal of Rheology,* vol. 31, no. 8, pp. 751-784, 1987.

[18] M. Kutz, Applied plastics engineering handbook: processing and materials, William Andrew, 2011.

[19] H. J. Wolf, "Screw plasticating of discontinuous fiber filled thermoplastic: Mechanisms and prevention of fiber attrition," *Polymer Composites,* vol. 15, pp. 375-383, 1994.

[20] K. Ramani, D. Bank and N. Kraemer, "Effect of screw design on fiber damage in extrusion compounding and composite properties," *Polymer composites,* vol. 16, pp. 258-266, 1995.

[21] B. E. Verweyst and C. L. Tucker, "Fiber Suspensions in Complex Geometries: Flow/Orientation Coupling," *The Canadian Journal of Chemical Engineering,* vol. 80, no. 6, pp. 1093-1106.

[22] R. B. Pipes, J. W. S. Hearle, A. J. Beaussart, A. M. Sastry and R. K. Okine, "A Constitutive Relation for the Viscous Flow of an Oriented Fiber Assembly," *Journal of Composite Materials,* vol. 25, no. 9, pp. 1204-1217, 1991.

[23] R. B. Pipes, "Anisotropic Viscosities of an Oriented Fiber Composite with a Power-Law Matrix," *Journal of Composite Materials,* vol. 26, no. 10, pp. 1536-1552, 1992.

[24] B. P. Heller, D. E. Smith and D. A. Jack, "Effects of extrudate swell and nozzle geometry on fiber orientation in Fused Filament Fabrication nozzle flow," *Additive Manufacturing* , Vols. 12, Part B, pp. 252-264, 2016.

[25] H. L. Tekinalp, V. Kunc, G. M. Velez-Garcia, C. E. Duty, L. J. Love, A. K. Naskar, C. A. Blue and S. Ozcan, "Highly Oriented Carbon Fiber-Polymer Composites via Additive Manufacturing," *Composites Science and Technology,* 2014.

[26] T. Mulholland, S. Goris, J. Boxleitner, T. A. Osswald and N. Rudolph, "Process-Induced Fiber Orientation in Fused Filament Fabrication," *Journal of Composites Science,* vol. 2, no. 3, 2018.

[27] M. Favre-Marinet and S. Tardu, Convective Heat Transfer: Solved Problems, 2010.

[28] T. L. Bergman, F. P. Incropera, D. P. DeWitt and A. S. Lavine, Fundamentals of heat and mass transfer, John Wiley & Sons, 2011.

[29] R. P. Wool, B.-L. Yuan and O. J. McGarel, "Welding of polymer interfaces," *Polymer Engineering \& Science,* vol. 29, no. 19, pp. 1340-1367, 1989.

[30] P.-G. De Gennes, "Reptation of a polymer chain in the presence of fixed obstacles," *The journal of chemical physics,* vol. 55, no. 2, pp. 572-579, 1971.

[31] A. Greco and A. Maffezzoli, "Statistical and kinetic approaches for linear low-density polyethylene melting modeling," *Journal of Applied Polymer Science,* vol. 89, no. 2, pp. 289-295, 2003.

[32] R. P. Wool and K. M. O'Connor, "Time dependence of crack healing," *Journal of Polymer Science: Polymer Letters Edition,* vol. 20, no. 1, pp. 7-16, 1982.

[33] E. Piorkowska and G. C. Rutledge, Handbook of polymer crystallization, John Wiley & Sons, 2013.

[34] P. P. Parlevliet, H. E. Bersee and A. Beukers, "Residual stresses in thermoplastic compositesâ€"A study of the literatureâ€"Part I: Formation of residual stresses," *Composites Part A: Applied Science and Manufacturing* , vol. 37, no. 11, pp. 1847-1857, 2006.

[35] P. Sunderland, W. Yu and J.-A. MÃ¥nson, "A thermoviscoelastic analysis of process-induced internal stresses in thermoplastic matrix composites," *Polymer Composites,* vol. 22, no. 5, pp. 579-592, 2001.

[36] C. E. Duty, T. Drye and A. Franc, "Material Development for Tooling Applications Using Big Area Additive Manufacturing (BAAM)," 2015.

[37] C. E. Duty, V. Kunc, B. Compton, B. Post, D. Erdman, R. Smith, R. Lind, P. Lloyd and L. Love, "Structure and mechanical behavior of Big Area Additive Manufacturing (BAAM) materials," *Rapid Prototyping Journal,* vol. 23, pp. 181-189, 2017.

[38] C. Hill, K. Rowe, R. Bedsole, J. Earle and V. Kunc, "Materials and Process Development for Direct Digital Manufacturing of Vehicles," in *SAMPE Long Beach 2016 Conference and Exhibition,* 2016.

[39] C. Hill, R. Bedsole, C. Duty, V. Kunc, K. Rowe, D. Riha and C. Ajinjeru, "Big Area Additive Manufacturing (BAAM) Materials Development and Reinforcement with Advanced Composites," 2018.

[40] B. Brenken, E. Barocio, A. Favaloro, V. Kunc and R. B. Pipes, "Fused filament fabrication of fiber-reinforced polymers: A review," *Additive Manufacturing,* vol. 21, pp. 1-16, 2018.

[41] J. M. Gardner, G. Sauti, J.-W. Kim, R. J. Cano, R. A. Wincheski, C. J. Stelter, B. W. Grimsley, D. C. Working and E. J. Siochi, "Additive Manufacturing of Multifunctional Components Using High Density Carbon Nanotube Yarn Filaments," 2016.

[42] B. G. Compton and J. A. Lewis, "3D-Printing of Lightweight Cellular Composites," *Advanced Materials,* vol. 26, pp. 5930-5935, 2014.

[43] C. Mahajan and D. Cormier, "3D printing of carbon fiber composites with preferentially aligned fibers," in *IIE Annual Conference. Proceedings,* 2015.

[44] M. Spoerk, C. Savandaiah, F. Arbeiter, G. Traxler, L. Cardon, C. Holzer and J. Sapkota, "Anisotropic properties of oriented short carbon fibre filled polypropylene parts fabricated by extrusion-based additive manufacturing," *Composites Part A: Applied Science and Manufacturing,* vol. 113, pp. 95-104, 2018.

[45] I. Ferreira, D. Vale, M. Machado and J. Lino, "Additive manufacturing of polyethylene terephthalate glycol/carbon fiber composites: An experimental study from filament to printed parts," *Proceedings of the Institution of Mechanical Engineers, Part L: Journal of Materials: Design and Applications*, p. 1464420718795197, 2018.

[46] R. Matsuzaki, M. Ueda, M. Namiki, T.-K. Jeong, H. Asahara, K. Horiguchi, T. Nakamura, A. Todoroki and Y. Hirano, "Three-dimensional printing of continuous-fiber composites by in-nozzle impregnation," *Scientific reports*, vol. 6, p. 23058, 2016.

[47] N. Li, Y. Li and S. Liu, "Rapid prototyping of continuous carbon fiber reinforced polylactic acid composites by 3D printing," *Journal of Materials Processing Technology*, vol. 238, pp. 218-225, 2016.

[48] X. Tian, T. Liu, Q. Wang, A. Dilmurat, D. Li and G. Ziegmann, "Recycling and remanufacturing of 3D printed continuous carbon fiber reinforced PLA composites," *Journal of Cleaner Production*, vol. 142, pp. 1609-1618, 2017.

[49] P. Bettini, G. Alitta, G. Sala and L. Di Landro, "Fused Deposition Technique for Continuous Fiber Reinforced Thermoplastic," *Journal of Materials Engineering and Performance*, vol. 26, pp. 843-848, Feb 2017.

[50] C. Yang, X. Tian, T. Liu, Y. Cao and D. Li, "3D printing for continuous fiber reinforced thermoplastic composites: mechanism and performance," *Rapid Prototyping Journal*, vol. 23, pp. 209-215, 2017.

[51] W. Hao, Y. Liu, H. Zhou, H. Chen and D. Fang, "Preparation and characterization of 3D printed continuous carbon fiber reinforced thermosetting composites," *Polymer Testing*, vol. 65, pp. 29-34, 2018.

[52] T. Liu, X. Tian, M. Zhang, D. Abliz, D. Li and G. Ziegmann, "Interfacial performance and fracture patterns of 3D printed continuous carbon fiber with sizing reinforced PA6 composites," *Composites Part A: Applied Science and Manufacturing*, vol. 114, pp. 368-376, 2018.

[53] "Markforged," [Online]. Available: https://markforged.com/. [Accessed 11 October 2018].

[54] G. D. Goh, V. Dikshit, A. P. Nagalingam, G. L. Goh, S. Agarwala, S. L. Sing, J. Wei and W. Y. Yeong, "Characterization of mechanical properties and fracture mode of additively manufactured carbon fiber and glass fiber reinforced thermoplastics," *Materials \& Design,* vol. 137, pp. 79-89, 2018.

[55] O. A. González-Estrada, A. Pertuz and Q. a. J. E. Mendez, "Evaluation of Tensile Properties and Damage of Continuous Fibre Reinforced 3D-Printed Parts," in *Key Engineering Materials*, 2018.

[56] A. N. Dickson, J. N. Barry, K. A. McDonnell and D. P. Dowling, "Fabrication of continuous carbon, glass and Kevlar fibre reinforced polymer composites using additive manufacturing," *Additive Manufacturing,* vol. 16, pp. 146-152, 2017.

[57] F. Van Der Klift, Y. Koga, A. Todoroki, M. Ueda, Y. Hirano and R. Matsuzaki, "3D printing of continuous carbon fibre reinforced thermo-plastic (CFRTP) tensile test specimens," *Open Journal of Composite Materials,* vol. 6, p. 18, 2015.

[58] L. G. Blok, M. L. Longana, H. Yu and B. K. S. Woods, "An investigation into 3D printing of fibre reinforced thermoplastic composites," *Additive Manufacturing,* vol. 22, pp. 176-186, 2018.

[59] G. W. Melenka, B. K. O. Cheung, J. S. Schofield, M. R. Dawson and J. P. Carey, "Evaluation and prediction of the tensile properties of continuous fiber-reinforced 3D printed structures," *Composite Structures,* vol. 153, pp. 866-875, 2016.

[60] Markforged, "Markforged - Material Specifications Composites," [Online]. Available: https://static.markforged.com/markforged_composites_datasheet.pdf. [Accessed 11 October 2018].

[61] M. A. Yardimci and S. GÃ¼Ã§eri, "Conceptual framework for the thermal process modelling of fused deposition," *Rapid Prototyping Journal,* vol. 2, no. 2, pp. 26-31, 1996.

[62] M. A. Yardimci, S. I. Guceri, M. Agarwala and S. C. Danforth, "Part quality prediction tools for fused deposition processing," in *Proceedings of the Solid Freeform Fabrication Symposium, Austin, TX*, 1996.

[63] J. Thomas and J. Rodriguez, "Modeling the fracture strength between fused deposition extruded roads," in *Proceedings of the 11th Solid Freeform Fabrication Symposium*, 2000.

[64] L. Li, Q. Sun, C. Bellehumeur and P. Gu, "Investigation of bond formation in FDM process," in *Solid Freeform Fabrication Symp., Austin, TX*, 2002.

[65] C. Bellehumeur, L. Li, Q. Sun and P. Gu, "Modeling of Bond Formation Between Polymer Filaments in the Fused Deposition Modeling Process," *Journal of Manufacturing Processes* , vol. 6, no. 2, pp. 170-178, 2004.

[66] Q. Sun, G. Rizvi, C. Bellehumeur and P. Gu, "Effect of processing conditions on the bonding quality of FDM polymer filaments," *Rapid Prototyping Journal,* vol. 14, no. 2, pp. 72-80, 2008.

[67] S. F. Costa, F. M. Duarte and J. A. Covas, "Towards modelling of Free Form Extrusion: analytical solution of transient heat transfer," *International Journal of Material Forming,* vol. 1, no. 1, pp. 703-706, Apr 2008.

[68] S. Costa, F. Duarte and J. Covas, "Thermal conditions affecting heat transfer in FDM/FFE: a contribution towards the numerical modelling of the process," *Virtual and Physical Prototyping,* vol. 10, no. 1, pp. 35-46, 2015.

[69] B. G. Compton, B. K. Post, C. E. Duty, L. Love and V. Kunc, "Thermal analysis of additive manufacturing of large-scale thermoplastic polymer composites," *Additive Manufacturing,* vol. 17, pp. 77-86, 2017.

[70] K. Pooladvand and C. Furlong, "Thermo-mechanical Investigation of Fused Deposition Modeling by Computational and Experimental Methods," in *Mechanics of Composite and Multi-functional Materials, Volume 7,* Cham, 2017.

[71] J. Yin, C. Lu, J. Fu, Y. Huang and Y. Zheng, "Interfacial bonding during multi-material fused deposition modeling (FDM) process due to inter-molecular diffusion," *Materials \& Design,* vol. 150, pp. 104-112, 2018.

[72] B. Brenken, E. Barocio, A. J. Favaloro and R. B. Pipes, "Simulation of Semi-Crystalline Composites in the Extrusion Deposition Additive Manufacturing Process," in *Science in the Age of Experience*, 2017.

[73] A. J. Favaloro, B. Brenken, E. Barocio and R. B. Pipes, "Simulation of Polymeric Composites Additive Manufacturing using Abaqus," in *Science in the Age of Experience*, 2017.

[74] A. Cattenone, S. Morganti, G. Alaimo and F. Auricchio, "Finite element analysis of Additive Manufacturing based on Fused Deposition Modeling (FDM): distortion prediction and comparison with experimental data.," *Journal of Manufacturing Science and Engineering*, 2018.

[75] C. T. Bellehumeur, M. Kontopoulou and J. Vlachopoulos, "The role of viscoelasticity in polymer sintering," *Rheologica Acta*, vol. 37, no. 3, pp. 270-278, 1998.

[76] O. Pokluda, C. T. Bellehumeur and J. Vlachopoulos, "Modification of Frenkel's model for sintering," *AIChE journal*, vol. 43, no. 12, pp. 3253-3256, 1997.

[77] P. K. Gurrala and S. P. Regalla, "Part strength evolution with bonding between filaments in fused deposition modelling," *Virtual and Physical Prototyping*, vol. 9, no. 3, pp. 141-149, 2014.

[78] Y. Zhang and Y. K. Chou, "3D FEA simulations of fused deposition modeling process," in *ASME 2006 International Manufacturing Science and Engineering Conference*, 2006.

[79] Y. Zhang and K. Chou, "A parametric study of part distortions in fused deposition modelling using three-dimensional finite element analysis," *Proceedings of the Institution of Mechanical Engineers, Part B: Journal of Engineering Manufacture*, vol. 222, pp. 959-968, 2008.

[80] M. R. Talagani, S. DorMohammadi, R. Dutton, C. Godines, H. Baid, F. Abdi, V. Kunc, B. Compton, S. Simunovic, C. Duty and others, "Numerical simulation of big area additive manufacturing (3D printing) of a full size car," *SAMPE Journal*, vol. 51, pp. 27-36, 2015.

[81] B. Brenken, A. Favaloro, E. Barocio, V. Kunc and R. B. Pipes, "Thermoviscoelasticity in Extrusion Deposition Additive Manufacturing Process Simulations," in *Proceedings of the American Society for Composites—Thirty-second Technical Conference*, 2017.

[82] M. Ramirez, S. G. Kravchenki, J. Ramirez, E. Barocio and R. B. Pipes, "Computational Damage Modeling of Additively Manufactured Short Fiber Composite Material," in *Science in the Age of Experience*, 2018.

[83] M. A. Ramirez, S. G. Kravchenko, J. A. Ramirez, E. E. Barocio and R. Byron, "Virtual Tensile Testing of Additively Manufactured Short Fiber Composite With Stochastic Morphology," in *SAMPE*, 2018.

[84] "TA Instruments - DMA Q800 Specifications," [Online]. Available: http://www.tainstruments.com/wp-content/uploads/dma.pdf. [Accessed 14 October 2018].

[85] "TA Instruments - DSC Q2000 Specifications," [Online]. Available: http://www.tainstruments.com/pdf/brochure/2012%20DSC%20Brochure%20r1.pdf. [Accessed 14 October 2018].

[86] V. Kunc, J. Lindah, R. B. Dinwiddie, B. K. Post, L. J. Love, C. Duty, M. Matlack, R. Fahey Jr and A. A. Hassen, "Investigation of In-autoclave Additive Manufacturing Composite Tooling," in *CAMX Conference, Anaheim, CA*, 2016.

[87] T. Z. Sudbury, R. Springfield, V. Kunc and C. Duty, "An assessment of additive manufactured molds for hand-laid fiber reinforced composites," *The International Journal of Advanced Manufacturing Technology*, pp. 1-6, 2016.

[88] E. Barocio, B. Brenken, A. J. Favaloro and R. B. Pipes, "Extrusion Additive Manufacturing of Composite Molds for High-Temperature Applications," in *SAMPE*, Seatle. WA., 2017.

[89] "Kflop," Dynomotion, [Online]. Available: https://dynomotion.com/KFLOP.html. [Accessed 17 October 2018].

[90] Dynomotion, "On-Line Help," 2014 8 2018. [Online]. Available: http://www.dynomotion.com/Help/index.htm. [Accessed 17 October 2018].

[91] C. Rauwendaal, "Polymer Extrusion," in *Polymer Extrusion (Fifth Edition)*, Fifth Edition ed., C. Rauwendaal, Ed., Hanser, 2014, pp. I - XVI.

[92] M. Rubinstein and R. H. Colby, Polymer physics, vol. 23, Oxford University Press New York, 2003.

[93] K. Ogata, Modern control engineering, vol. 1, Prentice hall, 2002.

[94] K. J. Åström and B. Wittenmark, Adaptive control, Courier Corporation, 2013.

[95] R. N. Haward, "Compressibility of polymers," *Journal of Polymer Science Part A-2: Polymer Physics*, vol. 7, pp. 219-229.

[96] "Sure Servo - AM Servo Systems User Manual," [Online]. Available: https://cdn.automationdirect.com/static/manuals/sureservomanual/sureservomanual.html. [Accessed 25 October 2018].

[97] N. I. "NI 6363 Device Specifications," 2016. [Online]. Available: http://www.ni.com/pdf/manuals/374651d.pdf. [Accessed 25 October 2018].

[98] N. I. "Datasheet NI 9214 and TB-9214," March 2016. [Online]. Available: http://www.ni.com/pdf/manuals/375138a_02.pdf. [Accessed 25 October 2018].

[99] L. "Implementing the PID Algorithm with the PID VIs," LabVIEW, 2017.

[100] N. I. C. "LabWindows/CVI," March 2016. [Online]. Available: http://www.ni.com/pdf/manuals/371685b.pdf. [Accessed 27 October 2018].

[101] D. S. "Simulia User Assistance 2017," 2018. [Online]. Available: https://help.3ds.com/2017/english/DSSIMULIA_Established/SIMULIA_Established_FrontmatterMap/SIMULIA_EstablishedDocSearchOnline.htm?ContextScope=all. [Accessed 28 October 2018].

[102] E. Barocio, B. Brenken, A. J. Favaloro, M. Ramirez, J. Ramirez and R. B. Pipes, "Prediction of the Degree of Bonding in the Extrusion Deposition Additive Manufacturing Process of Semi-Crystalline Polymer Composites," in *Science in the Age of Experience*, 2018.

[103] D. W. Hahn and M. N. Özisjk, Heat conduction, John Wiley & Sons, 2012.

[104] O. Rique, E. Barocio and W. Yu, "Experimental and Numerical Determination of the Thermal Conductivity Tensor for Composites Manufacturing Simulation," in *Proceedings of the American Society for Composites—Thirty-second Technical Conference*, 2017.

[105] J. Aboudi, "Effective thermoelastic constants of short-fiber composites," *Fibre Science and Technology*, vol. 20, pp. 211-225, 1984.

[106] A. S. T. M. Standard, *E1461, 2007,"Standard Test Method for Thermal Diffusivity by the Flash Method," ASTM International, West Conshohocken, PA.*

[107] R. Larsen, "Themophysical Properties of One Sample - TPRL 5533," Thermophysical Properties Research Laboratory, INC., West Lafayette, IN, 2017.

[108] A. S. T. M. Standard, *E1269, 2005,"Standard Test Method for Determining Specific Heat Capacity by Differential Scanning Calorimetry," ASTM International, West Conshohocken, PA.*

[109] J. E. Spruiell, "A review of the measurement and development of crystallinity and its relation to properties in meat polyphenylene sulfide and its fiber reinforced composites.," 2005.

[110] G. Reiter and G. R. Strobl, Progress in understanding of polymer crystallization @Bookreiter2007progress, Title = Progress in understanding of polymer crystallization, Author = Reiter, Günter and Strobl, Gert R, Publisher = Springer, Year = 2007, Volume = 714, File = :2007_Reiter,Strobl__Progress-in-Understanding-of-polymer-crystalliz.pdf:PDF @Bookreiter2007progress, Title = Progress in understanding of polymer crystallization, Author = Reiter, Günter and Strobl, Gert R, Publisher = Springer, Year = 2007, Volume = 714, File = :2007_Reiter,Strobl__Progress-in-Understanding-of-polymer-crystalliz.pdf:PDF, vol. 714, Springer, 2007.

[111] J. M. Kenny and A. Maffezzoli, "Crystallization kinetics of poly (phenylene sulfide)(PPS) and PPS/carbon fiber composites," *Polymer Engineering \& Science*, vol. 31, pp. 607-614, 1991.

[112] C. N. Velisaris and J. C. Seferis, "Crystallization kinetics of polyetheretherketone (peek) matrices," *Polymer Engineering \& Science*, vol. 26, pp. 1574-1581, 1986.

[113] L. M. Jiji and L. M. Jiji, Heat convection, Springer, 2006.

[114] S. Costa, F. Duarte and J. A. Covas, "Using MATLAB to compute heat transfer in free form extrusion," in *MATLAB-A Ubiquitous Tool for the Practical Engineer*, InTech, 2011.

[115] W. Churchill S. and R. Usagi, "A general expression for the correlation of rates of transfer and other phenomena," *AIChE Journal*, vol. 18, pp. 1121-1128.

[116] S. W. Churchill, "A comprehensive correlating equation for laminar, assisting, forced and free convection," *AIChE Journal*, vol. 23, pp. 10-16, 1 1977.

[117] S. W. Churchill and H. H. S. Chu, "Correlating equations for laminar and turbulent free convection from a vertical plate," *International Journal of Heat and Mass Transfer*, vol. 18, pp. 1323-1329, 1975.

[118] S. W. Churchill and R. U. Churchill, "A comprehensive correlating equation for heat and component transfer by free convection," *AIChE Journal,* vol. 21, pp. 604-606, 5 1975.

[119] G. C. Vliet, "Natural convection local heat transfer on constant-heat-flux inclined surfaces," *Journal of Heat Transfer,* vol. 91, pp. 511-516, 1969.

[120] T. Y. Na, "Numerical solution of natural convection flow past a non-isothermal vertical flat plate," *Applied Scientific Research,* vol. 33, pp. 519-543, Dec 1977.

[121] R. Goldstein, E. Sparrow and D. Jones, "Natural convection mass transfer adjacent to horizontal plates," *International Journal of Heat and Mass Transfer,* vol. 16, no. 5, pp. 1025-1035, 1973.

[122] J. Lloyd and W. Moran, "Natural convection adjacent to horizontal surface of various planforms," *Journal of Heat Transfer,* vol. 96, no. 4, pp. 443-447, 1974.

[123] K. Kitamura, A. Mitsuishi, T. Suzuki and F. Kimura, "Fluid flow and heat transfer of natural convection adjacent to upward-facing, rectangular plates of arbitrary aspect ratios," *International Journal of Heat and Mass Transfer,* vol. 89, pp. 320-332, 2015.

[124] W. M. Lewandowski, E. Radziemska, M. Buzuk and H. Bieszk, "Free convection heat transfer and fluid flow above horizontal rectangular plates," *Applied Energy,* vol. 66, no. 2, pp. 177-197, 2000.

[125] M. Prakash, S. Kedare and J. Nayak, "Numerical study of natural convection loss from open cavities," *International Journal of Thermal Sciences,* vol. 51, pp. 23-30, 2012.

[126] E. Bilgen and H. Oztop, "Natural convection heat transfer in partially open inclined square cavities," *International Journal of Heat and Mass Transfer,* vol. 48, no. 8, pp. 1470-1479, 2005.

[127] A. A. Mohamad, "Natural convection in open cavities and slots," *Numerical Heat Transfer, Part A: Applications,* vol. 27, no. 6, pp. 705-716, 1995.

[128] E. Bilgen and A. Muftuoglu, "Natural convection in an open square cavity with slots," *International Communications in Heat and Mass Transfer,* vol. 35, no. 8, pp. 896-900, 2008.

[129] M. M. Gonzalez, J. H. Palafox and C. A. Estrada, "Numerical study of heat transfer by natural convection and surface thermal radiation in an open cavity receiver," *Solar Energy*, vol. 86, no. 4, pp. 1118-1128, 2012.

[130] A. "Ansys Documentation - Release 16.2".

[131] J. N. Reddy, An introduction to continuum mechanics, Cambridge university press, 2013.

[132] "Engineering ToolBox," 2001. [Online]. Available: https://www.engineeringtoolbox.com/index.html. [Accessed 10 October 2018].

[133] "ResearchIR 4 - User's Guide," FLIR Systems, Inc., 2016.

[134] W. Minkina and S. Dudzik, Infrared thermography: errors and uncertainties, John Wiley \& Sons, 2009.

[135] J. Goldak, A. Chakravarti and M. Bibby, "A new finite element model for welding heat sources," *Metallurgical Transactions B*, vol. 15, pp. 299-305, Jun 1984.

[136] "Abaqus Online Documentation Server," Dassault Systemes, 2017. [Online]. Available: http://50.16.225.63/. [Accessed 15 February 2018].

[137] E. Barocio, B. Brenken, A. Favaloro, J. Ramirez, V. Kunc and R. B. Pipes, "Fusion Bonding Simulations of Semi-Crystalline Polymer Composites in the Extrusion Deposition Additive Manufacturing Process," in *Proceedings of the American Society for Composites—Thirty-second Technical Conference*, 2017.

[138] R. P. Wool and K. M. Oâ€™Connor, "A theory crack healing in polymers," *Journal of Applied Physics*, vol. 52, no. 10, pp. 5953-5963, 1981.

[139] J.-E. Zanetto, C. J. G. Plummer, P.-E. Bourban and J.-A. E. Månson, "Fusion bonding of polyamide 12," *Polymer Engineering \& Science*, vol. 41, no. 5, pp. 890-897, 2001.

[140] P.-E. Bourban, N. Bernet, J.-E. Zanetto and J.-A. E. Månson, "Material phenomena controlling rapid processing of thermoplastic composites," *Composites Part A: Applied Science and Manufacturing*, vol. 32, no. 8, pp. 1045-1057, 2001.

[141] R. H. Somani, B. S. Hsiao, A. Nogales, S. Srinivas, A. H. Tsou, I. Sics, F. J. Balta-Calleja and T. A. Ezquerra, "Structure Development during Shear Flow-Induced Crystallization of i-PP: In-Situ Small-Angle X-ray Scattering Study," *Macromolecules*, vol. 33, no. 25, pp. 9385-9394, 2000.

[142] H. An, B. Zhao, Z. Ma, C. Shao, X. Wang, Y. Fang, L. Li and Z. Li, "Shear-induced conformational ordering in the melt of isotactic polypropylene," *Macromolecules,* vol. 40, no. 14, pp. 4740-4743, 2007.

[143] P. De Gennes and L. Leger, "Dynamics of entangled polymer chains," *Annual Review of Physical Chemistry,* vol. 33, no. 1, pp. 49-61, 1982.

[144] S. Prager and M. Tirrell, "The healing process at polymer–polymer interfaces," *The Journal of Chemical Physics,* vol. 75, no. 10, pp. 5194-5198, 1981.

[145] K. Jud, H. H. Kausch and J. G. Williams, "Fracture mechanics studies of crack healing and welding of polymers," *Journal of Materials Science,* vol. 16, no. 1, pp. 204-210, 1981.

[146] P. Dara and A. Loos, "Thermoplastic Matrix Composite Processing Model, Virginia Polytechnic Institute," 1985.

[147] M. Tirrell, "Polymer Self-Diffusion in Entangled Systems," *Rubber Chemistry and Technology,* vol. 57, no. 3, pp. 523-556, 1984.

[148] K. Jud and H. H. Kausch, "Load transfer through chain molecules after interpenetration at interfaces," *Polymer Bulletin,* vol. 1, no. 10, pp. 697-707, 1979.

[149] F. Yang and R. Pitchumani, "Nonisothermal healing and interlaminar bond strength evolution during thermoplastic matrix composites processing," *Polymer Composites,* vol. 24, no. 2, pp. 263-278, 2003.

[150] S. C. Mantell and G. S. Springer, "Manufacturing Process Models for Thermoplastic Composites," *Journal of Composite Materials,* vol. 26, no. 16, pp. 2348-2377, 1992.

[151] A. C. Loos and M.-C. Li, "Non-Isothermal Autohesion Model for Amorphous Thermoplastic Composites," *Journal of Thermoplastic Composite Materials,* vol. 7, no. 4, pp. 280-310, 1994.

[152] J. Schell, J. Guilleminot, C. Binetruy and P. Krawczak, "Computational and experimental analysis of fusion bonding in thermoplastic composites: Influence of process parameters," *Journal of Materials Processing Technology,* vol. 209, no. 11, pp. 5211-5219, 2009.

[153] R. P. Wool, Polymer interfaces: structure and strength, Hanser, 1995.

[154] G. D. Smith, C. J. Plummer, P.-E. Bourban and J.-A. E. Månson, "Non-isothermal fusion bonding of polypropylene," *Polymer* , vol. 42, no. 14, pp. 6247-6257, 2001.

[155] C. J. G. Plummer, P.-E. Bourban, J.-E. Zanetto, G. D. Smith and J.-A. E. MÃ¥nson, "Nonisothermal fusion bonding in semicrystalline thermoplastics," *Journal of Applied Polymer Science,* vol. 87, no. 8, pp. 1267-1276, 2003.

[156] R. J. Young and P. A. Lovell, Introduction to polymers, CRC press, 2011.

[157] ASTM, *ASTM D5528 - Standard Test Method for Mode I Interlaminar Fracture Toughness of Unidirectional Fiber-Reinforced Polymer Matrix Composites*, 2013.

[158] L. A. Carlsson, D. F. Adams and R. B. Pipes, Experimental characterization of advanced composite materials, CRC press, 2014.

[159] E. Barocio, R. B. Pipes, B. Brenken, A. J. Favaloro and N. M. DeNardo, *Methods and apparatus for embedding heating circuits into articles made by additive manufacturing and articles made therefrom*, Google Patents, 2018.

[160] G. T. Mark and A. S. Gozdz, "Apparatus for fiber reinforced additive manufacturing". USA Patent US20140328963A1, 22 March 2013.

[161] G. T. Mark and A. S. Gozdz, "Methods for composite filament fabrication in three dimensional printing". USA Patent US9126365B1, 22 March 2013.

[162] G. T. Mark and A. S. Gozdz, "Three dimensional printer for fiber reinforced composite filament fabrication". USA Patent US9126367B1, 22 March 2013.

[163] D. Espalin, D. Marquez, A. Fernandez, C. Kim, E. MacDonald and R. Wicker, "Method and apparatus for wire handling and embedding on and within 3d printed parts". USA Patent US20170064840A1, 24 August 2015.

[164] R. B. Wicker, F. Medina, E. MacDonald, D. W. Muse and D. Espalin, "Methods and Systems For Embedding Filaments in 3D Structures, Structural Components, and Structural Electronic, Electromagnetic and Electromechanical Components/Devices". USA Patent US20140268604A1, 14 March 2013.

[165] F. N. Cogswell, "Patents by Inventor Frederic N. Cogswell," Patents from multiple years. [Online]. Available: https://patents.justia.com/inventor/frederic-n-cogswell. [Accessed 25 January 2018].

[166] "Simulia User Assistance 2017," Dassault Systemes, [Online]. Available: http://50.16.225.63/. [Accessed 18 January 2018].

[167] S.-Y. Fu, B. Lauke, E. Mäder, C.-Y. Yue and X. Hu, "Tensile properties of short-glass-fiber-and short-carbon-fiber-reinforced polypropylene composites," *Composites Part A: Applied Science and Manufacturing*, vol. 31, pp. 1117-1125, 2000.

[168] T. King, D. Blackketter, D. Walrath and D. Adams, "Micromechanics Prediction of the Shear Strength of Carbon Fiber/Epoxy Matrix Composites: The Influence of the Matrix and Interface Strengths," *Journal of Composite Materials*, vol. 26, no. 4, pp. 558-573, 1992.

[169] F. Ning, W. Cong, J. Qiu, J. Wei and S. Wang, "Additive manufacturing of carbon fiber reinforced thermoplastic composites using fused deposition modeling," *Composites Part B: Engineering*, vol. 80, pp. 369-378, 2015.

[170] M. L. Shofner, K. Lozano, F. J. RodrÃguez-MacÃas and E. V. Barrera, "Nanofiber-reinforced polymers prepared by fused deposition modeling," *Journal of Applied Polymer Science*, vol. 89, pp. 3081-3090, 2003.

[171] M. L. Shofner, F. J. Rodríguez-Macías, R. Vaidyanathan and E. V. Barrera, "Single wall nanotube and vapor grown carbon fiber reinforced polymers processed by extrusion freeform fabrication," *Composites Part A: Applied Science and Manufacturing*, vol. 34, pp. 1207-1217, 2003.

[172] A. R. T. Perez, D. A. Roberson and R. B. Wicker, "Fracture surface analysis of 3D-printed tensile specimens of novel ABS-based materials," *Journal of Failure Analysis and Prevention*, vol. 14, pp. 343-353, 2014.